

THE MINISTRY OF SCIENCE AND HIGHER EDUCATION OF THE RUSSIAN FEDERATION



ST. PETERSBURG STATE  
POLYTECHNICAL UNIVERSITY  
**JOURNAL**

---

---

Physics  
and Mathematics

---

---

**VOLUME 15, No.3.2,  
2022**

Peter the Great St. Petersburg  
Polytechnic University  
2022

# ST. PETERSBURG STATE POLYTECHNICAL UNIVERSITY JOURNAL. PHYSICS AND MATHEMATICS

## JOURNAL EDITORIAL COUNCIL

*A.I. Borovkov* – vice-rector for perspective projects;  
*V.A. Glukhikh* – full member of RAS;  
*D.A. Indeitsev* – corresponding member of RAS;  
*V.A.I. Rudskoy* – full member of RAS;  
*R.A. Suris* – full member of RAS;  
*A.E. Zhukov* – corresponding member of RAS.

## JOURNAL EDITORIAL BOARD

*V.K. Ivanov* – Dr. Sci. (phys.-math.), prof., SPbPU, St. Petersburg, Russia, – editor-in-chief;  
*A.E. Fotiadi* – Dr. Sci. (phys.-math.), prof., SPbPU, St. Petersburg, Russia, – deputy editor-in-chief;  
*V.M. Kapralova* – Candidate of Phys.-Math. Sci., associate prof., SPbPU, St. Petersburg, Russia, – executive secretary;  
*V.I. Antonov* – Dr. Sci. (phys.-math.), prof., SPbPU, St. Petersburg, Russia;  
*I.B. Bezprozvanny* – Dr. Sci. (biology), prof., The University of Texas Southwestern Medical Center, Dallas, TX, USA;  
*A.V. Blinov* – Dr. Sci. (phys.-math.), prof., SPbPU, St. Petersburg, Russia;  
*A.S. Cherepanov* – Dr. Sci. (phys.-math.), prof., SPbPU, St. Petersburg, Russia;  
*D.V. Donetski* – Dr. Sci. (phys.-math.), prof., State University of New York at Stony Brook, NY, USA;  
*V.V. Dubov* – Dr. Sci. (phys.-math.), prof., SPbPU, St. Petersburg, Russia;  
*D.A. Firsov* – Dr. Sci. (phys.-math.), prof., SPbPU, St. Petersburg, Russia;  
*P.A. Karasev* – Dr. Sci. (phys.-math.), prof., SPbPU, St. Petersburg, Russia;  
*A.S. Kheifets* – Ph.D., prof., Australian National University, Canberra, Australia;  
*O.S. Loboda* – Candidate of Phys.-Math. Sci., associate prof., SPbPU, St. Petersburg, Russia;  
*J.B. Malherbe* – Dr. Sci. (physics), prof., University of Pretoria, Republic of South Africa;  
*V.M. Ostryakov* – Dr. Sci. (phys.-math.), prof., SPbPU, St. Petersburg, Russia;  
*V.E. Privalov* – Dr. Sci. (phys.-math.), prof., SPbPU, St. Petersburg, Russia;  
*E.M. Smirnov* – Dr. Sci. (phys.-math.), prof., SPbPU, St. Petersburg, Russia;  
*A.V. Solov'yov* – Dr. Sci. (phys.-math.), prof., MBN Research Center, Frankfurt am Main, Germany;  
*A.K. Tagantsev* – Dr. Sci. (phys.-math.), prof., Swiss Federal Institute of Technology, Lausanne, Switzerland;  
*I.N. Toptygin* – Dr. Sci. (phys.-math.), prof., SPbPU, St. Petersburg, Russia;

The journal is included in the List of leading peer-reviewed scientific journals and other editions to publish major findings of theses for the research degrees of Doctor of Sciences and Candidate of Sciences.

The publications are presented in the VINITI RAS Abstract Journal and Ulrich's Periodical Directory International Database.

The journal is published since 2008 as part of the periodical edition 'Nauchno-tekhnicheskie vedomosti SPb-GPU'.

The journal is registered with the Federal Service for Supervision in the Sphere of Telecom, Information Technologies and Mass Communications (ROSKOMNADZOR). Certificate ПИ № ФС77-52144 issued December 11, 2012.

The journal is distributed through the CIS countries catalogue, the «Press of Russia» joint catalogue and the «Press by subscription» Internet catalogue. The subscription index is 71823.

The journal is in the **Web of Science** (Emerging Sources Citation Index), **Scopus**, the **Russian Science Citation Index** (RSCI) and the **Directory of Open Access Journals** (DOAJ) databases.

© Scientific Electronic Library (<http://www.elibrary.ru>).

No part of this publication may be reproduced without clear reference to the source.

The views of the authors may not represent the views of the Editorial Board.

Address: 195251 Politekhnicheskaya St. 29, St. Petersburg, Russia.

Phone: (812) 294-22-85.

<http://ntv.spbstu.ru/physics>

© Peter the Great St. Petersburg Polytechnic University, 2022

## PREFACE



### 9-я Международная школа-конференция по оптоэлектронике, фотонике, инженерии и наноструктурам / 9th International School and Conference on Optoelectronics, Photonics, Engineering and Nanostructures (SPb OPEN – 2022)

The 9th International School and Conference on Optoelectronics, Photonics, Engineering and Nanostructures (SPb OPEN–2022) was held on May 24–27, 2022. It continues the annual schools and seminars on physics and technology of nanostructures for young scientists, organized by Zhores Alferov since 2009.

The School was organized by the St. Petersburg Higher School of Economics, Peter the Great St. Petersburg Polytechnic University and the Alferov University with the support of the Russian Science Foundation, Photonics magazine, NT-MDT LLC, Azimut Photonics LLC. In contrast to last year, the conference was run fully in-person.

The conference was attended by 301 people, including 60 young Russian scientists, 94 graduate and 123 undergraduate students. The average age of the attendees was just under 27 years. Presentations were given in six panels:

- Synthesis and structural properties of semiconductor materials and nanostructures
- Lasers, solar cells, other optoelectronic devices
- Nanophotonics, spectroscopy, microresonators, optical properties, plasmonics
- Biophysics, nanobiotechnology, biophotonics
- Electrical, magnetic and microwave characteristics and devices
- Other aspects of nanotechnology

In addition to poster presentations from young scientists, the program included a series of keynote speeches by prominent researchers, outlining the main advances and challenges in various fields of physics and technology.

The keynote speakers included:

- Vladimir Belotelov, M. V. Lomonosov Moscow State University/Vernadsky Crimean Federal University
- Igor Bilenko, M. V. Lomonosov Moscow State University/Russian Quantum Center
- Andrey Bogdanov, ITMO University
- Valentina Zhurikhina, Peter the Great St. Petersburg Polytechnic University
- Natalia Kryzhanovskaya, HSE St. Petersburg
- Maxim Solodovnik, Southern Federal University
- Georgy Tsyrlin, Alferov University
- Alexey Shpilman, Gazprom Neft PJSC/HSE
- Yong Wang, Laser Institute, Jinan, China.





The conference proceedings are to be published in *St. Petersburg State Polytechnical University Journal: Physics and Mathematics*. The Program Committee of SPbOPEN-2022 hopes that the range of subjects presented at the conference will be of interest to the journal's audience. We would like to thank the journal for giving us the opportunity to publish the proceedings, and thank the reviewers for useful recommendations and constructive criticism. We express our gratitude to all participants of the conference.

We invite young scientists, graduate and undergraduate students to take part in the next School and Conference in 2023. Please visit <https://spb.hse.ru/spbopen/> for more details.

**A. E. Zhukov**

National Research University Higher School of Economics,  
St. Petersburg  
aezhukov@hse.ru



# Contents

## Condensed matter physics

<b>Kondratev V.M., Vyacheslavova E.A., Morozov I.A., Nalimova S.S., Moshnikov V.A., Gudovskikh A.S. Bolshakov A.D. Study of quasi 1-D silicon nanostructures adsorption properties.....</b>	10
<b>Kadinskaya S.A., Kondratev V.M., Kindyushov I.K., Kusnetsov A., Lihachev A.I., Naschekin A.V. Bolshakov A.D. Study of hydrothermal zinc oxide nanostructures photovoltaic properties.....</b>	16
<b>Arteev D.S., Sakharov A.V., Nikolaev A.E., Zavarin E.E., Tsatsulnikov A.F., Ustinov V.M. Optimization of InGaN-based luminescent heterostructures by genetic algorithm .....</b>	21
<b>Moiseev E.I., Kryzhanovskaya N.V., Zubov F.I., Nahorny A.V., Urmanov B.D., Fominykh N.A., Ivanov K.A., Mintairov S.A., Kalyuzhnyy N.A., Kulagina M.M., Maximov, M., Zhukov A. E. Investigation of far-field patterns of semiconductor microlasers with an active region based on InGaAs/GaAs quantum well-dots .....</b>	25
<b>Shkoldin V.A., Lebedev D.V., Permyakov D.V., Petukhov A.E., Golubok A.O., Arkhipov A.V., Samusev A.K. Mukhin I.S. Ultra-high vacuum formation of silver films for light-emitting tunnel junctions...</b>	31
<b>Soldatenkova M.D., Baeva E.M., Triznova A.D., Titova N.A., Zolotov P.I., Kolbatova A.I., Goltsman G.N. Effect of heat dissipation on the current-voltage characteristics of ultrathin NbN nanowires</b>	35
<b>Bakina K.A., Zhuk N.A., Sivkov V.N., Nekipelov S.V. X-ray spectral studies of doped bismuth-magnesium and bismuth-zinc tantalates .....</b>	41

## Simulation of physical processes

<b>Briushinin A.A., Davydov V.V. Synchronization systems of time scales and frequencies in polar latitudes by meteor radio channel .....</b>	45
<b>Isaeva A.S., Denisenko M.A., Kots I.N. Testing the layout of the rail condition monitoring system using LSTM recurrent neural networks .....</b>	51
<b>Rudavin N.V., Gerasin I.S., Mekhtiev E.E., Duplinsky A.V., Kurochkin Y.V. Synchronization protocol for MDI-QKD systems .....</b>	56
<b>Duplinsky A.V., Khmelev A.V., Merzlinkin V.E., Kurochkin V.L., Kurochkin Yu.V. Influence of polarization reference frame rotation on ground-receiver error rate in satellite quantum key distribution</b>	61
<b>Reutov A.A., Tayduganov A.S. QKD and phase modulator imperfections .....</b>	65

## Atom physics and physics of clusters and nanostructures

<b>Studzinskii V.M., Karabeshkin K.V., Kondrateva A.S., Fedorenko E.D., Karaseov P.A., Mishin M.V. Ion-beam-induced formation of gold nanostructures on polymethyl methacrylate film .....</b>	69
<b>Lendyashova V.V., Ilkiv I.V., Borodin B.R., Ubyivovk E.V., Reznik R.R., Talalaev V.G. Cirlin G.E. Submonolayer InAs Quantum Dots in Silicon grown by Molecular Beam Epitaxy .....</b>	75
<b>Slyusarenko N.V., Slyusareva E.A. Förster resonance energy transfer from colloidal quantum dots to xanthene dye in polymer film .....</b>	80
<b>Kondrateva A.S., Komarevtsev I.M., Enns Ya.B., Kazakin A.N., Mishin M.V. Effect of noble metal nanoparticles in transition metal oxide magnetron sputtering .....</b>	86

<b>Boudjemila L., Davydov V.V., Aleshin A.N., Malyshkin V. M., Terukov E. I. Electrical characteristics of CsPbI<sub>3</sub> and CsPbBr<sub>3</sub> lead halide perovskite nanocrystal films deposited on Si-c solar cells for high-efficiency photovoltaics .....</b>	<b>91</b>
--	-----------

### Experimental technique and devices

<b>Litvinov K.A., Radaev O.A., Kozlikova I.S., Sergeev V.A., Kulikov, A.A. Algorithm and installation for measuring the current lacing voltage in high-power RF and microwave bipolar and heterojunction bipolar transistors .....</b>	<b>97</b>
<b>Mikhailova O.A., Antifeev I.E., Petrov D.G., Davydov, R.V. Development of a device for picoampere currents measuring .....</b>	<b>102</b>
<b>Arinushkina K.G., Valov A.P., Davydov V.V. Improving metrological characteristics of a frequency standard based on cesium atoms .....</b>	<b>107</b>
<b>Trofimov P.I., Ivanova, T.V., Lazarenko, P.I., Fedyanina, M.E., Sinev I.S. Phase-change periodic surface structures for engineering of excitonic photoluminescence in WS<sub>2</sub> monolayers .....</b>	<b>113</b>
<b>Goldberg A.A., Kochetkov I.D., Davydov V.V. Research on the character of laser radiation propagation in a differential Anderson cuvette .....</b>	<b>118</b>
<b>Provodin D.S., Davydov V.V. New technique for control of liquid media state by optical method in express mode .....</b>	<b>124</b>

### Physical electronics

<b>Alymov G.V. Impact of the current pulse width on the speed of metal-insulator transition in VO<sub>2</sub> nanobeams .....</b>	<b>130</b>
<b>Kozlowski A.V., Stetsyura S.V. Dependence of light-addressable potentiometric sensor sensitivity on photo-induced processes in Si .....</b>	<b>135</b>
<b>Belozerov I.A., Uvarov I.V. Performance optimization of the cantilever-based MEMS switch .....</b>	<b>140</b>
<b>Kazakin A.N., Enns Ya.B., Uvarov A.V., Nikitina E.V. Fabrication and investigation of UV photodiode based on n-GaN / p-NiO heterojunction .....</b>	<b>145</b>
<b>Uvarov A.V., Baranov A.I., Maksimova A.A., Vyacheslavova E.A., Gudovskikh A.S. Study of recombination and transport properties of a-Si:H(i)/ μc-Si:H(n) contact system for crystalline silicon solar cells .....</b>	<b>150</b>
<b>Davydov M.N., Davydov V.V., Cherkassova R.D. Development of a small-sized NMR relaxometer for express monitoring of the state of the liquid medium .....</b>	<b>155</b>
<b>Savin D.D., Davydov V.V. Generator of highly stable microwave signals with low phase noise .....</b>	<b>161</b>

### Physical optics

<b>Gafurov E.M., Smirnov E.V. Reliability of 808 nm QCW laser diode arrays .....</b>	<b>167</b>
<b>Savelyev D.A. The comparison of the optical vortices focusing by silicon diffraction axicons and ring gratings with variable relief heights using high-performance computer systems .....</b>	<b>172</b>
<b>Popovskiy N.I., Davydov V.V., Rud V.Yu. Features of construction of fiber-optic communication lines with orthogonal frequency-division multiplexing .....</b>	<b>178</b>

<b>Kashapov A.I., Bezus E.A., Bykov D.A., Golovastikov N.V., Doskolovich L.L. Broadband light absorbers based on multilayer metal-insulator-metal structures .....</b>	<b>184</b>
<b>Ignatev A. N., Fomin A. V., Usmanov S. R. Wavelength stabilized laser module for high-power fiber laser pumping .....</b>	<b>190</b>
<b>Lebedeva E.S., Sedykh K.O., Venediktov I.O., Goltsman G.N., Sych D.V. Detection of orbital angular momentum of light by forked diffraction method .....</b>	<b>196</b>
<b>Shakhvoy R.A., Maksimova E.I. Gain-switched VSCEL as a quantum entropy source: the problem of quantum and classical noise .....</b>	<b>201</b>
<b>Naumova V.V., Davydov V.V., Mazing M.S., Zaitceva A.Yu. The new method of processing measurement results of tissue oxygen saturation abnormalities .....</b>	<b>206</b>
<b>Kurkova A.D., Davydov V.V. Veracity of the method of detecting scattered laser radiation for content measuring of particulate matter in air .....</b>	<b>212</b>
<b>Dmitrieva D.S., Davydov V.V. Development of the radiation situation monitoring system based on fiber-optic sensors for pools of nuclear power plants .....</b>	<b>218</b>
<b>Venediktov I.O., Sedykh K.O., Zolotov P.I., Kaurova N.S., Lebedeva E.S., Goltsman G.N., Sych D.V. Fabrication of diffraction gratings for generation of OAM light .....</b>	<b>224</b>
<b>Lukashev N.A., Davydov V.V. New optic system for low mass <sup>199</sup>Hg ion clock .....</b>	<b>229</b>
<b>Baryshnikova K.V., Sergaeva O.N., Petrov M.I. Silicon nanoantenna for control the polarization direction of radiation from standalone quantum light source .....</b>	<b>235</b>
<b>Shurupov D.N., Pchelkin G.A., Demidov V.V., Davydov V.V., Vakorina D.V. Hollow-core antiresonant optical fiber activated with YAG:Yb<sup>3+</sup> .....</b>	<b>240</b>
<b>Logunov S.E., Davydov R.V., Davydov V.V. Development of a fiber-optic system for monitoring the state of oxygen activity in the current flow of the coolant .....</b>	<b>246</b>
<b>Rodin S.A., Davydov V.V., Reznikov B.K., Isaenko D.I., Vakorina D.V. Optical communication channel for multifunctional ecological monitoring complex .....</b>	<b>253</b>

### Physical materials technology

<b>Kamalov A.M., Kolbe K.A., Pavlov A.A., Borisova M.E., Yudin V.E. Activation of polylactide films by cold plasma dielectric barrier discharge to improve the interaction of fibroblasts .....</b>	<b>257</b>
<b>Zhurina A.E., Pecherskaya E.A., Fimin A.V., Zinchenko T.O., Kozlov G.V. Polarization and electrophysical parameters of piezoceramic materials investigation .....</b>	<b>263</b>
<b>Vakulov Z.E., Tominov R.V., Dzyuba D.A., Shihovcov I.A., Smirnov V.A., Ageev O.A. Ferroelectric films for renewable energy .....</b>	<b>269</b>
<b>Mozhayko A.A., Gerashchenkov D.A., Gerashchenkova E.Yu., Davydov V.V. Laser surface treatment of aluminium: correlation between thermal modeling and experimental study .....</b>	<b>274</b>
<b>Shlepakov P.S., Uvarov I.V., Svetovoy V.B. Ruthenium as an electrode material for the fast electrochemical actuator .....</b>	<b>280</b>

**Yakovleva M.A., Vasin A.A., Dontsov A.E., Gulin A.A., Aybush A.V., Feldman T.B., Ostrovsky M.A.**  
*Physicochemical analysis of bisretinoid A2E photooxidative destruction products* ..... 285

### Biophysics and medical physics

**Kharlamova K.A., Makarov M.D.** *Peculiarity of electron density calculation during interaction of ultrashort laser pulse with nitrogenous base of DNA molecule adenine* ..... 291

**Serov E.D., Kavalier A.I., Kruglov V.A., Reznik V.S., Saraev A.S., Davydov V.V.** *Development of a control algorithm for a fluid flow monitoring system in a microfluidic system* ..... 296

**Tochilo U.A., Osychenko A.A., Zalessky A.D., Martirosyan D.Yu., Nadtochenko V.A.** *Femtosecond laser is an effective instrument to remove DNA in pronuclei of mouse zygotes* ..... 302

**Trifanova E. M., Koshelev A. V., Khaydukov K. V., Krylov I. V., Popov V. K.** *Photoluminescent  $\alpha$ -NaYbF<sub>4</sub>:Er<sub>0.02</sub>Ce<sub>0.02</sub>Zn<sub>0.1</sub> nanoparticles for bioimaging in visible and infrared ranges* ..... 306

**Gulin A.A., Dontsov A.E., Yakovleva M.A., Trofimova N.N., Aybush A.V., Vasin A.A., Ostrovsky M.A.** *Oxidative destruction of human RPE melanosomes induced by superoxide radicals leads to the formation of reactive aldehydes and ketones* ..... 311

**Osychenko A.A., Zalessky A.D., Tochilo U.A., Martirosyan D.Yu.** *Oocyte enucleation by 795 nm femtosecond laser is a precise and effective method of recipient cytoplasm preparation* ..... 317

### Physics of molecules

**Nikitina A.D., Nikolaeva A.A., Petrov M.I., Frizyuk K.S.** *Nonlinear circular dichroism in dielectric nanoparticle dimers and trimers* ..... 321

**Tikhomirov V.G., Chizhikov S.V., Gudkov A.G., Nikolaenkov A.V., Gudkov G.A.** *Optimization of heterostructure transistor parameters for the monolithic integrated circuits of the amplifying path of a medical radiothermograph* ..... 326

**Sidorov E.A., Kriger V.V., Nasirov P.D., Novikova S.A., Gribova E.D., Gladyshev P.P.** *Study of quantum dots conjugation with antibodies to be used in a lateral flow immunochromatographic assay* ... 331

**Kakovkina Yu.I., Isokjanov Sh.Sh., Lebedev E.A., Ryazanov R.M., Kitsyuk E.P.** *Features of the formation super C45-RuO<sub>2</sub> based planar supercapacitor structures* ..... 336

### Radiophysics

**Ryzhova D.A., Davydov V.V.** *Monitoring of radioactive contamination in the atmosphere using radar systems* ..... 340

**Makeev S.S.** *Method for constructing NMR signal spectra using the discrete Fourier transform* ..... 346

**Dorogov A.E., Fedorov G.P., Kalacheva D.A., Dmitriev A.Yu., Bolgar A.N., Abramov N.N., Astafiev O.V.** *Application of a broadband Josephson parametric amplifier* ..... 352

**Gureeva I.M., Davydov V.V.** *A new technique for researching the absorption signal fronts of laser radiation on blood vessels* ..... 358

**Shavshin A.V., Davydov V.V.** *Development of automatic gain control for a atomic frequency standard on rubidium-87 atoms* ..... 364

<b>Seliverstov S.V., Svyatodukh S.S., Prokhodtsov A.I., Goltsman G.N.</b> <i>Simulation of terahertz photonic integrated antenna</i> .....	370
<b>Klimenko D.Yu., Esikova N.A., Bulyanitsa A.L., Davydov R.V., Belov D.A.</b> <i>Processing of qPCR signals obtained on microfluidic chips in the measurement sequence disorder event</i> .....	375
<b>Gryaznova E.M., Davydov V.V., Malanin K.Yu.</b> <i>Application of a fiber-optic communication line for transmitting RF-signal in system for measuring parameters of active phased antenna arrays</i> .....	381
<b>Burtsev V.D., Rogozhkin K.A., Vosheva T.S., Khudykin A.A., Filonov D.S.</b> <i>Additive manufacturing of an antenna array</i> .....	388
<b>Bulatov N.O., Vosheva T.S., Khudykin A.A., Filonov D.S.</b> <i>RFID-based sensor for insect detection</i> .....	393
<b>Myazin N.S., Davydov V.V.</b> <i>Design improvements of nuclear magnetic resonance magnetometer to study magnetic mid-fields variations</i> .....	399
<b>Wang D., Davydov V.V.</b> <i>Possibility of using atomic clocks on mercury-199 ions in satellite navigation systems</i> .....	406
<b>Isupova E.V., Budnikov A.S., Shvetsov S.Y., Davydov V.V.</b> <i>Improvement of the characteristics of the frequency synthesizer in the quantum frequency standard on caesium-133 atoms</i> .....	412

## CONDENSED MATTER PHYSICS

Conference materials

UDC 538.9

DOI: <https://doi.org/10.18721/JPM.153.201>

### Study of quasi 1-D silicon nanostructures adsorption properties

V. M. Kondratev<sup>1,4</sup> ✉, E. A. Vyacheslavova<sup>1,2</sup>, I. A. Morozov<sup>1,2</sup>,

S. S. Nalimova<sup>2</sup>, V. A. Moshnikov<sup>2</sup>, A. S. Gudovskikh<sup>1,2</sup>, A. D. Bolshakov<sup>1,3,4</sup>

<sup>1</sup> Alferov University, Saint Petersburg, Russia;

<sup>2</sup> Saint Petersburg Electrotechnical University "LETI", Saint Petersburg, Russia;

<sup>3</sup> ITMO University, Saint Petersburg, Russia;

<sup>4</sup> Moscow Institute of Physics and Technology, Moscow, Russia

✉ [kvm\\_96@mail.ru](mailto:kvm_96@mail.ru)

**Abstract.** The work is aimed at study of quasi 1-D silicon nanostructures (nanowires) adsorption properties via electrical impedance spectroscopy. Nanowires were synthesized by cryogenic plasma chemical etching and transferred to auxiliary substrate with interdigital gold contacts. Further, nanowires were exposed to air, unsaturated vapors of ammonia and hydrochloric acid aqueous solutions with concentrations about 0.1–1.0 mmol·l<sup>-1</sup> followed by measurement of the nanowires impedance spectra. Changes in the impedance spectra of nanowires upon exposure under analyte vapors are considered in terms of a correlation between the adsorption properties of nanowires and their electrical characteristics.

**Keywords:** silicon, nanowires, 1D, electrical impedance spectroscopy, adsorption properties, acid sensor, alkali sensor

**Funding:** Authors thanks for support the Ministry of Science and Higher Education of the Russian Federation (grants № FSRM-2020-0011) and the strategic academic leadership program "Priority 2030" (Agreement 075-02-2021-1316 30.09.2021).

**Citation:** Kondratev V. M., Vyacheslavova E. A., Morozov I. A., Nalimova S. S., Moshnikov V. A., Gudovskikh A. S., Bolshakov A. D., Study of quasi 1-D silicon nanostructures adsorption properties, St. Petersburg State Polytechnical University Journal. Physics and Mathematics. 15 (3.2) (2022) 10–15. DOI: <https://doi.org/10.18721/JPM.153.201>

This is an open access article under the CC BY-NC 4.0 license (<https://creativecommons.org/licenses/by-nc/4.0/>)

Материалы конференции

УДК 538.9

DOI: <https://doi.org/10.18721/JPM.153.201>

### Исследование адсорбционных свойств квази 1-D наноструктур кремния

В. М. Кондратьев<sup>1,4</sup> ✉, Е. А. Вячеславова<sup>1,2</sup>, И. А. Морозов<sup>1,2</sup>,

С. С. Налимова<sup>2</sup>, В. А. Мошников<sup>2</sup>, А. С. Гудовских<sup>1,2</sup>, А. Д. Большаков<sup>1,3,4</sup>

<sup>1</sup> СПбАУ РАН им. Ж.И. Алфёрова, Санкт-Петербург, Россия;

<sup>2</sup> СПбГЭТУ "ЛЭТИ", Санкт-Петербург, Россия;

<sup>3</sup> Университет ИТМО, Санкт-Петербург, Россия;

<sup>4</sup> Московский физико-технический институт, Москва, Россия

✉ [kvm\\_96@mail.ru](mailto:kvm_96@mail.ru)

**Аннотация.** Работа направлена на изучение адсорбционных свойств нанонитей кремния методами спектроскопии электрического импеданса. Продемонстрирована корреляция между адсорбционными свойствами и электрическими характеристиками нанонитей в присутствии воздуха, ненасыщенных паров воды и водных растворов аммиака, а также соляной кислоты.

**Ключевые слова:** кремний, нанонити, 1Д, спектроскопия электрического импеданса, адсорбционные свойства, сенсор кислот, сенсор щелочей

**Финансирование:** Работа выполнена при финансовой поддержке Министерства науки и высшего образования Российской Федерации (грант № FSRM-2020-0011), а также при поддержке программы академического стратегического лидерства "Приоритет 2030" (Соглашение 075-02-2021-1316 30.09.2021)

**Ссылка при цитировании:** Кондратьев В. М., Вячеславова Е. А., Морозов И. А., Налимова С. С., Мошников В. А., Гудовских А. С., Большаков А. Д. Исследование адсорбционных свойств квази 1-Д наноструктур кремния // Научно-технические ведомости СПбГПУ. Физико-математические науки. 2022. Т. 15. № 3.2. С. 10–15. DOI: <https://doi.org/10.18721/JPM.153.201>

Статья открытого доступа, распространяемая по лицензии CC BY-NC 4.0 (<https://creativecommons.org/licenses/by-nc/4.0/>)

## Introduction

Active development of low-dimensional nanostructures based on various materials is carried out in all spheres of modern nanoelectronics. Quantum dots (0-D) are widely used in photocatalysis [1]. There are many light emitting [2-4] and waveguiding [2, 5] devices based on nanowires (NWs, 1-D). At the same time, thin semiconductor films is the common basic element of modern electronics [6]. High surface area and peculiar electronic properties compare to bulk material and thin films are the main reason for use of NWs in adsorption sensing [7-10]. Silicon is still the most accessible material for the production of NWs, both by epitaxial and «top-down» techniques [11, 12].

The existing works on Si NWs adsorption properties [13, 14] commonly consider small amounts of target adsorbates. This paper shows the possibility of detection both acidic and alkaline agents at concentrations below the "biological" level via electrical impedance spectroscopy and correlation between silicon NWs electrical impedance and their adsorption properties. For example  $\text{NH}_3$  and HCl at concentrations of about  $1 \text{ mmol}\cdot\text{l}^{-1}$  selected as target adsorbates of alkaline and acidic nature because they can be found in body fluids and breath and may indicate pathological changes in the body. At the same time, hydrochloric acid and ammonia are found in human body, nature and waste products of the factories and farms. In high concentrations these agents leads to irritation of respiratory system, as well as eye mucous membranes [15]. So development of novel approaches for their detection is of an importance.

## Materials and Methods

In this work silicon NWs are obtained using cryogen plasma chemical etching of Si (001) substrate (boron-doped substrate with the resistivity of  $12 \Omega\cdot\text{cm}$ ) in Oxford PlasmaLab System 100 ICP380. Anisotropic etching occurs on the silicon surface under the flow of oxygen and etcher ( $\text{O}_2/\text{SF}_6$ ) mixture. Primarily etched Si islands on the surface are passivated by a non-volatile  $\text{SiO}_x\text{F}_y$  compound, which prevents lateral etching. An increase in temperature after the etching interruption leads to volatilization of F and conversion of  $\text{SiO}_x\text{F}_y$  into the native oxide. The NWs morphology was investigated by scanning electron microscopy (SEM) by Zeiss Supra25 (Carl Zeiss, Germany) (Fig. 1).

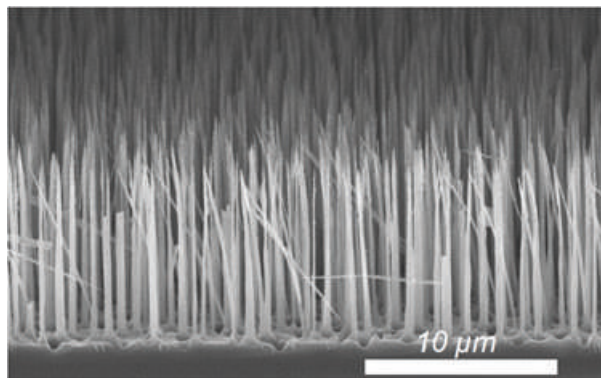


Fig. 1. SEM image of the vertical Si NWs

As-synthesized Si NWs (Fig. 1) were separated from Si (001) substrate by ultrasonication and transferred to an auxiliary substrate with concentric interdigital gold contacts (contact step of  $10 \mu\text{m}$ ) (Fig. 2, a). Gold–NWs contacts are found to be of the Schottky type, which

is proven by the voltage-current characterization obtained using Keithley 2400 source-meter, (Tektronix, USA) (Fig. 2, *b*). The current-voltage (*I-V*) characteristic demonstrates symmetry and a diode shape with a knee voltage of about 5V, which indicates the barrier nature of the conductivity.

The phenomenon of barrier conductivity at the nanowire-gold interfaces can be effectively used for  $\text{NH}_3$  and  $\text{HCl}$  detection as shown below via electric impedance spectroscopy of Si NWs under exposure of analyte vapor at 100mV bias in the frequency range from 100 Hz to 500 kHz (by impedance meter Z500P (Elins, Russia)). Impedance spectrum in a reference medium – air – is shown in Fig. 2, *c*.

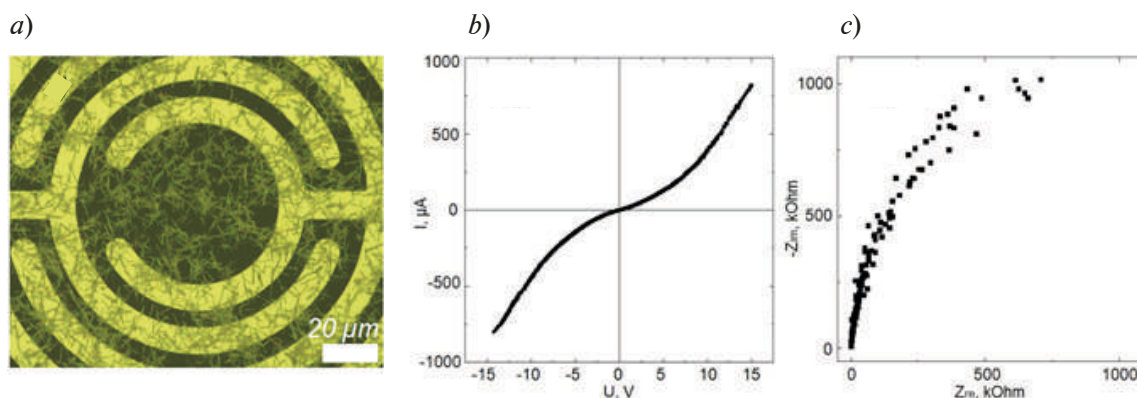


Fig. 2. Typical optical image of the Si NWs on the surface of an auxiliary substrate with concentric interdigital gold contacts (*a*); current-voltage characteristic (*b*); measured impedance spectrum in air conditions (*c*)

The impedance spectra were represented in Nyquist's plots – in the form of a dependence of the imaginary part ( $Z_{im}$ ) of the Si NWs impedance on the real one ( $Z_{re}$ ) – and analyzed for a shift due to the change in the environment.

### Results and Discussion

Vapor media with adsorbates were delivered to the NWs by natural evaporation of water and aqueous ammonia solutions (room temperature, atmospheric pressure) from a reservoir 4 cm (1.6 in) in diameter located at a distance of about 5 cm (2.0 in) below the NWs. A change in the NWs electrical impedance under action of the target adsorbates (vapors of  $\text{NH}_3$  and  $\text{HCl}$  aqua solutions with concentrations of 0.1 and 1.0  $\text{mmol}\cdot\text{l}^{-1}$ ) (Fig. 3, *b, c, e*) was measured and compared with the impedance in the water vapors medium (Fig. 3, *a*).

Analysis of the dependencies in Fig. 3 showed the presence in all spectra of a characteristic region in the frequency range from 25 kHz to 500 kHz which can be approximated by a semicircle with the center lying on the abscissa axis. At the same time, the diameter of such a semicircle decreases when water vapor changes to vapor of aqueous ammonia solutions and increases when changing to vapor of aqueous solutions of hydrochloric acid. In previous works, it was shown that the projection of this high-frequency region of the nanowire impedance spectrum onto the abscissa (real resistance) axis makes it possible to estimate the active resistance of NWs transferred to gold contacts and electrically connected in parallel to each other [11–12].

In air conditions a NWs surface is oxidized due to increase in temperature after the cryogenic plasmachemical etching interruption and volatilization of F with subsequent conversion of  $\text{SiO}_x\text{F}_y$  into the native oxide [11-12]. The interaction of  $\text{H}_2\text{O}$ ,  $\text{NH}_3$  and  $\text{HCl}$  vapors with NWs occurs by redox mechanisms:

1) hydration of the silicon oxidized surface by  $\text{OH}^-$  molecules from water vapors (breaking the bond between oxygen and silicon in the near-surface native oxide and its replacement with a more energetically advantageous one) [11-12];

2) for ammonia aqueous solution vapors it is a protonation of the hydrated surface of the nanowire by neutral  $\text{NH}_3$  molecules (separation of the proton  $\text{H}^+$  from the  $\text{OH}$  molecule on the surface of the nanowire) with formation of the  $\text{NH}_4^+$  ion (gas) [13-15];

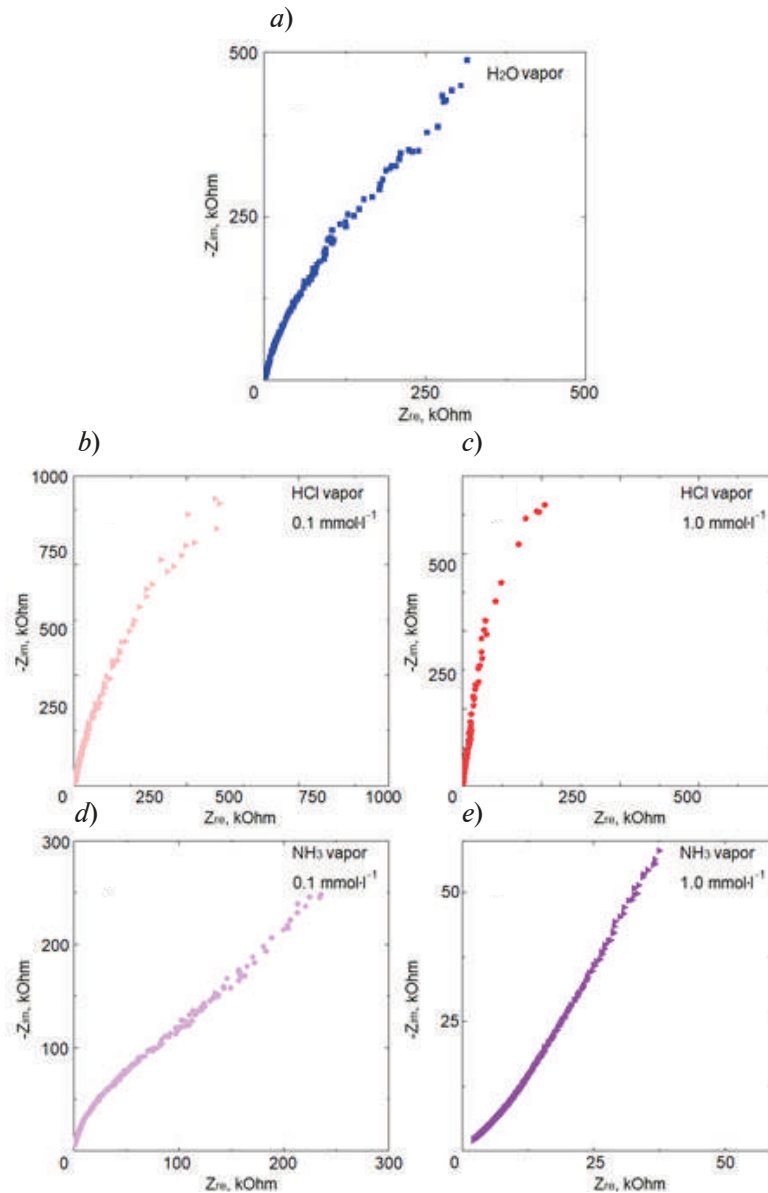


Fig. 3. Measured impedance spectra in: comparative medium of water vapor (a), 0.1 (b) and 1.0 mmol·l<sup>-1</sup> HCl aqueous solution vapors (c), 0.1 (d) and 1.0 mmol·l<sup>-1</sup> NH<sub>3</sub> aqueous solution vapors (e)

3) vapors of hydrochloric acid aqueous solution contain neutral Cl ions which presumably interact with the silicon surface followed by the removal of electrons from NWs with a subsequent increase in its resistance [16].

At the same time in both first and second cases described conduction electrons are injected into silicon NWs which affect the resistance and impedance of NWs.

It is also necessary to consider the multiple Schottky barriers at the gold-NWs interfaces which make a significant contribution to the impedance of NWs in air in the non-ohmic mode (Fig. 2). We believe that the impedance of silicon NWs in air is determined precisely by the contact resistance of the Schottky barriers, and the NWs themselves are significantly depleted.

However, in the presence of water vapor, ammonia, and hydrochloric acid, the impedance of NWs is determined precisely by the injection and rejection of electrons during the adsorption of molecules. Thus, the measurement concept proposed in Fig. 2 is suitable for silicon NWs adsorption properties analysis.

### Conclusion

Changes in the impedance spectra of NWs in the presence of air, H<sub>2</sub>O, NH<sub>3</sub> and HCl were considered in terms of a correlation between the adsorption properties of NWs and their electrical impedance.

We demonstrate the possibility of qualitative and quantitative gaseous (vapor) media analysis for the presence of ammonia and hydrochloric acid in extra low concentration via silicon NWs and impedance spectroscopy.

The selectivity between oxidizing and reducing gasses can be used for Si NWs based sensor fabrication.

### Acknowledgments

Authors thanks for support the Ministry of Science and Higher Education of the Russian Federation (grants № FSRM-2020-0011) and the strategic academic leadership program "Priority 2030" (Agreement 075-02-2021-1316 30.09.2021).

### REFERENCES

1. Zhang Q., Yang F., Zhou S., Bao N., Xu Z., Chaker M., Ma D., Broadband photocatalysts enabled by 0D/2D heterojunctions of near-infrared quantum dots/graphitic carbon nitride nanosheets, *Applied Catalysis B: Environmental*. 2020, 118879.
2. Kuznetsov A., Roy P., Kondratev V. M., Fedorov V. V., Kotlyar K. P., Reznik R. R., Vorobyev A. A., Mukhin I. S., Cirlin G. E., Bolshakov A. D., Anisotropic Radiation in Heterostructured "Emitter in a Cavity" Nanowire, *Nanomaterials*. 2022, 12(2), 241.
3. Kadinskaya S. A., Kondratev V. M., Kindyushov I. K., Kuznetsov A., Punegova K. N., Hydrothermal ZnO-based Nanostructures: Geometry Control and Narrow Band UV Emission, 2022 Conference of Russian Young Researchers in Electrical and Electronic Engineering (EIConRus). 2022, 958–961.
4. Kadinskaya S. A., Kondratev V. M., Kindyushov I. K., Labzovskaya M. E., Novikov B. V., Shtrom I. V., Lihachev A. I., Nashchekin A. V., Bolshakov A. D., Hydrothermal zinc oxide nanostructures: geometry control and narrow band UV emission, *J. Phys.: Conf. Ser.* 2022, 2227, 012007.
5. Kuznetsov A., Fominykh N., Kondratev V., Fedina S. V., GaP Nanowire Waveguides, 2022 Conference of Russian Young Researchers in Electrical and Electronic Engineering (EIConRus). 2022, 1126–1129.
6. Butle S. Z., et al., Progress, Challenges, and Opportunities in Two-Dimensional Materials Beyond Graphene, *ACS Nano*. 2013, 7(4), 2898.
7. Kondratev V. M., Kuznetsov A., Gridchin V. O., Fedina S. V., Aubekerov K., III–V Nanowires for Biological Ammonia Concentrations Detection, 2022 Conference of Russian Young Researchers in Electrical and Electronic Engineering (EIConRus). 2022, 970–974.
8. Kondratev V. M., et al., Gallium phosphide nanowires for "biological concentrations ammonia detection, *J. Phys.: Conf. Ser.* 2022, 2172, 012006.
9. Kondratev V. M., et al., III–V nanowires for ammonia detection, *J. Phys.: Conf. Ser.* 2021, 2086, 012186.
10. Kondratev V. M., Bolshakov A. D., Nalimova S. S., Technologically Feasible ZnO Nanostructures for Carbon Monoxide Gas Sensing, 2021 IEEE Conference of Russian Young Researchers in Electrical and Electronic Engineering (EIConRus). 2021, 1163–1166.
11. Kondratev V. M., et al., Silicon nanowires based adsorption sensors for CO and NH<sub>3</sub> detection, *J. Phys.: Conf. Ser.* 2021, 2103, 012229.
12. Kondratev V. M., et al., Silicon nanowires as multi-environment sensor elements for carbon monoxide and ammonia detection, *J. Phys.: Conf. Ser.*, 2021, 2015, 012068.
13. Zhou X. T., et al., Silicon nanowires as chemical sensors, *Chemical Physics Letters*. 2003, 369, 220.
14. Park I., et al., Top-down fabricated silicon nanowire sensors for real-time chemical detection, *Nanotechnology*. 2010, 21, 1, 015501.
15. Li C., et al., Impact of Ammonia on the Electrical Properties of P-Type Si Nanowire Arrays, *Journal of Applied Physics*. 2013, 114, 17.



16. Virji S., et al., Polyaniline Nanofiber Gas Sensors: Examination of Response Mechanisms, Nano Letters. 2004, 4(3), 491.

#### THE AUTHORS

**KONDRATEV Valeriy M.**  
kvm\_96@mail.ru  
ORCID: 0000-0002-3469-5897

**VYACHESLAVOVA Ekaterina A.**  
cate.viacheslavova@yandex.ru  
ORCID: 0000-0001-6869-1213

**MOROZOV Ivan A.**  
morivan@mail.ru

**NALIMOVA Svetlana S.**  
sskarpova@list.ru

**MOSHNIKOV Vyacheslav A.**  
vamoshnikov@mail.ru

**GUDOVSKIKH Alexander S.**  
gudovskikh@spbau.ru

**BOLSHAKOV Alexey D.**  
acr1235@mail.ru  
ORCID: 0000-0001-7223-7232

*Received 12.07.2022. Approved after reviewing 20.07.2022. Accepted 20.07.2022.*

Conference materials

UDC 537.9

DOI: <https://doi.org/10.18721/JPM.153.202>

## Study of hydrothermal zinc oxide nanostructures photovoltaic properties

S. A. Kadinskaya<sup>1,2</sup> ✉, V. M. Kondratev<sup>1,2</sup>, I. K. Kindyushov<sup>1</sup>, A. Kusnetsov<sup>1,2</sup>,  
A. I. Lihachev<sup>3</sup>, A. V. Nashchekin<sup>3</sup>, A. D. Bolshakov<sup>1,2,4</sup>

<sup>1</sup> Alferov University, Saint Petersburg, Russia;

<sup>2</sup> Moscow Institute of Physics and Technology, Dolgoprudny, Russia;

<sup>3</sup> Ioffe Institute, St. Petersburg, Russia;

<sup>4</sup> ITMO University, St. Petersburg, Russia

✉ skadinskaya@bk.ru

**Abstract.** Electrical properties of zinc oxide nanostructures were studied in terms of change in the impedance under infrared, red, green, blue, and ultraviolet illumination. Physical interpretation of photoabsorption in ZnO is given, and the prospect of using the synthesized structures as photosensitive elements is shown.

**Keywords:** hydrothermal synthesis, zinc oxide, impedance spectroscopy

**Funding:** The work was supported by the strategic academic leadership program "Priority 2030" (Agreement 075-02-2021-1316 30.09.2021).

SEM characterization was performed using equipment owned by the Federal Joint Research Center "Material science and characterization in advanced technology".

**Citation:** Kadinskaya S. A., Kondratev V. M., Kindyushov I. K., Kusnetsov A., Lihachev A. I., Naschekin A.V., Bolshakov A. D., Study of hydrothermal zinc oxide nanostructures photovoltaic properties, St. Petersburg State Polytechnical University Journal. Physics and Mathematics. 15 (3.2) (2022) 16–20. DOI: <https://doi.org/10.18721/JPM.153.202>

This is an open access article under the CC BY-NC 4.0 license (<https://creativecommons.org/licenses/by-nc/4.0/>)

Материалы конференции

УДК 537.9

DOI: <https://doi.org/10.18721/JPM.153.202>

## Исследование фотоэлектрических свойств гидротермальных наноструктур оксида цинка

С. А. Кадинская<sup>1,2</sup>, В. М. Кондратьев<sup>1,2</sup>, И. К. Киндюшов<sup>1</sup>, А. Кузнецов<sup>1,2</sup>,  
А. И. Лихачев<sup>3</sup>, А. В. Нащекин<sup>3</sup>, А. Д. Большаков<sup>1,2,4</sup>

<sup>1</sup> СПбАУ РАН им. Ж.И. Алфёрова, Санкт-Петербург, Россия;

<sup>2</sup> Московский физико-технический институт, Долгопрудный, Россия;

<sup>3</sup> ФТИ им. А.Ф. Иоффе, Санкт-Петербург, Россия;

<sup>4</sup> Университет ИТМО, Санкт-Петербург, Россия

✉ skadinskaya@bk.ru

**Аннотация.** Исследованы электрические свойства наноструктур оксида цинка по изменению импеданса в условиях ИК, красного, зеленого, синего и УФ освещения. Дана физическая интерпретация фотопоглощения в ZnO и показана перспективность использования синтезированных структур в качестве фоточувствительных элементов.



**Ключевые слова:** гидротермальный синтез, оксид цинка, спектроскопия импеданса

**Финансирование:** Работа выполнена при поддержке программы академического стратегического лидерства «Приоритет 2030» (Соглашение 075-02-2021-1316 от 30.09.2021).

СЭМ-характеристику выполняли на оборудовании, принадлежащем Федеральному объединенному исследовательскому центру «Материаловедение и характеризация в передовых технологиях».

**Ссылка при цитировании:** Кадинская С. А., Кондратьев В. М., Киндюшов И. К., Кузнецов А., Лихачев А. И., Нашекин А. В., Большаков А. Д. Исследование фотоэлектрических свойств гидротермальных наноструктур оксида цинка // Научно-технические ведомости СПбГПУ. Физико-математические науки. 2022. Т. 15. № 3.2. С. 16–20. DOI: <https://doi.org/10.18721/JPM.153.202>

Статья открытого доступа, распространяемая по лицензии CC BY-NC 4.0 (<https://creativecommons.org/licenses/by-nc/4.0/>)

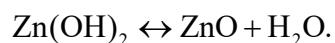
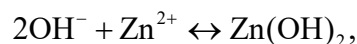
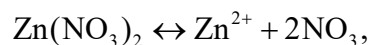
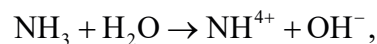
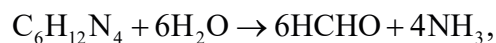
## Introduction

Zinc oxide (ZnO) is a wide-gap semiconductor material with band gap of 3,37 eV at room temperature [1]. This material is inexpensive, widespread, chemically stable, easy to synthesize, and non-toxic. ZnO is widely studied due to applications in light-emitting devices, nanoelectromechanical devices, sensors and others [1-5].

There are plenty of defect states occurring in ZnO that can either ruin the device performance or can be efficiently utilized, so control over the crystallinity is a major factor in ZnO nanostructures fabrication. Typical defects in ZnO are zinc and oxygen vacancies [6], which create levels enhancing non-radiative recombination, which can be used for development of photoabsorbing devices operating in the infrared (IR), visible, and ultraviolet (UV) wavelength ranges. However, the presence of oxygen and zinc vacancies also indicates a low crystalline perfection of the synthesized structures. This work is devoted to development of protocols for control of the morphology of ZnO structures synthesized using hydrothermal method and study of their photoelectric characteristics.

## Materials and Methods

Hydrothermal synthesis is a method of growing various materials and compounds, based on the use of physical and chemical processes that take place in aqueous solutions at slightly elevated temperatures often used to obtain ZnO nanostructures [7]. In our work, silicon substrates Si (111) are used for the hydrothermal synthesis of ZnO nanostructures since this material is known to be the most often used in nanoelectronics. Zinc acetate is used as a seed layer material. The following reactions take place during the growth process:



The growth solution consists of equimolar aqueous solutions of  $\text{Zn}(\text{NO}_3)_2$  and hexamethylenetetramine (HMTA). Sample #1 was synthesized without using surfactants (Fig. 1, *a*). Samples #2 and #3 were synthesized using sodium citrate and polyethylenimine (PEI) respectively (Fig. 1, *b*, *c*) allowing for lateral and vertical growth enhancement, respectively.

The resulting structures are found to possess branched NWs shape with an aspect ratio (length to thickness ratio) of about 10:1 (Fig. 1, *a*), quasi-two-dimensional nanostructures [8] in the shape of hexapods with  $D \sim 5 \mu\text{m}$ ,  $l \sim 1 \mu\text{m}$  (figure1(b)) and NWs with  $D \sim 100 \text{ nm}$  and  $l \sim 1 \mu\text{m}$  (Fig. 1, *c*).

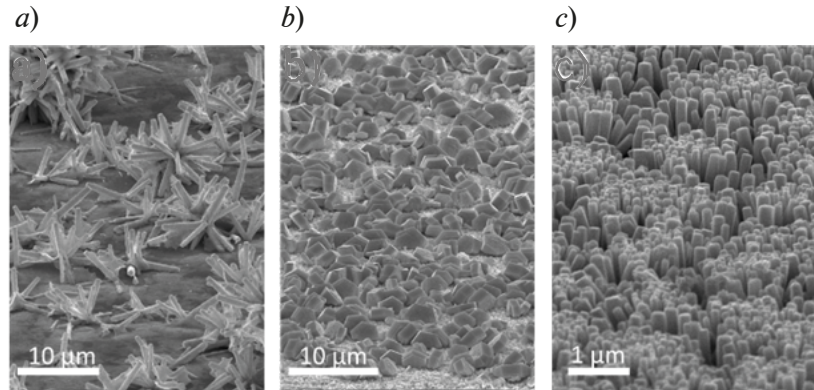


Fig. 1. Scanning electron microscopy (SEM) images of sample #1 (branched NWs) (*a*); sample #2 (hexapods) (*b*); sample #3 (vertical NWs) (*c*)

Electrical properties of the prepared samples were studied using Z500P impedance meter (Elins, Chernogolovka, Russia) in the frequency range from 100 Hz to 500 kHz by impedance spectroscopy. During the experiment, the impedance spectra were obtained under dark conditions, as well as under illumination with IR (850 nm), red (622 nm), green (570 nm), blue (470 nm), and UV (390 nm) LEDs. The power of the LEDs  $\sim 1 \text{ W}$ .

### Results and Discussion

The spectra of samples under different conditions are presented in Nyquist coordinates – the dependence of the imaginary part of the electrical impedance on the real one (Fig. 2). Spectra of samples can be visually divided into two parts: low-frequency (large impedance values) and high-frequency (10 kHz–500 kHz) in the form of a semicircle [9, 10], which is well described by an equivalent RC circuit, and the diameter of the semicircle corresponds to the resistance  $R$  of the material [11]. Analyzing the experimental data, we approximated the high-frequency part of the spectrum by a semicircle with the center lying on the x axis, which makes it possible to find the active electrical resistance of the zinc oxide structures lying between the electrical contacts. The change in the diameter of the approximating semicircles during the transition from dark conditions to illumination with a certain wavelength indicates a change in the active resistance of zinc oxide structures due to photoexcitation of carriers.

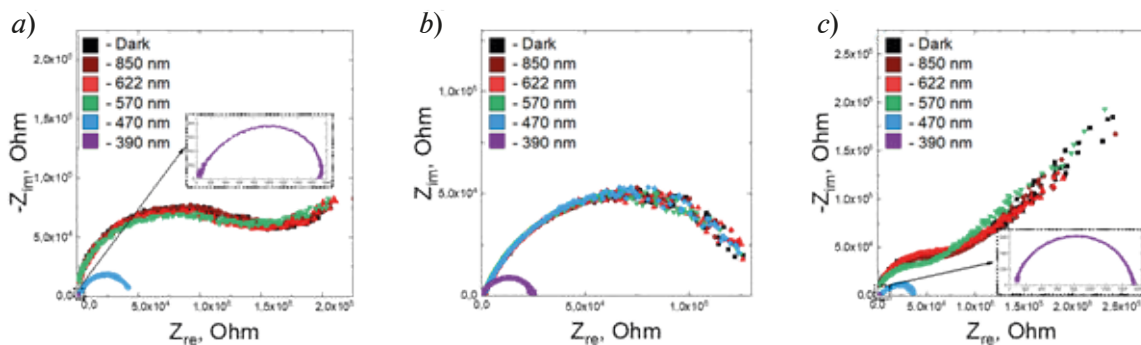


Fig. 2. Impedance spectra of sample #1 (*a*); sample #2 (*b*); sample #3 (*c*)



Figure 2 shows that no change in the resistance is observed for any of the samples when exposed under IR (850 nm) and red (622 nm) illumination. This is generally expected, due to wide-gap structure of ZnO. All the samples show high absorption when exposed near the absorption edge (390 nm). Table 1 shows the changes in resistance during illumination, obtained as a result of the analysis of the dependences shown in figure 2.

Table 1.

**Photoresistive response in three types of synthesized structures**

	570 nm	470 nm	390 nm
No surfactants	–	70%	99%
Sodium citrate	–	–	81,5%
PEI	26%	59,5%	98%

Structures synthesized without surfactants and using PEI also show photoconductivity under blue illumination ( $\lambda = 470$  nm). This behavior may be due to the presence of defect levels – zinc vacancies [7, 12, 13] in the band gap. The absence of absorption at a wavelength of 470 nm in the structures synthesized using sodium citrate indicates a high crystalline perfection of the structures. The sample synthesized using PEI also exhibits absorption at a wavelength of – 570 nm, which may be due to the presence of oxygen vacancies and interstitial Zn atoms [7, 14]. Further investigation of the nanostructures crystallinity will allow detailed interpretation of the demonstrated effects.

**Conclusion**

As a result of the work, samples of three morphology types were obtained: branched NWs, hexapods, vertical NWs. The change in photoabsorption depending on the wavelength of the LED radiation was studied by impedance spectroscopy. These changes are related to the crystallinity of the synthesized ZnO structures. The results obtained indicate that changing the hydrothermal growth chemistry is an effective way to control the optical properties of ZnO.

Thus, the zinc oxide structures synthesized in the course of this work are promising for their use as photosensitive elements.

**Acknowledgments**

The work was supported by the strategic academic leadership program "Priority 2030" (Agreement 075-02-2021-1316 30.09.2021).

SEM characterization was performed using equipment owned by the Federal Joint Research Center "Material science and characterization in advanced technology".

**REFERENCES**

1. Özgür Ü., Alivov Ya. I., Liu C., Teke A., Reshchikov M. A., Doğan S., Avrutin V., Cho S.-J., Morkoç H., A comprehensive review of ZnO materials and devices, *Journal of Applied Physics* 98 (2005) 041301.
2. Kondratev V. M., Bolshakov A. D., Nalimova S. S., Technologically Feasible ZnO Nanostructures for Carbon Monoxide Gas Sensing, 2021 IEEE Conference of Russian Young Researchers in Electrical and Electronic Engineering (EIConRus) (2021) 1163–1166.
3. Kadinskaya S. A., Kondratev V. M., Kindyushov I. K., Kuznetsov A., Punegova K. N., Hydrothermal ZnO-based Nanostructures: Geometry Control and Narrow Band UV Emission, 2022 Conference of Russian Young Researchers in Electrical and Electronic Engineering (EIConRus) (2022) 958–961.
4. Kadinskaya S. A., Kondratev V. M., Kindyushov I. K., Labzovskaya M. E., Novikov B. V., Shtrom I. V., Lihachev A. I., Nashchekin A. V., Bolshakov A. D., Hydrothermal zinc oxide nanostructures: geometry control and narrow band UV emission, *J. Phys.: Conf. Ser.* 2227 (2022) 012007.

5. Kuznetsov A., Roy P., Kondratev V. M., Fedorov V. V., Kotlyar K. P., Reznik R. R., Vorobyev A. A., Mukhin I. S., Cirlin G. E., Bolshakov A. D., Anisotropic Radiation in Heterostructured “Emitter in a Cavity” Nanowire, *Nanomaterials* 12(2) (2022) 241.
6. Galdámez–Martínez A., Santana G., Güell F., Martínez-Alanis P. R., Dutt A., Photoluminescence of ZnO nanowires: a review, *Nanomaterials* 10(5) (2020) 857.
7. Xu H. Y., Wang H., Zhang Y. C., He W. L., Zhu M. K., Wang B., Yan H., Hydrothermal synthesis of zinc oxide powders with controllable morphology, *Ceramics International* 30(1) (2004) 93–97.
8. Gerbreders V., Krasovska M., Sledevskis E., Gerbreders A., Mihailova I., Tamanisa E., Ogurcovs A., Hydrothermal synthesis of ZnO nanostructures with controllable morphology change, *CrystEngComm* 22 (2020) 1346–58.
9. Mhamdi A., Labidi A., Souissi B., Kahlaoui M., Yumak A., Boubaker K., Amlouk A., Amlouk M., Impedance spectroscopy and sensors under ethanol vapors application of sprayed vanadium-doped ZnO compounds, *Journal of Alloys and Compounds* 639 (2015) 648–658.
10. Li X., Qin Zh., Fu H., Li T., Peng R., Li Zh., Rini J. M., Liu X., Physical Interpretations of Nyquist Plots for EDLC Electrodes and Devices, *Biosensors and Bioelectronics* 177 (2021) 112672.
11. Mei B.-A., Munteshari O., Lau J., Dunn B., Pilon L., Physical interpretations of Nyquist plots for EDLC electrodes and devices, *J. Phys. Chem. C* 122(1) (2018) 194–206.
12. Lima S.A.M., Sigoli F.A., Jafelicci Jr M., Davolos M.R., Luminescent properties and lattice defects correlation on zinc oxide, *International Journal of Inorganic Materials*, 3(7) (2001) 749–754
13. Nikitenko V., NATO ASI Ser., Ser. 2: Math. Phys. Chem. 194 (2004) 69.
14. Lin B., Fu Z., Jia Y., Green luminescent center in undoped zinc oxide films deposited on silicon substrates, *Appl. Phys. Lett.* 79 (2001) 943.

#### THE AUTHORS

**KADINSKAYA Svetlana A.**

skadinskaya@bk.ru

ORCID: 0000-0003-2508-2244

**KONDRATEV Valeriy M.**

kvm\_96@mail.ru

ORCID: 0000-0002-3469-5897

**KINDYUSHOV Ivan K.**

Kindyushov@gmail.com

**KUSNETSOV Alexey**

alkuznetsov1998@gmail.com

ORCID: 0000-0001-7143-6686

**LIHACHEV Alexey I.**

lihachev\_alexey@bk.ru

ORCID: 0000-0003-3671-2600

**NASHCHEKIN Alexey V.**

nashchekin@mail.ioffe.ru

ORCID: 0000-0002-2542-7364

**BOLSHAKOV Alexey D.**

acr1235@mail.ru

ORCID: 0000-0001-7223-7232

*Received 02.08.2022. Approved after reviewing 03.08.2022. Accepted 04.08.2022.*

Conference materials

UDC 621.382

DOI: <https://doi.org/10.18721/JPM.153.203>

## Optimization of InGaN-based luminescent heterostructures by genetic algorithm

D. S. Arteev <sup>1</sup>✉, A. V. Sakharov <sup>1</sup>, A. E. Nikolaev <sup>1</sup>,  
E. E. Zavarin <sup>1</sup>, A. F. Tsatsulnikov <sup>2</sup>, V. M. Ustinov <sup>3</sup>

<sup>1</sup> Ioffe Institute, St. Petersburg, Russia;

<sup>2</sup> Submicron Heterostructures for Microelectronics, Research & Engineering Center, RAS, St. Petersburg, Russia;

<sup>3</sup> Peter the Great St. Petersburg Polytechnic University, St. Petersburg, Russia

✉ [ArteevDS@mail.ioffe.ru](mailto:ArteevDS@mail.ioffe.ru)

**Abstract.** A genetic algorithm was employed to optimize the Si doping profile of luminescence InGaN-based heterostructures. It was shown that, in the optimized structure, a ‘parasitic’ luminescence from GaN barrier layers could be suppressed while the efficiency remained the same as that of the best uniformly doped structure. Moreover, the optimized structure had a 2.6 times lower total Si concentration, which could be beneficial in terms of crystal quality of the grown layers.

**Keywords:** GaN, InGaN, doping, luminescence, optimization, genetic algorithm

**Funding:** The research is partially funded by the Ministry of Science and Higher Education of the Russian Federation as part of Strategic Academic Leadership program “Priority-2030” (contract No. 075-15-2021-1333 dated 30.09.2021).

**Citation:** Arteev D. S., Sakharov A. V., Nikolaev A. E., Zavarin E. E., Tsatsulnikov A. F., Ustinov V. M., Optimization of InGaN-based luminescent heterostructures by genetic algorithm, St. Petersburg State Polytechnical University Journal. Physics and Mathematics. 15 (3.2) (2022) 21–24. DOI: <https://doi.org/10.18721/JPM.153.203>

This is an open access article under the CC BY-NC 4.0 license (<https://creativecommons.org/licenses/by-nc/4.0/>)

Материалы конференции

УДК 621.382

DOI: <https://doi.org/10.18721/JPM.153.203>

## Оптимизация люминесцентных гетероструктур на основе InGaN с помощью генетического алгоритма

Д. С. Артеев <sup>1</sup>✉, А. В. Сахаров <sup>1</sup>, А. Е. Николаев <sup>1</sup>,  
Е. Е. Заварин <sup>1</sup>, А. Ф. Цацульников <sup>2</sup>, В. М. Устинов <sup>3</sup>

<sup>1</sup> ФТИ им. А. Ф. Иоффе, Санкт-Петербург, Россия;

<sup>2</sup> НТЦ микроэлектроники РАН, Санкт-Петербург, Россия;

<sup>3</sup> Санкт-Петербургский политехнический университет Петра Великого, Санкт-Петербург, Россия

✉ [ArteevDS@mail.ioffe.ru](mailto:ArteevDS@mail.ioffe.ru)

**Аннотация.** В данной работе представлены результаты оптимизации профиля легирования барьерного слоя в структурах на основе InGaN методом генетического алгоритма. Показано, что в оптимизированной структуре интенсивность «паразитной» люминесценции из GaN слоёв может быть существенно снижена, при этом эффективность излучения из квантовых ям остаётся такой же, как и в лучшей структуре с однородно легированным барьером. Кроме того, суммарная концентрация кремния в оптимизированной структуре в 2,6 раза ниже, что также является преимуществом с точки зрения кристаллического качества выращенных слоёв.

**Ключевые слова:** GaN, InGaN, легирование, люминесценция, оптимизация, генетический алгоритм

**Финансирование:** Работа выполнена при финансовой поддержке Министерства науки и высшего образования Российской Федерации в рамках программы стратегического академического лидерства «Приоритет-2030» (соглашение от 30.09.2021 № 075-15-2021-1333).

**Ссылка при цитировании:** Артеев Д. С., Сахаров А. В., Николаев А. Е., Заварин Е. Е., Цацульников А. Ф., Устинов В. М. Оптимизация люминесцентных гетероструктур на основе InGaN с помощью генетического алгоритма // Научно-технические ведомости СПбГПУ. Физико-математические науки. 2022. Т. 15. № 3.2. С. 21–24. DOI: <https://doi.org/10.18721/JPM.153.203>

Статья открытого доступа, распространяемая по лицензии CC BY-NC 4.0 (<https://creativecommons.org/licenses/by-nc/4.0/>)

### Introduction

Optimization of the design of semiconductor structures for achieving a better performance has been a hot topic from the earliest days of semiconductor industry. As epitaxial growth technology improved, fabrication of more and more complex heterostructures with a lot of different layers became possible. Obviously, it is impossible to experimentally grow and measure all possible structures to find the best one since it would require huge financial and time costs. Computer simulations could significantly reduce these costs. However, even in this case, it could be very challenging to find an optimal design of complex heterostructures ‘by hand’ due to enormous parameter space, especially when different parameters strongly affect each other, so conventional simulation methods may be inefficient.

A very promising approach to overcome the so called ‘curse of dimensionality’ is a genetic algorithm (GA). It is inspired by the process of the natural selection and rely on such operators as mutation, crossover and selection [1]. This simple but powerful method is suitable for optimization tasks in different areas of science. It is not widely used in semiconductor device design yet; however, there are several works demonstrating its applicability and efficiency [2 – 4].

In this study, we employ a GA to optimize a Si doping profile of the GaN barrier layer in multiple-quantum well (MQW) InGaN/GaN-based luminescence heterostructures.

### Simulation details

The calculations were performed in drift-diffusion approximation by self-consistent solving of Poisson’s equation and current continuity equations for electrons and holes. Quantum confinement and quantum tunneling effects were taken into account effectively using localization landscape theory [5]. The structure consisted of 1.5 nm  $\text{In}_{0.11}\text{Ga}_{0.89}\text{N}$  quantum wells (QWs) separated with 31 nm GaN quantum barriers (QBs). The QB was divided to 10 sublayers of different thickness, representing a ‘genotype’ of the sample (Fig. 1). Spontaneous and piezoelectric polarization charges were considered. The dependencies of mobility [6] and lifetime [7] for electrons and holes, as well as Si ionization energy [8], on Si concentration were implemented. Simulation were carried out using 1D-DDCC software [9] for semiconductor part together with Python scripting for GA part.

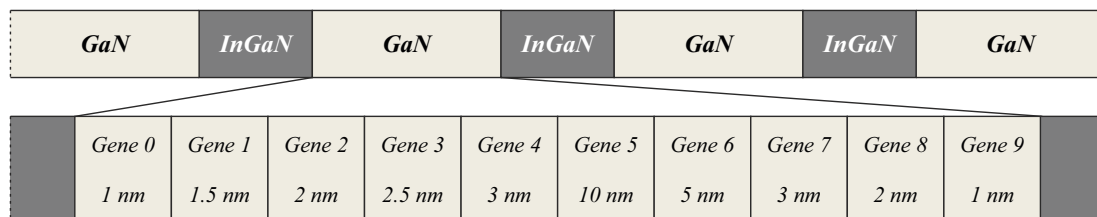


Fig. 1. Schematic of the genotype of the structures

## Results and Discussion

Obviously, an internal quantum efficiency (IQE) is wanted to be high. However, it is also preferable to keep a ‘parasitic’ luminescence from QB (both near band edge and yellow band) as low as possible. Therefore, we chose the following fitness function:

$$F = IQE^{1.5} \frac{R_{QW}}{R_{barrier}} \quad (1)$$

where  $R_{QW}$  and  $R_{barrier}$  are the radiative recombination rates in the QWs and QBs, respectively. The power of 1.5 shows the higher relative importance of  $IQE$  over the ratio of recombination rates.

First, in order to calibrate the model, a set of samples with uniformly doped QBs grown by metalorganic vapor phase epitaxy was investigated by photoluminescence, and the structures of the corresponding design were simulated. For simplicity, we used uniform generation rate of  $\sim 10^{23} \text{ cm}^{-3}\text{s}^{-1}$  (weak excitation regime). The maximum value  $F$  achieved is 6.3 ( $IQE=0.323$ ,  $R_{QW}/R_{barrier}=34.3$ ) for Si doping of  $2.2 \times 10^{18} \text{ cm}^{-3}$ , while  $F$  dramatically decreases for both lower and higher concentrations of Si (Fig. 2). Next, GA optimization was performed as follows. Optimization started with 21 structures with randomly assigned Si density in each sublayer. Then, 6 structures with the highest values of the fitness function were selected, and uniform crossover operator was applied pairwise to generate 15 new offspring. Additionally, one or two arbitrary genes of each offspring ‘mutated’, i.e. a random Si density was assigned. Thus, 6 old and 15 new specimens formed a new generation, and the process repeated.

After 100 generations, the best  $F$  achieved was 7.665 with almost the same  $IQE=0.333$  and  $R_{QW}/R_{barrier}=40.0$ , so the optimized structure had a slightly higher  $IQE$  and suppressed luminescence from GaN barrier layers. Figure 3 shows the total and ionized Si concentration in the best uniformly doped and the optimized structure. As one can see, they differ significantly. In the optimized structure, there is a thin highly doped region under the QW. As the distance to the upper QW increases, Si concentration gradually decreases to the minimum allowed value of  $1 \times 10^{17} \text{ cm}^{-3}$ . On the one hand, such nonuniform Si profile provides high free electron concentration in QWs (and, therefore, high radiative recombination rate in QWs), and enhanced carrier transport due to higher mobility and smooth band edges and reduced recombination due to low free electron concentration in the barrier layers on the other hand. The total Si concentration in the barrier layer is reduced by 2.6 times, which could be beneficial in terms of crystal quality of the grown layer.

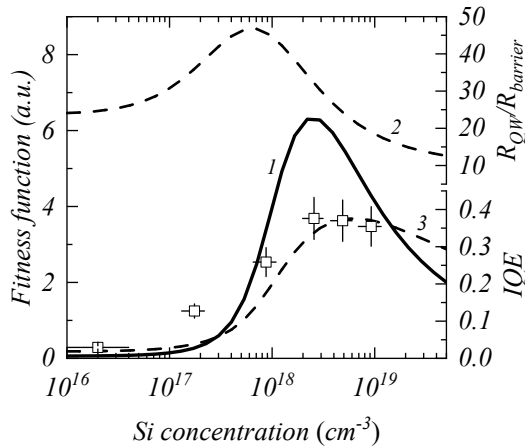


Fig. 2.  $F$  (1),  $R_{QW}/R_{barrier}$  (2) and  $IQE$  (3) vs. uniform Si doping concentration. Symbols are experimental PL intensities (in arbitrary unit).

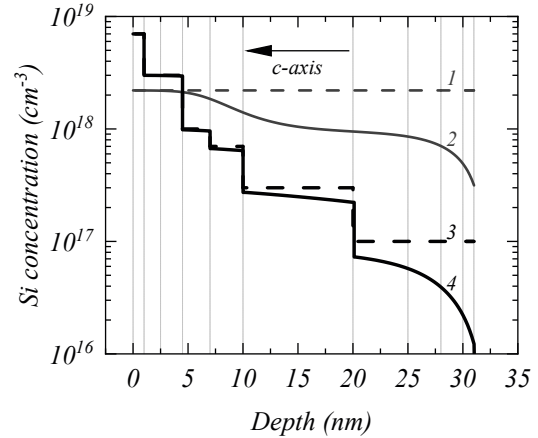


Fig. 3. Total and ionized silicon concentrations in the barrier layer for uniformly doped (1 and 2) and optimized structures (3 and 4, respectively).

## Conclusion

In this study, a genetic algorithm was successfully employed to optimize Si doping profile of luminescent InGaN-based multiple-quantum well heterostructures. It was shown that, in optimized structure with a gradually changing doping profile, a ‘parasitic’ luminescence from GaN barrier layers could be suppressed, while an internal quantum efficiency remained the same as that of the best uniformly doped structure. Moreover, the optimized structure has lower total dopant concentration, which could be beneficial in terms of crystal quality. Any additional parameters could be used as genes (e.g., Al or In molar fraction or thickness of the layers), and any dependencies of mobilities, lifetimes, recombination coefficients, etc. or other fitness function could be easily implemented.

## REFERENCES

1. Genetic algorithm – Wikipedia. URL: [https://en.wikipedia.org/wiki/Genetic\\_algorithm](https://en.wikipedia.org/wiki/Genetic_algorithm). Accessed April 04, 2022.
2. Zhu D., Schubert M. F., Cho J., Schubert E. F., Crawford M. H., Koleske D. D., Shim H., Sone C., Genetic algorithm for innovative device designs in high-efficiency III-V nitride light-emitting diode, *Applied Physics Express*, 5 (1) (2012) 012102.
3. Kim D. Y., Lin G.-B., Hwang S., Park J. H., Meyaard D., Schubert E. F., Ryu H.-Y., Kim. J. K., Polarization-engineered high-efficiency GaInN light-emitting diodes optimized by genetic algorithm, *IEEE Photonics Journal*, 7 (1) (2015) 1–9.
4. Pasaro A., Tanaka R. Y., Muraro A., Viera G. S., Abe N. M., Self-consistent optimization of multi-quantum well structures by a genetic algorithm, *IEEE Transactions on Magnetics*, 46 (8) (2010) 2759–2762.
5. Filoche M., Piccardo M., Wu Y.-R., Li C.-K., Weisbuch C., Mayboroda S., Localization landscape theory of disorder in semiconductors. I. Theory and modeling, *Physical Review B*, 95 (14) (2017) 144204.
6. Mnatsakanov T. T., Levinstein M. E., Pomortseva L. I., Yurkov S. N., Simin G. S., Asif Khan M., Carrier mobility model for GaN, *Solid-State Electronics*, 47 (1) (2003) 111–115.
7. Karpov S. Yu., Makarov Yu. N., Dislocation effect on light emission efficiency in gallium nitride, *Applied Physics Letters*, 81 (25) (2002) 4721–4723.
8. Jayapalan J., Skromme B. J., Vaudo R. P., Phanse V. M., Optical spectroscopy of Si-related donor and acceptor levels in Si-doped GaN grown by hydride vapor phase epitaxy, *Applied Physics Letters*, 73 (9) (1998) 1188–1190.
9. DDCC-1D – Optoelectronic Device Simulation Laboratory. URL: <http://yrwu-wk.ee.ntu.edu.tw/index.php/ddcc-1d>. Accessed April 04, 2022.

## THE AUTHORS

**ARTEEV Dmitri S.**  
ArteevDS@mail.ioffe.ru  
ORCID: 0000-0003-4447-8789

**SAKHAROV Alexei V.**  
Val@beam.ioffe.ru

**NIKOLAEV Andrey E.**  
Aen@mail.ioffe.ru

**ZAVARIN Evgenii E.**  
EZavarin@mail.ioffe.ru  
ORCID: 0000-0001-8380-3172

**TSATSULNIKOV Andrey F.**  
Andrew@beam.ioffe.ru  
ORCID: 0000-0002-5078-8946

**USTINOV Victor M.**  
Vmust@beam.ioffe.ru

*Received 29.07.2022. Approved after reviewing 11.08.2022. Accepted 17.08.2022.*

Conference materials

UDC 538.958

DOI: <https://doi.org/10.18721/JPM.153.204>

## Investigation of far-field patterns of semiconductor microlasers with an active region based on InGaAs/GaAs quantum well-dots

E. I. Moiseev<sup>1</sup>✉, N. V. Kryzhanovskaya<sup>1</sup>, F. I. Zubov<sup>2</sup>, A. V. Nahorny<sup>3</sup>,  
B. D. Urmanov<sup>3</sup>, N. A. Fominykh<sup>1</sup>, K. A. Ivanov<sup>1</sup>, S. A. Mintairov<sup>4</sup>,  
N. A. Kalyuzhnyy<sup>4</sup>, M. M. Kulagina<sup>4</sup>, M. V. Maximov<sup>2</sup>, A. E. Zhukov<sup>1</sup>

<sup>1</sup> HSE University, St Petersburg, Russia;

<sup>2</sup> Alferov University, St Petersburg, Russia;

<sup>3</sup> Institute of Physics of NAS of Belarus, Minsk, Belarus;

<sup>4</sup> Ioffe Institute, St Petersburg, Russia

✉ [emoiseev@hse.ru](mailto:emoiseev@hse.ru)

**Abstract.** This paper is the first study of the far-field patterns of semiconductor microlasers with an active region based on In<sub>0.4</sub>Ga<sub>0.6</sub>As/GaAs quantum well-dots. A theoretical model describing the far-field radiation pattern is developed. It is shown that in the vertical direction the radiation pattern has a narrow beam divergence (the most of the power is confined to 20 degrees) and is characterized by narrow lobes, the position and number of which are determined by the height of the waveguide relative to the substrate. It is found that in the horizontal direction, each optical mode has its own far-field pattern. A change in the injection current leads to a change in the dominant optical mode and in the far-field pattern. Deviation of the resonator shape from the circular one leads to chaotization of the peripheral modes and generation through more profound WGM-like modes. Reducing the diameter of the resonator leads to a reduction in the number of lobes of the horizontal radiation pattern.

**Keywords:** Microlaser, quantum dots, radiation pattern, directional output, emission field control, far-field emission

**Funding:** The study of the far fields was funded by RFBR and BRFR project number 20-52-04016, the development and modeling of the epitaxial structure are supported by the Basic Research Program at the National Research University Higher School of Economics (HSE University), mounting and soldering of samples are supported by the Ministry of Science and Higher Education of the Russian Federation under project #0791-2020-0002.

**Citation:** Moiseev E. I., Kryzhanovskaya N. V., Zubov F. I., Nahorny A. V., Urmanov B. D., Fominykh N.A., Ivanov K. A., Mintairov S. A., Kalyuzhnyy N. A., Kulagina M. M., Maximov M. V., Zhukov A. E., Investigation of far-field patterns of semiconductor microlasers with an active region based on InGaAs/GaAs quantum well-dots, St. Petersburg State Polytechnical University Journal. Physics and Mathematics. 15 (3.2) (2022) 25–30. DOI: <https://doi.org/10.18721/JPM.153.204>

This is an open access article under the CC BY-NC 4.0 license (<https://creativecommons.org/licenses/by-nc/4.0/>)

Материалы конференции

УДК 538.958

DOI: <https://doi.org/10.18721/JPM.153.204>

## Исследование картин дальнего поля полупроводниковых микролазеров с активной областью на основе квантовых ям-точек InGaAs/GaAs

Э. И. Моисеев<sup>1</sup>✉, Н. В. Крыжановская<sup>1</sup>, Ф. И. Зубов<sup>2</sup>, А. В. Нагорный<sup>3</sup>, Б. Д. Урманов<sup>3</sup>, Н. А. Фоминых<sup>1</sup>, К. А. Иванов<sup>1</sup>, С. А. Минтаиров<sup>4</sup>,  
Н. А. Калюжный<sup>4</sup>, М. М. Кулагина<sup>4</sup>, М. В. Максимов<sup>2</sup>, А. Е. Жуков<sup>1</sup>

<sup>1</sup> НИУ ВШЭ, Санкт-Петербург, Россия;

<sup>2</sup> Алферовский университет, Санкт-Петербург, Россия;

<sup>3</sup> Институт физики НАН Беларуси, Минск, Белоруссия;

<sup>4</sup> ФТИ им. А.Ф. Иоффе, Санкт-Петербург, Россия

✉ emoiseev@hse.ru

**Аннотация.** В работе впервые проведено исследование картин дальнего поля полупроводниковых микролазеров с активной областью на основе квантовых ям-точек  $\text{In}_{0.4}\text{Ga}_{0.6}\text{As}/\text{GaAs}$ . Разработана теоретическая модель, описывающая картину излучения в дальней зоне. Показано, что в вертикальном направлении диаграмма направленности имеет узконаправленный характер (основная часть мощности ограничивается в диапазоне 20 градусов) и характеризуется узкими лепестками направленности, положение и количество которых определяется высотой волновода относительно подложки. Установлено, что в горизонтальном направлении каждой оптической моде соответствует своя картина дальнего поля. Изменение тока накачки приводит к смене доминантной оптической моды и картины дальнего поля. Отклонение формы резонатора от круговой приводит к хаотизации периферийных мод и генерации через более углубленные МШГ-подобные. Уменьшение диаметра резонатора позволяет уменьшить количество лепестков горизонтальной диаграммы направленности.

**Ключевые слова:** микролазер, квантовые точки, диаграмма направленности, направленный вывод излучения, управление полями излучения, дальнее поле излучения

**Финансирование:** Исследование дальних полей выполнено при финансовой поддержке РФФИ в рамках научного проекта № 20-52-04016, разработка и моделирование эпитаксиальной структуры выполнены при поддержке Программы фундаментальных исследований НИУ ВШЭ, монтаж и пайка приборов выполнены при поддержке Министерством науки и высшего образования Российской Федерации по проекту № 0791-2020-0002.

**Ссылка при цитировании:** Моисеев Э. И., Крыжановская Н. В., Зубов Ф. И., Нагорный А. В., Урманов Б. Д., Фоминых Н. А., Иванов К. А., Минтаиров С. А., Калюжный Н. А., Кулагина М. М., Максимов М. В., Жуков А. Е. Исследование картин дальнего поля полупроводниковых микролазеров с активной областью на основе квантовых ям-точек  $\text{InGaAs}/\text{GaAs}$  // Научно-технические ведомости СПбГПУ. Физико-математические науки. 2022. Т. 15. № 3.2. С. 25–30. DOI: <https://doi.org/10.18721/JPM.153.204>

Статья открытого доступа, распространяемая по лицензии CC BY-NC 4.0 (<https://creativecommons.org/licenses/by-nc/4.0/>)

## Introduction

Semiconductor microlasers with a resonator supporting whispering gallery modes (WGM) are considered as promising elements for implementation of optical communication systems on a chip, detectors and biosensors with extremely high sensitivity [1], [2] and for fundamental research in quantum electrodynamics, in particular, realization of a strong coupling regime [3], open chaotic systems [4] and non-hermitian quantum mechanics [5].

Recently, results have been presented for microdisk lasers with an active region based on  $\text{In}_{0.4}\text{Ga}_{0.6}\text{As}/\text{GaAs}$  quantum well-dots (QWDs) [6] which demonstrate high output power of optical emission [7], the possibility of laser generation at elevated temperatures and optical data transmission with a speed up to 10 Gbit/sec [8]. The rotational symmetry of the resonator should lead to isotropic emission of radiation into free space. However, the spectral-angular dependences of the emission intensity in the far field are much more complicated as shown in this work.

## Materials and Methods

An epitaxial structure was grown by the MOCVD method on an n-doped GaAs (100) substrate. The active region represents 5 layers of InGaAs QWDs separated with 40 nm thick GaAs spacers. The active region was deposited in the middle of a 0.8  $\mu\text{m}$  thick GaAs waveguide layer confined



from both sides with AlGaAs claddings. Microdisk resonators with a height of about 5.5  $\mu\text{m}$  and diameters of 30, 50, 100 and 200  $\mu\text{m}$  were formed using photolithography and plasma chemical etching. AgMn/NiAu (AuGe/Ni/Au) metallization was used to form ohmic contacts to p+ GaAs cap layer (n+ substrate, respectively).

The GaAs wafer with microlasers was split into separate chips with single microlasers. The chips with microlasers were mounted on a heat sink. A 17.5  $\mu\text{m}$  diameter gold wire was used to electrically connect the microlaser to the contact pad (Fig. 1, *a*). A stabilized Keithley 2400 source was used for current pumping of the structures. The spectral-angle patterns of the far field were measured on a specialized automatic stand. The electroluminescence emission was injected into the optical fiber through an adapter. The collimator aperture was limited by an aperture to control the angular resolution ( $0.3^\circ$ ). The measurements were performed at room temperature and CW mode.

## Results and Discussion

The electroluminescence spectra of the microlasers contain narrow lines and a wide band corresponding to the spontaneous emission of the  $\text{In}_{0.4}\text{Ga}_{0.6}\text{As}/\text{GaAs}$  active region. With an increase in the pump current, the onset of lasing is observed (Fig. 1, *b*).

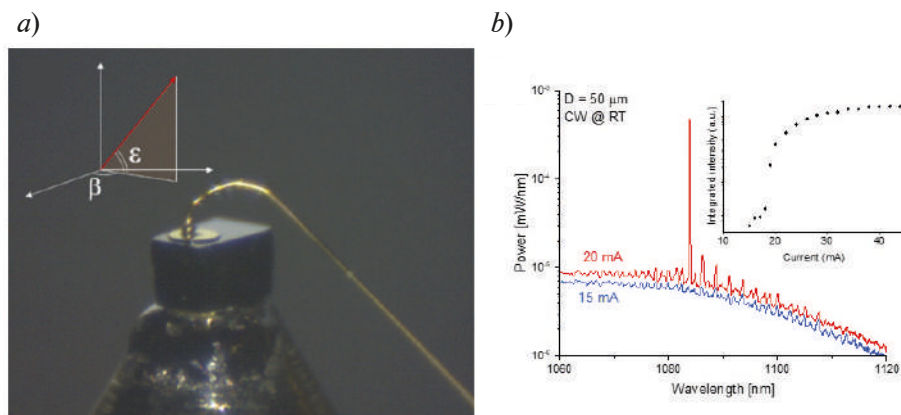


Fig. 1. Image of a heat sink-mounted chip with a 100  $\mu\text{m}$  microlaser (*a*); electroluminescence spectra of a 50  $\mu\text{m}$  microlaser below and above the threshold current ( $I_{\text{th}} = 20 \text{ mA}$ ) (*b*); inset: integrated line intensity as a function of pump current

Figure 2, *a* shows the angular distribution of the field intensity in the polar angle (in vertical direction) below and above the threshold current. The dependences show that the light is primarily emitted in the lateral direction and has an intensity modulation both below and above the threshold current.

Modeling of the vertical radiation pattern showed that changing the height of the active region relative to the surface of the substrate leads to a change in the number and position of the lobes of the radiation pattern (Fig. 2, *b*) and is caused by interference of radiation coming from the waveguide with radiation reflected from the surface of the substrate. In this case, the narrow-directional type of the vertical radiation pattern is retained, and the main part of the power is limited in the angular range of 20 degrees.

The horizontal (in-plane) radiation pattern below the threshold current is isotropic. However, above the threshold current includes modulation of the emission intensity (Fig. 3 *a, b*). The number of lobes of the radiation pattern increases as the diameter of the resonator increases. The experimentally observed number of peaks turns out to be much smaller than the number of the intensity maxima expected for the whispering gallery mode of the lowest radial order. For example, for a microlaser with a diameter of 30  $\mu\text{m}$ , 144 maxima of intensity are observed, while about 600 are expected. This discrepancy is probably due to the effect of frequency synchronization of spatial modes [9]-[11] and the formation of non-classical WGM in a resonator with a non-ideal form [12]-[13]. Numerical simulations of far-field patterns for Limaçon-shaped microlasers show that deviation of the resonator shape from the ideal (axially symmetric) one can lead to

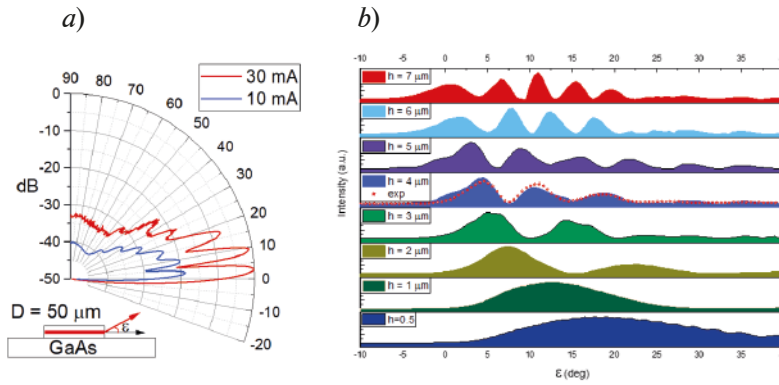


Fig. 2. Vertical directional pattern at different pump currents (a) and different heights of the active region relative to the substrate – model (solid lines) and experiment (dotted line) (b)

chaotization of peripheral modes and formation of WGM-like modes, which are characterized by a smaller number of directional lobes.

It was found that each optical mode corresponds to a different far-field pattern. For a microlaser with a resonator diameter of 50 μm, when the pump current is increased from 30 to 49 mA, a spectral long-wavelength shift of the laser line ( $\lambda_1$ ) occurs due to heating of the structure. In this case, the position of the lobes of the radiation pattern does not change (Fig. 3 c, d). At a pump current of 51 mA, the dominant mode is changed (from  $\lambda_1$  to  $\lambda_2$ ), which leads to a change in the position of the lobes of the horizontal radiation pattern.

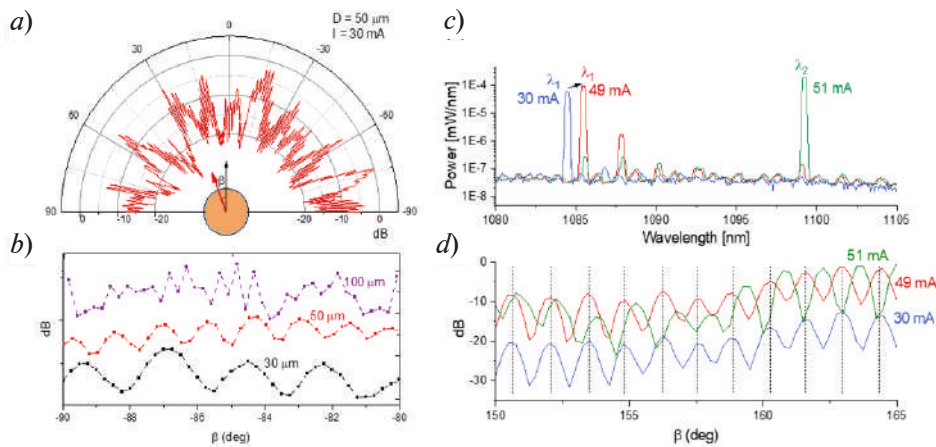


Fig. 3. Horizontal radiation pattern for a 50 μm microlaser (a) and results for structures with 30, 50, and 100 μm resonator diameters (b); electroluminescence spectra (c) and horizontal radiation pattern at different pump currents (d)

### Conclusion

In this work, we studied, for the first time, the far-field patterns of semiconductor microlasers with an active region based on  $\text{In}_{0.4}\text{Ga}_{0.6}\text{As}/\text{GaAs}$  quantum well-dots. A theoretical model describing the far-field radiation pattern is developed. It is shown that in the vertical direction the radiation pattern has a narrow directionality (the main part of the power is confined to 20 degrees) and is characterized by narrow lobes, the position and number of which are determined by the height of the waveguide relative to the substrate, which is determined during the fabrication of the structures.

It was found that in the horizontal direction, each optical mode corresponds to a different far-field pattern. A change in the pump current leads to a change in the dominant optical mode and the far-field pattern. Deviation of the resonator shape from the circular leads to chaotization of the peripheral modes and generation through more profound WGM-like, which are characterized by a smaller number of directional lobes. Reducing the diameter of the resonator leads to a decrease in the number of lobes of the horizontal radiation pattern.



## REFERENCES

1. He L., Özdemir Ş.K., Zhu J., Kim W., Yang L., Detecting single viruses and nanoparticles using whispering gallery microlasers // *Nature Nanotechnology*. 2011. № 7(6). C. 428–432. DOI:10.1038/nnano.2011.99.
2. Toropov N., Cabello G., Serrano M.P., Gutha R.R., Rafti M., Vollmer F., Review of biosensing with whispering-gallery mode lasers // *Light: Science & Applications*. 2021. № 1(10). C. 42. DOI:10.1038/s41377-021-00471-3.
3. Gayral B., Gérard J.-M., Sermage B., Lemaitre A., Dupuis C., Time-resolved probing of the Purcell effect for InAs quantum boxes in GaAs microdisks // *Applied Physics Letters*. 2001. № 19(78). C. 2828–2830.
4. Nöckel J.U., Stone A.D., Ray and wave chaos in asymmetric resonant optical cavities // *Nature*. 1997. № 6611(385). C. 45–47. DOI:10.1038/385045a0.
5. Lee S.-B., Yang J., Moon S., Lee S.-Y., Shim J.-B., Kim S.W., Lee J.-H., An K., Observation of an Exceptional Point in a Chaotic Optical Microcavity // *Physical Review Letters*. 2009. № 13(103). C. 134101. DOI:10.1103/PhysRevLett.103.134101.
6. Maximov M.V., Nadtochiy A.M., Mintairov S.A., Kalyuzhnyy N.A., Kryzhanovskaya N.V., Moiseev E.I., Gordeev N.Y., Shernyakov Y.M., Payusov A.S., Zubov F.I., Nevedomskiy V.N., Rouvimov S.S., Zhukov A.E., Light Emitting Devices Based on Quantum Well-Dots // *Applied Sciences*. 2020. № 3(10). C. 1038. DOI:10.3390/app10031038.
7. Moiseev E., Kryzhanovskaya N., Maximov M., Zubov F., Nadtochiy A., Kulagina M., Zadiranov Y., Kalyuzhnyy N., Mintairov S., Zhukov A., Highly efficient injection microdisk lasers based on quantum well-dots // *Optics Letters*. 2018. № 19(43). C. 4554. DOI:10.1364/OL.43.004554.
8. Zubov F., Maximov M., Kryzhanovskaya N., Moiseev E., Muretova M., Mozharov A., Kaluzhnyy N., Mintairov S., Kulagina M., Ledentsov N., Chorchos L., Ledentsov N., Zhukov A., High speed data transmission using directly modulated microdisk lasers based on InGaAs/GaAs quantum well-dots // *Optics Letters*. 2019. № 22(44). C. 5442. DOI:10.1364/OL.44.005442.
9. Choi M., Shinohara S., Harayama T., Dependence of far-field characteristics on the number of lasing modes in stadium-shaped InGaAsP microlasers // *Optics Express*. 2008. № 22(16). C. 17554. DOI:10.1364/oe.16.017554.
10. Harayama T., Sunada S., Ikeda K.S., Theory of two-dimensional microcavity lasers // *Physical Review A*. 2005. № 1(72). C. 013803. DOI:10.1103/PhysRevA.72.013803.
11. Kryzhanovskaya N. V., Zhukov A.E., Nadtochy A.M., Maximov M. V., Moiseev E.I., Kulagina M.M., Savelev A. V., Arakcheeva E.M., Lipovskii A.A., Zubov F.I., Kapsalis A., Mesaritakis C., Syvridis D., Mintairov A., Livshits D., Room-temperature lasing in microring cavities with an InAs/InGaAs quantum-dot active region // *Semiconductors*. 2013. № 10(47). C. 1387–1390. DOI:10.1134/S1063782613100187.
12. Song Q., Fang W., Liu B., Ho S.-T., Solomon G.S., Cao H., Chaotic microcavity laser with high quality factor and unidirectional output // *Physical Review A*. 2009. № 4(80). C. 041807. DOI:10.1103/PhysRevA.80.041807.
13. Alekseev P.A., Dunaevskiy M.S., Monakhov A.M., Dudelev V. V., Sokolovskii G.S., Arinero R., Teissier R., Baranov A.N., Half-disk laser: insight into the internal mode structure of laser resonators // *Optics Express*. 2018. № 11(26). C. 14433. DOI:10.1364/OE.26.014433.

## THE AUTHORS

**MOISEEV Eduard I.**

emoiseev@hse.ru

ORCID: 0000-0003-3686-935X

**ZHUKOV Alexey E.**

aezhukov@hse.ru

ORCID: 0000-0002-4579-0718

**KRYZHANOVSKAYA Natalia V.**

nkryzhanovskaya@hse.ru

ORCID: 0000-0002-4945-9803

**MAXIMOV Mikhail V.**

maximov@beam.ioffe.ru

ORCID: 0000-0002-9251-226X

**ZUBOV Fedor I.**

fzubov@hse.ru

ORCID: 0000-0002-3926-8675

**IVANOV Konstantin A.**

kivanov@hse.ru

ORCID: 0000-0003-2165-1067

**FOMINYKH Nikita A.**

nfominykh@hse.ru

ORCID: 0000-0003-3919-6410

**KALYUZHNYI Nikolay A.**

Nickk@mail.ioffe.ru

ORCID: 0000-0001-8443-4663

**KULAGINA Marina M.**

Marina.Kulagina@mail.ioffe.ru

ORCID: 0000-0002-8721-185X

**MINTAIROV Sergey A.**

Mintairov@scell.ioffe.ru

ORCID 0000-0002-6176-6291

**NAHORNY Aliaksey V.**

a.nahorny@ifanbel.bas-net.by

**URMANOV Boris D.**

boris-urmanov@mail.ru

*Received 19.07.2022. Approved after reviewing 04.08.2022. Accepted 09.08.2022.*

Conference materials

UDC 681.7.069.24

DOI: <https://doi.org/10.18721/JPM.153.205>

### Ultra-high vacuum formation of silver films for light-emitting tunnel junctions

V. A. Shkoldin <sup>1,2</sup>✉, D. V. Lebedev <sup>1,3,4</sup>, D. V. Permyakov <sup>2</sup>, A. E. Petukhov <sup>3</sup>,  
A. O. Golubok <sup>4</sup>, A. V. Arkhipov <sup>5</sup>, A. K. Samusev <sup>2</sup>, I. S. Mukhin <sup>1,5</sup>

<sup>1</sup> St. Petersburg Academic University, St. Petersburg, Russia;

<sup>2</sup> ITMO University, St. Petersburg, Russia;

<sup>3</sup> St. Petersburg State University, St. Petersburg, Russia;

<sup>4</sup> Institute for analytical instrumentation RAS, St. Petersburg, Russia;

<sup>5</sup> Peter the Great St. Petersburg Polytechnic University, St. Petersburg, Russia

✉ [shkoldin@spbau.ru](mailto:shkoldin@spbau.ru)

**Abstract.** Integrated photonics requires compact electrically driven sources of optical radiation for the use in high-performance integrated circuits with optical interconnections in a chip. Light-emitting tunnel junctions represent a promising option of such nanosized light sources, even if their present quantum efficiency is insufficient for practical implementation. We propose a technique for fabrication of such junctions by ultrahigh vacuum forming of thin silver films. Testing showed a high quality and high optical response of the produced films. Such films can serve as substrates for more complicated tunnel junction structures with yet higher quantum efficiency.

**Keywords:** scanning tunneling microscopy, tunnel contact, emission from a tunnel contact, silver film, photonics, ultrahigh vacuum

**Funding:** This study was funded by Russian Science Foundation, grant number 21-79-10346.

**Citation:** Shkoldin V. A., Lebedev D. V., Permyakov D. V., Petukhov A. E., Golubok A. O., Arkhipov A.V., Samusev A. K., Mukhin I. S., Ultra-high vacuum formation of silver films for light-emitting tunnel junctions, St. Petersburg State Polytechnical University Journal. Physics and Mathematics. 15 (3.2) (2022) 31–34. DOI: <https://doi.org/10.18721/JPM.153.205>

This is an open access article under the CC BY-NC 4.0 license (<https://creativecommons.org/licenses/by-nc/4.0/>)

Материалы конференции

УДК 681.7.069.24

DOI: <https://doi.org/10.18721/JPM.153.205>

### Формирование серебряных плёнок в ультра-высоком вакууме для светоизлучающих туннельных контактов

В. А. Школдин <sup>1,2</sup>✉, Д. В. Лебедев <sup>1,3,4</sup>, Д. В. Пермяков <sup>2</sup>,

А. О. Голубок <sup>4</sup>, А. В. Архипов <sup>5</sup>, А. К. Самусев <sup>2</sup>, И. С. Мухин <sup>1,5</sup>

<sup>1</sup> Академический университет имени Ж.И. Алфёрова РАН, Санкт-Петербург, Россия;

<sup>2</sup> Университет ИТМО, Санкт-Петербург, Россия;

<sup>3</sup> Санкт-Петербургский государственный университет кино и телевидения, Санкт-Петербург, Россия;

<sup>4</sup> Институт аналитического приборостроения РАН, Санкт-Петербург, Россия;

<sup>5</sup> Санкт-Петербургский политехнический университет Петра Великого, Санкт-Петербург, Россия

✉ [shkoldin@spbau.ru](mailto:shkoldin@spbau.ru)

**Аннотация.** Излучающий туннельный контакт является перспективной основой для наноразмерных электрически управляемых источников света, но обладает невысокой квантовой эффективностью для использования в фотонике. Предложен метод создания серебряных плёнок в ультра-высоком вакууме, дающих высокий оптический отклик в туннельном контакте.

**Ключевые слова:** сканирующая туннельная микроскопия, туннельный контакт, излучение из туннельного контакта, серебряная плёнка, фотоника

**Финансирование:** Работа выполнена при поддержке Российского Научного Фонда проект № 21-79-10346.

**Ссылка при цитировании:** Школдин В. А., Лебедев Д. В., Пермяков Д. В., Петухов А. Е., Голубок А. О., Архипов А. В., Самусев А. К., Мухин И. С. Формирование серебряных плёнок в ультра-высоком вакууме для светоизлучающих туннельных контактов // Научно-технические ведомости СПбГПУ. Физико-математические науки. 2022. Т. 15. № 3.2. С. 31–34. DOI: <https://doi.org/10.18721/JPM.153.205>

Статья открытого доступа, распространяемая по лицензии CC BY-NC 4.0 (<https://creativecommons.org/licenses/by-nc/4.0/>)

## Introduction

The progress of computing electronics encounters various limitations, such as heat dissipation efficiency and bandwidth of electrical connections. A prospective approach to conquer these problems consists in inclusion of photonic links and photonic computing components into integrated circuits. Present photonics technologies offer many of the necessary components, though the size difference between the modern CMOS electronic components and optical sources represents a bottleneck on the way to their integration [1].

Tunnel junctions provide a promising basis for construction of compact optical sources. The visible and near infrared light emission effect supported by inelastic electron tunneling has been known for about 50 years [2]. The size of the resulting light source is defined by the size of electrical contacts. However, at present the quantum efficiency of such sources remains insufficient for their practical implementation: its typical value is as low as  $10^{-6}$  photons per electron, and further efforts are necessary to increase this figure.

Here we report on our investigation of a method to fabricate clean Ag layers in ultrahigh vacuum (UHV) conditions, which represents an initial step to produce a light-emitting tunnel junctions.

## Experiment

Sample fabrication and characterization were performed in ultrahigh vacuum conditions at the pressure not worse than  $5 \cdot 10^{-9}$  mbar. All processes were conducted in a research modular platform Nanolab, which incorporates a scanning tunneling microscope (STM) Omicron VT AFM XA 50/500 (Scienta Omicron, Germany), equipment for thin film deposition, a low-energy electron diffractometer (LEED) and some other tools. The sample was fabricated on a highest quality vacuum cleaved mica (Ted Pella, USA) serving as a substrate.

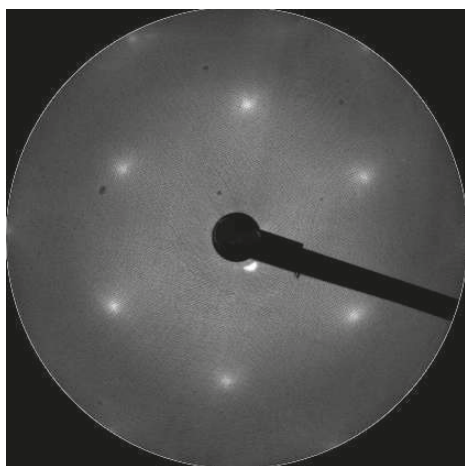


Fig. 1. Low energy electron diffraction pattern from Ag film

The mica plate was installed on a custom-made STM sample holder equipped with an optical lens. The plate was fixed by four screws; preliminary electric contact at its edges was secured with two-component silver-filled epoxy (EPO-TEK H21D). Then the top layer of mica was scratched and covered by a copper tape with an attached copper ring. After transferring the sample into the vacuum chamber, pumping and annealing, the copper tape was removed by pulling the ring with the chamber manipulator. The resulting cleaving exposed a clean mica surface. Then, a 30 nm layer of silver was deposited on the freshly cleaved mica by thermal evaporation. The silver film quality was estimated with the Low Energy Electrons Diffraction (LEED) technique: the bright peaks in the LEED image (Fig. 1) demonstrate its crystallinity.

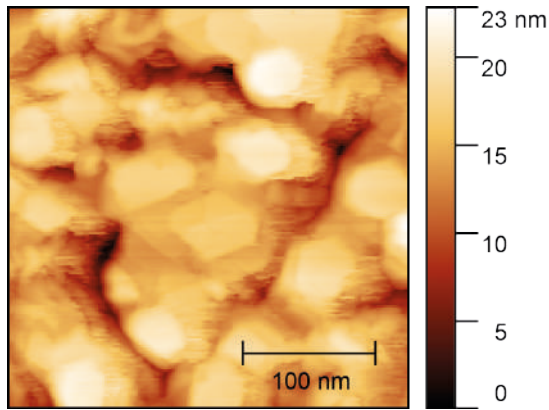


Fig 2. STM image of Ag film

Then the sample was examined by the STM. Surface topography images showed formation of large grains (Fig. 2). Studies of light emission induced by STM current were performed using the optical system described in detail in [3]: the emitted light was directed to a single photon counter ID120 (IDQuantique, Sweden) which work in visible and near infrared regions (400-900 nm). Quantum efficiency of the source based on the tunnel junction between the Ag film surface and a Pt/Ir STM tip was estimated to be about  $2 \cdot 10^{-6}$  photon per electron at  $-2.5$  V bias voltage. This estimate was calculated in the same way as the one in [4]. Notably, the current-voltage characteristics measured during the experiment showed

distinct features around  $\pm 2.5$  V, presumably associated with light emission from the tunnel junction assisted by optical levels [5].

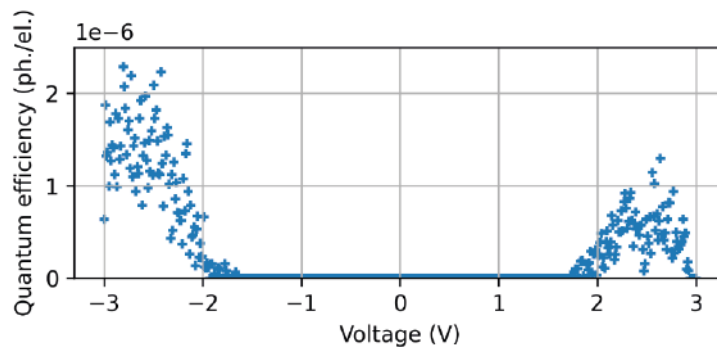


Fig. 3. Estimated quantum efficiency of tunnel junction between the silver film and Pt/Ir STM tip

### Conclusion

The tested silver film has a relatively high quantum efficiency, about  $2 \cdot 10^{-6}$  photon/el., as compared to the one of the previously studied gold films, which had efficiencies of about  $9 \cdot 10^{-7}$  photon/el.. This developed technique and material can be used for producing more complicated tunnel junctions coupled to nanoantennas.

### Acknowledgments

This work was supported by the Russian Science Foundation (project no. 21-79-10346 of the Russian Science Foundation). The studies were carried out using the equipment of the St. Petersburg State University Research Park “Centre for Physical methods of surface investigation”.

### REFERENCES

1. Parzefall M., Novotny L., Optical antennas driven by quantum tunneling: a key issues review. Reports on Progress in Physics. 11(82) (2019) 112401.
2. Lambe J., McCarthy S. L., Light Emission from Inelastic Electron Tunneling . Phys. Rev. Lett. 14(37) (1976) 923–925.
3. Lebedev D. V., Mozharov A. M., Bolshakov A. D., Shkoldin V. A., Permyakov D. V., Golubok A. O., Samusev A. K., Mukhin I. S., Indirect Detection of the Light Emission in the Local Tunnel Junction . physica status solidi (RRL) – Rapid Research Letters. 3(14) (2020) 1900607.
4. Lebedev D. V., Shkoldin V. A., Mozharov A. M., Larin A. O., Permyakov D. V., Samusev A. K., Petukhov A. E., Golubok A. O., Arkhipov A. V., Mukhin I. S., Nanoscale Electrically Driven Light Source Based on Hybrid Semiconductor / Metal Nanoantenna. The Journal of Physical Chemistry Letters. 20(13) (2022) 4612–4620.

5. Lebedev D. V., Shkoldin V. A., Mozharov A. M., Golubok A. O., Permyakov D. V., Samusev A. K., Mukhin I. S., Indirect observation of the light emission in the tunnel junction with metal nanodisk. AIP Conference Proceedings. 2300 (2020) 020080.

#### THE AUTHORS

**SHKOLDIN Vitaliy A.**

shkoldin@spbau.ru

ORCID: 0000-0002-1014-5401

**LEBEDEV Denis V.**

denis.v.lebedev@gmail.com

ORCID: 0000-0001-5389-2899

**PERMYAKOV Dmitry V.**

d.permyakov@metalab.ifmo.ru

ORCID: 0000-0003-2708-9140

**PETUKHOV Anatoliy E.**

anatoliy.petukhov@spbu.ru

ORCID: 0000-0001-9362-3589

**GOLUBOK Alexander O.**

aogolubok@mail.ru

ORCID: 0000-0001-9970-9172

**ARKHIPOV Alexander V.**

arkhipov@rphf.spbstu.ru

**SAMUSEV Anton K.**

a.samusev@metalab.ifmo.ru

ORCID: 0000-0002-3547-6573

**MUKHIN Ivan S.**

imukhin@yandex.ru

ORCID: 0000-0001-9792-045X

*Received 12.08.2022. Approved after reviewing 14.09.2022. Accepted 14.09.2022.*

Conference materials

UDC 538.9

DOI: <https://doi.org/10.18721/JPM.153.206>

### **Effect of heat dissipation on the current-voltage characteristics of ultrathin NbN nanowires**

M. D. Soldatenkova<sup>1,2</sup>✉, E. M. Baeva<sup>1</sup>, A. D. Triznova<sup>1</sup>, N. A. Titova<sup>1</sup>,  
P. I. Zolotov<sup>1</sup>, A. I. Kolbatova<sup>1,2</sup>, G. N. Goltsman<sup>1,2</sup>

<sup>1</sup> Moscow Pedagogical State University, Moscow, Russia;

<sup>2</sup> National Research University Higher School of Economics, Moscow, Russia

✉ [mdsoldatenkova@edu.hse.ru](mailto:mdsoldatenkova@edu.hse.ru)

**Abstract.** The nonlinear current-voltage characteristics of niobium nitride (NbN) nanowires have been studied experimentally at the vicinity of the resistive transition. We show that the nonlinear behavior of the current-voltage characteristics is in agreement with the thermal model considered the heat dissipation in NbN samples.

**Keywords:** superconductivity, superconducting transition, thermal activated phase-slips

**Funding:** This study was funded in the framework of the Russian Science Foundation grant No. 19-72-10101.

**Citation:** Soldatenkova M. D., Baeva E. M., Triznova A. D., Titova N. A., Zolotov P. I., Kolbatova A. I., Goltsman G. N., Effect of heat dissipation on the current-voltage characteristics of ultrathin NbN nanowires, St. Petersburg State Polytechnical University Journal. Physics and Mathematics. 15 (3.2) (2022) 35–40. DOI: <https://doi.org/10.18721/JPM.153.206>

This is an open access article under the CC BY-NC 4.0 license (<https://creativecommons.org/licenses/by-nc/4.0/>)

Материалы конференции

УДК 538.9

DOI: <https://doi.org/10.18721/JPM.153.206>

### **Влияние эффекта разогрева на вольт-амперные характеристики в ультратонких нанопроводах NbN**

М. Д. Солдатенкова<sup>1,2</sup>✉, Э. М. Баева<sup>1</sup>, А. Д. Тризнава<sup>1</sup>, Н. А. Титова<sup>1</sup>,  
Ф. И. Золотов<sup>1</sup>, А. И. Колбатова<sup>1,2</sup>, Г. Н. Гольцман<sup>1,2</sup>

<sup>1</sup> Московский Педагогический Государственный Университет, Москва, Россия;

<sup>2</sup> Национальный Исследовательский Университет Высшая Школа Экономики, Москва, Россия

✉ [mdsoldatenkova@edu.hse.ru](mailto:mdsoldatenkova@edu.hse.ru)

**Аннотация.** Экспериментально исследованы нелинейные вольт-амперные характеристики нанопроволок нитрида ниобия NbN в окрестности резистивного перехода. Показано, что нелинейное поведение вольт-амперных характеристик полностью согласуется с тепловой моделью релаксации тепла в NbN.

**Ключевые слова:** сверхпроводимость, сверхпроводящий переход, термические проскальзывания фазы

**Финансирование:** Работа выполнена в рамках гранта Российского научного фонда № 19-72-10101.

**Ссылка при цитировании:** Солдатенкова М. Д., Баева Э. М., Тризнава А. Д., Титова Н. А., Золотов Ф. И., Колбатова А. И., Гольцман Г. Н. Влияние эффекта разогрева на вольт-амперные характеристики в ультратонких нанопроводах NbN // Научно-технические ведомости СПбГПУ. Физико-математические науки. 2022. Т. 15. № 3.2. С. 35–40. DOI: <https://doi.org/10.18721/JPM.153.206>

Статья открытого доступа, распространяемая по лицензии CC BY-NC 4.0 (<https://creativecommons.org/licenses/by-nc/4.0/>)

## Introduction

Superconducting NbN nanowires have attracted a lot of interest as elements of superconducting circuits, detectors, and high frequency devices [1]. For instance, single photon detectors based on long superconducting NbN nanowires (SNSPD) [2] are extensively used in optical and infrared quantum technologies due to their ultimately high response speed, high system detection efficiency, and low dark count level [3]. One of the key parameters of SNSPDs, the dark count rate, is associated with the thermal activated phase slips (TAPS) [4]. Meanwhile, signatures of TAPS are observed in the temperature dependences of resistance [5,6] and the current-voltage (IV) characteristics [7,6] of narrow NbN wires. However, as shown in [5] only a part of the IV curve at low bias can be described by the TAPS model, and the non-linearity of the IV curve at high bias appears to be of thermal origin. Effect of joule heating on IV curves of superconductors has been known for a long time [8-10], but at the same time such an interpretation of the IV curves is complicated by lack of an accurate information about heat dissipation in thin wires and by presence of electronic inhomogeneities due to strong disorder in NbN films.

In this paper we study the effect of joule heating on ultrathin NbN nanowires at the resistive transition. We measure the current-voltage characteristics at the low-temperature part of the resistive transition. The data is analyzed in terms of the TAPS and thermal models. The latter model considers influence of heat dissipation on nonlinearities of the IV-curves in a one-dimensional (1D) NbN wire. As a key parameter for the thermal model, we take the Kapitza resistance [11], which has been measured via the noise thermometry above the superconducting transition. Our results show that the thermal model can adequately describe the nonlinearity of the IV curves at the resistive transition.

## Materials and Methods

The measurements described in this paper are performed on NbN wires, patterned from ultrathin NbN film deposited by RF magnetron sputtering on r-cut sapphire ( $\text{Al}_2\text{O}_3$ ) substrate. After deposition, NbN film is covered *in situ* by a 5-nm thick Si layer. The film has a thickness  $d \approx 3.5$  nm, the critical temperature  $T_c$  of 10 K, and the normal-state resistivity  $\rho$  of  $260 \mu\Omega \cdot \text{cm}$ . Finally, the film is patterned into two-contact bridges using the electron-beam lithography, the plasma-chemical etching and thermal evaporation of Ti/Au contact pads. The image of a representative sample obtained with the scanning electron microscope (SEM) is presented in (Fig. 1, a). The length  $L$ , the width  $w$  of samples A and B, and the normal-state resistance  $R$  at 20 K and at 300 K are listed in Table 1.

Table 1

Parameters of the studied NbN nanowires

	$w$ , nm	$L$ , $\mu\text{m}$	$R_{300\text{K}}$ , k $\Omega$	$R_{20\text{K}}$ , k $\Omega$	$T_c$ , K
A	70	4	35	43.73	10.4
B	70	4	35.84	43.82	10.2

Measurements of the resistance, the current-voltage characteristics, and voltage fluctuations are performed using of a cryogenic  $^4\text{He}$  dipstick. In this experiment, the bath temperature  $T_b$  is controlled by a position of the dipstick in the liquid  $^4\text{He}$  dewar. Resistance measurements, shown schematically in (Fig. 1, a), are performed with the standard lock-in technique in a quasifour-probe configuration. The bias current is varied in the range of 1 – 10 nA at the modulation frequency of 8 Hz. The output AC voltage signal is amplified by a SR560 preamplifier and measured with a SR830 lock-in. The experimental setup is designed using stainless steel coaxial lines and low-pass resistor-capacitor filters. For each of the devices the current-voltage characteristics are measured at the current-biased regime. The output DC voltage signal is amplified by a SR560 preamplifier and measured with a Keysight 34461A multimeter.

To determine the mechanism of heat dissipation in the studied samples, we measure the noise temperature  $T_N$  at the normal state above the superconducting transition using the noise thermometry [11]. Figure 1, *a* shows schematic of the experimental setup. Above  $T_c$ , the sample is biased with dc current  $I$ , and the excess current noise from the sample is passed through the resonance tank circuit at a central frequency of 46 MHz. The signal is amplified by a homemade low-temperature (LTamp) amplifier (with 6-dB gain and input current noise of  $10^{-27}$  A<sup>2</sup>/Hz) and room-temperature amplifiers and measured by a power detector. When calibrating a circuit with the Johnson-Nyquist noise, the current noise of the sample  $S_I$  can be extracted. Thus,  $T_N$  can be found using the Johnson-Nyquist relation  $T_N = S_I R_d / 4k_B$ , where  $R_d$  is the differential resistance of the sample,  $k_B$  is the Boltzmann constant. We assume that the length of NbN samples is much longer than the electron-phonon scattering length [12], which implies that an electron temperature  $T_e$  is uniform along the sample length. As a consequence,  $T_N$  can be considered equal to  $T_e$ .

### Results and Discussion

To obtain information about heat dissipation in NbN wires, we measure the heat flow rate. Figure 1, *b* displays results of the noise thermometry performed at  $T_b = 16$  K for two studied samples. The data, presented with symbols, follow a  $T_e^4$  dependence on the normalized Joule power  $P_2 D = I^2 R / A$ , where  $A = w \times L$  is the area of sample. The exponent  $n = 4$  revealed in  $P_2 D(T_e)$  dependence indicates that the thermal relaxation is limited by the Kapitza resistance [11]. For further analysis, we fit the experimental data with expression  $P_2 D = \sum_{2D} (T_e^4 - T_b^4)$ , considering  $\sum_{2D}$ , the two-dimensional cooling rate, as a fitting parameter (the black solid line in Figure 1, *b*). The obtained value of  $\sum_{2D} 120 \text{WK}^{-4} \text{m}^{-2}$  is close to results reported for NbN/Al<sub>2</sub>O<sub>3</sub> interface in [13], however it is in 1.5 times smaller than  $\sum_{2D}$  obtained in our previous work [11].

Next, we investigate the resistance of NbN samples at the vicinity of the resistive transition. A low-temperature tail of the resistance transition can be result of the TAPS contribution [5-6]. The resistivity caused by TAPS can be described in the framework of the Langer-Ambegaokar-McCumber-Halperin (LAMH) theory [14-15]:

$$R_{LAMH} = \frac{\pi \hbar}{2e^2} \frac{\hbar L}{\kappa_B T \xi(0) / \sqrt{T/T_C - 1}} \left( \frac{\Delta F}{\kappa_B T} \right)^{1/2} \frac{\pi \hbar}{8 \kappa_B (T_C - T)} e^{-\Delta F / \kappa_B T}, \quad (1)$$

with the condensation energy

$$\Delta F = 0.83 \frac{\pi \hbar}{2e^2} \frac{1}{R_{20K}} \frac{L}{\xi(0)} k_B T_C \left( 1 - \frac{T}{T_C} \right)^{3/2}. \quad (2)$$

Where  $\xi(0)$  is the Ginzburg-Landau coherence length. In the experiment,  $\xi(0)$  is determined using the relation  $\xi(0)2 = -\hbar / 2eTc(dBc_2(T)/dT)$  from the temperature dependency of the second critical magnetic field  $Bc_2(T)$ .

The LAMH model also predicts the finite voltage induced by TAPS, when the wire is biased with a current [14-15]:

$$V_{LAMH} = \frac{2e\kappa_B T}{\pi \hbar} R_{LAMH} \sinh \frac{\pi \hbar I}{2e\kappa_B T}. \quad (3)$$

In Figure 1, *b* we fit the temperature dependence of resistance (shown with the green symbols) by the TAPS model as  $R = (R_{20K}^{-1} + R_{LAMH}^{-1})^{-1}$ . One can see that the temperature dependence of resistance can be partially described by the LAMH model. Low-temperature residual resistance which is not described by TAPS can be result of superconducting properties of leads. For the sample B we obtain the similar results (not shown). The fitting parameter  $T_c$  is listed in Table 1.

In Figure 2, *a* we compare the current-voltage (IV) curves measured at the vicinity of the resistive transition (Fig. 2, *b*) with the LAMH model. One can see that only the low-bias part of the IV curve can be described with the LAMH model. Note that the comparable fits can be obtained in the framework of the Golubev-Zaikin theory [16] (not shown here). Similar results for fitting the IV curves with the LAMH model have been obtained for NbN wires in [5]. The discrepancy of the LAMH model with the experimental data can be related to the effect of joule heating. It is well-known that the thermal effect, accompanied with inhomogeneity of

superconducting properties, can lead to the nonlinearity of the current-voltage characteristics [8, 9] and fully describes the retrapping current [10,13].

To analyze the effect of joule heating on the IV curves at the resistive transition, we assume that the transition into superconducting state occurs by the formation of expanding superconducting domains. Here we neglect contributions of paraconductivity to broadening of the resistive transition and current conversion processes for simplicity. Similar to the thermal model reported in [9], we assume that electronic inhomogeneities and, hence, inhomogeneity of  $T_c$  along the length of the wire play a role.

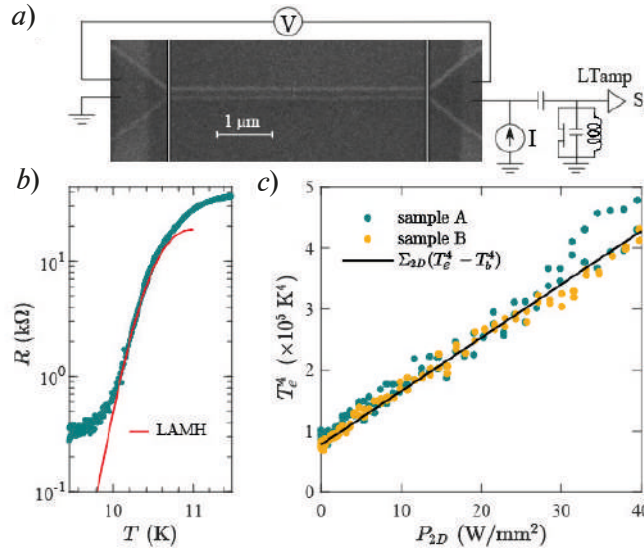


Fig. 1. SEM photo of a representative sample with a schematic sketch of the noise thermometry experiment (a); the temperature dependence of resistance for sample A on a logarithmic scale. The solid and dashed lines show the TAPS contribution to  $R(T)$  derived from the LAMH theory (b); the measured electron temperature  $T_e$  is presented as a function of joule power  $P_{2D}$  for samples A and B. The data are presented on a linear scale. The solid line shows a fit with the expression  $P_{2D} = \sum_{2D} (T_e^4 - T_b^4)$  with  $\sum_{2D} = 120WK^{-4}m^{-2}$  (c)

To describe the experimental data we consider a one-dimensional (1D) model (see a schematic representation of the model in (Fig. 2, a), in which joule heating is dissipated in the normal-state parts of the wire under the constant bias current and at finite bath temperature  $T_b$ . In this straightforward model, we consider that a segment of the wire is in the normal state if the local electron temperature  $T_e$  exceeds the local  $T_c$ . We also assume that the electron  $T_e$  and the phonon  $T_{ph}$  temperatures are constant over the normal region and their values do not depend on the size of the normal region. In the one-dimensional model, the non-zero resistance state can be simply determined by the part of the normal regions  $v_N$ . Thus, a decrease of the resistance with decreasing temperature is accompanied by a decrease of the portion of normal domains  $v_N(T) = R(T) / R_{20K}$ . With the noise thermometry we found that the electronic temperature and the electronic heat flow rate in the studied NbN nanowires are controlled by phonons escape to the substrate, known as the Kapitza resistance. Thus the electronic heat flow rate due to heat dissipation in the normal segments of the wire can be determined as:

$$\frac{I^2 R_{20K} v_N}{A_N} = \sum_{2D} (T_e^4 - T_b^4). \quad (4)$$

Here the joule power is normalized on the net area of normal parts in the 1D wire,  $A_N = v_N \times L \times w$ . This simple equation provides the average electron temperature  $T_e$  of the normal regions under the bias current  $I$ . Then, one can find the total voltage drop on the normal parts of the wire as  $V = I(dR(T) / dT)T_e$  using the average value of  $T_e$ . Figure 2 demonstrates the results of the thermal model with the solid blue lines. One can see that the simplified thermal model better describes the non-linearity of the IV curves than the TAPS model. These results indicate



that, similarly to recent observations in TiN [8], NbTiN [9], MoGe [10] wires, the nonlinearity of the IV curves at the resistive transition in NbN wires can be associated with the heating effect.

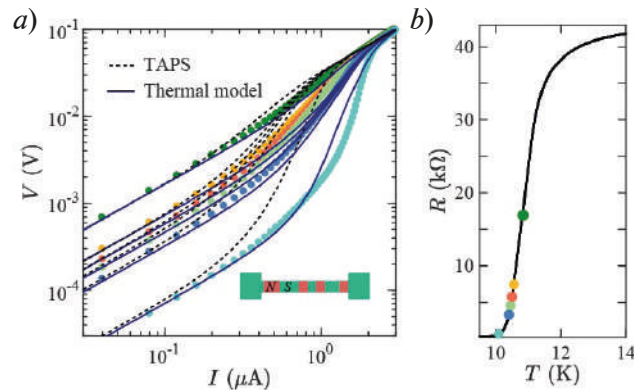


Fig. 2. The current–voltage characteristics of the NbN nanowire (sample A) at various bath temperatures on a log-log scale and a schematic representation of the model (“N” and “S” are superconducting and normal regions of the nanowire, respectively) (a); symbols show the experimental data measured at Tb marked by the same symbols at the resistive transition (panel (b)). The black dashed lines are fits by the LAMH theory (Eq. (3)). The blue solid lines demonstrate the results of the heating model discussed in the text

## Conclusion

In conclusion, we have shown that the current-voltage characteristics measured at the superconducting resistive transition in NbN nanowires can be quantitatively described by the thermal model considered the heat dissipation in NbN samples.

## REFERENCES

1. **Holzman I., Yachin Y.**, Superconducting Nanowires for Single-Photon Detection: Progress, Challenges, and Opportunities, *Advanced Quantum Technologies*. 2 (3-4) (2019) 1800058.
2. **Gol’tsman G., Okunev O., Chulkova G., Lipatov A., Semenov A., Smirnov K., Voronov B., Dzardanov A.**, Picosecond superconducting single-photon optical detector, *Applied Physics Letters*. 79 (6) (2001) 705–707.
3. **Smirnov K., Divochiy A., Vakhtomin Y., Morozov P., Zolotov P., Antipov A., Seleznev V.**, NbN single-photon detectors with saturated dependence of quantum efficiency, *Superconducting Science and Technology*. 31 (3) (2018), 035011.
4. **Murphy A., Semenov A., Korneev A., Korneeva Y., Gol’tsman G., Bezryadin A.**, Three temperature regimes in superconducting photon detectors: quantum, thermal and multiple phase-slips as generators of dark counts, *Scientific reports*. 5 (1) (2015) 1–10.
5. **Bell M., Sergeev A., Mitin V., Bird J., Verevkin A., Gol’tsman G.**, One-dimensional resistive states in quasi-two-dimensional superconductors, *Physical Review B*. 76 (9) (2007) 094521.
6. **Delacour C., Pannetier B., Villegier J.-C., Bouchiat V.**, Quantum and Thermal Phase Slips in Superconducting Niobium Nitride (NbN) Ultrathin Crystalline Nanowire: Application to Single Photon Detection, *Nano Letters*. 12 (7) (2012) 3501–3506.
7. **Elmurodov A.K., Peeters F.M., Vodolazov D.Y., Michotte S., Adam S., F. de Menten de Horne, L. Piraux, Lucot D., Mailly D.**, Phase-slip phenomena in NbN superconducting nanowires with leads, *Physical Review B*. 78 (21) (2008) 214519.
8. **Postolova S.V., Mironov A.Yu., Baturina T.I.**, Nonequilibrium Transport near the Superconducting Transition in TiN Films, *JETP Letters*. 100 (10) (2014) 635–641.
9. **Hortensius H.L., Driessen E.F.C., Klapwijk T.M.**, Possible Indications of Electronic Inhomogeneities in Superconducting Nanowire Detectors, *IEEE Transactions on Applied Superconductivity*, 23 (3) (2013) 2200705.
10. **Tinkham M., Free J.U., Lau C.N., Markovic N.**, Hysteretic I-V curves of superconducting nanowires. *Physical Review B*, 68 (13) (2003) 134515.

11. **Baeva E.M., Soldatenkova M.D., Zolotov P.I., Titova N.A., Triznova A.D., Lomakin A.I., Kardakova A.I., Goltsman G.N.**, Thermal relaxation in NbN films on crystalline substrates, IEEE Transactions on Applied Superconductivity, 32 (4) (2022) 1–5.
12. **Baeva E.M. et al.**, Thermal relaxation in metal films limited by diffuson lattice excitations of amorphous substrates, Physical Review Applied. 15 (5) (2021) 054014.
13. **Dane A. et al.**, Self-heating hotspots in superconducting nanowires cooled by phonon black-body radiation, Nature Portfolio, preprint (2021).
14. **Langer J.S. Ambegaokar V.**, Intrinsic resistive transition in narrow superconducting channels, Physical Review. 164 (2) (1967) 498.
15. **McCumber D.E. Halperin B.I.**, Time scale of intrinsic resistive fluctuations in thin superconducting wires, Physical Review B. 1 (3) (1970) 1054.
16. **Zaikin A.D., Golubev D.S., A. van Otterlo, Zimónyi G.T.**, Quantum phase slips and transport in ultrathin superconducting wires, Physical Review Letters. 78 (8) (1997) 1552–1555.

#### THE AUTHORS

**SOLDATENKOVA Maria D.**  
mdsoldatenkova@edu.hse.ru  
ORCID:0000-0002-9918-1811

**ZOLOTOV Philip I.**  
zolotov@scontel.ru  
ORCID:0000-0003-1729-7480

**BAEVA Elmira M.**  
baeva.elm@gmail.com  
ORCID:0000-0002-6805-2670

**KOLBATOVA Anna I.**  
anna\_kardakova@mail.ru  
ORCID:0000-0002-3441-3968

**TRIZNOVA Alexandra D.**  
sashatriznova@gmail.com

**GOLTSMAN Grigory N.**  
goltsman@rplab.ru  
ORCID:0000-0002-1960-9161

**TITOVA Nadezhda A.**  
titovana@mail.ru

*Received 14.08.2022. Approved after reviewing 16.08.2022. Accepted 06.09.2022.*

Conference materials

UDC 539.18

DOI: <https://doi.org/10.18721/JPM.153.207>

### **X-ray spectral studies of doped bismuth-magnesium and bismuth-zinc tantalates**

K. A. Bakina<sup>1</sup>✉, N. A. Zhuk<sup>2</sup>, V. N. Sivkov<sup>1</sup>, S. V. Nekipelov<sup>1,2</sup>

<sup>1</sup> FRC Komi SC UB RAS, Syktyvkar, Russia;

<sup>2</sup> Pitirim Sorokin Syktyvkar State University, Syktyvkar, Russia

✉ [tylxen@gmail.com](mailto:tylxen@gmail.com)

**Abstract.** Solid solutions of bismuth-magnesium tantalates and bismuth-zinc tantalates doped with 3d-metal atoms were studied by XPS and NEXAFS. It was shown that atoms of bismuth, magnesium and zinc in all the compounds under consideration have the charge states  $\text{Bi}^{3+}$ ,  $\text{Mg}^{2+}$  and  $\text{Zn}^{2+}$ , respectively, and the tantalum atoms, in turn, have an effective charge of  $+(5-\delta)$ .

**Keywords:** bismuth-magnesium, bismuth-zinc, tantalates

**Funding:** The study was funded by the Grant of the President of the Russian Federation (МК 3796.2021.1.2), the RFBR and the Komi Republic within the framework of research projects number 19-32-60018 and 20-42-110002 r-a. The study was supported by the Ministry of Science and Higher Education of Russia under Agreement No. 075-15-2021-1351 in part of research on NEXAFS spectroscopy.

**Citation:** Bakina K. A., Zhuk N. A., Sivkov V. N., Nekipelov S. V., X-ray spectral studies of doped bismuth-magnesium and bismuth-zinc tantalates, St. Petersburg State Polytechnical University Journal. Physics and Mathematics. 15 (3.2) (2022) 41–44. DOI: <https://doi.org/10.18721/JPM.153.207>

This is an open access article under the CC BY-NC 4.0 license (<https://creativecommons.org/licenses/by-nc/4.0/>)

Материалы конференции

УДК 539.18

DOI: <https://doi.org/10.18721/JPM.153.207>

### **Рентгеноспектральные исследования допированных танталатов висмута-магния и висмута-цинка**

К.А. Бакина<sup>1</sup>✉, Н.А. Жук<sup>2</sup>, В.Н. Сивков<sup>1</sup>, С.В. Некипелов<sup>1,2</sup>

<sup>1</sup> ФИЦ Коми научный центр УрО РАН, Сыктывкар, Россия;

<sup>2</sup> СГУ им. Питирима Сорокина, Сыктывкар, Россия

✉ [tylxen@gmail.com](mailto:tylxen@gmail.com)

**Аннотация.** На основе данных XPS- и NEXAFS-спектроскопии твёрдых растворов танталатов висмута-магния и висмута-цинка, допированных атомами меди и никеля, показано, что атомы висмута, магния и цинка во всех исследуемых соединениях обладают зарядовым состоянием  $\text{Bi}^{3+}$ ,  $\text{Mg}^{2+}$  и  $\text{Zn}^{2+}$ , соответственно, а атомы тантала имеют эффективный заряд  $+(5-\delta)$ .

**Ключевые слова:** висмут-магний, висмут-цинк, танталаты

**Финансирование:** Работа выполнена при финансовой поддержке Гранта Президента РФ (МК 3796.2021.1.2), РФФИ и Республики Коми в рамках научных проектов № 19-32-60018 и 20-42-110002 р-а и Министерства науки и высшего образования РФ в рамках соглашения № 075-15-2021-1351 в части NEXAFS-спектроскопии.

**Ссылка при цитировании:** Бакина К. А., Жук Н. А., Сивков В. Н., Некипелов С. В. Рентгеноспектральные исследования допированных танталатов висмута-магния и висмута-цинка // Научно-технические ведомости СПбГПУ. Физико-математические науки. 2022. Т. 15. № 3.2. С. 41–44. DOI: <https://doi.org/10.18721/JPM.153.207>

Статья открытого доступа, распространяемая по лицензии CC BY-NC 4.0 (<https://creativecommons.org/licenses/by-nc/4.0/>)

### Introduction

Doping of bismuth tantalates with atoms of various metals can lead to a significant change in their electrophysical properties, which can depend both on the type of doped atoms and on the degree of doping [1–4]. This work shows the results of NEXAFS and XPS studies of the electronic state and nature of interatomic interactions of 3d-metal atoms in bismuth-magnesium and bismuth-zinc tantalates doped with copper and nickel atoms at different degrees of doping  $\text{Bi}_2\text{Ta}_2\text{Mg}(\text{Zn})_{1-x}\text{Cu}(\text{Ni})_x\text{O}_9$  ( $x = 0.1–0.9$ ). The experimental particularities and the used equipment characteristics are described in detail elsewhere [4].

### Results and Discussion

Let us consider the results of spectral studies of bismuth-magnesium tantalates. Figure 1 shows the XPS spectra of bismuth-magnesium tantalates without doping and nickel-doped ones. It is clear that doping with nickel atoms slightly changes the spectral characteristics of bismuth, tantalum, and magnesium atoms. This indicates that the charge state of these atoms in the compounds under consideration is conserved.

Comparison of the XPS Bi 4f and Bi 5d spectra of the samples and  $\text{Bi}_2\text{O}_3$  oxide (Fig. 1 *a, b*) shows that the energy position and width of the peaks in the spectra of all samples almost completely coincide and correlate well with the spectra of  $\text{Bi}_2\text{O}_3$  oxide. Therefore, the bismuth atom in this compound has the  $\text{Bi}^{3+}$  charge state. In the case of tantalum atoms (Fig. 1 *a, c*), the absence of peak splitting and distortion clearly indicates that all tantalum atoms are in the same charge state. The energy position of the peaks has a shift towards lower energies compared to the binding energy in oxide  $\text{Ta}_2\text{O}_5$ , which is typical for a decrease in the effective positive charge. This evidence may be taken to mean that tantalum atoms have the same effective charge  $+(5-\delta)$ . The energy position of the peaks in the XPS Mg 1s spectra (Fig. 1 *d*) is characteristic of a divalent magnesium atom [5]. Thus, the charge state of these atoms here is  $\text{Mg}^{2+}$ .

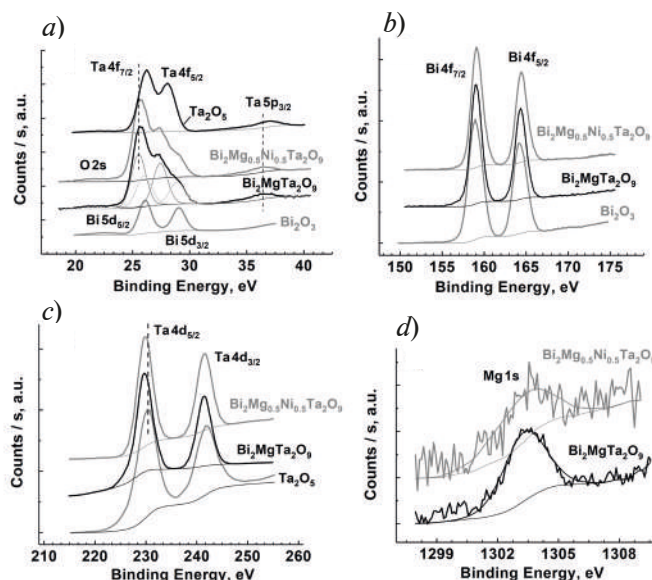


Fig. 1. XPS spectra of bismuth-magnesium tantalates without doping and XPS spectra of bismuth-magnesium tantalates, doped with nickel atoms

Comparison of the XPS and NEXAFS Ni 2p spectra of the samples with the ones of nickel oxide NiO (Fig. 2) shows that nickel atoms have the same charge state, since there is no splitting and distortion of the peaks. The energy positions of the peaks in XPS spectra (Fig. 2 *a*) is shifted



towards higher energies compared to the binding energies for the given levels in NiO oxide, which is characteristic of an increase in the effective positive charge. This suggests that nickel atoms have the same effective charge  $+(2+\delta)$ . NEXAFS spectra (Fig. 2 *b*) reflects that the charge state of nickel atoms is preserved when the degree of doping is changed.

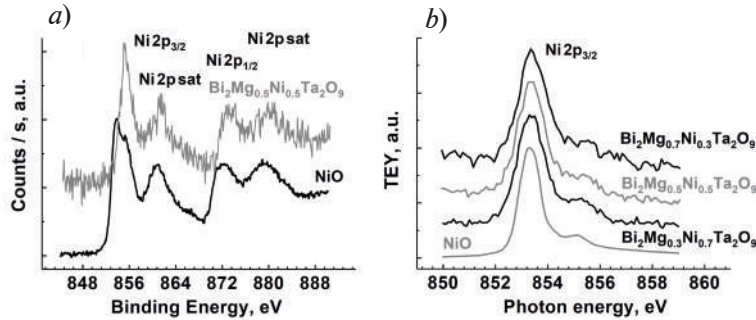


Fig. 2. XPS (*a*) and NEXAFS (*b*) Ni 2p spectra of Ni-doped bismuth-magnesium tantalates

Similar to samples doped with nickel atoms, in the case of doping with copper atoms, the shape of the spectra of bismuth, tantalum, and magnesium atoms remains almost unchanged. Consequently, the charge state of these atoms ( $\text{Bi}^{3+}$ ,  $\text{Ta}^{(5-\delta)+}$  and  $\text{Mg}^{2+}$ ) in the presented compounds is preserved. In this case, the behaviour of the introduced copper atoms is fundamentally different. Figure 3 shows the XPS and NEXAFS spectra of copper atoms in the samples at various degrees of doping. A comparison of the spectra shows that the samples contain Cu(I) and Cu(II) atoms.

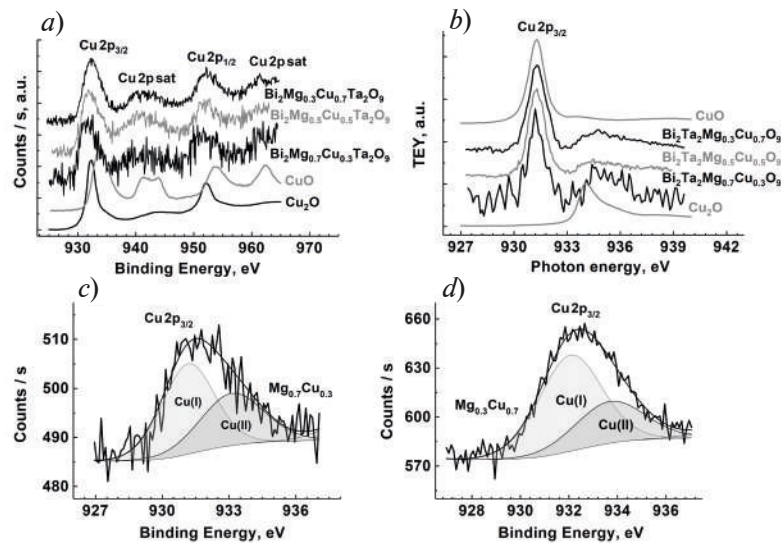


Fig. 3. XPS (*a*) and NEXAFS (*b*) Cu 2p spectra of Cu-doped bismuth-magnesium tantalates and decomposition of XPS Cu 2p spectra at  $x = 0.3$  (*c*), at  $x = 0.7$  (*d*)

From the analysis of XPS Cu 2p spectra (Fig. 3 *c*, *d*), it is possible to determine the contribution of Cu(I) and Cu(II) atoms to the corresponding spectra. The ratio of integral intensities Cu(I)/Cu(II) is 1.43 at  $x = 0.3$  and 2.08 at  $x = 0.7$ . Thus, the relative contribution of Cu(I) increases with increasing degree of doping with copper atoms, which indicates a change in the position of copper atoms in the structure of pyrochlores. Perhaps, at a low concentration, copper atoms are introduced into the positions of tantalum atoms, and with an increase in their concentration, they are partially introduced into the positions of bismuth atoms. A similar behaviour of all atoms is also observed in the samples of Ni- and Cu-doped bismuth-zinc tantalates.

### Conclusions

Thermally stable solid solutions of bismuth-magnesium (zinc) tantalates doped with nickel and copper atoms were obtained in a wide range of compositions. It follows from the NEXAFS and

XPS spectra that the bismuth, magnesium, and zinc atoms in all compounds have the  $\text{Bi}^{3+}$ ,  $\text{Mg}^{2+}$ , and  $\text{Zn}^{2+}$  charge state, while the tantalum atoms have an effective charge of  $+(5-\delta)$ . The doped nickel atoms have an effective charge of  $+(2+\delta)$ , and the copper atoms have the charge state  $\text{Cu}^+$  and  $\text{Cu}^{2+}$ .

## REFERENCES

1. Murugesan S., Huda M.N., Yan Y., Al-Jassim M.M., Subramanian V., Band-Engineered Bismuth Titanate Pyrochlores for Visible Light Photocatalysis, *J. Phys. Chem. C*. 114 (2010) 10598–10605.
2. Giampaoli G., Siritanon T., Day B., Li J., Subramanian M.A., Temperature in-dependent low loss dielectrics based on quaternary pyrochlore oxides, *Prog. Solid. State Ch.* 50 (2018) 16–23.
3. Zhuk N.A., Krzhizhanovskaya M.G., Koroleva A.V., Nekipelov S.V., Sivkov D.V., Sivkov V.N., Lebedev A.M., Chumakov R.G., Makeev B.A., Kharton V.V., Panova V.V., Korolev R.I., Spectroscopic characterization of cobalt doped bismuth tantalate pyrochlore. *Solid State Sciences*. 125 (2022) 106820.
4. Zhuk N.A., Krzhizhanovskaya M.G., Koroleva A.V., Reveguk A.A., Sivkov D.V., Nekipelov S.V., Thermal expansion, crystal structure, XPS and NEXAFS spectra of Fe-doped bismuth tantalate pyrochlore, *Ceramics International*. 48 (2022) 14849–14855.
5. Khairallah F., Glisenti A., XPS study of MgO nanopowders obtained by different preparation procedures, *Surface Science Spectra*. 13 (1) (2006) 58–71.

## THE AUTHORS

**BAKINA Ksenia A.**  
tylxen@gmail.com  
ORCID: 0000-0002-6687-6908

**SIVKOV Victor N.**  
sivkovvn@mail.ru  
ORCID: 0000-0001-9916-1514

**ZHUK Nadezhda A.**  
nzhuck@mail.ru  
ORCID: 0000-0002-9907-0898

**NEKIPELOV Sergey V.**  
nekipelovsv@mail.ru  
ORCID: 0000-0001-6749-738X

*Received 14.08.2022. Approved after reviewing 21.08.2022. Accepted 23.08.2022.*

## SIMULATION OF PHYSICAL PROCESSES

Conference materials

UDC 004.942

DOI: <https://doi.org/10.18721/JPM.153.208>

### Synchronization systems of time scales and frequencies in polar latitudes by meteor radio channel

A. A. Briushinin<sup>1</sup> ✉, V. V. Davydov<sup>1, 2, 3</sup>

<sup>1</sup> Peter the Great Saint-Petersburg Polytechnic University, Saint Petersburg, Russia;

<sup>2</sup> The Bonch-Bruевич Saint-Petersburg State University of Telecommunications, Saint Petersburg, Russia;

<sup>3</sup> All-Russian Research Institute of Phytopathology, Moscow Region, Russia

✉ [anatoliyb2000@mail.ru](mailto:anatoliyb2000@mail.ru)

**Abstract.** The necessity of using a meteor communication channel as a backup system for determining the coordinates of moving objects in polar latitudes and transmitting information is substantiated. The necessity of using a time scale synchronization system in the meteor communication channel has been established. The reasons that cause a failure in the transmission of information in the meteor communication channel are presented. A model for calculating the shift of time scales in the meteor communication channel is proposed. A method has been developed to reduce random errors and increase the noise immunity of the meteor communication channel. Recommendations are given on the choice of receiver parameters for synchronization with a given accuracy.

**Keywords:** meteor radio channel, meteor synchronization, synchronization of time scales, synchronization methods, duplex method, simulation model, noise-like signal, m-sequence, receiver sensitivity, registration threshold

**Citation:** Briushinin A. A., Davydov V. V., Synchronization systems of time scales and frequencies in polar latitudes by meteor radio channel, St. Petersburg State Polytechnical University Journal. Physics and Mathematics. 15 (3.2) (2022) 45–50. DOI: <https://doi.org/10.18721/JPM.153.208>

This is an open access article under the CC BY-NC 4.0 license (<https://creativecommons.org/licenses/by-nc/4.0/>)

Материалы конференции

УДК 004.942

DOI: <https://doi.org/10.18721/JPM.153.208>

### Системы синхронизации шкал времени и частот в полярных широтах по метеорному радиоканалу

A. A. Брюшинин<sup>1</sup> ✉, В. В. Давыдов<sup>1, 2, 3</sup>

<sup>1</sup> Санкт-Петербургский политехнический университет Петра Великого, Санкт-Петербург, Россия;

<sup>2</sup> Санкт-Петербургский государственный университет телекоммуникаций  
им. проф. М. А. Бонч-Бруевича, Санкт-Петербург, Россия;

<sup>3</sup> Всероссийский научно-исследовательский институт фитопатологии, Московская область, Россия

✉ [anatoliyb2000@mail.ru](mailto:anatoliyb2000@mail.ru)

**Аннотация.** Обоснована необходимость использования метеорного канала связи в качестве резервной системы для определения координат подвижных объектов в полярных широтах и передачи информации. Установлена необходимость использования системы синхронизации шкал времени в метеорном канале связи. Представлены причины, которые вызывают сбой в передаче информации в метеорном канале связи. Предложена модель расчета сдвига шкал времени в метеорном канале связи. Разработан способ для уменьшения случайных погрешностей и повышения помехозащищенности метеорного канала связи. Даны рекомендации по выбору параметров приемника для осуществления синхронизации с заданной точностью.

**Ключевые слова:** метеорный радиоканал, метеорная синхронизация, синхронизация шкал времени, методы синхронизации, встречный метод, имитационная модель, шумоподобный сигнал, m-последовательность, чувствительность приемника, порог регистрации

**Ссылка при цитировании:** Брюшинин А. А., Давыдов В. В. Системы синхронизации шкал времени и частот в полярных широтах по метеорному радиоканалу // Научно-технические ведомости СПбГПУ. Физико-математические науки. 2022. Т. 15. № 3.2. С. 45–50. DOI: <https://doi.org/10.18721/JPM.153.208>

Статья открытого доступа, распространяемая по лицензии CC BY-NC 4.0 (<https://creativecommons.org/licenses/by-nc/4.0/>)

## Introduction

The development of industry and trade, as well as mining, required new developments for communication systems and determining the coordinates of objects [1–10]. The most reliable among communication systems are fiber-optic lines [11–16], which can provide information transmission in difficult conditions. Among the coordinate determination systems, satellite navigation systems are in the greatest demand [1, 5, 6–9, 17–24]. When using satellite systems in northern latitudes (above 70 degrees latitude) to determine coordinates, a number of problems arise [25–27]. They are associated with the attenuation of the amplitude of the GLONASS signal by ionospheric disturbances (for example, the Northern lights, etc.). This creates large errors in determining the coordinates of the object [28, 29].

Under these conditions, navigation is carried out by ground-based pulse-phase radio navigation systems (PPRNS) that emit radio-pulse navigation signals [30–33]. The coordinates of the transmitting stations of the PPRNS are known in advance. The stations serve a certain area of the earth's surface. Transmitting stations work in groups forming a single chain. Each chain includes a master station and several slave stations, whose radio pulse emissions are synchronized with the signals of the master station. The emissions of the leading station of the chain are synchronized, for example, by precise time signals using quantum frequency standards [9, 16, 19, 32]. These standards need to be adjusted during the work. One of the adjustment options is offered in our work.

## Meteor synchronization

In northern latitudes, it is advisable to use the meteor radio channel as a backup channel for transmitting the exact time signal. The principle of meteor radio communication is based on the ability of ultrashort waves (VHF) to mirror the ionized traces formed as a result of the combustion of meteoroids in the Earth's atmosphere (Fig. 1) [33, 34].

It is known that the radiometeor communication channel is intermittent. The ionized trace is formed on average for 0.5 second, then it dissipates due to the process of bipolar (ambipolar) diffusion and it is necessary to wait for the formation of the next meteor trail. This disadvantage limits the scope of the radiometeor communication channel.

Due to the random location of the meteor trail in the synchronization systems of spatially remote time scales and frequencies on the meteor radio channel, the time of signal propagation is not known in advance, therefore, it is necessary to use two-way information transmission - the method is called active (two-way, duplex).

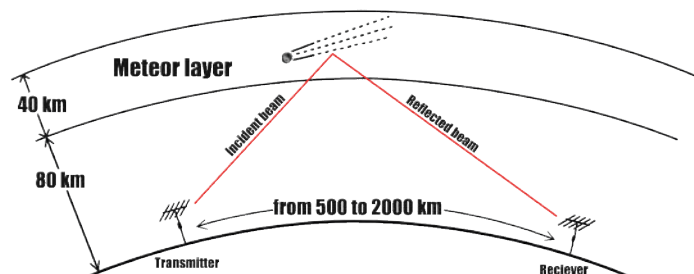


Fig. 1. The principal model of the meteor communication channel



To calculate the shift of the time scales  $\Delta T$ , it is necessary to calculate the propagation time of the signal  $t_p$ , for this, in addition to fixing the timestamp  $t_R^{(2)}$  by the receiver, the time  $t_T^{(1)}$  is fixed by the transmitter, after exchanging this information, a system of two equations is compiled:

$$\begin{cases} t_R^{(2)} = t_T^{(1)} + \Delta T + t_p, \\ t_R^{(1)} = t_T^{(2)} - \Delta T + t_p. \end{cases} \quad (1)$$

In total, we solve a system of two equations (1) with two unknowns:

$$\Delta T = \frac{1}{2} \left[ \left( t_R^{(2)} - t_R^{(1)} \right) + \left( t_T^{(2)} - t_T^{(1)} \right) \right]. \quad (2)$$

In this case, both simultaneous transmission of the timestamp (counter method) and alternate transmission is possible. Alternate transmission is suitable for a communication range of less than 500 km.

### Simulation model of time stamp transmission via meteor channel

Equation describing the power of the received signal reflected from an under-compacted trace [6]:

$$P_r(t) = A \cdot q^2 \cdot e^{-\frac{t}{\tau}}, \quad (3)$$

where  $A$  is the coefficient,  $q$  is the linear electron density,  $\tau$  is the attenuation constant,  $t$  is the time elapsed since the appearance of the trace.

All formulas for generating random distribution parameters are obtained by the inverse function method.

A random time for the appearance of a meteor trail  $t_0$ :

$$t_0 = -\frac{\ln(1-R)}{\lambda}, \quad (4)$$

where  $R$  is a random variable from a standard uniform distribution.

A random lifetime of the trail  $t_{life}$ :

$$t_{life} = -T_{mean} \ln(1-R), \quad (5)$$

where  $R$  is a random variable from a standard uniform distribution.

The experience of operating the COMET system has shown that the average lifetime of the trace is 0.5 seconds [8].

A random value of the linear electron density  $Q$ :

$$Q = \frac{q_{min}}{1-R + R \frac{q_{min}}{q_{max}}}, \quad (6)$$

where  $R$  is a random variable from a standard uniform distribution.

### Simulation results

The potential accuracy of measuring the arrival time of the timestamp directly depends on the signal-to-noise ratio and the width of the signal spectrum [9-10]:

$$\sigma_t = \frac{\alpha}{h F_{eff}}, \quad (7)$$

where  $\alpha = \frac{\sqrt{3}}{\pi}$ ,  $h$  – maximum signal-to-noise ratio at the output of the matched filter,  $F_{eff}$  – effective spectrum width.

We express from (7) the minimum value of the signal power at the receiver input to ensure the specified measurement accuracy (and hence synchronization):

$$P_r = \frac{\alpha^2 P_n}{2B(\sigma_t 2\Delta f)^2}. \quad (8)$$

Using (8), we calculate the minimum values of the signal amplitude  $U_r$  at the input of the receiver for a given accuracy.

A study of the dependence of the average waiting time of a meteor trail suitable for synchronization  $t_{wait}$  on the distance to the receiver showed that with an increase in the distance to the receiver, the waiting time increases, that is, the efficiency of the synchronization session decreases. In addition, an increase in the waiting time occurs when the power of the transmitter decreases (Fig. 2).

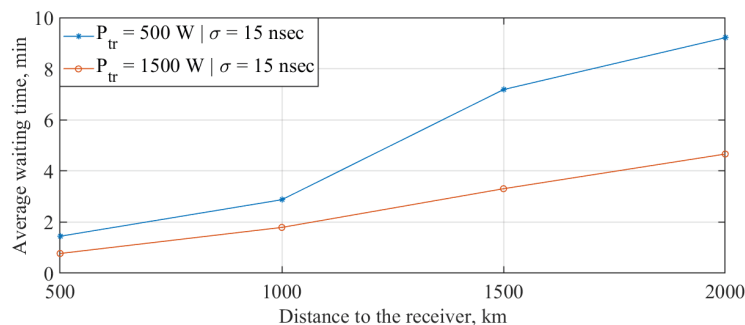


Fig. 2. The dependence of the average waiting time on the distance to the receiver or the different power of the transmitter

As can be seen in Fig. 2, the average waiting time does not exceed 40 minutes, which means that the transmission of a noise-like signal as a timestamp over a distance of 2000 km with a transmitter power of 1500 Watts and a given accuracy of 15 ns is possible, while it is necessary to have a receiver sensitivity of the order of  $1.26e-08$  V or less.

### Conclusion

Transmission as a timestamp of the m-sequence allows to increase the noise immunity and secrecy of the meteor radio communication system, as well as to reduce the random error. The use of highly stable quantum generators (frequency standards) in meteor communication channels makes it possible to further reduce the random error during channel synchronization.

### REFERENCES

1. Wang, D., Rud V.Y., Prospective directions for the development of microwave frequency standards for satellite navigation systems, *Journal of Physics: Conference Series*. 2086(1) (2021) 012073.
2. Semenov V.V., Nikiforov N.F., Ermak S.V., Calculation of stationary magnetic resonance signal in optically oriented atoms induced by a sequence of radio pulses, *Soviet journal of Communications Technology and Electronics*. 36(4) (1991) 59–63.
3. Lukashev N.A., Davydov R.V., Glinushkin A.P., Rud' V.Y., Improving characteristics of microwave frequency standard on Hg-199 ions for telecommunication systems, *Journal of Physics: Conference Series*. 1326(1) (2019) 012046.
4. Mihov E.D., Nepomnyashchiy O.V., Selecting informative variables in the identification problem *Journal of Siberian Federal University - Mathematics and Physics*. 9(4) (2016) 473–480.
5. Ryzhenko I.N., Lutsenko A.E., Varygin O.G., Nepomnyashchiy O.V., Carrier compensation mode implementation in satellite communication channels. In: *Proceedings of 2019 International Siberian Conference on Control and Communications, SIBCON 2019*, vol. 8729665 (2019) 23-29.
6. Petrov A.A., Myazin N.S., Kaganovskiy V.E., Rubidium atomic clock with improved metrological characteristics for satellite communication system, *Lecture Notes in Computer Science (including subseries Lecture Notes in Artificial Intelligence and Lecture Notes in Bioinformatics)*. 10531 LNCS (2017) 561–568.



7. **Arinushkina K.G., Valov A.P.**, Digital processing of optical signals in the frequency standard based in rubidium atoms - 87, In: Proceedings of ITNT 2021 - 7th IEEE International Conference on Information Technology and Nanotechnology, 2021 Samara, Russia, 20-24 September 2021. vol. 44026298 (2021) 44–49.
8. **Grevtseva A., Rud V.**, Method of processing velocity increase of measuring results of quantum frequency standard parameters for information transfer velocity increase in satellite communication systems, CEUR Workshop Proceedings. 2667 (2020) 15–18.
9. **Petrov A.A.**, New scheme of the microwave signal formation for quantum frequency standard on the atoms of caesium-133 Journal of Physics: Conference Series. 769(1) (2016) 012065.
10. **Kuzmin M.S., Rogov S.A.**, On the use of a multi-raster input of one-dimensional signals in two-dimensional optical correlators, Computer Optics. 43(3) (2019) 391–396.
11. **Fadeenko V.B., Pchelkin G.A., Davydov V.V., Rud V.Yu.**, Features of the transmission of microwave signals in the range of 8-12 GHz in the maritime radar station over fiber-optic communication line, Journal of Physics: Conference Series. 1400(4) (2019) 044010.
12. **Ermak S.V., Karseev A.U., Velichko E.N.**, Fiber-optic super-high-frequency signal transmission system for sea-based radar station Lecture Notes in Computer Science (including subseries Lecture Notes in Artificial Intelligence and Lecture Notes in Bioinformatics). 8638 LNCS (2014) 694–702.
13. **Sharova N.V., Fedorova E.V., Vologdin V.A.**, Fiber-optics system for the radar station work control, Lecture Notes in Computer Science (including subseries Lecture Notes in Artificial Intelligence and Lecture Notes in Bioinformatics). 9247 (2015) 712–721.
14. **Lenets V.A., Tarasenko M.Yu., Rodygina N.S.**, New method for testing of antenna phased array in X frequency range, Journal of Physics: Conference Series. 2018, 1038(1) (2018) 012037.
15. **Tarasenko M.Yu., Lenets V.A., Malanin K.Yu., Akulich N.V.**, Features of use direct and external modulation in fiber optical simulators of a false target for testing radar station, Journal of Physics: Conference Series. 1038(1) (2018) 012035.
16. **Popovskiy N.I., Rud V.Yu.**, Features of the construction of photonic integrated circuits for communication systems Journal of Physics: Conference Series 2086(1) (2021) 012163.
17. **Davydov R., Antonov V., Moroz A.**, Parameter Control System for a Nuclear Power Plant Based on Fiber-Optic Sensors and Communication Lines, In: IEEE International Conference on Electrical Engineering and Photonics (EExPolytech), Saint-Petersburg. Vol. 8906791 (2019) 295–297.
18. **Lukashev N.A., Moroz A.V.**, Compact microwave frequency standard on Hg-199 ions for navigation systems, Journal of Physics: Conference Series. 1236(1) (2019) 012068.
19. **Valov, A.P., Arinushkina, K.G.**, The use of digital data processing to improve the metrological characteristics of the rubidium frequency standard, Journal of Physics: Conference Series. 2086(1) (2021) 012070.
20. **Lukashev N.A., Rud V.Yu.**, Microwave frequency standard on Hg-199 ions for space stations and vehicles Journal of Physics: Conference Series. 1400(2) (2019) 022050.
21. **Petrov A. A.**, Digital Frequency Synthesizer for 133Cs-Vapor Atomic Clock, Journal of Communications Technology and Electronics. 62(3) (2017) 289–293.
22. **Petrov A.A., Shabanov V.E., Zalyotov D.V., Bulyanitsa A.L., Shapovalov D.V.**, Modernization of the frequency synthesizer of cesium atomic clock, IEEE International Conference on Electrical Engineering and Photonics, EExPolytech 2018, Saint-Petersburg, October 2018. vol. 8564389 (2018) 52–55.
23. **Zalyotov D. V., Shabanov V. E., Shapovalov D. V.**, Features of direct digital synthesis applications for microwave excitation signal formation in quantum frequency standard on the atoms of cesium, Journal Physics: Conference Series. 1124(1) (2018) 041004.
24. **Valov A.P., Lukashev N.A., Grebenikova N.M.**, Improving performance of quantum frequency standard with laser pumping, Proceedings of 18th International conference of Laser Optics ICLO-2018, Saint-Petersburg, Vol. 8435889 (2019) 271.
25. **Riehle F.**, Frequency standard. Basic and applications. WILEY-VCH Verlag CmbH Co. KGaA: New-York, 2008.
26. **Petrov A.A., Zaletov D.V., Shapovalov D.V.**, Peculiarities of Constructing a Scheme for Formation of a Microwave Excitation Signal in a Cesium Atomic Clock, Journal of Communications Technology and Electronics. 66(3) (2021) 295–299.
27. **Grevtseva A.S., Dmitriev R.A.**, Features of the formation of the frequency of the microwave excitation signal in the quantum frequency standard on rubidium atoms – 87, Journal of Physics:

Conference Series. 2086(1) (2021) 012055.

28. **Petrov A.A.**, Digital Frequency Synthesizer for  $^{133}\text{Cs}$ -Vapor Atomic Clock, Journal of Communications Technology and Electronics. 62(3) (2017) 289–293.

29. **Petrov A.A., Grebenikova N.M.**, Some Directions of Quantum Frequency Standard Modernization for Telecommunication Systems, Lecture Notes in Computer Science (including subseries Lecture Notes in Artificial Intelligence and Lecture Notes in Bioinformatics). 11118 LNCS (2018) 641–648.

30. **Davydov R., Kulikova M.**, Selection basis of an antenna for a radio receiver of a small-sized module of a pulse-phase radio navigation system of a moving object, In IEEE International Conference on Electrical Engineering and Photonics (EExPolytech 2020), Saint-Petersburg, Vol. 9244003 (2020) 38–41.

31. **Davydov R., Nagornaya A.**, The algorithm for processing signals of a pulse-phase radio navigation system in a quasi-differential mode using signals from global navigation satellite systems. In: IEEE International Conference on Electrical Engineering and Photonics (EExPolytech 2020), Saint-Petersburg, Vol. 9243977 (2020) 145–148.

32. **Valov A.P., Nagornaya A.I., Kulikova M.E., Glinushkin A.P.**, Method of improving the rubidium - 87 quantum frequency standard's metrological characteristics, Journal of Physics: Conference Series. 1695(1) (2020) 012169.

33. **Tolmachev S.V., Ryabov I.V., Chernov D.A.**, Hardware-software complex for meteor-burst communication, International Conference Systems of Signal Synchronization, Generating and Processing in Telecommunications, SINKHROINFO 2017, Vol. 7997565 (2017) 314–319.

34. **Mashkova E., Zavjalov S., Volvenko S., Xue W.**, Evaluation of the Transmission Efficiency of Multi-frequency Signals with an Unknown Initial Phase in the Meteor Burst Communication System, Springer Proceedings in Physics. 268 (2022) 545–553.

#### THE AUTHORS

**BRIUSHININ Anatolii A.**

anatoliyb2000@mail.ru

ORCID: 0000-0002-3129-1694

**DAVYDOV Vadim V.**

davydov\_vadim66@mail.ru

ORCID: 0000-0001-9530-4805

*Received 12.08.2022. Approved after reviewing 15.08.2022. Accepted 26.08.2022.*

Conference materials  
UDC 064.89.032.26  
DOI: <https://doi.org/10.18721/JPM.153.209>

## Testing the layout of the rail condition monitoring system using LSTM recurrent neural networks

M. A. Denisenko<sup>1</sup>, A. S. Isaeva<sup>1</sup> ✉, I. N. Kots<sup>1</sup>

<sup>1</sup>Southern Federal University, Taganrog, Russia

✉ isaevaas@sfedu.ru

**Abstract.** In this paper the solution of the multiclass classification problem of the events recognition during the movement of a bogie model along rails containing defects is described. Testing the layout of the rail condition monitoring system was described. The problem was solved using LSTM recurrent neural networks and implemented by Python programming language. The neural network was trained to classify three type of events used acceleration data. The method of the data collection and the description of the test stand is given. Conclusions about the efficiency of event recognition from a given set are made.

**Keywords:** rail defect monitoring, neural network, multiclass classification problem

**Funding:** The work was carried out at the expense of funds, task No. FENW-2020-0022 for the implementation of scientific research carrying out scientific research at the expense of the Federal budget, in terms of scientific activities on the topic "Development and research of methods and means of monitoring, diagnostics and forecasting state of engineering objects based on artificial intelligence".

**Citation:** Isaeva A. S., Denisenko M. A., Kots I. N., Testing the layout of the rail condition monitoring system using LSTM recurrent neural networks, St. Petersburg State Polytechnical University Journal. Physics and Mathematics. 15 (3.2) (2022) 51–55. DOI: <https://doi.org/10.18721/JPM.153.209>

This is an open access article under the CC BY-NC 4.0 license (<https://creativecommons.org/licenses/by-nc/4.0/>)

Материалы конференции  
УДК 064.89.032.26  
DOI: <https://doi.org/10.18721/JPM.153.209>

## Тестирование прототипа системы мониторинга состояния рельсового пути с использованием LSTM рекуррентных нейронных сетей

М.А. Денисенко<sup>1</sup>, А.С. Исаева<sup>1</sup> ✉, И.Н. Коц<sup>1</sup>

<sup>1</sup>Южный федеральный университет, г. Таганрог, Россия

✉ isaevaas@sfedu.ru

**Аннотация.** В статье описано решение задачи многоклассовой классификации событий при движении модели тележки по рельсам, содержащим дефекты. Задача была решена с использованием рекуррентных нейронных сетей LSTM и реализована на языке программирования Python. Дана методика сбора данных и описание испытательного стенда. Сделаны выводы об эффективности распознавания событий из заданного набора.

**Ключевые слова:** мониторинг дефектов рельсового пути, нейронные сети, многоклассовая классификация

**Финансирование:** Научные исследования выполнены за счет средств федерального бюджета, в рамках научной деятельности по теме «Разработка и исследование методов и средств мониторинга, диагностики и прогнозирования состояния инженерных объектов на основе искусственного интеллекта» (задание № FENW-2020-0022).

**Ссылка при цитировании:** Исаева А. С., Денисенко М. А., Коц И. Н. Тестирование прототипа системы мониторинга состояния рельсового пути с использованием LSTM

рекуррентных нейронных сетей // Научно-технические ведомости СПбГПУ. Физико-математические науки. 2022. Т. 15. № 3.2. С. 51–55. DOI: <https://doi.org/10.18721/JPM.153.209>

Статья открытого доступа, распространяемая по лицензии CC BY-NC 4.0 (<https://creativecommons.org/licenses/by-nc/4.0/>)

### Introduction

Improving the efficiency of detecting defects in the railway track is an urgent task for any state that implements railway communication on its territory. The large length of railway tracks (more than 85 thousand kilometers of general-purpose tracks in the Russian Federation) makes it difficult to regularly inspect them and detect defects. All over the world, systems for diagnosing the condition of railway tracks are being actively developed, including the use of artificial intelligence systems [1–3]. Development of monitoring systems installed on existing railway cars and (or) trains, transfer and aggregation of the received data, analysis and identification of places of possible defects seems to be a good strategy. Data from a microphone, an accelerometer, a gyroscope, a photos of a railway tracks, etc. could be analyzed. In this paper we used information about accelerations that a vehicle moving on rails is subjected to.

### Materials and Methods

A model of a railway bogie was designed and manufactured for this experiment. Bogie is completed with an NVIDIA Jetson module, a Bluetooth/WiFi wireless data transmission module, sensitive elements - an inertial accelerometer module, and a power bank. Figure 1 shows 3D model of a railway bogie and a railway bogie with installed components.

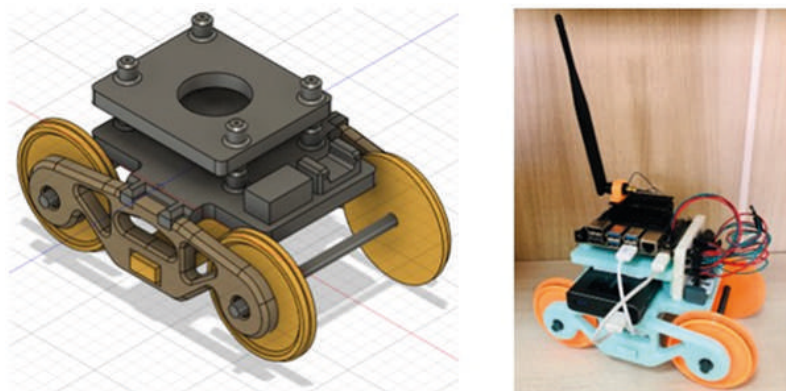


Fig. 1. 3D model of a railway bogie and a railway bogie with installed components

The rail track model consists of two metal L-shaped ( $3 \times 3$  cm) profiles 4 mm thick and 2 m long, fixed on wooden bars. The bogie rolls along the top edge of the profile. There are two such structures, so we have a total track length of 4 m and a joint that imitates a non-welded butt rail joint. The model was leveled and fixed on a solid base. A defect imitating rail spalling was applied to the working surface.

For the task of multiclass classification solving six variables were used: activity, user, timestamp, x-axis, y-axis, z-axis. Activity is the target variable and its takes three values: 1 (corresponds to the event "driving on rails"), 2 (corresponds to the event "non-welded joint of the rail track detected") and 3 (corresponds to the event "defect detected"). The x-axis, y-axis, z-axis are accelerations along the x, y, z axes. Numeric variables were normalized and converted to binary features, i.e., to a unitary code (one-hot encoding). In total, the training sample included 1957111 acceleration measurements, the test sample included 489275 measurements, that is, 80% and 20%, respectively, of the entire data set: 840,536 acceleration measurements were collected when a bogie model traveled on rails that did not contain defects, 775,118 acceleration measurements when a bogie model traveled along a joint, and 830,735 acceleration measurements when a bogie model traveled along a defect. Accelerations were taken at a sampling rate of 400 Hz.

In this case, since the data was collected for a specific task, the features are not sparse and the model does not contain redundant features for which it would be necessary to apply selection algorithms.

Figure 2 shows acceleration versus time graphs for three possible events: "driving on rails", "defect detected" and "non-welded joint of the rail track detected".

The sensor on railway bogie model is oriented as follows: the x-axis coincides with the direction of the bogie movement along the rails, the y-axis is perpendicular to the x-axis in the horizontal plane, and the z-axis is co-directed with the gravitational acceleration  $g$ .

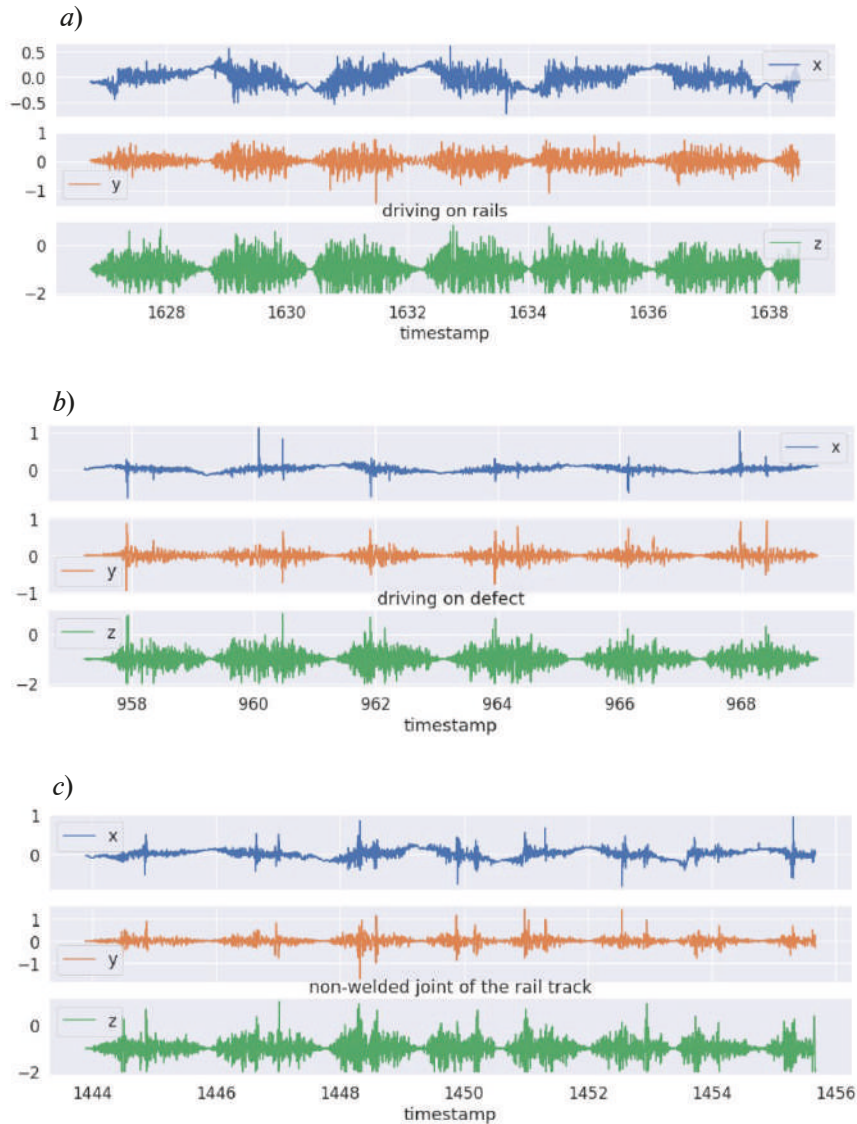


Fig. 2. Acceleration data: x-axis, y-axis and z-axis curves for "driving on rails" event (a), for "defect detected" event (b) and for "non-welded joint of the rail track detected" event (c)

Graphs in Figure 2 are built on 4000 values of the timestamp variable. Timestamp variable counts every 0.0025 second of the experiment, so it is slightly modified time scale. It can be seen from the graphs that 6-7 full round-trip cycles of the bogie movement fit into this time interval. This is important to note, since the entire set of data must be divided into frames for training the neural network, and we did it in such a way that each frame must include at least one full cycle of movement. During the training of the neural network, frames of 200 and 500 values of the timestamp variable were used.

To implement the event recognition algorithm, a network of long short-term memory (LSTM) was used. It is a one of recurrent neural networks. The LSTM network is well adapted to learning on the problems of classification, processing and forecasting of time series in cases where important events are separated by time lags with indefinite duration and boundaries. To improve the performance of the model, a bidirectional LSTM network (Bidirectional LSTM) was used.

Unlike a conventional LSTM network, a bidirectional LSTM network is trained on both the direct and external side of the input data [4].

The LSTM neural network was implemented using the Keras library. It consists of one layer of 164 neurons. The model was trained for 20 epochs, batch size = 32.

### Results and Discussion

The neural network determines the event with an accuracy of 93%. The largest number of errors occurs when defining “defect detected” event. The confusion matrix of the developed model is shown on Figure 3.

Despite a convolutional neural network (CNN) it is the most commonly used architecture for this type of problem [5], we have obtained good result with LSTM neural network. We suppose that data, collected not in the laboratory, but through a real railway bogie driving, would reduce the accuracy.

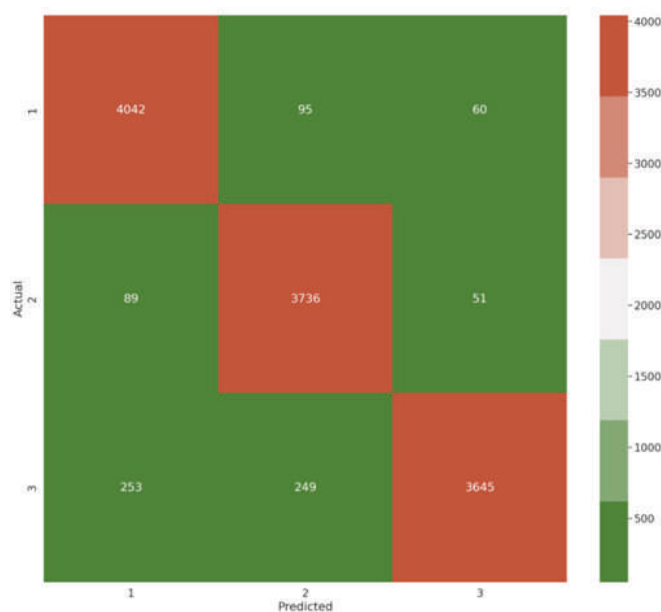


Fig. 3. Confusion matrix of the developed model

### Conclusion

The solution of the multiclass classification problem of the events recognition during the movement of a bogie model along rails containing defects and training of the LSTM recurrent neural networks is described in this paper. We obtained 93% accuracy of the events recognition.

### REFERENCES

1. **Giben X., Patel V. M., Chellappa R.**, Material classification and semantic segmentation of railway track images with deep convolutional neural networks IEEE International Conference on Image Processing (ICIP). 2015. Pp. 621–625.
2. **Gibert X., Vishal P., Chellappa R.**, Robust Fastener Detection for Autonomous Visual Railway Track Inspection 2015 IEEE Winter Conference on Applications of Computer Vision. 2015. Pp. 694–701.
3. **Yang C., Sun Y., Ladubec C., Liu Y.**, Developing Machine Learning-Based Models for Railway Inspection Applied Sciences. 2021. Vol. 11 (1) 13.
4. **Staudemeyer Ralf C., Morris Eric R.**, Understanding LSTM - a tutorial into Long Short-Term Memory Recurrent Neural Networks ArXiv. 2019
5. **Fawaz H., Forestier G., Weber J., Idoumghar L., Muller P. A.**, Deep learning for time series classification: a review. Data Mining and Knowledge Discovery. 2019. Vol. 33. No. 4. Pp. 917–963.



## THE AUTHORS

**DENISENKO Mark A.**

dema@sfedu.ru

ORCID: 0000-0001-5044-7482

**ISAEVA Alina S.**

isaevaas@sfedu.ru

ORCID: 0000-0002-5145-0963

**KOTS Ivan N.**

inkots@sfedu.ru

ORCID: 0000-0002-1257-7304

*Received 17.08.2022. Approved after reviewing 31.08.2022. Accepted 01.09.2022.*

Conference materials

UDC 535

DOI: <https://doi.org/10.18721/JPM.153.210>

## Synchronization protocol for MDI-QKD systems

N. V. Rudavin<sup>1,2</sup> ✉, I. S. Gerasin<sup>1,3,4</sup>, E. E. Mekhtiev<sup>3,4,5</sup>,

A. V. Duplinsky<sup>1,4,5</sup>, Y. V. Kurochkin<sup>1,3,4,5</sup>

<sup>1</sup> NTI Center for Quantum Communications, National University of Science and Technology MISiS, Moscow, Russia;

<sup>2</sup> HSE University, Moscow, Russia;

<sup>3</sup> Moscow Institute of Physics and Technology, Dolgoprudny, Moscow Region, Russia;

<sup>4</sup> Russian Quantum Center, Skolkovo, Moscow, Russia;

<sup>5</sup> QRate, Moscow, Russia

✉ [n.rudavin@goqrates.com](mailto:n.rudavin@goqrates.com)

**Abstract.** Commercial fiber quantum key distribution systems require the implementation of a protocol for synchronizing the frequency synthesizers of the transmitter and receiver nodes. Frequency mismatch may be due to temperature fluctuations, mechanical effects and imperfections in the technological processes. In this work, an algorithm for automatically adjusting Alice's and Bob's frequency to Charlie's frequency is proposed. After optimizing the algorithm parameters, it was tested on optical lines of different lengths.

**Keywords:** measurement-device-independent quantum key distribution, MDI-QKD, synchronization protocol, PD controller

**Funding:** The study was commissioned by JSCo «RZD».

**Citation:** Rudavin N. V., Gerasin I. S., Mekhtiev E. E., Duplinsky A. V., Kurochkin Y. V., Synchronization protocol for MDI-QKD systems, St. Petersburg State Polytechnical University Journal. Physics and Mathematics. 15 (3.2) (2022) 56–60. DOI: <https://doi.org/10.18721/JPM.153.210>

This is an open access article under the CC BY-NC 4.0 license (<https://creativecommons.org/licenses/by-nc/4.0/>)

Материалы конференции

УДК 535

DOI: <https://doi.org/10.18721/JPM.153.210>

## Протокол синхронизации для систем MDI-QKD

Н.В. Рудавин<sup>1,2</sup> ✉, И.С. Герасин<sup>1,3,4</sup>, Е.Е. Мехтiev<sup>3,4,5</sup>,

А.В. Дуплинский<sup>1,4,5</sup>, Ю.В. Курочкин<sup>1,3,4,5</sup>

<sup>1</sup> Центр НТИ «Квантовые коммуникации», Национальный исследовательский технологический университет МИСиС, г. Москва, Россия;

<sup>2</sup> Национальный исследовательский университет «Высшая школа экономики», г. Москва, Россия;

<sup>3</sup> Московский физико-технический институт, г. Долгопрудный, Московская область, Россия;

<sup>4</sup> Российский квантовый центр, Инновационный центр Сколково, г. Москва, Россия;

<sup>5</sup> КуРэйт, г. Москва, Россия

✉ [n.rudavin@goqrates.com](mailto:n.rudavin@goqrates.com)

**Аннотация.** Промышленная система квантового распределения ключей требует реализации протокола синхронизации генераторов опорных частот узлов передатчика и приемника. Расхождение частот может быть связано с температурными флуктуациями, механическим воздействием и неидеальностью технологических процессов. В данной работе предложен алгоритм автоматической подстройки частоты Алисы и Боба под частоту Чарли. После оптимизации параметров алгоритма было проведено его тестирование на оптических линиях различной длины.



**Ключевые слова:** детектор-независимое квантовое распределение ключей, КРК, протокол синхронизации, PD – регулятор

**Финансирование:** Исследовательская работа выполнена по заказу ОАО «РЖД».

**Ссылка при цитировании:** Рудагин Н. В., Герасин И. С., Мехтиев Э. Э., Дуплинский А. В., Курочкин Ю. В. Протокол синхронизации для систем MDI-QKD // Научно-технические ведомости СПбГПУ. Физико-математические науки. 2022. Т. 15. № 3.2. С. 56–60. DOI: <https://doi.org/10.18721/JPM.153.210>

Статья открытого доступа, распространяемая по лицензии CC BY-NC 4.0 (<https://creativecommons.org/licenses/by-nc/4.0/>)

## Introduction

Nowadays, the commercial implementation of fiber quantum key distribution (QKD) systems use crystal oscillators and several frequency multipliers as frequency synthesizers to generate the operating frequency. At the same time, the existing technological production process does not allow obtaining frequency synthesizers with identical output parameters. Moreover, modern crystal oscillators do not have high stability over long periods of time due to temperature fluctuations or mechanical stress. The discrepancy between the frequencies of the synthesizers is crucial for key generation. So, it is necessary to organize frequency synchronization system for experimental measurement-device-independent QKD protocol (MDI-QKD) fiber setup.

There are three main approaches to organize the synchronization protocol in QKD systems. The most common method for time synchronization of nodes in MDI-QKD fiber setups is to use a frequency synthesizer as a reference for all nodes. In this scheme, the generator is typically installed on Charlie's device and connected to Alice's and Bob's control boards via electrical cables [1, 2]. This synchronization method is traditionally used in proof of principle experiments. However, a significant disadvantage of this approach is that it is impossible to distribute Alice's and Bob's devices at a large distance from Charlie. Accordingly, this is critical for the commercial implementation of the QKD system but is excellent for laboratory testing.

The second method is based on computing the cross-correlation of transmitted and received qubit sequences [3]. The disadvantage of this approach is the necessity to use single photon detectors (SPD), which are the most technologically complex node of modern QKD systems. The last approach is to use high energy optical pulses sent by Alice through a quantum channel [4] or an additional fiber [5] to transmit the frequency of Alice's synthesizer. The use of a second fiber imposes additional requirements on the integration of the QKD system into existing telecommunication networks and increases the cost of the system.

## Materials and Methods

In the MDI-QKD protocol the secret key is distributed between the two transmitters (Alice and Bob) using the untrusted central node (Charlie). Since SPDs are located at Charlie's node, we cannot use qubit-based synchronization method. Therefore, for experimental MDI-QKD fiber setup we suggest to use quantum channel to transmit the synchronization signal. Since Alice and Bob are not connected by an optical fiber, we use a laser and a 50/50 beamsplitter to generate a synchronization signal on Charlie. The wavelengths of the synchronization laser and the signal laser are in different DWDM channels. In this configuration the sync pulses propagate in the opposite direction through the quantum channel. To eliminate their influence on the quantum signal and the SPDs, we use time-division multiplexing and WDM optical filters.

From the point of view of the theory of control of technical systems, the task of adjusting the frequency of one synthesizer to the frequency of another synthesizer can be considered as the task of designing and implementing an industrial control system (ICS). A phase-locked loop (PLL) system was chosen as the ICS. We use photodetectors to register the optical synchronization signal and to convert it into an electrical signal.

To obtain a phase error value between the synthesizers, the synchronization signal is sent to one of the inputs of the phase detector (PD). The signal from Alice's (Bob's) synthesizer is sent

to the second PD input. Then we tune the frequency by changing the voltage supplied to Alice's (Bob's) synthesizer. The value of the control signal is calculated using a proportional – derivative controller (PD controller). In general, the integral term is also used to calculate the correction, but during the experiments it was decided not to use it to simplify the optimization process of the gain coefficients. By using third and fifth order derivative terms we can achieve a high frequency tuning rate even if the initial frequencies of the synthesizers are very different:

$$u(n) = P + D + D^3 + D^5 + u(n-1) \quad (1)$$

where  $P$  is the proportional term, where  $D$  is the derivative term, where  $u(n-1)$  is the voltage on the frequency synthesizer, calculated in the previous iteration of the protocol. Terms for  $u(n)$  calculates as follows:

$$P = K_p \cdot (e(n) - \Delta e_{const}), \quad (2)$$

$$D = K_d \cdot (e(n) - e(n-1)), \quad (3)$$

$$D^3 = K_{d3} \cdot (e(n) - e(n-1))^3, \quad (4)$$

$$D^5 = K_{d5} \cdot (e(n) - e(n-1))^5, \quad (5)$$

where  $K_p$  is the proportional term coefficient, where  $K_d$  is the derivative term coefficient, where  $K_{d3}$  is the third order derivative term coefficient, where  $K_{d5}$  is the fifth order derivative term coefficient, where  $e(n)$  is the phase error value on current iteration, where  $e(n-1)$  is the phase error value on the previous iteration, where  $\Delta e_{const}$  is the target phase error value.

### Results

For proof of principle experiment we built experimental setup, consisting of Alice and Charlie. The proposed synchronization protocol has four hyperparameters – the gain coefficients of the terms of the controller. Using the method of experimental tuning with different sets of coefficients, their optimal values were found (Table 1).

**PD controller coefficients**

Coefficient	Value
$K_p$	$2 \times 10^{-3}$
$K_d$	$8 \times 10^{-3}$
$K_{d3}$	$3.2 \times 10^{-10}$
$K_{d5}$	$1.6 \times 10^{-8}$

To estimate the accuracy of the synchronization, we measured the frequency ratio of Alice's and Charlie's synthesizers with 75 km of fiber. During the experiment, the Keysight 53220A 350 MHz universal frequency counter was used, and the sampling rate was 1/60 Hz (Fig. 1). During the tests with optimal coefficients, we were able to achieve stable synchronization with accuracy up to the twelve decimal place. The experiment confirmed that the proposed protocol can be used in MDI-QKD experimental setups.

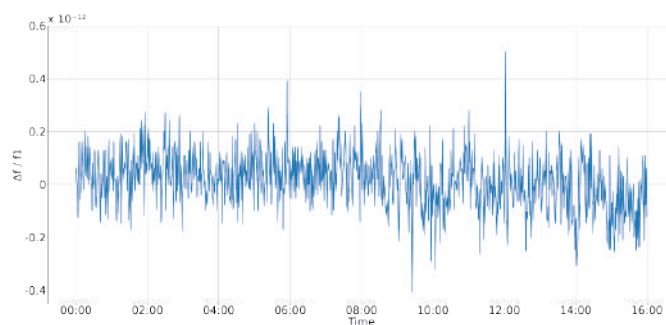


Fig. 1. The frequency ratio of Alice's and Charlie's synthesizers with 75 km of fiber for 16 hours



For the next experiment, the MDI-QKD fiber experiment setup was built and the proposed protocol was implemented on it. Both Alice and Bob were connected to Charlie by 75 kilometers of standard single-mode telecommunication optical fiber SMF-28e. As frequency counter was used Keysight 53220A with sampling rate of 1/60 Hz. We run the synchronization process using the coefficients from Table 1 and measured the frequency ratio during 16 hours (see Fig. 2). We can see the accuracy of the synchronization is up to the twelve decimal place, which is consistent with the results of the previous experiment.

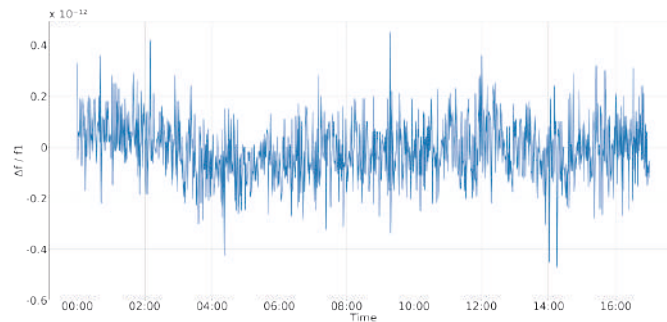


Fig. 2. The frequency ratio of Alice's and Bob's synthesizers with 150 km of fiber for 16 hours

### Conclusion

We have demonstrated frequency synchronization protocol for MDI-QKD setups, utilizing a laser and a 50/50 beamsplitter to transmit the synchronization signal and a PLL system to calculate the value of the control signal. Importantly, this method allows the use of a single optical fiber to transmit quantum and synchronization signals. The obtained results show that our approach allows us to maintain frequency synchronization at a high level. It is worth pointing out that this work has been carried out in a laboratory with fiber coils. It is necessary to perform a similar demonstration in the scenario of real telecommunication networks to confirm the robustness of the proposed protocol.

### REFERENCES

1. Tang Z., Liao Z., Xu F., Qi B., Qian L., Lo H. K., Experimental demonstration of polarization encoding measurement-device-independent quantum key distribution, *Physical review letters*. 112 (19) (2014) 190503.
2. Tang Z., Wei K., Bedroya O., Qian L., Lo H. K., Experimental measurement-device-independent quantum key distribution with imperfect sources, *Physical Review A*. 93 (4) (2016) 042308.
3. Cochran R., Gauthier D., Qubit-based clock synchronization for QKD systems using a Bayesian approach, *Entropy*. 23 (8) (2021) 988.
4. Tang Y. L., Yin H. L., Chen S. J., Liu Y., Zhang W. J., Jiang X., Pan J. W., Measurement-device-independent quantum key distribution over 200 km, *Physical review letters*. 113 (19) (2014) 190501.
5. Korzh B., Lim C. C. W., Houlmann R., Gisin N., Li M. J., Nolan, D., Zbinden H., Provably secure and practical quantum key distribution over 307 km of optical fibre, *Nature Photonics*. 9 (3) (2015) 163–168.

### THE AUTHORS

**RUDAVIN Nikita V.**  
n.rudavin@goqrates.com  
ORCID: 0000-0003-0264-5710

**GERASIN Ilia S.**  
i.gerasin@goqrates.com  
ORCID: 0000-0001-5084-7056

**MEKHTIEV EI E.**

mekhtiev@phystech.edu

ORCID: 0000-0002-9756-7016

**DUPLINSKY Alexander V.**

a.duplinsky@goqrata.com

ORCID: 0000-0003-2222-0752

**KUROCHKIN Yury V.**

yk@goqrata.com

ORCID: 0000-0001-5376-6358

*Received 12.08.2022. Approved after reviewing 31.08.2022. Accepted 31.08.2022.*

Conference materials

UDC 535.51

DOI: <https://doi.org/10.18721/JPM.153.211>

## Influence of polarization reference frame rotation on ground-receiver error rate in satellite quantum key distribution

A. V. Duplinsky<sup>1,2,6</sup> ✉, A. V. Khmelev<sup>1,2,4</sup>, V. E. Merzlinkin<sup>2,3</sup>,  
V. L. Kurochkin<sup>1,2,3,4</sup>, Yu. V. Kurochkin<sup>1,2,3,4,5</sup>

<sup>1</sup> QSpace Technologies, Moscow, Russia;

<sup>2</sup> QRate, Moscow, Russia;

<sup>3</sup> NTI Center for Quantum Communications, National University of Science and Technology MISiS, Moscow, Russia;

<sup>4</sup> Russian Quantum Center, Moscow, Russia;

<sup>5</sup> Moscow Institute of Physics and Technology, Dolgoprudny, Moscow Region, Russia;

<sup>6</sup> HSE University, Moscow, Russia

✉ [al.duplinsky@goqr.com](mailto:al.duplinsky@goqr.com)

**Abstract.** Quantum key distribution (QKD) in a space-Earth communication link is a difficult technical task. Aside from precise mutual pointing of the optical axes during the satellite QKD session, the polarization reference frame coincidence of the satellite and the receiving station is also required. Satellite motion causes a rotation of the polarization reference frame in respect to ground station measurements of quantum states, which contributes to the error rate in time. In order to reduce the quantum bit error rate, we designed and tested a polarization correction device for the receiving ground station that is included as a part of our data analysis and processing module. We have measured the polarization properties of the ground-based receiver and showed the evolution of four polarization states over time for a typical satellite passage. An average polarization extinction ratio is equal to 200:1 for the optical free-space receiver. We have calculated the maximum permitted deviation of the polarization reference frame at the performance of the compensation system, which is less than 5.8 degrees when bit error rate is equal to 1,5%.

**Keywords:** Quantum communications, quantum key distribution, polarimetry, extinction ratio, optical design, photon polarization, single photon detectors, free-space optics

**Funding:** Strategic academic leadership program “Priority 2030”, indicating number of the financial support of K1-2022-027.

**Citation:** Duplinsky A. V., Khmelev A. V., Merzlinkin V.E., Kurochkin V. L., Kurochkin Yu. V., Influence of polarization reference frame rotation on ground-receiver error rate in satellite quantum key distribution, St. Petersburg State Polytechnical University Journal. Physics and Mathematics. 15 (3.2) (2022) 61–64. DOI: <https://doi.org/10.18721/JPM.153.211>

This is an open access article under the CC BY-NC 4.0 license (<https://creativecommons.org/licenses/by-nc/4.0/>)

Материалы конференции

УДК 535.51

DOI: <https://doi.org/10.18721/JPM.153.211>

## Влияние вращения поляризационной системы отсчета на величину ошибок в эксперименте по квантовому распределению ключей со спутника на наземную станцию

А. В. Дуплинский<sup>1,2,6</sup> ✉, А. В. Хмелев<sup>1,2,4</sup>, В. Е. Мерзлинкин<sup>2,3</sup>,  
В. Л. Курочкин<sup>1,2,3,4</sup>, Ю. В. Курочкин<sup>1,2,3,4,5</sup>

<sup>1</sup> КуСпэйс Технологии, г. Москва, Россия;

<sup>2</sup> КурЭйт, г. Москва, Россия;

<sup>3</sup> НТИ Центр Квантовых коммуникаций, Национальный Университет  
Науки и Технологии МИСиС, г. Москва, Россия;

<sup>4</sup> Российский Квантовый Центр, г. Москва, Россия;

<sup>5</sup> Московский физико-технический институт, г. Долгопрудный, Россия;

<sup>6</sup> Национальный исследовательский университет «Высшая школа экономики», г. Москва, Россия

✉ al.duplinsky@goqrates.com

**Аннотация.** Квантовое распределение ключей по линии связи космос–Земля является сложной технической задачей. Помимо точного взаимного наведения оптических осей во время сеанса квантовой связи со спутником, также требуется совпадение поляризационной системы отсчета космического аппарата и приемной наземной станции. В статье представлены результаты тестов системы коррекции поляризации для наземной станции, которая входит в состав приемного модуля анализа и обработки данных. Проведены измерения поляризационных свойств наземной приемной станции для четырех поляризационных состояний от времени в ходе симуляции типичного пролёта спутника. Усредненный коэффициент поляризационной экстинкции для оптического приемника составил 200:1. Максимально допустимое отклонение поляризационной системы отсчета при работе системы компенсации составляет менее 5,8 градусов при ограничении итоговой величин ошибки в 1,5%.

**Ключевые слова:** Квантовые коммуникации, распределение квантовых ключей, поляриметрия, коэффициент экстинкции, оптическая схема, поляризация фотонов, детекторы одиночных фотонов, оптика свободного пространства

**Финансирование:** Программа стратегического академического лидерства «Приоритет-2030», проект № К1-2022-027.

**Ссылка при цитировании:** Дуплинский А. В., Хмелёв А. В., Мерзлинкин В. Е., Курочкин В. Л., Курочкин Ю. В. Влияние вращения поляризационной системы отсчета на величину ошибок в эксперименте по квантовому распределению ключей со спутника на наземную станцию // Научно-технические ведомости СПбГПУ. Физико-математические науки. 2022. Т. 15. № 3.2. С. 61–64. DOI: <https://doi.org/10.18721/JPM.153.211>

Статья открытого доступа, распространяемая по лицензии CC BY-NC 4.0 (<https://creativecommons.org/licenses/by-nc/4.0/>)

## Introduction

Quantum key distribution in a Space-Earth optical communication link is a challenging technical task [1,2]. The development of an equipment requires a solution of many issues including the precise optical axes pointing of a ground station and a satellite payload, but also the highly necessary polarization reference frame coincidence of them. The problem of pointing and tracking is successfully solved in our previous articles [3,4]. The solution to the polarization rotation problem is reported here.

The satellite reference frame has a time dependent rotation relatively at the ground station, even when the satellite system is stabilized along the nadir axis [5]. Such angular movement creates a shift in the angles of the polarization bases during a QKD communication with the satellite, which increases the error rate when decoding quantum states.

In this work we consider the effect of a time dependent rotation of the polarization basis and describe the method which helps to compensate this polarization deviation. The observed polarization characteristic of an optical ground station allows us to determine the maximum mismatch angle of polarization reference frames encoding and decoding photon states.

## Methods

A ground-based receiver for QKD is located in the Zvenigorod observatory, about 80 km from Moscow. A Ritchey–Chretien Alt–Az telescope with an aperture of 0.6 m and a focal length of 4.8 m is used to gather a quantum signal. The main optical part of the receiver for satellite quantum key distribution with a satellite consists of a mirror telescope, an optical signal processing unit, and a polarization analyzer (PA).

© Дуплинский А. В., Хмелёв А. В., Мерзлинкин В. Е., Курочкин В. Л., Курочкин Ю. В., 2022. Издатель: Санкт-Петербургский политехнический университет Петра Великого.



The polarization analyzer acts as a free-space decoder of quantum states that allows using the BB84 protocol for satellite-to-ground QKD. The optical signal analysis and processing system (APS) includes a motorized half-wave plate. Its time-dependent angular motion may be regulated by a predicted function to correct the rotation of the reference frame of polarization bases measurements, as shown in figure 1. By altering the angle of the half-wave plate fast axis, a unit can align the decoder's polarization reference frame in relation to the transmitter's polarized photons.

In order to test the compensating system, we simulate the relative rotation of the satellite to the Alt-Azimuth telescope polarization reference frame. A polarized laser source with an intense output power and a wavelength of roughly 850 nm is positioned in front of our receiving ground station. This source is mounted in a high-precision rotary holder, altering the angle of the output linear polarization.

Firstly, we should define the zero point of our receiver, setting a horizontal  $|H\rangle$ -polarization on the laser source. Rotating the half-wave plate of the compensation system in APS, we find its angular position that corresponds to the maximum number of clicks on the single photon detector coupled to the  $|H\rangle$ -channel of the polarization decoder.

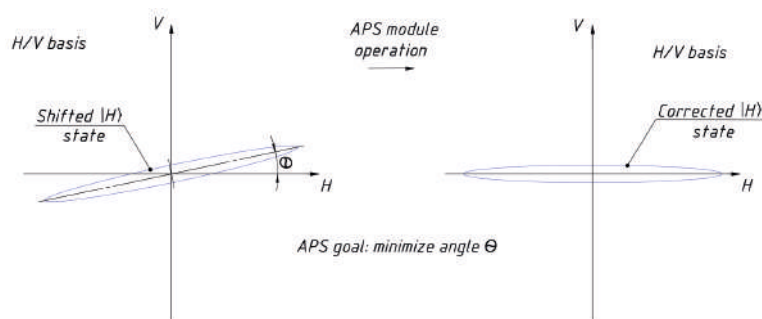


Fig. 1. Polarization conversion in APS module

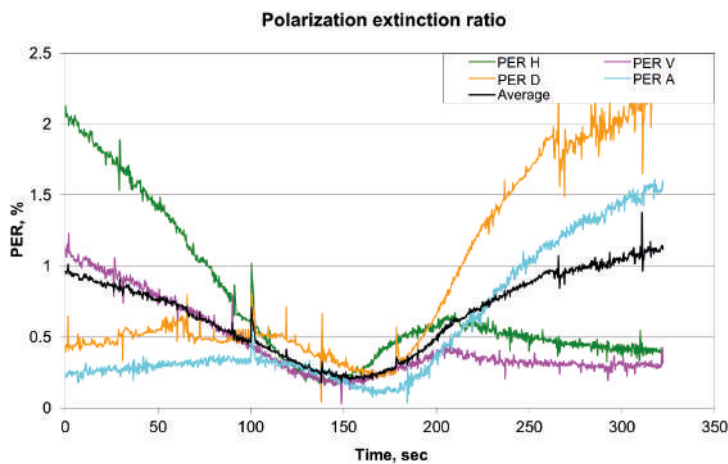


Fig.2. Polarization extinction ratio (PER) obtained in the local test

To obtain the expected error rate of the ground station, we measure the polarization characteristics of the optical receiver using an intense laser source with a polarization extinction ratio (PER) better than 4000:1. So, we start a polarization rotation of the laser source in a range of  $\pm 90$  degrees according to the predicted function and compensate it on the receiver, simultaneously. Such measurements are carried out for  $|H\rangle$  – horizontal polarization,  $|V\rangle$  – vertical polarization,  $|D\rangle$  – diagonal polarization and  $|A\rangle$  – anti-diagonal polarization decoder channels. The results of polarization extinction coefficient depending on time for these channels are presented in figure

2. The average value of the PER of these polarization states for our setup turned out to be less than 0.5% (Fig. 2).

### Results

Based on the PER values acquired from experiment for the stationary transmission of polarization states, the compensating mechanism appears to be operational. Because the simulation of the satellite QKD session was conducted in the presence of a strong optical signal, we can only estimate the optical  $QBER$  of our system without taking noise into account.

Let us estimate the permissible angular error of polarization reference frame rotation when the

upper bound of expected  $QBER$  is under 1.5%:

$$QBER_{exp} = QBER_{opt} + \frac{ER-1}{ER+1} \sin^2 \theta_{max}, \quad (1)$$

where  $ER$  – reciprocal of average PER,  $\theta$  – angular error value,  $QBER_{exp}$  – the specified (expected) limit parameter for error rate,  $QBER_{opt}$  – optical part of error rate.

Hence, taking into account  $ER^{opt} = 200$  from local polarization test and consequently  $QBER_{opt} = 0.5\%$ ,  $QBER_{exp} = 1.5\%$ , we can calculate  $\theta_{max}$ , using estimated and experimental measurements as follows:

$$\theta_{max} = \arcsin \sqrt{\frac{(ER+1) \cdot QBER_{opt}}{ER-1}}, \quad (2)$$

$$\theta_{max} = 5.78^\circ. \quad (3)$$

### Conclusion

We have demonstrated the work of the analysis and processing module in operating mode simulation. The APS module can successfully compensate for polarization reference frame rotation and the average optical  $QBER$  is 0.5%. Finally, we estimate the maximum allowed angular error for the compensation system, as a consequence of complexity of the precise satellite rotation prediction.

### Acknowledgments

We would like to thank colleagues at the Institute of Astronomy of the Russian Academy of Sciences for their assistance and support in the form of the strategic academic leadership program “Priority 2030”, indicating number of the financial support of K1-2022-027.

### REFERENCES

1. Liao, Sheng-Kai, et al., Satellite-to-ground quantum key distribution. Nature 549.7670 (2017) 43–47.
2. Han, Xuan, et al., Polarization design for ground-to-satellite quantum entanglement distribution. Optics Express 28.1 (2020) 369–378.
3. Khmelev, A. V., et al., Recording of a Single-Photon Signal from Low-Flying Satellites for Satellite Quantum Key Distribution. Technical Physics Letters (2021) 1–4.
4. Kurochkin, V. L., et al., Elements of satellite quantum network. International Conference on Micro-and Nano-Electronics 2021. Vol. 12157. SPIE, 2022.
5. Zhang, Ming, et al., Detection and compensation of basis deviation in satellite-to-ground quantum communications. Optics express 22.8 (2014) 9871–9886.

### THE AUTHORS

**DUPLINSKY Alexey V.**  
al.duplinsky@goqr.com  
ORCID: 0000-0002-2964-1800

**KUROCHKIN Vladimir L.**  
v.kurochkin@rqc.ru  
ORCID: 0000-0002-1599-9801

**KHMELEV Aleksandr V.**  
a.khmelev@goqr.com  
ORCID: 0000-0003-1511-1128

**KUROCHKIN Yury V.**  
yk@goqr.com  
ORCID: 0000-0001-5376-6358

**MERZLINKIN Vitalii E.**  
merzlinkin@yandex.ru  
ORCID: 0000-0002-4310-2619

*Received 15.08.2022. Approved after reviewing 08.09.2022. Accepted 08.09.2022.*

Conference materials

UDC 04.056.55

DOI: <https://doi.org/10.18721/JPM.153.212>

## QKD and phase modulator imperfections

Reutov A. A.<sup>1</sup>✉, Tayduganov A. S.<sup>1,2</sup>

<sup>1</sup>QRate, Skolkovo, Moscow, Russia;

<sup>2</sup>NTI Center for Quantum Communications, National University of Science and Technology MISiS,  
Moscow, Russia

✉ [aleksey.reutov@phystech.edu](mailto:aleksey.reutov@phystech.edu)

**Abstract.** Very often in practical schemes of quantum key distribution various realistic device imperfections are usually neglected. In this work we consider the imperfect phase-modulation encoding that might lead to a potential information leakage and study its effect on the secret key generation rate.

**Keywords:** quantum cryptography, QKD, state preparation

**Citation:** Reutov A. A., Tayduganov A. S., QKD and phase modulator imperfections, St. Petersburg State Polytechnical University Journal. Physics and Mathematics. 15 (3.2) (2022) 65–68. DOI: <https://doi.org/10.18721/JPM.153.212>

This is an open access article under the CC BY-NC 4.0 license (<https://creativecommons.org/licenses/by-nc/4.0/>)

Материалы конференции

УДК 04.056.55

DOI: <https://doi.org/10.18721/JPM.153.212>

## КРК и неидеальности фазового модулятора

А. А. Реутов<sup>1</sup> ✉, А. С. Тайдуганов<sup>1,2</sup>

<sup>1</sup>QRate, Сколково, г. Москва, Россия;

<sup>2</sup>НТИ Центр квантовых коммуникаций, Национальный университет  
науки и технологий МИСиС, г. Москва, Россия

✉ [aleksey.reutov@phystech.edu](mailto:aleksey.reutov@phystech.edu)

**Аннотация.** Очень часто в практических схемах распределения квантового ключа обычно пренебрегают различными реальными несовершенствами устройств. В этой работе мы рассматриваем неидеальности фазово-модуляционного кодирования, которые могут привести к потенциальной утечке информации и изучаем их влияние на скорость генерации секретного ключа.

**Ключевые слова:** квантовая криптография, КРК, приготовление состояний

**Ссылка при цитировании:** Реутов А.А., Тайдуганов А.С. КРК и неидеальности фазового модулятора // Научно-технические ведомости СПбГПУ. Физико-математические науки. 2022. Т. 15. № 3.2. С. 65–68. DOI: <https://doi.org/10.18721/JPM.153.212>

Статья открытого доступа, распространяемая по лицензии CC BY-NC 4.0 (<https://creativecommons.org/licenses/by-nc/4.0/>)

## Introduction

The quantum key distribution (QKD) is based on fundamental laws of quantum physics and theoretically provides security regardless eavesdropper's potential resources. However, the practical QKD implementations suffer from imperfections of realistic devices [1]. One of the sources of potential information leakage in practical BB84 [2] schemes is the imperfect state preparation by a phase modulator (PM) used for the qubit state encoding. This imperfection leads to an asymmetry between the bases, that can provide more efficient strategies for an eavesdropper [3]. In this work we consider the general quantum state description and introduce two possible phase modulation

uncertainties. Using the density matrix formalism, we provide a metrics of distinguishability between the BB84 bases in our model and estimate its effect on the secret key rate.

### Theory and Methods

In our setup the linearly polarized light is brought to the Alice's PM at an angle of  $45^\circ$  with respect to the crystal axes of the modulator with an error  $\delta\theta$ . In general, there is some phase difference  $\varphi$  between the field amplitudes along the ordinary and extraordinary axes. By applying an electric voltage along one of the axes, an additional phase difference  $\varphi_{bit}^{basis}$  (with some uncertainty  $\delta\varphi_{bit}^{basis}$ ) is created, which determines the basis and bit states.

Without uncertainty  $\delta\varphi_{bit}^{basis}$  and error  $\delta\theta$ , the polarization state, prepared by Alice in  $X'$  and  $Y'$  bases, can be described on the Bloch sphere (Fig. 1) in the following form,

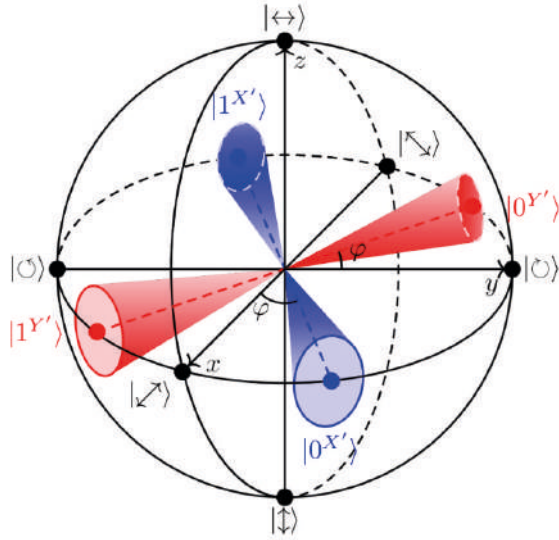


Fig. 1. Physical polarization states on the Bloch sphere; experimental phase uncertainties are schematically depicted as red and blue cones

$$\begin{aligned} |0^{X'}\rangle &= \frac{1}{\sqrt{2}}(|\leftrightarrow\rangle + e^{i\varphi}|\downarrow\rangle), \\ |1^{X'}\rangle &= \frac{1}{\sqrt{2}}(|\leftrightarrow\rangle + e^{i(\varphi+\pi)}|\downarrow\rangle), \\ |0^{Y'}\rangle &= \frac{1}{\sqrt{2}}(|\leftrightarrow\rangle + e^{i(\varphi+\pi/2)}|\downarrow\rangle), \\ |1^{Y'}\rangle &= \frac{1}{\sqrt{2}}(|\leftrightarrow\rangle + e^{i(\varphi-\pi/2)}|\downarrow\rangle), \end{aligned} \quad (1)$$

where  $|\leftrightarrow\rangle$  and  $|\downarrow\rangle$  are the standard horizontal and vertical polarization states. The general polarization state with PM imperfection corrections is given by

$$\begin{aligned} |\Psi_0^{X'}\rangle &= \cos\left(\frac{\pi}{4} - \frac{\delta\theta}{2}\right)|\leftrightarrow\rangle + e^{i(\varphi+\delta\varphi_1)}\sin\left(\frac{\pi}{4} - \frac{\delta\theta}{2}\right)|\downarrow\rangle, \\ |\Psi_1^{X'}\rangle &= \cos\left(\frac{\pi}{4} - \frac{\delta\theta}{2}\right)|\leftrightarrow\rangle + e^{i(\varphi+\pi+\delta\varphi_2)}\sin\left(\frac{\pi}{4} - \frac{\delta\theta}{2}\right)|\downarrow\rangle, \\ |\Psi_0^{Y'}\rangle &= \cos\left(\frac{\pi}{4} - \frac{\delta\theta}{2}\right)|\leftrightarrow\rangle + e^{i(\varphi+\pi/2+\delta\varphi_3)}\sin\left(\frac{\pi}{4} - \frac{\delta\theta}{2}\right)|\downarrow\rangle, \\ |\Psi_1^{Y'}\rangle &= \cos\left(\frac{\pi}{4} - \frac{\delta\theta}{2}\right)|\leftrightarrow\rangle + e^{i(\varphi-\pi/2+\delta\varphi_4)}\sin\left(\frac{\pi}{4} - \frac{\delta\theta}{2}\right)|\downarrow\rangle, \end{aligned} \quad (2)$$

where  $\delta\theta$  represents in Fig. 1 the deviation from the  $xy$  – plane on the Bloch sphere caused by e.g. the  $45^\circ$  fiber input error.

To describe the distinguishability between the states in two bases, the metric  $\Delta$  called the *imbalance of “quantum coin”* [4] is used. It can be expressed in terms of *fidelity*  $F$  [5]:

$$\Delta \equiv \frac{1 - \sqrt{F(\rho^{X'}, \rho^{Y'})}}{2}, \quad (3)$$

and fidelity  $F$  is given by

$$F(\rho^{X'}, \rho^{Y'}) \equiv \left( \text{Tr} \sqrt{\sqrt{\rho^{Y'}} \rho^{X'} \sqrt{\rho^{Y'}}} \right)^2, \quad (4)$$



where the density matrices  $\rho^{X'}$  and  $\rho^{Y'}$  are given by  $\rho^{basis} = (|\psi_0^{basis}\rangle\langle\psi_0^{basis}| + |\psi_1^{basis}\rangle\langle\psi_1^{basis}|) / 2$  and can be written (with help (2)) as:

$$\rho^{X'} = \frac{1}{2} \begin{pmatrix} 1 + \sin \delta\theta & \frac{1}{2} e^{-i\varphi} (e^{-i\delta\varphi_1} - e^{-i\delta\varphi_2}) \cos \delta\theta \\ \frac{1}{2} e^{i\varphi} (e^{i\delta\varphi_1} - e^{i\delta\varphi_2}) \cos \delta\theta & 1 - \sin \delta\theta \end{pmatrix}, \quad (5)$$

$$\rho^{Y'} = \frac{1}{2} \begin{pmatrix} 1 + \sin \delta\theta & -\frac{i}{2} e^{-i\varphi} (e^{-i\delta\varphi_3} - e^{-i\delta\varphi_4}) \cos \delta\theta \\ \frac{i}{2} e^{i\varphi} (e^{i\delta\varphi_3} - e^{i\delta\varphi_4}) \cos \delta\theta & 1 - \sin \delta\theta \end{pmatrix}.$$

It's leads us to the following result for fidelity:

$$F(\rho^{X'}, \rho^{Y'}) = \frac{1 + \sin^2 \delta\theta}{2} + \frac{\cos^2 \delta\theta}{2} \cos \frac{\delta\varphi_{12}}{2} \cos \frac{\delta\varphi_{34}}{2} + \frac{\cos^2 \delta\theta}{8} \sum_{j=3,4}^{i=1,2} (-1)^{i+j} \sin \delta\varphi_{ij}, \quad (6)$$

where designation  $\delta\varphi_{ij} = \delta\varphi_i - \delta\varphi_j$  is used. The minimum of (6) is achieved at  $\delta\theta = 0$  and  $\delta\varphi_{1(3)} = -\delta\varphi_{2(4)} = \pm \delta\varphi_{\max}$ ,

$$F_{\min} = \frac{1 + \cos^2 \delta\varphi_{\max}}{2}. \quad (7)$$

### Results and Discussion

Using explicit state parametrization (2), we provide the analytical computation of fidelity (6) and estimate the single-photon phase error rate correction according to [4]:

$$E_1^{phase} = E_1^{bit} + 4\Delta'(1-\Delta')(1-2E_1^{bit}) + 4(1-2\Delta')\sqrt{\Delta'(1-\Delta')E_1^{bit}(1-E_1^{bit})},$$

where the single-photon yield  $Y_1$  and bit error rate  $E_1^{bit}$  are determined via decoy-state technique taking into account the finite-key-size effects [6]. Here we consider the worst case, when only a part of the pulses reached to Bob due to losses, but all the different (in the sense of a quantum coin) and useful for eavesdropper pulses were not lost during transmission over the channel. That's way we use  $\Delta'$  instead of  $\Delta$ :

$$\Delta' = \frac{\Delta}{Y_1},$$

$E_1^{phase}$  is used for the secret key rate calculation [7],

$$r_{\text{sec}}^l = \frac{Q_1}{Q_\mu} [1 - h_2(E_1^{phase})] - f_{ec} h_2(E_\mu), \quad (8)$$

where  $Q_1$  is single-photon gain,  $Q_\mu$  is signal gain and  $E_\mu$  is measured quantum bit error. Then we study the effects of  $\delta\theta$  and  $\delta\varphi_{bit}^{basis}$  uncertainties on  $r_{\text{sec}}^l$ .

Our main result is presented in Fig. 2. One can see that for the 100 km-long optical line the critical (i.e. when  $r_{\text{sec}}^l \leq 0$  no secret key can be distributed) value of a phase disturbance is about  $1.5^\circ$ . For the length of 50 km our result is more promising – the key rate vanishes only for the phase error is about  $5^\circ$ .

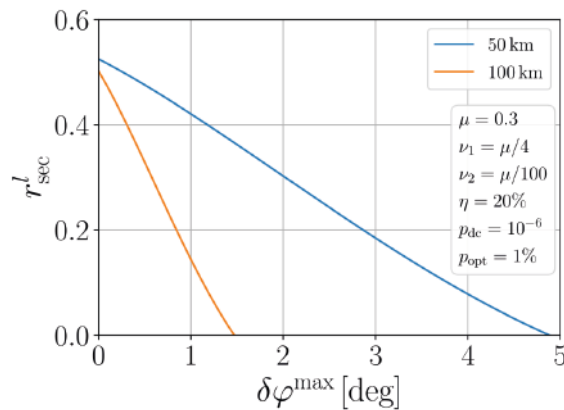


Fig. 2. Minimized secret key rate (7) (per bit) lower bound as function of maximum phase modulation error  $\delta\theta_{\max}$ . The parameters  $\mu$ ,  $\nu_1$ ,  $\nu_2$ ,  $\eta$ ,  $p_{\text{dc}}$ ,  $p_{\text{opt}}$  are signal, weak decoy and vacuum decoy intensities, quantum efficiency, dark count rate probability and probability of the optical error respectively. The simulation is run for the 50 km (orange line) and 100 km (blue line) optical fiber distances.

### Conclusion

From our research we conclude that rather precise ( $\sim 1^\circ$  for short distances and  $\sim 0.1^\circ$  for large distances) fine tuning of PM is required in order to have a reasonable secret key generation rate.

### Acknowledgments

The authors would like to acknowledge Arina Gavrilovich for thoughtful and productive discussions.

### REFERENCES

1. **Bennett, C. H., Brassard G.**, Quantum Cryptography: Public-Key Distribution and Coin Tossing, In: Proc. Of the IEEE Int. Conf. On Comp. Sys. And Sign. Process. (IEEE, 1984), 175–79.
2. **Gottesman D., Lo H.-K., Lütkenhaus N., Preskill J.**, Security of Quantum Key Distribution with Imperfect Devices, *Quant. Inf. Comput.* 4 (2004) 325–60.
3. **Jozsa R.**, Fidelity for Mixed Quantum States, *Journal of Modern Optics* 41 (12) (1994) 2315–23.
4. **Lo H.-K., Ma X., Chen K.**, Decoy State Quantum Key Distribution, *Phys. Rev. Lett.* 94 (2005) 230504.
5. **Lo H.-K., Preskill, J.**, Security of Quantum Key Distribution Using Weak Coherent States with Nonrandom Phases, *Quantum Info. Comput.*, 7 (5) (2007) 431–58.
6. **Trushechkin A. S., Kiktenko E. O., Fedorov A. K.**, Practical Issues in Decoy-State Quantum Key Distribution Based on the Central Limit Theorem, *Phys. Rev. A* 96 (2017) 022316.
7. **Xu F., Ma X., Zhang Q., Lo H.-K., Pan J.-W.**, Secure Quantum Key Distribution with Realistic Devices, *Rev. Mod. Phys.* 92 (May) (2020) 025002.

### THE AUTHORS

**REUTOV Aleksei A.**  
aleksey.reutov@phystech.edu  
ORCID: 0000-0001-5838-4770

**TAYDUGANOV Andrey S.**  
a.tayduganov@goqr.com

*Received 15.08.2022. Approved after reviewing 16.08.2022. Accepted 08.09.2022.*

## ATOM PHYSICS AND PHYSICS OF CLUSTERS AND NANOSTRUCTURES

Conference materials

UDC 539.1

DOI: <https://doi.org/10.18721/JPM.153.213>

### **Ion-beam-induced formation of gold nanostructures on polymethyl methacrylate film**

V. M. Studzinskii <sup>1</sup> ✉, K. V. Karabeshkin <sup>2</sup>, A. S. Kondrateva <sup>1</sup>,  
E. D. Fedorenko <sup>1</sup>, P. A. Karaseov <sup>1</sup>, M. V. Mishin <sup>3</sup>

<sup>1</sup> Peter the Great St. Petersburg Polytechnic University, St. Petersburg, Russia;

<sup>2</sup> Joint - Stock Company "Research and Production Enterprise "ELAR", St. Petersburg, Russia;

<sup>3</sup> Alferov University, St. Petersburg, Russia

✉ [svm.fl@mail.ru](mailto:svm.fl@mail.ru)

**Abstract.** In this work, we study the behavior of a thin gold layer on the surface of a polymethyl methacrylate (PMMA) film under irradiation with keV atomic P and molecular PF<sub>4</sub> ions. Transformation of both the gold layer and the PMMA film depends on the kind of ions used. Formation of gold nanoparticles is found in all cases. This process is less efficient than in the case of the ion-beam-induced Au layer dewetting on SiO<sub>2</sub> substrate. The formation of nanostructured regions in the polymer bulk was also established. The dependence of transmission in the IR range on the stage of formation of nanostructures has been investigated. The PMMA matrix destruction is low as revealed by FTIR investigation. Obtained structures could be used as efficient substrates for surface enhanced Raman scattering studies.

**Keywords:** gold nanoparticles, irradiation with ions, polymethyl methacrylate, molecular effect, nanomaterials, polymer

**Funding:** Work was supported by the Ministry of Science and Higher Education (project № FSRM-2020-0011).

**Citation:** Studzinskii V. M., Karabeshkin K. V., Kondrateva A. S., Fedorenko E. D., Karaseov P. A., Mishin M. V., Ion-beam-induced formation of gold nanostructures on polymethyl methacrylate film, St. Petersburg State Polytechnical University Journal. Physics and Mathematics. 15 (3.2) (2022) 69–74. DOI: <https://doi.org/10.18721/JPM.153.213>

This is an open access article under the CC BY-NC 4.0 license (<https://creativecommons.org/licenses/by-nc/4.0/>)

Материалы конференции

УДК 539.1

DOI: <https://doi.org/10.18721/JPM.153.213>

### **Ионно-индуцированное формирование наноструктур золота на пленке из полиметилметакрилата**

V. M. Studzinskii <sup>1</sup> ✉, K. V. Karabeshkin <sup>2</sup>, A. S. Kondrateva <sup>1</sup>,  
E. D. Fedorenko <sup>1</sup>, P. A. Karaseov <sup>1</sup>, M. V. Mishin <sup>3</sup>

<sup>1</sup> Санкт-Петербургский политехнический университет Петра Великого, Санкт-Петербург, Россия;

<sup>2</sup> Акционерное общество "Научно – производственное предприятие "ЭЛАР", Санкт-Петербург, Россия;

<sup>3</sup> Академический университет имени Ж.И. Алферова РАН, Санкт-Петербург, Россия

✉ [svm.fl@mail.ru](mailto:svm.fl@mail.ru)

**Аннотация.** В настоящей работе исследуется поведение тонкого слоя золота на поверхности пленки полиметилметакрилата (ПММА) при облучении атомарными ионами P и молекулярными ионами PF<sub>4</sub> с энергиями порядка кэВ. Поведение как слоя золота,

так и пленки ПММА зависит от типа используемых ионов. Формирование наночастиц золота происходит менее эффективно, чем при ионно-лучевом осушении слоя Au на подложке SiO<sub>2</sub>. Установлено также образование наноструктурированных областей в объеме полимера. Выявлена зависимость пропускания в ИК-диапазоне от стадии формирования наноструктур. С помощью ИК-Фурье анализа доказано, что при формировании наноструктур полимер хоть и претерпевает изменения, но все же остается ПММА. Полученные структуры могут быть использованы в качестве подложек для исследований методом поверхностно-усиленного комбинационного рассеяния.

**Ключевые слова:** золотые наночастицы, облучение ионами, полиметилметакрилат, молекулярный эффект, наноматериалы, полимер

**Финансирование:** Работа выполнена в рамках Государственного задания «Активные композитные материалы и методики анализа для (био)сенсорики» (код темы FSRM-2020-0011).

**Ссылка при цитировании:** Студзинский В. М., Карабешкин К. В., Кондратьева А. С., Федоренко Е. Д., Карасев П. А., Мишин М. В. Ионно-индуцированное формирование наноструктур золота на пленке из полиметилметакрилата // Научно-технические ведомости СПбГПУ. Физико-математические науки. 2022. Т. 15. № 3.2. С. 69–74. DOI: <https://doi.org/10.18721/JPM.153.213>

Статья открытого доступа, распространяемая по лицензии CC BY-NC 4.0 (<https://creativecommons.org/licenses/by-nc/4.0/>)

## Introduction

Nanocomposite materials are of widespread use in various fields from catalysis to sensing and more. Noble metal nanoparticles exhibit tuneable plasmon resonances over VIS-NIR spectral range. Incorporation of nanoparticles into a bulk matrix could increase hardness, wear resistance and other mechanical properties of a composite material. One can also tailor electrical conductivity, optical transmission and reflection, antimicrobial properties, temperature response, and many other characteristics. Noble metal, especially gold, nanoparticles have attracted attention, primarily due to their unique electronic, optical, thermal, chemical and biological properties, and, accordingly, promising potential applications in various fields, including biology and medicine, chemistry, photonics, materials science, and other interdisciplinary areas.

One of dry low-temperature techniques of gold nanoparticle synthesis is heating of a few nanometer thick gold layer [1], or its irradiation with accelerated ions [2]. This layer can be either deposited on a substrate, or buried ten to hundred nanometer deep. Moreover, metal ion implantation has been used to fabricate [3] and control the size, shape, and distribution [4-6] of metal nanoclusters in various matrices. In particular, carbon based polymer matrices are of interest due to possible biocompatibility of a composite [7]. Bombardment with small metallic clusters also can be successfully utilized to produce pinned or buried nanoparticles [8]. Besides a lot of efforts, there are still a number of unanswered questions; in particular, role of the relative density of collision cascades formed in the target by a fast ion during its stopping [9] is not clear. The influence of the substrate material on the process of particle formation can play a decisive role in the formation of nanoparticles. Local density of collision cascades formed by a stopping ion also affects radiation-related phenomena. Overlapping of collision sub-cascades formed by atomic constituents of a molecular ion gives rise to an increase in the density of the cumulative cascade formed by molecular ion. This fact let us study the effect of collision cascade density on formation of gold nanoparticles. This work is devoted to study change of a thin gold layer deposited on polymethylmethacrylate (PMMA) film under bombardment with accelerated molecular and monatomic ions.

## Materials and Methods. Fabrication

Monocrystalline (100) *n*-silicon was used as a sample substrate. It was cleaned in hydrochloric acid, followed by thorough rinse with distilled water and acetone. Polymeric film was deposited

by the drop-casting technique. 0,0104 g of polymethyl methacrylate was dissolved in 3,75 g of dichloroethane at 24° C. After that, 1 drop of solution was applied onto 1×1 cm<sup>2</sup> Si substrate. Samples were dried at room temperature for 24 hours. The thickness of the resulting PMMA films was about 250 nm, as measured by atomic force microscopy over iron needle applied scratch.

The gold deposition was carried out by vacuum thermal evaporation at a pressure of 10<sup>-5</sup> Torr using an Oxford Instruments setup. The substrate was kept at room temperature during the deposition. Thickness of the gold layer on a test silicon sample (without polymethylmethacrylate) was measured by Rutherford backscattering technique using 0,7 MeV He<sup>++</sup> ions (see [10] for details). Thickness of Au layer is 5,7 nm.

Finally, samples were irradiated at room temperature with P and PF<sub>4</sub> ions using 500 keV HVEE implanter. Ion energies were kept as 1,3 keV/amu, which is equal to 40 and 140 keV for P and PF<sub>4</sub> ions respectively. Ion irradiation parameters are presented in Table I. The irradiation fluences used to compare the effect of irradiation were selected to keep constant number of displacements of gold atoms (displacements per atom) after bombardment with monatomic and molecular ions [9]. The values of DPA<sub>Au</sub> were calculated from simulation data in the TRIM software package [11] as:

$$DPA_{Au} = nv \times D / n_{at},$$

where  $n_v$  is the average number of displacements of atoms per unit length produced by a single ion (cm<sup>-1</sup>);  $n_{at}$  is the concentration of atoms of a substance (for gold  $n_{at} = 5,9 \cdot 10^{22}$  cm<sup>-3</sup>); D is the fluence of incident ions (cm<sup>-2</sup>).  $n_v$  was determined using the TRIM code simulation with the default values of threshold displacement energies in gold and PMMA layers. Number of displacements generated by a molecular ion was calculated as a sum of displacements produced by a one P and four F monatomic ions.

Table 1

#### List of irradiation parameters

Dose, $DPA_{Au}$	Fluence, cm <sup>-2</sup>	
	P	PF <sub>4</sub>
0.27·10 <sup>-4</sup>	—	4·10 <sup>10</sup>
0.54·10 <sup>-4</sup>	22.58·10 <sup>10</sup>	8·10 <sup>10</sup>
0.27·10 <sup>-3</sup>	11.29·10 <sup>10</sup>	4·10 <sup>11</sup>
0.54·10 <sup>-3</sup>	22.58·10 <sup>11</sup>	8·10 <sup>11</sup>
0.54·10 <sup>-2</sup>	22.58·10 <sup>12</sup>	—
0.27·10 <sup>-1</sup>	11.29·10 <sup>13</sup>	4·10 <sup>13</sup>
0.27	11.29·10 <sup>14</sup>	4·10 <sup>14</sup>
0.54	22.58·10 <sup>14</sup>	8·10 <sup>14</sup>
0.81	33.87·10 <sup>14</sup>	12·10 <sup>14</sup>

In the image with a non-irradiated sample, one can see that the formation of inhomogeneous nanosized regions occurs, in contrast to silicon, on which uniform Au layer is obtained at the given film thickness. It is also seen variable shape of gold islands and no single pattern describing the shape of these islands cannot be identified from the data obtained. Ion irradiation modify this surface with some notable trends. Indeed, gold structures become smaller and formation of bubble-like structures is seen. Fig. 2, *a* shows area covered by gold nanostructures, as deduced from SEM images. It is seen that gold occupied area decreases under ion irradiation. It follows from Fig. 2, *a* that same level of surface modification with P ions requires a higher dose compare to PF<sub>4</sub> molecular ions.

AFM images show that nanostructures are formed on the surface (Fig. 1, *a, b, c*). A significant part of these structures is seriously different from the images obtained by SEM (Fig. 1, *d, e, f*).

Most of the works related to the accumulation of damage in substances were carried out on crystal substrates [2], or SiO<sub>2</sub>. The starting point for choosing the irradiation doses was the data from [7], where the results of PF<sub>4</sub> ion-beam – induced modification of a gold film on a silicon substrate are reported. The values of the irradiation doses used in this study and corresponding fluences are shown in the Table I.

Samples obtained were investigated by Fourier-Transform Infrared Spectroscopy (FTIR), atomic force microscopy (AFM) and scanning electron microscopy (SEM) after each irradiation step.

#### Results and Discussion

Figure 1 shows SEM and AFM images of a non-irradiated sample (Fig. 1, *a, d*) and samples irradiated with P ions (Fig. 1, *b, e*) and PF<sub>4</sub> ions (Fig. 1, *c, f*), at dose DPA<sub>Au</sub> = 0.81.

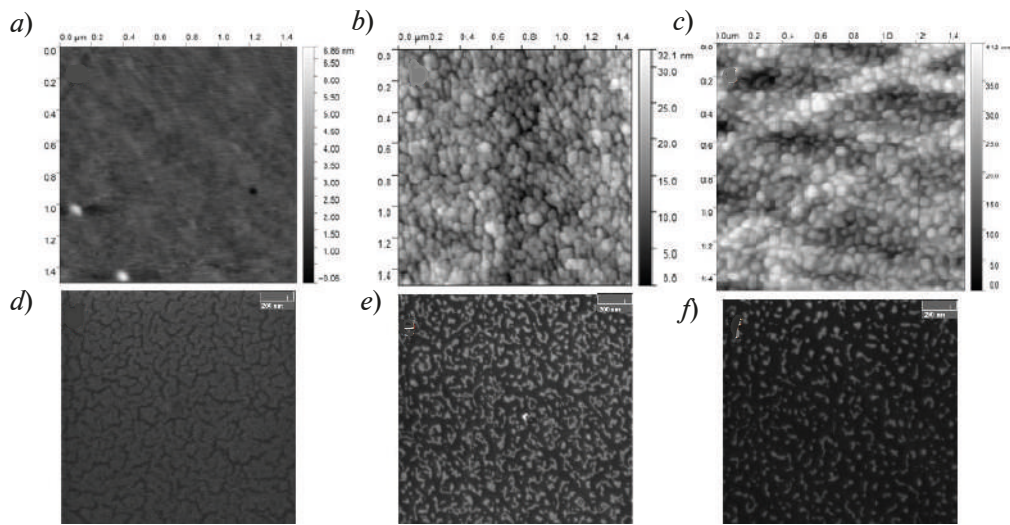


Fig. 1. SEM(*d, e, f*) and AFM(*a, b, c*) images of a non-irradiated sample (Fig. 1, *a, d*) and samples irradiated with P ions (Fig. 1, *b, e*) and PF<sub>4</sub> ions (Fig. 1 *c, f*), at dose  $DPA_{Au} = 0.81$

There are two possible ways in which the difference may have arisen. Possibly, degradation of the polymer occurs under heavy ion irradiation and gases are released under the surface, which form gas nanobubbles, observed on AFM images. There is also a probability that in during gold deposition and ion irradiation, gold atoms diffuse into the polymer layer. These pattern will not be visible in SEM images due to the light molecular weight of PMMA.

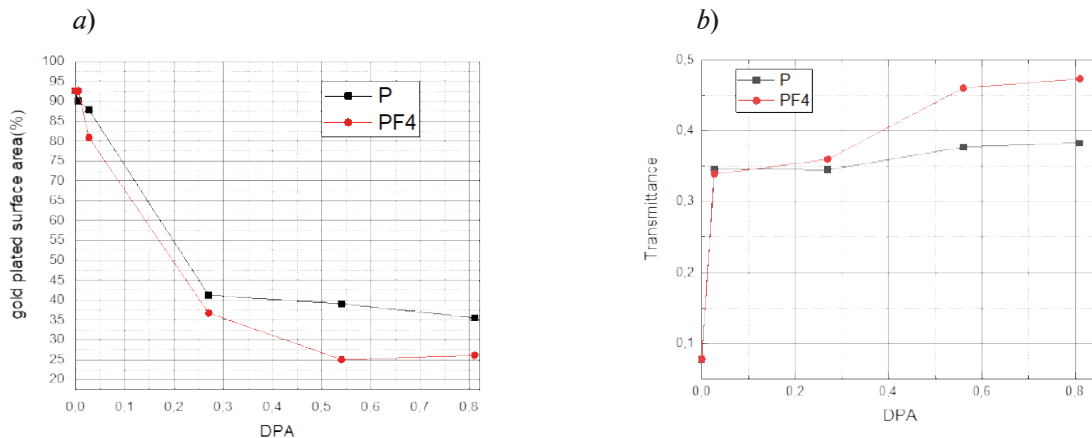


Fig. 2. Gold covered part of a surface as deduced from SEM (*a*) and IR transmission taken at 2000-2750 range (*b*) of irradiated samples as a function of ion dose

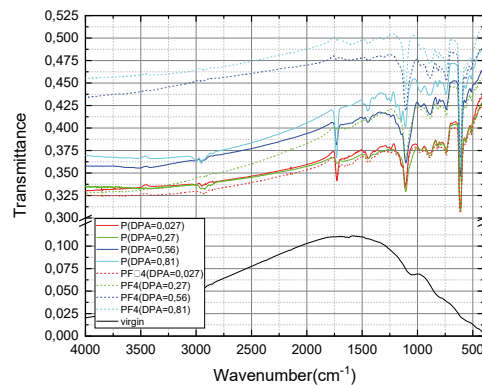


Fig. 3. FTIR spectra of samples: non-irradiated (black solid) and irradiated to various doses by P (solid colored) and PF<sub>4</sub> (dotted colored) ions

The transmission spectra in the IR spectral range taken from the samples are shown in the Fig.3. Several PMMA characteristic absorption peaks are visible at  $2940\text{cm}^{-1}$ ,  $1725\text{cm}^{-1}$ ,  $1144\text{cm}^{-1}$ ,  $988\text{cm}^{-1}$ . Overall transparency of the sample increases with the dose increase. Spectra of samples irradiated to highest doses used ( $\text{DPA}_{\text{Au}} = 0.81$ ) confirm that the polymer has not been destroyed. The characteristic PMMA group vibrations are still clearly visible (Fig.3). Also, it is seen from Fig. 3 *a* and *b* that the transmitted light intensity correlates well with the surface area occupied by the metal nanostructures. This area depends on the level to which the metal layer was modified (or else, which dose the samples were irradiated to). Thus, due to the high speed of Fourier spectra collecting, this finding let us recommend FTIR as a useful technique for fast analysis of the stage of the process of nanoparticle synthesis by ion bombardment.

### Conclusion

When applying a thin layer of gold on polymethyl methacrylate, nanostructures are formed on the surface, occupying almost the entire area. Irradiation with P and  $\text{PF}_4$  ions makes it possible to modify nanostructures, while irradiation with  $\text{PF}_4$  ions makes it possible to do this much more efficiently. In the process of modifying the gold layer, the PMMA substrate, although undergoing changes, is still not destroyed. It was also possible to observe the dependence of the transmission intensity in the IR range on the stage of formation of nanostructures, which makes it possible to use FTIR as a fast method for assessing the stage of formation of nanoparticles from thin metal layers on IR-transparent substrates. The formation of nanostructured regions in the polymer bulk was also established.

### Acknowledgments

Work was supported by the Ministry of Science and Higher Education (project № FSRM-2020-0011).

### REFERENCES

1. **Bespalova P., Enns Y., Kunkel T., Balanov V., Speshilova A., Vorobyev A., Mishin M., Karaseov P.**, Gold Nanoparticle Array Formation by Low-Temperature Annealing, in E. Velichko et al. (eds.), International Youth Conference on Electronics, Telecommunications and Information Technologies, Springer Proceedings in Physics 255, 2020, p.34.
2. **LoSavio R., Repetto L., Guida P., Angeli E., Firpo G., Volpe A., Ierardi V., Valbusa U.**, Control of the micrometric scale morphology of silicon nanowires through ion irradiation-induced metal dewetting. *Solid State Communications*, 240, 2016, p. 41–45.
3. **Mikhaylov A.N., Kostyuk A.B., Korolev D.S., Zhavoronkov I.Yu., Chugrov I.A., Belov A.I., Burdov V.A., Ershov A.V., Tetelbaum D.I.**, Formation of gold nanoparticles in single-layer and multi-layer ensembles of light-emitting silicon nanocrystals using ion implantation, *Bulletin of the Russian Academy of Sciences: Physics* 76, (2012) 214–217.
4. **Bizyaev I.S., Gabdullin P.G., Arkhipov A.V., Babyuk V.Y.**, Study of surface topography and emission properties of thin Mo and Zr films *Journal of Physics: Conference Series*, 1236 (1), 2019, 012019.
5. **Stepanov A.L., Nuzhdin V.I., Valeev V.F., Vorobev V.V., Rogova A.M., Osin Y.N.**, Study of silicon surface implanted by silver ions, *Vacuum*, 159 (2019), pp. 353–357.
6. **Modrić-Šahbazović A., Novaković M., Popović M., Schmidt E., Gazdić I., Bibić N., Ronning C., Rakočević Z.**, Formation of Ag nanoparticles in Si (100) wafers by single and multiple low energy Ag ions implantation, *Surface and Coatings Technology* 377, 2019, 124913.
7. **Prakash J., Tripathi A., Rigato V., Pivin J.C., Tripathi J., Chae K.H., Gautam S., Kumar P., Asokan K., Avasthi D. K.**, Synthesis of Au nanoparticles at the surface and embedded in carbonaceous matrix by 150 keV Ar ion irradiation, *J. Phys. D: Appl. Phys.* 44, 2011, 125302.
8. **Tuzhilkin M.S., Bespalova P.G., Mishin M.V., Kolesnikov I.E., Karabeshkin K.V., Karaseov P.A., Titov A.I.**, Formation of Au Nanoparticles and Features of Etching of a Si Substrate under Irradiation with Atomic and Molecular Ions, *Semiconductors* 54 (1), 2020, 137–143.
9. **Titov, A.I., Karaseov, P.A., Azarov, A.Yu., Kucheyev, S.O.**, Effects of the density of collision cascades: Separating contributions from dynamic annealing and energy spikes, *Nuclear Instruments and Methods in Physics Research Section B: Beam Interactions with Materials and Atoms*, 267 (16), 2009, 2701–2704.

10. Studzinsky, V.M., Mishin, M.V., Karaseov, P.A., Karabeshkin, K.V., Yurina, U.V., Ion-Beam-Induced Formation of Gold Plasmonic Structures on Polymer Film, 2020 IEEE International Conference on Electrical Engineering and Photonics (EExPolytech), 2020, pp. 216–218, doi: 10.1109/EExPolytech50912.2020.9243992.

11. Ziegler, J. F., Ziegler, M. D., Biersack, J.P., SRIM - The stopping and range of ions in matter (2010), Nucl. Instr. Meth. Phys.Res. B, 268(11–12), 2010, pp. 1818–1823.

#### THE AUTHORS

**STUDZINSKII Vitalii M.**

svm.fl@mail.ru

ORCID: 0000-0002-2149-2978

**FEDORENKO Elizaveta D.**

lizasever69@mail.ru

ORCID: 0000-0002-4292-9796

**KARABESHKIN Konstantin V.**

yanikolaus@yandex.ru

ORCID: 0000-0003-1770-1877

**KARASEOV Platon A.**

platon.karaseov@spbstu.ru

ORCID: 0000-0003-2511-0188

**KONDRATEVA Anastasia S.**

kondrateva\_n@spbau.ru

ORCID: 0000-0003-3915-9329

**MISHIN Maksim V.**

svm.fl@mail.ru

ORCID: 0000-0002-9195-3266

*Received 15.07.2022. Approved after reviewing 17.07.2022. Accepted 17.07.2022.*

Conference materials

UDC 621.315.592

DOI: <https://doi.org/10.18721/JPM.153.214>

### **Submonolayer InAs Quantum Dots in Silicon grown by Molecular Beam Epitaxy**

V. V. Lendyashova<sup>1,2</sup> ✉, I. V. Ilkiv<sup>1</sup>, B. R. Borodin<sup>3</sup>, E. V. Ubyivovk<sup>1</sup>,  
R. R. Reznik<sup>1,2,4,5</sup>, V. G. Talalaev<sup>6</sup>, G. E. Cirlin<sup>1,2,4,5</sup>

<sup>1</sup> St. Petersburg State University, St. Petersburg, Russia;

<sup>2</sup> Alferov University, St. Petersburg, Russia;

<sup>3</sup> Ioffe Physical Technical Institute of RAS, St Petersburg, Russia;

<sup>4</sup> ITMO University, St Petersburg, Russia;

<sup>5</sup> Institute for Analytical Instrumentation of the RAS, St. Petersburg, Russia;

<sup>6</sup> Martin-Luther-University Halle-Wittenberg, Halle, Germany

✉ erilerican@gmail.com

**Abstract.** The fabrication of composite material with embedded III-V quantum dots is of great interest due to promising silicon-based light emitting devices. In this work, the growth of self-assembled InAs quantum dots on Si substrates as well as subsequent capping layer formation by molecular beam epitaxy is presented. The evolution of size, density and shape of QDs are characterized by atomic-force microscopy. Bimodal size distribution of QDs at the submonolayer InAs coverage was observed. Full embedding into silicon matrix and dislocation free crystal structure of InAs QDs were confirmed by transmission electronic microscopy.

**Keywords:** quantum dots, semiconductors, molecular beam epitaxy

**Funding:** Samples growth was carried out under financial support of the Russian Science Foundation (Grant 19-72-30004). AFM studies of grown samples were done under financial support of the Ministry of Science and Higher Education of the Russian Federation, research project no. 2019-1442. Structural measurements of grown samples were done under financial support of St. Petersburg State University under research grant no. 92591131.

**Citation:** Lendyashova V. V., Ilkiv I. V., Borodin B. R., Ubyivovk E. V., Reznik R. R., Talalaev V. G., Cirlin G. E., Submonolayer InAs Quantum Dots in Silicon grown by Molecular Beam Epitaxy, St. Petersburg State Polytechnical University Journal. Physics and Mathematics. 15 (3.2) (2022) 75–79. DOI: <https://doi.org/10.18721/JPM.153.214>

This is an open access article under the CC BY-NC 4.0 license (<https://creativecommons.org/licenses/by-nc/4.0/>)

Материалы конференции

УДК 621.315.592

DOI: <https://doi.org/10.18721/JPM.153.214>

### **Субмонослойные InAs квантовые точки в кремнии, выращенные методом молекулярно-пучковой эпитаксии**

В.В. Лендяшова<sup>1,2</sup> ✉, И.В. Илькив<sup>1</sup>, Б.Р. Бородин<sup>3</sup>, Е.В. Убыйвовк<sup>1</sup>,  
Р.Р. Резник<sup>1,2,4,5</sup>, В.Г. Талалаев<sup>6</sup>, Г.Э. Цырлин<sup>1,2,4,5</sup>

<sup>1</sup> Санкт-Петербургский государственный университет, Санкт-Петербург, Россия;

<sup>2</sup> СПбАУ РАН им. Ж. И. Алфёрова, Санкт-Петербург, Россия;

<sup>3</sup> Физико-технический институт имени А. Ф. Иоффе РАН, Санкт-Петербург, Россия;

<sup>4</sup> Университет ИТМО, Санкт-Петербург, Россия;

<sup>5</sup> Институт аналитического приборостроения, Санкт-Петербург, Россия;

<sup>6</sup> Университет Галле-Виттенберг имени Мартина Лютера, Галле, Германия

✉ erilerican@gmail.com

**Аннотация.** Создание композитного материала с встроенными квантовыми точками  $A_3B_5$  представляет интерес для разработки светоизлучающих устройств на кремнии. В данной работе представлены результаты по синтезу методом молекулярно-пучковой эпитаксии самоиндуцированных квантовых точек InAs на подложках Si и их последующему наращиванию слоем кремния. Эволюция размеров, плотности и формы КТ исследовалась методом атомно-силовой микроскопии. Обнаружено, что при субмонослойном покрытии InAs наблюдается бимодальное распределение КТ по размерам. Полное внедрение в кремниевую матрицу и бездислокационная кристаллическая структура КТ InAs подтверждены данными просвечивающей электронной микроскопии.

**Ключевые слова:** квантовые точки, полупроводники, молекулярно-пучковая эпитаксия

**Финансирование:** Синтез образцов проводился при финансовой поддержке гранта РФФИ 19-72-30004. АСМ измерения были выполнены при поддержке Министерства науки и высшего образования Российской Федерации (проект 2019-1442). Структурные измерения выполнены в рамках реализации гос. задания Санкт-Петербургского государственного университета (92591131).

**Ссылка при цитировании:** Лендяшова В. В., Илькив И. В., Бородин Б. Р., Убийвовк Е. В., Резник Р. Р., Талалаев В. Г., Цырлин Г. Э. Субмонослойные InAs квантовые точки в кремнии, выращенные методом молекулярно-пучковой эпитаксии // Научно-технические ведомости СПбГПУ. Физико-математические науки. 2022. Т. 15. № 3.2. С. 75–79. DOI: <https://doi.org/10.18721/JPM.153.214>

Статья открытого доступа, распространяемая по лицензии CC BY-NC 4.0 (<https://creativecommons.org/licenses/by-nc/4.0/>)

## Introduction

Monolithic integration of III–V compound materials on silicon (Si) platform attracts intense research interest over years because it opens up new opportunities for the fabricating of photonic integrated circuits with optical data transmission systems [1]. Unfortunately, direct epitaxial growth of planar layer on Si suffers from large lattice mismatch and different expansion coefficients. In order to overcome this issue, a various methods have been proposed, such as the growth of the thick graded buffer layers [2], the insertion of several filter layers [3], migration-enhanced epitaxy growth of GaP [4]. Other interesting epitaxial approaches is based on the utilizing of Si substrates with special surface preparations, including the fabrication of V-grooved and 4 – 6° offcutted towards the [110] direction substrates [5], the patterning of substrate surfaces for confined lateral overgrowth [6]. Despite the great efforts and demonstration of several successful realizations, above mentioned methods still remain rather complex from the technological point of view. In turn, the growth of nanocomposite material consisting of III–V quantum dots (QDs) fully embedded in Si can be applied since they can be processed like Si. Several studies have been published on the fabrication of Si nanocomposite containing InAs QDs. Unfortunately, in spite of growth reports and morphological characterization [7–9], the photoluminescence emission, to our knowledge, was demonstrated only one-time [7]. One key point was to growth of 2 – 6 monolayer thickness QDs and the formation of dislocations in QDs was commonly observed [8]. In contrast, QDs with smaller size, which formation was found to occur at a smaller InAs coverage [9], may be more tolerant to dislocations.

Thus, the study of the mechanism of InAs dot formation on Si is of great interest. Here we report on the growth of submonolayer InAs QDs on Si by molecular beam epitaxy and fabrication of light emitting nanocomposite material.

## Materials and Methods

Growth experiments were carried out on Si(100)4° using 21EB200 Riber MBE system equipped with solid-state As, In effusion cells and e-beam evaporator for deposition of Si. Prior to growth wet chemical processing followed with degassing and annealing step at 950°C were performed to achieved atomically-clean Si(100) 2×1 surface. Afterwards, temperature was decreased to 600°C

and 50 nm Si buffer layer was formed. Then, self-assembled growth of InAs QDs was carried out at 400°C. The amount of InAs being deposited onto Si surface corresponded to equivalent film thickness of 0.3 – 3 monolayer (ML). It should be noted, that the growth rate of 0.01 nm/s was calibrated using standard procedure based on the measurements of reflection high-energy electron diffraction (RHEED) oscillation. The V/III was kept constant for all growth experiments and corresponded to ~20.

Topography investigation of the samples grown was performed on an Ntegra Aura (NT-MDT, Russia) scanning probe microscope in semi-contact mode using Si probes (HANC, TipsNano) with resonant frequency  $f_0 \approx 140$  kHz, spring constant  $k \approx 3.5\text{N}\cdot\text{m}^{-1}$  and tip curvature radius  $< 10$  nm.

Structural characterization of InAs QDs fully embedded in Si matrix was performed using Zeiss Libra 200FE transmission electron microscope (TEM) operated at 200 kV. Samples were prepared using conventional thinning processes including mechanical polishing and Ar-ion milling.

### Results and Discussion

We first probed the growth of InAs QDs using RHEED. One of the most important parameters that controls the size of the QDs is the amount of InAs. Under growth condition used in our experiments, the formation of QDs was clearly observed after 20s (0.8 ML) InAs deposition by transition appearing of 3D spots on streaky (2x1) RHEED pattern.

In order to gain information on the growth start of InAs on Si(001) a series of the samples with a various InAs coverage was grown. Figure 1 demonstrate the AFM images of the samples grown. The self-assembled InAs QDs are clearly can be identified on the bare Si surface in all cases. The InAs QDs size distribution was found to be inhomogeneous in all cases, as it can be seen in (Fig. 1, *d, e, f*). In detail, two types of QDs, which had irregular circular shape, were formed after the 0.3 ML growth. Relatively small InAs QDs were about 87 nm in the diameter and height of 5 nm. The bigger size QDs have 162 nm diameter and 14 nm height. The density of small and big QDs corresponded to 4 and  $1\ \mu\text{m}^{-2}$ .

The increasing of InAs coverage led to formation of QDs with bigger sizes, wherein the bimodal size distribution remained the same. It should be noted also, the dependence of QD densities on the coverage turned out to be different for two size types of QDs. In detail, density of small dots increases up to at 0.7 ML coverage and then decreases. At the same time, growth density of bigger size dots increases with the growth time, as well as the broadening of dot size occur. The reason for the peculiar behavior remains open. Nonetheless, it apparently can be connected with the coalescence of dots.

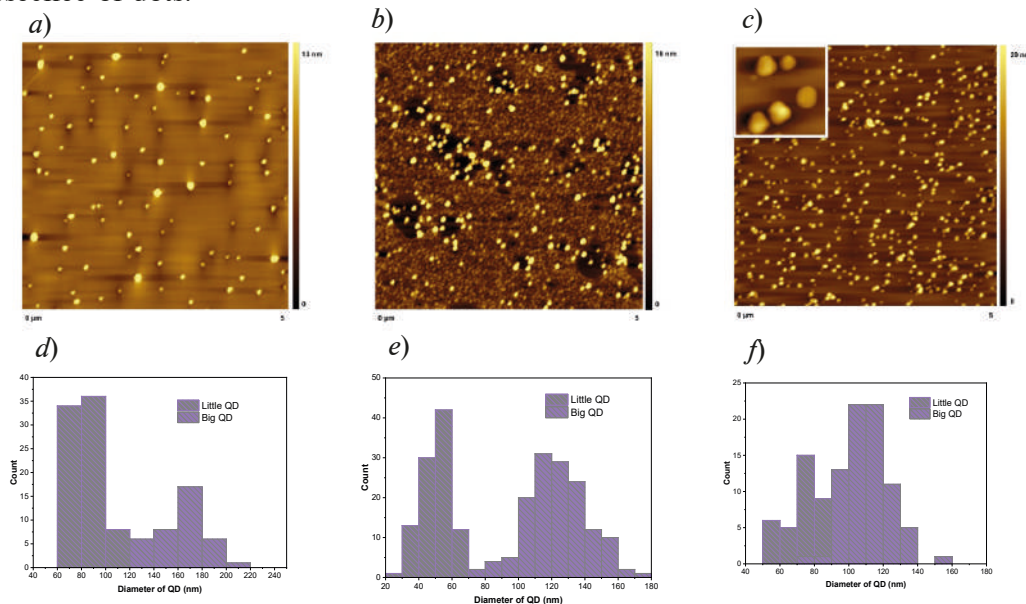


Fig. 1. The AFM images of s QDs with 0.3, 0.9, 1 ML InAs coverages (*a, b, c*); the size distribution of InAs QDs formed (*d, e, f*)

As it was mentioned above, one of the main tasks was the fabrication of Si nanocomposite with embedded InAs QDs. For this purpose, *in-situ* formation of Si capping layer was performed after the 0.3ML InAs QDs growth. At first, thin 10 nm Si layer was grown at the QDs growth temperature followed with the increasing substrate temperature to 500°C and growth of 20 nm Si. The evolution of RHEED pattern during the capping layer growth revealed the formation of amorphous Si layer at the first stage. More pronounced Si crystallization was achieved during subsequent overgrowth at higher substrate temperature. Investigation of the sample by TEM revealed that InAs QDs fully embedded inside Si matrix (Fig. 2). The size of InAs QDs measured by TEM corresponded to those measured with AFM. High-resolution TEM analysis confirmed the dislocation free crystal structure of InAs QDs.

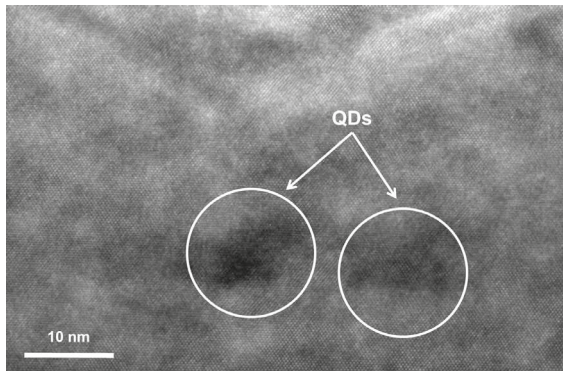


Fig. 2. TEM image of InAs QDs after the Si capping layer formation

### Conclusion

In summary, the growth of InAs QDs on the Si was demonstrated. The size distribution of submonolayer InAs QDs was found to be bimodal. The increasing in InAs coverage led to the increasing average dot diameters and to the broadening in size distribution. Capping of dots with Si opens up possibilities for the fabrication of composite materials with embedded QDs inside the Si matrix. Such material can be used for the realization of new light sources on Si platform.

### Acknowledgments

Samples growth was carried out under financial support of the Russian Science Foundation (Grant 19-72-30004). AFM studies of grown samples were done under financial support of the Ministry of Science and Higher Education of the Russian Federation, research project no. 2019-1442. Structural measurements of grown samples were done under financial support of St. Petersburg State University under research grant no. 92591131.

### REFERENCES

1. **Chen X. et al.**, The emergence of silicon photonics as a flexible technology platform, Proceedings of the IEEE. 106 (12) (2018) 2101–2116.
2. **Groenert M. E. et al.**, Monolithic integration of room-temperature cw GaAs/AlGaAs lasers on Si substrates via relaxed graded GeSi buffer layers, Journal of applied physics. 93 (1) (2003) 362–367.
3. **Wang T. et al.**, 1.3- $\mu\text{m}$  InAs/GaAs quantum-dot lasers monolithically grown on Si substrates, Optics express. 19 (12) (2011) 11381–11386.
4. **Grassman T. J. et al.**, Control and elimination of nucleation-related defects in GaP/Si (001) heteroepitaxy, Applied Physics Letters. 94 (23) (2009) 232106.
5. **Pukite P. R., Cohen P. I.**, Multilayer step formation after As adsorption on Si (100): Nucleation of GaAs on vicinal Si, Applied physics letters. 50 (24) (1987) 1739–1741.
6. **Sakawa S., Nishinaga T.**, Faceting of LPE GaAs grown on a misoriented Si (100) substrate, Journal of crystal growth. 115 (1-4) (1991) 145–149.
7. **Cirlin G. E. et al.**, Formation of InAs quantum dots on a silicon (100) surface, Semiconductor science and technology. 13 (11) (1998) 1262.
8. **Benyoucef M. et al.**, Nanostructured hybrid material based on highly mismatched III–V nanocrystals fully embedded in silicon, physica status solidi (a). 211(4) (2014) 817–822.
9. **Zhao Z. M. et al.**, Growth and characterization of InAs quantum dots on Si (001) substrates, Journal of crystal growth. 271 (3-4) (2004) 450–455.



## THE AUTHORS

**LENDYASHOVA Vera V.**

erilerican@gmail.com

ORCID: 0000-0001-8192-7614

**ILKIV Igor V.**

fiskerr@ymail.com

ORCID: 0000-0001-8968-3626

**BORODIN Bogdan R.**

brborodin@gmail.com

ORCID: 0000-0002-8673-4413

**UBYIVOVK Evgeny V.**

ubyivovk@gmail.com

ORCID: 0000-0001-5828-4243

**REZNIK Rodion R.**

moment92@mail.ru

ORCID: 0000-0003-1420-7515

**TALALAEV Vadim G.**

talalaev@mpi-halle.mpg.de

ORCID: 0000-0003-2559-889X

**CIRLIN George E.**

george.cirlin@mail.ru

ORCID: 0000-0003-0476-3630

*Received 21.07.2022. Approved after reviewing 08.08.2022. Accepted 14.08.2022.*

Conference materials

UDC 535.37, 538.975, 538.958, 538.935

DOI: <https://doi.org/10.18721/JPM.153.215>

## Förster resonance energy transfer from colloidal quantum dots to xanthene dye in polymer film

N. V. Slyusarenko <sup>✉</sup>, E. A. Slyusareva

Siberian Federal University, Krasnoyarsk, Russia

<sup>✉</sup> [sci\\_box@mail.ru](mailto:sci_box@mail.ru)

**Abstract.** In the work, a system with effective (up to 90%) Förster resonance energy transfer is implemented. The system includes thin gelatin films with embedded CdTe quantum dots (donors) and rose bengal xanthene dye (acceptor). The energy transfer mechanism revealed to be possible due to the high local concentration of fluorophores as well as careful selection of donor and acceptor spectral characteristics. The energy transfer was confirmed by the quenching of the donor photoluminescence in both steady-state and time-resolved measurements. The Stern-Volmer formalism and the Förster theory were used to estimate the constants and efficiency of energy transfer. It was shown that the photoluminescence spectrum of the system can be driven by changing the ratio of the donor-to-acceptor concentration.

**Keywords:** Förster Resonance Energy Transfer, FRET, colloidal quantum dots, nanocrystals, polymer film

**Funding:** This research was supported by the Ministry of Science and Higher Education of the Russian Federation (Grant MK–995.2022.1.2).

**Citation:** Slyusarenko N. V., Slyusareva E. A., Förster resonance energy transfer from colloidal quantum dots to xanthene dye in polymer film, St. Petersburg State Polytechnical University Journal. Physics and Mathematics. 15 (3.2) (2022) 80–85. DOI: <https://doi.org/10.18721/JPM.153.215>

This is an open access article under the CC BY-NC 4.0 license (<https://creativecommons.org/licenses/by-nc/4.0/>)

Материалы конференции

УДК 535.37, 538.975, 538.958, 538.935

DOI: <https://doi.org/10.18721/JPM.153.215>

## Резонансный перенос энергии Фёрстера от коллоидных квантовых точек к ксантеновому красителю в полимерной пленке

Н. В. Слюсаренко <sup>✉</sup>, Е. А. Слюсарева

Сибирский федеральный университет, г. Красноярск, Россия

<sup>✉</sup> [sci\\_box@mail.ru](mailto:sci_box@mail.ru)

**Аннотация.** В работе реализована система с эффективной (до 90%) резонансной передачей энергии Фёрстера. Система для реализации механизма переноса энергии состояла из тонких желатиновых пленок, с внедренными квантовыми точками CdTe и ксантеновым красителем бенгальский розовым, в качестве донора и акцептора энергии соответственно. Механизм переноса энергии оказался возможным благодаря высокой локальной концентрации флуорофоров в составе полимерной пленки, а также тщательному подбору спектральных характеристик донора и акцептора. Перенос энергии был подтвержден тушением и уменьшением времени жизни фотолюминесценции донора, используя методы стационарной и разрешенной во времени спектроскопии. Для оценки констант и эффективности переноса энергии использовались формализм Штерна-Фольмера и теория Фёрстера. Было показано, что спектром фотолюминесценции системы можно управлять, изменяя стехиометрию донорно-акцепторной пары.

**Ключевые слова:** Фёрстеровский перенос энергии, коллоидные квантовые точки, нанокристаллы, полимерные пленки

**Финансирование:** Работа выполнена в рамках Государственного задания Министер-

ства науки и высшего образования Российской Федерации «Допированные квантовыми точками полимерные пленки с перестраиваемой фотолюминесценцией» (номер гранта МК-995.2022.1.2).

**Ссылка при цитировании:** Слюсаренко Н.В., Слюсарева Е.А. Резонансный перенос энергии Фёрстера от коллоидных квантовых точек к ксантеновому красителю в полимерной пленке // Научно-технические ведомости СПбГПУ. Физико-математические науки. 2022. Т. 15. № 3.2. С. 80–85. DOI: <https://doi.org/10.18721/JPM.153.215>

Статья открытого доступа, распространяемая по лицензии CC BY-NC 4.0 (<https://creativecommons.org/licenses/by-nc/4.0/>)

## Introduction

Creation of light sources with adjustable spectral properties is of high interest in medicine [1], sensing [2], design of optoelectronic devices [3], lasers, photocatalysis and photopatterning [4]. Usually layers of several fluorophores are used to obtain a complex spectrum. In this case, it is necessary to simultaneously efficiently excite all components, which taking into account their different spectral properties is not always realizable.

One of the ways to obtain a complex spectrum in a wide spectral region is the implementation of the mechanism of nonradiative transfer of electronic excitation energy in a system of two fluorophores which is also called Förster Resonance Energy Transfer (FRET) [5]. This requires short-wavelength excitation of the donor, which partially transfers its energy to a longer-wavelength acceptor.

The efficiency of energy transfer depends on the degree of overlap between the photoluminescence spectra (PL) of the donor and absorption of the acceptor, the relative orientation of the dipole moments of transitions, and the distance between molecules [5]. Therefore, the key point for the implementation of this mechanism is the careful selection of the donor-acceptor pair and matrix.

The aim of the work was to create a luminophore in the form of a polymer film doped with semiconductor quantum dots (CdTe QDs) and xanthene dye (rose bengal). The photochemically stable QDs (donor) has a wide intense absorption spectrum from UV to the middle of the visible range and the acceptor has the ability to luminesce in the red region. The absorption, steady-state and time-resolved spectroscopy methods were used to determine the efficiency of spectral conversion. The results were interpreted using the Stern-Volmer formalism and the Förster theory.

## Materials and Methods

The water dispersible semiconductor quantum dots CdTe (CdTe QDs stabilized with thioglycolic acid) were supplied by PlasmaChem with a photoluminescence wavelength of  $550 \pm 5$  nm and a size of 2.6 nm. Rose bengal (RB) (4,5,6,7-Tetrachloro-2',4',5',7'-tetraiodofluorescein disodium salt) were supplied by Sigma-Aldrich. The stock solutions of CdTe QDs and rose bengal were  $10^{-4}$  и  $10^{-3}$  M respectively. Photographic gelatin type B were supplied by Vekton. All chemicals were used as delivered.

## Polymer films formation

The gelatin solution (1% wt.) in which quantum dots and dye were added was used to prepare polymer films. The concentration of quantum dots in the mixture was constant and equal to 8.2  $\mu$ M. The dye concentration was varied in the range of 1–67  $\mu$ M. Then the solutions were mixed on a magnetic stirrer and applied by dropping onto glass substrates. The samples were left for a day at room temperature as a result films without visible defects were obtained.

## The absorption and fluorescence measurements

The absorption spectra were recorded on a Lambda 35 (Perkin Elmer) spectrophotometer. The fluorescence spectra were measured on a Fluorolog 3–22 spectrofluorimeter (Horiba Scientific, USA) with excitation wavelength 453 nm. The spectra were corrected for the spectral sensitivity of the detector and the reabsorption effect.

The time-resolved measurements were performed using the DeltaHub timing module (Horiba, USA) upon excitation by a NanoLED N-453 pulsed laser diode with a maximum of 453 nm and pulse duration of  $< 1.3$  ns. The intensity decays were detected at the wavelengths corresponding to the maxima of the fluorescence spectra and described by a sum of three exponents using deconvolution analysis by the DAS6 software (Horiba Scientific, USA).  $\chi^2$  statistical criteria was applied. Average lifetime was calculated taking the amplitude contribution of the components into account.

The L-geometry was used for measurements of aqueous solutions of dyes and quantum dots dispersed in water using standard quartz cuvettes with a cross section of  $1 \times 1$  cm. The front-face geometry was used for measurements of polymer films doped with fluorophores. All measurements were carried out at room temperature.

### The analysis of changes in the photoluminescence spectrum depending on the stoichiometry of the fluorophores

Estimation of the change in the gravity center of the spectrum ( $GC$ ) which takes into account both changes in the position of the maximum and the shape of the contour was carried out to analyze the change in the PL spectrum [6]:

$$GC = \frac{\sum_i^j I(\lambda)\lambda}{\sum_i^j I(\lambda)}, \quad (1)$$

where  $GC$  – gravity center,  $I(\lambda)$  – intensity at the corresponding wavelength  $\lambda$ ,  $i$  and  $j$  – initial and final wavelengths, respectively.

### FRET model

According to the theory of Förster [5] the rate constant  $k_{ET}$  is determined by equation:

$$k_{ET}(r) = \frac{1}{\tau_D} \left( \frac{R_0}{r} \right)^6, \quad (2)$$

where  $\tau_D$  is the average lifetime of the donor,  $r$  is the distance between donor and acceptor,  $R_0$  is the Förster distance (the distance at which the energy transfer efficiency is 50%) and determined by:

$$R_0 = \left( \frac{9000 \ln 10}{128 \pi^5 n^4 N} \kappa^2 \Phi_D J \right)^{1/6}, \quad (3)$$

where  $\kappa^2$  is the dipole orientation factor,  $\Phi_D$  is the PL quantum yield of donor,  $n$  is refractive index of medium,  $N$  is Avogadro's number,  $J$  – spectral overlap between donor fluorescence and acceptor absorption and determined as follow:

$$J = \int I_D(\tilde{\nu}) \varepsilon_A(\tilde{\nu}) \tilde{\nu}^4 d\tilde{\nu} / \int I_D(\tilde{\nu}) d\tilde{\nu}, \quad (4)$$

where  $I_D(\tilde{\nu})$  is the intensity of the donor PL,  $\varepsilon_A(\tilde{\nu})$  is the molar extinction coefficient of the acceptor.

The transfer efficiency ( $E$ ) which is only a function of actual ( $r$ ) and Förster distance ( $R_0$ ):

$$E = \frac{1}{1 + (r/R_0)^6}. \quad (5)$$

The experimental transfer efficiency obtained by:

$$E = 1 - \frac{I_{DA}}{I_D} \text{ or } E = 1 - \frac{\tau_{DA}}{\tau_D}, \quad (6)$$

where  $I_D$  and  $I_{DA}$  is PL intensity,  $\tau_D$  and  $\tau_{DA}$  is average lifetime in absence (D) and presence (DA) of acceptor, respectively.

## Results and Discussion

Fig. 1 shows the absorption and photoluminescence spectra of quantum dots and rose bengal dye embedded in a gelatin film.

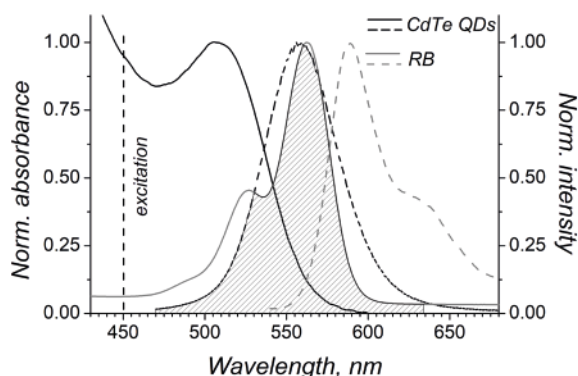


Fig. 1. Absorption and PL spectra of CdTe QDs (donor) and rose bengal (acceptor) in gelatin film

It is necessary to achieve a high degree of overlap between the photoluminescence spectrum of the donor and the absorption spectrum of the acceptor in order to implement energy transfer.

The spectral overlap and the Förster distance were obtained using **equations 3** and **4** which are  $4.94 \cdot 10^{-13} \text{ M}^{-1} \text{ cm}^{-3}$  and 4.5 nm, respectively. The orientation factor  $\kappa^2$  was chosen as for the case of static donor-acceptor orientations which do not change during the lifetime of the excited state. In this case  $\kappa^2 = 0.476$  [6]. The PL quantum yield of quantum dots in a polymer film was 20% and was estimated by the relative method.

Also, an important parameter for the implementation of energy transfer is the achievement of a high local concentration of fluorophores which cannot be achieved in aqueous solutions. The estimation of the local concentration for the implementation of energy transfer was carried out according to the equation:

$$C_0 = 3000 / 4\pi NR_0^3. \quad (7)$$

Based on the equation and the found value of the Förster distance, the local concentration turned out to be  $4.4 \cdot 10^{-3} \text{ M}$ . The concentration of quantum dots in polymer films was  $7.6 \cdot 10^{-3} \text{ M}$  and the dye varied in the range  $(1-62) \cdot 10^{-3} \text{ M}$  which gives confirmation the implementation of energy transfer in this system.

Experimental confirmation of energy transfer was recorded using stationary and time-resolved measurements (Fig. 2). A wavelength of 560 nm was chosen for recording donor PL quenching which corresponded to the maximum photoluminescence of CdTe quantum dots. It can be seen that with an increase in the dye concentration in the composition of the polymer film simultaneous quenching and a decrease in the PL lifetime occur which is evidence of energy transfer in the donor-acceptor system.

The energy transfer characteristics can be obtained on the basis of the Stern-Volmer quenching formalism. The quenching of PL intensity and decrease lifetime of donor as a function of acceptor concentration is describe by Stern-Volmer equation [7]:

$$\frac{I_{DA}}{I_D} = \frac{\tau_{DA}}{\tau_D} = 1 + K_{SV}[RB] = 1 + k_q \tau_D [RB], \quad (8)$$

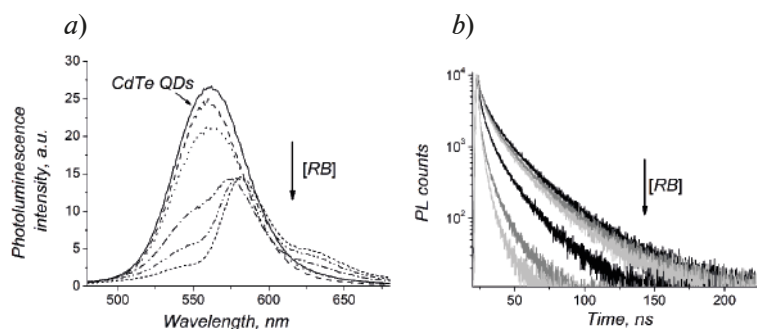


Fig. 2. The fluorescence steady-state spectra (a); time-resolved decays of CdTe QDs in gelatin films with increasing of the rose bengal concentration (b)

where  $K_{SV}$  – the Stern-Volmer quenching constant,  $k_q$  – bimolecular quenching constant, [RB] – concentration of dye.

The linear Stern-Volmer plots of  $I_{DA}/I_D$  and  $\tau_{DA}/\tau_D$  versus dye concentration is shown in (Fig. 3, a).

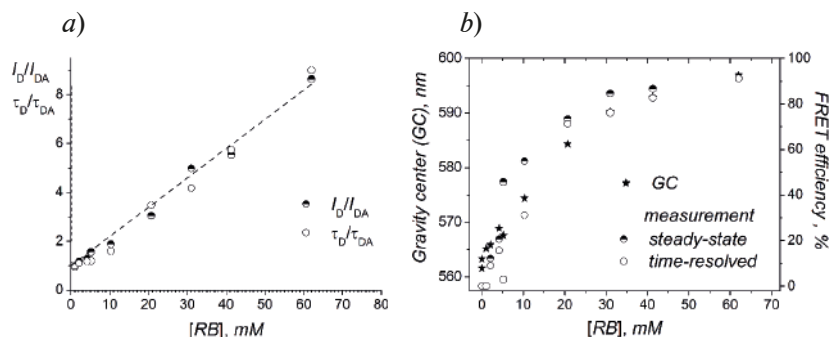


Fig. 3. The Stern-Volmer plots of  $I_{DA}/I_D$  and  $\tau_{DA}/\tau_D$  vs. concentration of dye (a). The gravity center and FRET efficiency vs. concentration of dye (b)

The Stern-Volmer constants are  $118.4 \pm 0.2 \text{ M}^{-1}$  and  $119.8 \pm 0.3 \text{ M}^{-1}$  for steady-state and time-resolved measurements, respectively. The energy transfer rate constants  $k_{ET}$  were estimated as  $(0.09-5.4) \times 10^8$  and  $(0.09-5.5) \times 10^8 \text{ s}^{-1}$  for steady-state and time-resolved measurements, respectively.

Figure 3, b shows the energy transfer efficiency obtained from steady-state and time-resolved measurements as a function of dye concentration as well as the change in the gravity center of the spectrum. The energy transfer efficiency reached 90%. It can be seen that an increase in the dye concentration leads to a change in the PL spectrum and an increase in the efficiency of energy transfer. It can be seen that after a concentration of about 40 mM there is no change in the FRET efficiency. The range of change in the gravity center for the donor-acceptor pair CdTe-rose bengal was 35 nm. Thus, by selecting and varying the ratio of fluorophores it is possible to tune the PL wavelength which can be used for a wide range of application where it is necessary to tune the PL spectrum.

### Conclusion

We examined polymer films with embedded QDs (donor) and rose bengal dye (acceptor) with spectral properties that ensure efficient transfer of electronic excitation energy. The donor is able to efficiently convert energy in the near UV and visible range and photochemically stable. The tuning of PL spectrum was adjusted by the donor-acceptor concentration ratio. The FRET efficiency up to 90% and red shift in the emission spectrum of the system of 35 nm occurred with increasing acceptor concentration. The maximum effect was achieved at an acceptor concentration more than 40 mM. The presented approaches and objects are promising for the creation of low-cost systems with tunable spectra.

### Acknowledgments

This research was supported by the Ministry of Science and Higher Education of the Russian Federation (Grant MK-995.2022.1.2).

### REFERENCES

1. Xing J., Gong Q., Akakuru O. U., Liu C., Zou R., Wu A., Research advances in integrated theranostic probes for tumor fluorescence visualization and treatment, *Nanoscale*. 12 (2020) 24311–24330.
2. Slyusarenko N. V., Gerasimova M. A., Slabko V. V., Slyusareva E. A., Temperature sensitivity of water-soluble CdTe and CdSe/ZnS quantum dots incorporated into biopolymer submicron particles, *Russian Physics Journal*. 60 (2017) 477–484.
3. Shu Y., Lin X., Hu H. Q. Z., Jin Y., Peng X., Quantum dots for display applications, *Angewandte Chemie*. 59 (50) (2020) 22312–22323.

4. **Devatha G., Rao A., Roy S., Pillai P. P.**, Förster Resonance Energy Transfer regulated multicolor photopatterning from single quantum dot nanohybrid films, *ACS Energy Letters*. 4 (7) (2019) 1710–1716.
5. **Förster T.**, Transfer mechanisms of electronic excitation energy, *Radiation Research Supplement*. 2 (1960) 326–339.
6. **Lakowicz J. R.**, Principles of fluorescence spectroscopy, Springer Science & Business Media, New York, 2006.

#### THE AUTHORS

**SLYUSARENKO Nina V.**

sci\_box@mail.ru

ORCID: 0000-0003-3249-4888

**SLYUSAREVA Evgenia A.**

eslyusareva@sfu-kras.ru

ORCID: 0000-0002-9124-3643

*Received 13.07.2022. Approved after reviewing 24.07.2022. Accepted 26.07.2022.*

Conference materials

UDC 620.3

DOI: <https://doi.org/10.18721/JPM.153.216>

### Effect of noble metal nanoparticles in transition metal oxide magnetron sputtering

A. S. Kondrateva<sup>1,2</sup>, I. M. Komarevtsev<sup>1,2</sup> ✉,

Ya. B. Enns<sup>1,2</sup>, A. V. Kazakin<sup>1,2</sup>, M. V. Mishin<sup>1,2</sup>

<sup>1</sup> Alferov University, St. Petersburg, Russia;

<sup>2</sup> Peter the Great Saint-Petersburg Polytechnic University, St. Petersburg, Russia

✉ [imk@spbstu.ru](mailto:imk@spbstu.ru)

**Abstract.** The purpose of this work is to study the transition metal oxides with metal nanoparticles structures formation features. A design technology is proposed, consisting of the oxide matrix magnetron sputtering, noble metal nanoparticles thermal evaporation and dewetting, and covering it with oxide. Gold nanoparticles, nickel and titanium oxides were used as materials under investigation. Metal-induced catalytic growth of nickel and titanium oxides on gold nanoparticles has been found. It is shown that the top layer being formed has a pronounced texture. During the process, cones are formed with an opening angle of 10–12° and a predominant growth direction coinciding with the crystallographic axis perpendicular to the (111) surface. The optical and electrical characteristics of the formed coatings were studied. The results obtained indicate a broad prospect of using the formed structures in the field of integrated optoelectronic devices.

**Keywords:** metal-induced catalytic growth, noble metal nanoparticle, transition metal oxides, optoelectronic device

**Funding:** This study was funded by Ministry of Education foundation grant number FSRM-2020-0011.

**Citation:** Kondrateva A. S., Komarevtsev I. M., Enns Ya. B., Kazakin A. N., Mishin M. V., Effect of noble metal nanoparticles in transition metal oxide magnetron sputtering, St. Petersburg State Polytechnical University Journal. Physics and Mathematics. 15 (3.2) (2022) 86–90. DOI: <https://doi.org/10.18721/JPM.153.216>

This is an open access article under the CC BY-NC 4.0 license (<https://creativecommons.org/licenses/by-nc/4.0/>)

Материалы конференции

УДК 620.3

DOI: <https://doi.org/10.18721/JPM.153.216>

### Влияние наночастиц благородных металлов на магнетронное распыление оксидов переходных металлов

А. С. Кондратьева<sup>1,2</sup>, И. М. Комаревцев<sup>1,2</sup> ✉, Я.Б. Эннс<sup>1,2</sup>,

А.В. Казакин<sup>1,2</sup>, М.В. Мишин<sup>1,2</sup>

<sup>1</sup> Алферовский университет, Санкт-Петербург, Россия;

<sup>2</sup> Санкт-Петербургский политехнический университет, Санкт-Петербург, Россия

✉ [imk@spbstu.ru](mailto:imk@spbstu.ru)

**Аннотация.** Целью данной работы является изучение особенностей формирования оксидов переходных металлов с металлическими наночастицами. Предложена технология формирования материалов, состоящая из магнетронного напыления оксидной матрицы, термокоагуляции наночастиц благородных металлов и покрытия их оксидом. В качестве исследуемых материалов использовались наночастицы золота, оксиды никеля и титана. Обнаружен металлоиндуцированный каталитический рост оксидов никеля и титана на наночастицах золота. Показано, что образующийся верхний слой имеет

ярко выраженную текстуру. В процессе образуются конусы с углом раскрытия  $10\text{--}12^\circ$  и преимущественным направлением роста, совпадающим с кристаллографической осью, перпендикулярной поверхности (111). Исследованы оптические и электрические характеристики сформированных покрытий. Полученные результаты указывают на широкую перспективу использования сформированных структур в области интегральных оптоэлектронных устройств.

**Ключевые слова:** металл-индуцированный каталитический рост, наночастицы благородных металлов, оксиды переходных металлов, оптоэлектронное устройство

**Финансирование:** Работа выполнена в рамках Государственного задания «Активные композитные материалы и методики анализа для (био)сенсорики» (код темы FSRM-2020-0011).

**Ссылка при цитировании:** Кондратьева А. С., Комаревцев И. М., Эннс Я. Б., Казакин А. Н., Мишин М. В. Влияние наночастиц благородных металлов на магнетронное распыление оксидов переходных металлов // Научно-технические ведомости СПбГПУ. Физико-математические науки. 2022. Т. 15. № 3.2. С. 86–90. DOI: <https://doi.org/10.18721/JPM.153.216>

Статья открытого доступа, распространяемая по лицензии CC BY-NC 4.0 (<https://creativecommons.org/licenses/by-nc/4.0/>)

## Introduction

For the last decades there is a growing need for functional layers with tailored optoelectrical properties, however the bare materials does not usually provide the required characteristics [1, 2]. Thereat, a mixture of materials with precisely guided organization in order to enhance the device features is required. In this respect the noble metal nanoparticles (NPs) dispersed inside semiconductor matrices have recently been under extensive study as high-performance active layers material in numerous integrated optoelectronic devices [3]. Generally, active layers are formed in thin film configuration by using chemical deposition (wet chemistry [4] or CVD [5]), and physical (magnetron deposition [6]). The former are convenient in that they allow the matrix and a filler formation in one process, the latter are more technologically applicable. A wide range of chemical and physical techniques are also used to obtain noble metal nanoparticles [7]. However, despite each of physical techniques requiring expensive deposition equipment, they produce films with sufficient control of NP size, size distribution, and spatial distribution within the layer.

This paper is focused on the metal oxide film (MOF) deposition on AuNPs research for potential enhancement of properties for optoelectronic devices. The purpose of this work is to study the transition metal oxides with metal nanoparticles structures formation features using nickel and titanium oxides as an example and to investigate the optical and electrical properties of the formed functional coatings.

## Materials and Methods

In this work,  $\text{TiO}_2$  films were obtained by reactive magnetron sputtering (DC) with a Ti target in an O/Ar gas mixture on amorphous quartz and Si substrates. The gas ratio varied in the range 0.2–1 at an operating pressure of 1.8 mTorr. NiO films were obtained by reactive magnetron sputtering (DC) with a Ni target in an O/Ar gas mixture on amorphous quartz and Si substrates. The gas ratio varied in the range 0.2–1 at an operating pressure of 1.8 mTorr. The film's thicknesses were controlled by ellipsometry and stands at 50–100 nm. The technique described in [8] were used for AuNP formation.

The structure of the samples were analyzed by scanning electron microscopy (SEM), using a JEOL JSM-7001F equipped with Energy Dispersion Spectroscopy (EDS) attachment Bruker XLash 6/30. Top-view and cross-sectional images were obtained using both secondary and backscattered electrons, respectively for morphology studies and atomic weight contrast of the Au NPs. The behavior of  $\text{TiO}_2$  and NiO on gold nanoparticles were investigated in terms of texturing and crystallinity. The technique described in [9] were used for electrical and optical experiments.

## Results and Discussion

SEM images of cleavages show two oxide layers, between which there is a clearly defined boundary (Fig.1). In both cases, the formation of an oxide layer with a pronounced structure was observed above the boundary. At the boundary, there are Au nanocrystallites, the average grain size of  $50 \pm 1$  nm.

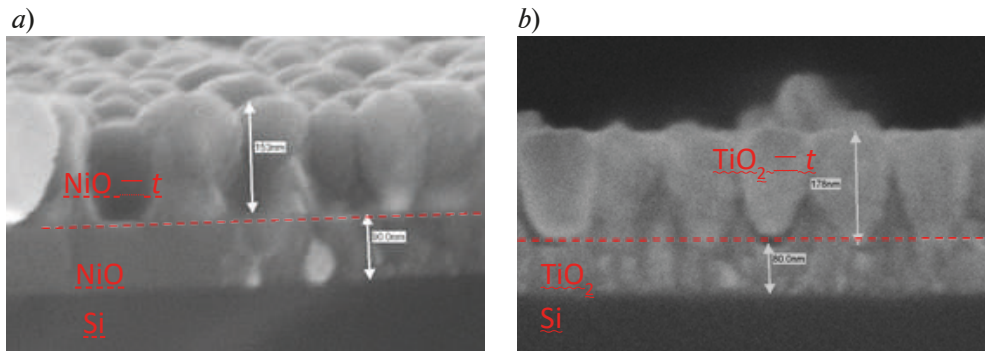


Fig. 1. Cross-sectional images of fabricated nanostructure (Si/NiO/AuNP/NiO (a) and Si/TiO<sub>2</sub>/AuNP/TiO<sub>2</sub>) (b)

In the case of Si/NiO/AuNP/NiO (SNAN) (Fig.2, a), the EDS results show the presence of O, Si, Ni and Au. In the case of SNAN, the average size of bunsenite crystallites in the lower and upper layers was  $35 \pm 2$  nm and  $45 \pm 1$  nm. The layers differ in the predominant orientation of crystallites (200) and (111), respectively. It was supposed that Au particles acted as a catalyst for the formation of nickel oxide textured in the (111) direction.

The EDS results for Si/TiO<sub>2</sub>/AuNP/TiO<sub>2</sub> (STAT) indicate the presence of O, Si, Ti, and Au. In the case of STAT (Fig.2, b), the average size of anatase crystallites was  $70 \pm 1$  nm, and for rutile,  $100 \pm 5$  nm. That is, the presence of Au particles also contributed to the formation of texture. That is, the presence of gold nanoparticles on the oxide surface provokes the formation of a textured oxide layer.

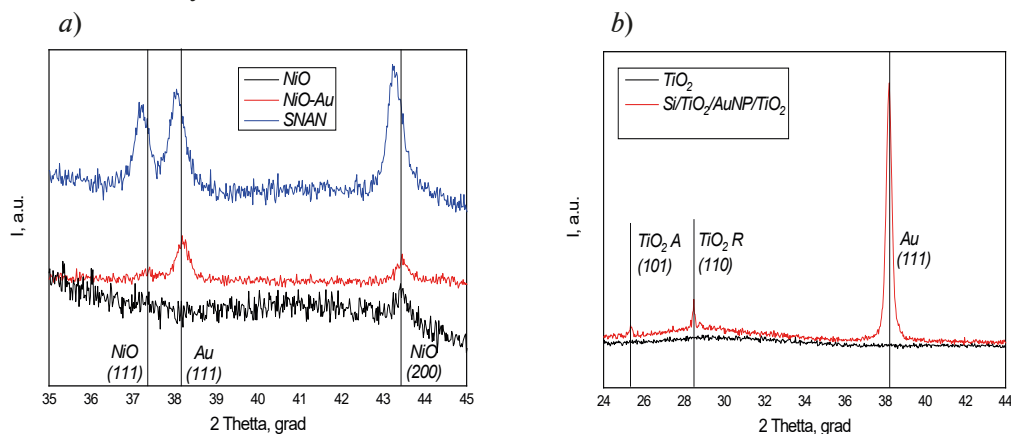


Fig. 2. XRD spectra of fabricated heterostructures

A similar behavior of systems is described for *a*-Si crystallization. It is known that a strong covalent bond is present in a bulk crystal, which is responsible for the high crystallization temperature. However, covalent bonds in *a*-Si weaken at the interface with the metal layer [10], which ensures a relatively high mobility of atoms at the interface. This fact can ensure the crystallization of *a*-Si at low temperatures. The bond weakening effect is a local electronic interaction, and the thickness of the free interfacial silicon layer is estimated at approximately 2 Si monolayers.

In immiscible metal/semiconductor systems, these two monolayers of interfacial free atoms in *a*-Si can mediate the low temperature crystallization process by (i) crystallizing at the metal interface and/or (ii) diffusing through the metal grain to the outer boundary of the system.



The ratio of the probabilities of the occurrence of these processes is determined by the ratio between the change in the "bulk" Gibbs energies and the change in the corresponding surface and interfacial energies. This process is called Metal-Induced Crystallization (MIC).

In the case of the considered oxide systems, directional crystallization is observed at the metal/semiconductor interface, which is supported by the additional introduction of material into the system during magnetron deposition of the material. During the process, cones are formed with an opening angle of 10-12° and a predominant growth direction coinciding with the crystallographic axis perpendicular to the (111) surface. A similar behavior of the deposit during magnetron sputtering was observed in the [11] for gold nanoparticles.

The formed structures showed a significant increase in the electrical response when illuminated with visible light [8], which indicates the prospects for the use of these materials as optically active layers in devices for various purposes.

### Conclusion

In this work the transition metal oxides with metal nanoparticles structures formation features were demonstrated. A novel technology is proposed, consisting of the oxide layer magnetron sputtering, Au nanoparticles thermal evaporation and dewetting. Through covering it with oxide the MIC growth of nickel and titanium oxides on gold nanoparticles has been found. The optical and electrical characteristics of the formed NiO and TiO<sub>2</sub> based coatings were investigated. The results obtained indicate a broad prospect of using the formed structures in the field of integrated optoelectronic devices.

### Acknowledgments

Authors wishing to acknowledge the Ministry of Education foundation for financial support assistance (№ FSRM-2020-0011).

### REFERENCES

1. **Lad R. J.**, Interactions at metal/oxide and oxide/oxide interfaces studied by ultrathin film growth on single-crystal oxide substrates, *Surface Review and Letters*. 2 (01) (1995) 109–126.
2. **Mallah A. R., Zubir M. N. M., Alawi O. A., Kazi S. N., Ahmed W., Sadri R., Kasaeian A.**, Experimental study on the effects of multi-resonance plasmonic nanoparticles for improving the solar collector efficiency, *Renewable Energy*. 187 (2022) 1204–1223.
3. **Kumar A, Choudhary P, Kumar A, Camargo P H, Krishnan V.**, Recent advances in plasmonic photocatalysis based on TiO<sub>2</sub> and noble metal nanoparticles for energy conversion, environmental remediation, and organic synthesis, *Small*. 18(1) (2022) 2101638.
4. **Tamm A., Acik I., Arroval T., Kasikov A., Seemen H., Marandi M., Krunks M., Mere A., Kukli K., Aarik J.**, Plasmon resonance effect caused by gold nanoparticles formed on titanium oxide films. *Thin Solid Films*. 616 (2016) 449–455.
5. **Kulczyk-Malecka J., Donaghy D., Delfour-Peyrethon B., Werner M., Chalker P. R., Bradley J. W., Kelly P. J.**, Nb-doped TiO<sub>2</sub> coatings developed by high power impulse magnetron sputtering-chemical vapor deposition hybrid deposition process, *Journal of Vacuum Science & Technology A: Vacuum, Surfaces, and Films*. 38 (3) (2020) 033410.
6. **Proença M., Borges J., Rodrigues M., Meira D., Sampaio P., Dias J., Pedrosa P., Martin N., Bundaleski N., Teodoro O., Vaz F.**, Nanocomposite thin films based on Au-Ag nanoparticles embedded in a CuO matrix for localized surface plasmon resonance sensing, *Applied Surface Science*. 484 (2019) 152–168.
7. **Bigall N., Eychmüller A.**, Synthesis of noble metal nanoparticles and their non-ordered superstructures, *Philosophical Transactions of the Royal Society A: Mathematical, Physical and Engineering Sciences*. 368 (1915) (2010) 1385–1404.
8. **Enns Y., Kondrateva A., Komarevtsev I., Kazakin A., Vyacheslavova E., Kuznetsov A., Andreeva V., Mishin M.**, Study of the optical properties of a NiO/AuNP/NiO nanocomposite film transferred onto a transparent flexible substrate, *Journal of Physics: Conference Series*. 2103 (1) (2021) 012106.
9. **Enns Y, Kondrateva A, Mishin M.**, The Simulation of Gold Nanoparticle in a TiO<sub>2</sub> Matrix Absorption and Reflection Spectra, *Journal of Physics: Conference Series*. 1695 (1) (2020) 012115.

10. Wang Z., Gu L., Philipp F., Wang J., Jeurgens L., Mittemeijer E., Metal-Catalyzed Growth of Semiconductor Nanostructures Without Solubility and Diffusivity Constraints, *Advanced Materials*. 23 (7) (2011) 854–859.

11. Soshnikov I.P., Dubrovsky V.G., Sibirev N.V., Barchenko B.T., Vertekha A.V., Ustinov G.E., Formation of arrays of GaAs whisker nanocrystals on a Si (111) substrate by magnetron deposition, *JTF Letters*. 32 (12) (2006) 28–33.

#### THE AUTHORS

**KONDRATEVA Anastasia S.**  
kondrateva\_n@spbau.ru  
ORCID: 0000-0003-3915-9329

**KAZAKIN Alexey V.**  
kazakin75@gmail.com  
ORCID: 0000-0001-8762-1587

**KOMAREVTSEV Ivan M.**  
imk@spbstu.ru  
ORCID: 0000-0001-5118-8152

**MISHIN Maxim V.**  
mishinm@spbau.ru  
ORCID: 0000-0002-9195-3266

**ENNS Yakob B.**  
Ennsjb@gmail.com  
ORCID: 0000-0003-4396-2368

*Received 27.07.2022. Approved after reviewing 04.08.2022. Accepted 16.08.2022.*

Conference materials

UDC 539.1

DOI: <https://doi.org/10.18721/JPM.153.217>

## Electrical characteristics of CsPbI<sub>3</sub> and CsPbBr<sub>3</sub> lead halide Perovskite nanocrystal films deposited on Si-c solar cells for high-efficiency photovoltaics

L. Boudjemila<sup>1</sup>✉, V. V. Davydov<sup>1,2,3</sup>, A. N. Aleshin<sup>4</sup>,  
V. M. Malyshev<sup>4</sup>, E. I. Terukov<sup>4</sup>

<sup>1</sup>Peter the Great Saint-Petersburg Polytechnic University, Saint Petersburg, Russia;

<sup>2</sup>The Bonch-Bruевич Saint Petersburg State University of Telecommunications, Saint Petersburg, Russia;

<sup>3</sup>All-Russian Research Institute of Phytopathology, Moscow Region, Russia;

<sup>4</sup>Ioffe Institute, St. Petersburg, Russia

✉ [lariessai21@gmail.com](mailto:lariessai21@gmail.com)

**Abstract.** The high performance of hybrid solar cells based on nanoparticles to improve optical and electrical performance is the subject of many current studies. For this purpose, nanoparticles of perovskite CsPbI<sub>3</sub> and CsPbBr<sub>3</sub> are used as their optical properties have provided good interaction with crystalline silicon (Si-c), the absorption coefficient ( $\alpha$ ) is significantly high in different ranges which increases the generation of photocurrent in the range 370-900nm. The degradation quickly reduces the efficiency and for specific results, developed equipment is required. CsPbI<sub>3</sub> has shown a textured surface while CsPbBr<sub>3</sub> surface is smooth, according to this better measurement for iodine content became possible.

**Keywords:** hybrid solar cells, nanoparticles, optical properties, perovskite, photocurrent, degradation factor

**Citation:** Boudjemila L., Davydov V. V., Aleshin A. N., Malyshev V. M., Terukov E. I. Electrical characteristics of CsPbI<sub>3</sub> and CsPbBr<sub>3</sub> lead halide perovskite nanocrystal films deposited on Si-c solar cells for high-efficiency photovoltaics, St. Petersburg State Polytechnical University Journal. Physics and Mathematics. 15 (3.2) (2022) 91–96. DOI: <https://doi.org/10.18721/JPM.153.217>

This is an open access article under the CC BY-NC 4.0 license (<https://creativecommons.org/licenses/by-nc/4.0/>)

Материалы конференции

УДК 539.1

DOI: <https://doi.org/10.18721/JPM.153.217>

## Электрические характеристики пленок нанокристаллов перовскита галогенидов свинца CsPbI<sub>3</sub> и CsPbBr<sub>3</sub>, нанесенных на Si-c солнечные элементы для высокоэффективной фотовольтаики

Л. Беджамилла<sup>1</sup>✉, В.В. Давыдов<sup>1,2,3</sup>, Ф. Н. Алешин<sup>4</sup>,  
В. М. Малышкин<sup>4</sup>, Е. И. Теруков<sup>4</sup>

<sup>1</sup>Санкт-Петербургский Политехнический университет Петра Великого,  
Санкт-Петербург, Россия;

<sup>2</sup>Санкт-Петербургский государственный университет телекоммуникаций  
им. проф. М. А. Бонч-Бруевича, Санкт-Петербург, Россия;

<sup>3</sup>Всероссийский научно-исследовательский институт фитопатологии, Московская область, Россия;

<sup>4</sup>Физико-Технический институт им. А.Ф. Иоффе, Санкт-Петербург, Россия

✉ [lariessai21@gmail.com](mailto:lariessai21@gmail.com)

**Аннотация.** Высокая производительность гибридных солнечных элементов на основе наночастиц для улучшения оптических и электрических характеристик является

предметом многих текущих исследований. Для этого по результатам предыдущей работы использованы наночастицы перовскита  $\text{CsPbI}_3$  и  $\text{CsPbBr}_3$ , их оптические свойства обеспечили хорошее взаимодействие с кристаллическим кремнием (Si-c), коэффициент поглощения ( $\alpha$ ) становится значительно выше в разных диапазонах, что увеличивает генерацию фототока в диапазоне 370-900нм. Фактор деградации быстро снижает эффективность, и для конкретных результатов требуется развитое оборудование.  $\text{CsPbI}_3$  показал текстурированную поверхность, в то время как поверхность  $\text{CsPbBr}_3$  является гладкой, в соответствии с этим стало возможным лучшее измерение содержания йода.

**Ключевые слова:** гибридные солнечные элементы, наночастицы, оптические свойства, перовскит, фототок, фактор деградации

**Ссылка при цитировании:** Беджамил Л., Давыдов В. В., Алешин Ф. Н., Малышкин В. М., Теруков Е. И. Электрические характеристики пленок нанокристаллов перовскита галогенидов свинца  $\text{CsPbI}_3$  и  $\text{CsPbBr}_3$ , нанесенных на Si-c солнечные элементы для высокоэффективной фотовольтаики // Научно-технические ведомости СПбГПУ. Физико-математические науки. 2022. Т. 15. № 3.2. С. 91–96. DOI: <https://doi.org/10.18721/JPM.153.217>

Статья открытого доступа, распространяемая по лицензии CC BY-NC 4.0 (<https://creativecommons.org/licenses/by-nc/4.0/>)

### Introduction

Recently, many research into improving performance and effectiveness of solar cells on perovskites has been provided. The research carried out to date makes it possible to consider the development of heterostructure tandem cells in order to limit various optical losses. As well as the Oxford Laboratories guarantee that currently, the best partner for Si-c is the perovskite material [1] due to the strong absorption of the light coefficient [2], tread structure [3], high mobility of charge carriers [4] and low manufacturing cost. Optically resonant nanostructures constitute a bridge between optics and nanometric scales, making it possible to reduce the confinement of light to the nanometric scale via the excitation of highly localized optical modes. This reduces a certain number of important optical devices such as wave guides, lasers, sensors, etc. historically, metal nanostructures paved the way to novel nanoscale optical phenomena and applications related to the effective light management in the deeply subwavelength regime [5]

This work mainly concerns how to improve the optical and electric properties of a solar cell with one junction by adding nanoparticles of perovskite of iodine and bromine  $\text{CsPbI}_3$  and  $\text{CsPbBr}_3$ , for their properties, strong absorption and/or emission, higher quantum yields of photoluminescence. This type of Np represents greater liaison energies of excitons and longer time of decrease of carriers by comparing them to those of massive crystals. [7]. The lead halide (Ncs)  $\text{CsPbI}_3$  and  $\text{CsPbBr}_3$  perovskite nanocrystals used in the current work are deposited on a crystalline silicon substrate coated with an ITO conductive layer. They are characterized respectively by a band gap granted between 1.75 and 2.13 eV [6] and 2.34 eV [8] while silicon band gap is 1.2 eV, which makes a varied heterostructure with a wider total band gap.

### Experimental Techniques of Elaboration and Characterization

The type of substrate used is crystalline silicon provided by Research and development center for thin-film technologies in energetics R&D Center TFTE LLC. Thin crystalline silicon substrates are doped to create the p-n junction. Subsequently, in order to reduce optical losses, the solar cells used are coated with a hydrogenated anti-reflection layer to reduce the risk of contamination. This layer is dark blue in color. It is commonly used as an insulator in microelectronics and as an antireflection layer in the photovoltaics. An additional layer is conductive ITO layer. And finally the deposition of  $\text{CsPbI}_3$  and  $\text{CsPbBr}_3$  perovskite nanoparticles is made. Two types of  $\text{CsPbI}_3$  and  $\text{CsPbBr}_3$  nanoparticles in the form of a compact solution were provided by the chemical laboratory of LETI University of Saint Petersburg.

The deposition of this solution is done by the spin coating technique. It is a deposition method which makes it possible to deposit a homogeneous film on a substrate. The film was deposited by centrifugation on the Si-c substrates at 2000 rpm for 30 s. The solution is dispersed at high speed. A homogeneous film is obtained. Molecular crystal synthesis of perovskite nanoparticles occurs during this deposition, during which the solvent evaporates, through a process of self-organization. And finally, an electrode made of ITO material with a thickness of 80 nm was deposited on top of the device by thermal evaporation. This structure is presented in Figure 1

After having prepared the substrates, the topography of the surface of the deposited layers is characterized by atomic force microscopy (AFM) of the SOLVER P47-PRO NT-MDT type. It makes it possible to quantitatively determine the roughness of surfaces as well as its thickness.

One of the most important properties of perovskite materials is the ability to emit light with high efficiency. The study of photoluminescence allows us to study this emission of light, the

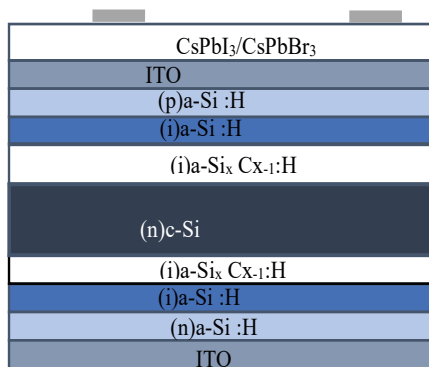


Fig. 1. The structure studied

nature of the halogen in the composition of the perovskite, or even whether the purity of the crystal is greater or lesser. The substrates were excited by ultraviolet LED UVTOP280TO39HS with a  $\lambda = 285$  nm. LED radiation focused on the surface of the samples using a quartz lens at an angle of  $10^\circ$  from the normal of the surface of the sample at a point 2 mm in diameter. The reflectance measurement was performed by the CARY5000 scan type spectrophotometer, which scans the entire ultraviolet, visible and near infrared solar spectrum from 200 to 2500 nm in R&D Center TFTE LLC.

The current-voltage (I-Vs) characteristics of the samples were measured in the vertical configuration by the two-probe scheme. The photocurrent current-voltage (I<sub>ph</sub>-V) curves of the solar cells were measured with a Keithley 2400 source meter under simulated lighting from a homemade lamp at a calibrated solar simulator intensity of  $50 \text{ mW/cm}^2$  at room temperature in the air, and the scan direction is from open circuit at 0.5 V to short circuit at  $-0.5$  V with variable pitch. The contacts with the flat electrodes were made using gold wire and copper.

### Investigation results and discussion

The morphology was examined using an atomic force microscope (AFM) for two types of Ncs in the form of thin films, formed from a solution, deposited by spin-coating under the same conditions. Figure 2a, b show the AFM images. There is a noticeable difference in surface texture for CsPbBr<sub>3</sub>, which is smooth and flat with complete absence of any spherical structure, unlike CsPbI<sub>3</sub> for which spherical structures of various sizes were present with a random distribution, with an RMS value of: Sq = 10.32 nm and 12.8 nm, respectively. Such a significant difference in RMS and average roughness can be explained by an increase in the size and density of CsPbI<sub>3</sub> crystals. The latter can be attributed to light trapping and reducing optical losses, which increase the rate of absorption.

In view of the graphs shown in Figure 3 we find that the ratio decrease results in a shift of the

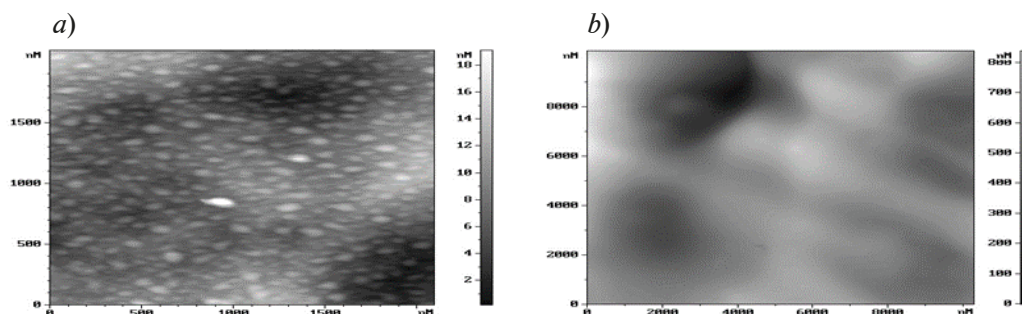


Fig.2. AFM images of CsPbI<sub>3</sub> (a) CsPbBr<sub>3</sub> (b)

reflectivity spectrum towards the near infrared region, which is due to an increase in the effective refractive index, the latter varies with the content of Ncs within the layer. Note also that the fringes are regularly spaced for Si-c and CsPbI<sub>3</sub>. This suggests that their refractive index is wavelength dependent in the same way. These effects are generally due to the increase in the depth refractive index of the layer. While for CsPbBr<sub>3</sub> the refractive index must be very different from the last two.

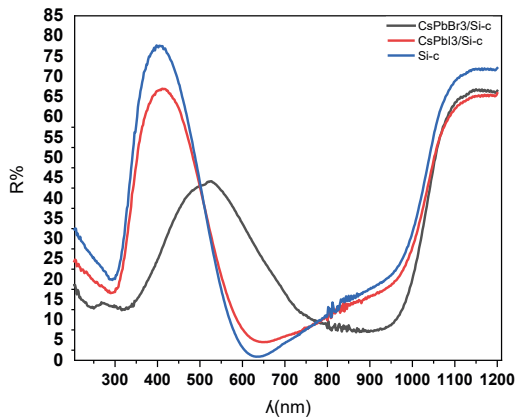


Fig. 3. Reflectance spectra of composite layers of perovskites and Si-c

The reflection rate remains quite high in the three substrates, which is far from meeting our expectations. And this is because of the absence of the anti-reflective layer which significantly decreases the reflection rate. Si-c and CsPbI<sub>3</sub> show quite similar results and for CsPbBr<sub>3</sub> the reflection rate is rather moderate, not exceeding 40%. The interaction of CsPbI<sub>3</sub> with Si-c is very weak while CsPbBr<sub>3</sub> gives another behavior totally different from Si-c.

For CsPbI<sub>3</sub>, the absorption rate is high in the range of 710–980 nm, while for CsPbBr<sub>3</sub> Ncs ( $\rho$ ) it is lower, but in a different range of 580–970 nm. This is related to the different role of Ncs as an indirect energy converter with Si-c. These results show a particular absorption in the UV region.

Figure 4 shows the photoluminescence spectra at ambient temperature of the thin films containing CsPbI<sub>3</sub> and MAPbI<sub>3</sub>, deposited on a crystalline silicon substrate.

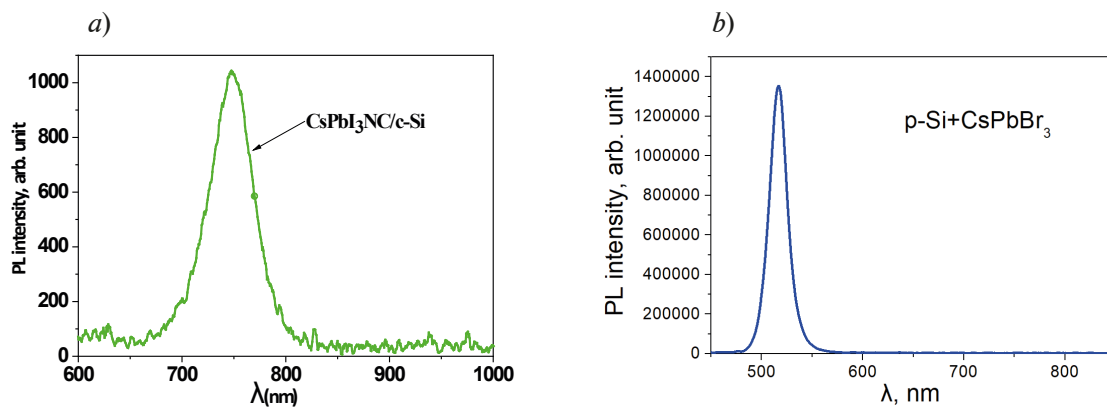


Fig. 4. Photoluminescence spectrum at room temperature for CsPbI<sub>3</sub> (a) and CsPbBr<sub>3</sub> (b)

The samples were excited with the 285 nm light. We find an emission peak centered at 2.47 eV for CsPbI<sub>3</sub> and MAPbI<sub>3</sub>. These are excitonic peaks, there are no peaks associated with possible defects, so it is intrinsic photoluminescence that we see on these spectra.

The PL intensity of iodine Ncs films at room temperature is observed with a maximum peak of about 740 nm, and the PL intensity of bromine Nc film has a maximum of about 550 nm, which confirms the results from literature [9]

The current-voltage characteristic  $I = f(V)$  of a solar cell makes it possible to determine the current as a function of the voltage for a given illumination. This measurement is carried out using a solar simulator whose irradiance spectrum is very close to the AM1.5 spectrum. The results obtained for the two types of perovskite nanoparticles CsPbI<sub>3</sub> and CsPbBr<sub>3</sub> are presented in Figure 5. The essential parameter of our study is the short-circuit current since the main gain obtained with the nanoparticle structure is at the level of  $J_{sc}$ . The measured current for CsPbI<sub>3</sub> nanoparticles is higher comparing it with CsPbBr<sub>3</sub>, and CsPbI<sub>3</sub> and CsPbBr<sub>3</sub> have higher current than the base substrates.

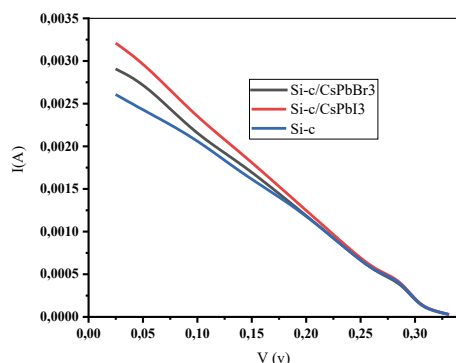


Fig. 5. The I-V characterization of CsPbI<sub>3</sub>, CsPbBr<sub>3</sub> and Si-c

The analysis of the dependences obtained shows that the currents coincide in the area of voltage increase. It is difficult to establish differences between the structures in terms of this dependence.

### Conclusion

However, 2D perovskite nanoparticles still offer a great potential due to the structure-dependent optic and electronic properties. Below the most important points are summarized from this work. The study of the external structure (morphology), a spherical form of nanoparticles makes a kind of textured surface which means it helps to provide an appropriated adjustment for optical optimization of

perovskite solar cells in addition, these nanoparticles are 0-dimension type. As a result, the size difference of CsPbI<sub>3</sub> and CsPbBr<sub>3</sub> leads to a different interaction with the semiconductor based on crystalline silicon: a different absorption peaks in different ranges for CsPbI<sub>3</sub> it is 350–450 nm, and for CsPbBr<sub>3</sub> 530–850 nm, which means, this improves the absorption of our heterostructure (before perovskites nanoparticles fast degradation). It has been found that the absorption coefficient of SCs with NC layers of inorganic perovskites is much higher in the visible region of the spectrum, which increases photocurrent generation in SCs in the range of 370–900 nm. The reflectance measurement shows that the combination CsPbBr<sub>3</sub>/c-Si shows a better absorbance in a different range comparing to CsPbI<sub>3</sub>/c-Si. The photocurrent measurements of Si-c coated with CsPbI<sub>3</sub> and CsPbBr<sub>3</sub> perovskites nanoparticles show higher photocurrent comparing them with Si-c.

I-V characteristic showed higher current for CsPbI<sub>3</sub> about 3,25 mA for a 1cm<sup>2</sup> substrate which proves that this kind of nanoparticles has higher electrical properties than CsPbBr<sub>3</sub> which gives the current is 2.88 mA. And substrates coated with active layer with perovskites have higher current then a simple substrate Si-c for which it is about 2,55 mA.

### REFERENCES

1. Jung S., Enhancement of Photoluminescence Quantum Yield and Stability in CsPbBr<sub>3</sub> Perovskite Quantum Dots by Trivalent Doping. *Nanomaterials*. 2020, 10 (4) 710.
2. Chen Q., De Marco N., Yang Y., Song T.B., Chen C.C., Zhao H., Hong Z., Zhou H., Yang Y., Under the spotlight: The organic-inorganic hybrid halide perovskite for optoelectronic applications. *Nano Today* 2015, 10, 355–396.
3. Noh J.H., Im S.H., Heo J.H., Mandal T.N., Seok S.I., Chemical management for colorful, efficient, and stable inorganic-organic hybrid nanostructured solar cells. *Nano Lett.* 2013, 13, 1764–1769.
4. Oga H., Saeki A., Ogomi Y., Hayase S., Seki S., Improved understanding of the electronic and energetic landscapes of perovskite solar cells: High local charge carrier mobility, reduced recombination, and extremely shallow traps. *J. Am. Chem. Soc.* 2014, 136, 13818–13825.
5. Zheludev N. I., Kivshar Y. S., *Nature Materials* 11, 917 (2012).
6. Almosni S., Robert C., Thanh T. N., Cornet C., Letoublon A., Quinci T., Levallois C., Perrin M., Kuyyalil J., Pedesseau L., Balocchi A., Barate P., Even J., Jancu J. M., Bertru N., Marie X., Durand O., Le Corre A., Evaluation of InGaPN and GaAsPN 18 materials lattice-matched to Si for multi-junction solar cells. *J. Appl. Phys.* 2013, 113 (12), 123509-123509-6.
7. Wei, Y., Lauret, J. S., Galmiche, L., Audebert, P., Deleporte, E., Strong exciton photon coupling in microcavities containing new fluorophenethylamine based perovskite compounds. *Opt. Express* 2012, 20 (9), 10399–10405.
8. Giovanni M., Temperature-Dependent Optical Band Gap in CsPbBr<sub>3</sub>, MAPbBr<sub>3</sub>, and FAPbBr<sub>3</sub> Single Crystals *J. Phys. Chem. Lett.* 2020, 11, 7, 2490–2496.
9. Stoumpos C. C., Malliakas C. D., Kanatsidis M. G., Semiconducting Tin and Lead Iodide Perovskites with Organic Cations: Phase Transitions, High Mobilities, and Near-Infrared Photoluminescent Properties (*Inorganic Chemistry*, A, 2015).

### THE AUTHORS

**BOUDJEMILA Linda**

ariessai21@gmail.com

ORCID: 0000-0003-3589-8941

**ALESHIN Andrey N.**

aleshin@transport.ioffe.ru

**DAVYDOV Vadim V.**

davydov\_vadim66@mail.ru

ORCID: 0000-0001-9530-4805

**MALYSHKIN Vladislav M.**

mal@gromco.com

**TERUKOV Evgenyi I.**

e.terukov@hevelsolar.com

*Received 05.08.2022. Approved after reviewing 21.09.2022. Accepted 21.09.2022.*

## EXPERIMENTAL TECHNIQUE AND DEVICES

Conference materials

UDC 621.396.6

DOI: <https://doi.org/10.18721/JPM.153.218>

### Algorithm and installation for measuring the current lacing voltage in high-power RF and microwave bipolar and heterojunction bipolar transistors

K. A. Litvinov<sup>1</sup> ✉, O. A. Radaev<sup>2</sup>, I. S. Kozlikova<sup>2</sup>, V. A. Sergeev<sup>1,2</sup>, A. A. Kulikov<sup>1</sup>

<sup>1</sup>Ulyanovsk State Technical University, Ulyanovsk, Russia;

<sup>2</sup>Ulyanovsk Branch of Kotelnikov Institute of Radio-Engineering and Electronics of RAS, Ulyanovsk, Russia  
✉ [sva@ulstu.ru](mailto:sva@ulstu.ru)

**Abstract.** Methods of measuring the current lacing voltage in high-power bipolar (BT) and heterojunction bipolar (HBT) RF and microwave transistors are considered. A method and installation for determining the current lacing voltage in a transistor without introducing the device into the hot spot mode by the steepness of the dependence of the variable component of the voltage at the emitter junction on the collector voltage at a given emitter current and the supply of the sum of linearly increasing and small alternating voltage to the collector is described. A critical drawback of the known methods for determining the voltage of the  $U_{KL}$  localization in BT and HBT is that the devices enter the hot spot mode thus the purpose of the work was to develop and experimentally test an algorithm and installation for measuring the voltage of the  $U_{KL}$  localization without introducing the device into the hot spot mode.

**Keywords:** microwave bipolar transistor, current lacing voltage, non-destructive method, measurement, installation

**Funding:** The work was supported by the Russian Science Foundation, the project No. 22-29-01134.

**Citation:** Litvinov K. A., Radaev O. A., Kozlikova I. S., Sergeev V. A., Kulikov A. A., Algorithm and installation for measuring the current lacing voltage in high-power rf and microwave bipolar and heterojunction bipolar transistors, St. Petersburg State Polytechnical University Journal. Physics and Mathematics. 15 (3.2) (2022) 97–101. DOI: <https://doi.org/10.18721/JPM.153.218>

This is an open access article under the CC BY-NC 4.0 license (<https://creativecommons.org/licenses/by-nc/4.0/>)

Материалы конференции

УДК 621.396.6

DOI: <https://doi.org/10.18721/JPM.153.218>

### Алгоритм и установка для измерения напряжения локализации тока в мощных ВЧ и СВЧ биполярных и гетеропереходных биполярных транзисторах

К. А. Литвинов<sup>1</sup> ✉, О. А. Радаев<sup>2</sup>, И. С. Козликова<sup>2</sup>,  
В. А. Сергеев<sup>1,2</sup>, А. А. Куликов<sup>1</sup>

<sup>1</sup>Ульяновский государственный технический университет, Ульяновск, Россия;

<sup>2</sup>Ульяновский филиал Института радиотехники и электроники  
им. В.А. Котельникова РАН, Ульяновск, Россия

✉ [sva@ulstu.ru](mailto:sva@ulstu.ru)

**Аннотация.** Рассмотрен метод измерения напряжения локализации тока  $U_{KL}$  в мощных биполярных (БТ) и гетеропереходных биполярных (ГБТ) ВЧ и СВЧ транзисторах. Описан метод и установка для определения напряжения локализации тока  $U_{KL}$  в транзисторе без введения прибора в режим горячего пятна по крутизне зависимости переменной

составляющей напряжения на эмиттерном переходе от коллекторного напряжения при заданном эмиттерном токе и при подаче на коллектор суммы линейно нарастающего и малого переменного напряжения. Существенным недостатком известных способов определения напряжения локализации  $U_{KL}$  в БТ и ГБТ является выход приборов в режим горячего пятна, поэтому целью работы являлась разработка и экспериментальная проверка алгоритма и установки для измерения напряжения локализации тока  $U_{KL}$  без введения исследуемого прибора в режим горячего пятна.

**Ключевые слова:** СВЧ биполярный транзистор, напряжение шнурования тока, неразрушающий метод, измерение, установка

**Финансирование:** Работа выполнена при поддержке Российского научного фонда, проект № 22-29-01134.

**Ссылка при цитировании:** Литвинов К. А., Радаев О. А., Козликова И. С., Сергеев В. А., Куликов А. А. Алгоритм и установка для измерения напряжения локализации тока в мощных ВЧ и СВЧ биполярных и гетеропереходных биполярных транзисторах // Научно-технические ведомости СПбГПУ. Физико-математические науки. 2022. Т. 15. № 3.2. С. 97–101. DOI: <https://doi.org/10.18721/JPM.153.218>

Статья открытого доступа, распространяемая по лицензии CC BY-NC 4.0 (<https://creativecommons.org/licenses/by-nc/4.0/>)

### Introduction

It is known that current distribution in high-power bipolar (BT), including heterojunction bipolar (HBT), loses stability at certain values of collector voltage of the  $U_{KL}$  localization under which the so-called "current cord" and "hot spot" (HS) are formed in the structure of the device [1–4]. The line of mode parameters in current-voltage coordinates corresponding to current lacing defines one of the boundaries of the safe operation area (SOA) of BT and HBT, going beyond which, even for a short time, leads either to irreversible destruction of the instrument structure and catastrophic failure of the device, or to degradation of the device [5]. Even in the absence of irreversible damage, strong overheating of the local region of the structure is accompanied by large thermal deformations, an increase in the number of dislocations and microcracks in the semiconductor, and accelerated MBT degradation.

A critical drawback of the known methods [6–8] for determining the voltage of the  $U_{KL}$  localization in BT and HBT is that the devices enter the HS mode thus the purpose of the work was to develop and experimentally test an algorithm and installation for measuring the voltage of the  $U_{KL}$  localization without introducing the device into the HS mode.

### Materials and Methods

According to the model presented in [9], for the case of defects of an electrophysical nature in the BT structure, the dependence of the variable voltage component  $\tilde{U}_{EB}$  on emitter junction from the collector voltage is described by the formula:

$$\tilde{U}_{EB}(U_K) = \tilde{U}_{EB}(0) \left[ 1 + \frac{b}{(1 - U_K/U_{KL})^2} \right], \quad (1)$$

where  $\tilde{U}_{EB}(0)$  is the amplitude of the alternating voltage at the emitter junction at a collector voltage  $U_{K0}$  close to zero;  $b$  – is a dimensionless parameter depending on the magnitude of the defect in the BT structure, and, as a rule,  $b \ll 1$ .

Based on this model, in [9] a non-destructive method and in [10] the installation are proposed for determining the  $U_{KL}$  at a given emitter current by three counts of the alternating voltage at the emitter at three collector voltages  $U_{K0}$ ,  $U_{K1}$ ,  $U_{K2}$  of a transistor included in a circuit with a common base, when the sum of a linearly increasing voltage and a small sinusoidal voltage is applied to the collector:

$$U_{EL} = \frac{U_{K2} - mU_{K1}}{1 - m}, \quad (2)$$

where  $m = \sqrt{\frac{a1-1}{a2-1}}$ ,  $a1 = \tilde{U}_{EB}(U_{K1})/\tilde{U}_{EB}(U_{K0})$ ,  $a2 = \tilde{U}_{EB}(U_{K2})/\tilde{U}_{EB}(U_{K0})$ .

The accuracy of this method strongly depends on the choice of collector voltage values, while there is a possibility of the device entering the HS mode. In order to exclude the devices from entering the HS mode and to increase the accuracy of determining the  $U_{KL}$  when setting the transistor mode, the new method proposes to measure the amplitude of the alternating emitter voltage at a low collector voltage; then measure the values of the collector voltage, at which the amplitude becomes equal to  $(1+k1)$  and  $(1+k2)$ , and the voltage  $U_{KL}$  is calculated by the formula:

$$U_{KL} = \frac{\sqrt{k2/k1}U_{K2} - U_{K1}}{\sqrt{k2/k1} - 1}, \tag{3}$$

where  $k1$  and  $k2$  are the given coefficients of response.

Figure 1 shows a characteristic type of BT dependence with current localization with specified levels, and Figure 2 shows a block diagram of the device implementing the method [11].

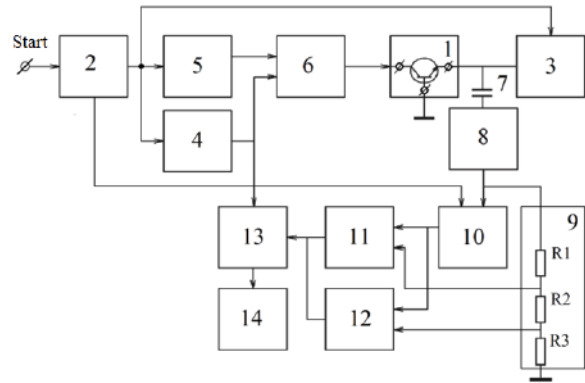
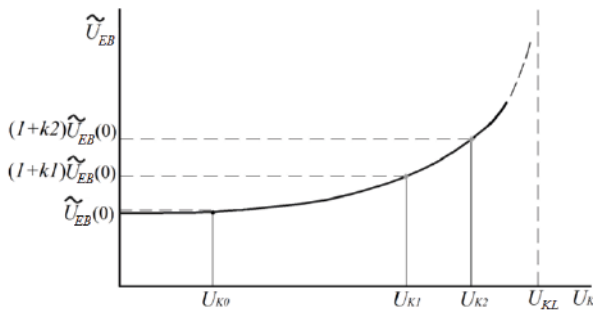


Fig. 1. Type of BT dependence with current localization and preset levels

Fig. 2. Block diagram of the device implementing the method

The device implementing the method contains a block 1 for connecting a transistor; a control device 2; a current source 3; a linearly increasing voltage generator 4; a low frequency generator 5; a power amplifier adder 6; a separating capacitor 7; an envelope extraction device 8; a resistive divider 9; a sampling and storage device 10; comparators 11 and 12; logger 13 and computer 14.

The device works according to the following algorithm. The tested transistor 1 is switched on according to the circuit with a common base. The device works according to the following algorithm. The tested transistor 1 is switched on according to the circuit with a common base. During the action of the control pulse  $T_{u3M}$  with a duration generated by the control unit 2 at the signal "start", the emitter current  $I_E^{u3M}$  is set by the current generator 3, and the sum of the linearly increasing and sinusoidal voltages is applied to the collector from the output of the power amplifier 6:

$$U_K(t) = U_{KM}t / T_{u3M} + U_m \sin \Omega t, \tag{4}$$

generated by the generator 4 linearly increasing voltage and the generator 5 low frequency. The variable voltage component  $\tilde{U}_{EB}(t)$  from the emitter of the transistor through the coupling capacitor 7 is fed to the input of the envelope selection device 8, from the output of which the envelope voltage of the variable voltage component at the emitter is fed to the input of the resistive divider 9 and the sampling and storage device 10. According to the second signal of the control device 2 at the time  $t_0$ , the sampling and storage device 10 remembers and stores the value of the amplitude of the variable component  $\tilde{U}_{EB}(0)$  of the voltage at the emitter junction of the transistor when the collector voltage is close to zero. The voltage from the output of the sampling and storage device 10 is supplied to the first inputs of the comparison devices 11 and 12, the second inputs of which receive signals from the first and second outputs of the resistive divider 9. The resistance values of resistors  $R_1$ ,  $R_2$  и  $R_3$  are chosen so that the voltage division

factor at the first output of divider 9 is equal to  $(1+k_1)$ , and at the output of the second one it is  $(1+k_2)$ , where  $k_1$  and  $k_2$  are the given coefficients of exceeding the initial amplitude  $\tilde{U}_{EB}(0)$ . At times  $t_1$  and  $t_2$ , when the voltages at the outputs of the resistive divider will be equal  $\tilde{U}_{EB}(0)$  comparison devices 11 and 12 generate short pulses, according to the signals of which the recorder 13 measures the voltages  $U_{K1}$  and  $U_{K2}$  at the output of the generator 4 and transfers them to the calculator 14, which calculates the desired localization voltage according to formula (3).

### Results and Discussion

An experimental sample of the device is implemented on the basis of an Arduino debugging board. The algorithm and the experimental device were tested on transistors of the KT903B type, some of the results are presented in the table 1. The measurements were carried out at an emitter current of 0.8 A, a collector voltage of 50 V, and a measurement time of 2.5 s.

Table 1

The results of determining  $U_{KL}$  for transistors of the KT903B type at two values of the coefficient  $k$

No. trans.	$U_{K2}$ at $k_2 = 0.8$ , V	$U_{K1}$ at $k_1 = 0.5$ , V	$U_{KL}$ , V
265	43	36	50.8
377	37	36	38.1
971	42	39	45.1
281	37	33	41.4

The use of the algorithm described above and the data processing unit made it possible to measure the dependence of the current lacing voltage on the emitter current for microwave transistors of the KT920B and KT925B types, see Fig. 3.

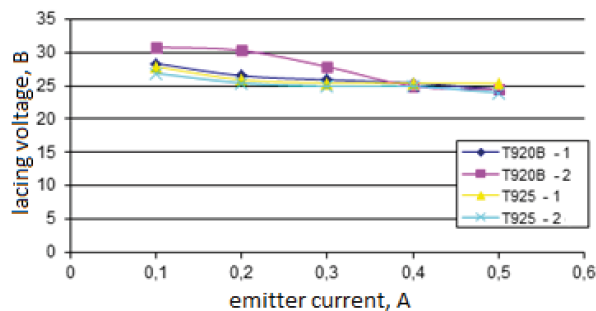


Fig. 3. Dependence  $U_{KL}$  transistors type KT920B and KT925B from emitter current

It can be seen from the Fig.3 that at lower emitter currents, the value of the localization voltage differs significantly from sample to sample. At high currents, the localization voltages practically coincide. To increase the reliability of rejection, it is necessary to set small emitter currents, at which the spread of  $U_{KL}$  values is greater. These results are consistent with known models of thermal instability in BT and HBT.

Defects that reduce the current lacing voltage also manifest themselves in an increase in the thermal resistance of the HBT. To verify this conclusion, the correlation between the lacing voltage  $U_{KL}$  and the thermal resistance  $R_{TRCB}$  of the collector-base junction was evaluated on a sample of transistors of the KT840B type;  $U_{KL}$  was measured on the described installation at a current of 1.5 A, and  $R_{TRCB}$  was measured with a thermal resistance meter at a current of 1.1 A. The correlation coefficient was  $-0.45$ , which confirms, taking into account the influence of other factors, the presence of a rather strong relationship between  $U_{KL}$  and  $R_{TRCB}$ . By selecting measurement modes, the relationship between the indicated parameters can probably be increased.

### Conclusion

Thus, using the described algorithm and installation, it was possible to measure the current lacing voltage localization voltage on several samples of transistors. In addition, it was found that there is some correlation between the voltage of the  $U_{KL}$  localization and the thermal resistance of the collector-base junction  $R_{TRCB}$ .

The values of collector voltage of the  $U_{KL}$  localization in the transistor structure can serve as a measure of defectiveness; therefore, the developed algorithm and installation will be widely used in the field of non-destructive input and output quality control of products at enterprises engaged in the manufacture of electronic equipment.

### REFERENCES

1. **Sergeev V. A.**, St. Petersburg Journal of Electronics, 2 (1997) 40–42.
2. **Sinkevich V. F.**, Electronic industry, 2, (2003) 232.
3. **Nenadovic N., et al.**, IEEE Trans. on Electron Devices, 12 (2004) 2175.
4. **Bagnoli P. E., Stefani F.**, IEEE Trans. on Components and Packaging Technologies, 2 (2009) 493.
5. **Liu W., et al.**, IEEE Trans. on Electron Devices, 2 (1996) 220.
6. **Ladbrooke P. et al.**, Patent US 20080228415, 2008.
7. **Scholten A. J. et al.**, IEEE Bipolar/BiCMOS Circuits and Technology Meeting (BCTM), 1 (2012).
8. **Gusev V. A., Kapranov I. Yu.**, Vestnik SevSTU. Ser. Informatics, electronics, communications : collection of scientific tr., 93 (106) (2008).
9. **Sergeev V. A., Dulov O. A., Kulikov A. A.**, News of universities. Electronics, 2 (10) (2009).
10. **Sergeev V. A., Dulov O. A., Kulikov A. A.**, Patent Russia, (2015) 2537519.
11. **Sergeev V. A. et al.**, Automation of control processes, 3 (96) (2017).

### THE AUTHORS

**LITVINOV Kirill A.**  
litvinovkirand@mail.ru  
ORCID: 0000-0003-1181-7406

**SERGEEV Viacheslav A.**  
sva@ulstu.ru  
ORCID: 0000-0003-4854-2813

**RADAEV Oleg A.**  
oleg.radaev.91@mail.ru  
ORCID: 0000-0002-8156-9412

**KULIKOV Alexander A.**  
kulikovaa36@yandex.ru

**KOZLIKOVA Irina S.**  
kozlikova95@mail.ru

*Received 08.08.2022. Approved after reviewing 15.08.2022. Accepted 18.08.2022.*

Conference materials

UDC 54.07

DOI: <https://doi.org/10.18721/JPM.153.219>

## Development of a device for picoampere currents measuring

O. A. Mikhailova<sup>1</sup> ✉, I. E. Antifeev<sup>2</sup>, D. G. Petrov<sup>2</sup>, R. V. Davydov<sup>1,3</sup>

<sup>1</sup> Peter the Great Saint-Petersburg Polytechnic University, Saint Petersburg, Russia;

<sup>2</sup> Institute of Analytical Instrumentation of the RAS, Russia;

<sup>3</sup> All-Russian Research Institute of Phytopathology, Moscow Region, Russia

✉ [lesya101201@gmail.com](mailto:lesya101201@gmail.com)

**Abstract.** One of the actual topics in microelectronics is the problem of measuring small currents. We have considered possible solutions to this problem, one of which is a current measurement method based on the use of an amplifier with differential inputs. The advantage of this scheme is that the high-precision measuring resistance is divided between two identical elements that are physically installed in the same orientation and at the same distance from the source of magnetic interference. Interference induced on two resistors in this case creates the same signals, which are suppressed at the output of the amplifier. To solve this problem, we have developed a stand for testing a device for measuring picoampere currents. The stand consists of a measuring unit, a digital-to-analog converter module and special software. The measuring unit consists of a differential amplifier stage, followed by a signal amplification circuit on an operational amplifier, the digital-to-analog converter module is implemented on the basis of an external input-output module L-CARD E20-10, and the L-Graph program was used for signal processing. As a result of the experiments, the ranges of measured values were confirmed.

**Keywords:** picoampere currents, current measurement, ADC

**Citation:** Mikhailova O. A., Antifeev I. E., Petrov D. G., Davydov R. V., Development of a device for picoampere currents measuring, St. Petersburg State Polytechnical University Journal. Physics and Mathematics. 15 (3.2) (2022) 102–106. DOI: <https://doi.org/10.18721/JPM.153.219>

This is an open access article under the CC BY-NC 4.0 license (<https://creativecommons.org/licenses/by-nc/4.0/>)

Материалы конференции

УДК 54.07

DOI: <https://doi.org/10.18721/JPM.153.219>

## Разработка устройства для измерения пикоамперных токов

О. А. Михайлова<sup>1</sup> ✉, И. Е. Антифеев<sup>2</sup>, Д. Г. Петров<sup>2</sup>, Р. В. Давыдов<sup>1,3</sup>

<sup>1</sup> Санкт-Петербургский Политехнический университет Петра Великого, Санкт-Петербург, Россия;

<sup>2</sup> Институт аналитического приборостроения РАН, Санкт-Петербург, Россия;

<sup>3</sup> Всероссийский научно-исследовательский институт фитопатологии, Московская область, Россия

✉ [lesya101201@gmail.com](mailto:lesya101201@gmail.com)

**Аннотация.** Одной из актуальных тем в микроэлектронике является проблема измерения малых токов. В данной работе показана схема прибора для измерения пикоамперных токов. Предложен принцип измерения токов, основанный на схеме усилителя с дифференциальными входами. В результате экспериментов были подтверждены диапазоны измеряемых величин.

**Ключевые слова:** пикоамперные токи, измерение тока, АЦП

**Ссылка при цитировании:** Михайлова О. А., Антифеев И. Е., Петров Д. Г., Давыдов Р. В. Разработка устройства для измерения пикоамперных токов // Научно-технические ведомости СПбГПУ. Физико-математические науки. 2022. Т. 15. № 3.2. С. 102–106. DOI: <https://doi.org/10.18721/JPM.153.219>

Статья открытого доступа, распространяемая по лицензии CC BY-NC 4.0 (<https://creativecommons.org/licenses/by-nc/4.0/>)



## Introduction

The problem of measuring currents remains relevant in various fields of science [1–8]. This is especially important when conducting physical experiments, for example, measuring the human magnetic field or examining samples during a long cycle, for example, polymerase chain reaction (PCR) [9–16]. The currents required in these cases must be measured with an accuracy of tens of picoamperes [11, 12, 17–19].

To measure currents in the world, magnetoelectric type devices are often used. This type of device does not allow measuring currents less than a few microamperes with an error of less than ten percent. There is a separate class of instruments - galvanometers. These devices are complex, capricious and require special conditions for use, such as protection from shaking, stable temperature and humidity.

Another way to solve the problem of measuring currents is to use microcircuits based on the Hall effect [20]. The principle of operation is based on the occurrence of an electric voltage on a magnetically sensitive element under the influence of a forming magnetic field resulting from the passage of an electric current through a nearby conductor. The main advantage of this measurement method is the absence of a resistive shunt, which results in no undesirable thermal energy release during the measurement. Although the use of this method is applicable for measuring ultra-low currents, it requires special conditions, for example, low temperatures close to absolute zero, as well as highly sensitive measuring equipment, which leads to difficulties in operating devices based on this principle.

Another measurement method can be products based on the use of current transformers. The principle of operation is based on the properties of the transformation of alternating electric current. The resulting alternating magnetic flux is captured by a magnetic circuit perpendicular to the direction of the primary current. This flux is created by the alternating current of the primary coil and induces an EMF in the secondary winding. After connecting the load, an electric current begins to flow through the secondary circuit. Thus, by selecting the required ratio of windings in the primary and secondary windings, you can immediately select the appropriate gain. The advantages of these devices are high accuracy and repeatability of the measured parameters, ease of use. However, the main disadvantage is the inapplicability of this approach in applications where it is necessary to measure direct currents.

The most common alternative solution is to use a resistive current sensor [21–23]. The principle is based on the dependence of voltage on the current passing through the measuring resistor. The advantage of this method of current measurement is the ease of use in both DC and AC circuits. The disadvantages include low noise immunity. To solve the above problem, various circuit solutions can be used.

The measurement methods discussed above have proven themselves in industry and household appliances and can be applied to solve the problem of analyzing small currents, but these solutions will lead to complex technical and technological solutions. Thus, the purpose of this work is to create a circuit solution that makes it possible to measure picoampere currents with high accuracy. We have proposed a method for measuring currents based on the use of an integrated current amplifier - an operational amplifier based on differential stages. The advantage of this circuit is that the high-resistance measuring resistance is shared between two identical elements that are physically mounted in the same orientation and at the same distance from the source of magnetic interference. Interference induced on two resistors, in this case, create the same signals, which are suppressed at the output of the amplifier [4]. This amplifier is capable of handling DC voltage amplification at sub-millivolt levels. The uniqueness of the chosen solution lies in the fact that we use standard techniques, but performed with high quality and simply. This is a special system with which we solve the problem of nanopore sequencing.

## Materials and Methods

To solve this problem, we have developed a stand for testing the device for measuring picoampere currents. The test bench consists of a measuring unit, a digital-to-analogue converter module and special software.

The measuring unit is based on the use of an operational amplifier with MOSFETs in the input circuits. The advantage of this circuit is that due to the use of MOSFETs, the input currents of the op-amp do not exceed 500 fA, which allows leveling the contribution of the op-amp in relation to the high-resistance measurement of resistance. This amplifier can handle DC amplification with levels in the tens of picoamps.

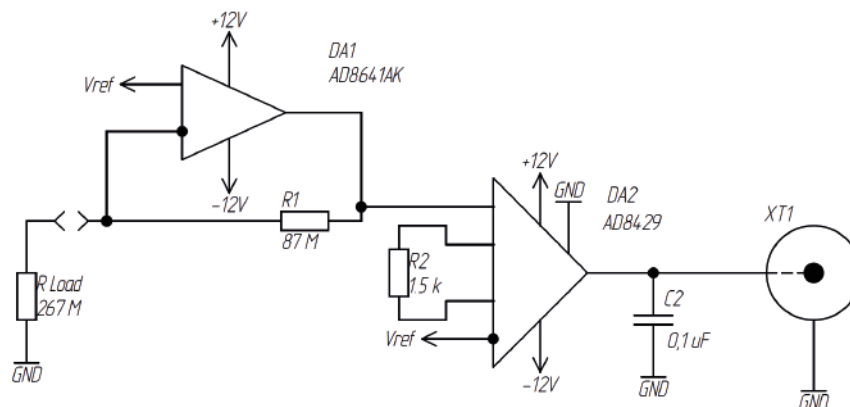


Fig.1. Circuit of the measuring equipment

The digital-to-analogue converter module is implemented on the basis of an external input-output module L-CARD E20-10. E20-10 is a high-speed ADC module with a USB interface for connecting to a PC. The E20-10 has 4 channels of 14bit/10MHz ADC with multiplexing function, 16 channels of digital input and output compatible with TTL logic, and 2 channels of DAC. The FPGA-based architecture with one ADC, switch and input buffer amplifiers in serially polled channels completely eliminates switching noise, third-order active low-pass filters in each channel improve the signal-to-noise ratio. Of the advantages of this ADC, among others, one can note the galvanic isolation of each channel, which provides high noise immunity.

To register, visualize, and process the analog signal, we used special software LGraph 2 (program) adapted to work with an external ADC L-CARD E20-10. A DT-9930 LCR meter was used for control measurement of the load resistor and current shunt. To control the measurement of the reference voltage and output signal frequency oscilloscope Tektronix MSO 2024B. For measuring test currents using a sample load resistor of 267 MΩ.

Changes in the current passing through the load resistor were changed by changing the reference voltage applied to the load resistor. The reference voltage was set using an external L-CARD E20-10 input/output module with a set voltage range of  $\pm 5V$  with a resolution of 12 bits. The parameters were measured in the range of  $\pm 3V$  with a sampling frequency of 50KHz. The measurement duration was 1 second. For each current measurement, 300 measurements were taken for subsequent averaging and calculation of statistical significance. Currents were measured from 0.1 nA to 0.4 nA in 0.025 nA steps.

### Results and Discussion

Based on the data obtained, a histogram of the distribution of the measured values was constructed (Fig. 2). Using the Kolmogorov-Smirnov test for the compliance of the sample with normal distributions, it was confirmed that the results obtained belong to the normal distribution and standard statistical methods of comparison can be applied to them. The correspondence of the obtained data to the normal distribution is also shown in Figure 2.

For each value of the tested current value, 300 measurements were carried out, after which these values were averaged and compared with each other. The graph for comparing the results is shown in Fig. 3. The step of changing the set current value was 0.025 nA, and the calculated RMS values do not exceed 0.0035 nA, which allows us to assert a significant difference in the experimentally obtained data.

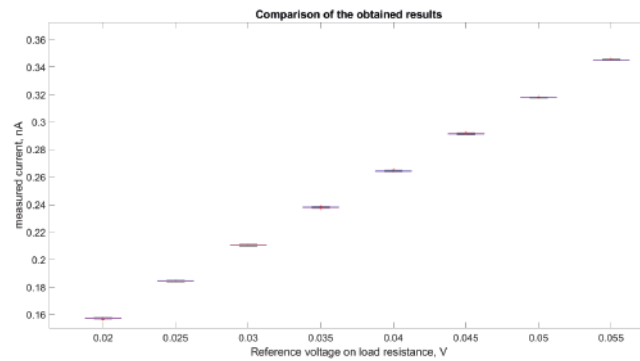


Fig.2. Comparison of the obtained results

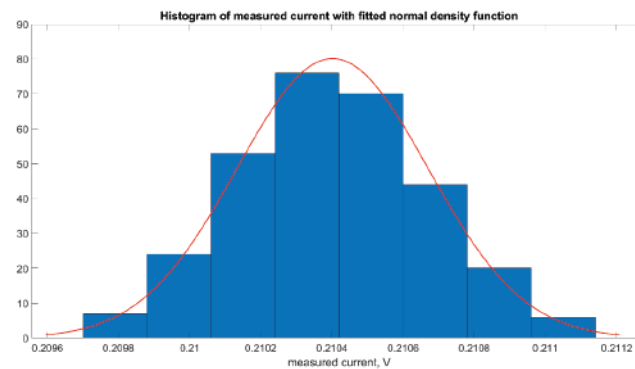


Fig.3. Histogram of current distribution

### Conclusion

As a result of the obtained data, we were convinced that the proposed circuit solution corresponds to the specified characteristics. The measuring stand allows measuring picoampere currents with an accuracy of  $\pm 10\text{pA}$ , and the results obtained correlate with the theoretical parameters of the circuit. A significant disadvantage of the measuring unit is the large leakage currents associated with the relatively low, compared with the analyzed samples, the resistance of the insulating material. In the manufacture of the measuring unit, a printed circuit board based on the FR4 insulating material was used, which does not allow achieving high electrical resistance. This parameter can be improved by using a separator based on polytetrafluoroethylene (PTFE).

### REFERENCES

1. Dyumin V., Smirnov K., Myazin N., Charge-coupled Device with Integrated Electron Multiplication for Low Light Level Imaging, Proceedings of the 2019 IEEE International Conference on Electrical Engineering and Photonics, EExPolytech. 8906868 (2019) 308–310.
2. Grevtseva A. S., Smirnov K. J., Rud V. Yu., Development of methods for results reliability raise during the diagnosis of a person's condition by pulse oximeter, Journal of Physics: Conference Series. 1135 (1) (2018) 012056.
3. Makeev S. S., Grevtzeva A. S., Glinushkin A. P., Matorin D. N., Possibilities of using spectral analysis in method of nuclear magnetic spectroscopy for condensed media investigation, Journal of Physics: Conference Series. 1695 (1) (2020) 012112.
4. Davydov V. V., Determination of the Composition and Concentrations of the Components of Mixtures of Hydrocarbon Media in the Course of its Express Analysis, Measurement Techniques. 62 (2) (2020) 1090–1098.
5. Davydov V. V., Grebenikova N. M., Smirnov K. Y., An Optical Method of Monitoring the State of Flowing Media with Low Transparency That Contain Large Inclusions, Measurement Techniques. 62 (6) (2019) 519–526.
6. Kuzmin M. S., Rogov S. A., On the use of a multi-raster input of one-dimensional signals in two-dimensional optical correlators, Computer Optics. 43 (3) (2019) 391–396.

7. **Logunov S. E., Vysoczky M. G.**, New method of researches of the magnetic fields force lines structure, *Journal of Physics: Conference Series*. 1038 (1) (2018) 012093.
8. **Mazing M. S., Zaitceva A. Yu., Kislyakov Yu. Ya., Kondakov N. S., Avdushenko S. A., Davydov V. V.**, Monitoring of Oxygen Supply of Human Tissues Using A Noninvasive Optical System Based on A MultiChannel Integrated Spectrum Analyzer, *International Journal of Pharmaceutical Research*. 12(2) (2020) 1974–1978.
9. **Reznik V. S., Kruglov V. A.**, Using of «bubble sensors» to control the quality of sequencing by the Illumina / Solexa method, *Journal of Physics: Conference Series*. 2086 (1) (2021) 012120.
10. **Kruglov V. A., Reznik V. S., Glinushkin A. P.**, Development of a hydraulic system for bridge amplification, *Journal of Physics: Conference Series*. 1695 (1) (2020) 012067.
11. **Reznik V. S., Kruglov V. A., Petrov A. I., Glinuchkin A. P., Rud V. Y.**, Development of a measuring device for the study of thermal processes during the polymerase chain reaction, *Journal of Physics: Conference Series*. 1410 (1) (2019) 012078.
12. **Davydov V. V., Kruzhalov S. V., Grebenikova N. M., Smirnov K. J.**, Method for Determining Defects on the Inner Walls of Tubing from the Velocity Distribution of the Flowing Fluid, *Measurement Techniques*. 61 (4) (2018) 365–372.
13. **Matvienko I. V., Bayramov V. M., Parygina N. A., Kurochkin V. E., Alekseev Y. I.**, Synthesis of Dihydroquinoline-Based Derivatives of Fluorescent Rhodamine Dyes for Nucleic Acid Analysis by a Real-Time Polymerase Chain Reaction, *Russian Journal of Bioorganic Chemistry*. 46 (3) (2020) 349–359.
14. **Fedorov A. A., Berdnikov A. S., Kurochkin V. E.**, The polymerase chain reaction model analyzed by the homotopy perturbation method, *Journal of Mathematical Chemistry*. 57 (4) (2019) 971–985.
15. **Davydov V. V., Davydova T. I.**, A nondestructive method for express testing of condensed media in ecological monitoring, *Russian Journal of Nondestructive Testing*. 53 (7) (2017) 520–529.
16. **Myazin N. S.**, Features of formation of structure of a nuclear magnetic resonance signal in weak magnetic field, *Journal of Physics: Conference Series*. 1135 (1) (2018) 012061.
17. **Natyrov A. N., Vlasova N. A., Matvienko I. V., Kurochkin V. E., Alexeev J. I.**, Synthesis of Unsymmetrical Polymethine Cyanine Fluorescent Dyes for Nucleic Acid Analysis by Real-Time PCR, *Russian Journal of Bioorganic Chemistry*. 44(5) (2018) 562–571.
18. **Davydov V. V., Dudkin V. I., Velichko E. N., Karseev A. Y.**, A Remote Nuclear-Resonance Magnetometer for Measuring Intense Nonuniform Fields, *Measurement Techniques*. 58 (5) (2015) 556–561.
19. **Davydov V. V., Dudkin V. I., Karseev A. Y.**, A two-channel nutation nuclear-magnetic magnetometer for remote control of the magnetic-field induction, *Instruments and Experimental Techniques*. 58 (6) (2015) 787–793.
20. **Hobbs P.**, Photodiode Monitoring with Op Amps, *Components & Technologies*, 3 (2009) 48–49.
21. **Salakhov R. F., Miskov D. N.**, Techniques for measuring the current in modern microelectronics, *Tests. Quality control and management*, 3 (2015) 9–62.
22. **Wenn D.**, Resistive current measurement methods for precise control in electronic circuits, *Components and technology*, 7 (2011) 156–158.
23. **Sakharov K. Y., Turkin V. A., Mikheev O. V., Sukhov A. V., Ugolev V. L., Denisov M. Y.**, Pulse measuring instruments electromagnetic fields and currents, *EMC Technologies*, 1 (72) (2020) 63–70.

#### THE AUTHORS

**MIKHAILOVA Olesya M.**  
mihajlova.oa@edu.spbstu.ru  
ORCID: 0000-0001-5925-1830

**PETROV Dmitriy G.**  
dimoon88@mail.ru  
ORCID: 0000-0002-7536-033X

**ANTIFEEV Ivan E.**  
antifeevie@bk.ru  
ORCID: 0000-0001-5546-7407

**DAVYDOV Roman V.**  
davydovroman@outlook.com  
ORCID: 0000-0003-1958-4221

*Received 15.08.2022. Approved after reviewing 19.08.2022. Accepted 05.09.2022.*

Conference materials

UDC 53

DOI: <https://doi.org/10.18721/JPM.153.220>

## Improving metrological characteristics of a frequency standard based on cesium atoms

K. G. Arinushkina<sup>1</sup>✉, A. P. Valov<sup>2</sup>, V. V. Davydov<sup>1, 2, 3</sup>

<sup>1</sup>Peter the Great Saint-Petersburg Polytechnic University, Saint Petersburg, Russia;

<sup>2</sup>The Bonch-Bruевич Saint Petersburg State University of Telecommunications, Saint Petersburg, Russia;

<sup>3</sup>All-Russian Research Institute of Phytopathology, Moscow Region, Russia

✉ k-arinushkina@mail.ru

**Abstract.** The necessity of constant modernization of quantum frequency standards (QFS) - atomic clocks, which are used in satellite navigation and telecommunication systems to solve new problems in terms of the speed of transmission of large amounts of information, etc., is substantiated. It is noted that among all atomic clocks, cesium QFSs occupy a special place. These standards are the primary frequency reference upon which the international time scale is based. The main goal of all QFS upgrades is to improve the metrological characteristics. In the case of its use on moving objects, its dimensions, weight and power consumption also become important characteristics. The article presents one of the options for reducing the influence of negative factors on the stability of the QFS. The problem of modernizing the cesium frequency standard by including a device for monitoring and stabilizing the temperature regime of its operation is considered.

**Keywords:** time scale, stabilization, automatic frequency control, frequency stabilizer, cesium frequency standard, operational amplifier, atomic beam tube

**Citation:** Arinushkina K. G., Valov A. P., Davydov V. V., Improving metrological characteristics of a frequency standard based on cesium atoms, St. Petersburg State Polytechnical University Journal. Physics and Mathematics. 15 (3.2) (2022) 107–112. DOI: <https://doi.org/10.18721/JPM.153.220>

This is an open access article under the CC BY-NC 4.0 license (<https://creativecommons.org/licenses/by-nc/4.0/>)

Материалы конференции

УДК 53

DOI: <https://doi.org/10.18721/JPM.153.220>

## Улучшение метрологических характеристик стандарта частоты на атомах цезия

К.Г. Аринушкина<sup>1</sup>✉, А.П. Валов<sup>2</sup>, В.В. Давыдов<sup>1, 2, 3</sup>

<sup>1</sup>Санкт-Петербургский Политехнический университет Петра Великого

Санкт-Петербург, Россия;

<sup>2</sup>Санкт-Петербургский государственный университет телекоммуникаций

им. проф. М. А. Бонч-Бруевича, Санкт-Петербург, Россия;

<sup>3</sup>Всероссийский научно-исследовательский институт фитопатологии, Московская область, Россия

✉ k-arinushkina@mail.ru

**Аннотация.** Обоснована необходимость постоянной модернизации квантовых стандартов частоты (КСЧ) — атомных часов, которые используются в спутниковых навигационных и телекоммуникационных системах. Основной целью всех модернизаций КСЧ является улучшение метрологических характеристик. В случае применения его на подвижных объектах, также важными характеристиками становятся его габариты, вес и энергопотребление. Представлен один из вариантов снижения влияния негативных факторов на стабильность работы КСЧ. Рассмотрена задача модернизации цезиевого стандарта частоты посредством включения в него устройства контроля и стабилизации температурного режима его функционирования.

**Ключевые слова:** шкала времени, стабилизация, автоматическая подстройка частоты, стабилизатор частоты, цезиевый стандарт частоты, операционный усилитель, атомно-лучевая трубка

**Ссылка при цитировании:** Аринушкина К. Г., Валов А. П., Давыдов В. В. Улучшение метрологических характеристик стандарта частоты на атомах // Научно-технические ведомости СПбГПУ. Физико-математические науки. 2022. Т. 15. № 3.2. С. 107–112. DOI: <https://doi.org/10.18721/JPM.153.220>

Статья открытого доступа, распространяемая по лицензии CC BY-NC 4.0 (<https://creativecommons.org/licenses/by-nc/4.0/>)

## Introduction

The contribution of methods for accurate measurements of frequency and time in the development of world science, technology, and economics is enormous [1–7]. As an example, we can cite global communication networks, satellite navigation systems (SNS), coordinated work using is impossible without stable frequency sources [7–13]. Frequency standards are used in GLONASS and GPS systems as synchronizing generators [7–9, 14–19]. The equipment is widely used in activities, various requirements for a high and stable frequency of master oscillators [1–7, 14–19, 20–27]. The implementation of available satellite navigation systems has a number of increased frequencies, which manifest themselves both with the observed environment and with the autonomy of the object itself. In spacecraft for remote sensing of the Earth, the quantum frequency standard plays a key role in the time scale for controlling the spacecraft and transmitting information to the ground [1–3, 7–10, 25–28].

One of the main factors affecting the accuracy is the system errors introduced by the equipment of the space complex. The errors associated with the operation of the onboard equipment of the satellite and the GNSS ground control complex are mainly due to the imperfection of the time-frequency and ephemeris support. (Satellite ephemeris - its predicted coordinates and motion parameters at a fixed point in time). Ephemeris-time support includes a set of hardware and software tools that measure the current parameters of the orbital motion of spacecraft, verify, correct and phasing onboard time scales, process measurement results and calculate ephemeris transmitted to consumers [25–29]. The accuracy of the GLONASS system at the moment is about 0.4 – 0.5 m. Such accuracy values for a number of areas are no longer enough. One way to improve the accuracy of geolocation is to improve the synchronization of the time scales of the satellites of the navigation system. So, if long-term instability of the master generators in the system is ensured at the level of  $3 \cdot 10^{-14}$ , then the error in matching satellite time scales will be 10 nanoseconds, which can reduce the geolocation error to 0.2 – 0.3 m. Therefore, the modernization of existing and the development of new highly stable sources of electromagnetic oscillations are one of the urgent tasks of improving the functional properties of geolocation satellite systems.

In this paper, we consider the problem of modernizing the cesium frequency standard by including in it a device for monitoring and stabilizing the temperature regime of its operation.

## Materials and Methods

The error in measuring the delays between the clock signals of spacecraft (SC) at the receiving point, which determines the accuracy of calculating the coordinates of the object, is determined by the error in the formation of time scales and the frequency stability of the reference oscillators (RO). An analysis of the requirements for the accuracy characteristics of the onboard synchronizing device shows that their implementation is possible only when quantum frequency standards are used as reference generators, operating in a continuous mode throughout the entire life of the spacecraft [1–3, 7–10, 25–30].

The highest frequency stability is achieved in quantum frequency standards, which operate on the basis of the phenomenon of selective (resonant) absorption and emission of electromagnetic field energy by quantum systems (atoms, molecules, ions). Depending on the quantum objects used, QFS are called atomic or molecular. Along with QFS, quartz standards are also used, the

oscillation frequency of which is determined by the natural frequency of the quartz resonator. The Cs-133 cesium frequency standard shown in Figure 1 is the primary frequency standard because the national time, frequency, and national time scale calibration schemes operate on the basis of the high-frequency energy transition in the Cs-133 atom.

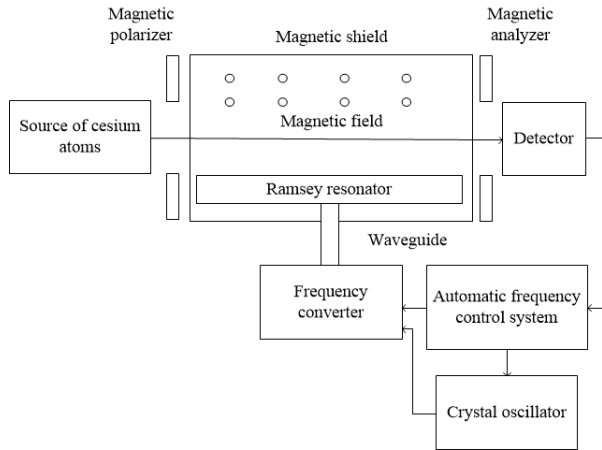


Fig. 1. The design of the cesium frequency standard

Required data for new applications  $AVAR < 1 \cdot 10^{-13}$  daily instability is not provided by the existing FS. To improve the characteristics of the FS, it is necessary to reduce the influence of a number of destabilizing factors, first of all, to reduce the instability of the magnetic field in the region of interaction between atoms and the electromagnetic field (long-term drift of the current source, its temperature dependence, the influence of an external magnetic field). This problem can be solved not only by creating new types of FSs, but also by modernizing existing ones. At the same time, a reduction in weight and dimensions, a reduction in energy consumption, and an improvement in their metrological characteristics can be achieved at the same time.

Traditionally, AFC circuits (Fig. 2) include a voltage-controlled oscillator, a frequency discriminator, and a reference signal source. In the AFC system of the quantum frequency standard (Fig. 4), the source of the reference signal is a quartz oscillator, and the control device acts as a frequency discriminator.

The signal from the ABT output is fed to the input of the automatic frequency control (AFC) system, which contains a matching amplifier (MA), a control device (CD), a crystal oscillator control device (CDXO) and a digital-to-analog converter (DAC).

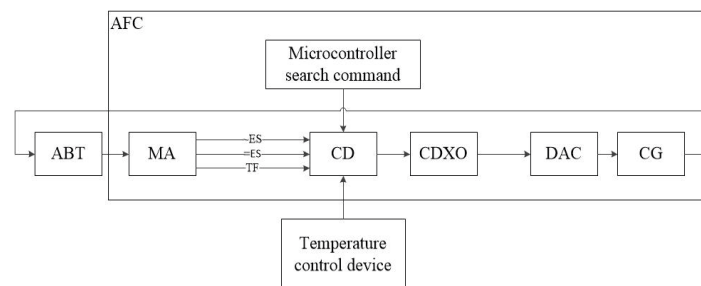


Fig. 2. Scheme of the AFC of the quantum frequency standard: ABT - atomic beam tube, MA - matching amplifier, CD - control device, QO - quartz oscillator, ES - error signal

The ABT output signal contains a constant component and a variable that characterizes the deviation of the signal from the average value of the ES components. This signal  $c$  with the help of a control device (CD) is converted into a control voltage supplied to the varicap fine-tuning the frequency of the CDXO. The AFC system generates a control voltage of magnitude and polarity, which allow compensating for the deviation of the actual frequency value (AFV) of the CG relative to the value corresponding to the frequency of the ABT atomic transition (5 MHz).

Preliminary setting of the CG frequency to the value at which the frequency of the microwave signal is close to the frequency of the atomic transition is carried out automatically.

The output voltage of the UUKG is supplied to the varicap of the CG frequency adjustment. Changing the voltage on the varicap CG leads to a change in the frequency of the CG and, consequently, to a change in the frequency of the microwave signal at the input of the ABT, which in turn leads to a change in the voltage at the output of the ABT in accordance with the resonance curve. The ambient temperature determines the voltage supplied to the control device in the automatic frequency control circuit (Fig. 2), and, consequently, the voltage supplied to the crystal oscillator. This leads to a mismatch between the frequencies of the microwave signal and

the atomic transition, which leads to errors in the matching of satellite time scales. Moreover, this process occurs regardless of whether the QFS uses highly stable laser radiation [38–42] or a magnetic field [43, 44] to create a population inversion in ABT.

### Results and Discussion

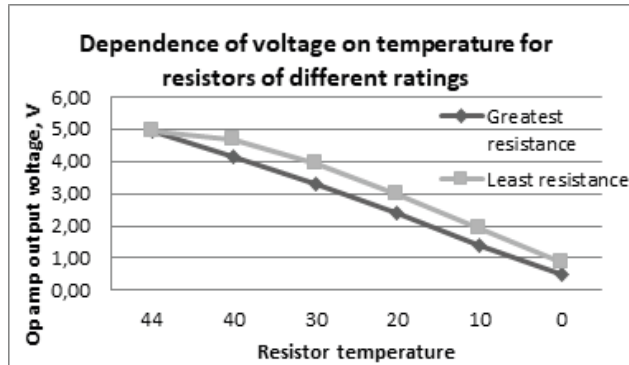


Fig. 3. Dependence of voltage on temperature for resistors of different ratings.

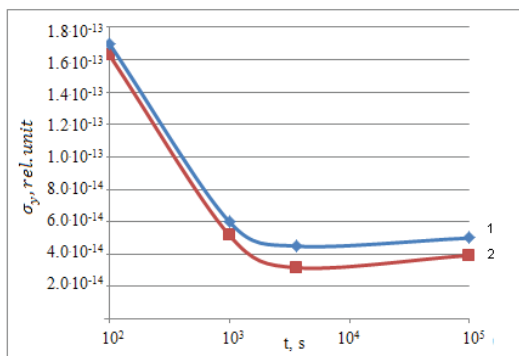


Fig. 4. Plot of the Allan variance  $\sigma_y$  versus time  $t$ . Graphs 1 and 2 correspond to the previously used AFC system in the QSC by us, respectively

The following principle is implemented in the system developed by us. The ambient temperature directly affects the resistance of the thermistor and the output signal of the operational amplifier (op-amp), which is located in the automatic frequency control system. Depending on the design of the resistor, there is a different change in voltage with temperature. This fact has not previously been given due attention. It was considered that dependence  $U(T)$  is linear. Our research has shown that this is not the case. On (Fig. 3) shows for example two dependencies for resistors of different ratings.

The result obtained shows that if the  $U(T)$  dependence becomes non-linear, an additional error appears. In the developed new AFC system, this error is eliminated. On (Fig. 4) shows the dependence of the change in the values of the Allan variance  $\sigma_{y(\tau)}$  on time  $\tau$  for the modernized and previous QFS designs.

The results obtained show an improvement in the Allan variance  $\sigma(\tau)$  by 5%. Studies of the operation of the QFS were carried out for 12 days in a temperature chamber. As a result of the research, it was found that the temperature coefficient of the frequency of the standard decreased by 1.35 times.

### Conclusion

The conducted experiments have shown the efficiency of using automatic frequency control systems with the thermal compensation device developed by us. As a result of using the device for compensating the temperature coefficient of frequency, the temperature sensitivity of the AFC system decreased by a factor of 1.3, which improves the synchronization of satellite time scales for spacecraft with Earth remote sensing systems.

### REFERENCES

1. Riehle F., Frequency standard. Basic and applications, WILEY-VCH Verlag GmbH Co. KGaA: New-York, 2008.
2. Almat N., Pellaton M., Moreno W., et al., Rb vapor-cell clock demonstration with a frequency-doubled telecom laser, Appl. Opt. 57 (2008) 4707.
3. Bandi T., Affolderbach C., Calosso C. E., et al., High-performance laser-pumped rubidium frequency standard for satellite navigation, Electron. Lett. 47 (2001) 698–699.
4. Myazin N. S., Dudkin V. I., Grebenikova N. M., Davydov R. V., Podstrigaev A. S., Fiber - optical system for governance and control of work for nuclear power stations of low power, Lecture Notes in Computer Science. 11660 (2019) 744–756.
5. Semenov V. V., Nikiforov N. F., Ermak S. V., Calculation of stationary magnetic resonance signal in optically oriented atoms induced by a sequence of radio pulses, Soviet journal of Communications



Technology and Electronics. 36 (4) (1991) 59–63.

6. **Davydov R., Antonov V., Moroz A.**, Parameter Control System for a Nuclear Power Plant Based on Fiber-Optic Sensors and Communication Lines, In: IEEE International Conference on Electrical Engineering and Photonics (EExPolytech), Saint-Petersburg, Russia, 13-15 October 2019. vol. 8906791 (2019) 295–297.

7. **Petrov A. A., Shabanov V. E., Zalyotov D. V., Bulyanitsa A. L., Shapovalov D. V.**, Modernization of the frequency synthesizer of cesium atomic clock, IEEE International Conference on Electrical Engineering and Photonics, EExPolytech 2018, Saint-Petersburg, October 2018. vol. 8564389 (2018) 52–55.

8. **Lukashev N. A., Davydov R. V., Glinushkin A. P., Rud' V. Y.**, Improving characteristics of microwave frequency standard on Hg-199 ions for telecommunication systems, Journal of Physics: Conference Series. 1326 (1) (2019) 012046.

9. **Lukashev N. A., Moroz A. V.**, Compact microwave frequency standard on Hg-199 ions for navigation systems, Journal of Physics: Conference Series. 1236 (1) (2019) 012068.

10. **Tarasov A. D., Milder O. B.**, Gradation trajectories as an analog of gradation curves in the metric cie lab space discrete approche, Computer Optics. 43 (1) (2018) 104–110.

11. **Kuzmin M. S., Rogov S. A.**, On the use of a multi-raster input of one-dimensional signals in two-dimensional optical correlators, Computer Optics. 43 (3) (2019) 391–396.

12. **Lukashev N. A., Petrov A. A., Grebenikova N. M.**, Improving performance of quantum frequency standard with laser pumping, Proceedings of 18th International conference of Laser Optics ICLO-2018 Saint-Petersburg, 2018, vol. 8435889, (2018) 271.

13. **Valov A. P., Arinushkina K. G., Davydov V. V.**, The use of digital data processing to improve the metrological characteristics of the rubidium frequency standard, Journal of Physics: Conference Series. 2086 (1) (2021) 012070.

14. **Arinushkina K. G., Valov A. P., Davydov V. V.**, Digital processing of optical signals in the frequency standard based in rubidium atoms - 87, In: Proceedings of ITNT 2021 - 7th IEEE International Conference on Information Technology and Nanotechnology, 2021 Samara, Russia, 20-24 September 2021. vol. 44026298 (2021) 44–49.

15. **Petrov A. A.**, Improvement frequency stability of caesium atomic clock for satellite communication system, Lecture Notes in Computer Science (including subseries Lecture Notes in Artificial Intelligence and Lecture Notes in Bioinformatics)/ 9247 (2015) 739–744.

16. **Lukashev N. A., Davydov V. V., Glinushkin A. P., Rud V. Yu., Lukyantsev V. S.**, Microwave low mass-dimensional frequency standard on Hg- 199 ions, Journal of Physics: Conference Series. 1410 (1) (2019) 012211.

17. **Petrov A. A., Grebenikova N. M.**, Some Directions of Quantum Frequency Standard Modernization for Telecommunication Systems, Lecture Notes in Computer Science (including subseries Lecture Notes in Artificial Intelligence and Lecture Notes in Bioinformatics). 11118 LNCS (2018) 641–648.

18. **Pashev G. P.**, Optimal algorithm for synchronizing the quantum clock timeline, Measurement Techniques. 59(6) (2016) 1005–1012.

19. **Grevtseva A., Rud V.**, Method of processing velocity increase of measuring results of quantum frequency standard parameters for information transfer velocity increase in satellite communication systems, CEUR Workshop Proceedings. 2667 (2020) 15–18.

20. **Mihov E. D., Nepomnyashchiy O. V.**, Selecting informative variables in the identification problem Journal of Siberian Federal University - Mathematics and Physics. 9 (4) (2016) 473–480.

21. **Ryzhenko I. N., Lutsenko A. E., Varygin O. G., Nepomnyashchiy O. V.**, Carrier compensation mode implementation in satellite communication channels. In: Proceedings of 2019 International Siberian Conference on Control and Communications, SIBCON 2019, vol. 8729665 (2019) 23–29.

22. **Fadeenko V. B., Pchelkin G. A., Davydov V. V., Rud V. Yu.**, Features of the transmission of microwave signals in the range of 8-12 GHz in the maritime radar station over fiber-optic communication line, Journal of Physics: Conference Series. 1400 (4) (2019) 044010.

23. **Petrov A. A., Vologdin V. A., Zalyotov D. V.**, Dependence of microwave – excitation signal parameters on frequency stability caesium atomic clock, Journal of Physics: Conference Series. 643 (1) (2015) 012087.

24. **Petrov A. A., Zalyotov D. V., Shabanov V. E., Shapovalov D. V.**, Features of direct digital synthesis applications for microwave excitation signal formation in quantum frequency standard on the

atoms of cesium, Journal Physics: Conference Series. 1124 (1) (2018) 041004.

25. **Grevtseva A. S., Dmitriev R. A.**, Features of the formation of the frequency of the microwave excitation signal in the quantum frequency standard on rubidium atoms – 87, Journal of Physics: Conference Series. 2086 (1) (2021) 012055.

26. **Petrov A. A.**, Digital Frequency Synthesizer for <sup>133</sup>Cs-Vapor Atomic Clock, Journal of Communications Technology and Electronics. 62(3) (2017) 289–293.

27. **Lukashev N. A., Rud V. Yu.**, Microwave frequency standard on Hg-199 ions for space stations and vehicles Journal of Physics: Conference Series. 1400 (2) (2019) 022050.

28. **Petrov A. A., Zaletov D. V., Shapovalov D. V.**, Peculiarities of Constructing a Scheme for Formation of a Microwave Excitation Signal in a Cesium Atomic Clock, Journal of Communications Technology and Electronics. 66(3) (2021) 295–299.

29. **Petrov A. A.**, New scheme of the microwave signal formation for quantum frequency standard on the atoms of caesium-133 Journal of Physics: Conference Series. 769 (1) (2016) 012065.

30. **Wang D., Davydov, V. V., Rud V. Y.** Prospective directions for the development of microwave frequency standards for satellite navigation systems Journal of Physics: Conference Series. 2086 (1) (2021) 012073.

### THE AUTHORS

**ARINUSHKINA Kseniya G.**

k-arinushkina@mail.ru

ORCID: 0000-0002-1156-2071

**VALOV Anton P.**

tony.valov2015@yandex.ru

ORCID: 0000-0001-9276-1736

**DAVYDOV Vadim V.**

davydov\_vadim66@mail.ru

ORCID: 0000-0001-9530-4805

*Received 12.07.2022. Approved after reviewing 21.07.2022. Accepted 12.09.2022.*

Conference materials

UDC 535.015

DOI: <https://doi.org/10.18721/JPM.153.221>

## Phase-change periodic surface structures for engineering of excitonic photoluminescence in $WS_2$ monolayers

P. I. Trofimov<sup>1</sup>✉, T. Ivanova<sup>1</sup>, P. I. Lazarenko<sup>2</sup>, M. Fedyanina<sup>2</sup>, I. S. Sinev<sup>1</sup>

<sup>1</sup> Department of Physics and Engineering, ITMO University, St. Petersburg, Russia;

<sup>2</sup> National Research University of Electronic Technology, Zelenograd, Moscow, Russia

✉ p.trofimov@metalab.ifmo.ru

**Abstract.** Due to their two-dimensional nature, transition metal dichalcogenide monolayers exhibit extremely strong sensitivity of their excitonic response to the permittivity of the surrounding medium. Here, we show that the intensity and wavelength of their excitonic photoluminescence can be spatially modulated by periodic structures induced by laser pulses in phase change material films.

**Keywords:** phase change materials,  $Ge_2Sb_2Te_5$ , transition metal dichalcogenides,  $WS_2$ , laser induced periodic surface structures, phase change gratings, exciton screening

**Funding:** The reported study was funded by RFBR according to the research project № 20-32-90220.

**Citation:** Trofimov P. I., Ivanova T. V., Lazarenko P. I., Fedyanina M. E., Sinev I. S., Phase-change periodic surface structures for engineering of excitonic photoluminescence in  $WS_2$  monolayers, St. Petersburg State Polytechnical University Journal. Physics and Mathematics. 15 (3.2) (2022) 113–117. DOI: <https://doi.org/10.18721/JPM.153.221>

This is an open access article under the CC BY-NC 4.0 license (<https://creativecommons.org/licenses/by-nc/4.0/>)

Материалы конференции

УДК 535.015

DOI: <https://doi.org/10.18721/JPM.153.221>

## Индукцированные лазером периодические поверхностные структуры с модуляцией фазового состояния для управления экситонной фотолюминесценцией монослоев $WS_2$

П. И. Трофимов<sup>1</sup>✉, Т. Иванова<sup>1</sup>, П. И. Лазаренко<sup>2</sup>,

М. Е. Федянина<sup>2</sup>, И. С. Синева<sup>1</sup>

<sup>1</sup> Физико-технический факультет, Университет ИТМО, Санкт-Петербург, Россия;

<sup>2</sup> Московский институт электронной техники, Зеленоград, Москва, Россия

✉ p.trofimov@metalab.ifmo.ru

**Аннотация.** Из-за своей двумерной природы монослои дихалькогенидов переходных металлов проявляют чрезвычайно сильную чувствительность своего экситонного отклика к диэлектрической проницаемости окружающей среды. В данной работе мы показываем, что интенсивность и длина волны их экситонной фотолюминесценции могут быть пространственно модулированы периодическими структурами, индуцированными лазерными импульсами в пленках материалов с фазовой памятью.

**Ключевые слова:** материалы с фазовой памятью,  $Ge_2Sb_2Te_5$ , дихалькогениды переходных металлов,  $WS_2$ , индуцированные лазером периодические поверхностные структуры, экранирование экситона

**Финансирование:** Исследование выполнено при финансовой поддержке РФФИ в рамках научного проекта № 20-32-90220.

**Ссылка при цитировании:** Трофимов П. И., Иванова Т. В., Лазаренко П. И., Федянина М.

Е., Синев И. С. Индуцированные лазером периодические поверхностные структуры с модуляцией фазового состояния для управления экситонной фотолюминесценцией монослоев  $WS_2$  // Научно-технические ведомости СПбГПУ. Физико-математические науки. 2022. Т. 15. № 3.2. С. 113–117. DOI: <https://doi.org/10.18721/JPM.153.221>

Статья открытого доступа, распространяемая по лицензии CC BY-NC 4.0 (<https://creativecommons.org/licenses/by-nc/4.0/>)

### Introduction

Two-dimensional transition metal dichalcogenides (TMDC) have attracted a lot of attention in photonics due to their strong excitonic effects, flexibility and tunability. Large exciton binding energy, and high quantum yield found in such materials already established them as a strong candidates for polaritonics, lasing and engineering of single photon emitters [1]. Moreover, the optical response of such systems can be manipulated using various methods such as gate voltage, doping, magnetic field and nonlinear effect which can influence the coupling constants in polariton systems, shift the wavelength of single photon emitters or control the handedness of circularly polarized light emission.

Another way to control the exciton binding energy in TMDC is to tune its dielectric environment, in particular static dielectric constant of the surrounding media which affects the exciton screening. Tuning of refractive index has already been implemented using various methods, such as chemical doping, optical pumping of free carriers in material, electrical or thermal switching of liquid crystals or  $VO_2$  based nanostructures [2]. From this standpoint, the phase switching between crystalline and amorphous phase of chalcogenide phase-change materials (PCM) might be a promising technique, as it provides tuning of both refractive index at optical frequencies and static dielectric permittivity [3]. Heating and subsequent melt-quenching of these materials induced by optical or electrical pulses results in rapid nanosecond-scale reversible switching between its phase states [4]. Furthermore, it was recently shown that the irradiation of PCM thin films with femtosecond laser pulses results in the formation of periodic modulation of the phase state of the film with period and direction defined by wavelength and polarization of the laser radiation [5]. The mechanism of their formation is well described within the concept of laser-induced periodic surface structures (LIPSS) [6].

In this work we studied how phase-change LIPSS formed in  $Ge_2Sb_2Te_5$  (GST) thin films and covered by a  $WS_2$  monolayer affect the optical properties of the latter, in particular the wavelength and the intensity of its excitonic photoluminescence.

### Results and Discussion

First we fabricated  $WS_2$ -GST heterostructures, the details of fabrication could be found in “Experiment Details” section. After that we studied the fabricated heterostructures with optical microscopy which allowed us to observe the reflection image of the sample, as well as the integrated photoluminescence (PL) signal, which was excited with UV range lamp and detected using a longpass filter. In the reflection image of the imprinted GST grating, one can observe the periodic modulation of the refractive index in the visible spectral range (Fig. 1, *a*). Such modulation confirms the formation of the periodic structures of different phase in GST film. In the image of the integral PL from the  $WS_2$  monolayer (Fig. 1, *b*) we observed the suppression of the PL signal in the areas of monolayer above the crystalline GST lines of the grating compared with high PL signal above amorphous ones. We interpret such modulation as the result of enhanced exciton screening in  $WS_2$  monolayer due to higher static dielectric permittivity of the crystalline GST [8], which in turn promotes the PL signal suppression.

To explore in more detail the impact of GST phase state on the  $WS_2$  monolayer optical response we mapped the photoluminescence spectra of the fabricated samples at room and cryogenic temperatures (see for the details of the mapping in Experimental section). The obtained spectra of the monolayer are shown in Figure 1, *c*. We observed the 616 nm exciton peak at 295 K (blue curve) and 593 nm at 6.3 K (red curve). To study how the modulation of the dielectric permittivity induced with GST phase grating affects the position and intensity of the PL signal we

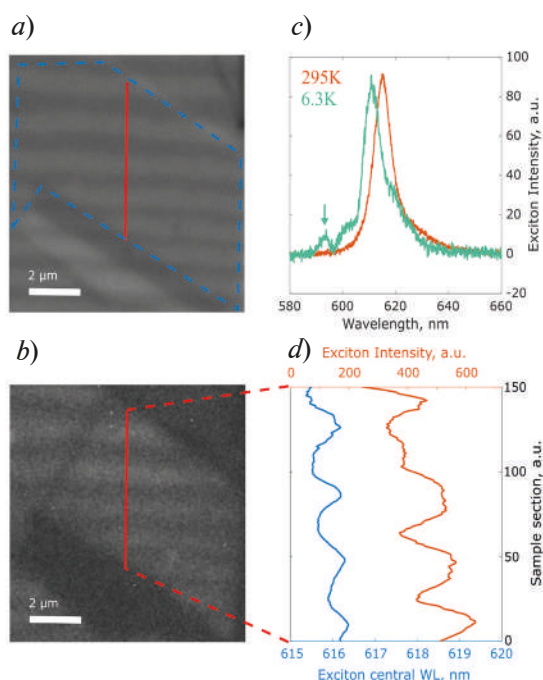


Fig. 1. Reflection (a) and integral photoluminescence from  $\text{WS}_2$  monolayer on a phase-change GST grating (b). Blue dashed line in denotes the area of the grating covered with transferred  $\text{WS}_2$  monolayer (a). Photoluminescence spectra of the  $\text{WS}_2$  monolayer at 295K (red) and 6.3K (green). Green arrow indicates the exciton peak at 6.3K (c). Spectral position (blue) and intensity of the exciton (orange) along its section (red line on (a, b)) at 295K (d)

simultaneously excited a large area of the monolayer. After that, using Lorentz fitting of the measured data, we extracted the peak position and intensity of the measured PL signal along a section perpendicular to the grating lines. We observed the suppression of the intensity and an approximately 0.5 nm blue shift of the PL signal above the crystalline lines (Fig. 1, d). Such a small change in the exciton spectral position despite the strong exciton intensity modulation is a result of two counteracting effects: renormalization of the band gap of the  $\text{WS}_2$  monolayer and a change in the exciton binding energy. We were unable to observe such modulation at cryogenic temperatures due to large aberrations of the optical setup which significantly lowered the spatial resolution of our system.

Finally, to complete the concept of manipulation of the excitonic response of the GST- $\text{WS}_2$  heterostructure, we studied the reversible switching of PL signal of the monolayer transferred onto a non-patterned as-deposited GST film (Fig. 2). During the experiment we switched GST film under the  $\text{WS}_2$  monolayer into crystalline state using CW 633 nm laser and observed the suppression of the PL signal (Fig. 2, b) along the whole structure in agreement with our previous results for GST phase grating. After that, we restored the initial

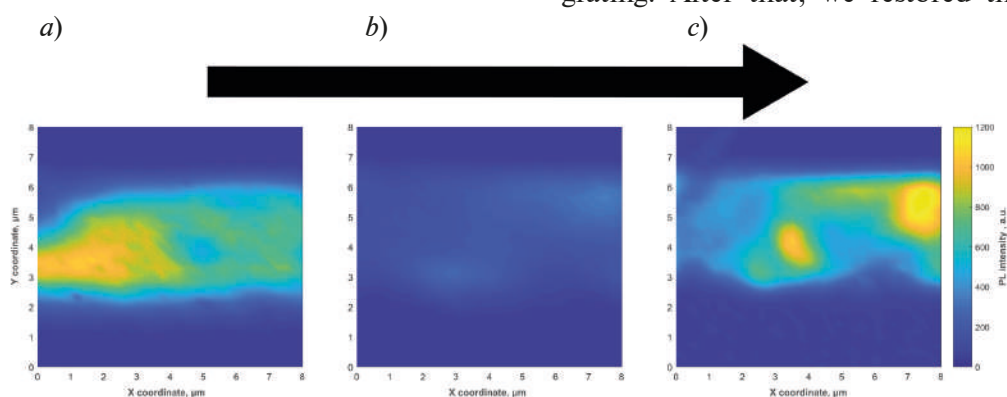


Fig. 2. Photoluminescence maps of the  $\text{WS}_2$  monolayer on GST film cycled through different phase states: as deposited amorphous state (a); crystalline state (b); reamorphized state (c)

amorphous state of the GST film using single femtosecond laser pulses (1047 nm, 20 Hz, 150 fs) which resulted in partial restoration of the exciton signal intensity (Fig. 2, c). The heterogeneity of PL signal observed during the experiment could be caused by increase of roughness of the GST film during its phase transformation which in turn resulted in different level of adhesion and local stress of the monolayer that significantly affected its photoluminescence intensity.

### Experiment Details

We fabricated WS<sub>2</sub>-GST LIPSS heterostructure in three steps. First, we deposited 50 nm film of Ge<sub>2</sub>Sb<sub>2</sub>Te<sub>5</sub> (GST) phase change material on a W substrate using magnetron sputtering. After that we irradiated the sample with femtosecond laser pulses (80 MHz, 290 fs, 700–2000 nm) while scanning it through the laser beam waist at a speed of 10–100 μm/s. This process resulted in the formation of periodic surface structures of the amorphous and crystalline GST phases, as described in our previous work [7]. Finally, we exfoliated the high quality monolayer flakes of WS<sub>2</sub> material from commercial bulk crystals and dry-transferred them onto the patterned GST film using scotch and custom-built transfer system.

To obtain maps of photoluminescence spectra of the fabricated samples at room and cryogenic temperatures we used CW laser source with 532 nm wavelength (Torus). The laser was focused onto the back focal plane of the objective to simultaneously excite a large area of the sample. To study the optical properties at cryogenic temperatures the sample was placed into the cell of a closed-cycle He cryostat which maintained a temperature of 6.3 K. The excited photoluminescence was collected with a high numerical aperture objective and focused with a large focal length lens onto the entrance slit of the spectrometer (Princeton Instruments) with a liquid nitrogen cooled CCD camera.

### Conclusion

To conclude, we studied the optical properties of the WS<sub>2</sub>-GST heterostructure. We showed that the photoluminescence response of the WS<sub>2</sub> monolayer, in particular, the spectral position and intensity of the excitonic PL peak can be modulated using LIPSS imprinted in the underlying GST film. We also demonstrated that cycling between crystalline and amorphous phase state of GST film covered with WS<sub>2</sub> monolayer results in suppression and partial restoration of its PL signal. These results shows great potential of phase-change LIPSS – TMD platform for dynamic control the excitonic response, utilizing the process of fast and reversible switching between GST phase states.

### Acknowledgments

The reported study was funded by RFBR according to the research project № 20-32-90220.

### REFERENCES

1. **Mak K. F., Shan J.**, Photonics and optoelectronics of 2D semiconductor transition metal dichalcogenides, *Nature Photonics* 2016, 10, 216–226.
2. **Cui et al.**, Tunable Metasurfaces Based on Active Materials, *Adv. Funct. Mater.* 2019, 29, 1806692.
3. **Wuttig M., Taubner T.**, Phase-change materials for non-volatile photonic applications, *Nature Photonics* 2017, 11, 465–476.
4. **Au Y-Y et al.**, Phase-change devices for simultaneous optical-electrical applications, *Sci. Rep.* 2017, 7, 9688.
5. **Kozyukhin S. et al.**, Specific Features of Formation of Laser-Induced Periodic Surface Structures on Ge<sub>2</sub>Sb<sub>2</sub>Te<sub>5</sub> Amorphous Thin Films under Illumination by Femtosecond Laser Pulses, *Phys. Status Solidi B* 2020, 257, 1900617.
6. **Bonse J., Gräf S.**, Maxwell Meets Marangoni—A Review of Theories on Laser-Induced Periodic Surface Structures, *Laser Photon. Rev.* 2020, 14, 10, 2000215.
7. **Trofimov P. et al.**, Rewritable and Tunable Laser-Induced Optical Gratings in Phase-Change Material Films, *ACS Appl. Mater. Interfaces* 2021, 13, 27, 32031–32036.
8. **Wuttig M., Yamada N.**, Phase-change materials for rewriteable data storage, *Nature Mater.* 2007, 6, 824–832.

### THE AUTHORS

**TROFIMOV Pavel I.**  
p.trofimov@metalab.ifmo.ru  
ORCID: 0000-0002-6426-2670

**IVANOVA Tatyana V.**  
tatyana.ivanova@metalab.ifmo.ru  
ORCID: 0000-0003-3320-9727



**LAZARENKO Petr I.**  
aka.jum@gmail.com  
ORCID: 0000-0003-4309-3481

**SINEV Ivan S.**  
i.sinev@metalab.ifmo.ru  
ORCID: 0000-0002-4246-7747

**FEDYANINA Maria E.**  
mfh.miet@gmail.com  
ORCID: 0000-0001-9779-2574

*Received 14.08.2022. Approved after reviewing 09.09.2022. Accepted 12.09.2022.*

Conference materials

UDC 535.8

DOI: <https://doi.org/10.18721/JPM.153.222>

## Research on the character of laser radiation propagation in a differential Anderson cuvette

A. A. Goldberg<sup>1</sup> ✉, I. D. Kochetkov<sup>1</sup>, V. V. Davydov<sup>1, 2, 3</sup>

<sup>1</sup>Peter the Great Saint-Petersburg Polytechnic University, Saint Petersburg, Russia;

<sup>2</sup>The Bonch-Bruевич Saint Petersburg State University of Telecommunications, Saint Petersburg, Russia;

<sup>3</sup>All-Russian Research Institute of Phytopathology, Moscow Region, Russia

✉ [artemiy.goldberg@mail.ru](mailto:artemiy.goldberg@mail.ru)

**Abstract.** The necessity of studying the nature of the propagation of laser radiation in the Anderson differential cuvette is substantiated in order to determine the optimal design parameters of a small-sized differential type refractometer. The construction of the Anderson differential cuvette is considered. A new method for studying the nature of the propagation of laser radiation in the differential Anderson cuvette is proposed. The trajectory of movement of the maximum of the laser radiation directive pattern in the cuvette, as well as beyond it (up to the sensor of the photodiode ruler on which the registration takes place) is plotted. An equation is obtained to study the changes in the nature of the propagation of laser radiation from various parameters of the differential cuvette, the reference liquid medium and the investigated liquid medium. A polynomial of the 12th degree is formed to obtain an analytical solution of the equation from the refractive index of the investigated medium.

**Keywords:** laser radiation, refraction, liquid, refractive index, Anderson's cuvette, refraction, displacement, polynomial

**Citation:** Goldberg A. A., Kochetkov I. D., Davydov V. V., Research on the character of laser radiation propagation in a differential Anderson cuvette, St. Petersburg State Polytechnical University Journal. Physics and Mathematics. 15 (3.2) (2022) 118–123. DOI: <https://doi.org/10.18721/JPM.153.222>

This is an open access article under the CC BY-NC 4.0 license (<https://creativecommons.org/licenses/by-nc/4.0/>)

Материалы конференции

УДК 535.8

DOI: <https://doi.org/10.18721/JPM.153.222>

## Исследование характера распространения лазерного излучения в дифференциальной кювете Андерсона

А. А. Гольдберг<sup>1</sup> ✉, И. Д. Кочетков<sup>1</sup>, В. В. Давыдов<sup>1, 2, 3</sup>

<sup>1</sup> Санкт-Петербургский Политехнический университет Петра Великого, Санкт-Петербург, Россия;

<sup>2</sup> Санкт-Петербургский государственный университет телекоммуникаций им. профессора М.А. Бонч-Бруевича, Санкт-Петербург, Россия;

<sup>3</sup> Всероссийский научно-исследовательский институт фитопатологии, Московская область, Россия

✉ [artemiy.goldberg@mail.ru](mailto:artemiy.goldberg@mail.ru)

**Аннотация.** Обоснована необходимость исследования характера распространения лазерного излучения в дифференциальной кювете Андерсона для определения оптимальных параметров конструкции малогабаритного рефрактометра дифференциального типа. Рассмотрена конструкция дифференциальной кюветы Андерсона. Предложена новая методика исследования характера распространения лазерного излучения в дифференциальной кювете Андерсона. Построена траектория движения максимума диаграммы направленности лазерного излучения в кювете, а также за её пределами (до сенсора фотодиодной линейки, на котором происходит регистрация). Получено уравнение для исследования изменения характера распространения лазерного излучения от различных параметров дифференциальной кюветы, эталонной и исследуемой жидкой



среды. Сформирован полином 12-й степени для получения аналитического решения уравнения относительно показателя преломления исследуемой среды.

**Ключевые слова:** лазерное излучение, рефракция, жидкость, показатель преломления, кювета Андерсона, преломление, смещение, полином

**Ссылка при цитировании:** Гольдберг А. А., Кочетков И. Д., Давыдов В. В. Исследование характера распространения лазерного излучения в дифференциальной кювете Андерсона // Научно-технические ведомости СПбГПУ. Физико-математические науки. 2022. Т. 15. № 3.2. С. 118–123. DOI: <https://doi.org/10.18721/JPM.153.222>

Статья открытого доступа, распространяемая по лицензии CC BY-NC 4.0 (<https://creativecommons.org/licenses/by-nc/4.0/>)

## Introduction

Reliable express control is becoming an important element in scientific research, industrial production and environmental monitoring [1–7]. The use of express control is necessary to obtain reliable information about the state of the environment at the sampling site in order to make an adequate decision [2, 8–11]. In addition, it is necessary to obtain further confirmation of the detected deviation in the sample on high-resolution devices [10–12]. In this case, the measurements carried out in express mode should not make irreversible changes to the sample of the medium, which will change its composition and physical structure [2, 11–15]. Taking into account these conditions, the number of methods and devices for express control is limited [1, 2, 6, 10–12, 16–18]. One of the devices that allows express control of the state of liquid medium with high precision at the sampling site is a refractometer.

High requirements for conducting experiments, the manufacture of complex mediums, for example, medical suspensions or medicaments for injection into veins, requires measurements of the refractive index  $n_m$  of a liquid medium with high precision over a large range of values [17–25]. A differential refractometer based on an Anderson cuvette, for measurements in which a reference liquid is used, is one of the possible solutions of these express control problems. The problem of measuring  $n_m$  with an error of 0.0001 over a large range of values is related to the lack of relations between different parameters in the design of the refractometer and the Anderson cuvette. This significantly limits the use of this type of refractometer.

### Anderson cuvette design and profile of laser radiation propagation

In the constructions of modern differential refractometers, three types of Anderson cuvettes

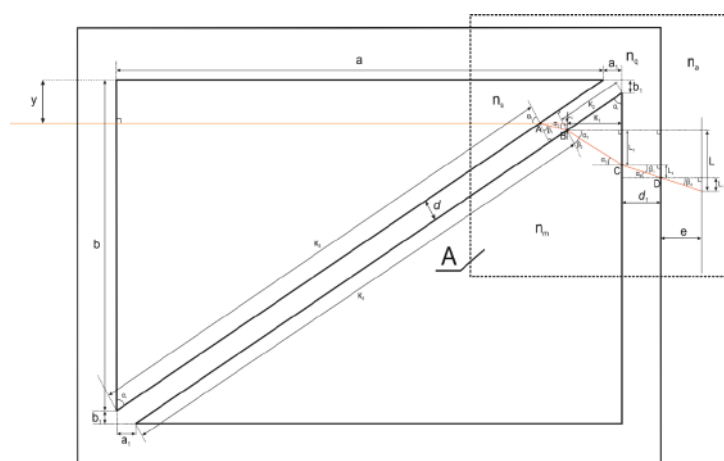


Fig. 1. Anderson cuvette and laser radiation propagation. Fragment A denotes the area for which the equation is derived to determine  $n_m$

(in the form of a square and two types in the form of a rectangle), which are made of quartz glass, are mainly used for measurements. On figure 1 is shown the propagation of laser radiation in the Anderson cuvette and after exiting it to the sensor of the photodiode ruler (the sensor is located at a distance  $e$  from the wall of the cuvette). The use of a photodiode ruler for registering laser radiation in refractometers is currently the most optimal solution [18–25].

In the construction of the differential refractometer designed by us, in contrast to those that were used earlier, it is proposed to use the measured value  $L$  (by shifting the maximum of laser radiation on the

photodiode ruler from the entry point  $y$  on the lateral surface of the Anderson cuvette of laser radiation) to determine the  $n_m$  value. The measurement error of  $\delta n_m$  in this case will be determined by ensuring that the maximum of laser radiation is registered on one photosensitive sensor. To determine the minimum value  $\delta n_m$ , it is necessary to establish the dependence between the change in the value  $L$  on the photodiode ruler on the parameters of the Anderson cuvette, the distance  $e$ , and the values  $n_m$  and  $n_s$ .

**The equation for research of laser radiation direction change in the time it dissemination in optical part of refractometer and ratio control**

To derive the equation and then verify the mathematical relations at the control points, the description of the nature of the change in the displacement of laser radiation on the photodiode ruler was divided into 4 parts:  $L_1, L_2, L_3$  and  $L_4$  (fragment A, Fig. 1).

For laser radiation in the considered fragment A (Fig. 1), the following relations were written down:

$$A: \frac{\sin \alpha_1}{\sin \beta_1} = \frac{n_q}{n_s}; B: \frac{\sin \alpha_2}{\sin \beta_2} = \frac{n_m}{n_q}; C: \frac{\sin \alpha_3}{\sin \beta_3} = \frac{n_q}{n_m}; D: \frac{\sin \alpha_4}{\sin \beta_4} = \frac{n_a}{n_q};$$

$$\alpha_1 = \alpha_3 + \beta_2, L_1 = e \operatorname{tg} \beta_4, L_2 = d_1 \operatorname{tg} \beta_3, L_3 = K_1 \operatorname{tg} \alpha_3, K_1 = (y - b_1 + L_4) \operatorname{tg} \alpha_1, \operatorname{tg} \alpha_1 = \frac{a}{b},$$

$$L_4 = |AB| \cdot \sin(\alpha_1 - \beta_1) = \frac{d}{\cos \beta_1} \sin(\alpha_1 - \beta_1) = d(\sin \alpha_1 - \cos \alpha_1 \operatorname{tg} \beta_1).$$

These relations allow us to express the values of  $L_1, L_2, L_3$  and  $L_4$  in terms of the parameters of the Anderson cuvette, the distance  $e$ , and also the values of the refractive indexes of the reference liquid  $n_s$  and the investigated liquid medium  $n_m$ .

$$L_4 = d \sin \alpha_1 \left( 1 - \frac{n_s \cos \alpha_1}{\sqrt{n_q^2 - n_s^2 \sin^2 \alpha_1}} \right), \operatorname{tg} \alpha_3 = \operatorname{tg}(\alpha_1 - \beta_2) = \frac{\operatorname{tg} \alpha_1 - \operatorname{tg} \beta_2}{1 + \operatorname{tg} \alpha_1 \operatorname{tg} \beta_2},$$

$$\frac{L_3}{K_1} = \operatorname{tg} \alpha_3 = \frac{\operatorname{tg} \alpha_1 - \frac{n_s \sin \alpha_1}{\sqrt{n_m^2 - n_s^2 \sin^2 \alpha_1}}}{1 + \operatorname{tg} \alpha_1 \frac{n_s \sin \alpha_1}{\sqrt{n_m^2 - n_s^2 \sin^2 \alpha_1}}} = \frac{\sin \alpha_1 \sqrt{n_m^2 - n_s^2 \sin^2 \alpha_1} - n_s \sin \alpha_1 \cos \alpha_1}{\cos \alpha_1 \sqrt{n_m^2 - n_s^2 \sin^2 \alpha_1} + n_s \sin^2 \alpha_1},$$

$$\begin{aligned} \sin \alpha_3 &= \sin(\alpha_1 - \beta_2) = \sin \alpha_1 \cos \beta_2 - \sin \beta_2 \cos \alpha_1 = \\ &= \sin \alpha_1 \sqrt{1 - \frac{n_s^2}{n_m^2} \sin^2 \alpha_1} - \frac{n_s}{n_m} \sin \alpha_1 \cos \alpha_1 = \frac{\sin \alpha_1}{n_m} \left( \sqrt{n_m^2 - n_s^2 \sin^2 \alpha_1} - n_s \cos \alpha_1 \right), \end{aligned}$$

$$\operatorname{tg} \beta_3 = \frac{L_2}{d_1} = \frac{\sin \alpha_1 \left( \sqrt{n_m^2 - n_s^2 \sin^2 \alpha_1} - n_s \cos \alpha_1 \right)}{\sqrt{n_q^2 - \sin^2 \alpha_1} \left( n_m^2 + n_s^2 \cos^2 \alpha_1 - n_s^2 \sin^2 \alpha_1 - 2n_s \cos \alpha_1 \sqrt{n_m^2 - n_s^2 \sin^2 \alpha_1} \right)},$$

$$\begin{aligned} L_1 = e \operatorname{tg} \beta_4; \frac{L_1}{e} = \operatorname{tg} \beta_4 &= \frac{\frac{\sin \alpha_1}{n_a} \left( \sqrt{n_m^2 - n_s^2 \sin^2 \alpha_1} - n_s \cos \alpha_1 \right)}{\sqrt{1 - \left( \frac{\sin \alpha_1}{n_a} \left( \sqrt{n_m^2 - n_s^2 \sin^2 \alpha_1} - n_s \cos \alpha_1 \right) \right)^2}} = \\ &= \frac{\sin \alpha_1 \left( \sqrt{n_m^2 - n_s^2 \sin^2 \alpha_1} - n_s \cos \alpha_1 \right)}{\sqrt{n_a^2 - \sin^2 \alpha_1} \left( n_m^2 - n_s^2 \sin^2 \alpha_1 + n_s^2 \cos^2 \alpha_1 - 2n_s \cos \alpha_1 \sqrt{n_m^2 - n_s^2 \sin^2 \alpha_1} \right)}. \end{aligned}$$

This allowed us to obtain the following equation for  $L$ :

$$L = L_1 + L_2 + L_3 + L_4 = \sin \alpha_1 \left( d \left( 1 - \frac{n_s \cos \alpha_1}{\sqrt{n_q^2 - n_s^2 \sin^2 \alpha_1}} \right) + \left( \sqrt{n_m^2 - n_s^2 \sin^2 \alpha_1} - n_s \cos \alpha_1 \right) \cdot \left( \frac{e}{\sqrt{n_a^2 - \sin^2 \alpha_1 (n_m^2 - n_s^2 \sin^2 \alpha_1 + n_s^2 \cos^2 \alpha_1 - 2n_s \cos \alpha_1 \sqrt{n_m^2 - n_s^2 \sin^2 \alpha_1})}} + \frac{d_1}{\sqrt{n_q^2 - \sin^2 \alpha_1 (n_m^2 + n_s^2 \cos^2 \alpha_1 - n_s^2 \sin^2 \alpha_1 - 2n_s \cos \alpha_1 \sqrt{n_m^2 - n_s^2 \sin^2 \alpha_1})}} + \frac{K_1}{\cos \alpha_1 \sqrt{n_m^2 - n_s^2 \sin^2 \alpha_1} + n_s \sin^2 \alpha_1} \right) \right). \quad (1)$$

A control check was performed for the obtained equation (1). The refractometers use laser radiation with  $\lambda = 632.8$  nm. For  $\lambda = 632.8$  nm, the value of  $n_q = 1.537826$ ,  $n_a = n_{air} = 1.000273$ ,  $d = 0.5$  mm,  $d_1 = 1$  mm,  $e = 20$  mm,  $y = 4$  mm. The test results are presented in table 1.

Table 1

**Calculation results of beam offset distance  $L$**

$n_s$ and $n_m$ values ( $n_s = n_m$ )	Cuvette (size 50 mm × 50 mm)
$n_{air} = 1.000273$	$L = 0.171129$
$n_{water} = 1.327412$	$L = 0.082450$
$n_{ethanol} = 1.361513$	$L = 0.071131$
$n_{petrol} = 1.437762$	$L = 0.043715$

Notations:  $L$  – displacement of the laser radiation after leaving the cuvette,  $n_s$  – refractive index of the reference liquid,  $n_m$  – refractive index of the investigated liquid.

To derive the analytical equation  $n_m$  ( $d$ ,  $L$ ,  $n_s$ ,  $e$ ,  $K_1$ ,  $d_1$ ,  $n_q$ ,  $\alpha_1$ ), the following notation is introduced:

$$\frac{L_4}{\sin \alpha_1} = d \left( 1 - \frac{n_s \cos \alpha_1}{\sqrt{n_q^2 - n_s^2 \sin^2 \alpha_1}} \right) = L'_4, \quad \frac{L}{\sin \alpha_1} - L'_4 = \frac{L - L_4}{\sin \alpha_1} = A,$$

$$\sqrt{n_m^2 - n_s^2 \sin^2 \alpha_1} - n_s \cos \alpha_1 = f_1; \quad f_2 = f_1 \sin \alpha_1,$$

$$A = f_1 \left( \frac{e}{\sqrt{n_a^2 - f_2^2}} + \frac{d_1}{\sqrt{n_q^2 - f_2^2}} + \frac{K_1}{\cos \alpha_1 (f_1 + n_s \cos \alpha_1) + n_s \sin^2 \alpha_1} \right).$$

In this case equation (1) is reduced to the following form.

$$\frac{A \sin \alpha_1}{f_2} = \frac{e}{\sqrt{n_a^2 - f_2^2}} + \frac{d_1}{\sqrt{n_q^2 - f_2^2}} + \frac{K_1}{f_2 \operatorname{tg} \alpha_1 + n_s}. \quad (2)$$

After various conversions equation (2) can be represented as a polynomial  $P(f_2)$ . The resulting equation (3) is a polynomial of the 12th degree from  $f_2$ , in which  $n_m$  is located. If we solve it for  $f_2$ , we will get an analytical expression for conducting research explicitly and calculating critical points (maximums and boundary conditions). This will be the subject of our further work.

### Conclusion

It is worth noting that the obtained equation (1) allows us to evaluate the possibility of measuring the  $n_m$  value with an error of 0.0001 when changing the distance  $L$  on the photodiode ruler corresponding to the distance between photosensitive sensors (the ruler design contains 1024 sensors). Using equation (1), it is possible to determine experimentally the parameters of the cuvette, the distance  $e$ , as well as the value  $n_s$ , so that when  $n_m$  changes by 0.0001, the maximum of laser radiation moves by one photosensitive sensor. It takes a lot of time and resources. There will also be difficulties when switching from one  $n_m$  measurement range to another (for example, from the range from 1.34 to 1.35 to the range from 1.52 to 1.53).

In the case of using an analytical solution for  $n_m$ , these difficulties can be identified and measurement techniques can be developed to eliminate them.

### REFERENCES

1. Grebenikova N. M., Davydov R. V., Rud V. Yu., Features of the signal registration and processing in the study of liquid flow medium by the refraction method, *Journal of Physics: Conference Series*. 1326 (1) (2019) 012012.
2. Davydov V. V., Determination of the Composition and Concentrations of the Components of Mixtures of Hydrocarbon Media in the Course of its Express Analysis, *Measurement Techniques*. 62 (2) (2020) 1090–1098.
3. Nalimov A. G., Kozlova E. S., Inversion of the longitudinal component of spin angular momentum in the focus of a left-handed circularly polarized beam, *Computer Optics*. 44 (5) (2020) 699–706.
4. Kuzmin M. S., Rogov S. A., On the use of a multi-raster input of one-dimensional signals in two-dimensional optical correlators, *Computer Optics*. 43 (3) (2019) 391–396.
5. Zhukov A. E., Moiseev E. I., Nadtochii A. M., Zubov F. I., Maximov M. V., The Effect of Self-Heating on the Modulation Characteristics of a Microdisk Laser *Technical Physics Letters*. 46 (6) (2020) 515–519.
6. Marusina M. Y., Fedorov A. V., Prokhorovich V. E., Tkacheva N. V., Mayorov A. L., Development of Acoustic Methods of Control of the Stress-Strain State of Threaded Connections, *Measurement Techniques*. 61 (3) (2018) 297–302.
7. Kruzhalov S. V., Vologdin V. A., Concerning some features of studying the flow of liquid media by a Doppler method, *Journal of Optical Technology (A Translation of Opticheskii Zhurnal)*. 84 (8) (2017) 568–573.
8. Myazin N. S., Smirnov K. J., Logunov S. J., Spectral characteristics of InP photocathode with a surface grid electrode, *Journal of Physics: Conference Series*. 929 (1) (2017) 012080.
9. Marusina M. Y., Karaseva E. A., Automatic segmentation of MRI images in dynamic programming mode Asian Pacific, *Journal of Cancer Prevention*. 19 (10) (2018) 2771–2775.
10. Mazing M. S., Zaitceva A. V., Davydov R. V., Application of the Kohonen neural network for monitoring tissue oxygen supply under hypoxic conditions, *Journal of Physics: Conference Series*. 2086 (1) (2021) 012116.
11. Myazin N. S., Yushkova V. V., Rud V. Y., On the possibility of recording absorption spectra in weak magnetic fields by the method of nuclear magnetic resonance, *Journal of Physics: Conference Series*. 1038 (1) (2018) 012088.
12. Davydov V. V., Davydova T. I., A nondestructive method for express testing of condensed media in ecological monitoring, *Russian Journal of Nondestructive Testing*. 53 (7) (2017) 520–529.
13. Davydov V. V., Measurement of Magnetic Susceptibility and Curie Constants of Colloidal Solutions in Ferrofluid Cells by the Nuclear Magnetic Resonance Method, *Measurement Techniques*. 60 (5) (2017) 491–496.
14. Smirnov K. J., Glagolev S. F., Tushavin G. V., High speed near-infrared range sensor based on InP/InGaAs heterostructures, *Journal of Physics: Conference Series*. 1124 (2) (2018) 022014.
15. Murzakhanov F., Mamin G. V., Orlinskii S., Gafurov M. R., Komlev V. S., Study of Electron-



Nuclear Interactions in Doped Calcium Phosphates by Various Pulsed EPR Spectroscopy Techniques. ACS Omega. 6(39) (2021) 25338–25349.

16. **Dudkin V. I., Karseev A. Y.**, A Compact Marked Nuclear-Magnetic Flowmeter for Measurement of Rapidly Varying Flow Rates of Liquid, Measurement Techniques. 58(3) (2015) 317–322.

17. **Dudkin V. I., Nikolaev D. I., Moroz A. V., Davydov R. V.**, Features of Studying Liquid Media by the Method of Nuclear Magnetic Resonance in a Weak Magnetic Field Journal of Communications Technology and Electronics. 66(10) (2021) 1189–1195.

18. **Grebenikova N. M., Smirnov K. J., Rud V. Yu., Artemiev V. V.**, Features of monitoring the state of the liquid medium by refractometer, Journal of Physics: Conference Series. 1135 (1) (2018) 012055.

19. **Davydov V. V., Smirnov K. J.**, An Optical Method of Monitoring the State of Flowing Media with Low Transparency That Contain Large Inclusions, Measurement Techniques. 62 (6) (2019) 519–526.

20. **Karabegov M. A.**, On certain information capabilities of analytical instruments, Measurement Techniques. 54 (10) (2012) 1203–1212.

21. **Karabegov M. A.**, Metrological and technical characteristics of total internal reflection refractometers, Measurement Techniques. 47 (11) (2004) 1106–1112.

22. **Grebenikova N. M.**, The effect of optical density of the flowing liquid on the measurement error of its refractive index, Journal of Physics: Conference Series. 1400 (6) (2019) 066029.

23. **Karabegov M. A.**, A method of increasing the accuracy of analytical instruments by structural correction, Measurement Techniques. 52 (10) (2009) 1126–1133.

24. **Moroz A. V.**, Effect of the Absorbance of a Flowing Liquid on the Error of the Refractive Index Measured with a Differential Refractometer, Journal: Optics and Spectroscopy. 128 (9) (2020) 1415–1420.

25. **Davydov V. V., Moroz A. V., Nikolaev D. I.**, New Method for Measuring the Refractive Index of Flowing Liquid Optics and Spectroscopy. 129 (8) (2021) 915–921.

#### THE AUTHORS

**GOLDBERG Artemiy A.**

artemiy.goldberg@mail.ru

ORCID: 0000-0002-1573-4619

**KOCHETKOV Igor D.**

K.Igor.D@yandex.ru

ORCID: 0000-0002-5046-6234

**DAVYDOV Vadim V.**

Davydov\_vadim66@mail.ru

ORCID: 0000-0001-9530-4805

*Received 04.08.2022. Approved after reviewing 12.08.2022. Accepted 13.08.2022.*

Conference materials

UDC 535.8

DOI: <https://doi.org/10.18721/JPM.153.223>

### **New technique for control of liquid media state by optical method in express mode**

D. S. Provodin<sup>1</sup> ✉, V. V. Davydov<sup>1, 2, 3</sup>

<sup>1</sup> Peter the Great Saint-Petersburg Polytechnic University, Saint Petersburg, Russia;

<sup>2</sup> The Bonch-Bruевич Saint Petersburg State University of Telecommunications, Saint Petersburg, Russia;

<sup>3</sup> All-Russian Research Institute of Phytopathology, Moscow Region, Russia

✉ [provodindanya@gmail.com](mailto:provodindanya@gmail.com)

**Abstract.** The necessity of express control of the state of liquid media in real time is substantiated. Various methods of express control of the state of liquid media are considered. The basic requirements for these methods are determined. An optical method for monitoring the state of liquid media using the phenomenon of refraction is presented. The use of a small-sized differential-type refractometer for express control of the state of liquid media is substantiated. Its design has been developed and a new principle for measuring the refractive index of the investigated liquid has been proposed. The results of experimental studies are presented.

**Keywords:** Refraction, express-control, laser radiation, liquid, refractive index, differential cuvette of Anderson, medium state

**Citation:** Provodin D. S., Davydov V. V., New technique for control of liquid media state by optical method in express mode, St. Petersburg State Polytechnical University Journal. Physics and Mathematics. 15 (3.2) (2022) 124–129. DOI: <https://doi.org/10.18721/JPM.153.223>

This is an open access article under the CC BY-NC 4.0 license (<https://creativecommons.org/licenses/by-nc/4.0/>)

Материалы конференции

УДК 535.8

DOI: <https://doi.org/10.18721/JPM.153.223>

### **Новая методика контроля состояния жидкой среды оптическим методом в экспресс режиме**

Д. С. Проводин<sup>1</sup> ✉, В. В. Давыдов<sup>1, 2, 3</sup>

<sup>1</sup> Санкт-Петербургский Политехнический университет Петра Великого, Санкт-Петербург, Россия;

<sup>2</sup> Санкт-Петербургский государственный университет телекоммуникаций  
им. профессора М.А. Бонч-Бруевича, Санкт-Петербург, Россия;

<sup>3</sup> Всероссийский научно-исследовательский институт фитопатологии, Московская об., Россия

✉ [provodindanya@gmail.com](mailto:provodindanya@gmail.com)

**Аннотация.** Рассмотрены различные методы экспресс-контроля состояния жидких сред. Обосновано использование малогабаритного рефрактометра дифференциального типа для экспресс-контроля состояния жидких сред. Разработана его конструкция и предложен новый принцип измерения показателя преломления исследуемой жидкости. Представлены результаты экспериментальных исследований.

**Ключевые слова:** Рефракция, экспресс-контроль, лазерное излучение, жидкость, показатель преломления, дифференциальная кювета Андерсона, состояние среды

**Ссылка при цитировании:** Проводин Д. С., Давыдов В. В. Новая методика контроля состояния жидкой среды оптическим методом в экспресс режиме // Научно-технические ведомости СПбГПУ. Физико-математические науки. 2022. Т. 15. № 3.2. С. 124–129. DOI: <https://doi.org/10.18721/JPM.153.223>

Статья открытого доступа, распространяемая по лицензии CC BY-NC 4.0 (<https://creativecommons.org/licenses/by-nc/4.0/>)

## Introduction

The development of scientific and technological progress has set a large number of tasks for scientists [1–6]. One of which is the express control of the state of liquids in real time [2, 7–11]. Its role in the modern world is very difficult to assess, since the number of negative factors that worsen the state of liquid media is constantly increasing [1, 2, 12–15]. Express control of the state of various media during experiments or in production is especially in demand. Or when conducting environmental monitoring, where there are no automated control systems [16–21]. In these cases, it is impractical to use expensive high-resolution equipment that require special operating conditions. To solve such problems, compact, reliable equipment with an autonomous power source is required [8, 12, 13, 16, 21–26]. In addition, ongoing studies of the state of the medium during express control should not change its physical structure and chemical composition [16–21]. This is necessary to obtain confirmation of the detected contamination in the environmental sample on high-resolution instruments in a stationary laboratory. One of the methods that satisfies these requirements is based on the phenomenon of refraction [21–25, 27, 28]. The refractive index of the medium  $n$  and the temperature  $T$  are measured. And the value of  $n$  is compared with the value of  $n$ , which corresponds to the standard state of the medium.

Currently, small-sized refractometers are used for express control of the state of the medium. The principle of their operation is based on the phenomenon of total internal reflection. (TIR) [28–34]. During their operation in various situations, especially in the field (environmental monitoring), a number of problems arise. One of them is related to the provision of the thermal stabilization mode for the measurement process of the refractive index of a liquid medium. It takes a certain time to ensure the required temperature during the measurement. It also requires a certain amount of electrical energy, which is limited by the capacity of the battery. In addition, the dynamic range of refractive index measurements for these devices is not large (usually no more than 0.03 –0.05). Such devices are designed for express control of a certain type of media or food products [30, 31, 34–36]. With strong pollution, the refractive index of the medium changes more significantly (more than 0.1 or 0.2). This will make it impossible to measure  $n$ . Uncertainty will arise (device does not work or unknown environment). The paper presents one of the solutions to these complex problems.

### The design of a differential refractometer with Anderson cuvette of Anderson and the principle of measuring the refractive index of a liquid medium

In the designs of differential refractometers developed earlier for find the value of the refractive index  $n_m$  measured angle  $\alpha$ . [27, 28, 34, 38]. For measurements in the field, this measurement method turned out to be difficult to implement, since it is necessary to provide accurate measurements of the rotation of optical elements to determine the angle  $\beta$ . When transferring the device, misalignment of the structure is possible. In addition, when measuring the angle  $\beta$ , the temperature  $T$  of the environment will affect the operation of the optical elements. This will lead to a large measurement error. Moreover, with this principle of measurement, it is quite difficult to ensure the small size of the design of the refractometer.

Therefore, we have developed a new method for measuring the refractive index  $n_m$  of the medium under study. This method is based on the derivation of an analytical equation for determining the shift  $L$  of the maximum of laser radiation on a photodiode line from the values of the refractive indices  $n_s$  and  $n_m$ , the parameters of the Anderson cuvette, and the place where laser radiation is injected into the cuvette. On figure 1 shows the layout of a laboratory model of a differential refractometer with an Anderson cuvette and a photodiode line that we developed.

The distance  $L$ , by which the radiation has shifted, the decision on the total displacement at beam refraction when entering the cuvette partition ( $L_1$ ), when leaving it ( $L_2$ ), when entering the cuvette wall ( $L_3$ ) and when leaving it ( $L_4$ ) (Fig. 1).

$$L = L_1 + L_2 + L_3 + L_4 \quad (1)$$

After carrying out various calculations at the boundaries of two media (reference liquid -

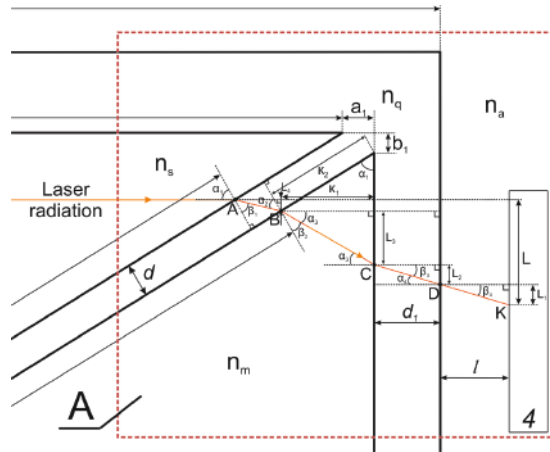


Fig. 1. Scheme of propagation of the laser radiation maximum in the Anderson differential cuvette and in the space up to the photodiode array

quartz, quartz - measured liquid, measured liquid - quartz and quartz-air), the following formula was obtained to calculate  $L$ :

$$\begin{aligned}
 L = \sin \alpha_1 & \left( d \left( 1 - \frac{n_s \cos \alpha_1}{\sqrt{n_q^2 - n_s^2 \sin^2 \alpha_1}} \right) + \left( \sqrt{n_m^2 - n_s^2 \sin^2 \alpha_1} - n_s \cos \alpha_1 \right) \right) \times \\
 & \times \left( \frac{e}{\sqrt{n_a^2 - \sin^2 \alpha_1 \left( n_m^2 - n_s^2 \sin^2 \alpha_1 + n_s^2 \cos^2 \alpha_1 - 2n_s \cos \alpha_1 \sqrt{n_m^2 - n_s^2 \sin^2 \alpha_1} \right)}} + \right. \\
 & + \frac{d_1}{\sqrt{n_q^2 - \sin^2 \alpha_1 \left( n_m^2 + n_s^2 \cos^2 \alpha_1 - n_s^2 \sin^2 \alpha_1 - 2n_s \cos \alpha_1 \sqrt{n_m^2 - n_s^2 \sin^2 \alpha_1} \right)}} + \\
 & \left. + \frac{K_1}{\cos \alpha_1 \sqrt{n_m^2 - n_s^2 \sin^2 \alpha_1 + n_s \sin^2 \alpha_1}} \right). \tag{2}
 \end{aligned}$$

We introduce the required parameters of the cuvette: width, length, wall thickness of the cuvette –  $b = 30$  mm,  $a = 40$  mm,  $d_1 = 2$  mm, respectively, the thickness of the partition  $d = 1$  mm, the distance from the cuvette to the photodiode bar –  $l = 30$  mm, let the beam at a distance  $y = 3.0$  mm from the top wall of the cuvette.

Let's check the formula (2) in the Matlab environment for the case when  $n_s = \text{nm}$ . The laser beam is displaced by a distance  $L = L_1$ , exits the cuvette at a right angle. It turned out the distance  $L_1 = 0.4365$  mm. This is consistent with experimental data.

### Results of the study of liquid media and discussion

The experiments performed have shown that the effect of ambient temperature  $T$  on the process of measuring  $\text{nm}$  is insignificant. This is due to the fact that the Anderson cuvette is made of quartz glass (the refractive index of quartz changes insignificantly when the temperature is measured from 276 to 313 K). The linear portion of the change in the dependence  $n(T)$  for quartz glass has been very well studied. The value of  $T$  is measured with an error of 0.1 K. During long-term measurements, the temperature of all objects, including the liquid medium, stabilizes. In some cases, a thermostat is used in refractometers to stabilize the temperature in the cuvette location area. This is effective for small cuvette sizes.

As an example, figure 2 shows the results of a study of the effect of metal scale in a pipeline on the state of drinking water at various temperatures  $T$ . The temperature change was carried out in an Anderson cuvette using a thermal stabilization scheme developed by us for a small-

sized model of a differential refractometer (Fig. 1). The results obtained showed the possibility of establishing the presence of metal scale in drinking water by changing the value of  $n$ . It should be noted that the nature of the change in  $n(T)$  for two media does not change, which means that the measurements are stable. Analysis of the obtained data shows the reliability of the differential refractometer we have developed.

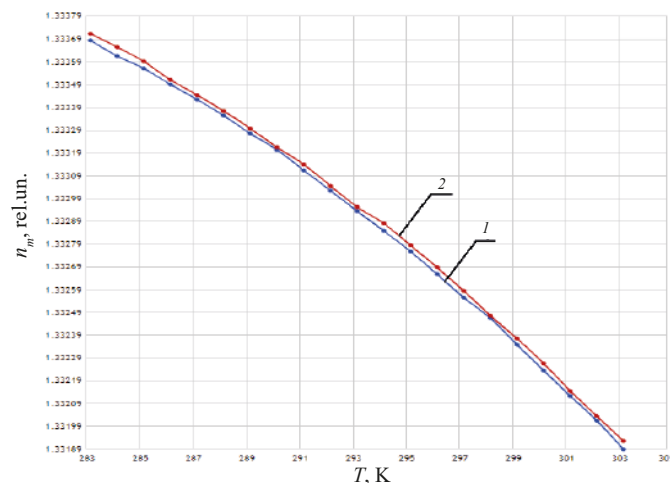


Fig. 2. Dependence of the change in the refractive index  $n_m$  of drinking water on temperature  $T$ .  
The graphs correspond to the state of drinking water:  
1- there are no oxides in the water, 2- there are oxides in the water.

It should be noted that the  $n_m$  measurement method developed by us makes it possible to set the measurement error depending on the range of  $n_m$  variation. For example, in the range of  $n_m$  variation from 1.4 to 1.5, using relation (2), by selecting the cuvette parameters, the refractive index of the reference liquid  $n_s$  and  $e$ , one can provide the following measurement mode (a change in the value of  $n_m$  by 0.0001 corresponds to a shift of the laser radiation maximum by one photosensitive sensor). For measurements is used a photodiode array with 1024 photosensitive sensors (1000 sensors are used to determine  $L$ ). In this case, the measurement error will be  $10^{-4}$ . Previously, this result was not possible.

### Conclusion

The results obtained allow us to consider that the design of the differential type refractometer proposed by us can be used to solve problems of express control of the state of liquid media in various situations. The results obtained by us allow us to consider that the design of the differential type refractometer proposed by us can be used to solve problems of express control of the state of liquid media in various situations. Our measurement accuracy of 0.0001 fully satisfies the strict requirements of express control, including medicines and biological solutions.

It should be noted that the results obtained by us make it possible, on the basis of a differential refractometer with an Anderson cuvette, to develop a first-class verification scheme for measuring the refractive index of liquid media. To do this, under laboratory conditions, for example, for the range of  $n_m$  in the range from 1.43 to 1.44, it is necessary to provide a change in the value of  $n_m$  by 0.00001 to shift the maximum of laser radiation by one photosensitive sensor. In this case, the measurement error will be  $10^{-5}$ , which is very close to the accuracy of the state standard.

### REFERENCES

1. Grebenikova N. M., Davydov R. V., Rud V. Yu., Features of the signal registration and processing in the study of liquid flow medium by the refraction method, Journal of Physics: Conference Series. 1326 (1) (2019) 012012.
2. Davydov V. V., Determination of the Composition and Concentrations of the Components of Mixtures of Hydrocarbon Media in the Course of its Express Analysis, Measurement Techniques. 62 (2) (2020) 1090–1098.

3. **Davydov R., Antonov V., Moroz A.**, Parameter Control System for a Nuclear Power Plant Based on Fiber-Optic Sensors and Communication Lines, IEEE International Conference on Electrical Engineering and Photonics (EExPolytech), Saint-Petersburg. Vol. 8906791 (2019) 295–297.
4. **Zubov F., Maximov M., Moiseev E., Kryzhanovskaya N., Zhukov A.**, Improved performance of InGaAs/GaAs microdisk lasers epi-side down bonded onto a silicon board Optics Letters. 46 (16) (2021) 3853–3856.
5. **Zhukov A. E., Moiseev E. I., Nadtochii A. M., Zubov F. I., Maximov M. V.**, The Effect of Self-Heating on the Modulation Characteristics of a Microdisk Laser Technical Physics Letters. 46 (6) (2020) 515–519.
6. **Kuzmin M. S., Rogov S. A.**, On the use of a multi-raster input of one-dimensional signals in two-dimensional optical correlators, Computer Optics. 43 (3) (2019) 391–396.
7. **Davydov V. V., Kruzhalov S. V., Grebenikova N. M., Smirnov K. J.**, Method for Determining Defects on the Inner Walls of Tubing from the Velocity Distribution of the Flowing Fluid, Measurement Techniques. 61 (4) (2018) 365–372.
8. **Myazin N. S., Smirnov K. J., Logunov S. J.**, Spectral characteristics of InP photocathode with a surface grid electrode, Journal of Physics: Conference Series. 929 (1) (2017) 012080.
9. **Davydov V. V., Kruzhalov S. V., Vologdin V. A.**, Concerning some features of studying the flow of liquid media by a Doppler method, Journal of Optical Technology (A Translation of Opticheskii Zhurnal). 84 (8) (2017) 568–573.
10. **Marusina M. Y., Karaseva E. A.**, Automatic segmentation of MRI images in dynamic programming mode Asian Pacific, Journal of Cancer Prevention. 19(10) (2018) 2771–2775.
11. **Marusina M. Y., Fedorov A. V., Prokhorovich V. E., Tkacheva N. V., Mayorov A. L.**, Development of Acoustic Methods of Control of the Stress-Strain State of Threaded Connections, Measurement Techniques. 61 (3) (2018) 297–302.
12. **Mazing M. S., Zaitceva A. V., Davydov R. V.**, Application of the Kohonen neural network for monitoring tissue oxygen supply under hypoxic conditions, Journal of Physics: Conference Series. 2086 (1) (2021) 012116.
13. **Davydov V. V., Dudkin V. I.**, On the Possibility of Express Recording of Nuclear Magnetic Resonance Spectra of Liquid Media in Weak Fields, Technical Physics. 63 (12) (2018) 1845–1850.
14. **Logunov S. E., Koshkin A. Y., Petrov A. A.**, Visualizer of magnetic fields, Journal of Physics: Conference Series. 741 (1) (2016) 012092.
15. **Logunov S. E., Vysoczky M. G., Mazing M. S.**, New method of researches of the magnetic fields force lines structure, Journal of Physics: Conference Series. 1038 (1) (2018) 012093.
16. **Myazin N. S., Yushkova V. V., Rud V. Y.**, On the possibility of recording absorption spectra in weak magnetic fields by the method of nuclear magnetic resonance, Journal of Physics: Conference Series. 1038 (1) (2018) 012088.
17. **Myazin N. S.**, Features of formation of structure of a nuclear magnetic resonance signal in weak magnetic field, Journal of Physics: Conference Series. 1135 (1) (2018) 012061.
18. **Davydov V. V., Davydova T. I.**, A nondestructive method for express testing of condensed media in ecological monitoring, Russian Journal of Nondestructive Testing. 53 (7) (2017) 520–529.
19. **Davydov V. V.**, Measurement of Magnetic Susceptibility and Curie Constants of Colloidal Solutions in Ferrofluid Cells by the Nuclear Magnetic Resonance Method, Measurement Techniques. 60 (5) (2017) 491–496.
20. **Smirnov K. J., Glagolev S. F., Tushavin G. V.**, High speed near-infrared range sensor based on InP/InGaAs heterostructures, Journal of Physics: Conference Series. 1124 (2) (2018) 022014.
21. **Davydov R. V., Dudkin V. I., Nikolaev D. I., Makeev S. S., Moroz A. V.**, Structure of a Nuclear Magnetic Resonance Signal in a Small Relaxometer. Journal of Communications Technology and Electronics. 66 (5) (2021) 632–636.
22. **Grebenikova N. M., Davydov R. V., Rud V. Yu.**, Features of the signal registration and processing in the study of liquid flow medium by the refraction method, Journal of Physics: Conference Series. 1326 (1) (2019) 012012.
23. **Grebenikova N. M., Smirnov K. J., Rud V. Yu., Artemiev V. V.**, Features of monitoring the state of the liquid medium by refractometer, Journal of Physics: Conference Series. 1135 (1) (2018) 012055.
24. **Grebenikova N. M., Rud V. Yu.**, The influence of optical density change on measurement error of refractive index in flowing liquid, Journal of Physics: Conference Series. 1410 (1) (2019) 012186.
25. **Grebenikova N. M., Smirnov K. J.**, Features of optical signals processing for monitoring the



state of the flowing liquid medium with a refractometer, *Journal of Physics: Conference Series*. 1368 (2) (2019) 022057.

26. **Davydov V. V., Dudkin V. I., Karseev A. Y.**, A Compact Marked Nuclear-Magnetic Flowmeter for Measurement of Rapidly Varying Flow Rates of Liquid, *Measurement Techniques*. 58 (3) (2015) 317–322.

27. **Davydov V. V.**, Some specific features of the NMR study of fluid flows *Optics and Spectroscopy* (English translation of *Optika i Spektroskopiya*). 121 (1) (2016) 18–24.

28. **Karabegov M. A.**, Metrological and technical characteristics of total internal reflection refractometers, *Measurement Techniques*. 47 (11) (2004) 1106–1112.

29. **Davydov V. V., Smirnov K. J.**, An Optical Method of Monitoring the State of Flowing Media with Low Transparency That Contain Large Inclusions, *Measurement Techniques*. 62(6) (2019) 519–526.

30. **Grebenikova N. M.**, The effect of optical density of the flowing liquid on the measurement error of its refractive index, *Journal of Physics: Conference Series*. 1400 (6) (2019) 066029.

31. **Davydov V. V., Dudkin V. I.**, Determination of the Composition and Concentrations of the Components of Mixtures of Hydrocarbon Media in the Course of its Express Analysis, *Measurement Techniques*. 62 (12) (2020) 1090–1098.

32. **Karabegov M. A.**, On certain information capabilities of analytical instruments, *Measurement Techniques*. 54 (10) (2012) 1203–1212.

33. **Davydov V. V., Moroz A. V., Makeev S. S., Dudkin V. I.**, Peculiarities of Registration of the Nuclear Magnetic Resonance Spectrum of a Condensed Medium During Express Control of Its State, *Optics and Spectroscopy*. 128 (10) (2020) 1678–1685.

34. **Karabegov M. A.**, A method of increasing the accuracy of analytical instruments by structural correction, *Measurement Techniques*. 52 (10) (2009) 1126–1133.

#### THE AUTHORS

**PROVODIN Daniil S.**  
provodindanya@gmail.com  
ORCID: 0000-0002-7007-9215

**DAVYDOV Vadim V.**  
davydov\_vadim66@mail.ru  
ORCID: 0000-0001- 9530- 4805

*Received 30.08.2022. Approved after reviewing 31.08.2022. Accepted 06.09.2022.*

## PHYSICAL ELECTRONICS

Conference materials

UDC 538.975

DOI: <https://doi.org/10.18721/JPM.153.224>

### Impact of the current pulse width on the speed of metal-insulator transition in VO<sub>2</sub> nanobeams

G. V. Alymov<sup>1</sup> ✉

<sup>1</sup>Moscow Institute of Physics and Technology (National Research University), Dolgoprudny, Russia

✉ [alymov@phystech.edu](mailto:alymov@phystech.edu)

**Abstract.** VO<sub>2</sub> undergoes an insulator-metal transition at ~ 68 °C, making it an attractive material for the development of tunable metasurfaces, steep-switching transistors, neuristors and other devices. Applications such as wireless communications call for ultrashort transition times, which are believed to be typically limited by heat dissipation. We consider the negative role of heat accumulation in the substrate, which slows down recovery after long heating pulses. Thermal simulations of VO<sub>2</sub> nanobeam gratings show that they can display two different behaviors: single-nanobeam-like in the short-pulse regime and film-like in the long-pulse regime. In the long-pulse regime, the recovery time depends linearly on the pulse duration and approximately quadratically on the hysteresis width, in agreement with analytical expressions. In the short-pulse regime, the dependence is much weaker. To achieve nanosecond recovery times, either the short-pulse regime must be used (pulse duration less than the time constant of heat diffusion between adjacent nanobeams), or hysteresis must be eliminated (e. g., by doping). Our results quantify the impact of the pulse duration and hysteresis on the switching time of VO<sub>2</sub> devices, clarify the conditions under which these factors are important, and therefore can guide the development of fast electronic/optoelectronic devices based on phase-change materials.

**Keywords:** vanadium dioxide, metal-insulator transition, nanobeams, nanowires, hysteresis, heat transfer

**Funding:** This work was supported by the grant No. 21-79-00209 of the Russian Science Foundation.

**Citation:** Alymov G. V., Impact of the current pulse width on the speed of metal-insulator transition in VO<sub>2</sub> nanobeams, St. Petersburg State Polytechnical University Journal. Physics and Mathematics. 15 (3.2) (2022) 130–134. DOI: <https://doi.org/10.18721/JPM.153.224>

This is an open access article under the CC BY-NC 4.0 license (<https://creativecommons.org/licenses/by-nc/4.0/>)

Материалы конференции

УДК 538.975

DOI: <https://doi.org/10.18721/JPM.153.224>

### Влияние длительности импульсов тока на скорость перехода металл-полупроводник в нанопроводах VO<sub>2</sub>

Г.В. Алымов<sup>1</sup> ✉

<sup>1</sup>МФТИ, Долгопрудный, Россия

✉ [alymov@phystech.edu](mailto:alymov@phystech.edu)

**Аннотация.** VO<sub>2</sub> претерпевает переход изолятор-металл при температуре ~ 68 °C, что делает его привлекательным материалом для создания управляемых метаповерхностей, транзисторов с высокой крутизной характеристики, нейристоров и других устройств. Такие применения, как беспроводная связь, требуют ультрабыстрых времён переключения, которые обычно ограничены теплоотводом. Мы рассматриваем негативную роль накопления тепла в подложке, которое замедляет восстановление изолирующего состояния после длинных импульсов нагрева. Тепловое моделирование решёток из нанопроводов VO<sub>2</sub> показало, что они могут вести себя двумя способами: как отдельные нанопровода в режиме коротких импульсов и как непрерывные плёнки



в режиме длинных импульсов. В режиме длинных импульсов время восстановления зависит линейно от длительности импульса и примерно квадратично от ширины гистерезиса, в согласии с аналитическими выражениями. В режиме коротких импульсов эти зависимости гораздо слабее. Для достижения наносекундных времён восстановления необходимо либо использовать режим коротких импульсов (длительность импульса меньше характерного времени диффузии тепла между соседними нанопроводами), либо устранить гистерезис (например, легированием). Таким образом, количественно охарактеризовано влияние длительности импульсов и ширины гистерезиса на время переключения устройств из VO<sub>2</sub>; прояснены условия, при которых эти факторы важны. Эти результаты могут быть использованы для создания быстрых электронных/оптоэлектронных устройств на фазовых переходах.

**Ключевые слова:** диоксид ванадия, переход металл-полупроводник, нанопровода, гистерезис, теплопередача

**Финансирование:** Работа поддержана грантом РФФИ № 21-79-00209.

**Ссылка при цитировании:** Алымов Г. В. Влияние длительности импульсов тока на скорость перехода металл-полупроводник в нанопроводах VO<sub>2</sub> // Научно-технические ведомости СПбГПУ. Физико-математические науки. 2022. Т. 15. № 3.2. С. 130–134. DOI: <https://doi.org/10.18721/JPM.153.224>

Статья открытого доступа, распространяемая по лицензии CC BY-NC 4.0 (<https://creativecommons.org/licenses/by-nc/4.0/>)

## Introduction

VO<sub>2</sub> undergoes a first-order insulator-metal transition (IMT) at  $T_c \sim 68$  °C, accompanied by an abrupt increase in conductivity and reflectivity. This makes it attractive for a range of applications in electronics and optoelectronics [1], including electrically and/or optically controlled metasurfaces [2], steep-switching transistors [3], and neuromorphic devices [4]. Previous theoretical and experimental work has shown that the switching speed of electrically controlled VO<sub>2</sub> devices is typically limited by the rate of heat dissipation [5, 6], while the “intrinsic” characteristic time of the IMT lies in the subpicosecond range [7]. (For completeness, we also mention reports on nonthermal electrically induced IMT in VO<sub>2</sub>, which requires a large defect concentration [8].)

Therefore, the most obvious ways of improving the transition speed in VO<sub>2</sub> are (i) downscaling (nanobeams, nanocrystals) and (ii) using substrates with good thermal conductivity (such as Al<sub>2</sub>O<sub>3</sub>). Both approaches have been successfully tested experimentally [9, 10].

But there remains another possibility, related to the nonstationary nature of heat flow in fast-switching devices. If the device remains in the metallic (high-temperature) phase long enough, heat will accumulate in the substrate and prevent efficient cooling of the device when heating current is switched off, thereby slowing down the reverse, metal-insulator transition (MIT). On the other hand, if VO<sub>2</sub> is heated by short current pulses and stays hot (metallic) only for short periods of time, the substrate will absorb less heat during the pulse, and the reverse switching will be faster. This is especially relevant for the combined optical/electrical control of VO<sub>2</sub> metasurfaces, when electric current is used to reduce the optical switching threshold and does not necessarily have to be pulsed [11].

In this work, we simulate heat transfer in periodic arrays of VO<sub>2</sub> nanobeams (nanobeam gratings) grown on single-crystal Al<sub>2</sub>O<sub>3</sub> and study the dependence of the recovery time on the duration of current pulses passing through the nanobeams. The role of hysteresis is also discussed.

## Model

We consider infinitely long VO<sub>2</sub> nanobeams of width  $w = 200$  nm and thickness  $h = 30$  nm grown on a single-crystal Al<sub>2</sub>O<sub>3</sub> substrate. The nanobeams form a periodic array with a period of 1 μm. They are heated by square current pulses (0.1 mA) to the IMT temperature and then cool down to the temperature of reverse, metal-insulator transition (MIT), switching back into the semiconducting phase. We calculate the switching time by numerically solving the heat equation, taking into account the latent heat of MIT and hysteresis. The switching time is defined as the interval between the end of a pulse and the moment when the whole nanobeam cools down below the MIT temperature. The ambient temperature is  $T_{env} = 25$  °C.

Material parameters used in the simulations:  $\text{Al}_2\text{O}_3$  heat capacity  $c_{\text{Al}_2\text{O}_3} = 3.5 \cdot 10^6 \text{ J}/(\text{m} \cdot \text{K})$ ,  $\text{Al}_2\text{O}_3$  thermal conductivity  $k_{\text{Al}_2\text{O}_3} = 30 \text{ W}/(\text{m} \cdot \text{K})$ ,  $\text{VO}_2$  heat capacity  $c_{\text{VO}_2} = 3 \cdot 10^6 \text{ J}/(\text{m}^3 \cdot \text{K})$ ,  $\text{VO}_2$  thermal conductivity in the metallic phase  $k_{\text{VO}_2, \text{M}} = 6 \text{ W}/(\text{m} \cdot \text{K})$ ,  $\text{VO}_2$  thermal conductivity in the semiconducting phase  $k_{\text{VO}_2, \text{I}} = 3.5 \text{ W}/(\text{m} \cdot \text{K})$ ,  $\text{VO}_2$  resistivity  $\rho_{\text{VO}_2, \text{M}} = 2 \cdot 10^{-2} \Omega \cdot \text{m}$ ,  $\rho_{\text{VO}_2, \text{I}} = 2 \cdot 10^{-6} \Omega \cdot \text{m}$ , latent heat of the IMT  $\Delta H_{\text{IMT}} = 2.7 \cdot 10^8 \text{ J}/\text{m}^3$ , transition temperatures  $(T_{\text{VO}_2, \text{I}} + T_{\text{MIT}})/2 = 68 \text{ }^\circ\text{C}$ ,  $T_{\text{IMT}} - T_{\text{MIT}} = \Delta T$ . The hysteresis width  $\Delta T$  was set to either 0, 10 or 20  $^\circ\text{C}$ . We assume that both  $\text{VO}_2$  phases coexist at  $T_{\text{IMT}}$  (during heating) or  $T_{\text{MIT}}$  (during cooling), and the properties of this mixed state (heat capacity, resistivity, enthalpy) are determined by the properties of each phase weighted by their molar fractions. Interface thermal resistance was neglected.

### Numerical simulations

The simulation results for three different hysteresis widths are shown in Fig. 1a. Indeed, long current pulses lead to slower switching, which is explained by the heat accumulation in the substrate (Fig. 1b, c). Two regimes are observed. When the pulse duration  $t_{\text{pulse}}$  is less than the characteristic timescale of heat diffusion between adjacent nanobeams ( $\sim 30 \text{ ns}$  in our simulations), the grating behaves as independent nanobeams, and the dependence of the recovery time on the pulse duration is rather weak (nanobeams are small and cannot dissipate much heat into the substrate). On the other hand, in the long-pulse limit the grating behaves as a continuous film, and the recovery time depends linearly on the pulse duration.

The effect of hysteresis is also pronounced. Hysteresis width  $\Delta T$  in  $\text{VO}_2$  can be controlled, e. g., by doping [12]. Wide hysteresis delays the reverse transition (MIT), because cooling  $\text{VO}_2$  from  $T_{\text{IMT}}$  to  $T_{\text{MIT}}$  requires more time than just dissipating the latent heat. (Fig. 1a) shows approximately quadratic dependence of the recovery time on the hysteresis width in the long-pulse limit, and a weaker, but still significant dependence in the short-pulse limit.

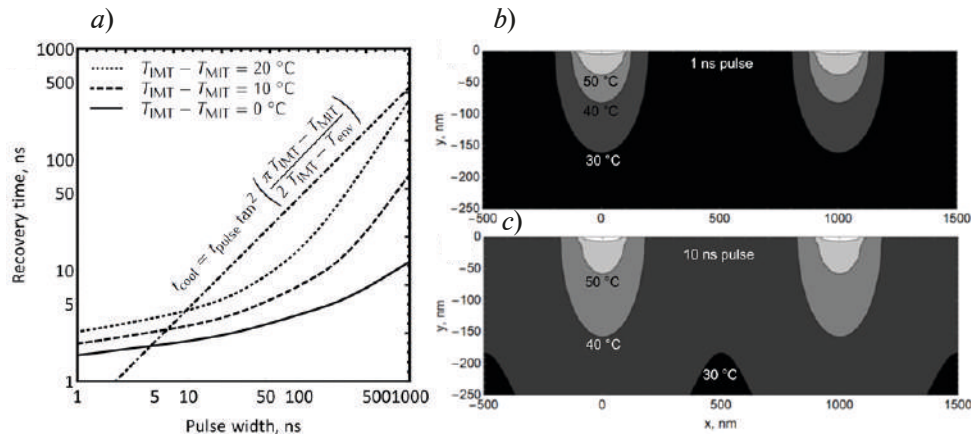


Fig. 1. Transition time in a periodic array of  $30 \text{ nm} \times 200 \text{ nm}$   $\text{VO}_2$  nanobeams (period  $1 \mu\text{m}$ ) on  $\text{Al}_2\text{O}_3$  substrate vs the duration of current pulses for three different hysteresis widths (a). Temperature distribution in the substrate after the end of a 1 ns, 0.1 mA pulse (b) or a 10 ns, 0.1 mA pulse (c)

### Analytical expressions

In the long-pulse limit, a nanobeam grating behaves as a continuous film. Assuming  $\text{VO}_2$  heats up to  $T_{\text{IMT}}$  almost instantaneously and neglecting its heat capacity and finite thickness, we can find the recovery time by solving the one-dimensional heat equation on a half-line with a boundary condition of constant temperature during the pulse, zero heat flux after the pulse, and again constant temperature during the MIT. In the presence of hysteresis, the main contribution to the recovery time is cooling from  $T_{\text{IMT}}$  to  $T_{\text{MIT}}$ , with the MIT itself being much faster:

$$t_{\text{recovery}} \equiv t_{\text{cool}} + t_{\text{MIT}} \approx t_{\text{pulse}} \tan^2 \left( \frac{\pi T_{\text{IMT}} - T_{\text{MIT}}}{2 T_{\text{IMT}} - T_{\text{env}}} \right). \quad (1)$$



Without hysteresis, the recovery time is determined by the duration of MIT and has an approximately square-root dependence on the pulse duration:

$$t_{\text{recovery}} = t_{\text{MIT}} = \left( \sqrt{t_{\text{pulse}}} + \sqrt{\frac{\pi}{4\kappa_{\text{Al}_2\text{O}_3} c_{\text{Al}_2\text{O}_3}} \frac{\Delta H_{\text{IMT}} h}{T_{\text{IMT}} - T_{\text{env}}}} \right)^2 - t_{\text{pulse}} \approx \sqrt{\frac{\pi t_{\text{pulse}}}{\kappa_{\text{Al}_2\text{O}_3} c_{\text{Al}_2\text{O}_3}} \frac{\Delta H_{\text{IMT}} h}{T_{\text{IMT}} - T_{\text{env}}}}. \quad (2)$$

In the short-pulse limit, the grating behaves as independent nanobeams. In this case, analytical expressions become complicated. Qualitatively, the weaker dependence of the recovery time on the pulse duration and hysteresis width can be traced to the fact that the finite width of a nanobeam sets a characteristic timescale of heat diffusion (in contrast to the case of a film, where the only timescale is the pulse duration, leading to a linear behavior of the recovery time).

### Conclusion

We have studied quantitatively the dependence of the recovery time in periodic arrays of VO<sub>2</sub> nanobeams on the duration of current pulses applied to VO<sub>2</sub> and hysteresis width (the difference in temperatures of insulator-metal and metal-insulator transitions).

The speed of metal-insulator transition in VO<sub>2</sub> nanobeam gratings depends on the heating protocol because of heat accumulation in the substrate. This dependence is especially pronounced when heat has enough time to diffuse between adjacent nanobeams, effectively blocking heat dissipation in lateral direction. In this case, the recovery time depends linearly on the duration of heating pulses. Hysteresis width has an even stronger influence on the recovery time, because cooling VO<sub>2</sub> to a lower temperature is slower than just dissipating a fixed amount of energy (latent heat).

To keep the recovery time in the nanosecond range, three approaches can be used: (1) using heating pulses shorter than the characteristic time of heat diffusion between adjacent nanobeams; (2) eliminating hysteresis (e. g., by doping [12]); (3) employing nonthermal field-induced transition not associated with significant heat dissipation (e. g., by applying low-fluence laser pulses or introducing a large number of defects into VO<sub>2</sub> [8]).

A significant influence of pulse duration on the recovery time has been observed in VO<sub>2</sub> thin films [13]. However, in two-dimensional films, the picture can be further complicated by filamentary conduction and the kinetics of domain walls. These factors are greatly suppressed in one- and zero-dimensional structures and arrays thereof.

Our results can serve as a guideline for the development of fast electronic/optoelectronic devices based on phase-change materials.

### REFERENCES

1. Yang Z., Ko C., Ramanathan S., Oxide electronics utilizing ultrafast metal-insulator transitions, *Annual Review of Materials Research*, 41 (2011) 337–367.
2. Shabanpour J., Beyraghi S., Cheldavi A., Ultrafast reprogrammable multifunctional vanadium-dioxide-assisted metasurface for dynamic THz wavefront engineering, *Scientific Reports* 10 (1) (2020) 1–4.
3. Shukla N. et al., A steep-slope transistor based on abrupt electronic phase transition, *Nature communications*, 6 (1) (2015) 1–6.
4. Del Valle J., Salev P., Kalcheim Y., Schuller I. K., A caloritronics-based Mott neuristor, *Scientific reports*, 10 (1) (2020) 1–10.
5. Markov P., Marvel R. E., Conley H. J., Miller K. J., Haglund Jr. R. F., Weiss S. M., Optically monitored electrical switching in VO<sub>2</sub>, *ACS Photonics*, 2 (8) (2015) 1175–1182.
6. Zhong X., Zhang X., Gupta A., LeClair P., Avalanche breakdown in microscale VO<sub>2</sub> structures, *Journal of Applied Physics*, 110 (8) (2011) 084516.
7. Cavalleri A., Dekorsy T., Chong H. H., Kieffer J. C., Schoenlein R. W., Evidence for a structurally-driven insulator-to-metal transition in VO<sub>2</sub>: A view from the ultrafast timescale, *Physical Review B*, 70 (16) (2004) 161102.
8. Kalcheim Y., Camjayi A., Del Valle J., Salev P., Rozenberg M., Schuller I. K., Non-thermal resistive switching in Mott insulator nanowires, *Nature communications*, 11 (1) (2020) 1–9.
9. Jerry M., Shukla N., Paik H., Schlom D. G., Datta S., Dynamics of electrically driven sub-

nanosecond switching in vanadium dioxide, 2016 IEEE Silicon Nanoelectronics Workshop (SNW) (2016) 26–27.

10. **Rodriguez-Vega M., Simons M. T., Radue E., Kittiwatanakul S., Lu J., Wolf S. A., Lukaszew R. A., Novikova I., Rossi E.**, Effect of inhomogeneities and substrate on the dynamics of the metal-insulator transition in VO<sub>2</sub> thin films, *Physical Review B*, 92 (11) (2015) 115420.

11. **Kaydashev V. E., Zhukov S., Kutepov M., Domaratskiy I., Slavich A.**, Metasurfaces based on Au and VO<sub>2</sub> for THz applications, Saratov Fall Meeting 2020, Saratov, Russia, 29 September – 2 October 2020.

12. **Chen S., Liu J., Wang L., Luo H., Gao Y.**, Unraveling mechanism on reducing thermal hysteresis width of VO<sub>2</sub> by Ti doping: A joint experimental and theoretical study, *The Journal of Physical Chemistry C*, 118 (33) (2014) 18938–18944.

13. **Adam G. B., Duchene J. C.**, Pulse investigation of switching delays in VO<sub>2</sub> coplanar devices, *IEEE Transactions on Electron Devices*, 19 (6) (1972), 820–825.

### THE AUTHORS

**ALYMOV Georgy V.**  
alymov@phystech.edu  
ORCID: 0000-0002-3957-5325

*Received 25.07.2022. Approved after reviewing 08.08.2022. Accepted 10.08.2022.*

Conference materials

UDC 538.971

DOI: <https://doi.org/10.18721/JPM.153.225>

## Dependence of light-addressable potentiometric sensor sensitivity on photo-induced processes in Si

A. V. Kozlowski<sup>1</sup> ✉, S. V. Stetsyura<sup>1</sup>

<sup>1</sup> Saratov State University, Saratov, Russia

✉ [kozlowsky@bk.ru](mailto:kozlowsky@bk.ru)

**Abstract.** The effect of photoelectron processes in *n*-Si and *p*-Si during the fabrication of the "Si/SiO<sub>2</sub>/SiN<sub>x</sub>/polyethyleneimine/glucose oxidase" sensor structure on the glucose sensitivity of a light-addressable potentiometric sensor (LAPS) depending on SiN<sub>x</sub> thickness was investigated. It was found that the illumination of the *n*-Si-based structure during the adsorption of the glucose oxidase enzyme doubles the sensitivity to glucose compared to the adsorption of glucose oxidase in the dark, and the best effect from photostimulated adsorption is achieved at a SiN<sub>x</sub> layer thickness of ~50 nm. At the same time, the sensitivity to D-glucose, measured in the LAPS mode, is 45% higher than the sensitivity of the capacitive sensor. Illumination of *p*-Si during glucose oxidase adsorption resulted in a slight decrease in sensor sensitivity. The results are explained by a change in the density of immobilized glucose oxidase molecules due to a change in the electrostatic forces of attraction between enzyme molecules and semiconductor upon illumination and photoinduced charge stabilization on the surface electronic states of the Si/SiO<sub>2</sub> and SiN<sub>x</sub>/polyethyleneimine interfaces in the case of photostimulated glucose oxidase adsorption.

**Keywords:** Semiconductor, sensor structures, silicon nitride, illumination, light-addressable potentiometric sensor

**Funding:** This study was funded by the Russian Science Foundation (project No. 22-22-00194, <https://rscf.ru/en/project/22-22-00194/>).

**Citation:** Kozlowski A. V., Stetsyura S. V., Dependence of light-addressable potentiometric sensor sensitivity on photo-induced processes in Si, St. Petersburg State Polytechnical University Journal. Physics and Mathematics. 15 (3.2) (2022) 135–139. DOI: <https://doi.org/10.18721/JPM.153.225>

This is an open access article under the CC BY-NC 4.0 license (<https://creativecommons.org/licenses/by-nc/4.0/>)

Материалы конференции

УДК 538.971

DOI: <https://doi.org/10.18721/JPM.153.225>

## Зависимость чувствительности светоадресуемого потенциометрического сенсора от фотоиндуцированных процессов в Si

А. В. Козловский<sup>1</sup> ✉, С. В. Стецюра<sup>1</sup>

<sup>1</sup> ФГБОУ ВО «СГУ имени Н.Г. Чернышевского», Саратов, Россия

✉ [kozlowsky@bk.ru](mailto:kozlowsky@bk.ru)

**Аннотация.** Исследовано влияние фотоэлектронных процессов в *n*-Si и *p*-Si при создании сенсорной структуры «Si/SiO<sub>2</sub>/SiN<sub>x</sub>/полиэтиленмин (ПЭИ)/глюкозооксидаза (GOx)» на чувствительность к глюкозе светоадресуемого потенциометрического сенсора (САПС) в зависимости от толщины слоя SiN<sub>x</sub>. Получено, что освещение структуры на основе *n*-Si при адсорбции фермента GOx увеличивает чувствительность к глюкозе в два раза по сравнению с адсорбцией GOx в темноте, а наилучший эффект от фотостимулированной адсорбции достигается при толщине слоя SiN<sub>x</sub> ~50 нм. Освещение *p*-Si во время адсорбции GOx приводило к небольшому снижению чувствительности сенсора. Результат объясняется изменением плотности иммобилизованных молекул GOx за

счет изменения электростатических сил притяжения при освещении и стабилизацией фотоиндуцированного заряда на поверхностных электронных состояниях интерфейсов Si/SiO<sub>2</sub> и SiN<sub>x</sub>/ПЭИ в случае применения фотостимулированной адсорбции GOx.

**Ключевые слова:** полупроводник, сенсорные структуры, нитрид кремния, освещение

**Финансирование:** Исследование выполнено за счет гранта Российского научного фонда № 22-22-00194, <https://rscf.ru/project/22-22-00194/>.

**Ссылка при цитировании:** Козловский А. В., Стецюра С. В. Зависимость чувствительности светоадресуемого потенциометрического сенсора от фотоиндуцированных процессов в Si // Научно-технические ведомости СПбГПУ. Физико-математические науки. 2022. Т. 15. № 3.2. С. 135–139. DOI: <https://doi.org/10.18721/JPM.153.225>

Статья открытого доступа, распространяемая по лицензии CC BY-NC 4.0 (<https://creativecommons.org/licenses/by-nc/4.0/>)

### Introduction

Electrolyte/insulator/semiconductor (EIS) structures are widely used to detect nano- and bio-objects ionized in solution due to the field effect. Also, EIS-structures are used to recognize enzymatic reactions [1], viruses [2], RNA/DNA sequencing [3]. Compared to capacitive EIS-sensors, light-addressable potentiometric sensors (LAPS) have a number of advantages, such as the ability to obtain spatial and temporal charge distribution over the surface of the transducer (scanning photoinduced impedance spectroscopy), which makes it possible to visually assess the dynamics of changes in the concentration of the analyte.

Previously, we reported on the effect of photoelectron processes in a silicon substrate on the glucose oxidase (GOx) adsorption. Photostimulation of the semiconductor during enzyme adsorption led to a change in the surface concentration of adsorbed molecules, which ultimately led to an increase in the glucose sensitivity of a capacitive EIS-sensor based on the Si/SiO<sub>2</sub>/polyethyleneimine (PEI)/GOx structure. However, the effectiveness of photostimulated layer-by-layer adsorption of the enzyme on a semiconductor with a passivating dielectric layer of silicon nitride has not been studied before. Silicon nitride is advantageous over SiO<sub>2</sub> because it allows greater sensitivity to changes in H<sup>+</sup> in solution due to the higher density of protonated groups on the surface. However, it should be taken into account that for the photostimulated adsorption method to be effective, one should limit oneself to nanoscale insulator thicknesses.

In this work, we studied the effect of both photo-stimulated layer-by-layer adsorption (PSA) of GOx and the thickness of the dielectric layer of Si/SiO<sub>2</sub>/SiN<sub>x</sub> structure on the sensitivity to glucose of LAPS based on Si/SiO<sub>2</sub>/SiN<sub>x</sub>/PEI/GOx structure.

### Materials and Methods

The sensor structures were fabricated using single-crystal (100) Si wafers (250 μm thickness) of *n*-type ( $\rho = 2 - 7 \Omega \text{ cm}$ ) and *p*-type ( $\rho = 9 - 15 \Omega \text{ cm}$ ). Initially, the wafers were boiled in a peroxide–ammonia solution (NH<sub>4</sub>OH : H<sub>2</sub>O<sub>2</sub> : H<sub>2</sub>O = 1 : 1 : 4 (vol.)) at 75°C during 10 min. Then wafers were rinsed in deionized water ( $\rho \sim 18.2 \text{ M}\Omega \text{ cm}$ ). Afterwards, wafers were cut into substrates of 10×10 mm<sup>2</sup>. A 300 nm nickel layer on the rear side of the sensor structure was applied by magnetron sputtering method. The rear-side contact was partially removed to create an illumination window for the light beams. A nitride silicon (SiN<sub>x</sub>) thin films approximately 50 and 150 nm thick were deposited on the front side Si by magnetron sputtering method (Angstrom Nexdep, USA). The SiN<sub>x</sub> surface contains primarily silanol groups with a small percentage of silamine groups. The silanol groups in solution exist as either negatively charged Si-O<sup>-</sup> or neutrally charged Si-OH functions due to protonated-deprotonated processes. The silamine groups can exist as neutral or positively charged functions. It can be noted that isoelectric point (IEP) of the SiN<sub>x</sub> surface is ca. pH=3.5 [4] and above this pH value the surface is negatively charged.

The glucose oxidase (GOx) form *Aspergillus niger* were used as enzyme molecules. Branched polyethyleneimine (PEI) with a molecular weight of 25 kDa was used as cationic polyelectrolyte to increase the adsorption of negatively charged GOx onto Si substrates with SiN<sub>x</sub> layer.



The organic molecules were adsorbed onto Si substrates from the aqueous solutions during 10 min followed by rinsing in deionized water ( $\rho \sim 18.2 \text{ M}\Omega \text{ cm}$ ) during 10 min and drying in nitrogen flow. The glucose solutions were prepared by dissolving D-glucose in the working buffer. As working buffer, a 0.2 mM potassium phosphate buffer solution ( $\text{pH} = 7.3$ ) containing 150 mM NaCl as an ionic strength adjuster was used. At ionic strength about of 150 mM, the  $1/e$  distance for the exponential decay of the surface potential is approximately 1 nm. At ionic strength about of 150 mM, the  $1/e$  distance for the exponential decay of the surface potential is approximately 1 nm. The size of the GOx molecule is  $6.0 \times 5.2 \times 7.7 \text{ nm}^3$  [5]. Thus, charged GOx molecules on substrate surface would have little influence on sensor signal.

The photo-stimulated layer-by-layer adsorption technique suggested in [6] was used to adsorb GOx from aqueous solution onto  $\text{Si}/\text{SiO}_2/\text{SiN}_x$  substrates covered with PEI. A halogen lamp (Philips 13186 EPX/EPV) was used to activate photoelectric processes in a silicon wafer during adsorption of polyelectrolyte molecules. The substrate was either in the dark or under illumination during the GOx adsorption, other things being equal.

Figure 1 schematically shows the experimental set-up, which has been utilised for the characterisation of LAPS with the adsorbed PEI and GOx layers. For the measurements, the prepared structure was mounted into an electrochemical cell, sealed by an O-ring and contacted on its front side by the electrolyte and Ag/AgCl reference electrode, and on its rear side by ohmic contact. The measurements have been performed at room temperature.

Before the adsorption of PEI and GOx, the pH-sensitive behaviour of the as-prepared  $\text{Si}/\text{SiO}_2/\text{SiN}_x$  structure has been investigated in buffer solutions of  $\text{pH} 5.89\text{--}7.77$  by LAPS method. For operation, a DC voltage is applied via the Ag/AgCl reference electrode. For the measuring procedure, about 0.5 mL of the working buffer or particular glucose solution was applied to the  $\text{SiN}_x$  surface, and photocurrent has been read out for after 10 min. During measurements, the substrates were illuminated from the rear side with modulated light. Red-LED ( $\lambda = 650\text{--}655 \text{ nm}$ ) is placed directly below the EIS-structure as a light source. An oscillator, which generates a 1 kHz rectangular signal, was provided the modulation of the red-light beam. After each measurement, front side region was rinsed with buffer solution.

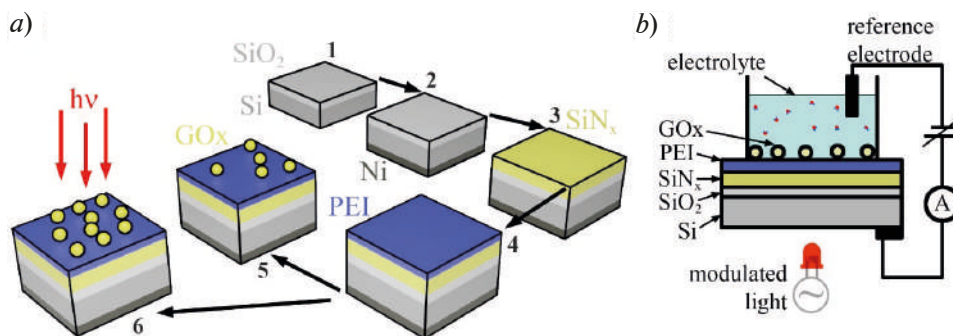


Fig. 1. Stages of fabrication a hybrid sensor structure: 1 - silicon wafer with an oxide layer after ammonia-peroxide treatment; 2 - deposition of a nickel contact and its partial etching on the rear side of the substrate; 3 - deposition of the  $\text{SiN}_x$  layer by magnetron sputtering; 4 - deposition polyethyleneimine molecules by layer-by-layer adsorption; 5 and 6 - deposition of GOx molecules in the dark (5) or under illumination (6) of semiconductor substrate (a). Schematic of light-addressable potentiometric sensors (b)

The glucose sensitivity of biosensors was studied by means of capacitance-voltage (EIS-sensor mode) and photocurrent-voltage (LAPS mode) measurements in glucose solutions with different content of D-glucose from 1 mM to 10 mM using a semiconductor device analyzer (Agilent B1500A, USA). Bias voltage was applied relative to the rear-side Si substrate.

## Results and Discussion

Figure 2 shows exemplarily a typical photocurrent-voltage curves response to pH changes. With increasing pH of the solution, photocurrent-voltage curves are shifted along the voltage axis in the

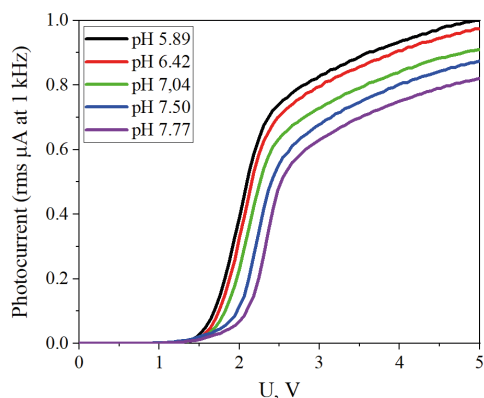


Fig. 2. Typical photocurrent-voltage curves of Si/SiO<sub>2</sub>/SiN<sub>x</sub>/PEI/GOx sensor structures measured in 0.1 M potassium phosphate buffer at different pH-values

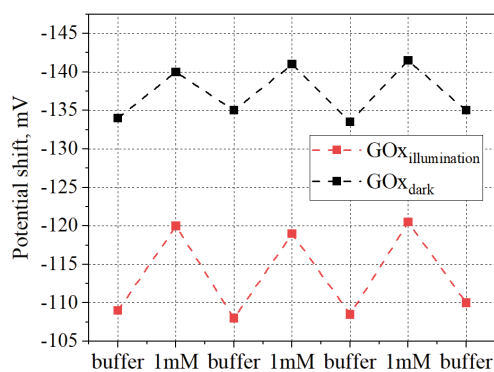


Fig. 3. Reproducibility of potential change during cyclic change of the working buffer solution (0.2 mM potassium phosphate buffer solution, pH = 7.3) by 1 mM D-glucose depending on the method of deposition of GOx molecules: in the dark or under illumination of silicon during GOx adsorption

direction to more positive voltage values. This is due to decrease in the H<sup>+</sup> concentration of on the LAPS surface. It was found that pH sensitivity is 1.57 times greater for a structure with SiN<sub>x</sub> thickness of 50 nm.

It was found that for LAPS with 150 nm of SiN<sub>x</sub>, where the GOx molecules were deposited in the dark, the sensitivity to D-glucose is 4.6 mV/mM. In the case of PSA – 7.4 mV/mM. For 50 nm of SiN<sub>x</sub>, the D-glucose sensitivity is 6.7 mV/mM and 12.3 mV/mM for GOx deposition in the dark and PSA, respectively

The repeatability of readings of the biosensor structure during multiple measurements was also recorded. The values of the potential shift were measured during several measurement cycles. After each measurement cycle in a 1 mM D-glucose solution, the structure was washed (0.2 mM potassium phosphate buffer, pH = 7.3) and potential shift was measured again. The experiments were carried out on the structures obtained using the GOx PSA and when GOx deposited in the dark. Figure 3 shows the results of 3 consecutive cycles.

The scatter of the potential shifts for structure obtained by dark deposition of GOx is 1.3 mV or 19 %. When using PSA, the shifts are more stable: changes are less than 0.6 mV or 5.3 %. In addition, it can be seen from Figure 3 that the response to the same glucose concentration is higher for the structure obtained with GOx PSA - a change of 11.3 mV versus 5-6 mV for the structure on which GOx was deposited in the dark. The results can be explained by the change in the density of immobilized GOx molecules induced by photoelectron processes in the Si substrate during adsorption of enzyme [6].

### Conclusion

It was found that the sensitivity to D-glucose of LAPS, prepared with PSA of enzyme molecules on a semiconductor substrate, twice the sensitivity of LAPS obtained without PSA. The PSA of GOx was studied for the first time for the structure of Si/SiO<sub>2</sub>/SiN<sub>x</sub>. The best effect of photostimulated adsorption was achieved with SiN<sub>x</sub> layer thickness ~50 nm. It can be noted that PSA at the stage of adsorption of enzyme molecules to increase the stability of biosensor signal. The results were explained by photoelectron processes in a hybrid structure that occur during the adsorption of a polyelectrolyte on a photosensitive substrate.

### Acknowledgments

The work was carried out at the expense of the Russian Science Foundation (project No. 22-22-00194, <https://rscf.ru/en/project/22-22-00194/>).

### REFERENCES

1. Werner C. F., Takenaga S., Taki H., Sawada K., Schöning M. J., Comparison of label-free ACh-imaging sensors based on CCD and LAPS, *Sensors and Actuators B: Chemical*. 177 (2013) 745–752.



2. Seo G., Lee G., Kim M. J., Baek S.-H., Choi M., Ku K. B., Lee C.-S., Jun S., Park D., Kim H. G., Kim S.-J., Lee J., Kim B. T., Park E. C., Kim S. I., Rapid Detection of COVID-19 Causative Virus (SARS-CoV-2) in Human Nasopharyngeal Swab Specimens Using Field-Effect Transistor-Based Biosensor, ACS Nano. 14 (2020) 5135–5142.
3. Gasparyan L., Mazo I., Simonyan V., Gasparyan F., DNA Sequencing: Current State and Prospects of Development, Open Journal of Biophysics. 9 (2019) 169–197.
4. Cloarec J.-P., Chevalier C., Genest J., Beauvais J., Chamas H., Chevolot Y., Baron T., Souifi A., pH driven addressing of silicon nanowires onto Si<sub>3</sub>N<sub>4</sub>/SiO<sub>2</sub> micro-patterned surfaces, Nanotechnology. 27 (2016) 295602.
5. Hecht H. J., Kalisz H. M., Hendle J., Schmid R. D., Schomburg D., Crystal Structure of Glucose Oxidase from Aspergillus niger Refined at 2.3 Å Resolution, Journal of Molecular Biology. 229 (1993) 153–172.
6. Kozłowski A. V., Stetsyura S. V., Dependence of field-effect biosensor sensitivity on photo-induced processes in Si and its conductivity type, Journal of Physics: Conference Series. 2086 (2021) 012189.

#### THE AUTHORS

**KOZŁOWSKI Alexander V.**  
kozłowsky@bk.ru  
ORCID: 0000-0002-3612-9776

**STETSYURA Svetlana V.**  
stetsyurasv@mail.ru  
ORCID: 0000-0002-4337-012X

*Received 12.08.2022. Approved after reviewing 15.08.2022. Accepted 26.08.2022.*

Conference materials

UDC 621.3

DOI: <https://doi.org/10.18721/JPM.153.226>

## Performance optimization of the cantilever-based MEMS switch

I. A. Belozеров<sup>1,2</sup> ✉, I. V. Uvarov<sup>1</sup>

<sup>1</sup>Valiev Institute of Physics and Technology of RAS, Yaroslavl Branch, Yaroslavl, Russia;

<sup>2</sup>P.G. Demidov Yaroslavl State University, Yaroslavl, Russia

✉ [igas2580@yandex.ru](mailto:igas2580@yandex.ru)

**Abstract.** Microelectromechanical system (MEMS) switches combine advantages of electromagnetic and semiconductor relays. However, a number of problems prevent the widespread use of these devices. One of them is high actuation voltage. In this work, voltage reduction is achieved by optimizing the shape of the electrodes. The switch is simulated by the finite element method. Dependences of the actuation voltage on the geometric parameters are obtained. The proposed shape of the electrodes reduces the voltage by almost two times compared to conventional design without deterioration of other working characteristics.

**Keywords:** MEMS switch, cantilever, actuation voltage, finite element method

**Funding:** This work is supported by the program № FFNN-2022-0017 of the Ministry of Science and Higher Education of Russia for Valiev Institute of Physics and Technology of RAS and the grant of President of the Russian Federation № МК-945.2021.4.

**Citation:** Belozеров I. A., Uvarov I. V., Performance optimization of the cantilever-based MEMS switch, St. Petersburg State Polytechnical University Journal. Physics and Mathematics. 15 (3.2) (2022) 140–144. DOI: <https://doi.org/10.18721/JPM.153.226>

This is an open access article under the CC BY-NC 4.0 license (<https://creativecommons.org/licenses/by-nc/4.0/>)

Материалы конференции

УДК 621.3

DOI: <https://doi.org/10.18721/JPM.153.226>

## Оптимизация рабочих характеристик МЭМС-переключателя на основе кантилевера

И. А. Белозеров<sup>1,2</sup> ✉, И. В. Уваров<sup>1</sup>

<sup>1</sup>Ярославский Филиал Физико-технологического института им. К.А. Валиева РАН, Ярославль, Россия;

<sup>2</sup>Ярославский государственный университет им. П.Г. Демидова, Ярославль, Россия

✉ [igas2580@yandex.ru](mailto:igas2580@yandex.ru)

**Аннотация.** МЭМС-переключатели сочетают в себе достоинства электромагнитных реле и полупроводниковых ключей, однако до сих пор не нашли широкого применения. Одной из причин является высокое напряжение срабатывания. В этой работе снижение напряжения достигается путем оптимизации формы электродов. Выполнено моделирование переключателя методом конечных элементов. Получены зависимости напряжения срабатывания от геометрических параметров конструкции. Предложенная форма электродов уменьшает напряжение практически вдвое по сравнению с классическим исполнением без ухудшения других рабочих характеристик.

**Ключевые слова:** МЭМС-переключатель, кантилевер, напряжение срабатывания, метод конечных элементов

**Финансирование:** Работа выполнена в рамках Государственного задания ФТИАН им. К.А. Валиева РАН Минобрнауки РФ по теме № FFNN-2022-0017, а также при финансовой поддержке гранта Президента Российской Федерации № МК-945.2021.4.

**Ссылка при цитировании:** Белозеров И. А., Уваров И. В. Оптимизация рабочих характеристик МЭМС-переключателя на основе кантилевера // Научно-технические

ведомости СПбГПУ. Физико-математические науки. 2022. Т. 15. № 3.2. С. 140–144.  
DOI: <https://doi.org/10.18721/JPM.153.226>

Статья открытого доступа, распространяемая по лицензии CC BY-NC 4.0 (<https://creativecommons.org/licenses/by-nc/4.0/>)

## Introduction

In recent decades, microelectromechanical systems (MEMS) have been actively developed in the world. MEMS switches for commutation of high-frequency signals receive a particular interest [1]. They combine advantages of electromagnetic relays and transistor-based devices: low insertion loss, good insulation and low power consumption combined with small size. In addition, MEMS switches are fabricated using microelectronic technology, which allows integration with other electronic components on a wide range of substrates, including Si [2], GaAs [3] and glass [4]. Such characteristics make MEMS switches attractive for use in 5G mobile network [5], reconfigurable antennas [6, 7], satellite communication systems [8], and other industries.

A typical MEMS switch is a metal beam with one fixed end (a cantilever), which is suspended above the driving and signal electrodes [9]. Applying voltage to the driving electrode makes the beam to bend under the electrostatic force and come in contact with the signal electrode. The classical design is simple and reliable, but it has high actuation voltage of about one hundred volts [10]. Such a voltage complicates the use of MEMS switches in modern electronic devices with an operating range of 3–5 V. This paper presents a technique for reducing the actuation voltage of a cantilever-based MEMS switch by optimizing the shape of the electrodes. Working characteristics are calculated using finite element method (FEM). The influence of the optimization on the resonant frequency of the cantilever, the switching time and the contact force are considered.

## Materials and Methods

The switch is schematically shown in Fig. 1. The movable electrode is an aluminum cantilever located above the driving and signal electrodes made of platinum. The cantilever has a length  $L = 50 \mu\text{m}$  and a thickness  $t = 2 \mu\text{m}$ . Its end with the coordinate  $x = 0$  is fixed. The width of the cantilever near the fixed end is  $W$ . The driving electrode has the length  $L_e$  and the width  $W_e$ . The air gap between the cantilever and the electrode is  $g_0 = 1.5 \mu\text{m}$ . The driving and signal electrodes have a thickness of 100 nm.

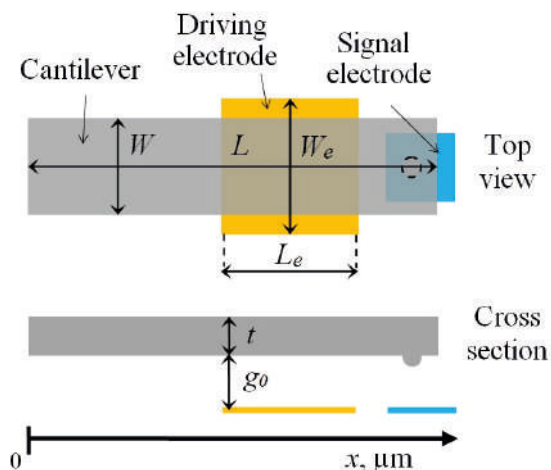


Fig. 1. Schematic illustration of the cantilever-based MEMS switch

The actuation voltage  $V_{pl}$  of the cantilever-based switch is given by the following expression [9]:

$$V_{pl} = \left( \frac{8k}{27\epsilon\epsilon_0 A} g_0^3 \right)^{\frac{1}{2}}, \quad (1)$$

where  $k$  is the spring constant of the beam,  $g_0$  is the gap between the beam and the electrode,  $A$  is the overlap area of the electrode and the beam, and  $\epsilon$  is the air permittivity. According to equation (1), the actuation voltage can be reduced by decreasing  $k$  and  $g$  and increasing  $A$ . However, the first method reduces the restoring force, thereby increasing the probability of stiction. The second way raises the capacitance between the cantilever and the signal electrode and degrades the radio frequency characteristics of the switch. In this work we consider the third method, which consists in optimizing the electrode shape.

Changing the design of the switch affects not only the actuation voltage, but also other characteristics such as switching time and contact force. The switching time  $t_{on}$  is determined by the following expression [9]:

$$t_{on} \approx 3.67 \frac{V_{pl}}{V_D} \frac{1}{2\pi f_0}, \quad (2)$$

where  $V_D$  is the voltage applied to the driving electrode, and  $f_0$  is the resonance frequency of the cantilever. The resonance frequency is calculated as follows [11]:

$$f_0 = \frac{1}{2\pi} \left( \frac{k}{m_{eff}} \right)^{\frac{1}{2}}, \quad (3)$$

where  $m_{eff}$  is the effective mass of the cantilever. The cantilever in the form of a rectangular parallelepiped has the mass of

$$m_{eff} = \frac{33}{140} m = \frac{33}{140} \rho W L t, \quad (4)$$

where  $\rho$  is the density of the cantilever material. The spring constant is expressed as

$$k = \frac{EW}{4} \left( \frac{t}{L} \right)^3, \quad (5)$$

where  $E$  is the Young's modulus of the cantilever material. The contact force  $F_C$  is determined by the difference between the electrostatic force  $F_{es}$  and the elastic force  $F_{el}$  acting on the cantilever in the closed state:

$$F_C = F_{es} - F_{el} \quad (6)$$

Expressions (1)–(6) allow estimation of the performance, but numerical methods provide more precise data. The switch is simulated in a verified FEM software. The model contains about  $10^6$  tetrahedral elements. The switch operates in air under normal conditions. The cantilever material is aluminum with the following properties:  $E = 70$  GPa,  $\rho = 2700$  kg/m<sup>3</sup>, Poisson's ratio 0.35. The cantilever is grounded, and an electric potential is applied to the driving electrode. The potential gradually increases until the electrostatic pull-in, when the position of the beam becomes unstable. The highest potential value for which the computer is able to calculate the cantilever position is considered as the actuation voltage.

### Results and Discussion

According to the simulation, the switch with  $W = 10$   $\mu\text{m}$ ,  $L_e = 18$   $\mu\text{m}$  and  $W_e = 12$   $\mu\text{m}$  has an actuation voltage of 146 V. This rather high value needs reduction. The decrease in  $V_{pl}$  is achieved by increasing the width of the electrode and the beam above it, as shown in the top inset of Fig. 2. This modification enlarges the overlap area of the electrode and the beam. The same figure shows the dependence of  $V_{pl}$  on the electrode width. The voltage goes down as the width increases, and for  $W_e = 22$   $\mu\text{m}$  it equals to 107 V. Further expansion may create a significant torque tending to rotate the cantilever around its axis. It may touch the driving electrode, and short circuit may occur. Therefore,  $W_e$  is limited to 22  $\mu\text{m}$ .

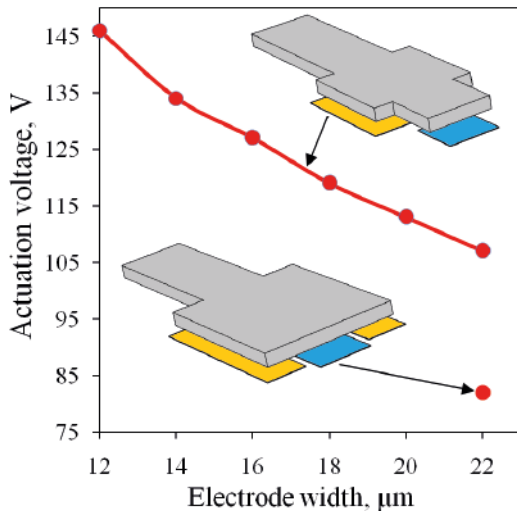


Fig. 2. Dependence of the actuation voltage on the width of the driving electrode

The actuation voltage of 107 V is still quite high and requires further reduction, which is achieved by extending the driving electrode towards the free end of the cantilever. The driving electrode goes around the signal one, as shown in the bottom inset of Fig. 2. The length of the electrode increases to  $L_e = 26$   $\mu\text{m}$ , and the actuation voltage decreases to 82 V. This value is acceptable, since it can be provided by a charge pump of the integrated driver [12].

Design optimization changes the switching time. According to expressions (3)–(5), the classical cantilever has a resonance frequency of 667 kHz. FEM simulation provides a close value of 664 kHz. The switch with widened electrode has the frequency of 567 kHz, while the design with widened and extended electrode



exhibits  $f_0 = 481$  kHz. The decrease in  $f_0$  is explained by the growing effective mass of the cantilever and is accompanied by the increase of the switching time. At  $V_D = V_{PI}$  the switch goes to the “on” state for 0.88, 1.03 and 1.21  $\mu\text{s}$ , respectively. However, this change is not significant. The switching time remains in the microsecond range, which is typical for a MEMS switches.

The contact force is calculated using a specially created model in which the cantilever is initially brought in contact with the signal electrode. The contact bump is a platinum cylinder of 0.5  $\mu\text{m}$  in height and 0.5  $\mu\text{m}$  in radius. The base of the cylinder is set in contact with the electrode. Since the cantilever originally has a deformed shape, it does not develop the elastic force. This force is introduced in the model according to the analytical calculations.

The dependences of the contact force on the driving voltage for three types of switches are shown in Fig. 3. Each curve is built in the range from  $V_{PI}$  to the “second pull-in” voltage, at which the cantilever touches the driving electrode. For the classic switch, this voltage equals to 357 V, while the other designs demonstrate 291 and 284 V.

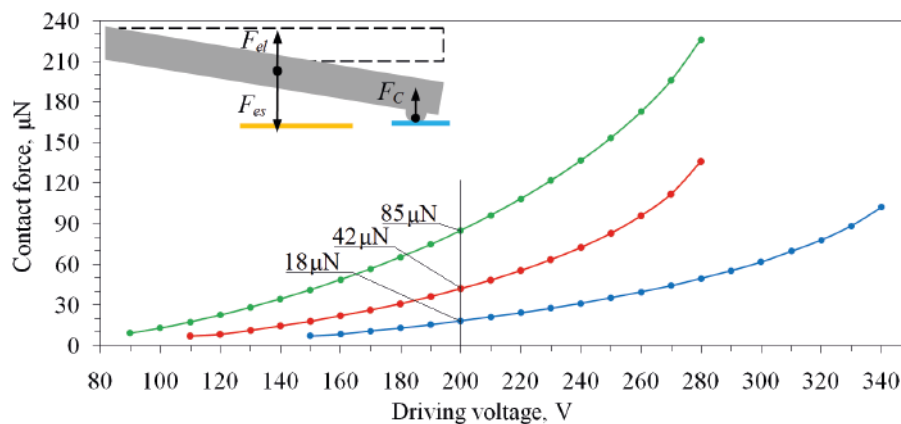


Fig. 3. Dependence of the contact force on the driving voltage. Blue color indicates the values for the classic version, while red color corresponds to the switch with the widened electrode, and the values for the switch with the widened and extended electrode are shown by green color

All the structures demonstrate the rise of the contact force with  $V_D$  due to the increase in the electrostatic force. However, the optimized switches exhibit significantly higher  $F_C$  compared to the classic design. At  $V_D = 200$  V, the contact force equals to 18, 42 and 85  $\mu\text{N}$ , respectively. This fact is explained by the increase in the overlap area between the electrode and the cantilever during optimization. The rise of  $F_C$  has a positive effect on the operation of the switch, since the contact resistance  $R$  decreases with the force according to the law  $R \sim F_C^{-1/3}$ . It is important to note that the elastic force remains unchanged ( $F_{el} = 16$   $\mu\text{N}$ ), since the bending part of the cantilever is located close to the fixed end and does not change size. Therefore, optimization of the electrode shape does not increase the probability of stiction.

### Conclusions

The paper considers an electrostatic MEMS switch based on the 50  $\mu\text{m}$  long and 2  $\mu\text{m}$  thick aluminum cantilever. Optimization of the electrode shape reduces its actuation voltage from 146 to 82 V. The switching time increases insignificantly and remains in the microsecond range. On the contrary, the contact force increases several times due to the increase in the working area of the electrostatic force. This change is considered positive because it should reduce the contact resistance. The optimization does not affect the restoring force and does not deteriorate the device performance.

### REFERENCES

1. Rebeiz G. M., Patel C. D., Han S. K., Ko C. H., Ho K. M. J., The search for a reliable MEMS switch. IEEE Microwave Magazine, 14(1) (2013) 57–67.

2. **Dai C. L., Chen J. H.**, Low voltage actuated RF micromechanical switches fabricated using CMOS-MEMS technique, *Microsystem Technologies*. 12(12) (2006) 1143–1151.
3. **Zheng W. B., Huang Q. A., Liao X. P., Li F. X.**, RF MEMS membrane switches on GaAs substrates for X-band applications, *Journal of Microelectromechanical Systems*. 14(3) (2005) 464–471.
4. **Zhang X., Adelegan O. J., Yamaner F. Y., Oralkan O.**, A fast-switching (1.35- $\mu$ s) low-control-voltage (2.5-V) MEMS T/R switch monolithically integrated with a capacitive micromachined ultrasonic transducer, *Journal of Microelectromechanical Systems*. 27 (2) (2018) 190–200.
5. **Shekhar S., Vinoy K. J., Ananthasuresh G. K.**, Low-voltage high-reliability MEMS switch for millimeter wave 5G applications, *Journal of Micromechanics and Microengineering*. 28 (2018) 075012.
6. Haupt R. L., Lanagan M., *Reconfigurable antennas*, *IEEE Antennas and Propagation Magazine*. 55 (1) (2013) 49–61.
7. **Haider N., Caratelli D., Yarovoy A. G.**, Recent developments in reconfigurable and multiband antenna technology, *International Journal of Antennas and Propagation*. 2013(10) (2013) 869170.
8. **Daneshmand M., Mansour R. R.**, RF MEMS satellite switch matrices, *IEEE Microwave Magazine*. 12 (5) (2011) 92–109.
9. **Rebeiz G. M.**, *RF MEMS: Theory, Design, and Technology*, Hoboken, New Jersey: John Wiley & Sons, 2003.
10. **Patel C. D., Rebeiz G. M.**, RF MEMS Metal-Contact Switches With mN-Contact and Restoring Forces and Low Process Sensitivity, *IEEE Transactions on Microwave Theory and Techniques*. 59 (5) (2011) 1230–1237.
11. **Bhushan B.**, *Handbook of Micro/Nanotribology*, CRC press, 1999.
12. **Goggin R., Fitzgerald P., Stenson B., Carty E., McDaid P.**, Commercialization of a reliable RF MEMS switch with integrated driver circuitry in a miniature QFN package for RF instrumentation applications, *IEEE MTT-S International Microwave Symposium*. (2015) ISBN:978-1-4799-8275-2.

#### THE AUTHORS

**BELOZEROV Igor A.**

igas2580@yandex.ru

ORCID: 0000-0001-5620-0608

**UVAROV Ilia V.**

i.v.uvarov@bk.ru

ORCID: 0000-0002-6882-0625

*Received 14.07.2022. Approved after reviewing 17.07.2022. Accepted 18.07.2022.*

Conference materials

UDC 621.383

DOI: <https://doi.org/10.18721/JPM.153.227>

## Fabrication and investigation of UV photodiode based on *n*-GaN / *p*-NiO heterojunction

A. N. Kazakin<sup>1,2</sup> ✉, Ya. B. Enns<sup>1,2</sup>, A.V. Uvarov<sup>1</sup>, E. V. Nikitina<sup>1</sup>

<sup>1</sup> Alferov University, St. Petersburg, Russia;

<sup>2</sup> Peter the Great Saint-Petersburg Polytechnic University, St. Petersburg, Russia

✉ [kazakin75@gmail.com](mailto:kazakin75@gmail.com)

**Abstract.** This paper presents the experimental results of the study of *n*-GaN/*p*-NiO heterojunction for application as a selective UV photodetector. Synthesis of *n*-type GaN layers was carried out by plasma-assisted molecular beam epitaxy (PA MBE) on GaN/c-Al<sub>2</sub>O<sub>3</sub> template substrates. The *p*-type layers were formed by reactive DC magnetron sputtering of NiO films followed by annealing. Post-annealing in an oxygen atmosphere at a temperature of 550 °C was used to improve the crystallinity of the deposited NiO films. The optical and electrical characteristics of individual semiconductor layers and *n*-GaN/*p*-NiO diode structure were studied. Photoluminescence spectra of GaN layers showed the presence of a narrow peak near 3.43 eV. The optical band gap of the NiO layers, determined by the edge of optical absorption, was 3.35 eV. The study of the *n*-GaN/*p*-NiO heterojunction current-voltage characteristics under light and dark conditions showed the selective sensitivity of the diode structure to UV radiation. Furthermore, the manufactured structure demonstrated the behavior of a self-powered photodiode. At a wavelength of 365 nm, the detectivity of the photodiode was  $6.8 \cdot 10^9$  Jones and the photoresponsivity was 3.64 mA/W.

**Keywords:** UV photodiode, gallium nitride, oxide semiconductors, DC magnetron sputtering, molecular beam epitaxy

**Funding:** The work was supported by the Ministry of Education and Science (grant №FSRM-2020-0008).

**Citation:** Kazakin A. N., Enns Ya. B., Uvarov A. V., Nikitina E. V., Fabrication and investigation of UV photodiode based ON *n*-GaN / *p*-NiO heterojunction, St. Petersburg State Polytechnical University Journal. Physics and Mathematics. 15 (3.2) (2022) 145–149. DOI: <https://doi.org/10.18721/JPM.153.227>

This is an open access article under the CC BY-NC 4.0 license (<https://creativecommons.org/licenses/by-nc/4.0/>)

Материалы конференции

УДК 621.383

DOI: <https://doi.org/10.18721/JPM.153.227>

## Изготовление и исследование УФ – фотодиода на основе гетероперехода *n*-GaN/*p*-NiO

А. Н. Казакин<sup>1,2</sup> ✉, Я. Б. Эннс<sup>1,2</sup>, А. В. Уваров<sup>1</sup>, Е. В. Никитина<sup>1</sup>

<sup>1</sup> Алферовский университет, Санкт-Петербург, Россия;

<sup>2</sup> Санкт-Петербургский политехнический университет, Санкт-Петербург, Россия

✉ [kazakin75@gmail.com](mailto:kazakin75@gmail.com)

**Аннотация.** В данной работе представлены экспериментальные результаты исследования гетероперехода *n*-GaN/*p*-NiO для УФ фотодиода. Синтез монокристаллических пленок нитрида галлия *n*-типа проводимости осуществлялся методом молекулярно-лучевой эпитаксии с плазменной активацией азотом на темплатных подложках GaN/c-Al<sub>2</sub>O<sub>3</sub>. Слои *p*-типа проводимости формировались методом реактивного магнетронного напыления на постоянном токе пленок полупроводникового оксида никеля. Последующий отжиг в кислородной среде при 550 °C использовался для улучшения кристалличности

осажденных пленок NiO. Проведены исследования оптических и электрических характеристик отдельных полупроводниковых слоев и диодных структур на их основе. Спектральная зависимость фотолюминесценции GaN показала наличие узкого пика в области энергии 3.43 эВ. Оптическая ширина запрещенной зоны NiO, измеренная по краю оптического поглощения, составила 3.35 эВ. Исследование вольт-амперных характеристик *n*-GaN/*p*-NiO гетероперехода при его облучении светом в видимой и ультрафиолетовой области спектра показало избирательную чувствительность фотодиодной структуры к УФ излучению. При этом изготовленная структура продемонстрировала работу в режиме фотоэлемента. На длине волны 365 нм удельная обнаружительная способность гетероструктуры составила  $6.8 \cdot 10^9 \text{ см} \cdot \text{Гц}^{0.5} \cdot \text{Вт}^{-1}$ , а величина фоточувствительности составила 3.64 мА/Вт.

**Ключевые слова:** УФ-фотодиод, нитрид галлия, оксидные полупроводники, магнетронное напыление на постоянном токе, молекулярно-лучевая эпитаксия

**Финансирование:** Работа выполнена в рамках Государственного задания (код темы [№FSRM-2020-0008]).

**Ссылка при цитировании:** Казакин А. Н., Эннс Я. Б., Уваров А. В., Никитина Е. В. Изготовление и исследование УФ – фотодиода на основе гетероперехода *n*-GaN/*p*-NiO // Научно-технические ведомости СПбГПУ. Физико-математические науки. 2022. Т. 15. № 3.2. С. 145–149. DOI: <https://doi.org/10.18721/JPM.153.227>

Статья открытого доступа, распространяемая по лицензии CC BY-NC 4.0 (<https://creativecommons.org/licenses/by-nc/4.0/>)

## Introduction

Improvement in technologies for the epitaxial growth of gallium nitride (GaN) contributed to the successful application of this material in high-frequency electronics and optoelectronic devices, such as light-emitting diodes and lasers [1, 2]. In addition, the high band gap of GaN makes this material promising for the development of selective UV photodetectors (wavelength  $\lambda < 400 \text{ nm}$ ). To create such devices, various photodiode structures based on homo- or heterojunctions can be used [3, 4]. However, due to numerous technological difficulties that arise during the synthesis of high-quality *p*-type GaN epitaxial layers [5], the use of homojunctions for UV photodiodes is less preferable compared to heterojunctions based on *n*-type GaN and another wide-gap *p*-type semiconductor. Among various *p*-type materials, nickel oxide (NiO) is most compatible with GaN in terms of such parameters as band gap and lattice parameter [6]. In addition, NiO is a direct gap semiconductor, has excellent chemical stability, and is easy to deposit with current microelectronics technologies. Therefore, the *n*-GaN/*p*-NiO heterostructure can be used in the future to create cheap and efficient UV photodiodes.

In this work, we analyze the possibility of creating a selective UV photodetector based on the *n*-GaN/*p*-NiO heterojunction.

## Materials and Methods

The design of the manufactured photosensitive sample is a planar structure with layers of GaN and NiO, which form a heterojunction, and metal layers, which form contact pads. Figure 1 shows the test sample design and the stages of fabrication process.

The synthesis of GaN layers was carried out on a Veeco Gen 200 industrial equipment by the PA MBE method [7]. The growth of the epitaxial layer was carried out on GaN/c-Al<sub>2</sub>O<sub>3</sub> template substrates, where 2 μm thick GaN sublayer was obtained by metal-organic vapor phase epitaxy. The subsequent growth of Si-doped GaN layers was carried out at constant substrate temperatures  $T_s = 700^\circ\text{C}$ , a gallium flow of ~0.25 μm/h, and an activated nitrogen flow of ~0.05 μm/h. The silicon doping used in the experiments made it possible to obtain an electron concentration in the GaN layers of  $\sim 3.7 \times 10^{18} \text{ cm}^{-2}$ .

The formation of NiO films was carried out using DC magnetron sputtering from a nickel target Ni (99.95%) in a mixture of working gases 30% O<sub>2</sub> / 70% Ar at a working pressure of 3 mTorr and magnetron power of 100 W. The deposition was carried out both on the surface of

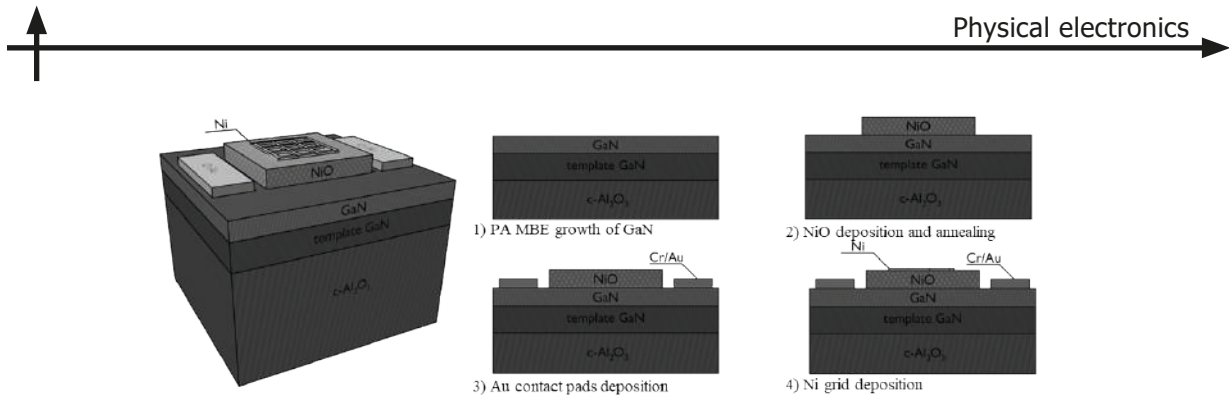


Fig. 1. Design and process flow of  $n$ -GaN/ $p$ -NiO photodetector

the GaN epitaxial film and on the glass (Corning 0211) for optical and electrical measurements of the obtained layer. Film thicknesses were determined using an Ambios XP-1 contact profilometer. Subsequent annealing of the NiO films at a temperature of 550°C and duration of 60 min was applied to improve the films quality, increase the resistivity and optical transmission of the films.

To form non-rectifying (ohmic) contacts, Cr/Au and Ni layers were used for contact to GaN and NiO, respectively. Contact metallization to the NiO layer was made in the form of a grid structure with an aperture of 3 mm, where the width of the grid band was 5  $\mu\text{m}$  with a period of 100  $\mu\text{m}$ .

In this work, optical transmission and reflection spectra of GaN and NiO layers were obtained using an AvaSpec-ULS2048XL-EVO-RS spectrometer and a xenon radiation source. The photoluminescence (PL) spectra of the structures were measured using an Accent RPM Sigma setup with 266 nm lasers. Based on the measurement results, the values of the optical band gap for semiconductor layers were obtained.

Measurement of dark and light current-voltage characteristics was carried out using a halogen radiation source and UV LEDs with a wavelength of 365 nm. The power density of the incident light of the UV LEDs (365 nm) was 2.3 mW.

## Results and Discussion

The thickness of the high-doped epitaxial GaN layers, measured using scanning electron microscopy, was about 300 nm. A detailed study of the morphology of the surface, composition and inner structure of the synthesized GaN layers is given in the article [7]. The epitaxial GaN layers on a sapphire substrate had a high transparency in the visible part of the spectrum, more than 90%. However, the spectral characteristics in the UV region showed a sharp drop in transmittance at a wavelength of 400 nm. This drop in transmission is probably due to the absorption of radiation by the substrate, which does not allow measurements to be made near the edge of GaN optical absorption. Figure 2, *a* shows the results of measuring the photoluminescence spectra of the synthesized layers. The main peak of photoluminescence lies near the energy of 3.43 eV and has an FWHM equal to 0.097 eV, as shown in the inset in figure 2, *a*.

The thickness of the NiO layer was about 300 nm. The as-deposited NiO films had high conductivity and low transparency. The resistivity of the film was 0.04  $\Omega\cdot\text{cm}$ . At the same time, the optical transmission of the film did not exceed 5%, as shown in figure 2, *b*. Subsequent annealing of the films at a temperature of 550°C and duration of 60 min led to an increase in the resistivity and optical transmission of the film. Figure 2, *b* shows that after annealing, the transmission of the film increased to 80% and has a sharp absorption edge. The optical band gap of NiO was 3.35 eV, as shown in the inset in figure 2, *b*. The value of film resistivity after annealing was 1460  $\Omega\cdot\text{cm}$ . An increase in the transparency and resistivity of NiO films after high-temperature annealing is due to a decrease in the concentration of intrinsic defects, which play the role of an acceptor impurity (nickel vacancies and interstitial oxygen atoms).

The current-voltage characteristics of  $n$ -GaN/ $p$ -NiO heterojunctions had the form of typical diode dependences, as shown in figure 3. Exposure of the samples to radiation in the visible region of the spectrum did not lead to a change in electrical characteristics. However, when the samples were irradiated with an LED with a wavelength of 365 nm, a shift of the I-V characteristic due to the occurrence of a photocurrent was recorded. Furthermore, the  $n$ -GaN/ $p$ -NiO heterojunction demonstrated the behavior of a self-powered photodiode. The dark current and photocurrent

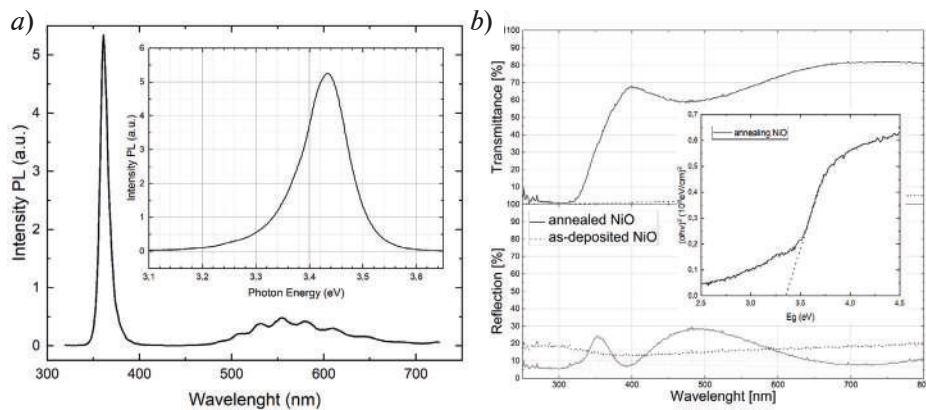


Fig. 2. Photoluminescence spectra of GaN (a); NiO optical transmittance, reflection spectra and (inset) the plot of  $(ahv)^2$  versus photon energy  $hv$  (b)

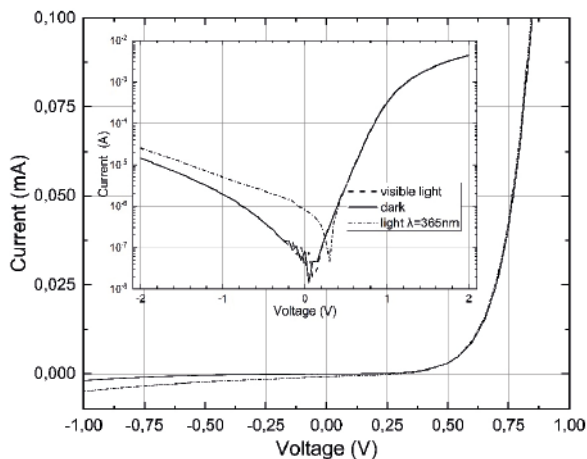


Fig. 3. I-V plot of the NiO/GaN photodetector on a linear scale and (inset) on a semi-log scale

can be calculated as in the article [8]. The photoresponsivity of the fabricated  $n$ -GaN/ $p$ -NiO photodetector at zero voltage was 3.64 mA/W, its detectivity was  $6.8 \cdot 10^9$  Jones.

were 0.08  $\mu\text{A}$  and 0.84  $\mu\text{A}$ , respectively. Open-circuit voltage was 0.29 V. (It is worth noting that even in the dark condition, a slight open-circuit voltage was also observed. Its value was about 0.05 V and changed slightly for different samples, which may be due to the presence of a built-in charge at the boundary of the GaN and NiO layers or the excess of the depletion region width over the NiO layer thickness.)

To quantify the sensitivity of our UV PDs compared to other ones, we used parameters such as photoresponsivity and detectivity. Photoresponsivity is defined as the photocurrent generated per unit power of incident light on the effective area of a photodiode. Detectivity ( $D^*$ ) of a UV PD is another parameter, meaning its ability to detect weak signals from noise environment. Both of these parameters

### Conclusion

In summary, we fabricated self-powered photodetector based on  $n$ -GaN/ $p$ -NiO heterojunction structure on  $c\text{-Al}_2\text{O}_3$  substrate. The photodetector exhibits a responsivity of 3.64 mA/W and detectivity of  $6.8 \cdot 10^9$  Jones, when exposed to a light with a wavelength of 365 nm at zero voltage. The NiO film as a  $p$ -type semiconductor layer for GaN-based diode was synthesized by a simple, scalable, and low-cost method. The study of the diode current-voltage characteristics under light and dark conditions showed the selective sensitivity of the diode structure to UV radiation. These results demonstrate the high quality of NiO/GaN heterojunction diodes and its great potential for future GaN based power electronics.

### Acknowledgments

The work was supported by the Ministry of Education and Science (grant №FSRM-2020-0008).

### REFERENCES

1. Wasisto H. S., Prades J. D., Głink J., Waag A., Beyond solid-state lighting: Miniaturization, hybrid integration, and applications of GaN nano- and micro-LEDs, Applied Physics Reviews. 6 (4) (2019) 041315–40.



2. Ueda T., GaN power devices: current status and future challenges, *Japanese Journal of Applied Physics*. 58 (2019), 0804–9.
3. Lee C. R., Seol K. W., Yeon J. M., Choi D. K., Ahn H. K., The effect of *p*-GaN: Mg layers on the turn-on voltage of *p*-*n* junction LED, *J. Cryst. Growth*. 222 (2001) 459–64.
4. Alivov Y. I., Van Nostrand J. E., Look D. C., Chukichev M. V., Ataev B. M., Observation of 430 nm electroluminescence from ZnO/GaN heterojunction light-emitting diodes, *Applied Physics Letters*. 83 (2003) 2943–5.
5. Enatsu Y., Gupta C., Keller S., Nakamura S., Mishra U.K., *P*-*n* junction diodes with polarization induced *p*-type graded in  $x$  Ga $_{1-x}$ N layer, *Semiconductor Science and Technology*. 32 (2017) 1–6.
6. Irwin M. D., Buchholz D. B., Hains A. W., Chang R. P. H., Marks T. J., *p*-type semiconducting nickel oxide as an efficiency-enhancing anode interfacial layer in polymer bulk-heterojunction solar cells, *Proc. Natl. Acad. Sci.* 105 (2008) 2783–7.
7. Mizerov A. M., Timoshnev S. N., Nikitina E. V., Sobolev M. S., Shubin K. Yu., Berezovskaia T.N., Mokhov D. V., Lundin W. V., Nikolaev A. E., Bouravlev A. D., On the Specific Features of the Plasma-Assisted MBE Synthesis of  $n \pm$  GaN Layers on GaN/*c*-Al $_2$ O $_3$  Templates, *Semiconductors*. 53(9) (2019) 1187–91.
8. Pansri S., Supruangnet R., Nakajima H., Rattanasuporn S., Noothongkaew S., Band offset determination of *p*-NiO/*n*-TiO $_2$  heterojunctions for applications in high-performance UV photodetectors, *Journal of Materials Science*. 55 (2020) 4332–44.

#### THE AUTHORS

**KAZAKIN Alexei N.**  
kazakin75@gmail.com  
ORCID: 0000-0001-8762-1587

**UVAROV Alexander V.**  
lumenlight@mail.ru  
ORCID: 0000-0002-0061-6687

**ENNS Yakov B.**  
ennsjb@gmail.com  
ORCID: 0000-0003-4396-2368

**NIKITINA Ekaterina V.**  
mail.nikitina@mail.ru  
ORCID: 0000-0002-6800-9218

*Received 22.07.2022. Approved after reviewing 25.07.2022. Accepted 27.07.2022.*

Conference materials

UDC 621.315.592.3

DOI: <https://doi.org/10.18721/JPM.153.228>

## Study of recombination and transport properties of a-Si:H(i)/ $\mu$ c-Si:H(n) contact system for crystalline silicon solar cells

A. V. Uvarov<sup>1,2</sup> ✉, A. I. Baranov<sup>1,2</sup>, A. A. Maksimova<sup>1,2</sup>,  
E. A. Vyacheslavova<sup>1,2</sup>, A. S. Gudovskikh<sup>1,2</sup>

<sup>1</sup> St. Petersburg Academic University of the Russian Academy of Sciences, Saint-Petersburg, Russia;

<sup>2</sup> St. Petersburg Electrotechnical University "LETI", Saint-Petersburg, Russia

✉ [lumenlight@mail.ru](mailto:lumenlight@mail.ru)

**Abstract.** This article is devoted to the study of the contact and recombination properties of the combination of a-Si:H(i)/ $\mu$ c-Si:H(n) layers. Numerical modeling of the band diagram as well as experimental study of the contact system with a silicon substrate has been carried out. The optimal values of the thicknesses of the contact layers are determined, which make it possible to obtain a low rate of carrier recombination and contact resistance.

**Keywords:** solar cells, silicon, amorphous silicon, effective lifetime

**Funding:** This work was supported by Ministry of Science and Higher Education of the Russian Federation (research project 0791-2020-0004).

**Citation:** Uvarov A. V., Baranov A. I., Maksimova A. A., Vyacheslavova E. A., Gudovskikh A. S., Study of recombination and transport properties of a-Si:H(i)/ $\mu$ c-Si:H(n) contact system for crystalline silicon solar cells, St. Petersburg State Polytechnical University Journal. Physics and Mathematics. 15 (3.2) (2022) 150–154. DOI: <https://doi.org/10.18721/JPM.153.228>

This is an open access article under the CC BY-NC 4.0 license (<https://creativecommons.org/licenses/by-nc/4.0/>)

Материалы конференции

УДК 621.315.592.3

DOI: <https://doi.org/10.18721/JPM.153.228>

## Исследование транспортных и рекомбинационных свойств контактной системы a-Si:H(i)/ $\mu$ c-Si:H(n) для фотоэлектрических преобразователей на основе кремния

A. V. Uvarov<sup>1,2</sup> ✉, A. I. Baranov<sup>1,2</sup>, A. A. Maksimova<sup>1,2</sup>,  
E. A. Vyacheslavova<sup>1,2</sup>, A. S. Gudovskikh<sup>1,2</sup>

<sup>1</sup> Санкт-Петербургский Академический университет - научно-образовательный центр нанотехнологий РАН, Санкт-Петербург, Россия;

<sup>2</sup> Санкт-Петербургский государственный электротехнический университет «ЛЭТИ» им. В.И. Ульянова (Ленина), Санкт-Петербург, Россия

✉ [lumenlight@mail.ru](mailto:lumenlight@mail.ru)

**Аннотация.** Данная статья посвящена исследованию контактных и рекомбинационных свойств комбинации слоев a-Si:H(i)/ $\mu$ c-Si:H(n) на подложках кристаллического кремния. Проведено численное моделирование зонной диаграммы, а также экспериментальное исследование транспортных свойств на кремниевой подложке. Определены оптимальные значения толщин контактных слоев, позволяющие получить низкую скорость рекомбинации носителей и контактное сопротивление.

**Ключевые слова:** фотоэлектрические преобразователи, кремний, аморфный кремний

**Финансирование:** This work was supported by Ministry of Science and Higher Education of the Russian Federation (research project 0791-2020-0004).



**Ссылка при цитировании:** Уваров А. В., Баранов А. И., Максимова А. А., Вячеславова Е. А., Гудовских А. С. Исследование транспортных и рекомбинационных свойств контактной системы a-Si:H(i)/  $\mu$ c-Si:H(n) для фотоэлектрических преобразователей на основе кремния // Научно-технические ведомости СПбГПУ. Физико-математические науки. 2022. Т. 15. № 3.2. С. 150–154. DOI: <https://doi.org/10.18721/JPM.153.228>

Статья открытого доступа, распространяемая по лицензии CC BY-NC 4.0 (<https://creativecommons.org/licenses/by-nc/4.0/>)

### Introduction

Silicon-based solar photovoltaic converters are an asymmetric diode structure with a heavily doped emitter and a lightly doped base. When such a structure is irradiated with optical radiation with a photon energy greater than the band gap of the base material, electron-hole pairs appear, which are separated by the field of the  $p$ - $n$  junction. However, the reverse process of recombination of electron-hole pairs also takes place, which occurs most intensively in the presence of defects in the volume and at the boundaries of the silicon substrate. This process leads to the transition of the energy of the absorbed radiation into heat losses. To reduce surface recombination, it is necessary to apply special passivating layers during the formation of contact and emitter layers of a solar cell. The contact to the silicon substrate should have a low specific contact resistance and good surface passivation. The quality of surface passivation is determined by the effective lifetime  $\tau_{\text{eff}}$  of nonequilibrium charge carriers by the limited rate of bulk and surface recombination [1]. To form contact layers to a silicon substrate, there are many contact systems that differ in the quality of passivation and specific contact resistance  $\rho_{\text{cont}}$ .

Table 1

**Typical parameters of different contact systems to  $n$ -type crystalline silicon**

	$J_{\text{rec}}$ , fA/cm <sup>2</sup>	$\rho_{\text{cont}}$ , $\Omega \cdot \text{cm}^2$	Ref.
P-diffused $n^+$	500	0.26	[2]
a-Si:H(i)/a-Si:H(n)	2	0.1	[3]
SiO <sub>x</sub> /poly-Si $n^+$	5	0.016	[4]
SiO <sub>x</sub> /TiO <sub>2</sub>	50	0.026	[5]
MgF <sub>x</sub> ( 1nm)/Al	1500	0.035	[6]

In this work, we study the a-Si:H(i)/ $\mu$ c-Si:H(n) contact system, which is characterized by the lowest recombination current at acceptable values of contact resistance.

### Materials and Methods

To study the specific contact resistance and recombination rate of nonequilibrium charge carriers contacts with different configurations of a-Si:H(i) and  $\mu$ c-Si:H(n) layers were deposited on  $n$ -type Si substrates by plasma-enhanced chemical vapor deposition at the temperature of 250 °C. We used phosphorus doped silicon substrates produced by the Czochralski method with a thickness of 380  $\mu$ m and resistivity 5 – 10  $\Omega \cdot \text{cm}$ . Monosilane (SiH<sub>4</sub>) and hydrogen (H<sub>2</sub>, 6N) gases were used as precursors in the deposition of a-Si:H and  $\mu$ c-Si:H. The  $\mu$ c-Si:H layers were doped with a donor impurity diluted with 1% phosphine (PH<sub>3</sub>) in hydrogen. Immediately prior to loading in the PECVD chamber, the substrates were treated in a 10% HF/H<sub>2</sub>O solution to remove natural oxide. Next, the vacuum chamber was evacuated to a residual pressure of <0.5 mTorr and heated to an operating temperature of 250 °C for 20 min. The a-Si:H deposition process was carried out from pure SiH<sub>4</sub> at a constant pressure of 350 mTorr and an RF power density of

11 mW/cm<sup>2</sup> at a rate of 8 nm/min. Immediately after that, a  $\mu\text{-Si:H}$  layer was deposited from a  $\text{SiH}_4(2\%)/\text{PH}_3(0.25\%)/\text{H}_2(97.75\%)$  gas mixture at a constant pressure of 700 mTorr and a power density of 11 mW/cm<sup>2</sup> at a rate of 1 nm/min. After cooling and removal from the PECVD chamber, all the described operations were repeated to form contact layers on the reverse side of the substrate. In this study, it is assumed that in this contact system there are no fixed charges inherent in dielectrics and, therefore, there is no drop in the effective lifetime at concentrations of non-equilibrium carriers less than  $10^{15} \text{ cm}^{-3}$  [7,8]. A 100 nm thick ITO layer in the form of TLM test contacts was deposited onto the structures obtained by magnetron sputtering. To do this, the samples were also treated in a 10% HF/H<sub>2</sub>O solution before being loaded into the BOC Edwards Auto 500 chamber. Then, for 40 min, pumping was carried out to a residual pressure of  $8 \cdot 10^{-6}$  mbar, while the temperature of the substrates remained at room temperature. ITO deposition was carried out using a magnetron sputtering system with an ITO target in an Ar/O<sub>2</sub> atmosphere at a pressure of  $1.24 \cdot 10^{-3}$  mbar and an RF source power of 65 W. To determine the contact resistance, a linear TLM method was used, consisting of 7 ITO contacts in the form of identical rectangular strips 5 mm wide and 0.96 mm long located in series at distances of 0.24  $\mu\text{m}$ , 0.46 mm, 0.85 mm, 1.66 mm, 3.25mm, 6.5mm apart. The I–V characteristics were measured in pairs between each two nearby contacts and the resistance  $R = R_s + 2R_c$  was determined, where  $R_s$  is the substrate resistance, and  $R_c$  is the contact resistance. Further, according to the obtained dependences of the resistance  $R$  on the distance between the contacts, the values of the specific contact resistance were determined. To evaluate the band structure of the contacts, numerical simulation was carried out using the Afors-HET 2.4.1 software package.

### Results and Discussion

The effective lifetime of nonequilibrium charge carriers in the obtained structures was studied using the photoluminescence decay (PLD) method. Based on the results of the study, a map of the lifetime distribution over the substrate surface was formed (Fig. 1).

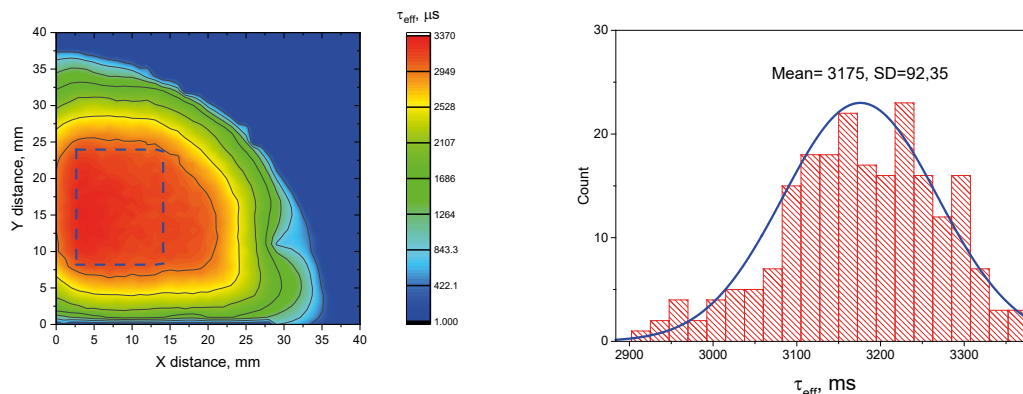


Fig. 1. The distribution of the effective lifetime over the surface and the histogram of the distribution of the effective lifetime in the "plateau" region

On the structures obtained, the lifetime is distributed inhomogeneously. A pronounced “plateau” is observed in the middle of the sample, which indicates a strong influence of the edges, especially at values greater than 1000  $\mu\text{s}$ . The decrease in the effective lifetime at the edges can be associated either with a higher concentration of defects at the edges, or with the inhomogeneity of the plasma-chemical deposition process. The size of the rims is 7 – 12 mm. A detailed analysis of the lifetime distribution over the surface in the "plateau" region showed that the average value is 3175  $\mu\text{s}$  with a standard deviation of 92.3  $\mu\text{s}$ . This indicates the high uniformity of the layers and the absence of contamination at the stages of preparation and plasma-chemical deposition.

The I–V characteristics of a-Si:H(i)/ $\mu\text{-Si:H}$ (n) contacts with different configurations of a-Si:H(i) contact layers were studied. The characteristics of the obtained contacts with the a-Si:H layer (i) have a nonlinear form, however, the values of the current density allow us to speak about the formation of a contact close to ohmic (Fig. 2.).



Table 2

**Transport and recombination properties of a-Si:H(i)/ $\mu$ c-Si:H(n) contacts with different thickness of i-layer**

	$\rho_{\text{cont}}, \Omega \cdot \text{cm}^2$	$\tau_{\text{eff max}}, \mu\text{s}$	S, cm/s	$J_o, \text{fA/cm}^2$
$\mu$ c-Si:H 10 nm	1.51	20	948.1	10450.4
a-Si:H 2.5 nm / $\mu$ c-Si:H 10 nm	4.42	3250	3.9	43.5
a-Si:H 5 nm / $\mu$ c-Si:H 10 nm	6.26	3450	3.6	39.7

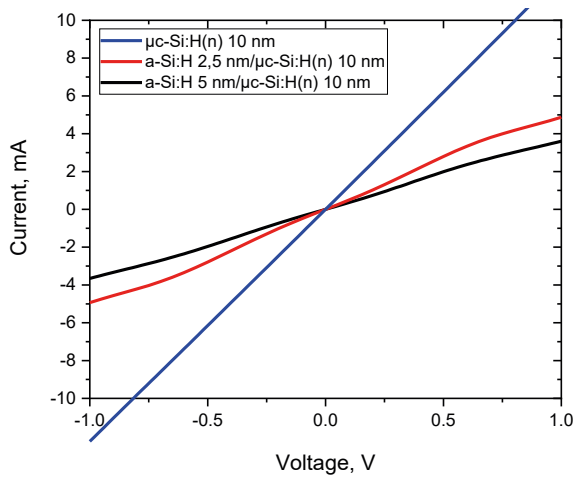


Fig. 2. I-V curve of a-Si:H(i)/ $\mu$ c-Si:H(n) contact system with different a-Si:H(i) layer thickness

It was noted that changing the thickness of the a-Si:H(i) layer from 5 nm to 2.5 nm led to a decrease in the contact resistance. At the same time, the I-V shape remained nonlinear with a distinct inflection at voltages of 0.5–0.7 V. It follows that the contact resistance is due to the formation of a barrier at the a-Si:H(i)/n-Si interface, and the value of this barrier depends on the thickness of the a-Si:H(i).

To explain the reason for the formation of a barrier at the a-Si:H(i)/n-Si interface, numerical simulation of the structure was carried out using the Afors-HET 2.5 software package (Fig. 3). This model shows the effect of the thickness of the a-Si:H(i) layer on the shape of the I V curve at a fixed concentration of dangling bonds.

It was noted that a high concentration of dangling Ndb bonds in the i layer (insufficient hydrogenation) can lead to screening of the n contact and the formation of a barrier in the substrate. A similar situation occurs when the degree of doping of the n-layer is less than the concentration of defects in the i-layer.

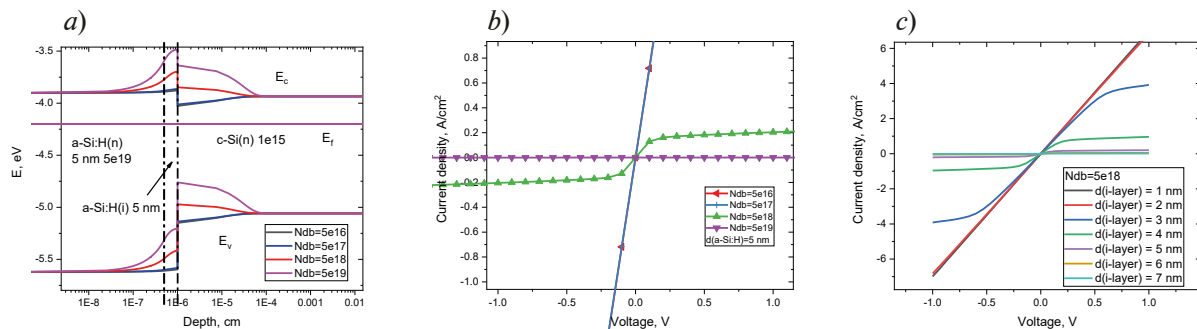


Fig. 3. Calculated band diagrams with different concentrations of defects in the a-Si:H(i) layer (a). I-V curves of structures with different concentrations of defects in a-Si:H(i) layers at a fixed thickness (b), and different thicknesses of an i-layer (c) at a fixed defect concentration.

Only in this case is the dependence of the contact resistance on the thickness of the i-layer observed. At small thicknesses, the n-layer works and the substrate is enriched with carriers. Pronounced S-shape may not appear in the presence of series resistance ( $R_{\text{substrate}}$ ). This model shows the effect of the thickness of the a-Si:H(i) layer on the shape of the I-V curve at a fixed concentration of dangling bonds. The characteristic S-shape appears at voltages of 0.2–0.7 V and i-layer thicknesses of 3 – 4 nm, which coincides with the values obtained in the experiment.

### Conclusion

The effect of the layer thickness in the a-Si:H(i)/a-Si:H(n) system on the contact and recombination parameters of the obtained structures was evaluated. It was noted that at a distance of 7–12 mm from the edges of the substrate, a decrease in the effective lifetime is observed. The maximum effective lifetime of nonequilibrium charge carriers in a substrate with a-Si:H 2.5 nm/ $\mu\text{c-Si:H}$  10nm contacts is 3250  $\mu\text{s}$ , which is close to the value of the volume lifetime for these silicon substrates. Passivating contact layers were formed to crystalline silicon substrates with a minimum resistivity of 4.42  $\Omega\cdot\text{cm}^2$ . It was shown that a high concentration of dangling bonds in the i-layer (insufficient hydrogenation) can lead to electric-field screening of the n-contact and the formation of a barrier in the substrate, which significantly increases the specific contact resistance. These results can be used in the formation of highly efficient photovoltaic converters based on amorphous and crystalline silicon.

### Acknowledgments

This work was supported by Ministry of Science and Higher Education of the Russian Federation (research project 0791-2020-0004)

### REFERENCES

1. Richter S., Glunz W., Werner F., Schmidt J., Cuevas A., Improved quantitative description of Auger recombination in crystalline silicon, *Physical Review B*. 86 (16), (2012).
2. Brendel R., Peibst R., Contact Selectivity and Efficiency in Crystalline Silicon Photovoltaics, *IEEE Journal of Photovoltaics*. 6 (6) (2016) 1413–1420.
3. Herasimenka S. Y., Dauksher W. J., Bowden S. G., >750 mV open circuit voltage measured on 50  $\mu\text{m}$  thick silicon heterojunction solar cell, *Applied Physics Letters*. 103 (5) (2013) 053511.
4. Yan D., Cuevas A., Bullock J., Wan Y., Samundsett C., Phosphorus-diffused polysilicon contacts for solar cells, *Solar Energy Materials and Solar Cells*. 142 (1) (2015) 75–82.
5. Yang X., Weber K., Hameiri Z., De Wolf S., Industrially feasible, dopant-free, carrier-selective contacts for high-efficiency silicon solar cells, *Progress in Photovoltaics: Research and Applications*. 25 (11) (2017) 896–904.
6. Wan Y. et al., Magnesium Fluoride Electron-Selective Contacts for Crystalline Silicon Solar Cells, *ACS Applied Materials & Interfaces*. 8 (23) (2016) 14671–14677.
7. Hoex B., Gielis J. J. H., van de Sanden M. C. M., Kessels W. M. M., On the c-Si surface passivation mechanism by the negative-charge-dielectric  $\text{Al}_2\text{O}_3$ , *Journal of Applied Physics*. 104 (11) (2008) 113703.
8. Schmidt J., Aberle A. G., Carrier recombination at silicon–silicon nitride interfaces fabricated by plasma-enhanced chemical vapor deposition, *Journal of Applied Physics*. 85 (7) (1999) 3626–3633.

### THE AUTHORS

**UVAROV Alexander V.**  
lumenlight@mail.ru  
ORCID: 0000-0002-0061-6687

**VYACHESLAVOVA Ekaterina A.**  
cate.viacheslavova@yandex.ru  
ORCID: 0000-0001-6869-1213

**BARANOV Artem I.**  
itiomchik@yandex.ru  
ORCID: 0000-0002-4894-6503

**GUDOVSKIKH Alexander S.**  
gudovskikh@spbau.ru  
ORCID: 0000-0002-7632-3194

**MAKSIMOVA Alina A.**  
deer.blackgreen@yandex.ru  
ORCID: 0000-0002-3503-7458

*Received 01.08.2022. Approved after reviewing 30.08.2022. Accepted 01.09.2022.*

Conference materials

UDC 53.082.79

DOI: <https://doi.org/10.18721/JPM.153.229>

## Development of a small-sized NMR relaxometer for express monitoring of the state of the liquid medium

M. N. Davydov<sup>1</sup> ✉, V. V. Davydov<sup>1,2,3</sup>, R. D. Cherkassova<sup>1</sup>

<sup>1</sup>Peter the Great St. Petersburg Polytechnic University, Saint-Petersburg, Russia;

<sup>2</sup>All-Russian Research Institute of Phytopathology, Moscow Region, Russia;

<sup>3</sup>The Bonch-Bruевич Saint-Petersburg State University of Telecommunications, Saint Petersburg, Russia

✉ [davydov.mn@edu.spbstu.ru](mailto:davydov.mn@edu.spbstu.ru)

**Abstract.** The necessity of developing devices for express monitoring of the state of the liquid medium at the sampling site is substantiated. The criteria for express control methods are substantiated. A design of a small-sized NMR relaxometer for express monitoring of the state of the medium has been developed. Experimental data are presented. The results obtained on the proposed small-sized NMR relaxometer were compared with the values obtained on an industrial NMR relaxometer.

**Keywords:** express control, NMR, nuclear magnetic resonance, instrumentation, relaxometer, NMR relaxometer, measuring equipment

**Citation:** Davydov M. N., Davydov V. V., Cherkassova R. D., Development of a small-sized NMR relaxometer for express monitoring of the state of the liquid medium, St. Petersburg State Polytechnical University Journal. Physics and Mathematics. 15 (3.2) (2022) 155–160. DOI: <https://doi.org/10.18721/JPM.153.229>

This is an open access article under the CC BY-NC 4.0 license (<https://creativecommons.org/licenses/by-nc/4.0/>)

Материалы конференции

УДК 53.082.79

DOI: <https://doi.org/10.18721/JPM.153.229>

## Разработка малогабаритного ЯМР-релаксометра для экспресс-контроля состояния жидкой среды

М. Н. Давыдов<sup>1</sup> ✉, В. В. Давыдов<sup>1,2,3</sup>, Р. Д. Черкассова<sup>1</sup>

<sup>1</sup>Санкт-Петербургский политехнический университет Петра Великого, Санкт-Петербург, Россия;

<sup>2</sup>Всероссийский научно-исследовательский институт фитопатологии, Московская область, Россия;

<sup>3</sup>Санкт-Петербургский государственный университет телекоммуникаций им. проф. М. А. Бонч-Бруевича, Санкт-Петербург, Россия

✉ [davydov.mn@edu.spbstu.ru](mailto:davydov.mn@edu.spbstu.ru)

**Аннотация.** Обоснована необходимость разработки приборов экспресс-контроля состояния жидкой среды на месте забора пробы. Обоснованы критерии, предъявляемые к методам экспресс-контроля. Разработана принципиальная схема малогабаритного ЯМР-релаксометра для экспресс-контроля состояния среды. Приведены экспериментальные данные. Полученные результаты на предложенном малогабаритном ЯМР-релаксометре были сравнены со значениями, получаемыми на промышленном ЯМР-релаксометре.

**Ключевые слова:** экспресс-контроль, ЯМР, ядерно-магнитный резонанс, приборостроение, релаксометр, ЯМР-релаксометр, измерительная техника

**Ссылка при цитировании:** Давыдов М. Н., Давыдов В. В., Черкассова Р. Д. Разработка малогабаритного ЯМР-релаксометра для экспресс-контроля состояния жидкой среды // Научно-технические ведомости СПбГПУ. Физико-математические науки. 2022. Т. 15. № 3.2. С. 155–160. DOI: <https://doi.org/10.18721/JPM.153.229>

Статья открытого доступа, распространяемая по лицензии CC BY-NC 4.0 (<https://creativecommons.org/licenses/by-nc/4.0/>)

### Introduction

Currently, there are many tasks in industrial production, in ecology, in physical and chemical experiments to control the state of the environment under study [1–8]. In some cases, the possibility of express monitoring of the state of the environment at the required time in difficult conditions is of particular importance [3, 6, 8, 9–11]. In most cases, the task of express control is only to establish whether there is a deviation from the standard state of the environment.

Therefore, increased requirements are imposed on the methods of measuring physical parameters during express control. It is necessary that the changes carried out do not make irreversible changes to the composition and structure of the environment under study [6, 8, 12–14]. This makes it possible, when detecting deviations from the standard state, to carry out further studies of the environment in stationary laboratories. Studies of various media using the phenomenon of nuclear magnetic resonance do not make irreversible changes to the medium, which allows this sample to be used for research on other devices [3, 6, 8, 14–18].

#### Modulation measurement technique and block diagram of NMR relaxometer

It is very difficult to register the NMR signal spectrum in a weak magnetic field [3, 6, 8, 18–20]. This problem can be solved by using a modulation technique to register the NMR signal. Monitoring of the state of the liquid medium is carried out by measuring the longitudinal  $T_1$  and  $T_2$  transverse relaxation times. According to the deviation of  $T_1$  and  $T_2$  from the standard, the presence of impurities in the medium is determined.

In the device developed by us, the NMR signal is obtained at the resonant frequency of protons. The Bloch equations are used in this case to describe the process of obtaining a signal at a resonant frequency. Figure 1 shows the developed design of the device.

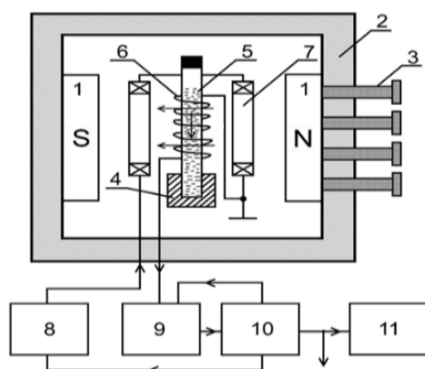


Fig. 1. Design of the NMR relaxometer: 1 – magnet, 2 – neutral for placing and centering magnets, 3 – adjusting screws, 4 – fixing device for the container with the test medium, 5 – container with the investigated medium, 6 – NMR signal registration coil, 7 – modulation coils, 8 – radio frequency generator, 9 – autodyne detector, 10 – processing and control device, 11 – oscilloscope

In the NMR signal registration coil of the relaxometer, the recorded signal from the medium under study is formed when the longitudinal and transverse components of the magnetization vector move, which are described by the Bloch equations [20–22]:

The results of the experiments performed show that in a small-sized NMR relaxometer, for any values of magnetic fields and modulation frequency  $f_m$  that satisfy the registration of an NMR signal in a weak field, it is impossible to ensure the fulfillment of the conditions for fast adiabatic passage through resonance [21, 22]. Therefore, to describe the line shape of the NMR resonance signal, taking into account the results of previous experiments and the identified features when using the modulation technique in a weak magnetic field [3, 6, 12, 20], it is proposed to introduce new coefficients into the Bloch equations. When using the

modulation technique for recording the NMR signal, the magnetic field in the system of Bloch equations must be taken into account in accordance with the following relationship:

$$H = H_0 + H_m \sin(\omega_m t), \tag{1}$$

where  $H_0$  is constant magnetic field,  $H_m$  is field created by the modulation coil,  $\omega_m$  is modulation frequency.

One of the features of NMR signal registration in a weak magnetic field using the modulation technique is that it should be performed only at the resonance frequency ( $\omega_{nmr} = \omega_0 = \gamma H_0$ ).



For most of the studied media, in the case of a detuning of the NMR signal detection frequency  $\omega_{nmr}$  from the resonance frequency  $\omega_0$ , the signal-to-noise ratio (SNR) can become less than 1.3 [3, 6, 11, 20-22]. At such a value of SNR, the operation of the NMR signal accumulation circuit in small-sized NMR relaxometers becomes inefficient [3, 6, 11, 20]. This does not allow performing various measurements with an error of no more than 1.5%. Considering this circumstance, frequency detuning is transformed into the following function:

$$\Delta\omega = \gamma H_m \sin(\omega_m t). \quad (2)$$

Relationship (2) is the new coefficient for the system of the Bloch equations. Another new coefficient, which is introduced in the Bloch equations, relates to the need to take into account the modulation of the weak magnetic field  $H_0$  in the magnetization of the investigated medium  $M$ . The new relation for  $M$ , which is substituted into Bloch equations, must be written in the following form:

$$M = \chi_0(H_0 + H_m \sin(\omega_m t)). \quad (3)$$

After substituting new coefficients (2) and (3) into the Bloch equations, they take the following form:

$$\begin{aligned} \frac{du(t)}{dt} + \frac{u(t)}{T_2} + \gamma H_m \sin(\omega_m t)v(t) &= 0, \\ \frac{dv(t)}{dt} + \frac{v(t)}{T_2} - \gamma H_m \sin(\omega_m t)u(t) + \gamma H_1 M_z(t) &= 0, \\ \frac{dM_z(t)}{dt} + \frac{M_z(t)}{T_1} - \frac{M}{T_1} - \gamma H_1 v(t) &= 0. \end{aligned} \quad (4)$$

The system of equations (4) is solved with respect to the components  $v(t)$ ,  $u(t)$  and  $M_z(t)$ , taking into account the initial conditions  $M_z(0) = \chi_0 H_0$ ,  $v(0) = 0$ ,  $u(0) = 0$ .

A feature of NMR signal registration in a weak magnetic field using the modulation technique is the need to fulfill the relation [3, 6, 18, 20]:

$$\gamma H_m > 10\Delta f_{nmr} \quad (5)$$

where  $H_m$  is magnitude of modulation field,  $\Delta f_{nmr}$  is natural line bandwidth of the NMR signal spectrum.

In weak magnetic fields with a high degree of uniformity, the value of  $\Delta f_{nmr}$  is determined by the relation [21, 22]:

$$\Delta f_{nmr} = \frac{1}{T_2}. \quad (6)$$

In turn, to measure the transverse relaxation time  $T_2$  in a small-sized NMR relaxometer by the decay of the envelope of the registered NMR signal with an error of less than 1.0 %, the modulation field period  $T_m$  is subjected to the condition [3, 6, 18, 20]:

$$T_m > 5T_2 \quad (7)$$

We have found that a decrease in the frequency of the modulation field  $f_m = 1 / T_m$  to fulfill condition (7) leads to a deterioration in the SNR due to a decrease in the accumulation rate. This deterioration due to the requirement of small dimensions for the NMR relaxometer cannot be fully compensated by an increase in  $H_1$  and  $H_m$ .

We found that in the case of applying the modulation technique in weak fields, in addition to fulfilling conditions (5) and (7), it is necessary to consider the complex nature of the dependence of the SNR on the amplitude of the modulation field  $H_m$ . It is necessary to set the amplitude of the modulation field to the maximum of the SNR.

To analytically determine the given value of the amplitude of the modulation field, it is necessary to obtain an analytical solution of the system (4).

### Experimental results

In Figure 2 shows the registered NMR signal in a weak magnetic field of 60 mT using the modulation technique at the resonant frequency of lithium nuclei at a temperature  $T=295.4$  K.

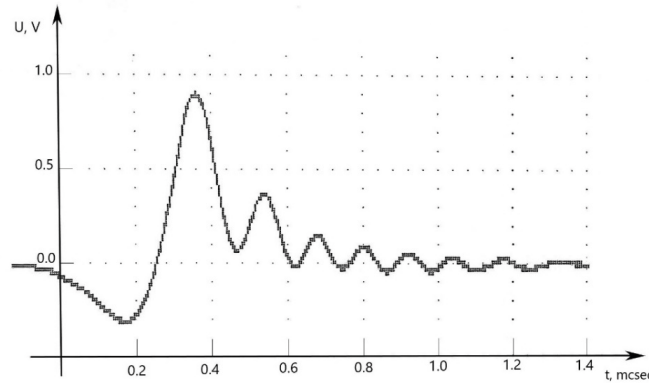


Fig. 2. Form of NMR signal obtained in a weak magnetic field of 60 mT using the modulation technique and accumulation when working with lithium nuclei.

The result obtained shows that the recorded NMR signal can be used to measure the relaxation times. For this medium  $T_1 = 24.872 \pm 0.532$  ms,  $T_2 = 0.160 \pm 0.005$  ms.

Table 1

#### Relaxation constant of liquid media

Medium	Small-sized NMR relaxometer		Industrial NMR relaxometer Minispec mq 20	
	$T_1$ , s	$T_2$ , ms	$T_1$ , s	$T_2$ , ms
Soviet Petrol standard A – 76	$1.432 \pm 0.007$	$146.05 \pm 0.73$	$1.4266 \pm 0.0029$	$145.35 \pm 0.29$
Soviet Petrol standard “Nefras C2-80/120”	$1.333 \pm 0.00$	$207.51 \pm 1.04$	$1.3403 \pm 0.0027$	$206.38 \pm 0.42$

Table 1 shows an example of the operation of a small-sized NMR relaxometer for express control of the state performed for the hydrocarbon medium. Table 1 presents the results of measurements of the longitudinal relaxation time  $T_1$  and transverse relaxation time  $T_2$  at a temperature of  $T = 291$  K. In Table 1 also presents the results of measurements of the relaxation times of these media obtained using an industrial NMR relaxometer Minispec mq 20.

Analysis of the measurement results of  $T_1$  and  $T_2$  shows that they match within the measurement error. The measurement error of  $T_1$  and  $T_2$  using the device developed by us is less than 1.0%. This value of the measurement error satisfies the requirements for devices for express control.

### Conclusion

The obtained results of studies of the state of various media and their comparison with the results of measurements obtained using instruments of higher accuracy confirm the possibility of using the developed small-sized NMR relaxometer for express control. Further improvement of the accuracy characteristics of a small-sized NMR relaxometer with a modulation technique for recording the NMR signal is planned to be carried out using new data that will be obtained after obtaining an analytical solution of the equations (4).



## REFERENCES

1. **Gryaznova E. M., Rud V. Y.**, On the possibility of using the optical method for express quality control of fruits, *Journal of Physics: Conference Series*. 2086 (1) (2021) 012143.
2. **Davydov R. V., Yushkova V. V., Stirmanov A. V., Rud V. Yu.**, A new method for monitoring the health condition based on nondestructive signals of laser radiation absorption and scattering, *Journal of Physics: Conference Series*. 1410 (1) (2019) 012067.
3. **Davydov V. V.**, Determination of the Composition and Concentrations of the Components of Mixtures of Hydrocarbon Media in the Course of its Express Analysis, *Measurement Techniques*. 62 (2) (2020) 1090-1098.
4. **Grebenikova N. M., Smirnov K. J., Rud V. Yu., Artemiev V. V.**, Features of monitoring the state of the liquid medium by refractometer, *Journal of Physics: Conference Series*. 1135 (1) (2018) 012055.
5. **Grebenikova N. M., Smirnov K. J.**, Features of optical signals processing for monitoring the state of the flowing liquid medium with a refractometer, *Journal of Physics: Conference Series*. 1368 (2) (2019) 022057.
6. **Davydov V. V., Davydova T. I.**, A nondestructive method for express testing of condensed media in ecological monitoring, *Russian Journal of Nondestructive Testing*. 53 (7) (2017) 520–529.
7. **Nikitina M., Grebenikova N., Dudkin V., Batov Y.**, Methodology for assessing the adverse effects of the use of nuclear energy on agricultural land, *IOP Conference Series: Earth and Environmental Science*. 390 (1) (2019) 012024.
8. **Gryznova E., Batov Y., Rud V.**, Methodology for assessing the environmental characteristics of various methods of generating electricity, *E3S Web of Conferences*. 140 (2019) 09001.
9. **Myazin N. S., Dudkin V. I., Grebenikova N. M.**, On the Possibility of Express Recording of Nuclear Magnetic Resonance Spectra of Liquid Media in Weak Fields, *Technical Physics*. 63 (12) (2018) 1845–1850.
10. **Grevtseva A. S., Smirnov K. J., Rud V. Yu.**, Development of methods for results reliability raise during the diagnosis of a person's condition by pulse oximeter, *Journal of Physics: Conference Series*. 1135 (1) (2018) 012056.
11. **Myazin N. S., Yushkova V. V., Rud V. Y.**, On the possibility of recording absorption spectra in weak magnetic fields by the method of nuclear magnetic resonance, *Journal of Physics: Conference Series*. 1038 (1) (2018) 012088.
12. **Kuzmin M. S., Rogov S. A.**, On the use of a multi-raster input of one-dimensional signals in two-dimensional optical correlators, *Computer Optics*. 43 (3) (2019) 391–396.
13. **Marusina M. Y., Karaseva E. A.**, Automatic segmentation of MRI images in dynamic programming mode Asian Pacific, *Journal of Cancer Prevention*. 19 (10) (2018) 2771–2775.
14. **Dyumin V., Smirnov K., Myazin N.**, Charge-coupled Device with Integrated Electron Multiplication for Low Light Level Imaging, *Proceedings of the 2019 IEEE International Conference on Electrical Engineering and Photonics, EExPolytech-2019*. Vol. 8906868 (2019) 308–310.
15. **Marusina M. Ya., Karaseva E. A.**, Application of fractal analysis for estimation of structural changes of tissues on MRI images *Russian Electronic Journal of Radiology*. 8 (3) (2018) 107–112.
16. **Gizatullin B., Gafurov M., Murzakhanov F., Mattea C., Stapf S.**, Molecular Dynamics and Proton Hyperpolarization via Synthetic and Crude Oil Porphyrin Complexes in Solid and Solution States, *Langmuir*. 37 (22) (2021) 6783–6791.
17. **Rakhmatullin I., Efimov S., Tyurin V., Varfolomeev M., Klochkov V.**, Qualitative and quantitative analysis of heavy crude oil samples and their SARA fractions with  $^{13}\text{C}$  nuclear magnetic resonance, *Processes*. 8 (8) (2020) 995–1009.
18. **Davydov R.V., Dudkin V.I., Nikolaev D.I., Makeev S.S., Moroz A.V.**, Structure of a Nuclear Magnetic Resonance Signal in a Small Relaxometer, *Journal of Communications Technology and Electronics*. 66 (5) (2021) 632–636.
19. **Kashaev R.S., Suntsov I.A., Tung C.V., Usachev A.E., Kozelkov O.V.**, Apparatus for Rapid Measurement of Oil Density and Molecular Mass Using Proton Magnetic Resonance, *Journal of Applied Spectroscopy*. 86 (2) (2019) 289–293.
20. **Davydov V.V., Dudkin V.I., Karseev A.Y.**, Governance of the Nutation Line Contour in Nuclear-Magnetic Flowmeters, *Russian Physics Journal*. 58 (2) (2015) 146–152.
21. **Leshe A.**, Nuclear induction, *Veb Deutscher Verlag Der Wissenschaften, Berlin*, 1963.
22. **Abragam A.**, The principles of nuclear magnetism, *Oxford at the Clarendon Press, Oxford UK*, 1961.

## THE AUTHORS

**DAVYDOV Maxim N.**

mdavydov2010@mail.ru

ORCID: 0000-0001-5406-1835

**DAVYDOV Vadim V.**

davydov\_vadim66@mail.ru

ORCID: 0000-0001-9530-4805

**CHERKASSOVA Regina D.**

rcherkasova01@mail.ru

*Received 04.08.2022. Approved after reviewing 08.08.2022. Accepted 15.08.2022.*

Conference materials

UDC 53.087

DOI: <https://doi.org/10.18721/JPM.153.230>

## Generator of highly stable microwave signals with low phase noise

D. D. Savin<sup>1</sup> ✉, V. V. Davydov<sup>1</sup>

<sup>1</sup> Peter the Great St. Petersburg Polytechnic University, Saint-Petersburg, Russia

✉ [savin\\_danila00@mail.ru](mailto:savin_danila00@mail.ru)

**Abstract.** The problems arising in various communication systems, determining coordinates, generating positional signals and others due to phase shifts between reference signals are considered. The necessity and relevance of the development of high-precision multichannel microwave generators is shown. The block diagram of the device is given. Active elements are selected that provide a given level of phase noise. The design of the generator of highly stable oscillations has been developed. The results of simulation of the operation of the generator during the formation of signals at a frequency of 100 MHz are presented.

**Keywords:** generator, microwave signal, synchronization system, channel, phase noise, stabilization, signal amplitude

**Citation:** Savin D. D., Davydov V. V., Generator of highly stable microwave signals with low phase noise, St. Petersburg State Polytechnical University Journal. Physics and Mathematics. 15 (3.2) (2022) 161–166. DOI: <https://doi.org/10.18721/JPM.153.230>

This is an open access article under the CC BY-NC 4.0 license (<https://creativecommons.org/licenses/by-nc/4.0/>)

Материалы конференции

УДК 53.087

DOI: <https://doi.org/10.18721/JPM.153.230>

## Генератор высокостабильных СВЧ сигналов с малыми фазовыми шумами

Д. Д. Савин<sup>1</sup> ✉, В. В. Давыдов<sup>1</sup>

<sup>1</sup> Санкт-Петербургский политехнический университет Петра Великого, Санкт-Петербург, Россия

✉ [savin\\_danila00@mail.ru](mailto:savin_danila00@mail.ru)

**Аннотация.** Рассмотрены проблемы, возникающие из-за фазовых сдвигов между опорными сигналами в различных системах связи, системах определения координат, генерации позиционных сигналов и другие. Показана необходимость и актуальность разработки высокоточных многоканальных СВЧ-генераторов. Приведена структурная схема устройства. Выбраны активные элементы, которые обеспечивают заданный уровень фазового шума. Разработан макет генератора высокостабильных колебаний. Представлены результаты моделирования работы генератора при формировании сигналов на частоте 100 МГц.

**Ключевые слова:** генератор, СВЧ сигнал, система синхронизации, канал, фазовый шум, стабилизация, амплитуда сигнала

**Ссылка при цитировании:** Савин Д. Д., Давыдов В. В. Генератор высокостабильных СВЧ сигналов с малыми фазовыми шумами // Научно-технические ведомости СПбГПУ. Физико-математические науки. 2022. Т. 15. № 3.2. С. 161–166. DOI: <https://doi.org/10.18721/JPM.153.230>

Статья открытого доступа, распространяемая по лицензии CC BY-NC 4.0 (<https://creativecommons.org/licenses/by-nc/4.0/>)

### Introduction

Currently, there is a large-scale development of technologies for the transmission of various information [1-6]. A considerable part of them is occupied by wireless signal transmission technologies, which require highly stable oscillators – heterodynes [7–9]. It should be noted that heterodynes are actively used in various radar systems, etc. [9–13]. In these systems, quantum frequency standards are used to ensure stability of operation [14–17]. When implementing the designs of quantum frequency standards, low-noise generators are indispensable devices, since standards in some cases must work autonomously for a long period of time (for example, in satellites in orbit, etc.) [16–22]. Highly stable microwave generators are indispensable in various radio engineering systems and experimental installations.

Modern designs of highly stable microwave generators have a number of disadvantages, among which are the relatively large size of the structure and the high cost. If there is more than one block in a device, for example, in a quantum frequency standard, requiring a high-frequency signal, the dimensions of such a device will be large. This creates problems with its use on satellites and mobile objects [22–25]. All this ultimately leads to an increase in the cost of the design of the device in which the microwave generator is installed, and the costs of its operation. In addition, these generators will not be synchronized, which leads to a phase difference between the signals that arrive at the corresponding blocks. In most cases, this situation is unfavorable, so they try to prevent it by including a synchronization block in the scheme. This will further increase the size and cost of the device.

An important point in this case is the characteristics of the signal (amplitude and noise). When adding new blocks to the device, the signal amplitude may decrease and the noise components in the output signal may increase. The presence of noise, especially phase noise, is extremely undesirable when solving tasks such as time synchronization and navigation [23–26]. In these tasks, the accuracy of determining special labels in the signal is extremely important. During the search for these labels, the moments of time when the signal amplitude crosses the zero value are determined. Phase noise distorts the signal, impairing the accuracy of determining these points.

Therefore, the development of new microwave generator circuits that will solve the problems described earlier, while introducing a minimum amount of phase noise into the original signal, is extremely relevant.

### Generator of highly stable microwave signals

Our paper presents a scheme for generating three highly stable synchronized microwave signals with low phase noise. The block diagram of the device developed by us is shown in Fig. 1. The device can be divided into two parts: a highly stable microwave signal generator (Fig. 1, *a*) and a splitter (Fig. 1, *b*).

We used an Ultra-Low Noise Microwave Signal Generator (HI-END RFSU40, 8 kHz — 40 GHz) as a microwave signal source. The technical characteristics of SSB Phase Noise Performance are shown in Fig. 2.

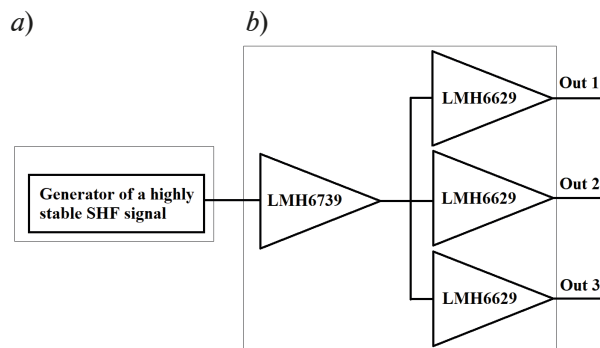


Fig. 1. Scheme of highly stable SHF signals generator with low phase noise: generator of a highly stable SHF signal (*a*); splitter (*b*)

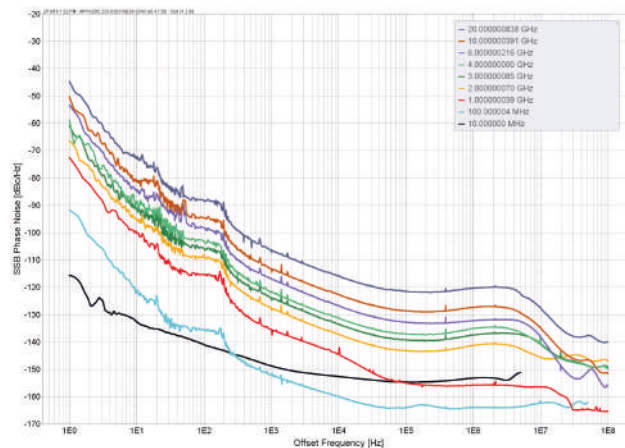


Fig. 2. The SSB Phase Noise Performance

To ensure the generation of highly stable signals, two differential amplifiers are used in the circuit. The LMH6739 amplifier with a gain of 1 is used as a buffer. It performs two important functions: firstly, it protects the generator from current surges that may occur in the second part of the device, and secondly, it maintains the signal amplitude at the desired level. In this case, the input noise, which is  $2.3 \text{ nV}/(\text{Hz})^{1/2}$  for this amplifier, will not be particularly amplified. The LMH6629 amplifier is low-noise-its input noise is  $0.69 \text{ nV}/(\text{Hz})^{1/2}$ . The minimum gain is 4, so the amplitude of the output signals will be greater than the input. Thus, three identical, synchronized signals are formed at the output.

### Simulation results of the generator operation

The NI Multisim 14.0 software package was used to build a model of the generator operation. The use of this program by other scientists has shown that it is possible to obtain a good agreement of theoretical results with the experiment. Fig. 3 shows a model of the device we developed, assembled in Multisim.

To take into account the physical features of resistors and capacitors, not ideal elements were used in the model. Their values were set in accordance with the E24 series. In the feedback circuit of the LMH6629 amplifier, the ratings were selected from the E96 series in order to provide a better gain value and reduce the influence of thermal noise.

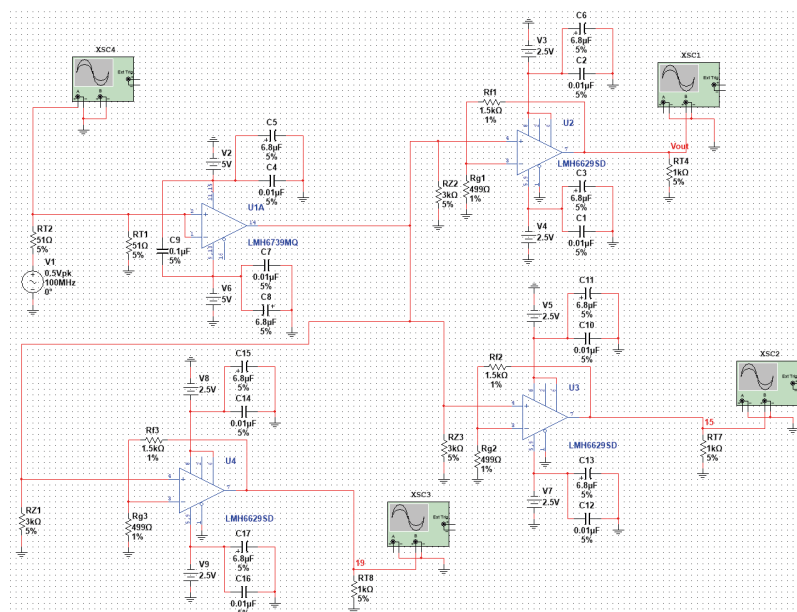


Fig. 3. A model of a generator of highly stable microwave signals with low phase noise in NI Multisim

Fig. 4 shows the result of modeling the operation of the microwave oscillator circuit – waveforms of signals from the HI-END RFSU40 output (highly stable signal) and from the Splitter output (output signal).

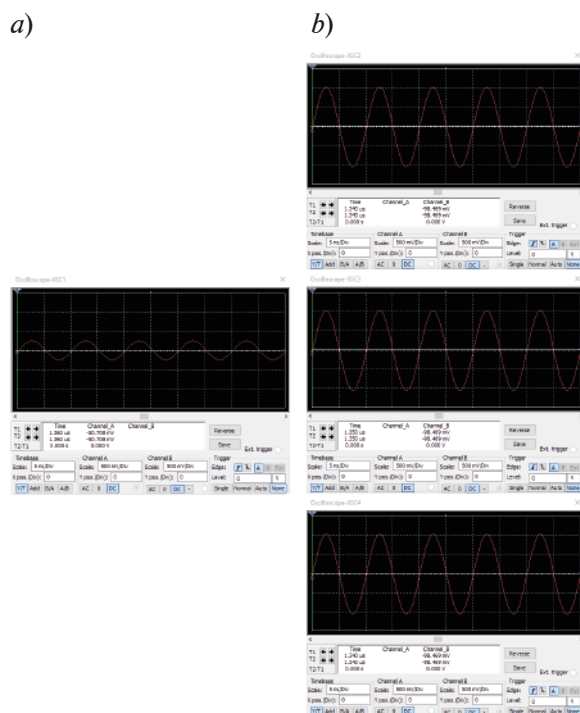


Fig. 4. Waveforms: highly stable signal (a), output signals (b)

The analysis of the obtained results shows that the amplitudes of the three microwave signals differ from each other by less than 0.2%, which meets the requirements that apply to these devices in time synchronization systems.

### Conclusion

The simulation results showed that the phases of the three generated microwave signals differ insignificantly from each other. An extremely small shift is associated with the imperfection of electronic elements. In this case, phase shift compensation is not needed.

It is established that the phase noise induced by the splitter is extremely small compared to the amplitudes of the signals. Their influence on the further operation of synchronization systems is insignificant. In addition, according to preliminary calculations, the size of the generator developed by us will be 60% smaller than the circuits currently used. The electric power consumption will also decrease. This is extremely important when using these synchronization systems on satellites.

### REFERENCES

1. **Davydov R., Antonov V., Moroz A.**, Parameter Control System for a Nuclear Power Plant Based on Fiber-Optic Sensors and Communication Lines, In: IEEE International Conference on Electrical Engineering and Photonics (EExPolytech), Saint-Petersburg, Russia, 13-15 October 2019. Vol. 8906791 (2019) 295–297.
2. **Dudkin V.I., Myazin N.S., Davydov R.V.**, On the Possibility of Studying Ferrofluids by a Nuclear Magnetic Magnetometer with a Flowing Sample, Journal of Communications Technology and Electronics. 65 (5) (2020) 558–564.
3. **Kislyakov Yu. Ya., Avdyushenko S. A., Kislyakova I. P., Zaitceva A. Yu.**, Analytical multisensory trainable system for diagnosing vocational aptitude of military medical specialists by ion content in the expired breath condensate, Journal of Computational and Theoretical Nanoscience. 16 (11) (2019) 4502–4507.



4. **Davydov V.V., Kruzhalov S.V., Vologdin V.A.**, Concerning some features of studying the flow of liquid media by a Doppler method *Journal of Optical Technology (A Translation of Opticheskii Zhurnal)*. 84 (8) (2017) 568–573.
5. **Antonov V.I., Davydov R.V., Maslikov V.I., Molodtsov D.V., Badenko V.L.**, Simulation of water flow management by the flood control facilities in the adjacent river basins, *Journal of Physics: Conference Series*. 1400 (7) (2019) 077049.
6. **Antonov V.I., Davydov R.V., Maslikov V.I., Molodtsov D.V., Chusov A.N.**, Mathematical models of operating regimes of flood control facility's system, *Journal of Physics: Conference Series*. 1368 (4) (2019) 042076.
7. **Moroz A. V., Davydov R. V.**, A New Scheme for Transmitting Heterodyne Signals Based on a Fiber-Optical Transmission System for Receiving Antenna Devices of Radar Stations and Communication Systems, *Lecture Notes in Computer Science (including subseries Lecture Notes in Artificial Intelligence and Lecture Notes in Bioinformatics)*. 11660 (2019) 710–718.
8. **Kislyakov Yu. Ya., Avdyushenko S. A., Kislyakova I. P., Zaitceva A. Yu.**, Analytical multisensory trainable system for diagnosing vocational aptitude of military medical specialists by ion content in the expired breath condensate, *Journal of Computational and Theoretical Nanoscience*. 16 (11) (2019) 4502–4507.
9. **Moroz A.V.**, Features of transmission bearing and heterodyne receivers for signals in fiber-optic communication line in active phased array antenna, *Journal of Physics: Conference Series*. 1410 (1) (2019) 012212.
10. **Wang D., Rud V.Y.**, Prospective directions for the development of microwave frequency standards for satellite navigation systems, *Journal of Physics: Conference Series*. 2086 (1) (2021) 012073.
11. **Mihov E.D., Nepomnyashchiy, O.V.**, Selecting informative variables in the identification problem, *Journal of Siberian Federal University: Mathematics and Physics*. 9 (4) (2016) 473–480.
12. **Ryzhenko I.N., Lutsenko A.E., Varygin O.G., Nepomnyashchiy O.V.**, Carrier compensation mode implementation in satellite communication channels 2019 International Siberian Conference on Control and Communications, *SIBCON 2019 – Proceedings*. Vol. 8729665 (2019).
13. **Lukashev N.A., Davydov R.V., Glinushkin A.P., Rud' V.Y.**, Improving characteristics of microwave frequency standard on Hg-199 ions for telecommunication systems. *Journal of Physics: Conference Series*. 1326 (1) (2019) 012046.
14. **Petrov A. A.**, Improvement frequency stability of caesium atomic clock for satellite communication system, *Lecture Notes in Computer Science (including subseries Lecture Notes in Artificial Intelligence and Lecture Notes in Bioinformatics)*. 9247 (2015) 739–744.
15. **Valov, A.P., Arinushkina, K.G.**, The use of digital data processing to improve the metrological characteristics of the rubidium frequency standard, *Journal of Physics: Conference Series*. 2086 (1) (2021) 012070.
16. **Petrov A. A.**, Digital Frequency Synthesizer for <sup>133</sup>Cs-Vapor Atomic Clock, *Journal of Communications Technology and Electronics*. 62 (3) (2017) 289 – 293.
17. **Lukashev N. A., Glinushkin A. P., Rud V. Yu., Lukyantsev V. S.**, Microwave low mass-dimensional frequency standard on Hg- 199 ions, *Journal of Physics: Conference Series*. 1410 (1) (2019) 012211.
18. **Petrov A. A., Grebenikova N. M.**, Some Directions of Quantum Frequency Standard Modernization for Telecommunication Systems, *Lecture Notes in Computer Science (including subseries Lecture Notes in Artificial Intelligence and Lecture Notes in Bioinformatics)*. 11118 LNCS (2018) 641–648.
19. **Grevtseva A., Rud V.**, Method of processing velocity increase of measuring results of quantum frequency standard parameters for information transfer velocity increase in satellite communication systems *CEUR Workshop Proceedings*. 2667 (2020) 15–18.
20. **Lukashev N. A., Rud V. Yu.**, Microwave frequency standard on Hg-199 ions for space stations and vehicles, *Journal of Physics: Conference Series*. 1400 (2) (2019) 022050.
21. **Petrov A. A., Zaletov D. V., Shapovalov D. V.**, Peculiarities of Constructing a Scheme for Formation of a Microwave Excitation Signal in a Cesium Atomic Clock, *Journal of Communications Technology and Electronics*. 66 (3) (2021) 295–299.
22. **Grevtseva A. S., Dmitriev R. A.**, Features of the formation of the frequency of the microwave excitation signal in the quantum frequency standard on rubidium atoms – 87, *Journal of Physics: Conference Series*. 2086 (1) (2021) 012055.

23. **Riehle F.**, Frequency standard. Basic and applications, WILEY-VCH Verlag GmbH Co. KGaA: New-York, 2008.

24. **Tarasov A. D., Milder O. B.**, Gradation trajectories as an analog of gradation curves in the metric Lie algebra space discrete approach, Computer Optics. 43 (1) (2018) 104–110.

25. **Arinushkina K. G., Valov A. P.**, Digital processing of optical signals in the frequency standard based in rubidium atoms - 87, In. Proceedings of ITNT 2021 - 7th IEEE International Conference on Information Technology and Nanotechnology, 2021 Samara, Russia, 20-24 September 2021. Vol. 44026298 (2021) 44–49.

26. **Petrov A. A., Vologdin V. A., Zalyotov D. V.**, Dependence of microwave – excitation signal parameters on frequency stability caesium atomic clock, Journal of Physics: Conference Series. 643 (1) (2015) 012087.

### THE AUTHORS

**SAVIN Danila D.**

savin\_danila00@mail.ru

ORCID: 0000-0002-2032-8535

**DAVYDOV Vadim V.**

davydov\_vadim66@mail.ru

ORCID: 0000-0001-9530-4805

*Received 13.08.2022. Approved after reviewing 19.09.2022. Accepted 19.09.2022.*

## PHYSICAL OPTICS

Conference materials

UDC 535.8

DOI: <https://doi.org/10.18721/JPM.153.231>

### Reliability of 808 nm QCW laser diode arrays

E. M. Gafurov<sup>1</sup> ✉, E. V. Smirnov<sup>1</sup>

<sup>1</sup> FSUE "RFNC-VNIITF named after Academ. E.I. Zababakhin", Snezhinsk, Russia

✉ [dep5@vniitf.ru](mailto:dep5@vniitf.ru)

**Abstract.** The dependence of radiative characteristics of 808 nm QCW laser diode arrays (LDAs) on power supply modes and thermostabilization temperature was studied. The accelerated lifetime test method is suggested at 6% duty cycle exceeding the nominal value by a factor of 2.5 and at two emitter junction temperatures of 65.0°C and 82.5°C. Accumulated total LDA operation time in the accelerated mode was more than  $7.0 \cdot 10^8$  pulses that allows predicting LDA operation time to be nearly  $3.5 \cdot 10^{10}$  pulses in nominal power supply modes (i.e. more than 60 thousand hours or 7.0 years of continuous work at 100 Hz frequency).

**Keywords:** Reliability, QCW laser diode arrays, Arrhenius model, accelerated lifetime tests.

**Citation:** Gafurov E. M., Smirnov E. V., Reliability of 808 nm QCW laser diode arrays, St. Petersburg State Polytechnical University Journal. Physics and Mathematics. 15 (3.2) (2022) 167–171. DOI: <https://doi.org/10.18721/JPM.153.231>

This is an open access article under the CC BY-NC 4.0 license (<https://creativecommons.org/licenses/by-nc/4.0/>)

Материалы конференции

УДК 535.8

DOI: <https://doi.org/10.18721/JPM.153.231>

### Исследование ресурсных характеристик импульсно-периодических матриц лазерных диодов

Э. М. Гафуров<sup>1</sup> ✉, Е. В. Смирнов<sup>1</sup>

<sup>1</sup> ФГУП «РФЯЦ-ВНИИТФ им. академ. Е.И. Забабахина», г. Снежинск, Россия

✉ [dep5@vniitf.ru](mailto:dep5@vniitf.ru)

**Аннотация.** Проведены исследования зависимости излучательных характеристик импульсно-периодических матриц ЛД (МЛД) с длиной волны излучения 808 нм от режимов питания и температуры термостабилизации. Предложен метод ускоренных ресурсных испытаний при коэффициенте заполнения импульсов 6%, превышающем номинальное значение в 2.5 раза, а также при двух значениях температуры эмиттеров 65.0°C и 82.5°C. Накопленное суммарное время работы МЛД в ускоренном режиме составило более  $7.0 \cdot 10^8$  импульсов, что позволяет прогнозировать длительность работы МЛД при номинальных режимах питания в течение около  $3.5 \cdot 10^{10}$  импульсов (более 60 тысяч часов или 7.0 лет непрерывной работы при частоте следования импульсов 100 Гц).

**Ключевые слова:** надежность, матрицы лазерных диодов, модель Аррениуса, ускоренные ресурсные тесты

**Ссылка при цитировании:** Гафуров Э. М., Смирнов Е. В. Исследование ресурсных характеристик импульсно-периодических матриц лазерных диодов // Научно-технические ведомости СПбГПУ. Физико-математические науки. 2022. Т. 15. № 3.2. С. 167–171. DOI: <https://doi.org/10.18721/JPM.153.231>

Статья открытого доступа, распространяемая по лицензии CC BY-NC 4.0 (<https://creativecommons.org/licenses/by-nc/4.0/>)

## Introduction

A large-scale research conducted by RFNC-VNIITF in the area of in-house development and production of diode-pumped solid-state laser (DPSSL) was focused on the design and production techniques of high-power QCW laser diode arrays (LDA) [1] with the following nominal characteristics: radiation power of 2.4 kW at 100 Hz frequency and 240 μs pulse width.

A major stage in production of LDAs and any other laser emitters (LEs) is to determine their reliability in the required operation modes. In turn, the rate of changing laser diode output characteristics which allows estimating reliability of products is affected by different degradation mechanisms of laser devices which can be determined only in the course of lifetime tests [2].

The topic of this research brings up the relevant issue related to long-term stability of LDA output characteristics and influence of different factors accelerating degradation process. On the one side, the lifetime of semiconductor laser emitters, including LDAs, depends on many factors, e.g. type of laser diodes (LDs) or laser diode bars (LDBs) used, LE design features, operation modes and operating conditions, that significantly complicates identification of degradation causes. On the other side, the lifetime of modern LEs exceeds tens of thousands of hours or 10<sup>9</sup> pulses thus making full-scale lifetime tests unfeasible under severe time constraints of up-to-date production.

Currently, the accelerated lifetime test method is commonly used to estimate LDA lifetime at the increased thermostabilization temperatures and/or optical radiation power, and this is the case of this study.

## Accelerated lifetime test method

Degradation of injection lasers is caused by a number of mechanisms acting at current transmission. The prevailing mechanism depends on many factors such as growth technology of heteroepitaxial wafers, improvement of crystal structure, semiconductor laser chips production technology, design and mounting of LDs or LDBs on the heat sinks, and operating conditions.

Mechanisms causing failures of semiconductor devices, including semiconductor LEs, are mainly based on chemical and physical processes with temperature-depending rates defined by the Arrhenius equation [3]:

$$v = A \exp(-E_a / kT), \quad (1)$$

where  $A$  is the proportionality coefficient defining reaction intensity, i.e. the rate of interaction events per reaction;  $E_a$  is the activation energy defining the energy barrier for different states in a reaction, eV;  $k$  is the Boltzmann constant ( $8.616 \cdot 10^{-5}$  eV/K); and  $T$  is the temperature in Kelvins.

Thus, to analyze and predict the degradation rate and, therefore, a semiconductor LE lifetime it is necessary to determine the activation energy representative for the specific degradation factor. In turn, the activation energy is determined by the analysis of several plots showing LDA optical radiation power vs. operating time at different power supply modes and thermostabilization temperatures.

As stated above, the increased temperature is one of the most common types of "loading", used when performing the accelerated lifetime tests. The Arrhenius model in its general form describes the influence of temperature, pumping current, and radiation power on lifetime. Based on the Arrhenius equation above it is possible to define acceleration coefficient,  $\tau_{T,P}$ , between lifetime under nominal operating conditions and that in the course of lifetime tests [4]:

$$\tau_{T,P} = \frac{\tau_1}{\tau_0} = \exp\left(\frac{E_a}{k} \left(\frac{1}{T_0} - \frac{1}{T_1}\right)\right) \left(\frac{P}{P_0}\right)^{-n} \left(\frac{I}{I_0}\right)^{-m}, \quad (2)$$

Where  $T_0$  and  $T_1$  are the heat-sink temperatures under nominal operating conditions and in the course of accelerated testing, respectively;  $\tau_0$  and  $\tau_1$  are the LE lifetimes under nominal conditions and in the course of the accelerated testing, respectively. The activation energy,  $E_a$ , is usually reported by the manufacturer of semiconductor crystal or is determined from the results of accelerated lifetime tests. Values  $n$  and  $m$  are positive constants.



The EOL-criterion can be a 20% increase in initial LE pumping current, required to maintain constant output radiation power [5], or a relative decrease in output radiation power by 20% at LE direct current [6].

### Experiment

Two samples of commercially available LDAs emitting at 795÷808 nm were studied. Chiller with heating function was used for LDA thermostabilization. Temperature of the array holder was controlled by TC-1388B calibrated thermoresistance.

Before studying LDA reliability it was necessary to determine those parameters of array power supply and external effects, whose change will have a direct impact on the degradation rate of the array radiative characteristics. For this purpose we examined the LDA power output and radiation wavelength vs. power supply parameters, i.e. pumping current amplitude, pulse frequency, and pulse width. The results of these studies, presented in Fig. 1, indicate that the change in LDB active region temperature and LDA radiation power depends on the integral value of duty cycle, whereas different combinations of pulse frequency and pulse widths do not lead to the deviation from the given linear dependence. This allows varying a limited set of parameters in the course of the accelerated lifetime tests, i.e. thermostabilization temperature of LDA heat-sink, duty cycle, and pumping current.

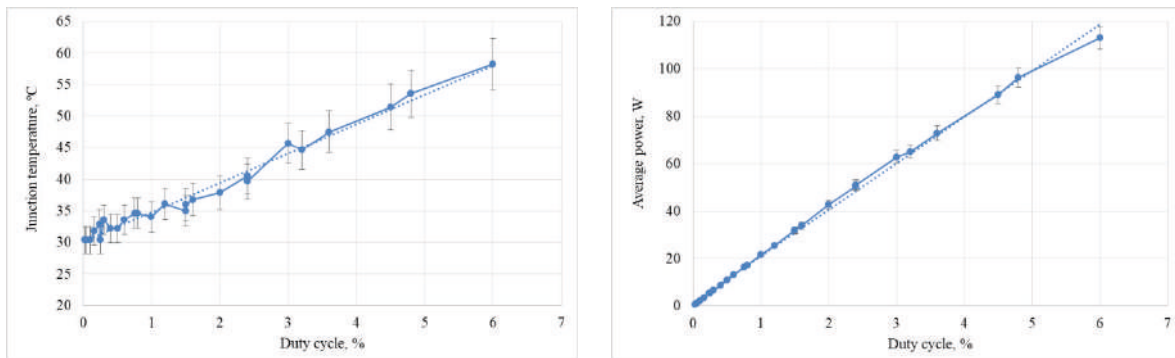


Fig. 1. Junction temperature and average radiation power vs. duty cycle

The temperatures of LDA holder were 25±0.5°C and 45±0.5°C for sample No. 1 and sample No. 2, respectively, in the absence of LDA power supply. According to the measurement results of LDA radiation wavelength, the temperatures of emitters (LDB active region) were 65.0±3.0°C for sample No. 1 and 82.5±3.0°C for sample No. 2 in LDA operation power supply modes at duty cycle of 6% and pumping current of 120A. For comparison, this temperature was 41.0±1.5°C in nominal operation modes of LDA power supply at duty cycle of 2.4%, pumping current of 120A and array holder temperature of 25±0.5°C, in the absence of power supply.

Fig. 2 presents LDA optical radiation power for sample No. 1 vs. shots in lifetime tests (discrete points) as well as the results of experimental data approximation by exponential function (solid line).

At the same time, the proportionality coefficient of approximation function exponent in Fig.2 is nothing else but the LDA degradation rate in the course of lifetime tests:

$$\frac{P(t)}{P_0} = \exp(-\nu * t), \tag{3}$$

where  $\nu$  is the LDA optical power degradation rate. This formula corresponds to the condition when the output power degradation rate slightly changes over time [6].

Then, the functional dependence of LDA degradation rate for two emitter temperatures was plotted as:

$$\ln(\nu) = \frac{E_a}{kt}. \tag{4}$$

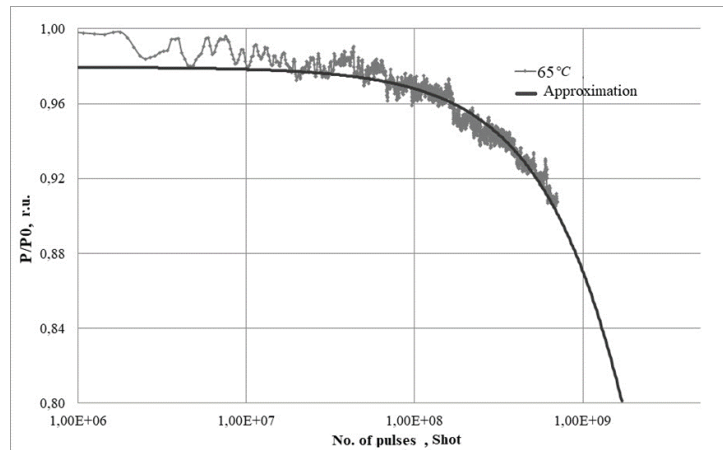


Fig. 2. The results of accelerated lifetime tests for LDA No. 1 at LDB junction temperature of 65 °C

According to Eq. 4, the slope of this plot is the desired activation energy. The LDA activation energy was  $E_a = 0.72 \pm 0.07$  eV. Next, using Eq. 2 and assuming power acceleration coefficient to be  $n = 2$  according to [4, 8], we obtained the acceleration coefficient,  $\tau_{T,P}$ , and the expected LDA failure-free operation time in the course of the accelerated test. Finally, we calculated the LDA lifetime in the nominal operation mode.

In our case, the calculated acceleration coefficients between lifetime under nominal operating conditions and in the course of accelerated lifetime tests were 0.032 for sample No. 1 and 0.012 for sample No. 2. This allows estimating the failure-free operation time of LDAs made by RFNC-VNIITF under nominal operating conditions to be  $3.5 \cdot 10^{10}$  pulses provided that the end of life in the course of the accelerated tests according to Fig. 2 will occur at  $1.1 \cdot 10^9$  pulses.

### Conclusion

The method for QCW LDA accelerated lifetime testing is suggested establishing the dependency of LDA failure-free operation time on thermostabilization temperature and power supply modes. The accelerated lifetime tests of two LDA samples made by RFNC-VNIITF were carried out. The tests were conducted at two LDB junction temperatures ( $65 \pm 3.0^\circ\text{C}$  for sample No. 1 and  $82.5 \pm 3.0^\circ\text{C}$  for sample No. 2) and the duty cycle increased by 2.5 times. The activation energy of degradation processes for the LDAs under study was  $E_a = 0.72 \pm 0.07$  eV.

The collected results of accelerated lifetime tests allow predicting LDA failure-free operation time in the nominal operation modes to be no less than  $3.5 \cdot 10^{10}$  pulses before EOL-criteria will be reached. LDA optical power degradation over time is likely caused by the gradual decrease in emitter quantum efficiency.

Further studies of LDA reliability will be proceeded to allow refining activation energies of degradation processes and power acceleration coefficient for the specific type of LDAs developed by RFNC-VNIITF.

### REFERENCES

1. **Milovidov N.I., Smirnov E.V., Fomin A.V.**, Diode laser array and method of producing same: Russian Federation Patent No. 2544875, IPC H01S 5/02 (2006.01), H01S 5/024 (2006.01), H01S 5/42 (2006.01) State Atomic Energy Corporation "ROSATOM", FSUE "RFNC-VNIITF named after Academ. E.I. Zababakhin".
2. **Ziegler M.**, Imaging Catastrophic Optical Mirror Damage in High-Power Diode Lasers, *J. Electron. Mat.* 39 (2010) 709–714.
3. **Stiller W.**, Arrhenius Equation and Non-Equilibrium Kinetics., W. Stiller. - M.: 3A, Mir2C (2000) 176.
4. **Wang J., Bao L., Devito M., et al.**, Reliability and Performance of 808nm Single Emitter Multi-mode Laser Diodes, SPIE proceedings. - Photonics West. (2010).
5. **Heiko Kissel Dr., Wilhelm Fassbender, Jörg Neukum Dr.**, Reliable high-power diode laser arrays for QCW operation with high duty cycles, *Photonics*. 1 (49) (2015).



6. **Walker C.L.**, Improved Catastrophic Optical Damage Level From Laser With Nonabsorbing Mirrors, C.L. Walker, A.C. Bryce, J.H. Marsh, IEEE Photonic. Technol. Lett. – (14) (2002) 1394–1396.
7. **Mitsudo Fukuda**, Materials and Reliability Handbook for Semiconductor Optical and Electron Devices, Springer New York Heidelberg Dordrecht London, (2013).
8. **Lawrence A. Johnson**, Laser Diode Burn-in and Reliability Testing. Lawrence, A. Johnson President, CEO and Founder ILX Lightwave. (2014).

#### THE AUTHORS

**GAFUROV Eldar M.**

dep5@vniitf.ru

ORCID: 0000-0002-7405-4242

**SMIRNOV Evgenii V.**

dep5@vniitf.ru

ORCID: 0000-0002-0162-4689

*Received 25.07.2022. Approved after reviewing 08.08.2022. Accepted 09.08.2022.*

Conference materials

UDC 535.42

DOI: <https://doi.org/10.18721/JPM.153.232>

## The comparison of the optical vortices focusing by silicon diffraction axicons and ring gratings with variable relief heights using high-performance computer systems

D. A. Savelyev<sup>1,2</sup>✉

<sup>1</sup> Samara National Research University, Samara, Russia

<sup>2</sup> Image Processing Systems Institute of RAS – Branch of the FSRC  
“Crystallography and Photonics” RAS, Samara, Russia

✉ [dmitrey.savelyev@yandex.ru](mailto:dmitrey.savelyev@yandex.ru)

**Abstract.** A study was made of the spatial distribution of the intensity of the Laguerre-super-Gaussian (1,0) modes with circular, radial and azimuthal polarization depending on the change in the height of silicon subwavelength optical elements, the height of which varied from 0.2 to 3 wavelengths. Simulation by the finite difference method in the time domain showed that a change in the height of the considered optical elements significantly affects the diffraction pattern in the near zone. The smallest focal spot size was obtained for "-" circular polarization at an element height equal to two wavelengths.

**Keywords:** optical vortices, sub-wavelength structures, FDTD, high performance computer systems, ring gratings

**Funding:** This study was funded by the Ministry of Science and Higher Education, as part of the implementation of the State assignment (project no. 0777-2020-0017) in the part «Introduction», by the Samara University Development Program for 2021-2030 as part of the Priority 2030 program with the support of the Government of the Samara Region in the part «Materials and Methods», scholarship of the President of the Russian Federation (SP-1173.2022.5) in the part «Results and Discussion» and was performed under the «ERA.Net RUS plus» program and funded by RFBR, project number 20-52-76021 in the part «Conclusion».

**Citation:** Savelyev D. A., The comparison of the optical vortices focusing by silicon diffraction axicons and ring gratings with variable relief heights using high-performance computer systems, St. Petersburg State Polytechnical University Journal. Physics and Mathematics. 15 (3.2) (2022) 172–177. DOI: <https://doi.org/10.18721/JPM.153.232>

This is an open access article under the CC BY-NC 4.0 license (<https://creativecommons.org/licenses/by-nc/4.0/>)

Материалы конференции

УДК 535.42

DOI: <https://doi.org/10.18721/JPM.153.232>

## Сравнение фокусировки оптических вихрей кремниевыми дифракционными аксиконами и кольцевыми решетками с переменной высотой рельефа с использованием высокопроизводительных компьютерных систем

Д. А. Савельев<sup>1,2</sup> ✉

<sup>1</sup> Самарский национальный исследовательский университет им. академика С.П. Королева г. Самара, Россия;

<sup>2</sup> Институт систем обработки изображений - филиал ФНИЦ  
«Кристаллография и фотоника» РАН, г. Самара, Россия

✉ [dmitrey.savelyev@yandex.ru](mailto:dmitrey.savelyev@yandex.ru)

**Аннотация.** В данной работе исследуется пространственное распределение интенсивности мод Лагерра-суперГаусса (1,0) с круговой, радиальной и азимутальной поляризацией в зависимости от изменения высоты кремниевых субволновых оптических элементов, высота которых менялась от 0.2 до 3 длин волн. Моделирование методом конечных разностей во временной области показало, что изменение высоты рассма-



триваемых оптических элементов существенным образом влияет на дифракционную картину в ближней зоне. Наименьший размер фокального пятна был получен для «-» круговой поляризации при высоте элемента равной двум длинам волн.

**Ключевые слова:** оптические вихри, субволновые структуры, FDTD, высокопроизводительные компьютерные системы, кольцевые решетки

**Финансирование:** Работа выполнена при поддержке Министерства науки и высшего образования, в рамках выполнения Государственного задания (проект № 0777-2020-0017) в части «Введение», в рамках реализации Программы развития Самарского университета на 2021-2030 годы в рамках программы "Приоритет-2030" при поддержке Правительства Самарской области в части «Материалы и методы», Стипендии Президента Российской Федерации (СП-1173.2022.5) в части «Результаты и обсуждение», а также под эгидой программы «ERA.Net RUS plus» при финансовой поддержке РФФИ в рамках научного проекта № 20-52-76021 в части «Заключение».

**Ссылка при цитировании:** Савельев Д. А. Сравнение фокусировки оптических вихрей кремниевыми дифракционными аксиконами и кольцевыми решетками с переменной высотой рельефа с использованием высокопроизводительных компьютерных систем // Научно-технические ведомости СПбГПУ. Физико-математические науки. 2022. Т. 15. № 3.2. С. 172–177. DOI: <https://doi.org/10.18721/JPM.153.232>

Статья открытого доступа, распространяемая по лицензии CC BY-NC 4.0 (<https://creativecommons.org/licenses/by-nc/4.0/>)

## Introduction

The structured laser beams [1], including those in the field of metamaterials and metasurfaces [2], are being actively studied in various fields of optics and photonics at present. In particular, it is known to use metasurfaces to generate an optical vortex in order to increase the throughput of optical communication systems [3]. Among structured beams, a special place is occupied by singular light beams [4], among which we should note beams with screw dislocations (optical vortices), which are currently being actively studied [5]. Optical vortices are known to be used for a number of applications, including the transmission of information over an optical fiber [6], in quantum informatics [7], and in wireless communication systems [8].

The introduction of a vortex phase singularity into the incident beam makes it possible to amplify the longitudinal component of uniformly polarized laser beams on the optical axis in the focal region [9], which makes it possible to change the diffraction pattern due to energy redistribution between the components of the electromagnetic field [10].

The presence of a strong longitudinal component in the focus region makes it possible to improve the optical resolution and is used for a number of applications, among which one can note optical manipulation and material processing [11].

Currently, the silicon and its compounds have a variety of applications [12, 13]. In particular, they are used for the manufacture of semiconductor devices [14], solar batteries [15], in medicine [16], as well as for solving photonics problems [17]. Due to the high refractive index of silicon, it is possible to obtain a high integration density [13], as well as to reduce the size of the focal spot during sharp focusing with optical microelements, including diffractive axicons [18].

The diffraction of optical vortices on silicon subwavelength microelements is studied in this paper: diffractive axicons and ring gratings of variable height. The influence of a change in the height of such elements on the subwavelength focusing of the considered laser beams is considered. Numerical calculations (3D) of laser radiation propagation were performed using the finite difference time domain method (FDTD) using high-performance computer systems.

## Materials and Methods

This section presents the simulation parameters, types of elements, input beam: wavelength  $\lambda = 1.55 \mu\text{m}$ , the size of the computational domain for the selected radiation wave  $x, y, z$  was in the range  $[-5.8\lambda; 5.8\lambda]$ . The spatial sampling step is  $\lambda/30$ , the time sampling step is  $\lambda/(60c)$ , where  $c$  is the speed of light. The thickness of the absorbing PML layer surrounding the compu-

tational domain on all sides is  $1.16\lambda$ . The source is located inside the substrate, which occupies the entire space below the relief and is immersed in the absorbing PML layer. The refractive index of the element is  $n = 3.47$ .

Let us consider the action of the simplest implementation of an axicon in the form of a binary diffractive axicon with a numerical aperture  $NA = 0.95$  (lattice period  $1.05\lambda$ ), whose phase takes values of 0 and  $\pi$  radians. The height of the relief of a binary element, corresponding to the phase  $\pi$  radians, with a refractive index of the material of the element  $n = 3.47$  is equal to:

$$h = \frac{\pi}{k(n-1)} \approx 0.2\lambda, \quad (1)$$

where  $\lambda$  is the wavelength of the considered laser radiation,  $n$  is the refractive index,  $k = 2\pi/\lambda$  is the wave number.

An optical vortex as an input beam significantly changes the focal pattern compared to a conventional one, for example, a Gaussian beam [9], and the direction of rotation of circular polarization becomes important. Let us call "-" circular polarization the polarization in which the sign of the circular polarization is opposite to the sign of the introduced vortex phase singularity. The case when the sign of the circular polarization is co-directed with the introduced vortex phase singularity will be called "+" circular polarization.

Previously, it was shown that at the second order of the optical vortex and higher for "-" circular polarization, a shadow round light spot was formed [9, 19]. In this paper, the first order of an optical vortex in an incident beam for this type of polarization is considered.

The beams with an amplitude distribution approximated by a super-Gaussian function are often used [20, 21] for the cases where a uniform intensity distribution over the beam cross section is required.

The Laguerre-superGauss (1,0) modes, mainly with "-" circular polarization, were considered as input laser radiation (cases for "+" circular, radial and azimuthal polarizations are also given) in this paper. The amplitude of the Laguerre-superGaussian mode (1,0) is given by:

$$A(r, \varphi) = r \cdot \exp\left[-\frac{r^p}{2\sigma^p}\right], \quad (2)$$

where  $\sigma$  is the beam size in  $\mu\text{m}$ ,  $p = 6$ .

### Results and Discussion

This section presents the study's results of the changing in the height relief effect of silicon microelements on the diffraction pattern in the near zone.

Figure 1 shows the results of propagation of the considered laser radiation through a diffractive axicon with a relief height  $h$  from  $0.2\lambda$  to  $3\lambda$ . The total intensity and intensity of the longitudinal

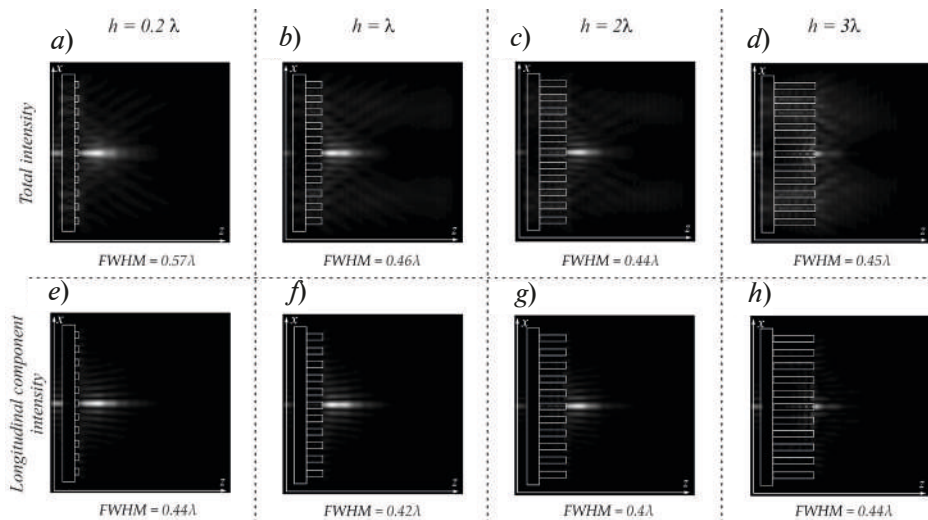


Fig. 1. The longitudinal cross section ( $xz$ ) of the Laguerre-superGauss mode (1,0) propagation (« $\leftrightarrow$ »circular polarization, intensity): total intensity ( $a, b, c, d$ ), longitudinal component intensity ( $e, f, g, h$ )

component of the electric field are shown. The size of the focal spot on the optical axis was estimated from the full width at half maximum (FWHM) of the all intensity.

All main maximums are formed outside the optical element. It should be noted that, at first, the size of the focal spot at the maximum decreases up to the height  $h = 2\lambda$ , and then an increase is observed. At a height  $h = 3\lambda$ , a significant shift of the maximum peak to the edge of the element relief is observed with a broadening of the focal spot size.

If estimate the value of the focal spot in the immediate vicinity of the element (at a distance of  $0.1\lambda$ ), then an increase in intensity is observed at all heights considered (from 40% at  $h = 0.2\lambda$  to 90% at  $h = 3\lambda$ ). The focal spot width was smaller than at the maximum and was  $\text{FWHM} = 0.36\lambda$  for heights from  $0.2\lambda$  to  $2\lambda$  and  $\text{FWHM} = 0.46\lambda$  for  $h = 3\lambda$ . The width of the focal spot for the longitudinal component of the electric field was less than the total width. It should also be noted that as the height of the relief increases, a reduction in the length of the light needle is observed.

The best value for the focal spot width was obtained for the height  $h = 2\lambda$  (total intensity). For this case, we will also consider other polarizations (“+” circular, radial and azimuthal). The results are shown in figure 2.

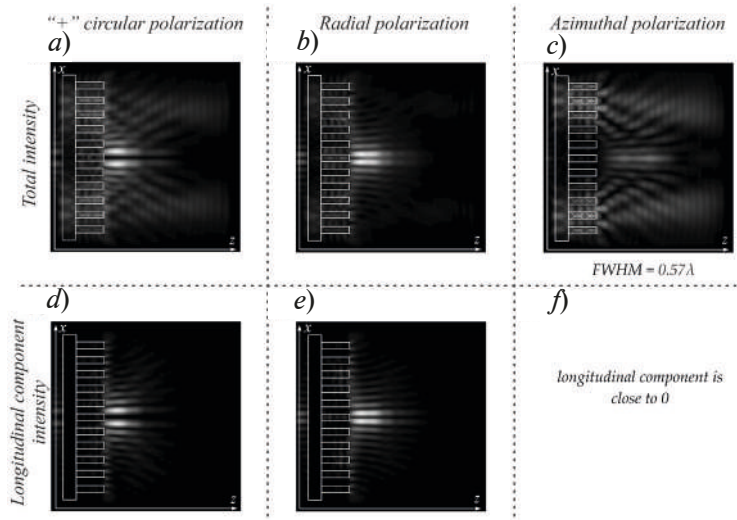


Fig. 2. The longitudinal cross section ( $xz$ ) of the Laguerre-superGauss mode (1,0) propagation, intensity: «+» circular polarization (a, d), radial polarization (b, e), azimuthal polarization (c)

As previously shown [18], the following is true for optical vortices of the first order: a zero value of the central focal spot indicates “+” circular polarization, and a nonzero one indicates “-” circular polarization. Similarly, for radial polarization there will be a zero value at the central focal point, and a non-zero value means azimuthal polarization.

Actually, you can see confirmation of this fact (Fig. 2). The rings obtained in the case of “+” circular polarization are smaller in length along the axis and the central shadow spot is larger than in the case of radial polarization (the length along the optical axis is greater). For the case of azimuthal polarization, the formation of a light needle on the optical axis is observed, but the intensity value is only 57% of the maximum. The size of the focal spot at the maximum on the optical axis is  $0.57\lambda$  and is formed at a distance of  $3.66\lambda$  from the edge of the relief.

Previous studies have shown that under certain conditions, a conventional round protrusion can be used to recognize polarization and focusing, and the focusing will be better than for a diffractive axicon with a similar grating size [18]. But the relief height also plays a key role [21].

In further studies, the central part of the relief changed, as shown in figure 3 (“-” circular polarization). Let's start from the height of the central cylinder  $h_1 = \lambda$ , the height of the remaining zones is the same and equal to  $0.2\lambda$ . Next, the height  $h_1$  has been increased to  $2\lambda$ , the height of the next zone will be equal to  $\lambda$ , and the rest by  $0.2\lambda$  (Fig. 3, b, e). And finally,  $h_1 = 3\lambda$ , the height of the first ring is  $2\lambda$ , the height of the second ring from the center is  $\lambda$ , and the rest are  $0.2\lambda$  each (Fig. 3, c, f).

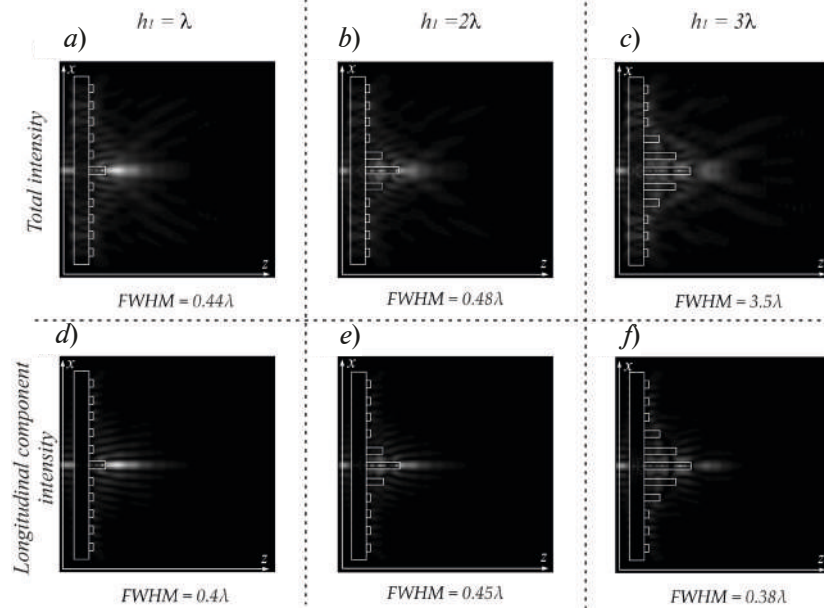


Fig. 3. The longitudinal cross section ( $xz$ ) of the Laguerre-super-Gauss mode (1,0) propagation on ring gratings with variable relief height:  $h_1 = \lambda$  (a, d),  $h_1 = 2\lambda$  (b, e),  $h_1 = 3\lambda$  (c, f)

It should be noted that only for the case  $h_1 = \lambda$ , the main maximum is formed outside of the element (at a distance of  $0.76\lambda$  from the edge of the element), so all FWHM values (Fig. 3) are given on the  $0.1\lambda$  from the edge of the central cylinder. That is, increasing the height in the selected format leads to the formation of an intensity peak inside the element. In the general case, a broadening of the focal spot size is observed outside the element; nevertheless, at  $h_1 = 3\lambda$  for the longitudinal component of the electric field, the result improved by 13.6% at a comparable intensity value.

### Conclusion

The simulation by the finite difference time domain method showed that a change in the height of subwavelength silicon elements significantly affects the diffraction pattern in the near zone. Diffractive axicons and annular gratings with different heights of individual grating rings were considered as such elements. The relief height of optical elements varied from  $0.2\lambda$  to  $3\lambda$ .

The Laguerre-superGaussian (1,0) modes with circular, radial, and azimuthal polarizations were considered as input laser radiation.

An analysis of the electric field intensity pattern showed that the smallest focal spot size was obtained for the diffractive axicon at  $h = 2\lambda$ : FWHM =  $0.44\lambda$  (for the maximum) and  $0.36\lambda$  (in the immediate vicinity of the element, at 65% of the total intensity). All main maxima for axicons were formed outside the optical elements. It should also be noted that as the height of the relief increases, a reduction in the length of the light needle of radiation is observed.

The results of numerical simulation for ring gratings with different heights showed that, in the general case, an increase in height leads to the formation of a maximum inside the element, however, at  $h_1 = 3\lambda$  for the longitudinal component of the electric field, the result improved by 13.6% at a comparable intensity value (outside, near the edge of the element).

### REFERENCES

1. Yan L., Kristensen P., Ramachandran S., Vortex fibers for STED microscopy, *Apl Photonics*. 4 (2) (2019) 022903.
2. Zhao Y., Askarpour A. N., Sun L., Shi J., Li X., Alù A., Chirality detection of enantiomers using twisted optical metamaterials, *Nature communications*. 8 (1) (2017) 1–8.
3. Ma X. et al., A planar chiral meta-surface for optical vortex generation and focusing, *Scientific Reports*. 5 (1) (2015) 1–7.
4. Cozzolino D., et al., Orbital angular momentum states enabling fiber-based high-dimensional quantum communication, *Physical Review Applied*. 11 (6) (2019) 064058.



5. Tkachenko G., Chen M., Dholakia K., Mazilu M., Is it possible to create a perfect fractional vortex beam, *Optica*. 4 (3) (2017) 330–333.
6. Pryamikov A., Alagashev G., Falkovich G, Turitsyn S., Light transport and vortex-supported wave-guiding in micro-structured optical fibres, *Scientific Reports*. (2020) 10 (1) 1–12.
7. Li S., Pan X., Ren Y., Liu H., Yu S., Jing J., Deterministic generation of orbital-angular-momentum multiplexed tripartite entanglement, *Physical Review Letters*. 124 (8) (2020) 083605.
8. Li S., et al., Efficient optical angular momentum manipulation for compact multiplexing and demultiplexing using a dielectric metasurface, *Advanced Optical Materials*. 8 (8) (2020) 1901666.
9. Savelyev D. A., Khonina S. N., Characteristics of sharp focusing of vortex Laguerre-Gaussian beams, *Computer Optics*. 39 (5) (2015) 654–662.
10. Khonina S. N., Alferov S. V., Karpeev S. V., Strengthening the longitudinal component of the sharply focused electric field by means of higher-order laser beams, *Optics Letters*. 38 (17) (2013) 3223.
11. Zhan, Q., Cylindrical vector beams: from mathematical concepts to applications, *Advances in Optics and Photonics*. 1 (2009) 1–57.
12. Cheng L., Mao S., Li Z., Han Y., Fu H. Y., Grating couplers on silicon photonics: design principles, emerging trends and practical issues, *Micromachines*. 11 (7) (2020) 666.
13. Mu X., Wu S., Cheng L., Fu H. Y., Edge couplers in silicon photonic integrated circuits: A review, *Applied Sciences*. 10 (4) (2020) 1538.
14. Myny K., The development of flexible integrated circuits based on thin-film transistors, *Nat. Electron*. 1 (2018) 30–39.
15. Garnett E., Yang P., Light trapping in silicon nanowire solar cells, *Nano Lett*. 10 (2010) 1082–1087.
16. Xu Y., et al., Silicon-based sensors for biomedical applications: a review, *Sensors*. 19(13) (2019) 2908.
17. Wu S., Mu X., Cheng L., Mao S., Fu H. Y., State-of-the-art and perspectives on silicon waveguide crossings: A review, *Micromachines*. 11 (3) (2020) 326.
18. Savelyev D., Kazanskiy N., Near-field vortex beams diffraction on surface micro-defects and diffractive axicons for polarization state recognition, *Sensors*. 21 (6) (2021) 1973.
19. Savelyev D. A., Khonina S. N., Golub I., Tight focusing of higher orders Laguerre-Gaussian modes, *AIP Conference Proceedings*. 1724 (2016) 020021.
20. Ding X., Ren Y. and Lu R., Shaping super-Gaussian beam through digital micro-mirror device, *Science China Physics, Mechanics & Astronomy*. 58(3) (2015) 1–6.
21. Savelyev D. A., The investigation of the features of focusing vortex super-Gaussian beams with a variable-height diffractive axicon, *Computer Optics*. 45 (2) (2021) 214–221.

## THE AUTHORS

**SAVELYEV Dmitry A.**

dmitrey.savelyev@yandex.ru

ORCID: 0000-0003-2282-3895

*Received 18.07.2022. Approved after reviewing 19.07.2022. Accepted 20.07.2022.*

Conference materials

UDC 535.8

DOI: <https://doi.org/10.18721/JPM.153.233>

## Features of construction of fiber-optic communication lines with orthogonal frequency-division multiplexing

N. I. Popovskiy<sup>1</sup> ✉, V. V. Davydov<sup>1, 2, 3</sup>, V. Yu. Rud<sup>3, 4</sup>

<sup>1</sup>The Bonch-Bruevich Saint Petersburg State University of Telecommunications, Saint Petersburg, Russia;

<sup>2</sup>Peter the Great Saint-Petersburg Polytechnic University, Saint Petersburg, Russia;

<sup>3</sup>All-Russian Research Institute of Phytopathology, Moscow Region, Russia;

<sup>4</sup>A.F. Ioffe Physicotechnical Institute, Saint Petersburg, Russia

✉ [nikitanikita24@mail.ru](mailto:nikitnikita24@mail.ru)

**Abstract.** The necessity of studying the features of building fiber-optic communication lines with multiplexing using orthogonal frequency division of channels is substantiated. The main properties of such systems are considered, as well as ways to improve operational characteristics to improve the quality of communication and economic benefits are studied. The necessity of developing such systems for future use in optical transport networks, cloud and high-performance computing systems is substantiated.

**Keywords:** large volumes of information, fiber-optic communication line, multiplexing, non-linear distortions, system bandwidth

**Citation:** Popovskiy N. I., Davydov V. V., Rud V. Yu., Features of construction of fiber-optic communication lines with orthogonal frequency-division multiplexing, St. Petersburg State Polytechnical University Journal. Physics and Mathematics. 15 (3.2) (2022) 178–183. DOI: <https://doi.org/10.18721/JPM.153.233>

This is an open access article under the CC BY-NC 4.0 license (<https://creativecommons.org/licenses/by-nc/4.0/>)

Материалы конференции

УДК 535.8

DOI: <https://doi.org/10.18721/JPM.153.233>

## Особенности построения волоконно-оптических линий связи с ортогональным частотным разделением каналов

Н. И. Поповский<sup>1</sup> ✉, В. В. Давыдов<sup>1, 2, 3</sup>, В. Ю. Рудь<sup>3, 4</sup>

<sup>1</sup>Санкт-Петербургский государственный университет телекоммуникаций им. проф. М. А. Бонч-Бруевича, Санкт-Петербург, Россия;

<sup>2</sup>Санкт-Петербургский Политехнический университет Петра Великого Санкт-Петербург, Россия;

<sup>3</sup>Всероссийский научно-исследовательский институт фитопатологии, Московская область, Россия;

<sup>4</sup>Физико-технический институт им. А.Ф. Иоффе, Санкт-Петербург, Россия

✉ [nikitanikita24@mail.ru](mailto:nikitnikita24@mail.ru)

**Аннотация.** Обоснована необходимость исследования особенностей построения волоконно-оптических линий связи с мультиплексированием с использованием ортогонального частотного разделения каналов. Рассмотрены основные свойства таких систем. Отмечены способы улучшения их эксплуатационных характеристик для повышения качества связи и финансовой рентабельности. Обоснована необходимость разработки таких систем для будущего использования в оптических транспортных сетях, облачных и высокопроизводительных вычислительных системах.

**Ключевые слова:** большие объемы информации, волоконно-оптическая линия связи, мультиплексирование, нелинейные искажения, пропускная способность системы

**Ссылка при цитировании:** Поповский Н. И., Давыдов В. В., Рудь В. Ю. Особенности построения волоконно-оптических линий связи с ортогональным частотным разделением каналов // Научно-технические ведомости СПбГПУ. Физико-математические науки. 2022. Т. 15. № 3.2. С. 178–183. DOI: <https://doi.org/10.18721/JPM.153.233>

Статья открытого доступа, распространяемая по лицензии CC BY-NC 4.0 (<https://creativecommons.org/licenses/by-nc/4.0/>)

### Introduction

The development of scientific and technological progress required the transfer of large amounts of information to solve various tasks [1–8]. To implement communication systems, channels have been developed using various principles for transmitting information [4, 9–15]. The most widely used fiber-optic communication lines (FOCL), since they use allows you to transfer large amounts of information at high rate [16–22]. The communication channel with FOCL is resistant to various external influences, which allows it to be used in various systems [20–29]. The constant increase in requirements for the speed of information transfer and an increase in its volume has led to the search for new solutions.

Recently, there has been an increased interest in the transmission of signals with orthogonal frequency multiplexing along the optical path, since this method has a well-developed hardware and software implementation of signal transmission and high spectral efficiency [30–33]. The features of OFDM signal generation lead to large signal outliers and, as a consequence, to the output of signal amplitudes from the linear section of the transmission characteristics of optoelectronic components of the optical path and to the transition of these devices to a nonlinear mode of operation. Consequently, there are nonlinear distortions that fall into the frequency band of the channels of the OFDM signal subcarriers and worsen the signal-to-noise ratio.

With the development of access networks to increase bandwidth, the use of frequency multiplexing technology of orthogonal subcarrier channels may become an alternative to traditional passive optical networks. In such networks, it is economically advantageous to use direct modulation of the laser diode radiation intensity on the transmitting side and direct photodetector detection of the signal on the receiving side. In the considered fiber-optic transmission system, the formation of an optical signal occurs in a technically simple way – the OFDM signal is created in the electrical range and then "transmitted" to the optical range with the modulation power according to the intensity of the optical carrier.

### Features of optical systems with frequency division of channels

One of the unique and most attractive properties of OFDMA networks is its asynchronous nature. Unlike TDM networks, it does not require time coordination between receiver and transmitter. Asynchronous FDMA allows subscribers to send their signals at any time without prior time coordination. The amount of noise interference will randomly change during the bit length of time in accordance with the relative positions of the cross correlations with the required autocorrelation peak, as shown in Figure 1.

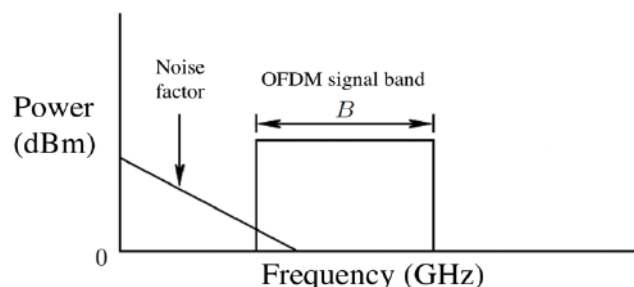


Fig. 1. The spectrum of signal at the output of the photodetection

To ensure spectral efficiency in the optical range, the methods of single-band modulation of the optical carrier and the technology of dense spectral multiplexing are used. However, with the single-band implementation of the OFDM signal and its transmission over an optical fiber, not only the distortion of the subcarrier levels occurs due to chromatic dispersion, but also during photodetection, there are beat noises between subcarriers that are located in the low-frequency region in the photocurrent spectrum. These noises do not allow the use of the entire bandwidth of the fiber-optic linear path.

### Experimental implementation of the OFDM network

Figure 2 shows the relative emission spectrum of a laser diode when modulated by an OFDM signal in the frequency band from 4.096 GHz to 8.192 GHz (the frequency range is 64 MHz, the number of subcarriers is 128). As can be seen from Fig. 2, the OFDM signal is distorted due to interference falling into the bandwidth of subcarrier channels. The source of such interference is clipped pulses that occur when the level of the OFDM signal exceeds the threshold value of the modulation current. It is possible to avoid these interferences and improve the energy budget of access networks by using external modulation of the optical carrier with an OFDM signal. An even greater increase in spectral efficiency can be achieved by using single-band external modulators, for example, based on the Mach-Zender.

The influence of quadrature nonlinearity with respect to the field during the conversion of an optical signal into an electric one was also studied. By analogy with Fig. 2, when the OFDM photo signal is detected, noises also appear in the low frequency region in the photocurrent spectrum, these noises are caused by beats between subcarriers.

Figure 3, *a* shows the radio frequency spectrum of the signal on the transmitter side, where the radio frequency power is approximately  $-12$  dBm. Figure 3, *b* shows the radio frequency spectrum on the receiver side after 50 km of SMF fiber. The radio frequency power decreases to  $-50$  dBm, this decrease in power is associated with an increase in the length of the fiber, which increases attenuation.

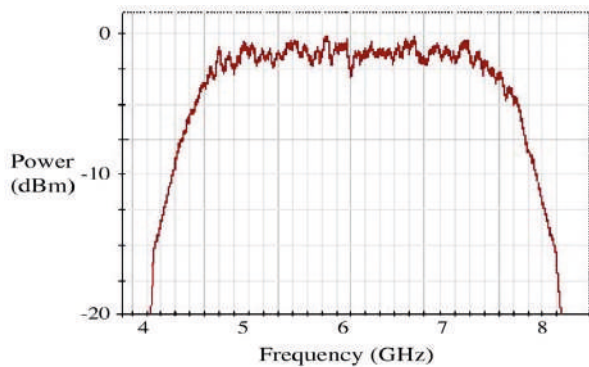


Fig. 2. The spectrum of signal at the output of the laser diode

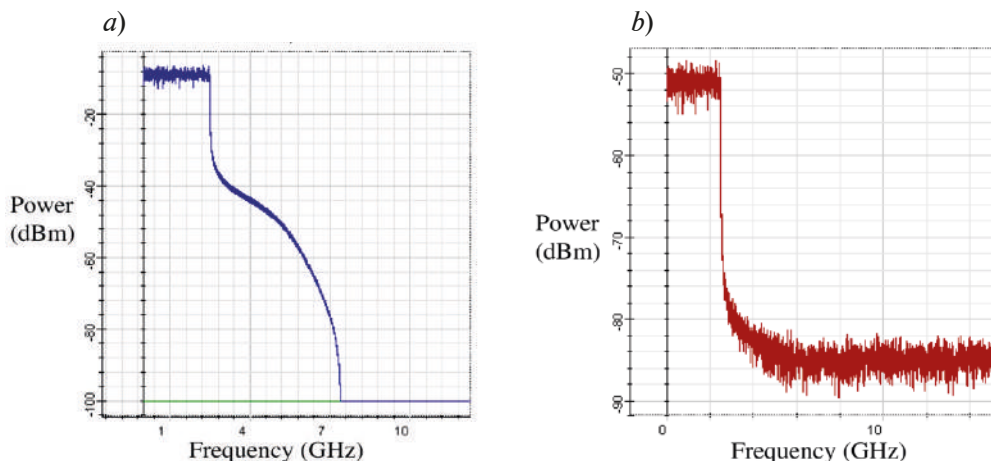


Fig. 3. Radio frequency spectrum of the signal on the transmitter side (*a*); radio frequency spectrum of the signal on the receiver side (*b*)

Figure 4, *a* shows an example of optical carrier phase fluctuations during one sample when transmitting  $N = 128$  subcarrier channels of the QPSK format with a frequency interval between them of 64 MHz. It can be seen that FCM leads to the appearance of high-frequency (relative to channel frequencies) phase fluctuations. In Figure 4, *b* shows the phase distribution density as a histogram.

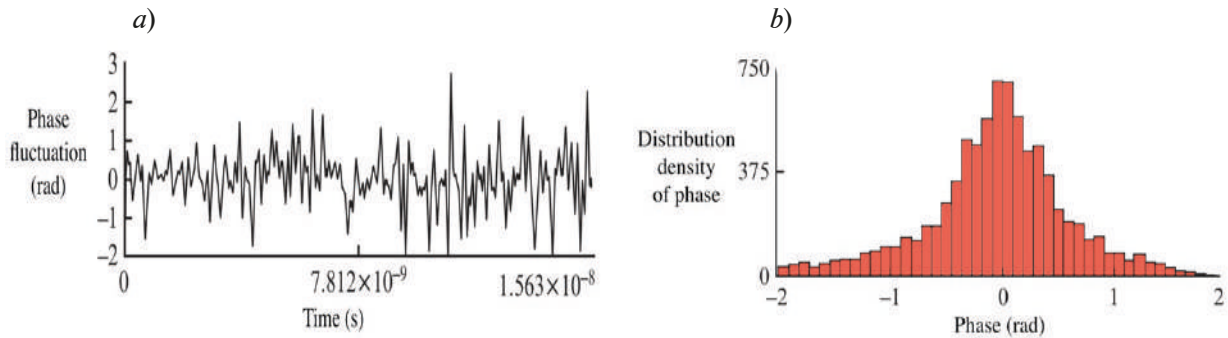


Fig. 4. Phase fluctuation due to FCM during one sample (*a*); the phase distribution density when transmitting  $N = 128$  subcarrier channels of the QPSK format with a frequency interval between them of 64 MHz (*b*)

The analysis shows that the average value of the fluctuating phase tends to zero, and its standard deviation – to 0.707, which indicates the independence of the standard value of XPM from the number of channels at  $N > 32$ .

### Conclusion

The main factor limiting the frequency band in access networks is the use of a direct photodetector according to technical and economic indicators. Note that an increase in the frequency band of the OFDM signal is possible due to the elimination of interference in the low-frequency spectrum of the photocurrent using circuit solutions in the receiving part of the equipment. In addition, it is possible to use methods of correcting coding in subcarrier channels, allowing to overcome strong interference in the channels. However, these and other technical solutions can increase the cost of equipment, so they require justification of economic feasibility when implemented in access networks.

The simulation results show that high-frequency channels with subcarriers are most susceptible to distortion due to chromatic dispersion. These distortions manifest themselves in the form of a decrease in the signal level in these channels. It is shown that the limiting factors of the bandwidth are the total frequency band occupied by the OFDM signal and the value of the specific chromatic dispersion coefficient of the optical fiber at the operating wavelength.

The simulation results showed that for access networks where a standard optical fiber with a length of 50 km is used in the optical infrastructure, the total frequency band of the OFDM signal at a wavelength of 1.55 microns should not exceed 8 GHz.

### REFERENCES

1. **Bandi T., Affolderbach C., Calosso C.E., et al.**, High-performance laser-pumped rubidium frequency standard for satellite navigation, *Electron. Lett.* 47 (2001) 698–699.
2. **Myazin N. S., Dudkin V. I., Grebenikova N. M., Davydov R. V., Podstrigaev A. S.**, Fiber - optical system for governance and control of work for nuclear power stations of low power, *Lecture Notes in Computer Science.* 11660 (2019) 744–756.
3. **Semenov V. V., Nikiforov N. F., Ermak S. V.**, Calculation of stationary magnetic resonance signal in optically oriented atoms induced by a sequence of radio pulses, *Soviet journal of Communications Technology and Electronics.* 36 (4) (1991) 59–63.
4. **Davydov R., Antonov V., Moroz A.**, Parameter Control System for a Nuclear Power Plant Based

on Fiber-Optic Sensors and Communication Lines, In: IEEE International Conference on Electrical Engineering and Photonics (EExPolytech), Saint-Petersburg, Russia, 13-15 October 2019. vol. 8906791 (2019) 295–297.

5. **Petrov A. A., Shabanov V. E., Zalyotov D. V., Bulyanitsa A. L., Shapovalov D. V.**, Modernization of the frequency synthesizer of cesium atomic clock, IEEE International Conference on Electrical Engineering and Photonics, EExPolytech 2018, Saint-Petersburg, October 2018. vol. 8564389 (2018) 52–55.

6. **Lukashev N. A., Davydov R. V., Glinushkin A. P.**, Improving characteristics of microwave frequency standard on Hg-199 ions for telecommunication systems, Journal of Physics: Conference Series. 1326 (1) (2019) 012046.

7. **Lukashev N. A., Moroz A. V.**, Compact microwave frequency standard on Hg-199 ions for navigation systems, Journal of Physics: Conference Series. 1236 (1) (2019) 012068.

8. **Valov, A. P., Arinushkina, K. G.**, The use of digital data processing to improve the metrological characteristics of the rubidium frequency standard, Journal of Physics: Conference Series. 2086 (1) (2021) 012070.

9. **Mihov E. D., Nepomnyashchiy O. V.**, Selecting informative variables in the identification problem Journal of Siberian Federal University - Mathematics and Physics. 9 (4) (2016) 473–480.

10. **Ryzhenko I. N., Lutsenko A.E., Varygin O. G., Nepomnyashchiy O. V.**, Carrier compensation mode implementation in satellite communication channels. In: Proceedings of 2019 International Siberian Conference on Control and Communications, SIBCON 2019, vol. 8729665 (2019) 23–29.

11. **Fadeenko V. B., Pchelkin G. A., Davydov V. V., Rud V. Yu.**, Features of the transmission of microwave signals in the range of 8-12 GHz in the maritime radar station over fiber-optic communication line, Journal of Physics: Conference Series. 1400 (4) (2019) 044010.

12. **Petrov A. A., Grebenikova N. M.**, Some Directions of Quantum Frequency Standard Modernization for Telecommunication Systems, Lecture Notes in Computer Science (including subseries Lecture Notes in Artificial Intelligence and Lecture Notes in Bioinformatics). 11118 LNCS (2018) 641–648.

13. **Petrov A. A.**, Digital Frequency Synthesizer for 133Cs-Vapor Atomic Clock, Journal of Communications Technology and Electronics. 62(3) (2017) 289–293.

14. **Petrov A. A., Zaletov D. V., Shapovalov D. V.**, Peculiarities of Constructing a Scheme for Formation of a Microwave Excitation Signal in a Cesium Atomic Clock, Journal of Communications Technology and Electronics. 66 (3) (2021) 295–299.

15. **Wang, D., Davydov, V. V., Rud, V. Y.** Prospective directions for the development of microwave frequency standards for satellite navigation systems Journal of Physics: Conference Series. 2086 (1) (2021) 012073.

16. **Myazin N., Neronov Y., Dudkin V.**, On the need for express control of the quality of consumer goods within the concept 'Internet of things' IOP Conference Series, Materials Science and Engineering. 497 (1) (2019) 012111.

17. **Dudkin V. I., Velichko E. N., Karseev A. Yu.**, Fiber-optic system for simulating accidents in the cooling circuits of a nuclear power plant Journal of Optical Technology (A Translation of Opticheskii Zhurnal) 82 (3) (2015) 132–135.

18. **Sharova N. V., Fedorova E. V., Vologdin V. A.**, Fiber-optics system for the radar station work control, Lecture Notes in Computer Science (including subseries Lecture Notes in Artificial Intelligence and Lecture Notes in Bioinformatics). 9247 (2015) 712–721.

19. **Ermak S. V., Karseev A. U., Velichko E. N.**, Fiber-optic super-high-frequency signal transmission system for sea-based radar station Lecture Notes in Computer Science (including subseries Lecture Notes in Artificial Intelligence and Lecture Notes in Bioinformatics). 8638 LNCS (2014) 694–702.

20. **Andreeva E. I., Potapov I. A.**, Possibilities of Using Optical Solitons in High-Speed Systems, Springer Proceedings in Physics. 255 (2021) 241–245.

21. **Andreeva E. I., Potapov I. A.**, Feature of Optical Soliton Sequence Propagation in Single-Mode Fiber, Journal of Physics: Conference Series. 1695 (1) (2020) 012125.

22. **Davydov R. V., Dmitrieva D. S., Pilipova V. M., Dudkin V. I., Andreeva E. I.**, The research of radioactive exposure compensation on optical material for optical fibers by powerful laser radiation Proceedings - International Conference Laser Optics 2020, ICLO 2020, Saint-Petersburg, Russia, vol. 9285820 (2020) 76.

23. **Andreev D. P., Andreeva E. I.**, Fiber Optic Attenuator, Journal of Physics: Conference Series. 2086 (1) (2021) 012128.



24. **Moroz, A. V.**, Features of transmission bearing and heterodyne receivers for signals in fiber-optic communication line in active phased array antenna, *Journal of Physics: Conference Series*. 1410 (1) (2019) 012212.
25. **Moroz, A. V.**, Fiber-optical system for transmitting heterodyne signals in active phased antenna arrays of radar stations, *Journal of Physics: Conference Series*. 1368 (2) (2019) 022024.
26. **Lenets V. A., Tarasenko M. Yu., Rodygina N. S.**, New method for testing of antenna phased array in X frequency range, *Journal of Physics: Conference Series*. 2018, 1038 (1) (2018) 012037.
27. **Tarasenko M. Yu., Lenets V. A., Malanin K. Yu., Akulich N. V.**, Features of use direct and external modulation in fiber optical simulators of a false target for testing radar station, *Journal of Physics: Conference Series*. 1038 (1) (2018) 012035.
28. **Tarasenko M. Y., Lenets V. A., Akulich N. V., Yalunina T. R.**, Features of use direct and external modulation in fiber optical simulators of a false target for testing radar station, *Lecture Notes in Computer Science (including subseries Lecture Notes in Artificial Intelligence and Lecture Notes in Bioinformatics)*. 10531 LNCS (2017) 227–232.
29. **Davydov R. V., Savelev I. K., Lenets V. A., Rud' V. Y.**, Fiber-optic transmission system for the testing of active phased antenna arrays in an anechoic chamber, *Lecture Notes in Computer Science (including subseries Lecture Notes in Artificial Intelligence and Lecture Notes in Bioinformatics)*. 10531 LNCS (2017) 177–183.
30. **Wang D., Zhang M., Li Z., Li J., Fu M., Cui Y.**, Modulation format recognition and OSNR estimation using CNN-based deep learning, *IEEE Photonics Technol.* 29 (19) (2017) 1667-1670.
31. **Popovskiy N., Davydov V., Gureeva I., Rud V. Y.**, Development to high-rate fiber optic communication line with code division multiplexing, *ACM International Conference Proceeding Series*. 2021 (2021) 527–531.
32. **Popovskiy N. I., Davydov V. V., Valiullin L. R.**, Features of the construction of fiber-optic communication lines with code division multiplexing, *Journal of Physics: Conference Series*. 1695 (1) (2020) 012120.
33. **Popovskiy N. I., Davydov V. V., Rud V. Yu.**, Features of the construction of photonic integrated circuits for communication systems *Journal of Physics: Conference Series* 2086(1) (2021) 012163.

## THE AUTHORS

### **POPOVSKIY Nikita I.**

nikitanikita24@mail.ru

ORCID: 0000-0003-3457-0370

### **DAVYDOV Vadim V.**

davydov\_vadim66@mail.ru

ORCID: 0000-0001-9530-4805

### **RUD Vasilij Yu.**

rudvas.spb@gmail.com

ORCID: 0000-0002-5731-0849

*Received 22.07.2022. Approved after reviewing 22.08.2022. Accepted 25.08.2022.*

Conference materials

UDC 535.3

DOI: <https://doi.org/10.18721/JPM.153.234>

### **Broadband light absorbers based on multilayer metal-insulator-metal structures**

A. I. Kashapov<sup>1,2</sup> ✉, E. A. Bezus<sup>1,2</sup>, D. A. Bykov<sup>1,2</sup>,  
N. V. Golovastikov<sup>1,2</sup>, L. L. Doskolovich<sup>1,2</sup>

<sup>1</sup>IPSI RAS – Branch of the FSRC “Crystallography and Photonics” RAS, Samara, Russia;

<sup>2</sup>Samara National Research University, Samara, Russia

✉ [ar.kashapov@outlook.com](mailto:ar.kashapov@outlook.com)

**Abstract.** We study optical properties of multilayer resonant metal-insulator structures. It is shown that a simple three-layer metal-insulator-metal (MIM) structure can provide near-perfect absorption of light (more than 90%) in a 732 nm-wide wavelength range. We demonstrate that by making the MIM structure slightly more complex by adding additional layers and optimizing their thickness, it is possible to broaden the near-perfect absorption band by almost a factor of two, covering the visible, near ultraviolet and near-infrared wavelength ranges with an average absorption level of 98.5%. Both structures provide a considerably low sensitivity to changes in the angle of incidence of the incident light. The obtained results can be applied for solar energy harvesting, photovoltaics and thermophotovoltaics, absorption filtering, and sensing.

**Keywords:** broadband light absorption, metal-insulator structures, resonant diffractive structures

**Funding:** This work was funded by the Ministry of Science and Higher Education of the Russian Federation (state assignment for research to Samara University (laboratory “Photonics for Smart Home and Smart City”, project FSSS-2021-0016), investigation of the broadband MIM absorbers; and state assignment to the FSRC “Crystallography and Photonics” RAS (agreement 007-GZ/Ch3363/26), implementation of the simulation software) and by the Russian Science Foundation (project 19-19-00514, analytical design the of initial “double” MIM structure).

**Citation:** Kashapov A. I., Bezus E. A., Bykov D. A., Golovastikov N. V., Doskolovich L. L., Broadband light absorbers based on multilayer metal-insulator-metal structures, St. Petersburg State Polytechnical University Journal. Physics and Mathematics. 15 (3.2) (2022) 184–189. DOI: <https://doi.org/10.18721/JPM.153.234>

This is an open access article under the CC BY-NC 4.0 license (<https://creativecommons.org/licenses/by-nc/4.0/>)

Материалы конференции

УДК 535.3

DOI: <https://doi.org/10.18721/JPM.153.234>

### **Широкополосные абсорберы света на основе многослойных структур металл-диэлектрик-металл**

А. И. Кашапов<sup>1,2</sup> ✉, Е. А. Безус<sup>1,2</sup>, Д. А. Быков<sup>1,2</sup>,  
Н. В. Головастикова<sup>1,2</sup>, Л. Л. Досколович<sup>1,2</sup>

<sup>1</sup>Институт систем обработки изображений РАН – филиал ФНИЦ «Кристаллография и фотоника» РАН, г. Самара, Россия;

<sup>2</sup>Самарский национальный исследовательский университет имени академика С.П. Королёва, г. Самара, Россия

✉ [ar.kashapov@outlook.com](mailto:ar.kashapov@outlook.com)

**Аннотация.** Исследованы оптические свойства многослойных резонансных металло-



диэлектрических (МДМ) структур. Показано, что путем усложнения простой трехслойной МДМ структуры, состоящего в добавлении дополнительных слоев и оптимизации их толщины, можно расширить полосу близкого к полному поглощения, охватив при этом диапазон длин волн от ближнего УФ до ближнего ИК включительно. Полученные результаты могут найти применение в фотовольтаике и термо-фотогальванике, сенсорики и для создания поглощающих оптических фильтров.

**Ключевые слова:** широкополосное поглощение света, металлодиэлектрические структуры, резонансные дифракционные структуры

**Финансирование:** Работа выполнена при финансовой поддержке Министерства науки и высшего образования Российской Федерации (государственное задание Самарскому университету (лаборатория «Фотоника для умного дома и умного города», проект ФССС-2021-0016), исследование широкополосных поглощающих МДМ-структур и государственное задание ФНИЦ «Кристаллография и фотоника» РАН (соглашение № 007-ГЗ/ЧЗ363/26 в части разработки программных средств для моделирования) и Российского научного фонда (проект 19-19-00514, аналитический расчет исходных «двойных» МДМ-структур).

**Ссылка при цитировании:** Кашапов А. И., Безус Е. А., Быков Д. А., Головастиков Н. В., Досколович Л. Л. Широкополосные абсорберы света на основе многослойных структур металл-диэлектрик-металл // Научно-технические ведомости СПбГПУ. Физико-математические науки. 2022. Т. 15. № 3.2. С. 184–189. DOI: <https://doi.org/10.18721/JPM.153.234>

Статья открытого доступа, распространяемая по лицензии CC BY-NC 4.0 (<https://creativecommons.org/licenses/by-nc/4.0/>)

## Introduction

Light absorbers based on nanophotonic structures are promising for a wide range of applications, including solar energy harvesting, photovoltaics and thermophotovoltaics, photodetection, absorption filtering, and sensing. Metal-insulator layered structures are widely used for broadband absorption of light [1–3]. One of the possible geometries of broadband absorbing structures is a set of pairs of metal and dielectric layers [1–3]. For example, in recent work [3], a non-resonant structure consisting of pairs of  $\text{MgF}_2$  – Cr layers was studied, which provides absorption exceeding 90% in a wavelength range with a width of about 1  $\mu\text{m}$  (900–1900 nm).

In our recent works [4, 5], we theoretically proved the possibility of obtaining an exact zero in the reflection spectrum of a three-layer metal-insulator-metal (MIM) structure at a given wavelength and angle of incidence by choosing the layer thicknesses. In the case, in which the lower metal layer of the MIM structure is sufficiently thick, it will “prohibit” the transmission of light through the structure, and, therefore, a zero in the reflection spectrum  $R$  will simultaneously mean complete absorption  $A = 1 - R$ . By combining two MIM structures, it is possible to obtain a reflection zero of the 2<sup>nd</sup> order in the spectrum of such a double MIM structure [6]. The authors of the present work believe that this is an important factor for broadening the band of near-perfect light absorption. In this work, absorbers based on single and double MIM structures are studied. It is shown that the optimization of the thicknesses of double MIM structures makes it possible to significantly expand the near-perfect absorption band. The broader near-perfect absorption band is explained by the presence of several resonances supported by the double MIM structure. The structure presented in this work absorbs more than 90% (98.5% on average) of the incident light with wavelengths ranging from 360 nm to 1750 nm, which is wider than the corresponding range in similar works [2, 3].

## Materials and Methods

As it was noted earlier, an MIM structure can provide complete absorption due to the proper choice of layer thicknesses [5]. Let us consider an MIM structure with metal and dielectric layers made of chromium (Cr) and silicon dioxide ( $\text{SiO}_2$ ), respectively. The refractive indices for

chromium and silicon dioxide were taken from the source [7]. The absorption spectra of metal-dielectric structures were calculated using an in-house implementation of the enhanced transmission matrix method [8]. As the optimization algorithm, we used the standard implementation of the interior-point algorithm in the MATLAB environment.

### Results and Discussion

Fig. 1, *a* shows the high absorption bandwidth at 90% (near-perfect absorption) at normal incidence as a function of the wavelength  $\lambda_0$ , at which total absorption is achieved. It is important to note that in order to obtain the graph in (Fig. 1, *a*), for each wavelength  $\lambda_0$ , the thicknesses of the MIM structure layers were calculated from the condition of zero reflection (total absorption) at this wavelength [5]. It can be seen from (Fig. 1, *a*) that a simple three-layer structure provides a wide near-perfect absorption band in the near-IR. Also, in Fig. 1, *a*, bold dots show the wavelengths used to calculate the structures, the spectra of which are shown in (Fig. 1, *b*). Consider a structure providing total absorption at a wavelength of 1300 nm. The thicknesses of the structure layers are described by the array [5.5, 197.1, 200.0] nm. In (Fig. 1, *b*), the yellow solid line shows the absorption spectrum of this structure, and the black dotted line shows the absorption level of 90%. Note that the width of the near-perfect absorption band is 732 nm (968–1700 nm).

The thicknesses of the layers of the MIM structure can be optimized to broaden the absorption band. For this, the following objective function can be used:

$$F(h) = \int_{\lambda_1}^{\lambda_2} A(h, \lambda) d\lambda, \quad (1)$$

where  $A$  is the absorption,  $h$  is the array of thicknesses of the structure layers,  $\lambda_1$  and  $\lambda_2$  are the boundaries of the “target” wavelength range, in which it is required to obtain high absorption.

Fig. 1, *c* shows the absorption spectra of the “initial” MIM structure (blue line) and the structure with optimized thicknesses (red line) maximizing the function (1). In this case, the thicknesses of the initial MIM structure were used as the starting point for the optimization. The thicknesses of the resulting optimized MIM structure are described by the following array: [6.0, 197.1, 167.0] nm. It can be seen from (Fig. 1, *c*) that the optimization of the thicknesses of the layers of the MIM structure makes it possible to only slightly increase the width of the absorption band.

For most applications, it is important for the absorption to remain high as the angle of incidence of the incident light changes. Fig. 1, *d* shows a rather low sensitivity to changes in a wide range of angles of incidence. In addition, let us note that concerning the application of photonic absorbing structures for solar energy harvesting, modern techniques in the field of reinforcement learning enable effectively choosing the position of a solar panel with such a coating, so the “uncovered” ranges of incidence angles can be compensated by such approaches [9].

Next, we make the studied structure more complex by “combining” two MIM structures with a SiO<sub>2</sub> dielectric layer separating them. Thus, we will obtain the following configuration (which we will refer to as “double” MIM structure): Cr-SiO<sub>2</sub>-Cr-SiO<sub>2</sub>-Cr-SiO<sub>2</sub>-Cr. The structure calculated in this way has a broader near-perfect absorption band (Fig. 2, *a*) as compared to the simple three-layer structure. In the vicinity of the wavelength, at which total absorption is provided, the absorption spectrum can be approximated by the function  $P_4(\lambda) = 1 - \alpha\lambda^4$  (Fig. 2, *a*). It should be noted that the thickness of the upper chromium layer of such a structure is close to zero, and, as the results of numerical simulation demonstrate, the exclusion of this layer does not affect its optical properties. Thus, we have obtained a structure in the SiO<sub>2</sub>-Cr-SiO<sub>2</sub>-Cr-SiO<sub>2</sub>-Cr configuration, the layer thicknesses of which are described by the array [217.9, 5.6, 422.8, 8.9, 199.6, 200.0] nm.

Let us now consider the possibility of broadening the near-perfect absorption band by numerically optimizing the six layer thicknesses of the obtained structure. The objective function (1) given above can also be used to optimize the thicknesses of a multilayer structure. The spectra of three-layer structures in Fig. 1, *b* show a sharp drop in absorption with the shift to the visible wavelength range. Let us choose  $\lambda_1 = 380$  nm and  $\lambda_2 = 1200$  nm to expand the near-perfect absorption band of the multilayer MIM structure to the visible range. The thicknesses of the “double” MIM structure were used as the starting point for maximizing the objective function (1).

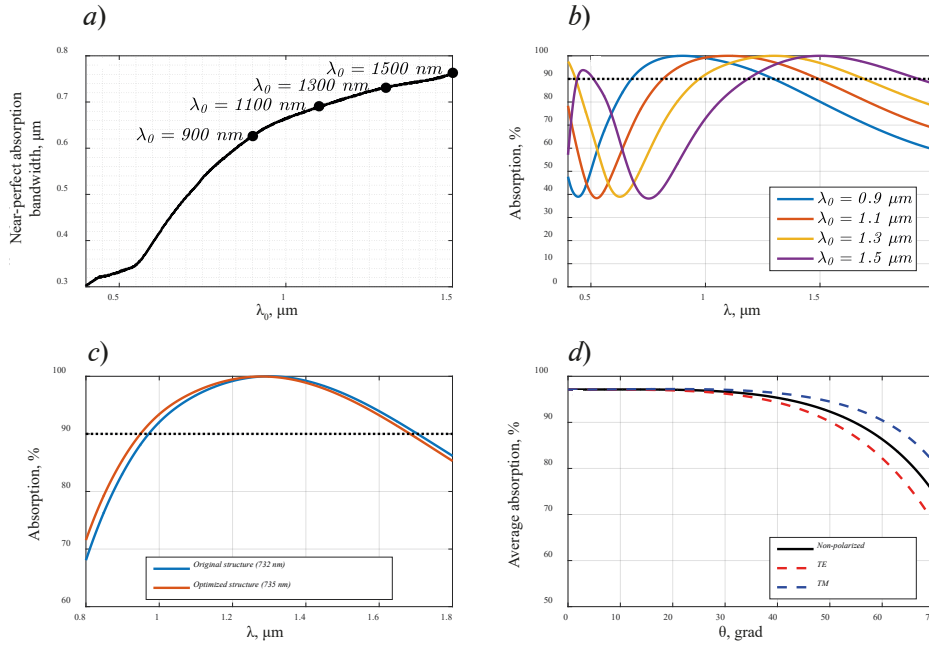


Fig. 1. Bandwidth of near-perfect absorption (at the level of 90%) vs. wavelength, at which total absorption is achieved, the black bold dots show the structures used to calculate the spectra in Fig. 1, *b* (a); absorption spectra of MIM structures calculated from the condition of zero reflection at normal incidence at different wavelengths, the dotted black line shows the absorption level of 90% (*b*); absorption spectrum of the analytically calculated MIM structure (blue line) and the structure with optimized thicknesses (red line) (*c*); average absorption over the wavelength range from 968 nm to 1700 nm vs. the angle of incidence for unpolarized light (black solid line), TE-polarized (red dashed line), and TM-polarized (blue dashed line) light (*d*)

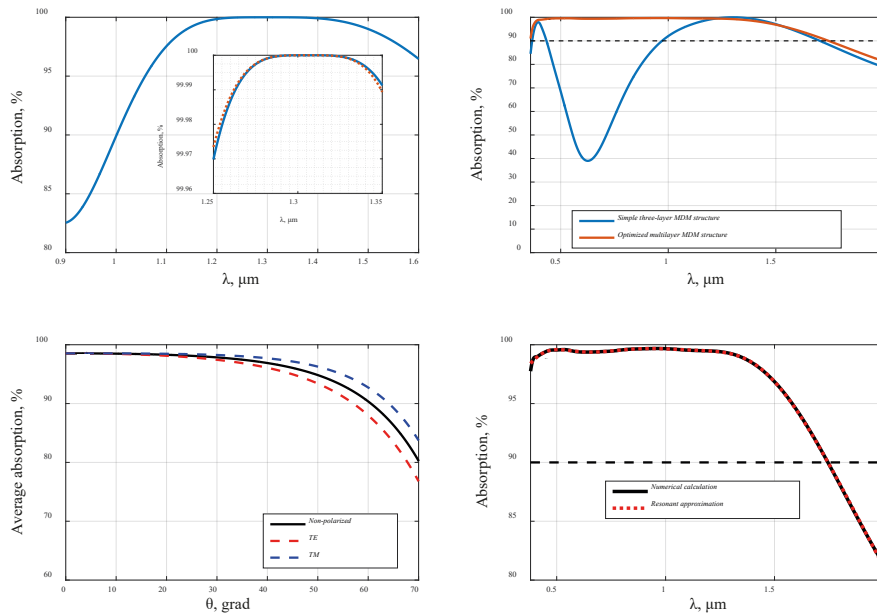


Fig. 2. Absorption spectrum of the “double” MIM structure without the upper metal layer and its approximation by the function  $P_4(\lambda) = 1 - \alpha\lambda^4$  (inset) (*a*); absorption spectra of the three-layer MIM structure (blue line) and the optimized multilayer MIM structure (red line), the black dashed line shows the absorption level of 90% (*b*); Average absorption in the 360-1750 nm wavelength range vs. angle of incidence for unpolarized light (black solid line), TE-polarized (red dashed line), and TM-polarized (blue dashed line) light (*c*); numerically calculated spectrum of the optimized structure (black solid line) and its resonant approximation by expression (2) (red dashed line) (*d*)

The red line in (Fig. 2, *b*) shows the absorption spectrum of the optimized structure, the thicknesses of which are described by the following array: [91.7, 5.0, 95.7, 12.3, 87.6, 223.0] nm.

Fig. 2, *b* shows that the addition of two dielectric layers separated by a metal layer to the three-layer MIM structure and subsequent optimization of their thicknesses makes it possible to extend the near-complete absorption band to the visible wavelength range, and that the width of the near-perfect absorption band of such a structure is almost two times greater than the corresponding value in the case of a simple three-layer structure. Also, the obtained structure provides rather low sensitivity to a change in the angle of incidence of the incident light (Fig. 2, *c*).

It should be noted that this effect has a resonant nature and is due to the excitation of eigenmodes supported by such a structure. Hence, the absorption spectrum of the six-layer structure can be approximated by the following expression:

$$A(\lambda) = 1 - \left| \rho \prod_{i=1}^3 \frac{\lambda - \lambda_{i,z}}{\lambda - \lambda_{i,p}} \right|^2, \quad (2)$$

where  $\rho$  is the non-resonant reflection coefficient,  $\lambda_{i,z}$  and  $\lambda_{i,p}$  are the complex wavelengths corresponding to zeros and poles (eigenmodes) of the reflection coefficient  $r(\lambda)$ , respectively.

In Fig. 2, *d*, the red dashed line shows the resonant approximation (2) of the numerically calculated spectrum of the multilayer MIM structure with optimized thicknesses (black solid line). As it can be seen from Fig. 2, *d*, the resonant model well approximates the obtained result, which confirms the assumption about the resonant nature of the studied effect. The numerically obtained approximation parameters (2) are given in Table. 1.

Table 1

**Numerical values of approximation parameters (2) for the absorption spectrum of the optimized six-layer structure.**

Approximation parameter	$\rho$	$\lambda_{1,z}$ , $\mu\text{m}$	$\lambda_{2,z}$ , $\mu\text{m}$	$\lambda_{3,z}$ , $\mu\text{m}$	$\lambda_{1,p}$ , $\mu\text{m}$	$\lambda_{2,p}$ , $\mu\text{m}$	$\lambda_{3,p}$ , $\mu\text{m}$
Value	0.837	0.485+ 0.083i	0.909+ 0.189i	1.273+ 0.187i	0.452+ 0.270i	0.921+ 1.489i	1.297+ 0.466i

### Conclusion

We demonstrated that a three-layer metal-insulator-metal structure can provide a wide near-perfect absorption band in the near-IR wavelength range, and high absorption is also maintained for a wide range of incidence angles. It has also been shown that the combination of MIM structures can significantly increase the width of near-perfect absorption band, and, in addition, the structure calculated in this way is a good starting point for numerical optimization of the thicknesses of a multilayer metal-insulator structure in order to extend the high absorption band to the visible and also to partially cover the near ultraviolet wavelength range. The resonant nature of the high absorption effect in the considered metal-insulator structures was also shown. The authors believe that this structure is promising for various practical applications, since layered structures, in contrast to structures with patterned layers (diffraction gratings and metasurfaces), are relatively easy to fabricate. The obtained results can be applied to solar energy harvesting, photovoltaics and thermophotovoltaics, photodetection, absorption filtering and sensing.

### REFERENCES

1. Yu P., Besteiro L. V., Huang Y., Wu J., Fu L., Tan H. H., Jagadish C., Wiederrecht G. P., Govorov A. O., Wang Z., Broadband Metamaterial Absorbers, *Adv. Opt. Mat.* 7 (3) (2019) 1800995.
2. Deng H., Li Z., Stan L., Rosenmann D., Czaplewski D., Gao J., Yang X., Broadband perfect absorber based on one ultrathin layer of refractory metal, *Opt. Lett.* 40 (11) (2015) 2592–2595.



3. **Chen T.-A., Yub M.-J., Lu Y.-J., Yen T.-J.**, Ultra-broadband, lithography-free, omnidirectional, and polarization-insensitive perfect absorber, *Sci. Rep.* 11 (2021) 5173.
4. **Kashapov A. I., Doskolovich L. L., Bezus E. A., Bykov D. A., Soifer V. A.**, Spatial differentiation of optical beams using a resonant metal-dielectric-metal structure, *J. Opt.* 23 (2) (2021) 023501.
5. **Kashapov A. I., Doskolovich L. L., Bykov D. A., Bezus E. A., Nesterenko D. V.**, Optical differentiator based on a trilayer metal-dielectric structure, *Comp. Opt.* 45 (3) (2021) 356–363.
6. **Doskolovich L.L., Kashapov A.I., Bezus E.A., Bykov D.A.**, Optical properties of cascaded metal-dielectric-metal structures and their application to the differentiation of optical signals, *Photonic. Nanostruct. Fundam. Appl.* 52 (2022) 101069.
7. Refractive index database. URL: <https://refractiveindex.info/>. Accessed Apr. 1, 2022.
8. **Moharam M. G., Pommet D. A., Grann E. B., Gaylord T. K.**, Stable implementation of the rigorous coupled-wave analysis for surface-relief gratings: enhanced transmittance matrix approach, *J. Opt. Soc. Am. A.* 12 (5) (1995) 1077–1086.
9. **Perera A.T.D., Kamalaruban P.**, Applications of reinforcement learning in energy systems, *Ren. Sust. En. Rev.* 137 (2021) 110618.

### THE AUTHORS

**KASHAPOV Artem I.**  
ar.kashapov@outlook.com  
ORCID: 0000-0002-7367-6277

**GOLOVASTIKOV Nikita V.**  
nikita.golovastikov@gmail.com  
ORCID: 0000-0002-0123-252X

**BEZUS Evgeni A.**  
evgeni.bezus@gmail.com  
ORCID: 0000-0001-7496-8960

**DOSKOLOVICH Leonid L.**  
leonid@ipsiras.ru  
ORCID: 0000-0001-8649-028X

**BYKOV Dmitry A.**  
bykovd@gmail.com  
ORCID: 0000-0002-9576-2360

*Received 14.07.2022. Approved after reviewing 17.07.2022. Accepted 18.07.2022.*

Conference materials

UDC 621.373.826

DOI: <https://doi.org/10.18721/JPM.153.235>

## Wavelength stabilized laser module for high-power fiber laser pumping

A. N. Ignatev<sup>1</sup>, A. V. Fomin<sup>1</sup>, S. R. Usmanov<sup>1</sup>, ✉

<sup>1</sup> FSUE "RFNC-VNIITF named after Academ. E. I. Zababakhin", Snezhinsk, Russia

✉ [dep5@vniitf.ru](mailto:dep5@vniitf.ru)

**Abstract.** The paper presents the results of development of wavelength stabilized laser modules where wavelength stabilization is achieved due to volume Bragg gratings with a 976 nm operating wavelength. The module was designed to spatially combine the light from six high-power laser diodes with its subsequent coupling into a silica fiber with a core diameter of 105  $\mu\text{m}$  and a numerical aperture of 0.15. Stabilization scheme was realized, where volume Bragg gratings were placed behind the lenses used for light collimation along the slow axis. Laser diode performance was studied for volume Bragg gratings with different reflectivity factors. The measurement results were used to determine optimum reflectivity of volume Bragg gratings; the spectral and power characteristics of the manufactured laser module were measured. The volume Bragg gratings allowed for significant, down to 0.5 nm, narrowing of the laser module spectrum width and wavelength stabilization over the entire range of operating currents. In continuous mode, the manufactured laser module power reached 43.6 W at a pumping current of 10 A and a thermal stabilization temperature of 25°C.

**Keywords:** high-power laser diodes, volume Bragg grating, volume holographic grating, wavelength stabilization

**Citation:** Ignatev A. N., Fomin A. V., Usmanov S. R., Wavelength stabilized laser module for high-power fiber laser pumping, St. Petersburg State Polytechnical University Journal. Physics and Mathematics. 15 (3.2) (2022) 190–195. DOI: <https://doi.org/10.18721/JPM.153.235>

This is an open access article under the CC BY-NC 4.0 license (<https://creativecommons.org/licenses/by-nc/4.0/>)

Материалы конференции

УДК 621.373.826

DOI: <https://doi.org/10.18721/JPM.153.235>

## Лазерный модуль со стабилизацией длины волны излучения для накачки мощных волоконных лазеров

А. Н. Игнатьев<sup>1</sup>, А. В. Фомин<sup>1</sup>, С. Р. Усманов<sup>1</sup>, ✉

<sup>1</sup> ФГУП «РФЯЦ-ВНИИТФ им. академ. Е.И. Забабахина», г. Снежинск, Россия

✉ [dep5@vniitf.ru](mailto:dep5@vniitf.ru)

**Аннотация.** В работе представлены результаты разработки лазерных модулей со стабилизацией длины волны излучения с помощью объемных брэгговских решеток с рабочей длиной волны 976 нм. В качестве модуля накачки использовался лазерный модуль с пространственным объединением излучения шести мощных лазерных диодов с последующим вводом в кварц-кварцевое волокно с диаметром сердцевины 105 мкм и числовой апертурой 0,15. Проведены исследования характеристик лазерных диодов при использовании объемных брэгговских решеток с различными коэффициентами отражения, определен оптимальный коэффициент отражения объемных брэгговских решеток, измерены спектральные и мощностные характеристики изготовленного лазерного модуля. Ширина спектральной линии излучения лазерного модуля составила 0,5 нм, стабилизация длины волны излучения наблюдалась во всем диапазоне рабочих токов. Мощность изготовленного лазерного модуля составила 43,6 Вт в непрерывном режиме работы при токе накачки 10 А и температуре термостабилизации 25°C.

**Ключевые слова:** мощные лазерные диоды, объемная брэгговская решетка, стабилизация длины волны



**Ссылка при цитировании:** Игнатьев А. Н., Фомин А. В., Усманов С. Р. Лазерный модуль со стабилизацией длины волны излучения для накачки мощных волоконных лазеров // Научно-технические ведомости СПбГПУ. Физико-математические науки. 2022. Т. 15. № 3.2. С. 190–195. DOI: <https://doi.org/10.18721/JPM.153.235>

Статья открытого доступа, распространяемая по лицензии CC BY-NC 4.0 (<https://creativecommons.org/licenses/by-nc/4.0/>)

### Introduction

Laser modules (LMs) based on high-power laser diodes (LDs) used to be a conventional source for high-power fiber laser pumping [1–3]. One of the most important LM characteristics is its pumping efficiency determined, among other factors, by spectral characteristics of the LM used. For pumping the ytterbium fiber lasers, LMs with spectral ranges of 915 nm, 940 nm, and 976 nm are used, while the latter are of the greatest interest as this spectral range corresponds to the absorption peak of ytterbium-doped fibers having maximum absorption coefficient [4]. At the same time, the width of the fiber absorption peak in this region is rather narrow, which imposes certain restrictions on the pump modules used since the spectral width of high-power LDs can reach several nanometers and the typical temperature shift of the lasing wavelength is 0.3 nm/°C [5, 6]. One of the ways to improve the LM spectral characteristics is to use an additional optical element as an output mirror of the LD external resonator. As for LMs that are commercially available nowadays, the most popular schemes are those where this additional optical element is represented by volume Bragg gratings, or volume holographic gratings, that are easy to operate and have smallest dimension, if compared to other schemes [6–8]. Spectral width of LD can be narrowed to less than 0.5 nm and the temperature drift of wavelength can be reduced to 0.01 nm/°C [4].

### LD wavelength stabilization using volume Bragg gratings

Volume Bragg gratings (VBGs) are the optical elements with a periodic change in the refractive index, that can fully or partially reflect the incident radiation. The principle of radiation wavelength stabilization with the help of VBG is based on the placement of this element on the laser beam path so that part of the radiation returns to the LD's resonator. Under certain conditions, this feedback suppresses the generation of neighboring longitudinal modes of LD's own resonator, radiation is generated only at the VBG operating wavelength, and the width of the LD spectral line narrows to a value corresponding to the spectral width of the VBG reflection [9]. The extension of range of operating currents and temperatures for which wavelength stabilization is observed is achieved in two ways, namely, by increasing the portion of radiation that returns to the LD resonator and reducing the reflectivity of AR-coating of the LD output facet [10]. In order to increase the portion of feedback, VBG is usually placed behind the optical elements used for the LD light collimation. At that, schemes are common, in which VBGs are mounted both behind the lenses for collimating the LD light divergence along the fast axis [11], and behind the lenses for collimating the divergence of light along the slow axis [7]. Besides, there are schemes where the periodic structure of the refractive index is integrated directly into the lens for collimation of light along the fast axis, which combines the properties of both the VBG and the collimating lens. Though easy to operate and adjust, these optical elements have certain disadvantages, such as significant exceedance of the spectral width of the stabilized LDs compared to that of the VBG reflection [12].

In this work, basic design version of a self-developed LM was used [13], whose optical scheme is designed to spatially combine the radiation from several LDs with its subsequent coupling into a silica fiber with a core diameter of 105  $\mu\text{m}$  and a numerical aperture of 0.15. This LM design allowed for installation of the VBG onto the surface area of a heatsink between the lenses used for collimation of light divergence along the slow axis and the rotary mirrors. Multimode broad area single emitter LDs with the emitter width of 94  $\mu\text{m}$  and the cavity length of 3.6 mm were used as the LM radiation sources. Output facet reflectivity of LDs was less than 0.1%, the LD wavelength corresponded to the range of (965 – 968.5) nm at a pumping current of 1 A and a

thermal stabilization temperature of 25°C. The LD spectral width was (4–6) nm and the average pumping current shift of wavelength amounted to 1 nm/A (Figure 1).

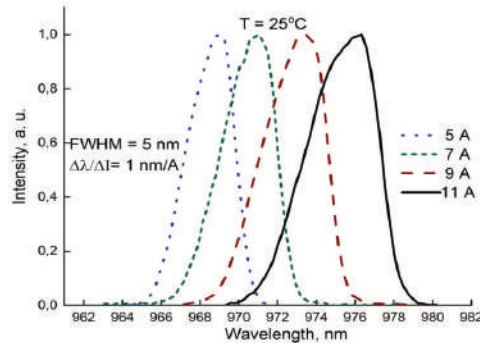


Fig. 1. LD spectrum vs. current

To stabilize the LD wavelength, the VBGs with characteristics presented in Table 1 were used.

Table 1

**Spectral characteristics of VBG**

Parameter	Value
Wavelength, nm	976 ± 0.5
Reflectivity, %	8;10;12
Spectral width, nm	0.5
AR-Coating	0.5
Thickness, mm	0.7

**Experimental results**

As a part of this work, we studied the possibility to manufacture an LM with a spectral range of 976 nm and a power of more than 40 W when wavelength is stabilized over the entire range of LM operating currents, i.e. from 1 A to 10 A. As noted above, one of the ways to increase the stabilization range is to use the VBG with a high reflectivity factor. In this work, to stabilize the LD wavelength, the VBGs with reflectivity factors (8–12)% were used. Figure 2 shows the change in the LD’s power vs. current characteristic depending on the reflectivity of the VBG used to stabilize the wavelength.

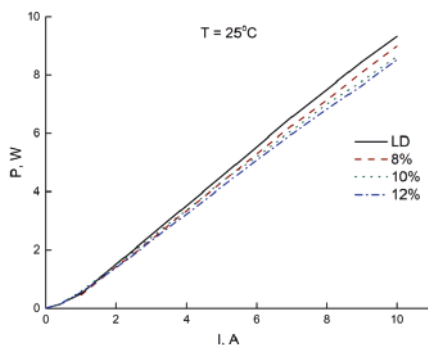


Fig.2. LD’s power vs. current curve for VBGs with different reflectivity factors

As can be seen from Figure 2, an increase in the VBG reflectivity leads to a decrease in the slope of the curve. Besides, the use of a high-reflectivity VBG increases the probability of LD failure at maximum pumping current [14, 15]. Thus, the task of determining the optimal characteristics of VBG can be reduced to finding the lowest reflectivity of VBG, at which wavelength stabilization is observed over the entire range of LM operating currents. The VBG was aligned by angular rotation in the direction of the fast and slow axes of the LD while continuously recording the LD spectrum. Figure 3, a, b, c shows the LD spectral data recorded after the mounting of VBG with reflectivity R = 8%.

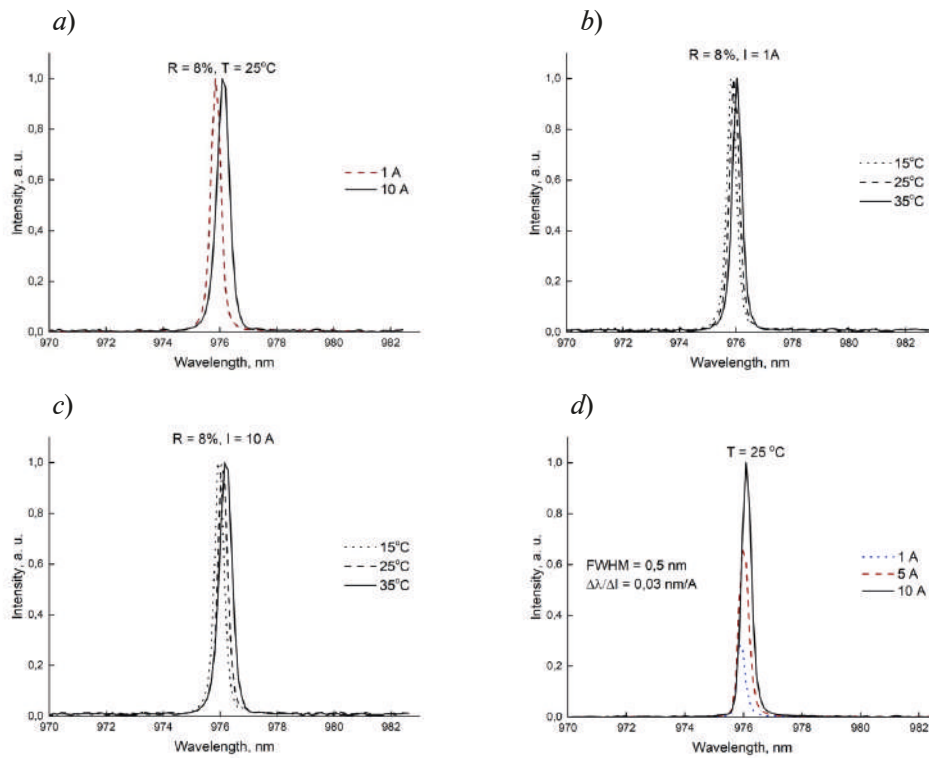


Fig. 3. LD spectrum vs. current (a); LD spectrum vs. temperature at 1 A (b); LD spectrum vs. temperature at 10 A (c); LM spectrum vs. current (d)

It can be seen from Figure 3 that wavelength stabilization was observed at all LD's operating currents in the temperature range from 15°C to 35°C. It should be noted that similar results have been achieved for VBG with reflectivity factors of 10% and 12%. Additionally, the generation of the second peak of radiation with a wavelength corresponding to that of the LD was observed only in the case of insufficiently accurate VBG alignment, and angular displacement of VBG in the direction of the fast axis turned out to be most sensitive to misalignment. Since VBGs with lower reflectivity factor are more preferable from the perspective of long life and maximum power of the LM, the VBGs with reflectivity of ~ 8% were chosen to be used in the experimental prototype LMs. To minimize displacement during its installation, the VBG was fixed to the base using a low-shrinkage UV-curable adhesive. The LM spectrum is shown in Figure 3, d and its power verses current curve is given in Figure 4. Maximum radiation power of the LMs manufactured was 43.6 W in continuous mode of operation at a current of 10 A and a thermal stabilization temperature of 25°C. Wavelength stabilization was observed at all operating currents of the LM.

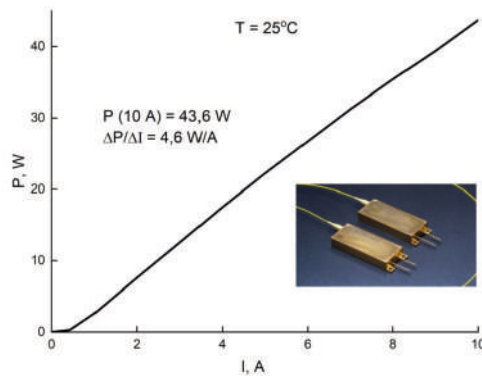


Fig. 4. Power vs. current curve of the LM

### Conclusion

Wavelength stabilized LM of ~44 W was designed and manufactured, where wavelength stabilization is realized in continuous mode of operation at a pumping current of 10 A and a thermal stabilization temperature of 25°C. For the LDs with output facet reflectivity less than 0.1%, the VBG with reflectivity of ~8% was demonstrated to be an optimal choice to achieve wavelength stabilization over the entire range of LM operating currents, provided that the VBG is properly aligned and installed. Due to the use of VBG, the LM spectral width narrowed to 0.5 nm and the pumping current shift of wavelength decreased to ~0.03 nm/A.

### REFERENCES

1. Haag M., Kohler B., Biesenbach J., Brand T., Novel high-brightness diode laser device, In: Proceedings of SPIE. High-Power Diode Laser Technology and Applications V. Vol. 6546 (64560T) (2007).
2. Wessling C., Hengesbach St., Geiger J., Dolkemeyer J., Traub M., Hoffman D., 50 W passively cooled, fiber coupled diode laser at 976 nm for pumping fiber lasers using 100 μm fiber bundles, In: Proceedings of SPIE. High-Power Diode Laser Technology and Applications VI, Vol. 6876 (687614) (2008).
3. Kelemen M., Gilly J., Friedmann P., Hilzensauer S., Ogradowski I., Kissel H., Biesenbach J., Diode lasers optimized in brightness for fiber laser pumping, In: Proceedings of SPIE. High-Power Diode Laser Technology XVI, Vol. (10514) (105140F) (2018).
4. Kohler B., Brand T., Haag M., Wavelength stabilized high-power diode laser modules, In: Proceedings of SPIE. High-Power Diode Laser Technology and Applications VII, Vol. 7198 (719810) (2009).
5. Samson B., Frith G., Diode pump requirements for high power fiber lasers, In: International Congress on Applications of Lasers & Electro-Optics, Paper 501 (2007) 228–233.
6. Volodin B., Dolgy S., Melnik E., Downs E., Shaw J., Ban V., Wavelength stabilization and spectrum narrowing of high-power multimode laser diodes and arrays by use of volume Bragg gratings, Optic Letters, Vol. 29, Issue 16 (2004) 1891–1893.
7. Xu D., Ma D., Yu Z., Xu L., Chen X., Kilowatt wavelength-stabilized CW and QCW diode laser, In: Proceedings of SPIE. High-Power Diode Laser Technology XVIII, Vol. 11262 (112620C) (2020).
8. Venus G., Smirnov V., Glebov L., Spectral stabilization of laser diodes by external Bragg resonator, In: Solid State Diode Lasers Technol. Rev. (2004).
9. Gapontsev V., Moshegov N., Trubenko P., Komissarov A., etc. High-brightness 9XX-nm pumps with wavelength stabilization, In: Proceedings of SPIE. High-Power Diode Laser Technology and Applications VIII, Vol. 7583 (75830A) (2010).
10. Volodin B., Dolgy S., Melnik E., Downs E., Shaw J., Ban V., Performance enhancement of the high-power laser diodes and arrays by use of the volume Bragg grating technology, In: Proceedings of SPIE. High-Power Diode Laser Technology and Applications III, Vol. 5711 (2005).
11. Steckman G., Liu W., Platz R., Volume Holographic Wavelength Stabilized Laser Diodes. IEEE Journal of selected topics in quantum electronics, Vol. 13 (3) (2007) 672–678.
12. Hengesbach S., Witteb U., Traubb M., Hoffmann D., Simulation and analysis of volume holographic gratings integrated in collimation optics for wavelength stabilization, In: Proceedings of SPIE. High-Power Diode Laser Technology and Applications IX, Vol. 7918 (79180 A) (2011).
13. Fomin A. V., Usmanov S. R., Ignatev A. N., Kadigrob E. V., Fiber coupled laser module with brightness exceeding 10 MW/cm<sup>2</sup>·sr, Technical Physics. 4 (92) (2022) 616–619.
14. Takiguchi Y., Asatsuma T., Hirata S., Effect of the threshold reduction on a catastrophic optical mirror damage in broad-area semiconductor lasers with optical feedback. In: Proceedings of SPIE. High-Power Diode Laser Technology and Applications IV, Vol. 6104 (61040X) (2006).
15. Leonhäuser B., Kissel H., Unger A., Köhler B., Biesenbach J., Feedback-induced catastrophic optical mirror damage (COMD) on 976 nm broad area single emitters with different AR reflectivity, In: Proceedings of SPIE. High-Power Diode Laser Technology and Applications XII, Vol. 8965 (896506) (2014).



## THE AUTHORS

**IGNATEV Andrey N.**

dep5@vniitf.ru

ORCID: 0000-0002-3724-7221

**FOMIN Alexey V.**

dep5@vniitf.ru

**USMANOV Sergey R.**

dep5@vniitf.ru

*Received 19.07.2022. Approved after reviewing 28.07.2022. Accepted 29.07.2022.*

Conference materials

UDC 535.015

DOI: <https://doi.org/10.18721/JPM.153.236>

## Detection of orbital angular momentum of light by forked diffraction method

E. S. Lebedeva <sup>1</sup>✉, K. O. Sedykh <sup>1,2</sup>, I. O. Venediktov <sup>1,3</sup>, G. N. Goltsman <sup>1,3,4</sup>, D. V. Sych <sup>5</sup>

<sup>1</sup> Moscow State Pedagogical University, Moscow, Russia;

<sup>2</sup> National University of Science and Technology MISiS, Moscow, Russia;

<sup>3</sup> National Research University Higher School of Economics, Moscow, Russia;

<sup>4</sup> Russian Quantum Center, Skolkovo, Moscow, Russia;

<sup>5</sup> P.N. Lebedev Physical Institute, Moscow, Russia

✉ [narniyall02@gmail.com](mailto:narniyall02@gmail.com)

**Abstract.** Orbital angular momentum (OAM) is a characteristic of wave describing its spiral phase front. These waves can be applied in various fields such as quantum communications and computations, hence, there is a need for a compact and simple method of its generation and detection. Here we describe an experimental realization of OAM light beams via the forked diffraction method.

**Keywords:** orbital angular momentum (OAM), vortex light, detection, computer-generated holographic gratings, topological charge

**Funding:** The study was supported by the Russian Foundation for Basic Research, Sirius University of Science and Technology, JSC Russian Railways and Educational Fund “Talent and success,” Project 20-32-51004, the Russian Science Foundation, grant 21-72-10119.

**Citation:** Lebedeva E. S., Sedykh K. O., Venediktov I. O., Goltsman G. N., Sych D. V., Detection of orbital angular momentum of light by forked diffraction method, St. Petersburg State Polytechnical University Journal. Physics and Mathematics. 15 (3.2) (2022) 196–200. DOI: <https://doi.org/10.18721/JPM.153.236>

This is an open access article under the CC BY-NC 4.0 license (<https://creativecommons.org/licenses/by-nc/4.0/>)

Материалы конференции

УДК 535.015

DOI: <https://doi.org/10.18721/JPM.153.236>

## Детектирование орбитального углового момента света методом вилочной дифракции

Е. С. Лебедева <sup>1</sup>✉, К. О. Седых <sup>1,2</sup>, И. О. Венедиктов <sup>1,3</sup>, Г. Н. Гольцман <sup>1,3,4</sup>, Д. В. Сыч <sup>5</sup>

<sup>1</sup> Московский педагогический государственный университет, Москва, Россия;

<sup>2</sup> Национальный исследовательский технологический университет «МИСиС», Москва, Россия;

<sup>3</sup> Национальный исследовательский университет «Высшая школа экономики», Москва, Россия;

<sup>4</sup> Российский Квантовый Центр, Сколково, Москва, Россия;

<sup>5</sup> Физический институт им. П.Н. Лебедева РАН, Москва, Россия

✉ [narniyall02@gmail.com](mailto:narniyall02@gmail.com)

**Аннотация.** Орбитальный угловой момент (ОУМ) — характеристика волны, описывающая ее спиральный фазовый фронт. Волны с этой характеристикой могут быть применены в различных областях — таких, как квантовые коммуникации и вычисления. Отсюда возникает необходимость в простом и компактном способе генерации и детектирования волн с ОУМ. В данной работе описывается экспериментальная реализация ОУМ световых пучков методом вилочной дифракции.



**Ключевые слова:** угловой момент (ОУМ), закрученный свет, детектирование, голографические решетки, топологический заряд.

**Финансирование:** Исследование выполнено при поддержке гранта РФФИ, Научно-технологического университета «Сириус», ОАО РЖД и Образовательного Фонда «Талант и успех», № 20-32-51004 и гранта РНФ № 21-72-10119.

**Ссылка при цитировании:** Лебедева Е. С., Седых К., Венедиктов И. О., Гольцман Г. Н., Сыч Д. В. Детектирование орбитального углового момента света методом вилочной дифракции // Научно-технические ведомости СПбГПУ. Физико-математические науки. Т. 15. № 3.2. С. 196–200. DOI: <https://doi.org/10.18721/JPM.153.236>

Статья открытого доступа, распространяемая по лицензии CC BY-NC 4.0 (<https://creativecommons.org/licenses/by-nc/4.0/>)

## Introduction

Quantum communications is a novel technology in the field of information transmission which enables ultimate signal protection from eavesdropping. In the simplest version, quantum information is encoded in a two-dimensional degree of freedom, e.g., polarization of light. The use of higher-dimensional degrees of freedom significantly improves quantum communication protocols, for example, providing longer secure communication distance [1-4]. Orbital angular momentum (OAM) of light is a degree of freedom which can be used for multidimensional quantum information encoding. Currently, there are several methods for generation and detection of OAM. Here we consider the forked diffraction method which is remarkably flexible and simple in use and allows for both generation and detection of OAM with the same equipment. The method employs special holographic masks which we produce by lithography.

## Theoretical

The local wave vector of a plane wave Gaussian beam is parallel to the direction of beam propagation (Fig. 1,*a*). In contrast (Fig. 1,*b*), beams that carry OAM have a non-zero tangential component of the local wave vector, so the wave has a spiral phase front [5-8]. The number of revolutions around the center of the beam is a topological property which does not depend on the local perturbations, hence OAM is described by the topological charge  $L$ . The magnitude corresponds to the number of revolutions, and the sign reflects the direction (negative  $L$  stands for clockwise and positive  $L$  for counterclockwise rotation) [5]. The maximum modulus of the topological charge determines dimensionality of the OAM degree of freedom which can be used to transmit information in high-dimensional quantum communications.

Many methods of generation and detection have been already described in literature. The method of forked holographic gratings, which we have chosen for our experiment, employs special holographic masks (Fig. 1,*c*). Each holographic pattern is generated by a special program and

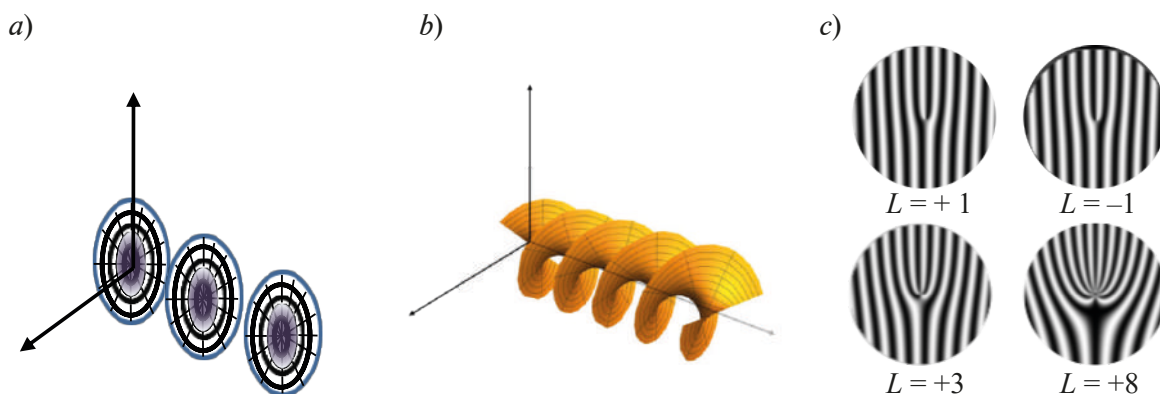


Fig. 1. Phase and intensity front of the initial Gauss beam (*a*); spiral phase front of an OAM carrier (*b*); diffraction patterns for  $L = \pm 1, +3, +8$  (*c*)

corresponds to a specific charge [8]. Diffraction of a wave on such masks changes its topological charge, for example, diffraction of a plane wave produces waves with OAM, while diffraction of an OAM wave can result in a plane wave.

In general, a grating with  $+L$  transforms the initial Gaussian beam into a diffracted one, where the zero's (central) diffraction order keeps with topological charge of the initial beam, the first (right) diffraction order has the same  $L$  as the grating, the minus first (left) diffraction order has  $-L$ , and each subsequent order changes the topological charge by  $+L$  or  $-L$ . The charge of each subsequent order increases due to a specific pattern: the lines bend more and more in the direction from the center of the pattern. Therefore, the size of gratings must be comparable to the width of the original beam, such that the beam passes through it entirely.

One of the significant advantages of this method is that the same gratings are used to detect OAM in the received beam. To detect an OAM beam, it is sufficient to transform it back into the original Gaussian beam [6]. To do this with help of forked holographic gratings, it is necessary to select the first diffraction order with  $+L$  (as its topological charge is equal to the charge to which the pattern corresponds) and let it pass through the plate with a charge equal to  $-L$ , in other words, the inverted one [5, 9]. Topological charge of the resultant beam becomes 0, which means it turns back into the Gaussian beam. Since our grating is made of a reflective material, the pattern formed by the slotted lattice can be considered as inverted at the reflection.

### Experimental Setup

The diffraction patterns were cut on the niobium plates on a sapphire substrate. For this experiment, gratings with patterns corresponding to  $L = \pm 1, \pm 3, \pm 8$  are used. Each pattern is produced in slightly different sizes for greater measurement accuracy. Gratings of 0.3 mm in size (denoted as Grid 1 in Fig. 2,*a*) were used to generate OAM, and of 0.2 mm (denoted as Grid 2 in Fig. 2,*a*) to detect it. When passing through a large lattice, the rays are more intense, which simplifies the detection process, as well as the resulting pattern has less artifacts (side spots) around diffraction orders.

The source of the Gaussian beam was a red free-space CW laser at 650 nm (Fig. 2,*a*). The beam fell orthogonally on the first grating, transforming into a diffraction pattern at its output. The first right order was selected on the obtained picture and guided through the diaphragm to block all other orders and then was focused by converging lens ( $F = 40$  mm) and completely reflected from the second grid which detects OAM.

In the measurement process, an important condition for observing the proper image is to maintain the straight direction of the beam after passing through the first grating, the diaphragm, and the lens (the same applies to the reflection from the second grating). Otherwise, there will be distortions of the pattern and even the absence of some orders during the detection.

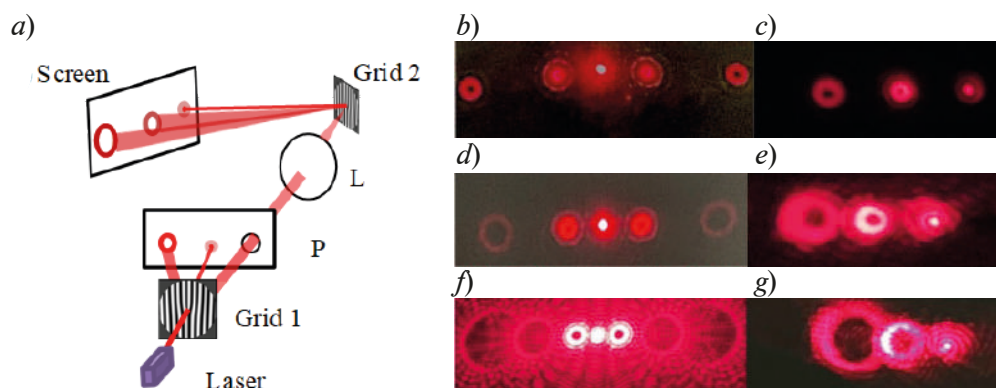


Fig.2 Experimental setup: laser, first grating Grid 1 ( $L = +1, +3, +8$ ), pinhole P, converging lens L, second grating Grid 2 ( $L = -1, -3, -8$ ) (a); pattern generated by grating with  $L = +1$  (b); pattern formed by detected beam ( $L = +1$ ) after reflection from second grating of the same charge (c); pattern generated by grating with  $L = +3$  (d); detected beam with  $L = +3$  (e); pattern generated by grating with  $L = +8$  (f); detected beam with  $L = +8$  (g)



## Results and discussion

After passing through the first grating, the Gaussian beam transforms into the required diffraction pattern (Fig. 2, *b*): at the central order we have  $L = 0$ , so the beam remains Gaussian, the right order has charge  $+l$ , the left order has charge  $-l$ . The fact that the charges of the first orders have equal charge magnitude can be confirmed by comparing the size of the dark “core” of the beams. Each subsequent diffraction order has lower intensity (thus we select the first order), a larger size and a smaller width of the “ring” itself, which confirms that the topological charge increased with each order. The larger  $L$  of the lattice, the faster topological charge increases with each order (Fig. 2, *d, f*).

When the selected order is focused on the second lattice and reflected from it, it forms a new pattern (Fig. 2, *c, e, g*). The central order keeps the charge of the original beam (in our case,  $L = +1, +3, +8$ ). In the left, its charge modulus increases by  $L$  of the grating, and in the first right order the beam becomes Gaussian back and thus his OAM is detected. This can also be judged by how the intensity is distributed: in the resulting pattern, the Gaussian beam is not the brightest, and the brightness decreases with each order starting from the first. Summarizing all these facts, it can be concluded that the efficiency of generating OAM beams with topological charges of  $+1, +3$  and  $+8$  is proven experimentally.

## Conclusion and Outlook

Results of our experiment confirms the possibility of generation and detection of OAM light beams via the forked diffraction method. This method significantly simplifies the study and the use of OAM beams, and enables numerous applications, e.g., quantum communication protocols and molecule identification in biochemistry [7], to name a few. Now, we have shown OAM beams with an integer topological charge. In future, we also consider manipulations with superpositions of two different OAM charges, low light intensity at the level of single photons, and the use of OAM photons in the field of quantum communications.

## Acknowledgments

We acknowledge Natalia Kaurova and Philip Zolotov for gratings fabrication, Dr. Ledesma, and Mr. Pabon for sharing program for diffraction masks generating. D.S. acknowledges financial support by Russian Foundation for Basic Research, Sirius University of Science and Technology, JSC Russian Railways and Educational Fund “Talent and success,” project number 20-32-51004.

E.L. acknowledges financial support by a grant from the Russian Science Foundation No. 21-72-10119.

## REFERENCES

1. Sych D., Grishanin B., Zadkov V., Critical error rate of quantum-key-distribution protocols versus the size and dimensionality of the quantum alphabet November 2004 Physical Review A 0523312.
2. Sych D., Grishanin B., Zadkov V., Analysis of limiting information characteristics of quantum-cryptography protocols, Quantum electronics. 35 (1) (2005) 80–84.
3. Sych D., Grishanin B., Zadkov V., Quantum key distribution with a continuous alphabet, Laser Physics. 14 (10) (2004) 1314–1321.
4. Sych D., Leuchs G., Quantum key distribution with multi letter alphabets, Optics and spectroscopy. 108 (April) (2010) 326–330.
5. Chen R., Zhou H., Moretti M., Wang X., Li J., Orbital Angular Momentum Waves: Generation, Detection and Emerging Applications, IEEE Communication Surveys & Tutorials. 22 (November) (2019) 840–868.
6. Allen L., Beijersbergen M B., Spreeuw R.J. C., Woerdman J. P., Orbital angular momentum of light and the transformation of Laguerre-Gaussian laser modes, Physical Review. A 45 (1992) (11).
7. Stepanov I. V., Fatkhiev D. M., Lyubopytov V. S., Kutluyarov R. V., Grakhova E. P., Neumann N., Khonina S. N. Sultanov A. K., Wavelength-Tunable Vortex Beam Emitter Based on Silicon Micro-Ring with PN Depletion Diode, Sensors. 22(3) (2022) 929.
8. Mair A., Vaziri A., Weihs G., Zeilinger A., Entanglement of Orbital Angular Momentum States of Photons, Nature. 412 (6844) (2001) 313–316.
9. Cunha A. B., Figueira G., André P. S., Generation of Orbital Angular Momentum Beams November 2015 CONF TELE 2015, Aveiro, 108.

## THE AUTHORS

**LEBEDEVA Elizaveta**

narniyall02@gmail.com

ORCID: 0000-0002-1429-3794

**GOLTSMAN Gregory**

goltsman@rplab.ru

ORCID: 0000-0002-1960-9161

**SEDYKH Ksenia**

kseniaolegovna98@gmail.com

ORCID: 0000-0001-6316-5337

**SYCH Denis**

denis.sych@gmail.com

ORCID: 0000-0002-4188-0951

**VENEDIKTOV Iliia**

ilia1999ven@gmail.com

ORCID: 0000-0001-8461-5931

*Received 14.08.2022. Approved after reviewing 16.08.2022. Accepted 31.08.2022.*

Conference materials

UDC 621.373.8

DOI: <https://doi.org/10.18721/JPM.153.237>

### **Gain-switched VCSEL as a quantum entropy source: the problem of quantum and classical noise**

R. A. Shakhovoy <sup>1, 2</sup>✉, E. I. Maksimova <sup>1</sup>,

<sup>1</sup>QRate LLC, Skolkovo, Russia;

<sup>2</sup>National University of Science and Technology MISiS, Moscow, Russia

✉ [r.shakhovoy@goqrates.com](mailto:r.shakhovoy@goqrates.com)

**Abstract.** We consider the problem of quantum noise extraction from polarization swapping in a gain-switched VCSEL. The principle of operation of a quantum random number generator is based on the generation of laser pulses with one of two orthogonal polarization states, followed by digitization of polarization-resolved pulses with a comparator. At intensity values of laser pulses close to the threshold value of the comparator, the contribution of the classical noise of the photodetector will have a crucial role in making a decision on the choice of a logical zero or one. We show how to evaluate the contribution of classical noise and how to calculate the quantum reduction factor required for post-processing.

**Keywords:** quantum random number generators, vertical surface emitting laser, quantum noise extraction

**Citation:** Shakhovoy R. A., Maksimova E. I., Gain-switched VCSEL as a quantum entropy source: the problem of quantum and classical noise, St. Petersburg State Polytechnical University Journal. Physics and Mathematics. 15 (3.2) (2022) 201–205. DOI: <https://doi.org/10.18721/JPM.153.237>

This is an open access article under the CC BY-NC 4.0 license (<https://creativecommons.org/licenses/by-nc/4.0/>)

Материалы конференции

УДК 621.373.8

DOI: <https://doi.org/10.18721/JPM.153.237>

### **Вертикально-излучающий лазер в режиме переключения усиления как источник квантовой энтропии**

Р.А. Шаховой <sup>1, 2</sup>✉, Е.И. Максимова <sup>1</sup>

<sup>1</sup>ОАО «КуРЭйт», Сколково, Россия;

<sup>2</sup>Университет науки и технологий МИСиС, г. Москва, Россия

✉ [r.shakhovoy@goqrates.com](mailto:r.shakhovoy@goqrates.com), ✉ [e.maksimova@goqrates.com](mailto:e.maksimova@goqrates.com)

**Аннотация.** В работе рассмотрена проблема извлечения квантового шума из переключения поляризации в вертикально излучающем лазере в режиме переключения усиления. Принцип работы квантового генератора случайных чисел основан на генерации импульсов лазерного излучения с одним из двух поляризационных состояний с последующей оцифровкой разрешенных по поляризации импульсов с помощью компаратора. При значениях интенсивности лазерных импульсов, близких к пороговому значению компаратора, решающим в принятии решения о выборе логического нуля или единицы будет вклад классических шумов фотоприемника. В работе показано, как оценить вклад классических шумов и как рассчитать квантовый фактор сжатия, необходимый для проведения постобработки.

**Ключевые слова:** квантовый генератор случайных чисел, вертикально-излучающий лазер, извлечение квантового шума

**Ссылка при цитировании:** Шаховой Р. А., Максимова Е. И. Вертикально-излучающий лазер в режиме переключения усиления как источник квантовой энтропии // Научно-технические ведомости СПбГПУ. Физико-математические науки. Т. 15. № 3.2. С. 201–205. DOI: <https://doi.org/10.18721/JPM.153.237>

Статья открытого доступа, распространяемая по лицензии CC BY-NC 4.0 (<https://creativecommons.org/licenses/by-nc/4.0/>)

### Introduction

Random number generators (RNGs) play a primary role in modern cryptographic applications. Due to the development of quantum cryptography, a special place among RNGs occupy now quantum RNGs (QRNGs), which use various quantum sources of entropy. Over the past 15-20 years, a number of approaches have been proposed to obtain quantum randomness; however, optical QRNGs, which employ laser noise, have gained the most popularity. Laser noise can be associated with various effects, e.g., with temperature-related fluctuations of the laser cavity length or with pump fluctuations. However, at relatively high frequencies, laser noise is associated mainly with spontaneous emission occurring due to zero-point oscillations of an electromagnetic field, which have purely quantum nature and are generally considered to have the properties of white noise. Due to this, laser noise can be employed as a high-frequency source of quantum entropy.

The main difference between optical QRNGs based on laser noise lies in how the noise is measured. Thus, interference-based optical QRNGs use *phase* noise of laser radiation, which is converted into amplitude fluctuations in the interferometer and then is readily measured with conventional photodetectors. In lasers that do not have fixed polarization of light, one may also use fluctuations of the *polarization state* in addition to phase fluctuations. Such an approach can be used, e.g., in a vertical-cavity surface-emitting laser (VCSEL). A VCSEL-based QRNG employing spontaneous polarization switching was first described in [1], where the author demonstrated the random bit generation rate up to 2 Mbps. Recently, we discussed a simple optical scheme of a QRNG based on a gain-switched VCSEL, which allows generating the sequence of random “on-off” pulses at several gigahertz [2]. Experimental demonstration of theoretical calculations performed there have been published in [3]. In the present article, we consider the problem of quantum noise extraction from polarization swapping in a gain-switched VCSEL. We use the approach developed in [4], namely, we introduce for the QRNG under consideration the *quantum reduction factor* containing information on the amount of classical noise “falling” into the digitized random sequence due to fluctuations in the photodetector. We also describe how this classical noise can be filtered out with the post-processing procedure.

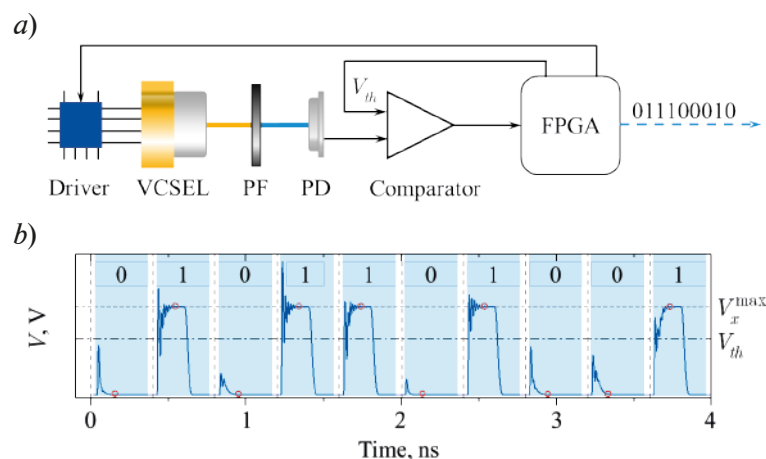


Fig. 1. Simplified scheme of a VCSEL-based QRNG (a); pulses at the comparator input and the results of the digitization (b)

### Simulations

A simplified scheme of the proposed QRNG is shown in Fig. 1,*a*. A gain-switched VCSEL is driven by a high-frequency laser driver, which is, in turn, controlled by the computer or FPGA. Laser output is followed by the polarization filter (PF) that allows obtaining polarization-resolved optical pulses, which are converted into the electrical signal via a broadband photodetector (PD). Random bits are obtained by digitizing pulses with a comparator, whose threshold voltage is calculated in the FPGA, which also performs post-processing procedures including randomness extraction.

In Fig. 1,*b*, we simulated the digitization process of polarization-resolved laser pulses. It was assumed in simulations that the polarizer in Fig. 1,*a* passes to the photodetector the  $x$ -linear polarization. Laser pulses were simulated with VCSEL rate equations given in [1]; the calculated signal was then processed with a low-pass digital filter (30 GHz bandpass) to simulate the finite bandwidth of the photodetector. The level of the comparator threshold ( $V_{th}$ ) is shown by the dash-dotted line in Fig. 1,*b*; red circles correspond to the moments of the comparator latch actuation. The result of digitization ('0'-s or '1'-s) is shown in the corresponding frames (each time frame is shown by the blue rectangle).

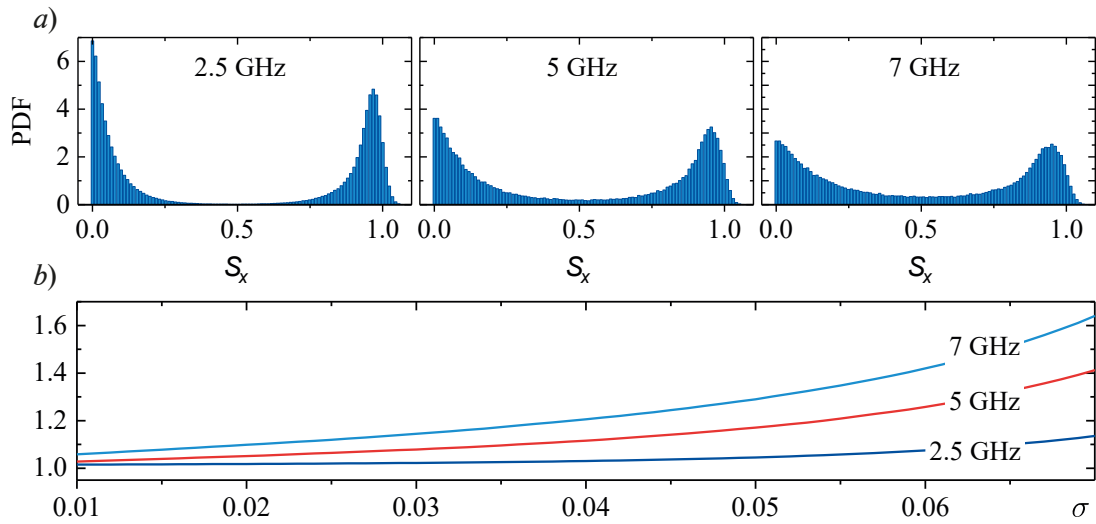


Fig. 2. Probability densities of the normalized integral signal  $S_x$  (a) and dependences of the reduction factor  $\tilde{\Gamma}$  on the photodetector's noise  $\sigma$  (b) at different pulse repetition rates

Generally, a laser pulse at the VCSEL output contains both polarization components ( $x$  and  $y$ ), such that polarization state of a given pulse can be referred to as “quasi-elliptical”. Relative contribution of orthogonal components is a random quantity; however, it depends on the width of the pulse and the rate of relaxation processes (transients). To demonstrate this, we calculated probability density function (PDF) of the normalized integral signal  $S_x$  at three different repetition rates (Fig. 2,*a*). In the ideal case, we would get two peaks at the values  $S_x = 0$  and  $S_x = 1$ , which means that all optical power goes into one particular linear polarization ( $y$  and  $x$  respectively). However, due to the finiteness of transients,  $S_x$  could take intermediate values between 0 and 1. The influence of transients becomes more prominent when decreasing the pulse width, which is clearly seen in Fig. 2,*a*, where the area under the PDF curve in the middle of the histogram is increased when increasing the pulse repetition rate from 2.5 to 7 GHz. Polarization-resolved laser pulses ( $x$ -pulses in our case) that fall into this intermediate region are the most affected by classical (non-quantum) noises of the photodetector; therefore, 0'-s and 1'-s resulted from digitization of such pulses can be considered as “untrusted” bits. The proportion of these bits can be thought of as a quantum reduction factor  $\tilde{\Gamma}$ , whose value determines how much the raw random sequence should be “compressed” using the randomness extractor. We propose the following formula to find  $\tilde{\Gamma}$ :

$$\tilde{\Gamma} = \frac{1}{H_\infty(1-P)}, \quad (1)$$

where  $H_\infty$  is the min-entropy of the raw random sequence, and  $P$  is the probability to obtain the pulse with the  $S_x$  value inside some “window” around the middle of the probability distribution, whose width is proportional to the relative r.m.s. value of the photodetector noise  $\sigma$  (“measured” in terms of the normalized value  $S_x$ ).

We also calculated the dependence of  $\tilde{\Gamma}$  on the photodetector’s noise  $\sigma$  at different pulse repetition rates (see Fig. 2,*b*). One can see that the reduction factor  $\tilde{\Gamma}$  grows when increasing the pulse repetition rate and begins to grow faster with increasing  $\sigma$ . It means that it does not make much sense to increase the repetition rate of laser pulses if the photodetector is quite noisy.

### Post-processing

The digitized random sequence in the proposed scheme must be subjected to the randomness extraction procedure with the reduction factor  $\tilde{\Gamma}$ , defined by . We may, however, use a deterministic extractor, e.g., the von Neumann extractor [5], which extracts randomness regardless the value of the reduction factor. The von Neumann extractor discards repeated bits in a sequence and replaces the two-bit words ‘01’ and ‘10’ with bits ‘0’ and ‘1’, respectively. Unfortunately, this extractor reduces the length of a sequence by at least 4 times, which is not very efficient. Therefore, one generally uses instead a seeded extractor. In cryptographic applications, an extractor with a seed is generally implemented in the form of 2-universal hash functions, whose efficiency is guaranteed by the leftover hash lemma [6]. A common way to implement 2-universal hashing is to multiply the input raw sequence by a random binary matrix [7]. Without loss of generality, one may always use for these purposes random Boolean Toeplitz matrices, which allow significantly saving the seed length. In our case, the randomness extractor is then divided into three steps:

For a “raw” binary sequence of length  $n$ , determine the length of the output sequence  $m$  by the formula:

$$m = n/\tilde{\Gamma}.$$

Generate the Toeplitz matrix using the “seed” of length  $m + n - 1$  bits.

Multiply the Toeplitz matrix by the raw sequence. This yields the resulting random sequence.

It is important to discuss the method of obtaining the seed. By default, it is assumed that the seed is obtained from a strong source of entropy, i.e., one that allows getting truly random bits. If the RNG being developed is not a strong source of entropy, then an additional source of entropy must be used. We propose, however, the following algorithm to obtain the seed. When switching-on the QRNG, the system buffers a raw random sequence of a given (relatively small) length. Then, this sequence is subjected to a deterministic extractor, e.g., the von Neumann extractor. The random sequence obtained after the extractor can be now used as a seed in hashing algorithms. “Equipped” with such a procedure, the QRNG under consideration is an autonomous source of entropy that does not need an additional entropy source, i.e., the device can operate even in the absence of a pre-memorized random sequence.

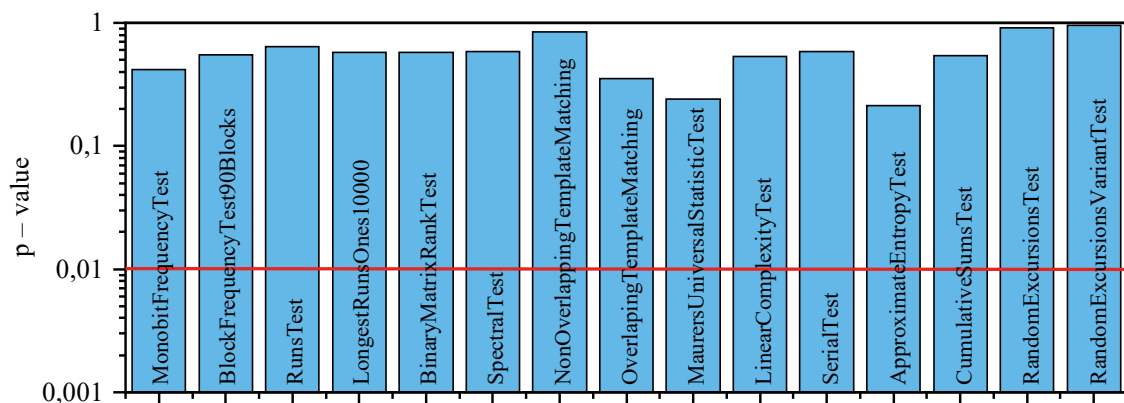


Fig. 3. NIST statistical test result



One of the common ways to test the quality of randomness, is to perform statistical tests, e.g., NIST tests [8]. Unfortunately, we did not have an access to real (obtained in the experiment) random numbers; however, we have a fairly detailed theoretical model, which may be used to follow the whole route the laser noise “travels” from spontaneous emission to the sequence of random bits. For this, we simulated  $10^6$  laser pulses similar to those shown in Fig. 1(b). To “digitize” them, the energy of each pulse (area under the pulse) was calculated and compared with a certain threshold energy. The obtained random bits were then grouped into  $k$ -bit words (we put  $k = 8$ ), which we denote as  $x[i]$ . The sequence of  $x[i]$  were processed with a second-order FIR filter according to the following formula:  $y[i] = \text{mod}(x[i] + 2x[i-1] + x[i-2], 2^k)$ , where each  $y[i]$  is an  $i$ th output word. The obtained data were then concatenate to a (“filtered”) random bit string. After filtering, we processed the data with the randomness extractor described above. Finally, we performed NIST tests with random bits; the results of the test are summarized in Fig. 3. As one can see, the obtained random sequence successfully passed all the test.

### Conclusion

We propose here an approach for quantum noise extraction from polarization swapping in a gain-switched VCSEL and proposed a simple method to get a seed for hashing the raw random sequence without an additional entropy source. The discussed algorithms allow developing a fully autonomous QRNG with proven “quantumness” of generated random bits.

### Acknowledgments

Authors are grateful to Vladimir Meshkov for valuable comments.

### REFERENCES

1. Chizhevsky V. N., Bistable vertical cavity laser with periodic pump modulation as a random bits generator, *Optics and Spectroscopy*, 108 (3) (2010) 343–346.
2. Shakhovoy R., Maksimova E., Sharoglazova V., Puplauskis M., Kurochkin Y., Fast and compact VCSEL-based quantum random number generator, *Journal of Physics: Conference Series*, 1984 (1) (2021) 012005.
3. Quirce A., Valle A., Quantum random number generation based on polarization switching in gain-switched VCSELs, *Optics Express*, 30 (7) (2022) 10513–10527.
4. Shakhovoy R., SychD., Sharoglazova V., Udaltsov A., Fedorov A., Kurochkin Y., Quantum noise extraction from the interference of laser pulses in optical quantum random number generator, *Optics Express*, 28 (5) (2020) 6209–6224.
5. Neumann von J., Various Techniques Used in Connection With Random Digits, *J. Res. Nat. Bur. Stand. Appl. Math. Series*, 3 (1951) 36–38.
6. Nisan N., Ta-Shma A., Extracting Randomness: A Survey and New Constructions, *Journal of Computer and System Sciences*, 58 (1) (1999) 148–173.
7. Krawczyk H., LFSR-based Hashing and Authentication, In: *Proceedings of the Advances in Cryptology – CRYPTO ’94*, Berlin, Heidelberg, 1994, 129–139.
8. Rukhin A., Soto J., Nechvatal J., Smid M., Barker E., Leigh S., Levenson M., Vangel M., Banks D., Heckert A., Dray J., Vo S., A statistical test suite for random and pseudorandom number generators for cryptographic applications, NIST Special Publication 800-22 revision 1a, (2010).

### THE AUTHORS

**SHAKHOVOY Roman**  
r.shakhovoy@goqrates.com  
ORCID: 0000-0003-2750-0518

**MAKSIMOVA Elizaveta**  
e.maksimova@goqrates.com  
ORCID: 0000-0002-1600-0377

*Received 20.07.2022. Approved after reviewing 04.08.2022. Accepted 08.09.2022.*

Conference materials

UDC 535.243.25

DOI: <https://doi.org/10.18721/JPM.153.238>

### **New method of processing measurement results of tissue oxygen saturation abnormalities**

V. V. Naumova <sup>1</sup>✉, V. V. Davydov <sup>1, 2, 3</sup>, M. S. Mazing <sup>4</sup>, A. Yu. Zaitceva <sup>4</sup>

<sup>1</sup> Peter the Great St. Petersburg Polytechnic University, St. Petersburg, Russia;

<sup>2</sup> Bonch-Bruевич Saint Petersburg State University of Telecommunications, St. Petersburg, Russia;

<sup>3</sup> All-Russian Research Institute of Phytopathology, Moscow Region, Russia;

<sup>4</sup> Institute for Analytical Instrumentation of the Russian Academy of Sciences, St. Petersburg, Russia

✉ [naumova.vv@edu.spbstu.ru](mailto:naumova.vv@edu.spbstu.ru)

**Abstract.** The necessity of monitoring the oxygen status of human tissues to detect various diseases at different stages is substantiated. A noninvasive intelligent blood filling control complex for lower limb ischemia using a multisensory system based on optical sensors and machine learning methods is presented. The results are presented, indicating the possibility of automated detection of deviations from the norm of the parameters of blood filling of the extremities.

**Keywords:** intellectual complex, oxygen status, laser radiation, pulse, lower limb ischemia, machine learning

**Citation:** Naumova V. V., Davydov V. V., Mazing M. S., Zaitceva A. Yu., New method of processing measurement results of tissue oxygen saturation abnormalities, St. Petersburg State Polytechnical University Journal. Physics and Mathematics. 15 (3.2) (2022) 206–211. DOI: <https://doi.org/10.18721/JPM.153.238>

This is an open access article under the CC BY-NC 4.0 license (<https://creativecommons.org/licenses/by-nc/4.0/>)

Материалы конференции

УДК 535.243.25

DOI: <https://doi.org/10.18721/JPM.153.238>

### **Новый метод обработки результатов измерений нарушений кислородного насыщения тканей**

В. В. Наумова <sup>1</sup>✉, В. В. Давыдов <sup>1, 2, 3</sup>, М. С. Мазинг <sup>4</sup>, А. Ю. Зайцева <sup>4</sup>

<sup>1</sup> Санкт-Петербургский Политехнический университет Петра Великого  
Санкт-Петербург, Россия;

<sup>2</sup> Санкт-Петербургский государственный университет телекоммуникаций  
им. проф. М. А. Бонч-Бруевича, Санкт-Петербург, Россия;

<sup>3</sup> Всероссийский научно-исследовательский институт фитопатологии, Московская область, Россия;

<sup>4</sup> Институт Аналитического приборостроения РАН, Санкт-Петербург, Россия

✉ [naumova.vv@edu.spbstu.ru](mailto:naumova.vv@edu.spbstu.ru)

**Аннотация.** Обоснована необходимость контроля кислородного статуса тканей человека для выявления различных заболеваний на различной стадии. Представлен неинвазивный интеллектуальный комплекс контроля кровенаполнения при ишемии нижних конечностей с использованием мультисенсорной системы на основе оптических датчиков и методов машинного обучения. Представлены результаты, свидетельствующие о возможности автоматизированного выявления отклонений от нормы параметров кровенаполнения конечностей.



**Ключевые слова:** интеллектуальный комплекс, кислородный статус, лазерное излучение, импульс, ишемия нижних конечностей, машинное обучение

**Ссылка при цитировании:** Наумова В. В., Давыдов В. В., Мазинг М. С., Зайцева А. Ю. Новый метод обработки результатов измерений нарушений кислородного насыщения тканей // Научно-технические ведомости СПбГПУ. Физико-математические науки. Т. 15. № 3.2. С. 206–211. DOI: <https://doi.org/10.18721/JPM.153.238>

Статья открытого доступа, распространяемая по лицензии CC BY-NC 4.0 (<https://creativecommons.org/licenses/by-nc/4.0/>)

## Introduction

The deterioration of the ecological state of the environment has led to a number of negative factors. One of them is associated with the deterioration of people's health. Therefore, personalized monitoring of human health is increasing every year in most countries of the world [1-4]. Among the methods for solving these problems, the greatest preference is given to non-invasive [1-9]. Diagnostics with their use, especially in personalized medicine, is becoming increasingly relevant all over the world [2-4, 6-8, 10-12]. Among noninvasive methods, various optical devices that do not violate the integrity of tissues and structures of the human body are most in demand [2-4, 6-8, 10-15]. Their main advantages are ease of use, high performance and, most importantly, the ability to perform diagnostics outside of a medical institution at any time without limiting the number of applications [1, 3, 4, 6-8, 11-13, 16]. One of the significant directions is the development of optical methods for monitoring blood flow in human limbs using a multichannel spectrum analyzer [17]. Abnormalities in the state of blood flow in the vessels of the extremities detected by optical methods may be associated with the development of dangerous pathologies, such as diabetes mellitus, atherosclerosis and others. Methods based on nuclear magnetic resonance, which are used to confirm many of the identified factors by optical methods, can be used only in stationary laboratories [18-21].

In the modern world, more than 200 million people suffer from lower limb ischemia of varying severity. Atherosclerosis is the primary factor of disability of the population of the Russian Federation. It is in Russia that the highest rate of amputations in atherosclerotic pathology of the lower extremities. Every year, about forty thousand patients in the Russian Federation undergo amputation of the lower extremities, in which the mortality according to various data varies from 10% to 49%. In the Russian Federation, ischemia of the lower extremities of varying severity is currently registered in 1.5 million patients. Therefore, the diagnosis of such vascular pathologies at various stages is one of the most significant tasks in modern medicine.

The purpose of this study is to create a prototype of an intelligent diagnostic optical system for non-invasive monitoring of disorders of oxygen saturation of human lower limb tissues. The method is based on a combination of using machine learning methods and optical methods for registering spectra using a multichannel analyzer having operating wavelengths in the range from 410 to 940 nm. Groups of subjects with different risks of blood supply disorders were formed using a mathematical analysis of the results obtained using the principal component method.

## Materials and Methods

A non-invasive intelligent complex for optical analysis of the oxygen status of human tissues in lower limb ischemia consists of two modules. The first, the sensor unit, is a set of chips that consists of three sensor devices. Multispectral sensors can be used for spectral identification in the range from visible to infrared. Each of the three sensor devices has 6 built-in optical filters, the spectral response of which is determined in the range from 410 to 940 nm with a pulse duration at the level of half the amplitude of 20 nm. The second, the software block, is presented in the form of a mathematical model for processing the results obtained [22]. On the screen of a personal computer, we receive measurement results, which are presented

as a multidimensional array of information. At the output, we have a diagram of the change in the readings of optical sensors over time. Using machine learning methods and principal components, the result has the form of a “point” in two-dimensional space. This method of displaying the results is especially convenient for grouping groups of subjects. derivatives. diabetes, atherosclerosis and others.

This experiment was conducted on the basis of the Almazov National Medical Research Center of the Ministry of Health of the Russian Federation. The study involved a man aged 67 with a diagnosis of diabetes mellitus. The man has an affected left leg and a relatively healthier right one. Measurements were carried out on both legs. The location of the optical system was the lower part of the shin. diabetes, atherosclerosis and others.

The optical system readings were recorded in three time intervals. First, the condition of rest for 1 minute 40 seconds in a standing position. This was followed by the patient performing low-intensity physical activity (3 metabolic units (MET)) within 5 minutes. The final stage, the process of recovery of the subject after performing load tests for 1 minute 40 seconds. Measurements were carried out once for a healthy leg and twice for the affected one with an interval of 10 minutes for complete recovery of the body. diabetes, atherosclerosis and others.

Physical exertion causes significant changes in the blood filling of the extremities and disorders in hemodynamics, as a result of which pathophysiological conditions can be more pronounced, the identification of which helps to diagnose hidden diseases, for example, diabetes mellitus, atherosclerosis and others.

### Results and Discussion

A mathematical analysis of the measurement results was performed, which were recorded by the optical system, healthy and affected lower extremities of the subject with diabetes mellitus.

Various responses of the patient’s limbs to physical activity were obtained, the results of the ranking were visualized, which made it possible to identify hidden patterns in the change in blood filling of the limbs according to the indications of optical sensors at various points in the experiment.

As a reference, measurements were made from the patient’s healthy leg at rest in a standing position, when performing low-intensity physical activity (3 metabolic units), as well as during recovery.

Fig. 1 shows the measurement results of the patient’s healthy leg. It can be seen from the graph that at rest in the standing position, as well as when performing a load, the sensor readings vary in the same range of values, but in the process of recovery, the indicators are lowered.

Then the optical system was moved to the other leg in the same way as the previous one. Next, the affected leg was measured twice with an interval of 10 minutes for the full recovery of the body after the previous physical activity. The sensor remained in the same place throughout the recovery, as well as the subsequent experiment.

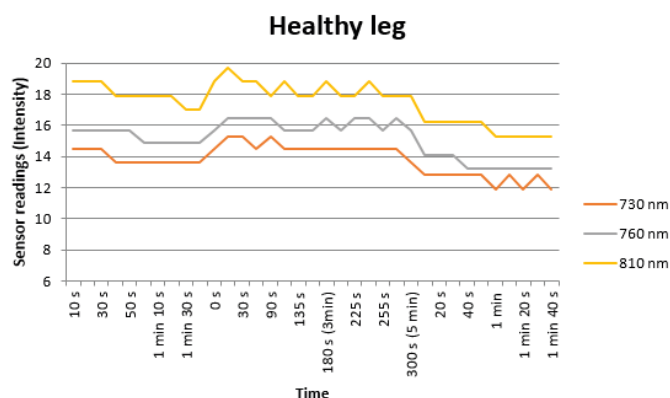


Fig. 1. Sensor readings (intensity) depending on the time at rest, physical activity and the process of restoring the patient’s healthy leg for wavelengths of 730,760, 810 nm

The measurement results of the affected leg are shown in Figs. 2 and 3. In comparison with the “Healthy Leg” graph, we can trace a clearly different trend in changing sensor readings. Firstly, the range of values at rest is several values lower in the affected leg than in the healthy one. Secondly, with the beginning of physical activity, we see a sharp jump in readings up, similarly, at the end of the load, a sharp decline in values.



Fig. 2. Sensor readings (intensity) depending on the time at rest, physical activity and the recovery process of the patient’s diseased leg for wavelengths of 730,760, 810 nm (1 measurement)

In addition, there is a difference in the graphs “Sore leg (1 measurement)” and “Sore leg (2 measurement)”, which may be caused by the registration of measurements after the onset of the state of “acute training”, the appearance of which may occur after several load tests in a row

According to the data obtained above, it can be said that a small shift of the sensor may occur at the beginning of the load. Distortions in the data caused by the sensor shift are proposed to be detected and removed using statistical data processing methods and machine learning methods. In addition, for the purpose of more rigid fixation of the optical system, options for changing the design of the sensor, as well as other types of fixing the device to the measurement site, will be considered.

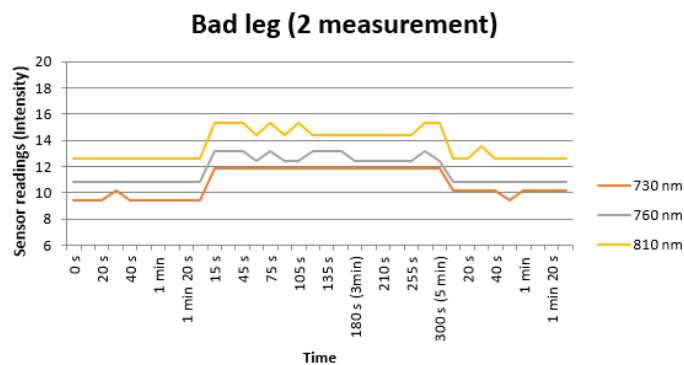


Fig. 3. Sensor readings (intensity) depending on the time at rest, physical activity and the recovery process of the patient’s diseased leg for wavelengths of 730,760, 810 nm (2 measurement)

### Conclusion

The obtained results of the study reflect the relevance of the methodological approach to solving the problems of non-invasive control of human health and performance, and also indicate the possibility of intelligent automated detection of violations of oxygen saturation of tissues with ischemia of the lower extremities of a person and allow medical personnel to make a preliminary decision on the presence or absence of pathology.

## REFERENCES

1. **Charlton P. H., Bonnici T., Tarassenko L., Alastruey J., Clifton D. A., Beale R., Watkinson P. J.**, Extraction of respiratory signals from the electrocardiogram and photoplethysmogram: technical and physiological determinants, *Physiol. Meas.* 38(2017) 669–690.
2. **Dontas A. S., Taylor H. L., Keys A.**, Carotid pressure plethysmograms. Effects of age, diastolic blood pressure, relative body weight and physical activity, *Arch Kreislaufforsch.* 36(1961) 49–58.
3. **Grevtseva A. S., Smirnov K. J., Rud V. Yu.**, Development of methods for results reliability raise during the diagnosis of a person's condition by pulse oximeter, *Journal of Physics: Conference Series.* 1135(1) (2018) 012056.
4. **Grevtseva A. S., Smirnov K. J., Greshnevikov K. V., Rud, V. Yu., Glinushkin, A. P.**, Method of assessment the degree of reliability of the pulse wave image in the rapid diagnosis of the human condition, *Journal of Physics: Conference Series.* 1368(2) (2019) 022072.
5. **Marusina M. Y., Karaseva E. A.**, Automatic segmentation of MRI images in dynamic programming mode Asian Pacific, *Journal of Cancer Prevention.* 19(10) (2018) 2771–2775.
6. **Davydov R. V., Rud V. Yu., Yushkova V. Y.**, On the possibility of analysis using the wavelet transform of the pulse waveform from the bloodstream, *Journal of Physics: Conference Series.* 1695(1) (2020) 012064.
7. **Davydov R. V., Yushkova V. V., Stirmanov A. V., Rud V. Yu.**, A new method for monitoring the health condition based on nondestructive signals of laser radiation absorption and scattering, *Journal of Physics: Conference Series.* 1410(1) (2019) 012067.
8. **Charlton P. H., Bonnici T., Tarassenko L., Watkinson P. J., Alastruey J.**, An impedance pneumography signal quality index: Design, assessment and application to respiratory rate monitoring, *Biomedical Signal Processing and Control.* 65(2021) 102339.
9. **Myazin N. S., Yushkova V. V., Rud V. Y.**, On the possibility of recording absorption spectra in weak magnetic fields by the method of nuclear magnetic resonance, *Journal of Physics: Conference Series.* 1038(1) (2018) 012088.
10. **Ushakov N., Markvart A., Kulik D., Liokumovich L.**, Comparison of pulse wave signal monitoring techniques with different fiber-optic interferometric sensing elements, *Photonics.* 8(5) (2021) 142–146.
11. **Davydov R. V., Antonov V. I., Yushkova V. V., Grebenikova N. M., Dudkin V. I.**, A new algorithm for processing the absorption and scattering signals of laser radiation on a blood vessel and human tissues, *Journal of Physics: Conference Series.* 1236(1) (2019) 012079.
12. **Charlton P. H., Harana J. M., Vennin S., Chowienczyk P., Alastruey J.**, Modeling arterial pulse waves in healthy aging: a database for in silico evaluation of hemodynamics and pulse wave indexes, *American Journal of Physiology - Heart and Circulatory Physiology.* 317(5) (2019) H1062–H1085.
13. **Davydov R. V., Antonov V. I., Yushkova V. V., Rud' V. Yu., Smirnov K. J.**, A new method of processing a pulse wave in rapid diagnosis of the human health, *Journal of Physics: Conference Series.* 1400(6) (2019) 066037.
14. **Dyumin V., Smirnov K., Myazin N.**, Charge-coupled Device with Integrated Electron Multiplication for Low Light Level Imaging, *Proceedings of the 2019 IEEE International Conference on Electrical Engineering and Photonics, EExPolytech.* 8906868 (2019) 308–310.
15. **Grebenikova N. M., Smirnov K. J., Rud V. Yu., Artemiev V. V.**, Features of monitoring the state of the liquid medium by refractometer, *Journal of Physics: Conference Series.* 1135(1) (2018) 012055.
16. **Kislyakov Yu. Ya., Avdyushenko S. A., Kislyakova L. P.**, Analytical multisensory trainable system for diagnosing vocational aptitude of military medical specialists by ion content in the expired breath condensate, *Journal of Computational and Theoretical Nanos Science.* 16(11) (2019) 4502–4507.
17. **Mazing M. S., Zaitceva A. Yu., Kislyakov Yu. Ya., Kondakov N. S., Avdushenko S. A., Davydov V. V.**, Monitoring of Oxygen Supply of Human Tissues Using A Noninvasive Optical System Based on A MultiChannel Integrated Spectrum Analyzer, *International Journal of Pharmaceutical Research.* 12(2) (2020) 1974–1978.
18. **Dyachenko S. V., Vaseshenkova M. A., Martinson K. D., Cherepkova I. A., Zhernovoi A. I.**, Synthesis and properties of magnetic fluids produced on the basis of magnetite particles, *Russian Journal of Applied Chemistry.* 89(5) (2016) 690–696.
19. **Myazin N. S.**, Features of formation of structure of a nuclear magnetic resonance signal in weak magnetic field, *Journal of Physics: Conference Series.* 1135(1) (2018) 012061.



20. **Davydov V. V.**, Determination of the Composition and Concentrations of the Components of Mixtures of Hydrocarbon Media in the Course of its Express Analysis, Measurement Techniques. 62(2) (2020) 1090–1098.

21. **Myazin N. S., Dudkin V. N., Davydov R. V.**, Peculiarities of Monitoring the State of a Flowing Medium by the Method of Nuclear Magnetic Resonance, Technical Physics Letters. 46(1) (2020) 55–58.

22. **Zaitceva A. Yu., Kislyakova L. P., Kislyakov Yu. Ya., Avduchenko S. A.**, Development of a multi-sensor analytical trainable system for non-invasive evaluation of adaptedness status of hazardous occupation specialists, Journal of Physics: Conference Series. 1400(3) (2019) 033022.

#### THE AUTHORS

**NAUMOVA Victoria**

Naumova.vv@edu.spbstu.ru

ORCID: 0000-0002-6577-1223

**MAZING Maria**

mazmari@mail.ru

ORCID: 0000-0003-1739-9671

**Davydov Vadim**

Davydov\_vadim66@mail.ru

ORCID: 0000-0001-9530-4805

**ZAITCEVA Anna**

anna@da-24.ru

ORCID: 0000-0003-0334-2770

*Received 11.08.2022. Approved after reviewing 17.08.2022. Accepted 18.08.2022.*

Conference materials

UDC 535.361.12

DOI: <https://doi.org/10.18721/JPM.153.239>

## Veracity of the method of detecting scattered laser radiation for content measuring of particulate matter in air

A. D. Kurkova <sup>1</sup>✉, V. V. Davydov <sup>1</sup>

<sup>1</sup> Peter the Great St. Petersburg Polytechnic University, St. Petersburg, Russia

✉ alexsa99k@gmail.com

**Abstract.** The problem of measuring the parameters of dust particles in the environment is currently relevant for residents of densely populated cities. Measurements of the size and size distribution function of dust particles are carried out using instruments based on the method of scattering of laser radiation. The analysis of the measurement method based on the spherical particle model and the theory of Mie diffraction theory is carried out. The indicatrices of laser radiation scattering by particles 2.5 and 10  $\mu\text{m}$  in size are calculated. The size distribution function of particles is estimated under the condition that the intensity of scattered laser radiation is measured for at least two scattering angles. The possibility of erroneous indication of measurement results by widely used portable measuring devices for dust parameters is shown.

**Keywords:** particle concentration, air pollution, particulate matter PM2.5, Mie scattering theory, scattering indicatrix, particle size distribution

**Citation:** Kurkova A. D., Davydov V. V., Veracity of the method of detecting scattered laser radiation for content measuring of particulate matter in air, St. Petersburg State Polytechnical University Journal. Physics and Mathematics. 15 (3.2) (2022) 212–217. DOI: <https://doi.org/10.18721/JPM.153.239>

This is an open access article under the CC BY-NC 4.0 license (<https://creativecommons.org/licenses/by-nc/4.0/>)

Материалы конференции

УДК 535.361.12

DOI: <https://doi.org/10.18721/JPM.153.239>

## Надежность метода детектирования рассеянного лазерного излучения при измерении содержания твердых частиц в воздухе

А. Д. Куркова <sup>1</sup>✉, В. В. Давыдов <sup>1</sup>

<sup>1</sup> Санкт-Петербургский политехнический университет Петра Великого,

Санкт-Петербург, Россия

✉ alexsa99k@gmail.com

**Аннотация.** Проблема измерения параметров частиц пыли в окружающей среде в настоящее время актуальна для жителей густонаселенных городов. Измерения размера и функции распределения по размерам частиц пыли осуществляются с помощью приборов, работа которых основана на методе рассеяния лазерного излучения. Выполнен анализ метода измерения, базирующегося на сферической модели частиц и теории дифракции Ми. Вычислены индикатрисы рассеяния лазерного излучения на частицах размером 2,5 и 10 мкм. Проведена оценка функции распределения частиц по размерам при условии измерения интенсивности рассеянного лазерного излучения не менее чем при двух углах рассеяния. Показана возможность ошибочной индикации результатов измерений широко применяемыми портативными измерительными приборами параметров пыли.

**Ключевые слова:** концентрация частиц, загрязнение воздуха, частицы PM2.5, теория рассеяния Ми, индикатриса рассеяния, распределение частиц по размерам

**Ссылка при цитировании:** Куркова А. Д., Давыдов В. В. Надежность метода детектирования рассеянного лазерного излучения при измерении содержания твердых частиц в воздухе // Научно-технические ведомости СПбГПУ. Физико-математические науки. Т. 15. № 3.2. С. 212–217. DOI: <https://doi.org/10.18721/JPM.153.239>

Статья открытого доступа, распространяемая по лицензии CC BY-NC 4.0 (<https://creativecommons.org/licenses/by-nc/4.0/>)

### Introduction

In recent years, industrial production in the world is rapidly gaining momentum. The state of the environment is constantly getting worse. The number of green spaces and other natural barriers that clean up the environment is decreasing [1–3]. These negative processes lead to an increase in dust in the air [4–6]. The highest concentration of dust is formed mainly in densely populated areas of cities and poses a great danger to residents. This is due to the fact that transport, industrial emissions and smog from thermal power plants are the main sources of dust particles [3, 7–9]. Particularly dangerous to humans are particulate matter with a size of 2.5 microns ( $PM_{2.5}$ ). They overcome the natural protective barriers of a person, penetrating the body through the mucous surface of the respiratory organs, and then spreading inside, overcoming the protective membranes of the body and penetrating directly into the cell. The problem is that the accuracy of commercial portable measuring instruments for dust parameters is not high ( $\pm 15\%$ ), since the device registers particles larger than  $2.5 \mu m$ , while in fact the size of the registered particles is less than  $2.5 \mu m$  [10–12]. It is these particles that have a negative impact on human health.

Fig. 1 shows the concentration distribution of particulate matter in the world. Countries marked in blue are those with less than  $10 \mu g/m^3$  (safe level according to the World Health Organization). Green corresponds to countries with up to  $12 \mu g/m^3$  (safe level according to the US assessment criteria), then from yellow on a gradient to red and brown as the danger increases.

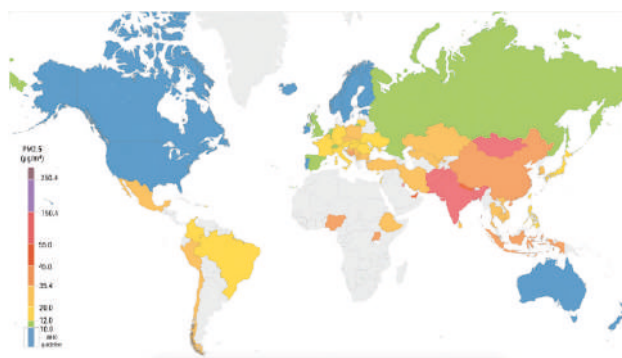


Fig. 1. Concentration of particulate matter  $PM_{2.5}$  in the world

### Materials and Methods

The proposed measurement method is based on the Mie diffraction theory [13, 14]. This is the most commonly used theory, which describes the scattering of laser radiation by spherical particles. Taking into account the small size of dust particles, they can be considered spherical in comparison with the distances and the volume in which the measurements are made. The radiation scattering pattern on a particle can be described over the entire angular range from  $0^\circ$  to  $360^\circ$  depending on the amplitude and wavelength. To use this theory for measurements, it is necessary to know the optical properties of the system under study (complex refractive index, its real and imaginary parts). For example, for quartz dust particles in air, this value of « $n$ » is on the order of  $1.5 - 0.05i$ , where  $i$  is an imaginary unit. The value of the imaginary part makes it possible to take into account the specificity of the particle surface structure, for example, roughness. The amplitude function of the scattered field is determined by solving the vector wave equation as a series in functions containing Legendre polynomials, and the coefficients of the scattered field series are expressed in terms of the Riccati–Bessel functions and their derivatives.

### Results and Discussion

Based on the Mie scattering equations, one can calculate the dependence of the scattered light on the scattering angle for particles of different sizes. Fig. 2 shows the calculated dependences of the scattered light intensity  $s$  on the scattering angle  $\theta$  for silica particles with sizes of 2.5 and 10  $\mu\text{m}$ .

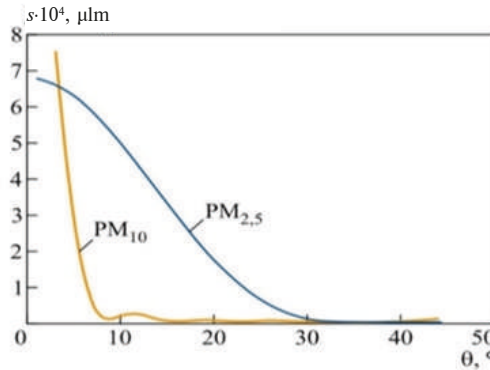


Fig. 2. Scattered light intensity as a function of the scattering angle for particles of sizes 2.5 and 10  $\mu\text{m}$

For small particle sizes, the radiation scattering indicatrix is concentrated in a sufficiently large scattering angle ( $\theta > 20^\circ$ ), and for large particles, on the contrary, in a small angle ( $\theta < 10^\circ$ ). At large scattering angles for very small particles, the intensities of the scattered radiation are very small, and at small angles little scattering is observed. For particles smaller than 2.5  $\mu\text{m}$ , it cannot be established that the scattering intensities are extremely low compared to particles with sizes  $d \geq 2.5$ . It is on this fact that the selection of small particles by scattering angles is based [14–17].

Dependences of the scattered light intensity on the scattering angle can be shown on the polar diagram (Fig. 3).

For particles with a size of 2.5  $\mu\text{m}$ , the intensity is maximum at  $\theta = 45^\circ$ , and for larger particles,  $\theta \approx 10^\circ$ . When designing simple instruments for estimating particle concentration, information about these scattering angles is taken into account. To fix the photodetectors, selective angles between  $10^\circ$  and  $45^\circ$  are chosen. When using four photodetectors, it is desirable to choose the angle values at the points of the curves where the intensity derivative is maximum (Fig. 2). The highest value of the derivative for the  $PM_{2.5}$  curve is achieved at  $\theta = 20^\circ$ , and for the  $PM_{10}$  curve, at  $\theta \approx 6^\circ$ . It is not without reason that we are talking about the number of photodetectors, since when using only one recorder it is impossible to obtain truthful data on the number concentration of particles. To achieve a lower measurement error, the number of sensors is usually increased to four.

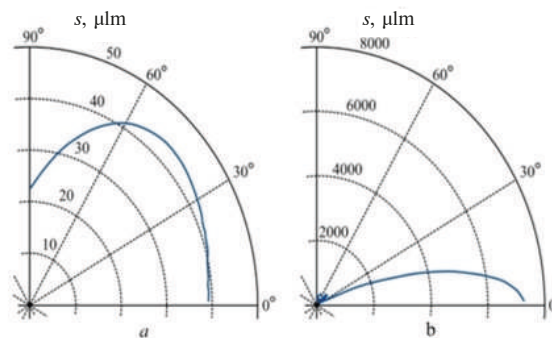


Fig. 3. Polar plot of scattering intensity for particles sized 2  $\mu\text{m}$  (a) and 8  $\mu\text{m}$  (b)



Thus, at a certain angle to the laser beam, the scattered radiation intensity will depend on the particle size. Scattered radiation is usually focused using a flat convex lens. A point in space where one photodiode is located registers scattered radiation not only from particles of a certain size, but also from all particles on which scattering occurs. The scattering indicatrix simply indicates that at a certain angle, a particle of a certain size has a maximum scattering intensity. However, particles of other sizes will also contribute to the total intensity of scattering at this angle. Therefore, a single photodetector, which is at an angle  $\theta$  relative to the laser beam, registers scattered radiation from particles of all sizes.

To search for the distribution of particle concentration on their size using several photodetectors, we take as the calculated particle concentration, where  $i$  is the particle size, in our case  $n_1$  denotes  $PM_{2,5}$ ,  $n_2$  denotes  $PM_4$ ,  $n_3$  denotes  $PM_6$ ,  $n_4$  denotes  $PM_8$ . Let  $s_1$  be the value of the photodetector signal, which is at an angle  $\theta$  to the laser beam. Then we can write

$$s_1 = \alpha_{11}n_1 + \alpha_{12}n_2 + \alpha_{13}n_3 + \alpha_{14}n_4, \quad (1)$$

where  $\alpha_{11}$ ,  $\alpha_{12}$ ,  $\alpha_{13}$ ,  $\alpha_{14}$  are coefficients that take into account the intensity of scattered radiation for each particle size and some technical properties of photodetectors.

For four photodetectors, we denote the signals as  $s_1$ ,  $s_2$ ,  $s_3$ ,  $s_4$  and write down the system of linear inhomogeneous equations:

$$\begin{cases} s_1 = \alpha_{11}n_1 + \alpha_{12}n_2 + \alpha_{13}n_3 + \alpha_{14}n_4 \\ s_2 = \alpha_{21}n_1 + \alpha_{22}n_2 + \alpha_{23}n_3 + \alpha_{24}n_4 \\ s_3 = \alpha_{31}n_1 + \alpha_{32}n_2 + \alpha_{33}n_3 + \alpha_{34}n_4 \\ s_4 = \alpha_{41}n_1 + \alpha_{42}n_2 + \alpha_{43}n_3 + \alpha_{44}n_4, \end{cases} \quad (2)$$

Considering that each counter receives scattered light only from a particle of a certain size, the distribution is calculated using four values  $s_1$ ,  $s_2$ ,  $s_3$ ,  $s_4$ :

$$\begin{cases} s_1 = \alpha_{11}n_1 \\ s_2 = \alpha_{22}n_2 \\ s_3 = \alpha_{33}n_3 \\ s_4 = \alpha_{44}n_4, \end{cases} \quad (3)$$

But the actual signals correspond to the solution of the system of inhomogeneous linear equations (2). The difference between these values is the reason for the errors in estimates of the calculated concentration. Fig. 4 shows two distribution functions of particles, actual and calculated from the readings of photodetectors. For particles of different concentrations, readings based only on the signals of the photodetector do not match the actual concentrations. It follows from Fig. 4 that the particle sizes obtained from instrument readings based on only certain signals from four photodetectors in accordance with the system of equations (3) differ significantly from the actual sizes of the same particles calculated from (2). In any of the two experiments, the estimate of the concentration of  $PM_{2,5}$  particles only from the signals of photodetectors (ignoring equation (2)) will be much higher than the actual one. The above analysis indicates that the readings of portable devices with several photodetectors do not correspond to the real concentration of particles.

To obtain a smoother curve of the distribution function, it is necessary to increase the number of laser counters in the device located at a small distance from each other. However, the concentration values will be relative, since they are expressed in units of photodetector readings. To obtain actual mass concentration values, it is necessary to collect the particles after they have passed the laser beam and weigh them. Only after these actions, it is possible to construct the particle size distribution function depending on their mass concentration.

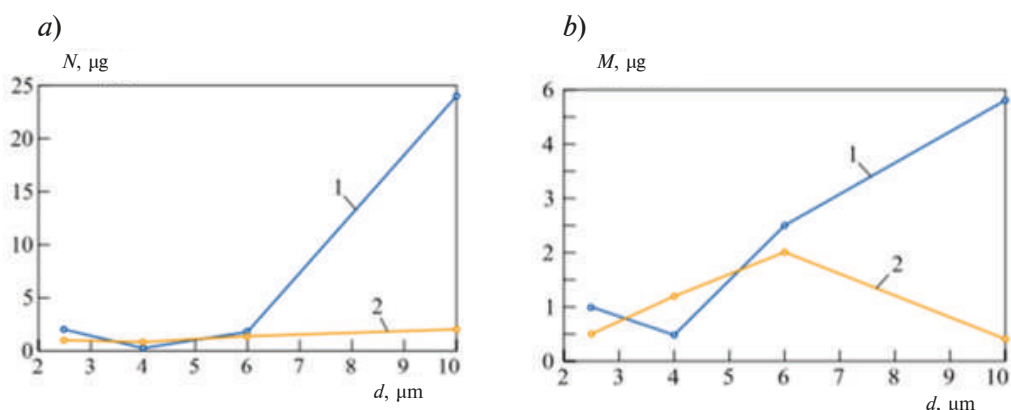


Fig. 4. Theoretical (1) and actual (2) particle distribution using one (a) and four (b) sensors

### Conclusion

The revealed measurement errors are inherent in both simple and complex devices designed to determine the number concentration of particles. Instruments based on the simple correspondence of a particular angle to a particle size can have measurement errors of almost 100%, in particular for  $\text{PM}_{2.5}$  hazardous particles. The particle size distribution can be easily obtained from the readings of several photodetectors at selected scattering angles. But an increase in the number of counters does not guarantee the authenticity of the results, since there are other errors due to the size of the angle, the finite size of the aperture in the working gap, as well as changes in the nature of the particles, which manifest themselves in a change in the imaginary part of the refractive index.

### REFERENCES

1. Antonov V.I., Davydov R.V., Maslikov V.I., Molodtsov D.V., Chusov A.N., Mathematical models of operating regimes of flood control facility's system, *Journal of Physics: Conference Series*. 1368 (4) (2019) 042076.
2. Davydov V. V., Determination of the Composition and Concentrations of the Components of Mixtures of Hydrocarbon Media in the Course of its Express Analysis, *Measurement Techniques*. 62 (2) (2020) 1090–1098.
3. Myazin N.S., Davydov V.V., Yushkova V.V., Rud V.Y., A new method of determining the state of water and agricultural areas in real time Environmental Research, *Engineering and Management*. 75 (2) (2019) 28–35.
4. Grevtseva A., Diuldin M., Savchenko I., Druzhinina G., Valov A., Investigation of the dustiness of various zones of a metropolis and a set of measures to reduce the negative impact of dust on living organisms, *IOP Conference Series: Earth and Environmental Science*. 578 (1) (2020) 012058.
5. Davydov R. V., Rud V. Yu., and Yushkova V.Y., On the possibility of analysis using the wavelet transform of the pulse waveform from the bloodstream, *Journal of Physics: Conference Series*. 1695 (1) (2020) 012064.
6. Davydov R. V., Yushkova V. V., Stirmanov A. V., and Rud V. Yu., A new method for monitoring the health condition based on nondestructive signals of laser radiation absorption and scattering, *Journal of Physics: Conference Series*. 1410 (1) (2019) 012067.
7. Davydov V.V., Kiryukhin A.V., Nuclear-Magnetic Flowmeter-Relaxometers for Monitoring Coolant and Feedwater Flow and Status in Npp Atomic Energy. 127 (5) (2020) 274–279.
8. Myazin N. S., Smirnov K. J., and Logunov S. J., Spectral characteristics of InP photocathode with a surface grid electrode, *Journal of Physics: Conference Series*. 929 (1) (2017) 012080.
9. Myazin N. S., Features of formation of structure of a nuclear magnetic resonance signal in weak magnetic field, *Journal of Physics: Conference Series*. 1135 (1) (2018) 012061.



10. **Loomis D., Huang W., Chen G.**, The International Agency for Research on Cancer (IARC) evaluation of the carcinogenicity of outdoor air pollution: focus on China, *Chinese Journal of Cancer*. 33(4) (2014) 189–196.
11. **Grebenikova N. M.**, The effect of optical density of the flowing liquid on the measurement error of its refractive index, *Journal of Physics: Conference Series*. 1400 (6) (2019) 066029.
12. **Borghi F., Spinazze A., Campagnolo D., Cattaneo A., Cavallo D.M.**, Precision and accuracy of a direct-reading miniaturized monitor in PM<sub>2.5</sub> exposure assessment *Sensors (Switzerland)*. 18 (9) (2018) 3089.
13. **Bohren C. F., and Huffman D. R.**, *Absorption and Scattering of Light by Small Particles*, New York, 1983.
14. **Davydov V. V., Kruzhalov S. V., and Vologdin V. A.**, Concerning some features of studying the flow of liquid media by a Doppler method: *Journal of Optical Technology (A Translation of Opticheskii Zhurnal)*. 84 (8) (2017) 568–573.
15. **Rovelli S., Cattaneo A., Binda G., Bollati V., Cavallo D.M.**, How to obtain large amounts of location- and time-specific PM<sub>2.5</sub> with homogeneous mass and composition? A possible approach, from particulate collection to chemical characterization *Atmospheric Pollution Research*. 12 (10) (2021) 101193.
16. **Yu X., Shi Y., Wang T., and Sun X.**, Sensor for measuring to concentration PM<sub>2.3</sub>, *Plose One*. 12 (8) (2017) 1–15.
17. **Mariselvam A.K., Padmanabhan K., Sivanesan S.**, Reliability of Results of Measurements of Air Pollution by Solid Particles by the Method of Detection of Scattered Laser Radiation Measurement Techniques. 63 (4) (2020) 266–272.
18. **Davydov V.V., Kruzhalov S.V., Vologdin V.A.**, Concerning some features of studying the flow of liquid media by a Doppler method *Journal of Optical Technology (A Translation of Opticheskii Zhurnal)*. 84 (8) (2017) 568–573.

#### THE AUTHORS

**KURKOVA Alexandra**  
kurkova.ad@edu.spbstu.ru  
ORCID: 0000-0002-3729-1943

**DAVYDOV Vadim**  
Davydov\_vadim66@mail.ru  
ORCID: 0000-0001- 9530- 4805

*Received 11.08.2022. Approved after reviewing 18.08.2022. Accepted 08.09.2022.*

Conference materials

UDC 53.087.44

DOI: <https://doi.org/10.18721/JPM.153.240>

## **Development of the radiation situation monitoring system based on fiber-optic sensors for pools of nuclear power plants**

D. S. Dmitrieva <sup>1</sup>✉, V. V. Davydov <sup>2</sup>

<sup>1</sup> Bonch-Bruевич Saint Petersburg State University of Telecommunications, St. Petersburg, Russia;

<sup>2</sup> Peter the Great St. Petersburg Polytechnic University, St. Petersburg, Russia

✉ [dmitrievadiana1405@gmail.com](mailto:dmitrievadiana1405@gmail.com)

**Abstract.** The necessity of development of the remote monitoring system of the radiation situation based on fiber-optic sensors for pools of nuclear power plants is substantiated. New method of building of communication line with fiber-optic sensor for controlling exposure dose of radioactive radiation in the large range of changes (several orders of magnitude) in remote mode is suggested. The design of sensor to provide measurements for long distance (more than 10 km from the location of the monitoring center) is developed. Functional capabilities of the fiber-optic sensor are identified. Experimental results are presented.

**Keywords:** fiber-optic sensor, exposure dose, fiber optic communication line, laser radiation,  $\gamma$ -radiation, spray pools

**Citation:** Dmitrieva D. S., Davydov V. V., Development of the radiation situation monitoring system based on fiber-optic sensors for pools of nuclear power plants, St. Petersburg State Polytechnical University Journal. Physics and Mathematics. 15 (3.2) (2022) 218–223. DOI: <https://doi.org/10.18721/JPM.153.240>

This is an open access article under the CC BY-NC 4.0 license (<https://creativecommons.org/licenses/by-nc/4.0/>)

Материалы конференции

УДК 53.087.44

DOI: <https://doi.org/10.18721/JPM.153.240>

## **Разработка системы контроля радиоактивной обстановки на основе волоконно-оптических датчиков для водных бассейнов атомных электрических станций**

Д. С. Дмитриева <sup>1</sup>✉, В. В. Давыдов <sup>2</sup>

<sup>1</sup> Санкт-Петербургский государственный университет телекоммуникаций им. проф. М.А. Бонч-Бруевича, Санкт-Петербург, Россия;

<sup>2</sup> Санкт-Петербургский политехнический университет Петра Великого, Санкт-Петербург, Россия

✉ [dmitrievadiana1405@gmail.com](mailto:dmitrievadiana1405@gmail.com)

**Аннотация.** В статье обоснована необходимость разработки системы дистанционного контроля радиоактивной обстановки на основе волоконно-оптических датчиков для водных бассейнов АЭС. Предложена новая конструкция волоконно-оптических датчика, определены его функциональные возможности. Представлены результаты экспериментальных исследований.

**Ключевые слова:** волоконно-оптический датчик, экспозиционная доза, волоконно-оптическая линия связи, лазерное излучение, гамма-излучение, брызгальные бассейны

**Ссылка при цитировании:** Дмитриева Д. С., Давыдов В. В. Разработка системы контроля радиоактивной обстановки на основе волоконно-оптических датчиков для водных бассейнов атомных электрических станций // Научно-технические ведомости СПбГПУ. Физико-математические науки. Т. 15. № 3.2. С. 218–223. DOI: <https://doi.org/10.18721/JPM.153.240>

Статья открытого доступа, распространяемая по лицензии CC BY-NC 4.0 (<https://creativecommons.org/licenses/by-nc/4.0/>)

## Introduction

In the modern world, environmental degradation is constantly happening for various reasons [1–9]. This is due to both objective and subjective factors [10–16]. One such factor is related to the increasing use of radioactive materials in various fields of industry, energy, and science [17–19]. In this case nuclear power plants are the most dangerous objects [20–24]. Despite the large number of protective screens and ceilings, has increased the number of radioactive releases, the consequences of which cannot be eliminated for a long time. In addition to the reactors, the spray pools used for continuous cooling of NPP equipment pose a danger. In the case of leakage, spray pools also often become sources of releases into the atmosphere due to the ingress the liquid radioactive waste into the water. Due to the presence of a nozzles system, some of drops containing radionuclides are carried by the wind outside the spray pools. Moreover, the natural water evaporation from the pool surface also leads to a change in radiation situation in the atmosphere. So, this is the reason, why the great attention is paid to possibility if control the radiation level in pools of nuclear power plants.

The great attention is paid to possibility of remote control the radiation situation in pools of NPP. Monitoring of the radioactive radiation power is associated with several difficulties. Such control must be carried out continuously in real time Moreover, in some cases it is necessary to carry out the control in automatic mode at the distance of several kilometers from the location of the monitoring center. Most dosimetry devices cannot cope with this task. Devices often go off, and communication systems, which are used for transmitting information about radiation level to monitoring center, are out of order because of radiation accumulation [25–27]. The maintenance of such monitoring systems is rather difficult, due to the radiation accumulation on the instrument case and its functional units, which poses a great danger to humans.

One of the ways of implementation the constant control of radiation level is the use of fiber-optic sensors. But sensors developed nowadays could not provide measurements at a high  $D_R$  value due to the long-term natural relaxation of the optical fiber.

Since the exposure dose of radiation in monitoring zone can change by several orders of magnitude in a fairly short period of time, the natural relaxation of optical fiber, which is used in sensors, can take  $10^6$  s and more.

Moreover, it is impossible to use more powerful radiation sources in fiber-optic sensors developed nowadays (sensors based on the laser radiation polarization under the  $\gamma$ -radiation influence provide measurements on low powers of about 5mW). The use of more powerful radiation is not possible because of the risk of damage photosensitive layer in photodetector module. Thus, the development of the radiation situation monitoring system based on fiber-optic sensors capable of withstanding high levels of exposure dose, is extremely actual.

## Materials and Methods

It is necessary to provide additional research of  $\gamma$ -influence on the optical fiber for develop the system of monitoring the radiation situation based on the fiber-optic sensors for pools of nuclear power plants. To provide the research we have assembled an experimental setup, which was discussed previously, as well as previously obtained experimental results [25–29]. In contrast to similar research, losses measurements were carried out both at the moment of  $\gamma$ -radiation influence on optical fiber, and immediately after its termination. In this case, there is no large time interval between the  $\gamma$ -radiation influence and the beginning of measurements.

The radiation-induced losses were determined with using the following formula:

$$\alpha_s = 10 \log(P_{out} / P_{in}) / L, \quad (1)$$

where  $P_{in}$  is the power input into the optical fiber,  $P_{out}$  is the power output from the optical fiber,  $L$  is the length of the optical fiber.

A set of transmitting and receiving optical modules from one company was used for measurements, allowing to obtain a higher signal-to-noise ratio of the recorded optical signal at a low power of laser radiation. Modified transmitting module DMPO131-23M (company Dilaz) transmits at a wavelength  $\lambda = 1550$  nm at a radiation power from 0 to 5.4 mW. Receiving optical module DFDMSH40-16M (company Dilaz) has highly sensitivity in a wavelength of 980–1550 nm. Fig.1 shows the dependences of the losses  $\alpha_s$  in single-mode fibers with various alloying percentage from the exposure dose of  $\gamma$ -radiation.

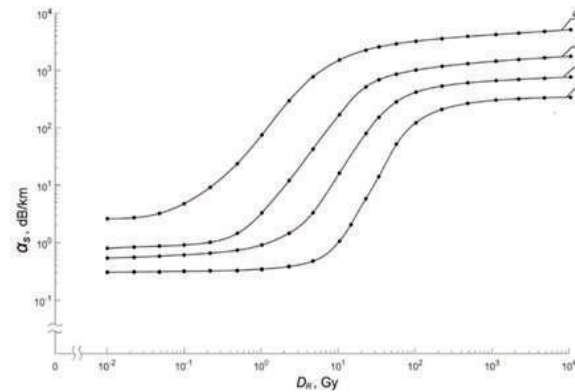


Fig. 1. Dependence of the  $\alpha_s$  changes on irradiation dose  $D_R$  at a wavelength  $\lambda = 1550$  nm on single-mode fiber with a  $\text{SiO}_2\text{--GeO}_2$  core at  $T = 294.2$  K  
Curves 1, 2, 3 and 4 correspond to different alloying in %: 1.5; 4.0; 10.0 and 20.0

Analysis of the obtained results show that the velocity of color centers in optical fiber under the  $\gamma$ -radiation influence depends on the change in the alloying percentage. In a case of increase in alloying percentage the losses in optical fiber increase, sensitivity to changes of exposure dose of radiation. The increase of fiber optic sensitivity to  $D_R$  changes allows to register the changes in small exposure dose values, which lead to decrease of the laser radiation power at the output of FOCL by 0.2 dB.

Fig. 2 shows the research results of velocity of the optical properties recovery after  $\gamma$ -radiation influence.

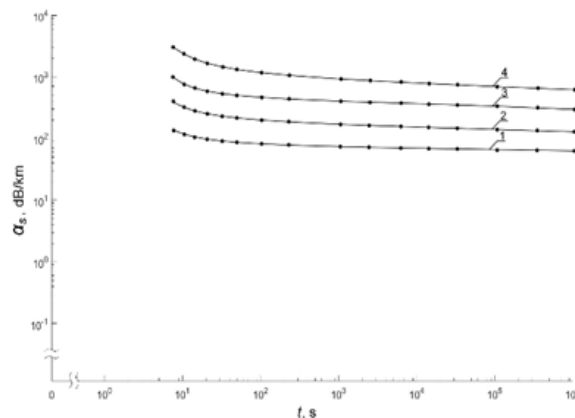


Fig. 2. Changes of losses  $\alpha_s$  vs  $t$  at the wavelength  $\lambda = 1550$  nm on single-mode fiber with  $\text{SiO}_2\text{--GeO}_2$  core at  $T = 294.2$  K  
Curves 1, 2, 3 and 4 correspond to different alloying in %: 1.5; 4.0; 10.0 and 20.0



Obtained results show that with an increase of the alloying percentage of optical fiber, the relaxation velocity of color centers increases. Optical properties of fiber recovery proceeds faster

### Results and Discussion

Obtained results make it possible to propose the following design of the fiber-optic sensor as the basis for the system for monitoring the radiation situation in the NPP pools. An optical fiber with 200 m long with a  $\text{SiO}_2\text{-GeO}_2$  core with alloying 20%, which connects to an optical fiber with a pure quartz core through optical connectors. To accelerate the relaxation natural process of fiber in this design is used the previously developed method to control the  $E$  center formation for trunk FOCL. To test the efficiency of the proposed design, was provided the research of velocity of the optical properties recovery after  $\gamma$ -radiation influence with a dose of 100 G.

In this study, we used pulsed laser radiation with a wavelength  $\lambda = 1310$  nm with a duration of 0.1 s with various powers during 10 s. The measurements were made with a laser radiation of various powers. The research results are presented in Figs. 3 and 4.

Analysis of the obtained results confirmed the possibility of increase the relaxation velocity with using the additional laser radiation. The optical properties recover in less 10 s. Moreover, as the result of the research it was found, that the optical fiber recovery proceeds faster using pulsed laser radiation, rather than continuous.

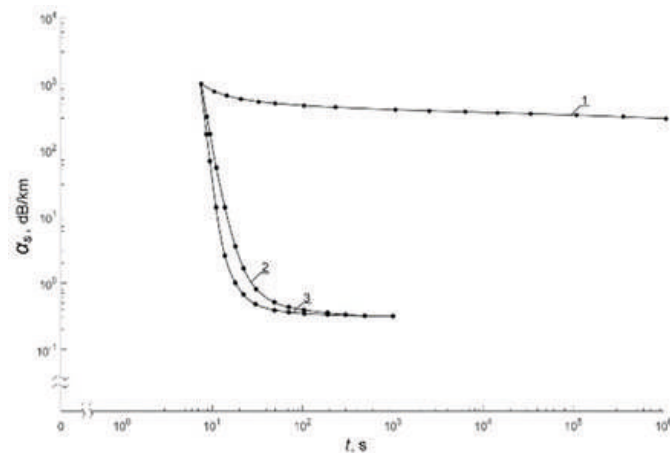


Fig. 3. Dependence of the change in losses  $\alpha_s$  on time  $t$  at a wavelength  $\lambda = 1550$  nm for single-mode fiber with a  $\text{SiO}_2\text{-GeO}_2$  core (alloying 10.0 %) and polymer cladding at  $T = 294.3$  K  
Curves 1, 2 and 3 correspond to different laser radiation powers at wavelength  $\lambda = 1310$  nm in mW: 0; 40; 80

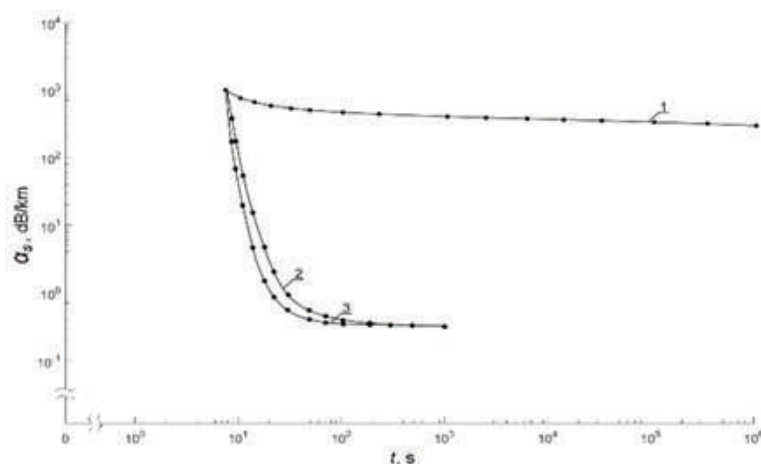


Fig. 4. Dependence of the change in losses  $\alpha_s$  on time  $t$  at a wavelength  $\lambda = 1550$  nm for single-mode fiber with a  $\text{SiO}_2\text{-GeO}_2$  core (alloying 10.0 %) and polymer cladding at  $T = 294.3$  K  
Curves 1, 2 and 3 correspond to different laser radiation powers at wavelength  $\lambda = 1310$  nm in mW at: 0; 20; 40

### Conclusion

Obtained results showed a reliable work of developed sensor in continuous mode. Using it allows to control the radiation dose from 0.1 to 1000 G in real time in NPP pools.

Moreover, the developed fiber-optic sensor for remote control of radiation situation has one feature, that differed it from the previously used. At a certain value of radiation exposure dose and power of the additional laser radiation, a static equilibrium can occur between two processes: color centers formation and their relaxation. Losses value increases for a certain period less than 1% from its initial state. In this case, fiber-optic sensor for monitoring radiation situation will be in standby mode of a radioactive release. In this case, influence of the background  $\gamma$ -radiation, which is also present in pools of nuclear power plants, is successfully compensated.

### REFERENCES

1. **Reznik V. S., Kruglov V. A., Petrov A. I., Glinuchkin A. P., Rud V. Y.**, Development of a measuring device for the study of thermal processes during the polymerase chain reaction, *Journal of Physics: Conference Series*. 1410(1) (2019) 012078.
2. **Mazing M. S., Zaitceva A. Yu., Kislyakov Yu. Ya., Kondakov N. S., Avdushenko S. A., Davydov V. V.**, Monitoring of Oxygen Supply of Human Tissues Using A Noninvasive Optical System Based on A MultiChannel Integrated Spectrum Analyzer, *International Journal of Pharmaceutical Research*. 12(2) (2020) 1974–1978.
3. **Kislyakov Yu. Ya., Avdyushenko S. A., Kislyakova I. P., Zaitceva A. Yu.**, Analytical multisensory trainable system for diagnosing vocational aptitude of military medical specialists by ion content in the expired breath condensate, *Journal of Computational and Theoretical Nanoscience*. 16(11) (2019) 4502–4507.
4. **Gryaznova E. M., Rud V. Y.**, On the possibility of using the optical method for express quality control of fruits, *Journal of Physics: Conference Series*. Vol. 2086(1) (2021) 012143.
5. **Davydov R. V., Yushkova V. V., Stirmanov A. V., Rud V. Yu.**, A new method for monitoring the health condition based on nondestructive signals of laser radiation absorption and scattering, *Journal of Physics: Conference Series*. 1410(1) (2019) 012067.
6. **Davydov R. V., Rud V. Yu., Yushkova V.Y.**, On the possibility of analysis using the wavelet transform of the pulse waveform from the bloodstream, *Journal of Physics: Conference Series*. 1695(1) (2020) 012064.
7. **Grevtseva A. S., Smirnov K. J., Rud V. Yu.**, Development of methods for results reliability raise during the diagnosis of a person's condition by pulse oximeter, *Journal of Physics: Conference Series*. 1135(1) (2018) 012056.
8. **Makeev S. S., Grevtseva A. S., Glinushkin A. P., Matorin D. N.**, Possibilities of using spectral analysis in method of nuclear magnetic spectroscopy for condensed media investigation, *Journal of Physics: Conference Series*. 1695(1) (2020) 012112.
9. **Davydov V. V., Grebenikova N. M., Smirnov K. Y.**, An Optical Method of Monitoring the State of Flowing Media with Low Transparency That Contain Large Inclusions, *Measurement Techniques*. 62(6) (2019) 519–526.
10. **Myazin N. S.**, Features of formation of structure of a nuclear magnetic resonance signal in weak magnetic field, *Journal of Physics: Conference Series*. 1135(1) (2018) 012061.
11. **Marusina M. Ya., Karaseva E. A.**, Application of fractal analysis for estimation of structural changes of tissues on MRI images, *Russian Electronic Journal of Radiology*. 8(3) (2018) 107–112.
12. **Logunov S. E., Vysoczky M. G.**, New method of researches of the magnetic fields force lines structure, *Journal of Physics: Conference Series*. 1038(1) (2018) 012093.
13. **Kuzmin M. S., Rogov S. A.**, On the use of a multi-raster input of one-dimensional signals in two-dimensional optical correlators, *Computer Optics*. 43(3) (2019) 391–396.
14. **Davydov V. V., Grebenikova N. M., Smirnov K. Y.**, An Optical Method of Monitoring the State of Flowing Media with Low Transparency That Contain Large Inclusions, *Measurement Techniques*. 62(6) (2019) 519–526.
15. **Davydov V. V.**, Determination of the Composition and Concentrations of the Components of Mixtures of Hydrocarbon Media in the Course of its Express Analysis, *Measurement Techniques*. 62(2) (2020) 1090–1098.
16. **Davydov V. V., Davydova T. I.**, A nondestructive method for express testing of condensed media in ecological monitoring, *Russian Journal of Nondestructive Testing*. 53(7) (2017) 520–529.



17. **Murzakhanov F. F., Mamin G. V., Goldberg M. A., Gafurov M. R., Orlinskii S. B.**, EPR of Radiation-Induced Nitrogen Centers in Hydroxyapatite: New Approaches to the Study of Electron-Nuclear Interactions, *Russian Journal of Coordination Chemistry/Koordinatsionnaya Khimiya*. 46(11) (2020) 729–737.
18. **Kiryakova T. N., Marusina M. Ya., Fedchenkov P. V.**, Automatic methods of contours and volumes determination of zones of interest in MRI images, *Russian Electronic Journal of Radiology*. 7(2) (2017) 117–127.
19. **Myazin N. S., Dudkin V. I., Grebenikova N. M.**, On the Possibility of Express Recording of Nuclear Magnetic Resonance Spectra of Liquid Media in Weak Fields, *Technical Physics*. 63(12) (2018) 1845–1850.
20. **Antonov V.I., Davydov R.V., Maslikov V.I., Molodtsov D.V., Badenko V.L.**, Simulation of water flow management by the flood control facilities in the adjacent river basins, *Journal of Physics: Conference Series*. 1400(7) (2019) 077049.
21. **Nikitina M., Grebenikova N., Dudkin V., Batov Y.**, Methodology for assessing the adverse effects of the use of nuclear energy on agricultural land, *IOP Conference Series: Earth and Environmental Science*. 390(1) (2019) 012024.
22. **Gryznova E., Batov Y., Rud V.**, Methodology for assessing the environmental characteristics of various methods of generating electricity, *E3S Web of Conferences*. 140 (2019) 09001
23. **Davydov R., Myazin N., Dudkin V.**, The Multifunctional Nuclear Magnetic Flowmeter for Control to the Consumption and Condition of Coolant in Nuclear Reactors, *Energies*. 15(5) (2022) 1748.
24. **Davydov R., Antonov V., Moroz A.**, Parameter Control System for a Nuclear Power Plant Based on Fiber-Optic Sensors and Communication Lines, In: *IEEE International Conference on Electrical Engineering and Photonics (EExPolytech)*, Saint Petersburg, Russia, 13–15 October 2019. Vol. 8906791 (2019) 295–297.
25. **Dmitrieva D.S., Pilipova V.M., Davydov R.V., Davydov V.V., Rud V.Y.**, Fiber-optical communication line with a system for compensation of radiation-induced losses during the transmission of information, *Lecture Notes in Computer Science (including subseries Lecture Notes in Artificial Intelligence and Lecture Notes in Bioinformatics)*. 12526 LNCS (2020) 348–356.
26. **Tomashuk A.L., Filippov A.V., Kashaykin P.F., Guryanov A.N., Semjonov S.L.**, Behavior of strain-assisted self-trapped holes in pure-silica optical fibers upon pulsed-X-ray irradiation, *Journal of Non-Crystalline Solids*. 566 (2021) 120880.
27. **Kashaykin P.F., Tomashuk A.L., Vasiliev S.A., Zarenbin A.V., Semjonov S.L.**, Radiation Resistance of Single-Mode Optical Fibers at  $\lambda = 1.55 \mu\text{m}$  under Irradiation at IVG.1M Nuclear Reactor, *IEEE Transactions on Nuclear Science*. 67(10) (2020) 2162–2171.
28. **Dmitrieva D.S., Pilipova V.M., Dudkin V.I., Davydov V.V., Rud V.Yu.**, The possibility of controlling the relaxation rate of color centers in the optical fibers, *Journal of Physics: Conference Series*. 1697(1) (2020) 012145.
29. **Girard S., Kuhnhen J., Gusarov A., Boukenter A., Marcandella C.**, Radiation effects on silica-based optical fibers: Recent advances and future challenges, *IEEE Transactions on Nuclear Science*. 60(3), 6457426 (2013) 2015–2036.

## THE AUTHORS

**DMITRIEVA Diana**

dmitrievadiana1405@gmail.com

ORCID: 0000-0002-2561-6245

**DAVYDOV Vadim**

davydov\_vadim66@mail.ru

ORCID: 0000-0001-9530-4805

*Received 13.08.2022. Approved after reviewing 16.08.2022. Accepted 14.09.2022.*

Conference materials

UDC 535.44

DOI: <https://doi.org/10.18721/JPM.153.241>

## Fabrication of diffraction gratings for generation of OAM light

I. O. Venediktov<sup>1,2</sup>, K. O. Sedykh<sup>2,3</sup>, P. I. Zolotov<sup>1,2</sup>, N.S. Kaurova<sup>2</sup>,  
E. S. Lebedeva<sup>1</sup>, G. N. Goltsman<sup>1,2,3,4</sup>, D. V. Sych<sup>1,5,6</sup>

<sup>1</sup> National Research University Higher School of Economics, Moscow, Russia;

<sup>2</sup> Moscow State Pedagogical University, Moscow, Russia;

<sup>3</sup> National University of Science and Technology MISiS, Moscow, Russia;

<sup>4</sup> Russian Quantum Center, Skolkovo, Moscow, Russia;

<sup>5</sup> Sirius University, Sochi, Russia;

<sup>6</sup> P. N. Lebedev Physical Institute, Moscow, Russia

✉ [ilia1999ven@gmail.com](mailto:ilia1999ven@gmail.com)

**Abstract.** In this work we describe fabrication of diffraction gratings for generation of light with orbital angular momentum (OAM). OAM light characterized by topological charge  $l$  and modes with different  $l$  are orthogonal, which makes OAM light useful in quantum communication and tomography. We demonstrate fabrication route of diffraction gratings with computer generated hologram pattern on sapphire substrate and niobium reflective coat for generation of OAM light of visible spectrum.

**Keywords:** orbital angular momentum (OAM), vortex light, computer-generated holograms (CGH)

**Funding:** This study was funded by Russian Foundation for Basic Research, Project 21 72 10117.

**Citation:** Venediktov I. O., Sedykh K. O., Zolotov P. I., Kaurova N. S., Lebedeva E. S., Goltsman G. N., Sych D. V., Fabrication of diffraction gratings for generation of OAM light, St. Petersburg State Polytechnical University Journal. Physics and Mathematics. 15 (3.2) (2022) 224–228. DOI: <https://doi.org/10.18721/JPM.153.241>

This is an open access article under the CC BY-NC 4.0 license (<https://creativecommons.org/licenses/by-nc/4.0/>)

Материалы конференции

УДК 535.44

DOI: <https://doi.org/10.18721/JPM.153.241>

## Изготовление дифракционных решеток для генерации света с орбитальным угловым моментом

И. О. Венедиктов<sup>1,2</sup>, К. О. Седых<sup>2,3</sup>, Ф. И. Золотов<sup>1,2</sup>, Н. С. Каурова<sup>2</sup>,  
Е. С. Лебедева<sup>1</sup>, Г. Н. Гольцман<sup>1,2,3,4</sup>, Д. В. Сыч<sup>1,5,6</sup>

<sup>1</sup> Национальный исследовательский университет «Высшая школа экономики», Москва, Россия;

<sup>2</sup> Московский педагогический государственный университет, Москва, Россия;

<sup>3</sup> Национальный исследовательский технологический университет «МИСиС», Москва, Россия;

<sup>4</sup> Российский Квантовый Центр, Сколково, Москва, Россия;

<sup>5</sup> Университет «Сириус», Сочи, Россия;

<sup>6</sup> Физический институт им. П. Н. Лебедева РАН, Москва, Россия

✉ [ilia1999ven@gmail.com](mailto:ilia1999ven@gmail.com)



**Аннотация.** В данной работе рассматривается изготовление дифракционных решеток для генерации света с угловым орбитальным моментом (ОУМ), ОУМ свет характеризуется топологическим зарядом  $l$ , моды с различным значением  $l$  являются ортогональными, что делает ОУМ свет полезным в применении в квантовой криптографии и томографии. В данной работе мы описываем маршрут производства дифракционных решеток на сапфировой подложке с отражающим покрытием из нитрида ниобия для генерации света с ОУМ в видимом диапазоне.

**Ключевые слова:** орбитальный угловой момент (ОУМ), закрученный свет, компьютерные голограммы (CGH)

**Финансирование:** Исследование было выполнено при финансировании РФФИ, проект 21 72 10117.

**Ссылка при цитировании:** Венедиктов И. О., Седых К. О., Золотов Ф. И., Каурова Н. С., Лебедева Е. С., Гольцман Г. Н., Сыч Д. В. Изготовление дифракционных решеток для генерации света с орбитальным угловым моментом // Научно-технические ведомости СПбГПУ. Физико-математические науки. Т. 15. № 3.2. С. 224–228. DOI: <https://doi.org/10.18721/JPM.153.241>

Статья открытого доступа, распространяемая по лицензии CC BY-NC 4.0 (<https://creativecommons.org/licenses/by-nc/4.0/>)

## Introduction

Light has 2 angular momentum characteristics - spin angular momentum and orbital angular momentum. Usually light has only spin angular momentum, because wave vector  $k$  has no component perpendicular to the direction of propagation. Light with non-zero orbital angular momentum has linear phase dependence on azimuthal angle through constant  $l$ , which leads to appearance of  $k$  component tangent to phase plane. Mode with defined  $l$  can be described in terms of generalized Laguerre polynomial of order  $l$ . Those modes are orthogonal which makes modes with different  $l$  perfectly distinguishable and allows us to use OAM light for high dimensional quantum communication [1-4] and quantum tomography. There are several ways of generating OAM light such as spiral phase plates [5], cylindrical mode converters [6], Q-plates [7], pitch-fork holograms [8]. The last method is using diffraction gratings for generating OAM light. Pattern for this holograms can be obtained by computing interference pattern of OAM light and plane wave. Then we can load those patterns on SLM and use it as diffraction grating, which allows to change patterns very fast [9]. But also we can just make solid diffraction gratings out of some transparent material with reflective coat material. This method has advantages over SLM because of accuracy of pattern of diffraction gratings, which in case of SLM is limited by size of micro mirrors which are used to modulate intensity.

## Fabrication route of diffraction grating

Firstly, we need to compute pattern for diffraction grating. For this we need to calculate interference pattern of OAM light and plane wave. Circle mask was applied on initial waves phase distributions and therefore pattern has circular form. OAM and plane wave must be represented just by their phase terms, not taking into account spatial amplitude distribution (1).

$$I(x, y) = \left| e^{i\vec{k}\cdot\vec{r}} + e^{i\theta} \right|^2. \quad (1)$$

The plane wave must be at some angle relative to OAM light to form strip structure. Amplitudes of OAM and plane wave must be equal for high contrast of the pattern. As substrate for gratings double polished sapphire was used and NbN was used as reflective coat. Width of sapphire is 400  $\mu\text{m}$  ( $\pm 5\%$ ) and width of NbN is 60 nm. NbN was deposited by magnetron deposition in nitrogen atmosphere and then was etched in SF<sub>6</sub>/Ar plasma forming diffraction pattern. The darkest parts of interference picture in Fig. 1 were etched, therefore gratings were designed for transmission diffraction.

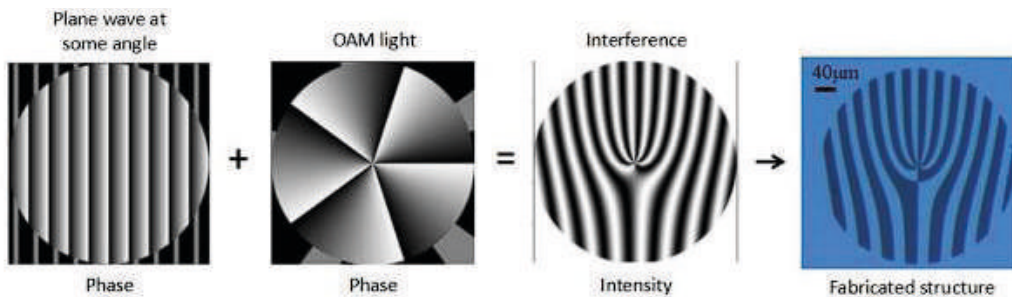


Fig. 1. Computing of hologram pattern and fabricated diffraction grating for  $l = 5$

### Fabricated structure

We fabricate array of diffraction gratings on sapphire plate. On the structure we arrange 12 fork-diffraction gratings for different number of  $l$  and with different grating period. Periods of  $20 \mu\text{m}$  and  $30 \mu\text{m}$  represented. Several periods were made for testing how it will affect generation of OAM. It can be seen from the micrograph in Fig. 1 that the pattern was produced accurately and all irregularities are order of wavelength and can't affect diffraction pattern.

### Simulation

We perform computer simulations in order to calculate how the gratings generate OAM. To simulate the process of light propagation, we use a plane wave with constant intensity as the initial wave. Then the intensity of the plane wave is multiplied by spatial grating pattern. Afterwards, we use fast Fourier transform to calculate far-field intensity. Calculation results are provided in Fig. 2. Then intensity plane was multiplied by grating pattern to simulate propagation through plane. Then we use fast Fourier transform to calculate far field intensity. Results of simulations provided in Fig. 2. Topological charge  $l = 5$  is chosen for simulation. It can be seen that in the center of intensity plane picture we have gauss beam with  $l = 0$ . Also we have two OAM beams with  $l = 5$  and  $l = -5$  at the first orders. The fact that charges are opposite can be proven by phase diagram in Fig. 2, *a*. We can see two helical phase fronts, which are twisted in opposite directions, which means that charges are opposite, because charge defines direction of rotation of phase front. Phase diagram also shows us that  $l = 5$  (by absolute value) because of shape of

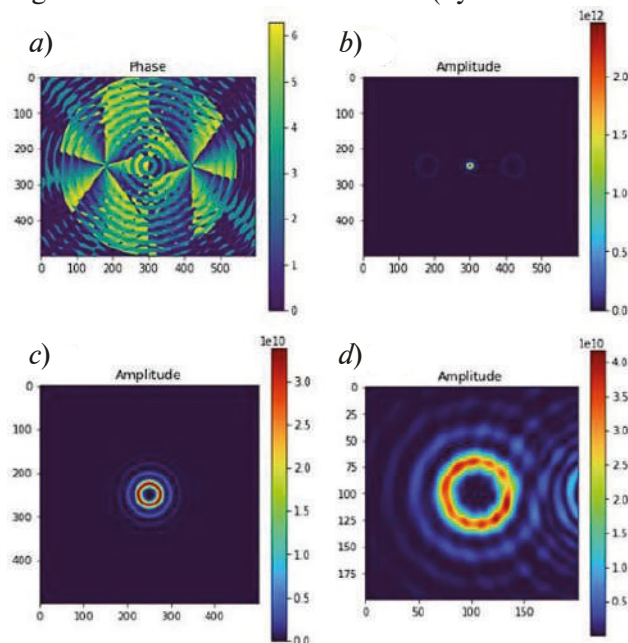


Fig. 2. Phase profile of the OAM light generated by grating (*a*), intensity profile of the OAM light generated by grating (*b*), ideal OAM light generated by simulation without grating (*c*), enlarged picture of OAM mode with  $l = 5$  generated by grating (*d*)

phase front of OAM beams, it has exactly 5 periodically changing regions, which is evidence of helical shape of phase front. Fig. 2,*c* shows the intensity profile of beam with  $l = 5$  is provided. Fig. 3,*d* shows enlarged intensity profile of beam with  $l = 5$  generated by gratings. It can be seen that profiles look the same which also proves that needed charge was obtained. Also we need to comment that circle mask was used during simulation and therefore in Fig. 2,*a* we can see circle and region with zero phase.

Simulation of generation of OAM light with  $l = 5$  was also provided for larger field of screen to see other orders of diffraction and check if they appear. In this case we did not use circular mask to see all orders and not nullify them. Results of simulation can be seen in Fig. 3. It can be seen from Fig. 3,*a* that phase still periodically changes with azimuthal angle, corresponding to  $l = 5$ , but phase profile for higher orders has more difficult structure which can be explained by overlapping of different orders. As  $l$  grows the radius of the beam also grows while distance between orders stays the same, therefore overlapping occurs which leads to interference of different orders. The overlapping can be also seen from Fig. 3,*b* where second order interfering with first order leading to appearance to interference strips between orders. The possible overlap is not good for generation because we may need to use different orders of OAM light from one grating. To prevent this situation, we may just use more strips in grating which can be done by increasing angle between plane wave and helical phase front during computation of diffraction pattern.

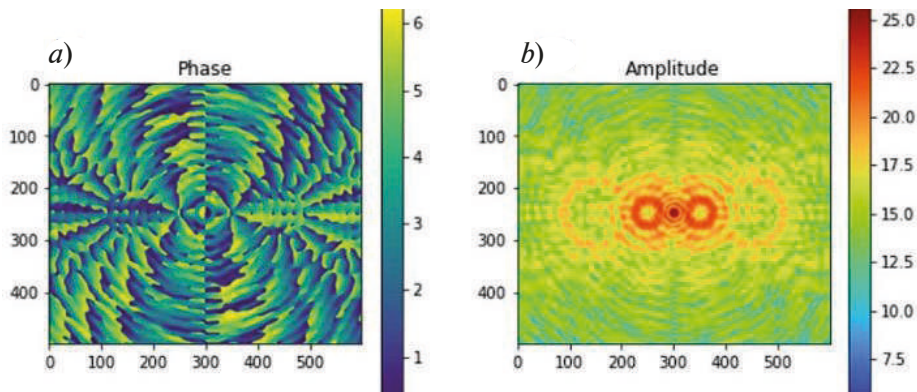


Fig 3. Phase profile of OAM light after grating (*a*), intensity profile of OAM light after grating in logarithmic scale (*b*)

### Conclusion

We have designed and fabricated a set of holographic diffraction gratings for generation of light with orbital angular momentum. We confirmed both in computer simulations and experiment that gratings with different periods and patterns produce the desired topological charges. Our work has great potential for developing compact structures for generating of light with orbital angular momentum which is particularly suitable for high-dimensional quantum communications.

### Acknowledgments

We thank Dr. Ledesma and Mr. Pabon for sharing program for CGH generating program and also useful literature. D.S. acknowledges financial support by Russian Foundation for Basic Research, Sirius University of Science and Technology, JSC Russian Railways and Educational Fund “Talent and success,” project number 20-32-51004.

### REFERENCES

1. Sych D., Grishanin B., and Zadkov V., Critical error rate of quantum-key-distribution protocols versus the size and dimensionality of the quantum alphabet November 2004 Physical Review A 0523312.
2. Sych D., Grishanin B., and Zadkov V., Analysis of limiting information characteristics of quantum-cryptography protocols 2005 Quantum electronics 35 (1) 80–84.
3. Sych D., Grishanin B., and Zadkov V., Quantum key distribution with a continuous alphabet Laser Physics 14 (10) (2004) 1314–1321.

4. **Sych D. and Leuchs G.**, Quantum key distribution with multi letter alphabets April 2010 Optics and spectroscopy, 108 326–33.
5. **Allen L., Beijersbergen M. W., Spreeuw R. J., Woerdman J. P.**, Helical- wavefront laser beams produced with a spiral phaseplate. J P, Optics Communications 112 (5–6): 321 (1994).
6. **Allen L., Beijersbergen M. W., Spreeuw R. J., Woerdman J. P.**, Orbital angular momentum of light and the transformation of Laguerre-Gaussian laser modes. Physical Review A 45(11) (1992) 8185–8189.
7. **Marrucci L., Manzo C., Paparo D.**, Optical Spin-to-Orbital Angular Momentum Conversion in Inhomogeneous Anisotropic Media. Physical Review Letters 96 (16): 163905 (2006).
8. **Heckenberg N. R., McDuff R., Smith C. P., White A. G.**, Generation of optical phase singularities by computer-generated holograms. Optics Letters 17 (3).
9. **Mirhosseini, M., Magaca-Loaiza O. S., Chen C., Rodenburg B., Malik M., Boyd R. W.**, Rapid generation of light beams carrying orbital angular momentum. Optics Express. 21(25) (2013) 30196.

#### THE AUTHORS

**VENEDIKTOV Ilia**  
ilia1999ven@gmail.com  
ORCID: 0000-0001-8461-5931

**LEBEDEVA Elizaveta**  
narniyall02@gmail.com  
ORCID: 0000-0002-1429-3794

**SEDYKH Ksenia**  
kseniaolegovna98@gmail.com  
ORCID: 0000-0001-6316-5337

**GOLTSMAN Gregory**  
goltsman@rplab.ru  
ORCID: 0000-0002-1960-9161

**ZOLOTOV Phillip**  
zolotov@scontel.ru  
ORCID: 0000-0003-1729-7480

**SYCH Denis**  
denis.sych@gmail.com  
ORCID: 0000-0002-4188-0951

**KAUROVA Natalia**  
kaurova@scontel.ru

*Received 14.08.2022. Approved after reviewing 16.08.2022. Accepted 24.08.2022.*

Conference materials

UDC 53.043

DOI: <https://doi.org/10.18721/JPM.153.242>

## New optic system for low mass $^{199}\text{Hg}$ ion clock

N. A. Lukashev <sup>1</sup>✉, V. V. Davydov <sup>1, 2</sup>

<sup>1</sup> Peter the Great St. Petersburg Polytechnic University, St. Petersburg, Russia;

<sup>2</sup> Bonch-Bruевич Saint Petersburg State University of Telecommunications, St. Petersburg, Russia

✉ [n-lukash@list.ru](mailto:n-lukash@list.ru)

**Abstract.** The necessity of modernization of quantum frequency standards (QFS), atomic clocks, which are used in satellite navigation and telecommunication systems, is substantiated. The main goal of all QSC upgrades is to improve the metrological characteristics. In the case of its use on moving objects, its dimensions, weight and power consumption also become important characteristics. The new developed optic system has been applied to low mass ion clock prototype. With its help it has become possible to significantly take up short term stability and temperature coefficients. The prospects for using this design in various moving objects are considered.

**Keywords:** time scale, optical system, mercury ions, atomic clock, stabilization, automatic frequency control

**Citation:** Lukashev N. A., Davydov V. V., New optic system for low mass  $^{199}\text{Hg}$  ion clock, St. Petersburg State Polytechnical University Journal. Physics and Mathematics. 15 (3.2) (2022) 229–234. DOI: <https://doi.org/10.18721/JPM.153.242>

This is an open access article under the CC BY-NC 4.0 license (<https://creativecommons.org/licenses/by-nc/4.0/>)

Материалы конференции

УДК 53.043

DOI: <https://doi.org/10.18721/JPM.153.242>

## Новая оптическая система для малогабаритных атомных часов на ионах ртути-199

Н. А. Лукашев <sup>1</sup>✉, В. В. Давыдов <sup>1, 2</sup>

<sup>1</sup> Санкт-Петербургский политехнический университет Петра Великого, Санкт-Петербург, Россия;

<sup>2</sup> Санкт-Петербургский государственный университет телекоммуникаций им. проф. М.А. Бонч-Бруевича, Санкт-Петербург, Россия

✉ [n-lukash@list.ru](mailto:n-lukash@list.ru)

**Аннотация.** Обоснована необходимость модернизации квантовых стандартов частоты (КСЧ) — атомных часов, которые используются в спутниковых навигационных и телекоммуникационных системах. Основной целью всех модернизаций КСЧ является улучшение метрологических характеристик. В случае применения его на подвижных объектах, также важными характеристиками становятся его габариты, вес и энергопотребление. Разработанная новая оптическая система была применена к прототипу ионных часов с малой массой. С его помощью удалось значительно улучшить кратковременную стабильность. Рассмотрены перспективы использования данной конструкции в различных подвижных объектах.

**Ключевые слова:** шкала времени, оптическая система, ионы ртути, атомные часы, стабилизация, автоподстройка частоты

**Ссылка при цитировании:** Лукашев Н. А., Давыдов В. В. Новая оптическая система для малогабаритных атомных часов на ионах ртути-199 // Научно-технические ведомости СПбГПУ. Физико-математические науки. Т. 15. № 3.2. С. 229–234. DOI: <https://doi.org/10.18721/JPM.153.242>

Статья открытого доступа, распространяемая по лицензии CC BY-NC 4.0 (<https://creativecommons.org/licenses/by-nc/4.0/>)

### Introduction

In the modern world, generators of highly stable oscillations (frequency standards) are used by humanity to solve various problems [1–5]. The highest accuracy among them is possessed by quantum frequency standards, which are actively used to solve various problems [6–11]. One of these tasks is related to ensuring a stable reference oscillation on a moving object [1, 6, 8, 12–17]. For various reasons, atomic clocks used in satellite systems experience a frequency delay, which is compensated during communication with the ground [12–22]. With a long-term absence of communication to adjust the time scale, delays will accumulate [22–26]. This may lead to various problems. For example, fractions of a second might spell the difference between reaching Mars safely and missing it entirely.

In the last years there is a common trend in developing new highly stable frequency standards, because of the growing demand from developing navigation and telecommunication systems [1–5]. Mostly these new designs are cold ion traps or laser-based. Ionic standards have somewhat worse stability indicators, but they compete with standards based on neutral atoms in terms of accuracy, since a single ion in a Paul trap is weakly subject to external perturbations. In addition, ion traps are compact (volume up to 1 dm<sup>3</sup>) and less sensitive to the settings of the cooling and interrogating laser fields. In CIS-countries, optical clocks are being created for ultracold strontium atoms with a relative error of part costs at the level of 10<sup>-17</sup> (VNIIFTRI), and work is also underway on the creation of optical clocks on single ions of ytterbium, aluminum, and neutral thulium atoms.

As it has been mentioned, there are several uses for ultra-stable clocks in space and on Earth that necessitate a tiny package size. Deep-space vehicles, for example, have strong physical size limits for onboard instruments; total spacecraft mass (unfueled) is frequently less than 400 kg, with projected trends toward even less mass. Current paper describes the newly developed optical system for one of these standards, the ion-based Hg-199 for telecommunication and space applications [23, 28, 29]. This device stands from other common “brothers” with its high tolerance to great G-values, which makes it a solid candidate for onboard use.

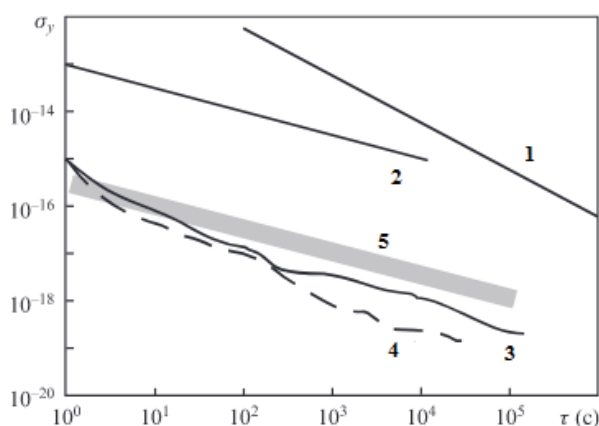


Fig. 1. Clock stability: gas chamber based 1, ion beam based 2, femtosecond laser 3, 4, optical standards device 5 of the cesium frequency standard

## Materials and Methods

We have developed a high-performance  $^{199}\text{Hg}^+$  trapped-ion clock with frequency stability near  $2 \cdot 10^{-16}$ . The ion-trapping technologies developed for this clock are critical to achieving this level of stability. The ion trap design for the liter clock is based on “ion-shuttling” between a linear quadrupole and a linear multipole, similar to what is utilized in ground clocks [1, 3]. However, improvements and redesigns in the vacuum and optical systems are required to achieve the 1 to 2 liter size requirement.

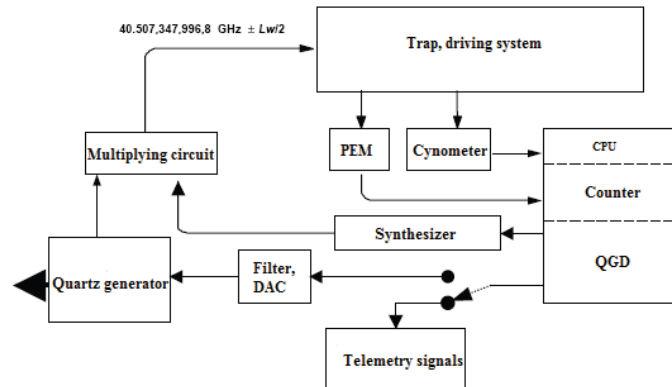


Fig. 2. Block diagram for the developed standard

Optical standards may be the perfect solution for onboard use right now for the high stability, those based on ultracold atoms and femtosecond lasers are too fragile for onboard applications.

The Hg-199 standard conceptually has a negative feedback loop where the magnetic trap provides the controller with information regarding its resonance shift. The photon counter determines time interval  $\tau$  that could be varied in a certain range depending on deployment conditions: from 1 to 10 seconds, the number of registered photons by PEM: from  $10^4$  to  $5 \cdot 10^5$ . The driving system produces processing commands judging by the number of photons emitted with the help of the newly developed algorithm in order to drive the frequency of the main quartz generator and also the power circuits. Voltage output from these circuits passes transformer coils and corrects the magnetic field in the trap in order to ensure stable and precise maintenance of the device. The programmable part consists of CPU, counter and quartz generator driver (QGD), quartz generator itself receives the error signal information and shifts the produced frequency to resonance. The whole work is performed inside the counter and CPU-related parts, thus taking the most crucial tasks, digital and analog circuitry are also separated making it easier for developers to maintain the device as well as further reducing its size.

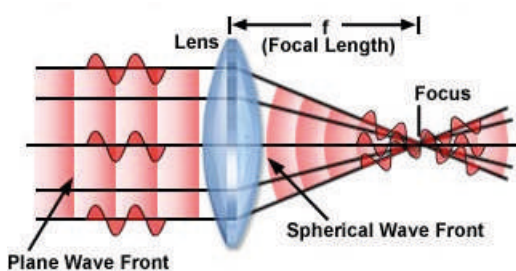


Fig. 3. Wave diagram through a perfect lens

Trap and its containing substance must be preserved at the operating state. Multiplying loop, controlling CPU and the optical system inside the trap are dedicated to this task.

While some optical components of the focusing system act as components that create an image, others are provided for all kinds of transformations of the illuminating beam, and also perform filtering and transmitting functions. The image-forming components of the optical system are considered to be a converging lens (located in or near the illuminator), a condenser, an objective, an eyepiece tube (or eyepiece) and refractive components or a video camera lens. But some of these components are not typically image-forming, and their properties are of primary importance in determining the property of the final microscopic image.

Awareness of the role of individual lenses, the elements that make up the optical system, is considered the main one for understanding the process of formation of a focusing beam in an optical system. A perfect lens is considered to be a simple, image-creating component (Fig. 3):

flawlessly corrected, free of aberrations and focused light into 1 point. A parallel, paraxial beam of light, refracted in a converging lens, is focused at its focal point or focus (it is labeled Focus in Fig. 3). These lenses are often referred to as positive lenses because they help converge a convergent (converging) light beam more sharply and slow down the diverging beam. Light from a point source placed at the focal point of the lens emerges from it in a parallel, paraxial beam (direction from right to left in Fig. 3). The distance between a lens and its focus is called the focal length of the lens, denoted  $f$  in Fig. 3.

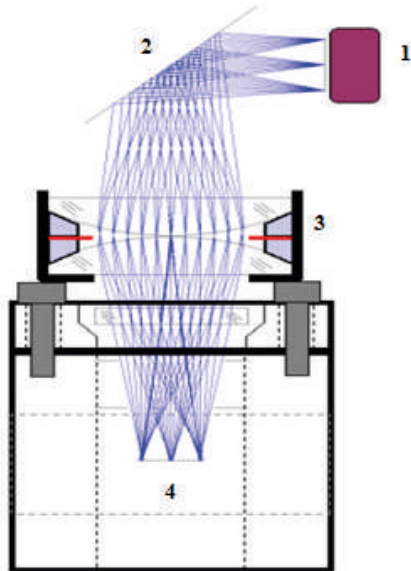


Fig. 4. UV Optical system: source 1, refractors 2, focus system 3, working substance 4

The optical system that collects appropriate ultraviolet (UV) fluorescence from the trapped Hg ions is crucial for achieving the desired short-term stability. The apparatus depicted in Fig. 4 was conceived and built by us, and it is utilized for both concentrating the source light from a  $^{202}\text{Hg}$  lamp onto the trapped ions and capturing fluorescence from these ions. The dielectric-coated folding mirror acts as a dichroic reflector, reflecting 194-nm ion fluorescent light with  $>95\%$  reflectance and parasitic 254-nm light from a neutral Hg transition with just 10 % reflectance. Because stray light limits the stability, it is critical to remove the 10 stronger 254-nm light from the beam because it is situated inside the UV-sensitive photomultiplier tube's detection band.

This system is integrated with the ion trap assembly. The electronics modules that control the photomultiplier tubes, pulse amplifier–discriminator, and discharge lamp are housed in the same enclosure as the lens, mirrors, and detectors/source. The ground clock used three independently movable optics modules to optimize ion fluorescence, but the single-module approach to the optical package here is different. The three identical optical arms of the integrated optical system described here may be placed on the bench such that their focuses fall in the same place. Since the production and assembly of the optical package have been recently completed, the optical alignment process is just getting started.

### Results and Discussion

Fig. 5 shows the dependence of the change in the values of the Allan variance  $\sigma_y(\tau)$  on time  $\tau$  for the laboratory design of atomic clocks.

The experimental results show that the Allan dispersion  $\sigma(\tau)$  satisfies the requirements that apply to the accuracy characteristics of atomic clocks. Studies of the operation of atomic clocks were carried out for 12 days in a temperature chamber.

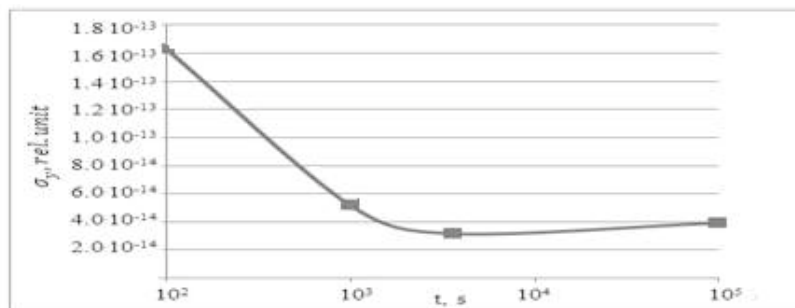


Fig. 5. Plot of Allan variance  $\sigma_y$  versus time  $t$



## Conclusion

The obtained results have shown that the developed optical systems for the small-sized design of atomic clocks on mercury-199 ions can be used in the basic model for satellite systems. In addition to this design, it is necessary to develop a thermal stabilization unit for the optical part, taking into account the space use of atomic clocks.

## REFERENCES

1. **Riehle F.**, Frequency standard. Basic and applications, WILEY-VCH Verlag GmbH Co. KGaA: New-York, 2008.
2. **Dudkin V.I., Myazin N.S., Davydov R.V.**, On the Possibility of Studying Ferrofluids by a Nuclear Magnetic Magnetometer with a Flowing Sample, *Journal of Communications Technology and Electronics*. 65 (5) (2020) 558–564.
3. **Mihov E.D., Nepomnyashchiy O.V.**, Selecting informative variables in the identification problem *Journal of Siberian Federal University - Mathematics and Physics*. 9(4) (2016) 473–480.
4. **Ryzhenko I.N., Lutsenko A.E., Varygin O.G., Nepomnyashchiy O.V.**, Carrier compensation mode implementation in satellite communication channels. In: *Proceedings of 2019 International Siberian Conference on Control and Communications, SIBCON 2019*, vol. 8729665 (2019) 23–29.
5. **Davydov R., Antonov V., Moroz A.**, Parameter Control System for a Nuclear Power Plant Based on Fiber-Optic Sensors and Communication Lines, In: *IEEE International Conference on Electrical Engineering and Photonics (EExPolytech)*, Saint Petersburg, Russia, 13-15 October 2019. vol. 8906791 (2019) 295–297.
6. **Petrov A. A., Grebenikova N. M.**, Some Directions of Quantum Frequency Standard Modernization for Telecommunication Systems, *Lecture Notes in Computer Science (including subseries Lecture Notes in Artificial Intelligence and Lecture Notes in Bioinformatics)*. 11118 LNCS (2018) 641–648.
7. **Semenov V. V., Nikiforov N. F., Ermak S. V.**, Calculation of stationary magnetic resonance signal in optically oriented atoms induced by a sequence of radio pulses, *Soviet journal of Communications Technology and Electronics*. 36(4) (1991) 59–63.
8. **Petrov A.A., Myazin N.S., Kaganovskiy V.E.**, Rubidium atomic clock with improved metrological characteristics for satellite communication system, *Lecture Notes in Computer Science (including subseries Lecture Notes in Artificial Intelligence and Lecture Notes in Bioinformatics)*. 10531 LNCS (2017) 561–568.
9. **Fadeenko V.B., Pchelkin G.A., Rud V.Yu.**, Features of the transmission of microwave signals in the range of 8-12 GHz in the maritime radar station over fiber-optic communication line, *Journal of Physics: Conference Series*. 1400(4) (2019) 044010.
10. **Sharova N.V., Fedorova E.V., Vologdin V.A.**, Fiber-optics system for the radar station work control, *Lecture Notes in Computer Science (including subseries Lecture Notes in Artificial Intelligence and Lecture Notes in Bioinformatics)*. 9247 (2015) 712–721.
11. **Lenets V.A., Tarasenko M.Yu., Rodygina N.S.**, New method for testing of antenna phased array in X frequency range, *Journal of Physics: Conference Series*. 2018, 1038(1) (2018) 012037.
12. **Petrov A. A.**, New scheme of the microwave signal formation for quantum frequency standard on the atoms of caesium-133 *Journal of Physics: Conference Series*. 769(1) (2016) 012065.
13. **Grevtseva A., Rud V.**, Method of processing velocity increase of measuring results of quantum frequency standard parameters for information transfer velocity increase in satellite communication systems, *CEUR Workshop Proceedings*. 2667 (2020) 15–18.
14. **Valov, A.P., Arinushkina, K.G.**, The use of digital data processing to improve the metrological characteristics of the rubidium frequency standard, *Journal of Physics: Conference Series*. 2086(1) (2021) 012070.
15. **Petrov A. A.**, Digital Frequency Synthesizer for <sup>133</sup>Cs-Vapor Atomic Clock, *Journal of Communications Technology and Electronics*. 62(3) (2017) 289–293.
16. **Arinushkina K. G., Valov A. P.**, Digital processing of optical signals in the frequency standard based in rubidium atoms - 87, In: *Proceedings of ITNT 2021 - 7th IEEE International Conference on Information Technology and Nanotechnology*, 2021 Samara, Russia, 20-24 September 2021. vol. 44026298 (2021) 44–49.
17. **Petrov A. A.**, Improvement frequency stability of caesium atomic clock for satellite communication system, *Lecture Notes in Computer Science (including subseries Lecture Notes in Artificial Intelligence and Lecture Notes in Bioinformatics)*. 9247 (2015) 739–744.

18. **Lukashev N. A., Rud V. Yu.**, Microwave frequency standard on Hg-199 ions for space stations and vehicles *Journal of Physics: Conference Series*. 1400(2) (2019) 022050.
19. **Zalyotov D. V., Shabanov V. E., Shapovalov D. V.**, Features of direct digital synthesis applications for microwave excitation signal formation in quantum frequency standard on the atoms of cesium, *Journal Physics: Conference Series*. 1124(1) (2018) 041004.
20. **Petrov A. A., Shabanov V. E., Zalyotov D. V., Bulyanitsa A. L., Shapovalov D. V.**, Modernization of the frequency synthesizer of cesium atomic clock, *IEEE International Conference on Electrical Engineering and Photonics, EExPolytech 2018, Saint Petersburg, October 2018*. vol. 8564389 (2018) 52–55.
21. **Grevtseva A. S., Dmitriev R. A.**, Features of the formation of the frequency of the microwave excitation signal in the quantum frequency standard on rubidium atoms – 87, *Journal of Physics: Conference Series*. 2086(1) (2021) 012055.
22. **Lukashev N.A., Moroz A.V.**, Compact microwave frequency standard on Hg-199 ions for navigation systems, *Journal of Physics: Conference Series*. 1236(1) (2019) 012068.
23. **Wang, D., Rud, V.Y.** Prospective directions for the development of microwave frequency standards for satellite navigation systems *Journal of Physics: Conference Series*. 2086(1) (2021) 012073.
24. **Petrov A. A., Zaletov D. V., Shapovalov D. V.**, Peculiarities of Constructing a Scheme for Formation of a Microwave Excitation Signal in Cesium Atomic Clock, *Journal of Communications Technology and Electronics*. 66(3) (2021) 295–299.
25. **Lukashev N.A., Valov A.P., Grebenikova N.M.**, Improving performance of quantum frequency standard with laser pumping, *Proceedings of 18th International conference of Laser Optics ICLO-2018, Saint Petersburg*. Vol. 8435889 (2018) 271.
26. **Valov A.P., Davydov V.V., Rud V.Y.**, The method of improving the parameters of the microwave excitation signal in the rubidium - 87 quantum frequency standard, *Journal of Physics: Conference Series*. 1410(1) (2019) 012246.
27. **Valov A., Davydov V., Rud V., Lukashev N.**, On the need to use the median signal filtering method to improve the metrological characteristics of the rubidium frequency standard during processing and transmitting large data arrays, *CEUR Workshop Proceedings*. 2667 (2020) 102–105.
28. **Lukashev N. A., Davydov R. V., Glinushkin A.P., Rud' V.Y.**, Improving characteristics of microwave frequency standard on Hg-199 ions for telecommunication systems, *Journal of Physics: Conference Series*. 1326(1) (2019) 012046.
29. **Lukashev N. A., Glinushkin A. P., Rud V. Yu., Lukyantsev V. S.**, Microwave low mass-dimensional frequency standard on Hg- 199 ions, *Journal of Physics: Conference Series*. 1410(1) (2019) 012211.
30. **Petrov A.A., Grebennikova N.M.**, On the Potential Application of Direct Digital Synthesis in the Development of Frequency Synthesizers for Quantum Frequency Standards *Journal of Communications Technology and Electronics*. 63(11) (2018) 1281–1285.

#### THE AUTHORS

**LUKASHEV Nikita**

n-lukash@list.ru

ORCID: 0000-0002-0841-0624

**DAVYDOV Vadim**

davydov\_vadim66@mail.ru

ORCID: 0000-0001-9530-4805

*Received 15.08.2022. Approved after reviewing 31.08.2022. Accepted 08.09.2022.*

Conference materials  
UDC 535.015, 535.58  
DOI: <https://doi.org/10.18721/JPM.153.243>

## Silicon nanoantenna for controlling the polarization direction of radiation from standalone quantum light source

K. V. Baryshnikova <sup>1</sup>✉, O. N. Sergaeva <sup>1</sup>, M. I. Petrov <sup>1</sup>

<sup>1</sup>ITMO University

✉ [k.baryshnikova@metalab.ifmo.ru](mailto:k.baryshnikova@metalab.ifmo.ru)

**Abstract.** The emission control of standalone quantum sources has recently attracted the interest of the scientific community due to the growing technological capabilities for fabrication and on-demand positioning of these emitters. Here we report on simulation of silicon-on-insulator prismatic nanoantenna possessing resonantly induced bianisotropy that provides a strong dependence of its emission on the location of the quantum emitter inside the system. Obtained results could potentially be used in sensing, nanoscale light control, and quantum computing applications.

**Keywords:** quantum islands, silicon nanoantenna, radiation pattern, numerical simulation, nanophotonics

**Funding:** This research was supported by the Russian Science Foundation (project 21-72-20184). K.V.B. acknowledges the financial support from BASIS foundation and The Russian Federation President Grant Council, project no. МК-2818.2022.1.2.

**Citation:** Baryshnikova K. V., Sergaeva O. N., Petrov M. I., Silicon nanoantenna for controlling the polarization direction of radiation from standalone quantum light source, St. Petersburg State Polytechnical University Journal. Physics and Mathematics. 15 (3.2) (2022) 235–239. DOI: <https://doi.org/10.18721/JPM.153.243>

This is an open access article under the CC BY-NC 4.0 license (<https://creativecommons.org/licenses/by-nc/4.0/>)

Материалы конференции  
УДК 535.015, 535.58  
DOI: <https://doi.org/10.18721/JPM.153.243>

## Кремниевая наноантенна для контроля поляризации излучения одиночного квантового источника света

К. В. Барышникова <sup>1</sup>✉, О. Н. Сергаева <sup>1</sup>, М. И. Петров <sup>1</sup>

<sup>1</sup>Университет ИТМО

✉ [k.baryshnikova@metalab.ifmo.ru](mailto:k.baryshnikova@metalab.ifmo.ru)

**Аннотация.** В последнее время управление эмиссией одиночных источников излучения привлекает интерес научного сообщества в связи с ростом технологических возможностей по созданию и позиционированию таких излучателей. В этой работе мы сообщаем о моделировании наноантенны в виде призмы на базе кремния-на-изоляторе, поддерживающей резонансно возбуждаемый бианизотропный отклик и обеспечивающей сильную зависимость характеристик излучения от положения квантового излучателя внутри наноструктуры. Полученные результаты могут применяться в области зондирования, управления светом на наномасштабе и, в перспективе, для создания квантовых компьютеров.

**Ключевые слова:** квантовые островки, кремниевая наноантенна, диаграмма направленности, поляризация, численное моделирование, нанофотоника

**Финансирование:** Работа выполнена при поддержке Российского научного фонда (проект № 21-72-20184). К.В.Б. благодарит финансовую поддержку фонда Базис и Президента Российской Федерации, номер гранта МК-2818.2022.1.2.

**Ссылка при цитировании:** Барышникова К. В., Сергаева О. Н., Петров М. И. Кремниевая наноантенна для контроля поляризации излучения одиночного квантового источника света // Научно-технические ведомости СПбГПУ. Физико-математические науки. Т. 15. № 3.2. С. 235–239. DOI: <https://doi.org/10.18721/JPM.153.243>

Статья открытого доступа, распространяемая по лицензии CC BY-NC 4.0 (<https://creativecommons.org/licenses/by-nc/4.0/>)

## Introduction

The creation of efficient compact photon emission sources has a wide range of potential applications, primarily in optical communication lines and information processing systems, including quantum computers. To increase variability of procedures that can be performed on a single chip, the number of independently controlled emitters should be reduced – at best to unity. Only recently it became possible to create standalone emitter, located on demand, in silicon wafer [1]. Herewith, silicon-on-insulator-based nanostructures attract great scientific interest due to the possibility of efficient light control at the nanoscale via excitation of both electric and magnetic Mie-type resonances [2, 3, 4].

Here we study silicon nanoresonators placed on an insulator substrate with an individual emitter precisely located inside and focus on the effect how polarization in the far field zone depends on the light source position. It is favorable for developing efficient emission sources with controllable polarization in the measurable zone [5–6].

We have previously studied the effects of induced bianisotropy in asymmetric nanoresonators and nanoclusters in [7, 8], and have shown that the coupling between electric and magnetic multipoles in such structures results in interesting effects, including polarizability-dependent modes excitation and directional scattering. These concepts can be applied and developed to control the emission from the quantum islands in silicon nanostructures. Based on our discussions with colleagues, proposed designs can be manufactured with accuracy  $\pm 10$  nm by the methods of electron beam lithography and plasma etching from a bare layer with controllable positioned emitters. The last one can be obtained via techniques discussed in [1] which can be briefly represented as follows: the structure is grown at 600 °C using molecular-beam epitaxy on a SOI substrate with buffer layer and contain several layers of Ge(Si) QDs interspersed with intermediate Si layers.

## Materials and Methods

Different polarizations of incident electromagnetic wave can excite different modes inside the prismatic nanoparticle at the same frequency. Moreover, degenerated modes have completely different field distribution, corresponding to the transverse electric and transverse magnetic types (see Fig. 1,c). It becomes possible due to bianisotropy induced in the nanoresonator. Bianisotropy appears in resonators with a lack of the inversion symmetry and manifests itself in the excitation of multipoles inside a resonator which are not presented in the incident plane wave [9]. In the case when the resonator's optical size is comparable with the incident wavelength, bianisotropic response can be easily presented in the following form:

$$\begin{aligned}\vec{p} &= \varepsilon_0 \hat{\alpha}^{EE} \vec{E} + \frac{1}{c} \hat{\alpha}^{EH} \vec{H}, \\ \vec{m} &= \varepsilon_0 \hat{\alpha}^{HH} \vec{H} + \frac{1}{Z_0} \hat{\alpha}^{HE} \vec{E},\end{aligned}\tag{1}$$

where  $\vec{E}$  and  $\vec{H}$  are the electric and magnetic fields of the incident wave at the dipoles coordinates,  $c$  is the speed of light,  $Z_0$  is the free space impedance,  $\varepsilon_0$  is the vacuum permittivity, and  $\hat{\alpha}^{EE}, \hat{\alpha}^{EH}, \hat{\alpha}^{HE}, \hat{\alpha}^{HH}$  are the second rank polarizability tensors.

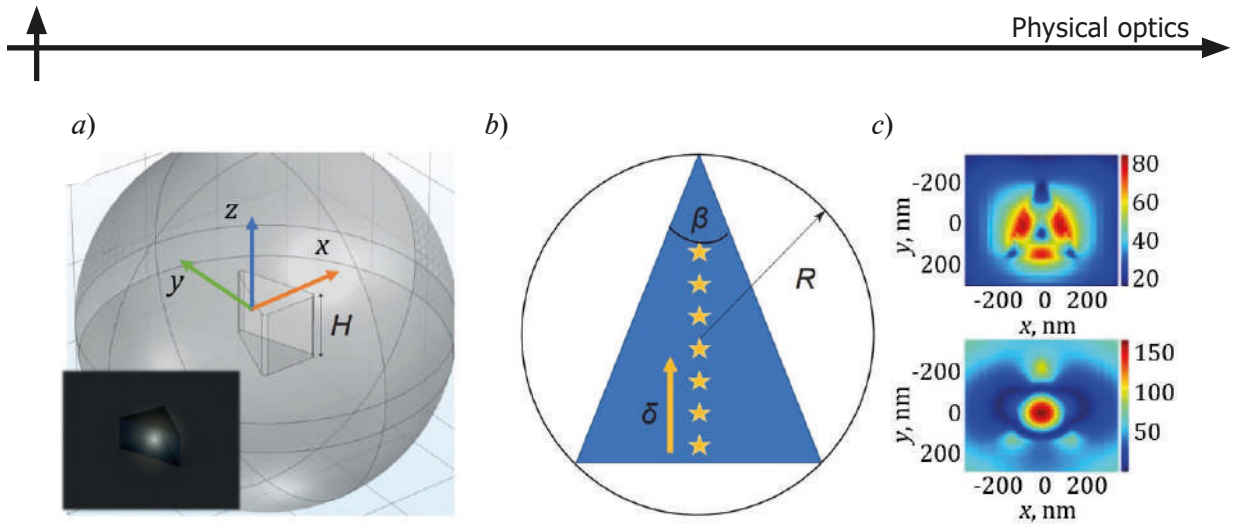


Fig. 1. Scheme of a silicon prismatic nanoresonator with an embedded point emitter: COMSOL model view (a); the inset shows a prismatic nanoparticle with a single emitter, artistic view; cut plane of the prism parallel to the substrate (b); the asterisks mark different positions of the emitter. Electric field distributions on the cut plane shown in Fig. 1,b excited in the prism illuminated by plane waves with two orthogonal polarizations (c)

The last figure was adopted with permission from [8]

By tuning the geometrical parameters, it is possible to create a structure where bianisotropic excitation of the magnetic dipole from the incident wave's electric field arises resonantly at the same frequency with the simple electric dipole resonance in the orthogonal polarization (see [8] for details). Due to the reciprocity principle, different modes excited in the nanoparticle have different polarization in the emitted far field. In order to enhance modes with different field distributions it is necessary to place the emitters differently inside the nanoresonators. In this case, the coupling between the emitter and the resonator modes strongly depends on its location and orientation, and the desired mode can be excited.

We carried out numerical calculations of the characteristics of the proposed nanosystem on a substrate in the COMSOL Multiphysics software. The emitter was modelled as a point dipole source oriented parallel to the substrate's surface and located inside the silicon nanoparticle at various positions. The material properties of crystalline silicon were emulated via refractive index equal to 3.5, which silicon has in the infrared range, and the refractive index of quartz substrate has taken to be 1.5. Particle's environment was air.

### Results and Discussion

Fig. 1,a,b shows the scheme of a considered structure, a silicon triangular prism on a quartz substrate. Parameters of the structure were chosen in accordance with optimized geometry from [7]. Here,  $H = 382$  nm,  $R = 282$  nm,  $\beta = 40^\circ$ . Point dipole was located in a plane parallel to the substrate at a distance  $H/2$  from it, different positions of the emitter along the triangle symmetry axis with different values of shift  $\delta$  from the base side were modeled. The corners of the prism were smoothed in the simulation, as there will be no sharp corners in the fabricated samples.

Simulations showed that the radiation from the structure goes predominantly into the substrate, however, the experimental setup, for which we developed the design of the nanostructure, collects the light from the ambient air side. Therefore, it is more important to analyze the radiation in the upward direction. Its features depend strongly on the location and orientation of the emitter. Thus, it is possible to find the location where emission in the upward direction has only  $y$ -polarization (e.g. along prism triangle's height), no matter how the emitting source is polarized. Fig. 2 shows emitted light polarization maps in the far field zone area above the investigated nanostructure for two positions of the source, 150 nm and 300 nm away from the short side of the triangle at the prism base and for different orientations of the emitter. As seen in the first row of Fig. 2, radiation in the considered area have both two polarizations in the observation direction upward from the substrate, along the triangle base and along its height. And the second row shows that for another emitter position both  $x$ - and  $z$ -oriented dipoles bring  $y$ -polarized contribution to the emitted light, while contribution of  $x$ -oriented dipole into the far field radiation is negligibly small. The

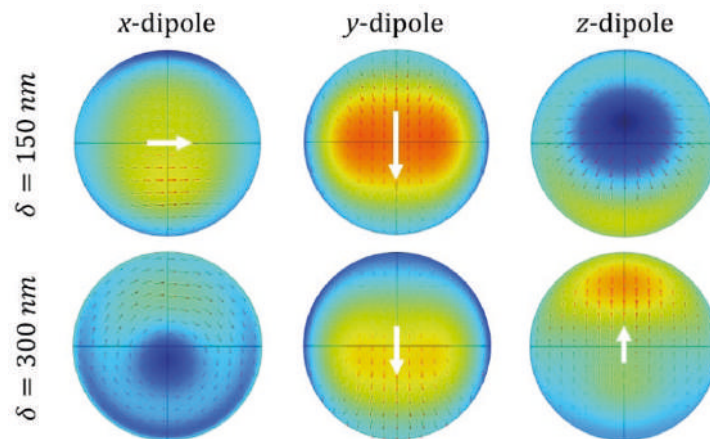


Fig. 2. Maps showing the electric field direction on the half-spherical surface above the structure in the far field wave zone. White arrows indicate direction and magnitude of the light's electric field in the upward direction. Two rows correspond to the two different emitter locations, three columns correspond to the three different emitter orientation directions

$x$ -dipole radiation dominates over the  $y$ -dipole one, meanwhile in the second row the  $y$ -dipole dominates over the two other orientations. The  $z$ -dipole radiation in the upward direction is low in both considered cases.

The direction of the dipole moment of the electron transition in the experimentally fabricated nanoislands strongly depends on shape and geometry and, thus, can be assumed unknown, so we consider all three polarizations of quantum emitter. It means that  $x$ -,  $y$ - and  $z$ - dipoles are excited with the same probability. However, if radiation at a chosen angle can “choose” the orientation of the dipole depending on its location, and we can manipulate and control the emitter location inside the nanostructure, we can use this mechanism to obtain the photoluminescence polarized on demand. Moreover, the luminescence signal of Ge-Si nanoislands is characterized by a large width [1], which makes it possible to interact with non-degenerated nanoresonator modes depending on their location. It expands the scope of possible designs sufficiently and opens a new route to design active metadevices.

These results are of a big interest of author's collaborators and the first experiments with standalone quantum nano-islands have been already performed based on the designs shown in this paper.

### Conclusion

We have demonstrated a prismatic nanoresonator on a substrate in which different electromagnetic modes can be excited depending on the location of the incorporated light emitter. Different modes radiate into the far field zone in a different manner, and the dominant polarization is strongly dependent on the emitter location. This result can be used for generation of a polarized luminescence signal as well as for determining the emitter location by analyzing the polarization of the radiation.

### Acknowledgments

The authors acknowledge A. V. Novikov, M. V. Stepikhova, V. A. Zinovyev, Zh. V. Smagina for fruitful discussions.



## REFERENCES

1. Smagina Zh.V., Novikov A.V., Stepikhova M.V., Zinovyev V.A., Rodyakina E.E., Nenashev A.V., Sergeev S.M., Peretokin A.V., Kuchinskaya P.A., Shaleev M.V., Gusev S.A., Dvurechenskii A.V., Luminescence of spatial ordered single and groups of Ge(Si) nanoislands embedded in photonics crystals, *Semiconductors* (2020) 54, 8, 708–715.
2. Staude I., Pertsch T., Kivshar Yu. S., All-Dielectric Resonant Meta-Optics Lightens up, *ACS Photonics* (2019) 6, 4, 802–814.
3. Kuznetsov A. I., Miroschnichenko A. E., Brongersma M. L., Kivshar Y. S., Luk'yanchuk B., Optically resonant dielectric nanostructures, *Science* (2016) Vol. 354, No. 6314, aag2472.
4. Staude I., Khardikov V. V., Fofang N. T., Liu S., Decker M., Neshev D. N., Luk T. S., Brener I., Kivshar Yu. S., Shaping Photoluminescence Spectra with Magnetoelectric Resonances in All-Dielectric Nanoparticles, *ACS Photonics* (2015) 2, 2, 172–177.
5. Rutckaia V., Heyroth F., Schmidt G., Novikov A., Shaleev V., Savelev R. S., Schilling J., Petrov M., Coupling of Germanium Quantum Dots with Collective Sub-radiant Modes of Silicon Nanopillar Arrays, *ACS Photonics* (2021) 8 (1), 209–217.
6. Zinovyev V.A., Zinovieva A.F.; Nenashev A.V.; Dvurechenskii A.V., Katsuba A.V., Borodavchenko O.M., Zhivulko V.D., Mudryi A.V., Self-assembled epitaxial metal-semiconductor nanostructures with enhanced GeSi quantum dot luminescence, *Journal of Applied Physics* (2020) 127, 243108.
7. Markovich D., Baryshnikova K., Shalin A., Samusev A., Krasnok A., Belov P., Ginzburg P., Enhancement of artificial magnetism via resonant bianisotropy. *Scientific reports* (2016) 6, 1–8.
8. Evlyukhin A. B., Poleva V. A., Prokhorov A. V., Baryshnikova K. V., Miroschnichenko A. E., Chichkov B. N., Polarization switching of quasi-trapped modes and near field enhancement in bianisotropic all-dielectric metasurfaces, *Laser Photonics Rev.* (2021) 15(12), 2100206.
9. Poleva, M., Frizyuk, K., Baryshnikova, K., Bogdanov, A., Petrov, M., Evlyukhin, A., Multipolar theory of bianisotropic response. arXiv preprint arXiv:2205.01082 (2022).

## THE AUTHORS

**BARYSHNIKOVA Kseniia**  
k.baryshnikova@metalab.ifmo.ru  
ORCID: 0000-0002-3753-3543

**PETROV Mihail**  
m.petrov@metalab.ifmo.ru  
ORCID: 0000-0001-8155-9778

**SERGAEVA Olga**  
o.sergayeva@metalab.ifmo.ru  
ORCID: 0000-0003-0922-8768

*Received 29.08.2022. Approved after reviewing 01.09.2022. Accepted 08.09.2022.*

Conference materials

UDC 535

DOI: <https://doi.org/10.18721/JPM.153.244>

### Hollow-core antiresonant optical fiber activated with YAG:Yb<sup>3+</sup>

D. N. Shurupov <sup>1</sup>✉, G. A. Pchelkin <sup>2</sup>, V. V. Demidov <sup>3</sup>, V. V. Davydov <sup>1,2</sup>, D. V. Vakorina<sup>2</sup>

<sup>1</sup> Peter the Great St. Petersburg Polytechnic University, St. Petersburg, Russia;

<sup>2</sup> Bonch-Bruевич Saint Petersburg State University of Telecommunications, St. Petersburg, Russia;

<sup>3</sup> JSC S.I. Vavilov State Optical Institute, St. Petersburg, Russia

✉ shurupoff.dm@yandex.ru

**Abstract.** This article presents methods for modifying the structures of an antiresonant optical fiber with a hollow cardiovascular system, with the help of which it is possible to detect a large number of active substances without resorting to the ways and technological processes of cardiovascular diseases. To obtain luminescence centers, a hollow antiresonant fiber is bound to capillaries with a solution of a YAG:Yb<sup>3+</sup> composite and an organic solvent of dimethylformamide. After the procedure, several processing options are identified that cause the stocks of blanks to dry under normal conditions at a temperature of 150 °C and heat treatment at a temperature of 1000 °C. As a result, film tissues based on YAG:Yb<sup>3+</sup> were formed inside the capillaries. The obtained luminescence peaks in the main and one of the additional peaks for YAG:Yb<sup>3+</sup>.

**Keywords:** hollow core antiresonant optical fiber, activated optical fiber, luminescence

**Citation:** Shurupov D. N., Pchelkin G. A., Demidov V. V., Davydov V. V., Vakorina D.V., Hollow-core antiresonant optical fiber activated with YAG:Yb<sup>3+</sup>, St. Petersburg State Polytechnical University Journal. Physics and Mathematics. 15 (3.2) (2022) 240–245. DOI: <https://doi.org/10.18721/JPM.153.244>

This is an open access article under the CC BY-NC 4.0 license (<https://creativecommons.org/licenses/by-nc/4.0/>)

Материалы конференции

УДК 535

DOI: <https://doi.org/10.18721/JPM.153.244>

### Полое антирезонансное оптическое волокно, активированное YAG:Yb<sup>3+</sup>

Д. Н. Шурупов <sup>1</sup>✉, Г. А. Пчелкин <sup>2</sup>, В. В. Демидов <sup>3</sup>, В. В. Давыдов <sup>1</sup>, Д. В. Вакорина <sup>2</sup>

<sup>1</sup> Санкт-Петербургский политехнический университет Петра Великого, Санкт-Петербург, Россия;

<sup>2</sup> Санкт-Петербургский государственный университет телекоммуникаций  
им. проф. М.А. Бонч-Бруевича, Санкт-Петербург, Россия;

<sup>3</sup> АО «НПО Государственный оптический институт им. С. И. Вавилова», Санкт-Петербург, Россия

✉ shurupoff.dm@yandex.ru

**Аннотация.** В статье представлен способ модификации структуры антирезонансного оптического волокна с полый сердцевинной, с помощью которого можно сформировать слой активного вещества, не прибегая к дорогим и технологически сложным процессам CVD. Чтобы получить центры люминесценции, полое антирезонансное волокно с четырьмя капиллярами заполняли раствором композита YAG:Yb<sup>3+</sup> и органического растворителя диметилформамида. После процедуры заполнения происходило несколько этапов последующей обработки, которые включали в себя сушку заполненной заготовки в печи в нормальных условиях при температуре 150 °C и ее термообработку при температуре 1000 °C. В результате внутри капилляров формировались тонкие пленки на основе YAG:Yb<sup>3+</sup>. Полученные пики люминесценции соответствуют основному и одному из дополнительных пиков для YAG:Yb<sup>3+</sup>.



**Ключевые слова:** полое антирезонансное оптическое волокно, активированное оптическое волокно, люминесценция

**Ссылка при цитировании:** Шурупов Д. Н., Пчелкин Г. А., Демидов В. В., Давыдов В. В., Вакорина Д. В. Полое антирезонансное оптическое волокно активированное YAG:Yb<sup>3+</sup> // Научно-технические ведомости СПбГПУ. Физико-математические науки. Т. 15. № 3.2. С. 240–245. DOI: <https://doi.org/10.18721/JPM.153.244>

Статья открытого доступа, распространяемая по лицензии CC BY-NC 4.0 (<https://creativecommons.org/licenses/by-nc/4.0/>)

## Introduction

In the modern world, it is hardly possible to do without the use of optical fiber. [1–8]. Optical fiber is actively used to solve the problems of information transmission, object detection, etc. [5, 6, 9–16]. Optical fibers are also used in various systems to control physical processes and the operation of different devices [17–26]. In addition, the development of optical fibers allows them to be used in areas that were previously occupied by other materials [27–29]. One of these areas is associated with luminescence.

Nanosized lanthanide-activated phosphors are widely used as base materials for the manufacture of fluorescent labels, contrast agents, upconverting media, lighting elements, and displays [30–32]. The practical value of oxide phosphors is determined by their strong emission in the visible and infrared (IR) regions of the spectrum, long lifetime, increased Stokes shift, resistance to photobleaching, low toxicity, as well as their ease of preparation and commercial availability of raw materials [32].

The creation of activated nanosized phosphors based on YAG:Yb<sup>3+</sup> usually occurs using a variety of methods such as hydrothermal synthesis, sol-gel process, polyol process, codeposition method, aerosol pyrolysis and solution-fuel synthesis. The crystal structure and emissive properties of phosphors are very dependent on the way in which they were obtained.

The polymer-salt method is a liquid-phase process in which mixtures of inorganic compounds and soluble organic polymers are used as film-forming compositions. This approach makes it possible to form one-component or multicomponent coatings from oxide nanoparticles on the substrate surface. The polymer-salt method, in contrast to the sol-gel processes, does not contain the stage of colloid formation. As a result, film-forming compositions do not contain a mixture of colloidal particles, which facilitates the application of highly uniform coatings. The polymer-salt method is simple and economical, and makes it possible to reduce the temperature of nanocrystal synthesis.

Recently, the polymer-salt method has been used to deposit YAG:Nd<sup>3+</sup> nanocrystals inside a microstructured fiber [33]. The results of the analysis of the resulting fiber showed the presence of nanocrystals with YAG:Nd<sup>3+</sup> luminescence spectra. However, due to the too small transverse dimensions of the channels, the modifying solution filled the preform inhomogeneously, which led to an uneven distribution of nanocrystals inside the resulting fiber.

This study is aimed at developing a prototype of an active quartz optical fiber with nanosized YAG:Yb<sup>3+</sup> phosphors uniformly distributed (in the transverse and longitudinal directions) inside the fiber. The main criteria for the development of preforms were the limited number and large internal diameter of the capillaries in order to eliminate the inhomogeneity of filling with the modifying solution.

## Optical system and research methodology

The design of the hollow antiresonance fiber had to be simple to fill with a modifying solution, and the fiber should also have a bandwidth in the spectral regions close to the photoluminescence excitation wavelength of 940 and 975 nm and the reflection wave characteristic of 1030 nm. For these purposes, a fiber with formed capillaries with a diameter of 310 μm, an internal diameter of 200 μm and internal capillaries with a diameter of 48 μm and a wall of 8 μm perfectly suited. The design of the capacitor is shown in Fig. 1.



Fig. 1. Construction of a hollow antiresonant light guide

The raw material for the synthesis of the modifying solution was a composite based on  $\text{YAG:Yb}^{3+}$  dissolved in dimethylformamide in a ratio of 1 part solid to 3 parts solvent.

The formation of thin-film uniform luminescent coatings on the inner surfaces of the capillaries took place in several stages, which included a sequence of operations, the first stage was the impregnation of the workpiece. To simplify the process of blank impregnation with a modifying solution, the air pressure in the channels was reduced, which in turn made it possible to evenly fill the air channels.

After filling the preform proceeded to the second stage, which consisted of convective drying of the filled preform at a temperature of  $150^\circ\text{C}$  for 4 hours. To prevent uneven distribution of the substance, the excess of the modifying solution was removed before drying, which

made it possible to form composite layers on the inner surfaces of the fiber capillaries.

In order to form a sufficient layer of composite inside, the first and second steps were repeated 3 times before proceeding to the last step.

At the last stage, the dried workpiece was heat treated at a temperature of  $1000^\circ\text{C}$  for 2 hours. As a result of heat treatment, chemical decomposition of solvent residues and metal salts occurred, followed by the formation of thin films based on  $\text{YAG:Yb}^{3+}$  inside the capillaries.

The result of the fiber after heat treatment at a temperature of  $1000^\circ\text{C}$  is shown in Fig. 2.

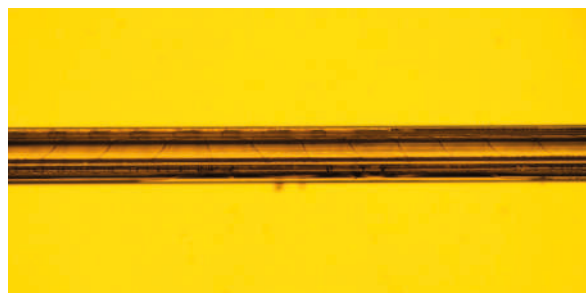


Fig. 2. Capillary with formed thin films inside

### Results and Discussion

After the filling and heat treatment procedures, it was decided to test the light transmission of the resulting fiber to make sure that the resulting fiber transmits light at the wavelengths we need in the range of 940-1050 nm. To check the light transmission of the fiber, light from a 64642 HLX halogen lamp (Osram) was applied to its input, and the dependence of the signal level on the wavelength was taken using an AQ-1212B spectrophotometer (Ando Electric Corporation). The resulting dependence is shown in Fig. 3, the dot on the graph marks the absorption wavelength (975 nm) for  $\text{YAG:Yb}^{3+}$ .

To study the luminescence spectrum of the resulting fiber, a setup was used that included a 64642 HLX halogen lamp (Osram) as a light source, an MDR-23 monochromator (LOMO) for applying a signal with a wavelength of 975 nm to the fiber input, an AQ-1212B spectrophotometer (Ando Electric Corporation), a germanium photodiode for the 900-1700 nm spectral range, an eLockIn 204 optical amplifier (Anfatec Instruments), and an AQ-1135E optical power meter (Ando Electric Corporation). Using a multimode fiber with a length of  $\sim 150$  cm, radiation from a monochromator with a wavelength of 975 nm was transmitted to the resulting fiber. The output signal was monitored from 1000 to 1200 nm to eliminate the influence of the input radiation. The resulting dependence is shown in Fig. 4.

The resulting luminescence peaks correspond to the main 1030 nm and one of the additional peaks 1066 nm for  $\text{YAG:Yb}^{3+}$ .



Fig. 3. Transmission spectrum of the resulting fiber



Fig. 4. Dependence of the signal level on the wavelength when applying to the input wavelength of 975 nm

### Conclusion

To obtain luminescence centers, a hollow antiresonance fiber with four capillaries was filled with a solution of a YAG:Yb<sup>3+</sup> composite and an organic solvent of dimethylformamide. After the filling procedure, several stages of subsequent processing took place, which included drying the filled billet in an oven under normal conditions at a temperature of 150 °C and its heat treatment at a temperature of 1000 °C. As a result, thin films based on YAG:Yb<sup>3+</sup> were formed inside the capillaries. The resulting luminescence peaks correspond to the main and one of the additional peaks for YAG:Yb<sup>3+</sup>. The presented method for modifying the structure of an antiresonant optical fiber with a hollow core makes it possible to form active layers of YAG:Yb<sup>3+</sup> crystals with a thickness of several hundred nanometers without using conventional CVD processes, which are usually technologically complex and expensive.

Data on the spectral and luminescent properties of the fabricated fiber confirmed the presence of YAG:Yb<sup>3+</sup> nanophosphors with the main emission peak at a wavelength of 1030 nm.

### REFERENCES

1. Popovskiy N., Gureeva I., Rud V.Y., Development to high-rate fiber optic communication line with code division multiplexing, ACM International Conference Proceeding Series. 2021 (2021) 527–531.
2. Popovskiy N.I., Valiullin L.R., Features of the construction of fiber-optic communication lines with code division multiplexing, Journal of Physics: Conference Series. 1695(1) (2020) 012120.

3. **Davydov R.V., Savelev I.K., Lenets V.A., Rud' V.Y.**, Fiber-optic transmission system for the testing of active phased antenna arrays in an anechoic chamber, *Lecture Notes in Computer Science (including subseries Lecture Notes in Artificial Intelligence and Lecture Notes in Bioinformatics)*. 10531 LNCS (2017) 177–183.
4. **Tarasenko M.Y., Lenets V.A., Akulich N.V., Yalunina T.R.**, Features of use direct and external modulation in fiber optical simulators of a false target for testing radar station, *Lecture Notes in Computer Science (including subseries Lecture Notes in Artificial Intelligence and Lecture Notes in Bioinformatics)*. 10531 LNCS (2017) 227–232.
5. **Lenets V.A., Tarasenko M.Yu., Rodygina N.S.**, New method for testing of antenna phased array in X frequency range, *Journal of Physics: Conference Series*. 2018, 1038(1) (2018) 012037.
6. **Moroz, A.V.**, Features of transmission bearing and heterodyne receivers for signals in fiber-optic communication line in active phased array antenna, *Journal of Physics: Conference Series*. 1410(1) (2019) 012212.
7. **Mihov E.D., Nepomnyashchiy O.V.**, Selecting informative variables in the identification problem *Journal of Siberian Federal University - Mathematics and Physics*. 9(4) (2016) 473–480.
8. **Ryzhenko I.N., Lutsenko A.E., Varygin O.G., Nepomnyashchiy O.V.**, Carrier compensation mode implementation in satellite communication channels. In: *Proceedings of 2019 International Siberian Conference on Control and Communications, SIBCON 2019*, vol. 8729665 (2019) 23–29.
9. **Ermak S.V., Karseev A.U., Velichko E.N.**, Fiber-optic super-high-frequency signal transmission system for sea-based radar station *Lecture Notes in Computer Science (including subseries Lecture Notes in Artificial Intelligence and Lecture Notes in Bioinformatics)*. 8638 LNCS (2014) 694–702.
10. **Davydov R., Antonov V., Moroz A.**, Parameter Control System for a Nuclear Power Plant Based on Fiber-Optic Sensors and Communication Lines, In: *IEEE International Conference on Electrical Engineering and Photonics (EExPolytech)*, Saint Petersburg, Russia, 13-15 October 2019. vol. 8906791 (2019) 295–297.
11. **Petrov A. A., Shabanov V. E., Zalyotov D. V., Bulyanitsa A. L., Shapovalov D. V.**, Modernization of the frequency synthesizer of cesium atomic clock, *IEEE International Conference on Electrical Engineering and Photonics, EExPolytech 2018*, Saint Petersburg, October 2018. vol. 8564389 (2018) 52–55.
12. **Fadeenko V.B., Pchelkin G.A., Davydov V.V., Rud V.Yu.**, Features of the transmission of microwave signals in the range of 8-12 GHz in the maritime radar station over fiber-optic communication line, *Journal of Physics: Conference Series*. 1400(4) (2019) 044010.
13. **Petrov A. A., Grebenikova N. M.**, Some Directions of Quantum Frequency Standard Modernization for Telecommunication Systems, *Lecture Notes in Computer Science (including subseries Lecture Notes in Artificial Intelligence and Lecture Notes in Bioinformatics)*. 11118 LNCS (2018) 641–648.
14. **Dudkin V.I., Velichko E.N., Karseev A.Yu.**, Fiber-optic system for simulating accidents in the cooling circuits of a nuclear power plant *Journal of Optical Technology (A Translation of Opticheskii Zhurnal)* 82(3) (2015) 132–135.
15. **Sharova N.V., Fedorova E.V., Vologdin V.A.**, Fiber-optics system for the radar station work control, *Lecture Notes in Computer Science (including subseries Lecture Notes in Artificial Intelligence and Lecture Notes in Bioinformatics)*. 9247 (2015) 712–721.
16. **Myazin N., Neronov Y., Dudkin V.**, On the need for express control of the quality of consumer goods within the concept 'Internet of things' *IOP Conference Series, Materials Science and Engineering*. 497(1) (2019) 012111.
17. **Myazin N. S., Dudkin V. I., Grebenikova N. M., Davydov R. V., Podstrigaev A. S.**, Fiber-optical system for governance and control of work for nuclear power stations of low power, *Lecture Notes in Computer Science*. 11660 (2019) 744–756.
18. **Andreeva E.I., Potapov I.A.**, Feature of Optical Soliton Sequence Propagation in Single-Mode Fiber, *Journal of Physics: Conference Series*. 1695(1) (2020) 012125.
19. **Tarasenko M.Y., Lenets V.A., Akulich N.V., Yalunina T.R.**, Features of use direct and external modulation in fiber optical simulators of a false target for testing radar station, *Lecture Notes in Computer Science (including subseries Lecture Notes in Artificial Intelligence and Lecture Notes in Bioinformatics)*. 10531 LNCS (2017) 227–232.
20. **Petrov A. A., Zaletov D. V., Shapovalov D. V.**, Peculiarities of Constructing a Scheme for Formation of a Microwave Excitation Signal in a Cesium Atomic Clock, *Journal of Communications Technology and Electronics*. 66(3) (2021) 295–299.



21. **Petrov A. A.**, Digital Frequency Synthesizer for  $^{133}\text{Cs}$ -Vapor Atomic Clock, *Journal of Communications Technology and Electronics*. 62(3) (2017) 289–293.
22. **Kuzmin M. S., Rogov S. A.**, On the use of a multi-raster input of one-dimensional signals in two-dimensional optical correlators, *Computer Optics*. 43(3) (2019) 391–396.
23. **Grebenikova N. M., Smirnov K. J., Rud V. Yu., Artemiev V. V.**, Features of monitoring the state of the liquid medium by refractometer, *Journal of Physics: Conference Series*. 1135(1) (2018) 012055.
24. **Myazin N.S., Smirnov K.J., Logunov S.E.**, Spectral characteristics of InP photocathode with a surface grid electrode, *Journal of Physics: Conference Series*. 929(1) (2017) 012080.
25. **Pchelkin G.A.**, Features of the transmission of microwave signals at offshore facilities, *Journal of Physics: Conference Series*. 1368(2) (2019) 022045.
26. **Petrov A. A., Grebenikova N.M.**, On the Potential Application of Direct Digital Synthesis in the Development of Frequency Synthesizers for Quantum Frequency Standards, *Journal of Communications Technology and Electronics*. 63(11) (2018) 1281–1285.
27. **Dyumin V., Smirnov K., Myazin N.**, Charge-coupled Device with Integrated Electron Multiplication for Low Light Level Imaging, *Proceedings of the 2019 IEEE International Conference on Electrical Engineering and Photonics, EExPolytech*. Vol. 8906868 (2019) 308–310.
28. **Evstropiev S.K., Demidov V.V., Bulyga D.V., Nikonorov N.V., Dukelskii K.V.**, YAG : R $^{3+}$  (R = Ce, Dy, Yb) nanophosphor-based luminescent fibre-optic sensors for temperature measurements in the range 20–500 C, *Quantum Electronics*. 52(1) (2022) 94–99.
29. **Mazing M. S., Zaitceva A. Yu., Kislyakov Yu. Ya., Kondakov N. S., Avdushenko S. A.**, Monitoring of Oxygen Supply of Human Tissues Using A Noninvasive Optical System Based on A MultiChannel Integrated Spectrum Analyzer, *International Journal of Pharmaceutical Research*. 12(2) (2020) 1974–1978.
30. **Brunckova H., Mudra E., Rocha L., Strečkova M., Medvecký P.**, Nanostructure and luminescent properties of bimetallic lanthanide Eu/Gd, Tb/Gd and Eu/Tb coordination polymers, *Inorganics*. 9(10) (2021) 77.
31. **Gálico D.A., Ovens J.S., Sigoli F.A., Murugesu M.**, Room-Temperature Upconversion in a Nanosized Ln $_{15}$  Molecular Cluster-Aggregate, *ACS Nano* 15(3) (2021) 5580–5588.
32. **de Sousa Filho P.C., Serra O.A.**, Red, green, and blue lanthanum phosphate phosphors obtained via surfactant-controlled hydrothermal synthesis, *Journal of Luminescence*. 129(12) (2009) 1664–1668.
33. **Matrosova, A., Evstropiev, S., Demidov, V., Nikonorov, N., Aseev, V., Kuzmenko, N., Dukelskii, K., Komarov, A., Oreshkina, K.**, “Silica microstructure-based optical fibers activated by YAG:Nd $^{3+}$  nanocrystals,” *Proc. SPIE*, 11355, 1135508 (2020).

#### THE AUTHORS

**SHURUPOV Dmitry**  
shurupoff.dm@yandex.ru  
ORCID: 0000-0001-5223-2354

**DAVYDOV Vadim**  
davydov\_vadim66@mail.ru  
ORCID: 0000-0001-9530-4805

**PCHELKIN Grigoriy**  
beegrig@mail.ru  
ORCID: 0000-0003-4517-930X

**VAKORINA Daria**  
cementary.ley@gmail.com

**DEMIDOV Vladimir**  
demidov@goi.ru

*Received 12.09.2022. Approved after reviewing 29.09.2022. Accepted 30.09.2022.*

Conference materials

UDC 535.92

DOI: <https://doi.org/10.18721/JPM.153.245>

### **Development of a fiber-optic system for monitoring the state of oxygen activity in the current flow of the coolant**

S. E. Logunov <sup>1, 2</sup>✉, R. V. Davydov <sup>2</sup>, V. V. Davydov <sup>1, 2, 3</sup>

<sup>1</sup> Bonch-Bruevich Saint Petersburg State University of Telecommunications, St. Petersburg, Russia;

<sup>2</sup> Peter the Great St. Petersburg Polytechnic University, St. Petersburg, Russia;

<sup>3</sup> All-Russian Research Institute of Phytopathology, Moscow Region, Russia

✉ [sema-logunov@ya.ru](mailto:sema-logunov@ya.ru)

**Abstract.** The need to develop an optical system for remote monitoring of the state of the coolant in the current flow in the first circuit of the nuclear reactor of a nuclear power plant has been substantiated. A method for monitoring the state of the coolant by changing the nature of the evolution of oxygen activity is presented. A fiber-optic system has been developed to study the nature of the change in the evolution of the oxygen activity of the coolant in the current flow. The results of the study of the evolution of oxygen activity in the current flow of the coolant are presented. The nature of the change in the evolution of oxygen activity in the event of the ingress of foreign particles into the coolant (carbon steel particles from welded joints) is determined.

**Keywords:** fiber-optic system, oxygen activity, coolant

**Citation:** Logunov S. E., Davydov R. V., Davydov V. V., Development of a fiber-optic system for monitoring the state of oxygen activity in the current flow of the coolant, St. Petersburg State Polytechnical University Journal. Physics and Mathematics. 15 (3.2) (2022) 246–252. DOI: <https://doi.org/10.18721/JPM.153.245>

This is an open access article under the CC BY-NC 4.0 license (<https://creativecommons.org/licenses/by-nc/4.0/>)

Материалы конференции

УДК 535.92

DOI: <https://doi.org/10.18721/JPM.153.245>

### **Разработка волоконно-оптической системы для контроля состояния кислородной активности в текущем потоке теплоносителя**

С. Е. Логунов <sup>1, 2</sup>✉, Р. В. Давыдов <sup>2</sup>, В. В. Давыдов <sup>1, 2, 3</sup>

<sup>1</sup> Санкт-Петербургский государственный университет связи им. проф. М.А. Бонч-Бруевича, Санкт-Петербург, Россия;

<sup>2</sup> Санкт-Петербургский политехнический университет Петра Великого, Санкт-Петербург, Россия;

<sup>3</sup> Всероссийский научно-исследовательский институт фитопатологии, Московская область, Россия

✉ [sema-logunov@ya.ru](mailto:sema-logunov@ya.ru)

**Аннотация.** Обоснована необходимость разработки оптической системы дистанционного контроля состояния теплоносителя в текущем потоке в первом контуре ядерного реактора атомной электрической станции. Представлен метод контроля состояния теплоносителя по изменению характера эволюции кислородной активности. Разработана волоконно-оптическая система для исследования характера изменения эволюции кислородной активности теплоносителя в текущем потоке. Представлены результаты исследования эволюции кислородной активности в текущем потоке теплоносителя. Определен характер изменения эволюции кислородной активности в случае попадания инородных частиц в теплоноситель (частицы углеродной стали со сварных соединений).



**Ключевые слова:** волоконно-оптическая система, активность кислорода, теплоноситель

**Ссылка при цитировании:** Логунов С. Э., Давыдов Р. В., Давыдов В. В. Разработка волоконно-оптической системы для контроля состояния кислородной активности в текущем потоке теплоносителя // Научно-технические ведомости СПбГПУ. Физико-математические науки. Т. 15. № 3.2. С. 246–252. DOI: <https://doi.org/10.18721/JPM.153.245>

Статья открытого доступа, распространяемая по лицензии CC BY-NC 4.0 (<https://creativecommons.org/licenses/by-nc/4.0/>)

## Introduction

In the context of increasing consumption of electrical energy, improving the efficiency of various power plants is one of the tasks of applied physics [1–6]. Currently, four types of power plants (hydroelectric power plants (HPP), thermal (CHP), nuclear (NPP) and solar (SPP)) and solar (SPP) are mainly used for the production of electrical energy in the world.) [2, 3, 6–9]. The share of other types of power plants in the world and electricity production is insignificant [10, 11].

For the sustainable development of nuclear energy, it is necessary to solve a large number of problems [12–15], which are related to the improvement of methods and devices for controlling chain reactions, in the development of new devices for monitoring the operation of nuclear reactors, etc. The solution of these problems required conducting studies of the evolution of oxygen activity in the flow of various liquid media used as a coolant in nuclear reactors at nuclear power plants [15–18].

Oxygen activity  $^{16}\text{O}(n,p)^{16}\text{N}$  is associated with the interaction of oxygen nuclei that are part of one of the parts of the coolant - water with neutrons with an energy of more than 9 MeV, which are present in the reactor zone due to the flow of a chain reaction. Currently, in systems with nuclear reactors, monitoring of the state of oxygen activity in the current flow of the coolant is not implemented. The content of  $^{131}\text{I}$  is controlled. This characterizes the poisoning of the reactor zone with xenon. In some cases, the activity of corrosion products is monitored. In new models of reactors, reference nuclides, primarily  $^{60}\text{Co}$ , are controlled, as this characterizes the tightness of the fuel. In some models of nuclear reactors, the activity of nuclear reactors is implemented continuous monitoring of the amount of coolant leakage from the first circuit to the second outside the central protective system of the reactor based on the registration of gamma radiation of the isotope  $^{16}\text{N}$  in the pair. This allows in some cases to prevent an emergency situation.

Therefore, the aim of the work is to develop a method for studying the evolution of oxygen activity arising in the current flow of the coolant, and its practical implementation.

## Features and a new method for studying the evolution of oxygen activity

A feature of oxygen activity is that it occurs only when a nuclear reactor is operating at high capacities and subsides immediately after the chain reaction stops. Therefore, without the use of a working nuclear reactor, it is impossible to conduct its research.

Another feature of the studies of the evolution of the oxygen activity of the coolant in the current flow is that they need to be carried out for a long time within the central protective zone of the reactor. For this reason, special ionization chambers, which are located inside protective lead collimators, designed for research in laboratories, are almost impossible to use in the reactor compartment, since they have significant dimensions and have high requirements for protection against temperature, electromagnetic interference, etc. Several of these factors also exclude the use of devices that record  $\gamma$  radiation in steam.

Taking into account these features, we have developed the following method to study the evolution of oxygen activity. It has been established that under the influence of  $\gamma$  radiation, the optical fiber darkens (radiation-induced losses  $\alpha_s$  increase) [19–21]:

$$\alpha_s = -10 \lg(P_{\text{out}}/P_{\text{in}})/l, \quad (1)$$

where  $P_{\text{in}}$  is the laser power introduced into the optical fiber,  $P_{\text{out}}$  is the power at the output of the optical fiber,  $l$  is the length of the optical fiber.

The effect of increasing  $\alpha_s$  is based on the formation of electron-hole pairs. Knocking out oxygen, the electron takes its place in the cyclic spatial structure [19–22]. Various centers of coloration and ‘electronic’ connections with different lifetimes are formed [19–25].

Studies [19–27] have shown that if the exposure dose of radiation is low, then the number of formed color centers and ‘electronic’ compounds is not large. Destruction in the glass mesh does not occur. Transparency (one of the main properties of optical fibers) persists for a long time. The fiber darkens weakly. With an increase in the exposure dose of irradiation, the number of these formations increases, the rate of darkening of the fiber increases. Losses increase.

Fig. 1 presents the results of studies of the change in  $\alpha_s$  from time  $t$  when exposed to  $\gamma$  radiation duration of 4–6 s (exposure dose of radiation 162.3 Gy) for different composition of the core of the optical fiber.

The results obtained show that by changing the percentage of doping of the core of an optical fiber (for example, with germanium oxide  $\text{GeO}_2$ ), it is possible to change its sensitivity to the effects of  $\gamma$  radiation. Establish a working point when recording  $\gamma$  radiation at the  $\alpha_s(t)$  dependence site with the maximum steepness of the slope (Fig. 1). This will make it possible in some cases to record bursts of oxygen activity from the decay of a small number of nuclei of  $^{16}\text{N}$ . After recording bursts of oxygen activity, it is necessary to quickly restore the optical properties of the fiber. Natural processes proceed extremely slowly [19-25, 28, 29]. Therefore, we propose to use additional laser radiation with  $\lambda = 547$  nm to clean the fiber. Fig. 2 shows an example of a process for controlling the relaxation processes of the color centers and ‘electronic’ compounds in the optical fiber after the cessation of exposure to  $\gamma$  radiation with an exposure dose of 162.3 Gy while maintaining a radioactive background.

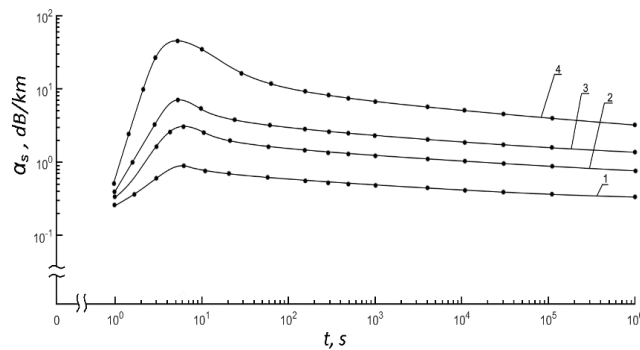


Fig. 1. Dependence of change in  $\alpha_s$  on time  $t$  at wavelength  $\lambda = 1310$  nm for single-mode fiber at  $T = 296.4$  K

Graphs 1, 2, 3, and 4 correspond to different types of optical fiber core:

pure quartz  $\text{SiO}_2$ ;  $\text{SiO}_2\text{--GeO}_2$  (doping 3.5 %);  $\text{SiO}_2\text{--GeO}_2$  (doping 15 %);  $\text{SiO}_2\text{--GeO}_2$  (doping 25%)

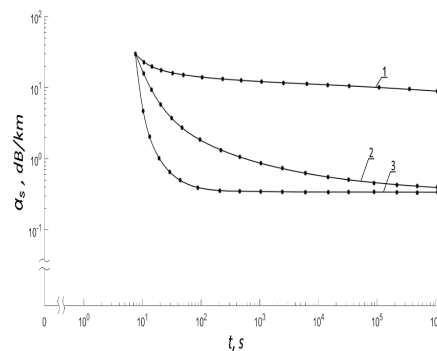


Fig. 2. Dependence of change in losses  $\alpha_s$  on time  $t$  at wavelength

$\lambda = 1310$  nm for single-mode fiber with a core  $\text{SiO}_2\text{--GeO}_2$  (doping 15.0 %) at  $T = 296.4$  K

Graphs 1, 2 and 3 correspond to the power of pulsed laser radiation at wavelength  $\lambda = 547$  nm in mW: 0; 120; 500

The results obtained show that optical fiber restores its optical properties. The transparency of the optical fiber is restored. The number of color centers decreases - the fiber brightens. The absorption of laser radiation at the color center becomes smaller. The output power is increased. This is one feature. The Rayleigh scattering of laser radiation by color centers, which makes the main contribution to the power loss of laser radiation at a wavelength of 1550 nm, is also significantly reduced. Second characteristic.

Since we use low-power laser radiation at 1550 nm, absorption losses are not considered, since they are small compared to scattering losses in this wavelength range.

Let us assume that during the decay of the nucleus  $^{16}\text{N}$   $\gamma$ -quanta are emitted in all directions in the same way. In addition, in the first approximation, in accordance with quantum theory [30, 31], when one  $\gamma$ -quantum interacts with an optical fiber, one center of color or one 'electronic' compound is formed. In this case, the value of  $E$  is spent on the formation of  $N$ . The centers of color can be calculated using the following ratio:

$$E = S \cdot N \cdot h\nu / \sigma = S \cdot N \cdot h \cdot c / (\lambda \cdot \sigma) \quad (2)$$

where  $\sigma$  is the cross-section of the interaction (scattering) of the  $\gamma$ -quantum on oxygen atoms  $\text{O}_2$  in the optical fiber,  $S$  is the area of interaction of the optical fiber with the  $\gamma$ -quanta,  $N$  is the number of emitted  $\gamma$ -quanta,  $\lambda$  is the wavelength of radiation  $\gamma$  - quantum from decay of  $^{16}\text{N}$ .

In the decay of a nucleus of  $^{16}\text{N}$ , the emission of  $\gamma$ -quanta corresponds to 7F of the spectrum line ( $\lambda = 0.254$  nm). Then the value of  $N$  can be determined using the following relation:

$$N = \sigma \cdot \lambda \cdot t_\gamma \cdot (P_{\text{in}} - P_{\text{out}}) / (S \cdot h \cdot c) \quad (3)$$

The values of laser radiation power  $P_{\text{in}}$  and  $P_{\text{out}}$  are measured. The value of the  $\sigma$  is set experimentally, since it depends on the percentage of doping of the core of the optical fiber with germanium oxide  $\text{GeO}_2$ , as well as on the temperature of the optical fiber  $T_c$ . The value of the exposure time  $\gamma$ -quanta the optical fiber is defined by the following formula:  $t_\gamma = \pi L_s d_p^2 / 4q$ , where  $d_p$  is the inner diameter of the pipeline, coolant flow rate is  $q$ ,  $L_s$  is the distance between the protective screens. Therefore, the measurement function  $q$  it is also necessary to implement in the fiber-optic system we are developing. To do this, we have previously developed a method for measuring  $q$  [32, 33].

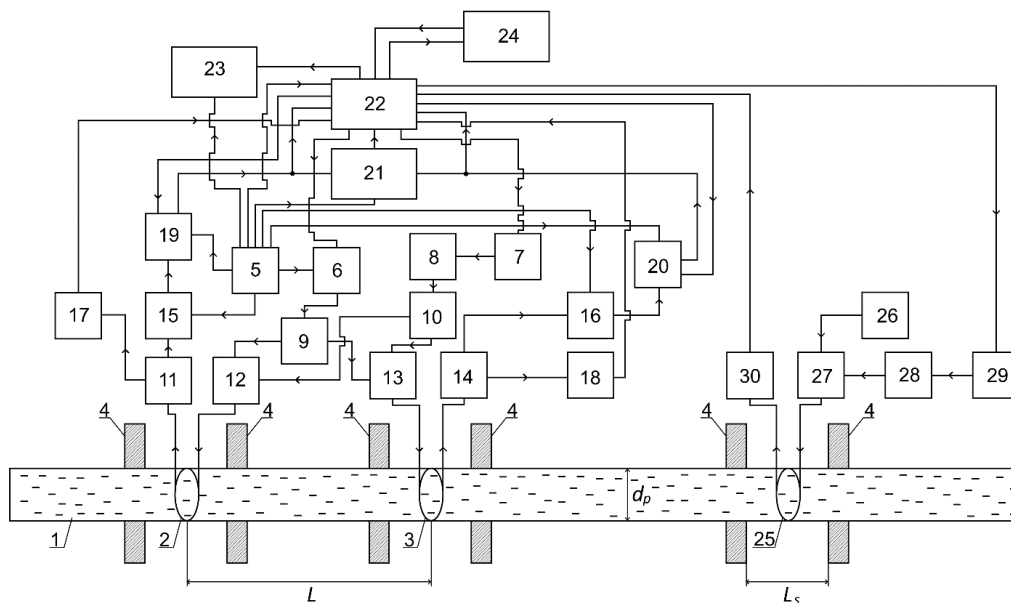


Fig. 3. Structural diagram of the fiber-optic system: pipeline with coolant 1; coils 2, 3 and 25 with optical fiber (sensors); protective radiation shields 4; multifunctional power supply driver 5; transmitting optical module 6 and 26; multifunctional power supply driver 7 and 29; semiconductor laser 8 and 28; optical dividers 9 and 10; multiplexers 11, 12, 13, 14 and 27; photodetectors 15, 16 and 30; optical power meters 17 and 18; comparators 19 and 20; logical device 21; processing and control device 22; display device 23; central computer 24

### Fiber-optic system and the results of experimental studies of the evolution of oxygen activity

Fig. 3 presents a structural diagram of the developed fiber-optic system, which takes into account the features of the study of the evolution of oxygen activity established by us.

To do this, in the developed system (Fig. 3) three coils 2, 3 and 25 with optical single-mode fiber are used, placed at a distance of 3 and 1.5 m from each other (Fig. 1). It should be noted that in the operating conditions of nuclear power plants, the distances of  $L$  and  $L_1$  are extremely difficult and not always expedient to change. The function of changing  $L$  and  $L_1$  is necessary in the case of various studies on the experimental model of the reactor, since the value of the flow rate of the coolant  $q$  during the conduct and a number of experiments must be changed over a large range (at least two orders of magnitude).

We note the main points of the work of the fiber-optic system developed by us. From the transmitting optical module 6, radiation with  $\lambda = 1550$  nm (radiation power  $P_m$  is regulated from 0.1 to 20 mW) through the optical divider 9 ( $N = 2$ ) enters the inputs of multiplexers 12 and 13. Wavelength  $\lambda = 1550$  nm for measuring loss  $\alpha_s(t)$  Laser radiation is selected for the following reasons. In addition, the 'tails' of phonon and electron absorption in the wavelength region of 1.0–1.6  $\mu\text{m}$  do not make a significant contribution to optical losses, the data on which are used to study changes in the nature of the oxygen activity of the coolant.

The other inputs of these multiplexers are supplied with laser radiation with  $\lambda = 457$  nm from the diode-pumped semiconductor laser 8 (SSP-ST-457-F). The radiation content of  $P_L$  is adjustable from 1 to 1000 mW. The multifunctional power supply driver 7 allows the laser 8 to operate in both continuous and pulsed modes. The wavelength from the range of laser radiation 440–485 nm (blue part of the spectrum) to control the relaxation rate of the color centers and «electronic» connections is chosen for the following reasons. On the one hand, with longer optical fiber lengths, it is necessary to ensure the lowest value of the Rayleigh scattering coefficient (CRC) so that the additional laser radiation carries out the maximum cleaning of the glass. On the other hand, the lower limit of laser radiation at a temperature of  $T = 307$  K for effective purification of  $E'$  centers is  $\lambda = 217$  nm [22]. All other color centers that change the optical properties of laser radiation passing through the fiber have loss regions in the longer wavelength part of the spectrum [19, 34, 35]. When cleaning the fiber, it is desirable to reduce losses of all kinds. Given the fact that our temperature is much higher than in [22], laser radiation with  $\lambda = 457$  nm was chosen, since it is likely that it can touch the 'tail' of the spectrum of  $E'$  centers, since at high temperatures it shifts and expands.

In Fig. 4, as an example, the dependence of the change  $N$  in the coil location zone 25 on time  $t$  for various values  $q$ . A solution ( $\text{H}_2\text{O} + \text{H}_3\text{VO}_3$ ) with plutonium nitride filling at a temperature  $T_G = 960$  K was used as a coolant.

The analysis of the results obtained in Fig. 4 shows that the oxygen activity in the coolant is distributed in time randomly. By adjusting the flow rate of the coolant  $q$ , it is possible to partially control the  $N$  distribution function in the registration zone of  $\gamma$ -quanta coils with optical fiber.

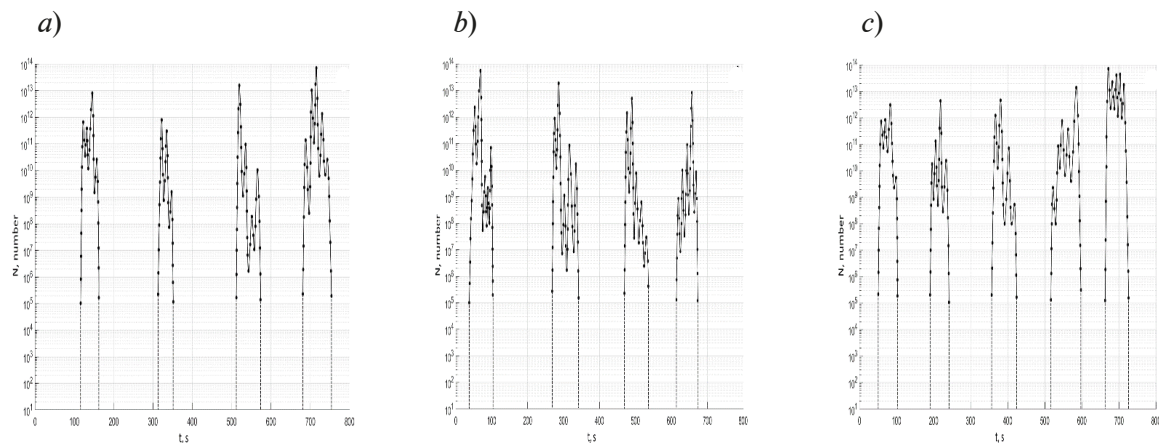


Fig. 4. Dependence of change  $N$  on time  $t$   
Curves in (a), (b) and (c) correspond to  $q$  in  $\text{m}^3/\text{s}$ : 0.169; 0.339; 0.678



## Conclusion

The results obtained showed the reliable operation of the developed design of the fiber-optic system to control the evolution of oxygen activity in the current flow of the coolant.

It is established that increasing the sensitivity of the new method of studying the evolution of oxygen activity, it is necessary to use laser radiation of wavelengths of the UV range.

In the case of additional calibration, it is possible to use the developed fiber-optic system to control the radiation level in the central zone of the reactor. This is necessary to ensure the independence of measurements when using devices with photoelectronic multipliers (PMFs) to solve these problems.

## REFERENCES

1. Myazin N.S., Makeev S.S., Dudkin V.I., Method for Monitoring the Longitudinal Relaxation Time of Flowing Liquids Over the Entire Range of Flow Rate Measurements Measurement Techniques, 2020, 63(5) 368–374.
2. Treshcheva M., Anikina I., Sergeev V., Skulkin S., Treshchev D., Selection of Heat Pump Capacity Used at Thermal Power Plants under Electricity Market Operating Conditions. Energies 2021, 14, 226. <https://doi.org/10.3390/en14010226>.
3. Sergeev V., Anikina I., Kalmykov K., Using Heat Pumps to Improve the Efficiency of Combined-Cycle Gas Turbines. Energies 2021, 14, 2685. <https://doi.org/10.3390/en14092685>.
4. Davydov V.V., Dudkin V.I., Karseev A.Y., Formation of the nutation line in NMR measuring systems with flowing samples Technical Physics Letters, 2015, 41(4) 355–358.
5. Davydov V.V., Dudkin V.I., Karseev A.U., Nuclear magnetic flowmeter - Spectrometer with fiber-optical communication line in cooling systems of atomic energy plants Optical Memory and Neural Networks (Information Optics), 2013, 22(2) 112–117.
6. Moroz A.V., Davydov R.V., Davydov V.V., A New Scheme for Transmitting Heterodyne Signals Based on a Fiber-Optical Transmission System for Receiving Antenna Devices of Radar Stations and Communication Systems Lecture Notes in Computer Science (including subseries Lecture Notes in Artificial Intelligence and Lecture Notes in Bioinformatics), 2019, 11660 LNCS 710–718.
7. Boudjemila L., Malyshkin V.G., Rud V.Y., Features of Degradation of Silicon-based Solar Photovoltaic Cells Journal of Physics: Conference Series, 2021, 2086(1), 012079.
8. Bobyl A., Malyshkin V., Dolzhenko V., Grabovets A., Chernoiivanov V., Scientific activity in the problems of technical and economic modeling of solar stations. An example of unstable climatic conditions. IOP Conf. Ser. Mater. Sci. Eng. 2019, 390, 012047. <https://doi.org/10.1088/1755-1315/390/1/012047>.
9. Boudjemila L., Mahmoudi B., Khenfer K., Valiullin L.R., Electrical characterization of nitride silicon layers SiN<sub>x</sub> enriched in silicon at different stoichiometry - Photovoltaic application. Journal of Physics: Conference Series, 2020, 1695(1), 012204.
10. Elistratov V.V., Diuldin M.V., Denisov R.S., Justification of project and operation modes of hybrid energy complexes for arctic conditions. IOP Conf. Ser. Mater. Sci. Eng. 2018, 180, 012006. <https://doi.org/10.1088/1755-1315/180/1/012006>.
11. Myazin N.S., Yushkova V.V., Rud' V.Y., A new method of determining the state of water and agricultural areas in real time Environmental Research, Engineering and Management, 2019, 75(2) 28–35.
12. Davydov V.V., Myazin N.S., Kiryukhin A.V., Nuclear-Magnetic Flowmeter-Relaxometers for Monitoring Coolant and Feedwater Flow and Status in Npp Atomic Energy, 2020, 127(5) 274–279.
13. Alekseev P.N., Gagarinskii A.Y., Kalugin M.A., Fomichenko P.A., Asmolov V.G., On a Strategy for the Development of Nuclear Power in Russia. At. Energy 2019, 126, 207–212. <https://doi.org/10.1007/s10512-019-00538-w>.
14. Davydov V.V., Dudkin V.I., Velichko E.N., Karseev A.Yu., Fiber-optic system for simulating accidents in the cooling circuits of a nuclear power plant Journal of Optical Technology (A Translation of Opticheskii Zhurnal), 2015, 82(3) 132–135.
15. Semenikhin A.V. Saunin Y.V., Rysnyi S.I., Method of Determining the Reliability of Real-Time In-reactor Monitoring of VVER. At. Energy 2018, 124, 8–13. <https://doi.org/10.1007/s10512-018-0367-8>.
16. Lee K.H. Kim M.G. Lee J.I. Lee P.S., Recent Advances in Ocean Nuclear Power Plants. Energies 2015, 8, 11470–11492. <https://doi.org/10.3390/en81011470>.
17. Davydov V.V., Dudkin V.I., Karseev A.Y., A Compact Nuclear Magnetic Relaxometer for the Express Monitoring of the State of Liquid and Viscous Media Measurement Techniques, 2014, 57(8) 912–918.

18. **Abramov L.V., Baklanov A.V., Bakmetiev A.M., Kiselev V.V.**, OKBM Afrikantov Experience in Developing Methods and Computer Codes for Reliability Analysis and Probabilistic Safety Analysis of Nuclear Installations. *At. Energy* 2020, 129, 98–102. <https://doi.org/10.1007/s10512-021-00713-y>.
19. **Girard S., Kuhnenn J., Gusarov A., Brichard B., Van Uffelen M., Ouerdane Y., Boukenter A., Marcandella C.**, *IEEE Transactions on Nuclear Science*. 60(3). 2015(2013). DOI: 10.1109/TNS.2012.2235464.
20. **Dmitrieva D.S., Pilipova V.M., Rud V.Y.**, *Lecture Notes in Computer Science (including subseries Lecture Notes in Artificial Intelligence and Lecture Notes in Bioinformatics)*. 12526 LNCS. 348(2020).
21. **Kashaykin P.F., Tomashuk A.L., Salgansky M.Y., Guryanov A.N., Dianov E.M.**, *Journal of Applied Physics*. 121(21). 213104(2017).
22. **Tomashuk A.L., Zabezhailov M.O.**, *Journal of Applied Physics*. 10(8). 083103(2011).
23. **Wen J., Peng G.-D., Luo W., Chen Z., Wang T.**, *Optics Express*. 19(23). 23271(2011).
24. **Kim Y., Ju S., Jeong S., Lee S.H., Han W.T.**, *Optics Express*. 24(4). 3910(2016).
25. **Dmitrieva D.S., Pilipova V.M., Dudkin V.I., Rud V.Yu.**, The possibility of controlling the relaxation rate of color centers in the optical fibers *Journal of Physics: Conference Series*. 1697(1). 012145(2020).
26. **Antonov V., Angelina M.**, Parameter Control System for a Nuclear Power Plant Based on Fiber-Optic Sensors and Communication Lines *Proceedings of the 2019 IEEE International Conference on Electrical Engineering and Photonics, EExPolytech 2019*, 2019 42–45, 8906791.
27. **Davydov V., Gureeva I., Davydov R., Dudkin V.**, Flowing Refractometer for Feed Water State Control in the Second Loop of Nuclear Reactor *Energies*, 2022, 15(2), 457.
28. **Dmitrieva D.S., Pilipova V.M., Davydov V.V., Valiullin L.R.**, About compensation of radiation - Induced losses in optical fibers *Journal of Physics: Conference Series*, 2020, 1695(1), 012130.
29. **Dmitrieva D., Pilipova V., Andreeva E., Dudkin V.**, Method for determination of negative influence to  $\gamma$  - radiation on fiber optic information transmission systems *Proceedings of ITNT 2020 - 6th IEEE International Conference on Information Technology and Nanotechnology*, 2020, 9253348.
30. **Dudkin V., Petrunkin V., Rubinov S., Uspenskiy L.**, Study electronic spin echo method phase relaxation  $e'$  -centers in  $\gamma$ -irradiated quartz glass. *Solid State Physics* 1986 Vol. 28 No 5 P. 1296-1301.
31. **Kashaykin P.F., Tomashuk A.L., Salgansky M.Y., Azanova I.S., Tsibinogina M.K., Dimakova T.V., Guryanov A.N., Dianov E.M.**, *Journal of Technical Physics*. 89(5). 752(2019).
32. **Dudkin V., Logunov S., Bobyl A.**, Optical Method for Controlling the Flow Rate of the Coolant in Nuclear Reactors *Proceedings of the 2021 International Conference on Electrical Engineering and Photonics, EExPolytech 2021*, 2021 179–183.
33. **Davydov V.V., Dudkin V.I., Karseev A.Y.**, A Compact Marked Nuclear-Magnetic Flowmeter for Measurement of Rapidly Varying Flow Rates of Liquid *Measurement Techniques*, 2015, 58(3) 317–322.
34. **Dmitrieva D.S., Pilipova V.M., Rud V.Y.**, Fiber-optical communication line with a system for compensation of radiation-induced losses during the transmission of information *Lecture Notes in Computer Science (including subseries Lecture Notes in Artificial Intelligence and Lecture Notes in Bioinformatics)*, 2020, 12526 LNCS 348–356.
35. **Davydov V.V., Dudkin V.I., Karseev A.Y., Vologdin V.A.**, Special Features in Application of Nuclear Magnetic Spectroscopy to Study Flows of Liquid Media *Journal of Applied Spectroscopy*, 2016, 82(6) 1013–1019.

## THE AUTHORS

**LOGUNOV Semen**

sema-logunov@ya.ru

ORCID: 0000-0002-6251-3333

**DAVYDOV Vadim**

davydov\_vadim66@mail.ru

ORCID: 0000-0001-9530-4805

**DAVYDOV Roman**

davydovroman@outlook.com

ORCID: 0000-0003-1958-4221

*Received 14.08.2022. Approved after reviewing 22.08.2022. Accepted 23.08.2022.*

Conference materials

UDC 681.7

DOI: <https://doi.org/10.18721/JPM.153.246>

### Optical communication channel for multifunctional ecological monitoring complex

S. A. Rodin <sup>1</sup>✉, V. V. Davydov <sup>2</sup>, B. K. Reznikov <sup>1</sup>,  
D. I. Isaenko <sup>1</sup>, D. V. Vakorina <sup>1</sup>

<sup>1</sup> Bonch-Bruevich Saint Petersburg State University of Telecommunications, St. Petersburg, Russia;

<sup>2</sup> Peter the Great St. Petersburg Polytechnic University, St. Petersburg, Russia

✉ [psnp.174.sut@gmail.com](mailto:psnp.174.sut@gmail.com)

**Abstract.** The necessity of transmitting information from a multifunctional complex for environmental monitoring located on a high-voltage power line via a fiber-optic communication line is substantiated. The features of the transmission of this information are noted. A fiber-optic communication line has been developed to transmit information over distances up to 200 km without the use of optical amplifiers. The research results of its main characteristics are presented. The prospects for further use of this type of FOCL are determined.

**Keywords:** environmental monitoring, information transmission, electromagnetic environmental, optical communication line, losses, time separation of information, dispersion

**Citation:** Rodin S. A., Davydov V. V., Reznikov B. K., Isaenko D. I., Vakorina D. V., Optical communication channel for multifunctional ecological monitoring complex, St. Petersburg State Polytechnical University Journal. Physics and Mathematics. 15 (3.2) (2022) 253–256. DOI: <https://doi.org/10.18721/JPM.153.246>

This is an open access article under the CC BY-NC 4.0 license (<https://creativecommons.org/licenses/by-nc/4.0/>)

Материалы конференции

УДК 681.7

DOI: <https://doi.org/10.18721/JPM.153.246>

### Оптический канал связи для многофункционального комплекса экологического мониторинга

С. А. Родин <sup>1</sup>✉, В. В. Давыдов <sup>2</sup>, Б. К. Резников <sup>1</sup>,  
Д. И. Исаенко <sup>1</sup>, Д. В. Вакорина <sup>1</sup>

<sup>1</sup> Санкт-Петербургский государственный университет телекоммуникаций им. проф. М.А. Бонч-Бруевича, Санкт-Петербург, Россия;

<sup>2</sup> Санкт-Петербургский политехнический университет Петра Великого, Санкт-Петербург, Россия

✉ [psnp.174.sut@gmail.com](mailto:psnp.174.sut@gmail.com)

**Аннотация.** Обоснована необходимость передачи информации от многофункционального комплекса для экологического мониторинга, размещенного на высоковольтной линии электропередачи по волоконно-оптической линии связи. Отмечены особенности передачи данной информации. Разработана волоконно-оптической линии связи для передачи информации на расстояния до 200 км без использования оптических усилителей. Представлены результаты исследования ее основных характеристик. Определены перспективы дальнейшего использования данного типа ВОЛС.

**Ключевые слова:** экологический мониторинг, передача информации, электромагнитный фон, оптическая линия связи, потери, временное разделение каналов, дисперсия

**Ссылка при цитировании:** Родин С. А., Давыдов В. В., Резников Б. К., Исаенко Д. И., Вакорина Д. В. Оптический канал связи для многофункционального комплекса экологического мониторинга // Научно-технические ведомости СПбГПУ. Физико-математические науки. Т. 15. № 3.2. С. 253–256. DOI: <https://doi.org/10.18721/JPM.153.246>

Статья открытого доступа, распространяемая по лицензии CC BY-NC 4.0 (<https://creativecommons.org/licenses/by-nc/4.0/>)

### Introduction

The deterioration of ecology and emergence of different negative factors for various reasons led to a decrease in the quality of the air environment [1–2], that affects the person health [2–3]. Especially in areas that are at distances of 200 km or less from industrial areas [2–5]. With strong wind currents, various contaminants are carried in the air [3–4], which then fall out in the form of precipitation, etc. Therefore, the state of the environment must be monitored continuously. This also allows new sources of pollution to be identified.

To implement measures to control the environment state, a large number of different devices (nuclear-magnetic, optical, etc.) have been developed [5]. All of them are designed to determine a certain type of pollution. Taking into account the fact that now pollution is complex in composition and type, the spread of such control is clearly not enough. Therefore, various environmental measuring systems are used, which should operate in a continuous mode. In areas where there are sources of electrical energy, there are no problems with the placement of environmental measuring complexes. Difficulties arise in remote areas from settlements. In these cases, we propose to place an environmental measuring complex in the upper part of a high-voltage power transmission line (TL). Information about the state of the environment can be transmitted via a communication system that is attached to the neutral cable. Taking into account the large number of electromagnetic interferences in the signal transmission zone and large distances, it is most expedient in this case to use a fiber-optic communication line (FOCL). Optical fiber does not respond to various electromagnetic interferences.

In our work, one of the possible variants of this measuring complex for environmental monitoring with a unidirectional fiber-optic communication line for information transmission is presented. The task to be solved also included the requirements related to the fact that the design of the FOCL was low-budget, since an optical channel with a single-mode fiber is allocated for the transmission of each measured parameter of the state of the environment.

### Multifunctional ecological monitoring complex design

Fig. 1 shows a diagram of a multifunctional environmental monitoring complex with an optical communication channel. The scheme includes power supply, sensors, transceiver, microcontroller.

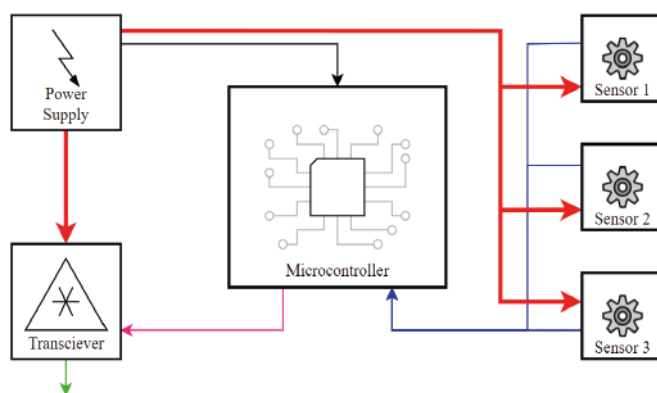


Fig. 1. Scheme of the environmental monitoring complex

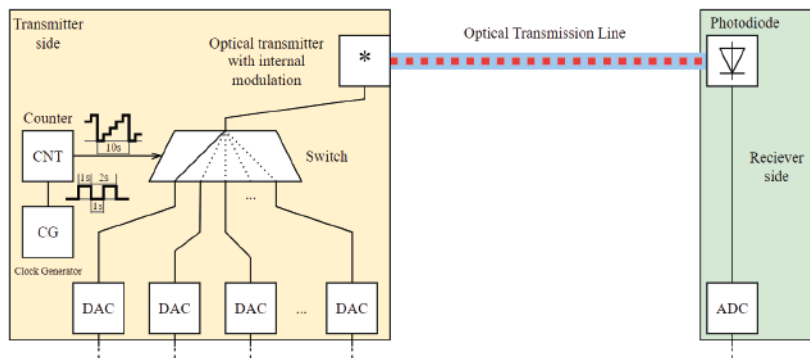


Fig. 2. Structural diagram of a fiber-optic transmission system

It assumes the use of a low-power DC power supply powered by a 220 V (50 Hz) mains. However, when the monitoring complex is placed in close proximity to power transmission towers or on the towers themselves, it is possible to organize power supplies from a strong electromagnetic field. In this case, an inductor and a voltage equalizing circuit are used up to the required 5 V for operation. In this case, the parameters of the inductor are determined individually, depending on the power of the electromagnetic field and the power consumption of sensors used.

### Optical channel of communication

In the environmental monitoring complex, an important component is a fiber-optic communication channel. This is necessary if the multifunctional complex is located on high-voltage power lines, in which case there will be no problems with electrical energy. The block diagram of the fiber-optic communication channel is shown in Fig. 2.

A one-way fiber-optic communication system is used to transmit information. The amount of transmitted information is not large (only values from environmental parameters). Therefore, it is more expedient to use direct modulation in a transmitting optical module with a wavelength of  $\lambda = 1550$  nm.

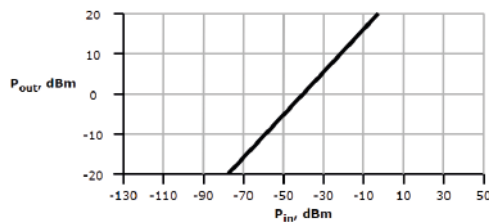


Fig. 3. Dynamic range of the optical communication channel

A feature of the developed optical communication channel is the temporal division of the transmitted information about the state of the environment over one single-mode fiber. This allows, on the one hand, to optimize the design of the FOCL for information transmission. On the other hand, to provide a higher stability of the optical communication channel from various factors. For this, a clock generator is used. The signal from this generator is fed to the counter, which alternately closes and opens the electronic keys. Through these switches, the input of the transmitting laser module receives an analog signal

from the measuring sensors, which modulates the laser radiation in amplitude.

A standard single-mode G.652 fiber is used to transmit information. Optical isolators when transmitting information in one direction are not advisable to use.

### Experiments

To determine the functionality of developed optical channel were calculated to most important parameters such as system speed and energy balance.

The results of the experiments and calculations show that system speed is only 11.72 ns which is fully associated with the specified requirements. Also, as a result of calculations, a positive value of the energy balance which is 6.7 dB was obtained, therefore, the balance is observed.

The modulated optical signal is recorded by a photodiode, which converts the received optical signal into an electrical voltage. This signal is then sent to an analog-to-digital converter. The most important characteristic in this case is the dynamic range of the developed optical communication channel. The results of measuring the dynamic range are presented in Fig. 3.

Analysis of the obtained results shows that the dynamic range is more than 40 dBm, which is sufficient for stable information transmission. This shows a possibility of transmitting the necessary information over distances up to 250 km with high stability.

### Conclusions

The obtained results show the reliability of the developed optical information transmission channel. The information is stably transmitted in a complex electromagnetic environment over distances up to 250 km.

It should be noted that the developed optical communication channel is universal. It can be expanded to transmit information from up to 32 sensors and measurement systems in real time. In this case, only one single-mode fiber is used for information.

Unlike other structures of this type, the developed optical communication channel for analog signals has low power consumption and low cost.

### REFERENCES

1. Gryaznova E. M., Rud V. Y., On the possibility of using the optical method for express quality control of fruits, Journal of Physics: Conference Series. Vol. 2086(1) (2021) 012143.
2. Davydov V. V., Determination of the Composition and Concentrations of the Components of Mixtures of Hydrocarbon Media in the Course of its Express Analysis, Measurement Techniques. 62(2) (2020) 1090–1098.
3. Nikitina M., Grebenikova N., Dudkin V., Batov Y., Methodology for assessing the adverse effects of the use of nuclear energy on agricultural land, IOP Conference Series: Earth and Environmental Science. 390(1) (2019) 012024.
4. Gryznova E., Batov Y., Rud V., Methodology for assessing the environmental characteristics of various methods of generating electricity, E3S Web of Conferences. 140 (2019) 09001.
5. Mazing M. S., Zaitceva A. Yu., Kislyakov Yu. Ya., Kondakov N. S., Avdushenko S. A., Davydov V. V., Monitoring of Oxygen Supply of Human Tissues Using A Noninvasive Optical System Based on A MultiChannel Integrated Spectrum Analyzer, International Journal of Pharmaceutical Research. 12(2) (2020) 1974–1978.

### THE AUTHORS

**RODIN Sergei**  
psnp.174.sut@gmail.com  
ORCID: 0000-0001-7722-3323

**ISAENKO Dmitry**  
isaenko-d@mail.ru

**DAVYDOV Vadim**  
davydov\_vadim66@mail.ru  
ORCID: 0000-0001-9530-4805

**VAKORINA Daria**  
vakorina.dv@mail.ru

**REZNIKOV Bogdan**  
rznkff@gmail.com

*Received 15.08.2022. Approved after reviewing 16.08.2022. Accepted 20.09.2022.*

## PHYSICAL MATERIALS TECHNOLOGY

Conference materials

UDC УДК 537.525

DOI: <https://doi.org/10.18721/JPM.153.247>

### Activation of polylactide films by cold plasma dielectric barrier discharge to improve the interaction of fibroblasts

A.M. Kamalov <sup>1</sup>✉, K.A. Kolbe <sup>2</sup>, A.A. Pavlov <sup>1</sup>, M.E. Borisova <sup>1</sup>, V.E. Yudin <sup>2</sup>

<sup>1</sup> Peter the Great St. Petersburg Polytechnic University, St. Petersburg, Russia;

<sup>2</sup> Institute of Macromolecular Compounds RAS, St. Petersburg, Russia

✉ [spb.kamalov@gmail.com](mailto:spb.kamalov@gmail.com)

**Abstract.** This work focuses on DBD (dielectric barrier discharge) surface modification of polylactide (PLA) films. The film samples were treated in a cold plasma in order to optimize their biological properties and interaction with human skin fibroblasts. Optimal film processing modes for the increased proliferative activity of cells have been found.

**Keywords:** DBD plasma, polylactide, fibroblast, modification, contact angle

**Funding:** The study was performed as part of grant МК-4346.2022.4 of the Ministry of Science and Higher Education of the Russian Federation for young scientists.

**Citation:** Kamalov A. M., Kolbe K. A., Pavlov A. A., Borisova M. E., Yudin V. E., Activation of polylactide films by cold plasma dielectric barrier discharge to improve the interaction of fibroblasts, St. Petersburg State Polytechnical University Journal. Physics and Mathematics. 15 (3.2) (2022) 257–262. DOI: <https://doi.org/10.18721/JPM.153.247>

This is an open access article under the CC BY-NC 4.0 license (<https://creativecommons.org/licenses/by-nc/4.0/>)

Материалы конференции

УДК УДК 537.525

DOI: <https://doi.org/10.18721/JPM.153.247>

### Активация полилактидных пленок диэлектрическим барьерным разрядом в холодной плазме для улучшения взаимодействия с фибробластами

A. M. Камалов <sup>1</sup>✉, К. А. Колбе <sup>2</sup>, А. А. Павлов <sup>1</sup>, М. Э. Борисова <sup>1</sup>, В. Е. Юдин <sup>2</sup>

<sup>1</sup> Санкт-Петербургский политехнический университет Петра Великого, Санкт-Петербург, Россия;

<sup>2</sup> Институт высокомолекулярных соединений РАН, Санкт-Петербург, Россия

✉ [spb.kamalov@gmail.com](mailto:spb.kamalov@gmail.com)

**Аннотация.** В данной работе была проведена модификация поверхности полилактидных пленок PLA с помощью барьерного разряда с целью оптимизации их биологических свойств при взаимодействии с культурой дермальных фибробластов человека. Найдены оптимальные режимы обработки пленок в газовом разряде, позволяющей повысить пролиферативную активность клеток.

**Ключевые слова:** барьерный разряд, плазма, полилактид, фибробласты, угол смачивания

**Финансирование:** Работа выполнена в рамках гранта для молодых ученых при Министерстве науки и высшего образования РФ МК-4346.2022.4.

**Ссылка при цитировании:** Камалов А. М., Колбе К. А., Павлов А. А., Борисова М. Э., Юдин В. Е. Активация полилактидных пленок диэлектрическим барьерным разрядом в холодной плазме для улучшения взаимодействия с фибробластами // Научно-технические ведомости СПбГПУ. Физико-математические науки. Т. 15. № 3.2. С. 257–262. DOI: <https://doi.org/10.18721/JPM.153.247>

Статья открытого доступа, распространяемая по лицензии CC BY-NC 4.0 (<https://creativecommons.org/licenses/by-nc/4.0/>)

### Introduction

Poly lactide is a weakly hydrophobic polymer [1] (water contact angle (WCA) ranges from 55° to 80°), its surface is prone to nonspecific protein adsorption, which promotes bacterial adhesion [2]. Therefore, it is important to improve the wettability of the surface in order to improve the biocompatibility and antibacterial properties of PLA, which define the biological processes occurring in the surface layers [3].

Plasma treatment is a popular method of polymer surface modification [4]. Plasma is an ionized gas achieved in a high electric field, which can be high-temperature or low-temperature at different pressure [5]. The DBD (dielectric barrier discharge) modification occurs only on the surface of the material, the volume properties do not change [6]. Moreover, it is a process that changes the surface in a controlled, reproducible and homogenous way, so it can be used even in cases where the surface has an irregular geometry [7]. The main effects of plasma treatment are [5]:

- Surface cleaning, removal of organic contaminants
- Surface degradation (etching)
- Cross-linking
- Surface functional groups modification.

The occurring processes depend on the gas used for plasma production and determine physical and chemical properties of the sample surface [8]. For example, when chemically active gases such as oxygen, fluorine or ammonia are used, chemical changes occur; in case of oxygen, new peroxide, hydroperoxide, carboxyl or hydroxyl groups are formed on the surface, which leads to the immobilization of other compounds [9]. Inert gas plasmas, produced from helium or argon, enable the process of extensive cross-linking. In any case, DBD creates numerous reactive particles such as ions, radicals, electrons, photons and other excited particles, so other secondary reactions should be expected.

The goal of this work was to optimize the surface modification method of PLA films in a DBD (in air at atmospheric pressure). The aim of this modification was to improve the biocompatibility and bioactivity of materials during the interaction with human skin fibroblasts.

### Materials and Methods

The objects of this study are samples of polylactide films, which thickness was  $25 \pm 5 \mu\text{m}$ . The samples were produced using a DSM Xplore micro-extruder and a DSM Film Device Machine.

Dielectric barrier discharge (DBD) was generated in the ionization chamber consisting of ceramic plates with electrodes divided by air medium (the gap thickness  $h = 1 \text{ mm}$ ). Partial discharges that modified the polymer film surface appeared in the air gap. The cell capacitance was 8.8 pF; the electrode area was 11 cm<sup>2</sup>. To provide sufficient amounts of oxygen, air was blown through the ionization chamber during plasma treatment of polymer films. Partial discharges in this cell developed uniformly over the whole surface of ceramic plates. The polylactide film was placed into the gas-discharge gap, as shown in Fig. 1. The source of high-voltage signals was a TVS-110 flyback transformer with Zero Voltage Switching (ZVS) driver in the primary coil. The schematic diagram of the DBD setup is presented in Fig. 1.

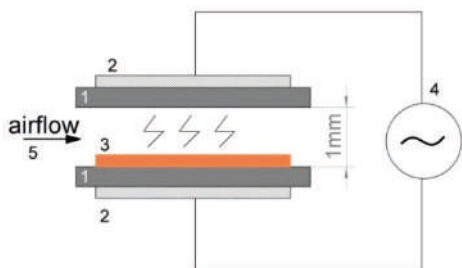


Fig. 1. Schematic of the DBD setup: ceramic plates 1; electrodes 2; PI film sample 3; high-voltage generator 4; fan 5



The voltage providing stable activity of partial discharges was 2.6–2.7 kV at a frequency of 25 kHz. Use of high-frequency alternating voltage caused an increase in the frequency of partial discharges. The repetition frequency of discharges was 40 kHz. As such, the energy densities employed in this work were within the range 0.01–8.6 J/cm<sup>2</sup>. The treatment time varied from 0.5 to 10 min.

Using a ZEISS Axio Scope.A1, the changes in the surface of PLA films after DBD modification were spotted.

The water contact angle (WCA) of a polylactide film was determined by the sessile drop method with the use of a DSA30 instrument (Kruss, Germany) in 24 h after plasma activation. The measurements were carried out at room temperature using 17  $\mu$ L drops of distilled water and hexadecane. The WCA values were calculated in 5 s after precipitation of drops using the DSA4 software. The values were determined in 5 areas randomly distributed over the surface.

Mechanical properties were investigated using an Instron 5943 testing machine; the sample length was 20 mm, and stretching rate was 1 mm/min. 10 measurements were taken at each point. Each experiment was repeated twice.

To analyze the biocompatibility of materials *in vitro*, a strain of skin fibroblasts from a healthy donor (collection of cell cultures of the Institute of Cytology RAS) was used. The cells were cultured in a nutrient medium in a CO<sub>2</sub> incubator (Thermo Fisher Scientific, USA) at a temperature of 37 °C, a CO<sub>2</sub> concentration of 5% and high humidity.

To determine the viability and proliferative activity of cells after 4 days of cultivation on the surface of experimental samples, a MTT test was used. The nutrient medium was replaced with a solution of MTT (thiazolyl blue tetrazolium bromide) (Thermo Fisher Scientific, USA) and the samples were incubated for 2 hours.

After the incubation, the solution was removed and the formed formazan crystals were extracted into DMSO (dimethyl sulfoxide). The optical density of the solution was measured using a Spectrastar Nano spectrophotometer (BMG Labtech, Germany) at a wavelength of 570 nm. The number of viable cells was estimated by the optical density.

## Results and Discussion

The effect of DBD exposure time on the microrelief of PLA films was recorded using a light microscope, micrographs are shown in Fig. 2.

Fig. 2 suggests that an increase in the DBD exposure time changes the relief of the films significantly. The density and depth of surface defects increase with the processing time. The size of the craters ranges from 1 microns to 5 microns. The developed film roughness will provide better adhesion of fibroblasts.

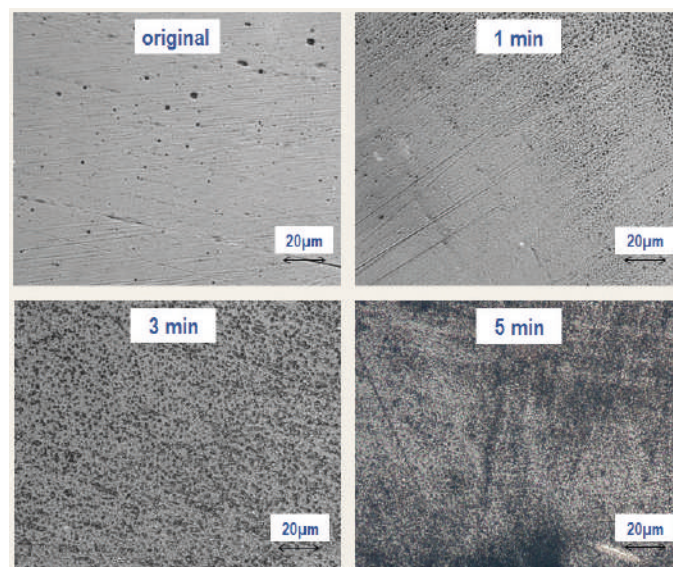


Fig. 2. Micrographs of PLA films after different DBD exposure times

Fig. 3. shows that the contact angle decreases from  $55^\circ$  to  $43.5^\circ$  at 1 minute, then the angle begins to increase; tends to the initial value of the contact angle ( $55^\circ$ ). This can be caused by the processes of degradation and chemical cross-linking in the surface layer of PLA during the DBD. High adhesion and proliferative activity of fibroblasts are provided by hydrophilic materials, so the chosen treatment time range is from 0.5 min to 3 min.

It is a known fact that the mechanical properties of polymer films change after the plasma treatment. The results are shown in Fig. 4.

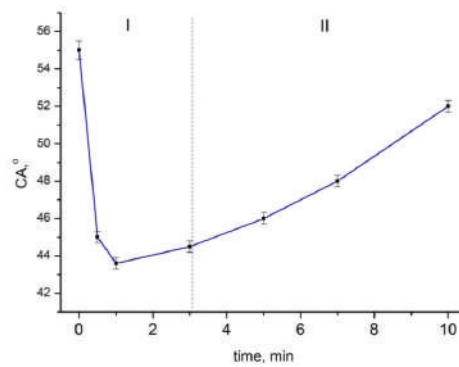


Fig. 3. Water contact angle (WCA) of the PLA samples versus DBD exposure time  
Area I refers to a decrease in the WCA, area II refers to an increase in the WCA on the treated surface of the PLA film

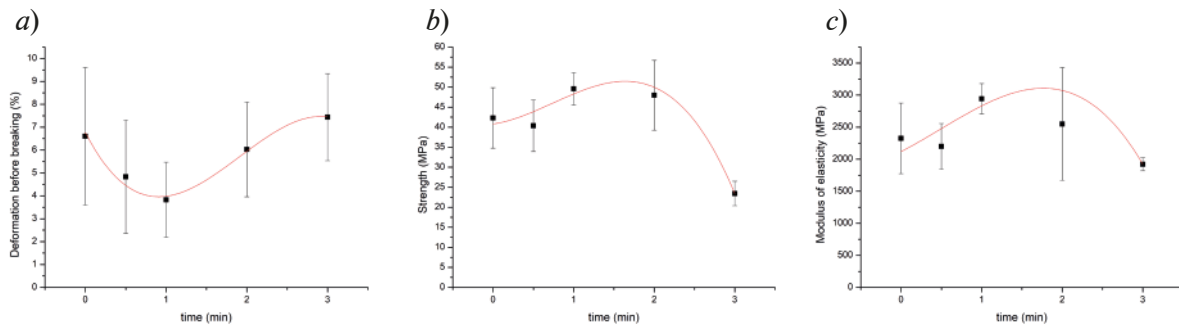


Fig. 4. Mechanical properties of the original and modified PLA films  
Deformation before breaking (a), strength (b), modulus of elasticity (c)

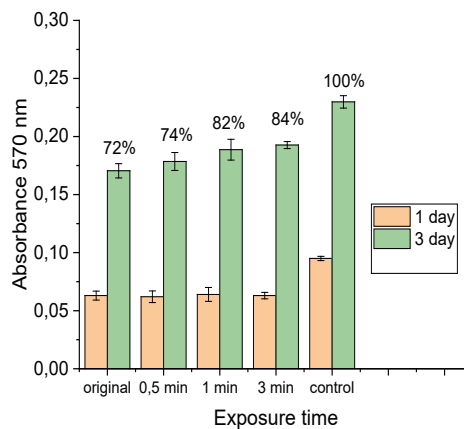


Fig. 5. Cell viability of human dermal fibroblasts cultivated on the surface of PLA films for 1 and 3 days



The plot suggests that after 1 minute of DBD exposure, the elongation of PLA decreases to  $4 \pm 1.5\%$ , the mechanical strength and the modulus of elasticity increase. This indicates the modification of films in DBD.

To analyze the biological properties of PLA films *in vitro*, a culture of human dermal fibroblasts was used. After 1 day of cell culture on the surface of films and culture plastic (control sample), cell adhesion was analyzed using a MTT test. It has been shown that all samples of PLA films have appropriate biocompatibility to maintain cell adhesion. Modification of the PLA matrix surface does not cause significant changes in the level of cell adhesion (Fig. 5). After 3 days of cell culture on the surface of PLA and culture plastic, a MTT test was used to determine the optimal treatment properties for maintaining an even distribution of cells on the surface of the material and a high level of their proliferative activity. The test showed that the optimal treatment time is in range from 1 min to 3 min.

### Conclusion

The results of the study show that PLA films can be modified in DBD to increase the proliferative activity of fibroblasts. When the DBD exposure time is in range from 1 to 3 minutes with energy density of partially discharges about  $8.6 \text{ J/cm}^2$ , cell viability can be increased by 10–12% compared to an untreated PLA film. This result appears to be caused by a hydrophilic surface (WCA  $44^\circ$ ) and a homogeneous rough relief of the treated PLA films.

### Acknowledgments

This study was funded by Grant for young scientists the Ministry of Education and Science Russia MK-4346.2022.4.

### REFERENCES

1. Cai K., Yao K., Lin S., Yang Z., Li X., Xie H., Qing T., Gao L., Poly(D,L-lactic acid) surfaces modified by silk fibroin: effects on the culture of osteoblast *in vitro*, *Biomaterials*. 23 (2002) 1153–1160.
2. Jiang L., Zhu W., Qian H., Wang C., Chen Y., Liu P., Fabrication of PMPC/PTM/ PEGDA micropatterns onto polypropylene films behaving with dual functions of antifouling and antimicrobial activities, *J. Mater. Chem. B*. 7 (2019) 5078–5088.
3. Suganya A., Shanmugavelayutham G.C.S., Rodríguez, Study on plasma prefunctionalized PVC film grafted with TiO<sub>2</sub>/PVP to improve blood compatible and antibacterial properties, *J. Phys. D Appl. Phys.* 50 (2017) 1–12.
4. Goddard J.M., Hotchkiss J.H., Polymer surface modification for the attachment of bioactive compounds, *Prog. Polym. Sci.* 32 (2007) 698–725.
5. Minati L., Migliaresi C., Lunelli L., Viero G., Dalla Serra M., Speranza G., Plasma assisted surface treatments of biomaterials, *Biophys. Chem.* 229 (2017) 151–164.
6. Suganya A., Shanmugavelayutham G.C.S., Rodríguez, Study on structural, morphological and thermal properties of surface modified polyvinylchloride (PVC) film under air, argon and oxygen discharge plasma, *Mater. Res. Express*. 3 (2016) 1–16.
7. Sonmez T., Fazeli Jadidi M., Kazmanli K., Birer Ö., Ürgen M., Role of different plasma gases on the surface chemistry and wettability of RF plasma treated stainless steel, *Vacuum*. 129 (2016) 63–73.
8. Kim J.G.H.M.C., Yang S.H., Boo J.-H., Surface treatment of metals using an atmospheric pressure plasma jet and their surface characteristics, *Surf. Coating. Technol.* (2003) 839–844.
9. Bahrami N., Nouri Khorasani S., Mahdavi H., Ghiaci M., Mokhtari R., Low-pressure plasma surface modification of polyurethane films with chitosan and collagen biomolecules, *J. Appl. Polym. Sci.* 136 (2019) 1–10.

## THE AUTHORS

**KAMALOV Almaz**

spb.kamalov@gmail.com

ORCID: 0000-0003-2044-957X

**KOLBE Konstantin**

kkolbe@yandex.ru

ORCID: 0000-0002-2304-1759

**PAVLOV Andrey**

pavlov.aa.hv@mail.ru

ORCID: 0000-0001-5459-7509

**BORISOVA Margarita**

vladimirl.borisov@gmail.com

ORCID: 0000-0003-0761-6302

**YUDIN Vladimir**

yudinve@gmail.com

ORCID: 0000-0002-5517-4767

*Received 11.07.2022. Approved after reviewing 24.07.2022. Accepted 26.07.2022.*

Conference materials

UDC 53.096

DOI: <https://doi.org/10.18721/JPM.153.248>

### **Polarization and electrophysical parameters of piezoceramic materials investigation**

A. E. Zhurina <sup>1</sup>✉, E. A. Pecherskaya <sup>1</sup>, A. V. Fimin <sup>1</sup>, T. O. Zinchenko <sup>1</sup>, G. V. Kozlov <sup>1</sup>,

<sup>1</sup> Penza State University, Penza, Russia

✉ [gelya.zhurina@mail.ru](mailto:gelya.zhurina@mail.ru)

**Abstract.** The effect of temperature and electric field strength on the polarization and dielectric relaxation of the  $\text{Ba}_{0.85}\text{Ca}_{0.15}\text{Zr}_{0.1}\text{Ti}_{0.9}\text{O}_3$  piezoceramic material has been studied. Experimental studies were carried out using the automated information-measuring system developed by the authors. It is based on the modified Sawyer–Tower circuits, which make it possible to measure the hysteresis loops of the polarization dependences on the electric field strength in the ferroelectric phase at different temperatures.

**Keywords:** temperature, polarization, piezoceramics

**Citation:** Zhurina A. E., Pecherskaya E. A., Fimin A. V., Zinchenko T. O., Kozlov G. V., Polarization and electrophysical parameters of piezoceramic materials investigation, St. Petersburg State Polytechnical University Journal. Physics and Mathematics. 15 (3.2) (2022) 263–268. DOI: <https://doi.org/10.18721/JPM.153.248>

This is an open access article under the CC BY-NC 4.0 license (<https://creativecommons.org/licenses/by-nc/4.0/>)

Материалы конференции

УДК 53.096

DOI: <https://doi.org/10.18721/JPM.153.248>

### **Исследование поляризации и электрофизических параметров пьезокерамических материалов**

А. Е. Журина <sup>1</sup>✉, Е. А. Печерская <sup>1</sup>, А. В. Фимин <sup>1</sup>, Т. О. Зинченко <sup>1</sup>, Г. В. Козлов <sup>1</sup>

<sup>1</sup> Пензенский государственный университет, г. Пенза, Россия

✉ [gelya.zhurina@mail.ru](mailto:gelya.zhurina@mail.ru)

**Аннотация.** Исследовано влияние температуры и напряженности электрического поля на поляризованность и диэлектрическую релаксацию пьезокерамического материала  $\text{Ba}_{0.85}\text{Ca}_{0.15}\text{Zr}_{0.1}\text{Ti}_{0.9}\text{O}_3$ . Экспериментальные исследования выполнены с помощью разработанной авторами автоматизированной информационно-измерительной системы. В ее основе – модифицированные схемы Сойера – Тауэра, которые позволяют измерять петли гистерезиса зависимостей поляризованности от напряженности электрического поля в сегнетоэлектрической фазе при разных температурах.

**Ключевые слова:** температура, поляризация, пьезокерамика

**Ссылка при цитировании:** Журина А. Е., Печерская Е. А., Фимин А. В., Зинченко Т. О., Козлов Г. В. Исследование поляризации и электрофизических параметров пьезокерамических материалов // Научно-технические ведомости СПбГПУ. Физико-математические науки. Т. 15. № 3.2. С. 263–268. DOI: <https://doi.org/10.18721/JPM.153.248>

Статья открытого доступа, распространяемая по лицензии CC BY-NC 4.0 (<https://creativecommons.org/licenses/by-nc/4.0/>)

### Introduction

Materials based on barium titanate ( $\text{BaTiO}_3$ ) are promising piezomaterials. It has been found that the dielectric and piezoelectric properties of  $\text{BaTiO}_3$  can be improved by adding elements such as Ca, Sr, Mg or Zr. It is stated in [1] that the BCZT ceramics having the composition  $\text{Ba}_{0.85}\text{Ca}_{0.15}\text{Zr}_{0.1}\text{Ti}_{0.9}\text{O}_3$  has the most uniform microstructure.

### BCZT Piezoceramic Polarization Study

Heating ceramic samples to a glassy phase with subsequent cooling to room temperature leads to the fact that during cooling in the crystal cells a phase transition occurs, as a result of which the vectors of spontaneous piezoceramics polarization in the entire set of crystal lattices do not take the same direction, while regions (domains) appear. ) having the same direction of spontaneous polarization [2]. In [3],  $\text{Ba}_{0.85}\text{Ca}_{0.15}\text{Zr}_{0.1}\text{Ti}_{0.9}\text{O}_3$  (BCZT) ceramics were obtained using a conventional solid solution. Experimental studies of the dependences of the electrophysical parameters of the samples on temperature, electric field strength, and the surface morphology were studied using a scanning electron microscope. Based on the studies results [3], a graph of the dependence of the  $\text{Ba}_{0.85}\text{Ca}_{0.15}\text{Zr}_{0.1}\text{Ti}_{0.9}\text{O}_3$  polarization on temperature and the strength of the external electric field was plotted (Fig. 1).

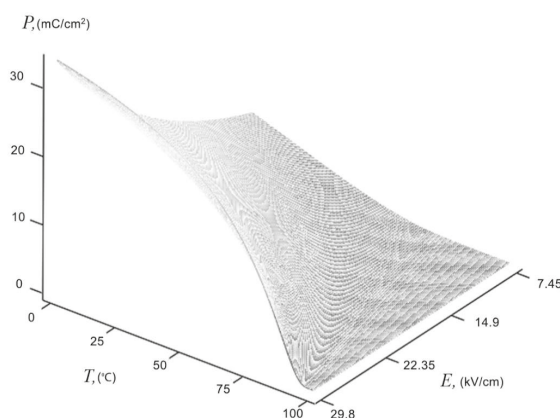


Fig. 1. Dependence of  $\text{Ba}_{0.85}\text{Ca}_{0.15}\text{Zr}_{0.1}\text{Ti}_{0.9}\text{O}_3$  polarization  $P$  ( $\text{mC}/\text{cm}^2$ ) on temperature  $T$  ( $^\circ\text{C}$ ) and external electric field strength  $E$  ( $\text{kV}/\text{cm}$ )

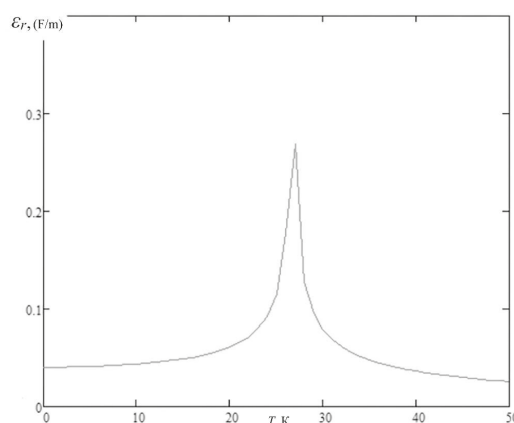


Fig. 2. Dependence of the  $\text{Ba}_{0.85}\text{Ca}_{0.15}\text{Zr}_{0.1}\text{Ti}_{0.9}\text{O}_3$  complex permittivity on temperature

For a detailed study of the  $\text{Ba}_{0.85}\text{Ca}_{0.15}\text{Zr}_{0.1}\text{Ti}_{0.9}\text{O}_3$  polarization, it is necessary to consider dielectric relaxation. In the case of dielectric relaxation, the polarization response to an external electric field is considered [4]. Dielectric relaxation is usually associated with the dynamics of electric dipoles of individual molecules or molecules groups, ions or electrons, passing between allowed energy levels. In the case of orientational polarization, the dipole moments of elementary dipoles remain constant in magnitude, but the directions change due to the thermal motion manifestation [5].

The activation energy of the dielectric relaxation was calculated using the Debye relation [6], the Debye relaxation can be expressed using the complex permittivity. The complex dielectric function is formed by summing the imaginary and real parts [7, 8], dependence of the imaginary part of the permittivity temperature [7]. The dependence of the  $\text{Ba}_{0.85}\text{Ca}_{0.15}\text{Zr}_{0.1}\text{Ti}_{0.9}\text{O}_3$  complex permittivity on temperature is shown in Fig. 2.

To study the phenomenon of dielectric hysteresis of the polarization  $P$  dependence on the electric field strength  $E$ , the authors proposed an automated information-measuring system based on the modified Sawyer-Tower method [9, 10]. Fig. 3 shows the experimental dependence of the polarization of a ferroelectric ceramic sample based on barium titanate on the intensity electric field at a temperature of  $80^\circ\text{C}$ .

The automated methods developed by the authors make it possible to estimate the coercive field (marked as "2" and "5" in Fig. 3) and the residual polarization (marked as "3" and "4" in Fig. 3, respectively), as well as calculate the values of other electrophysical parameters, including the tangent of the dielectric loss angle, relative permittivity [11, 12].

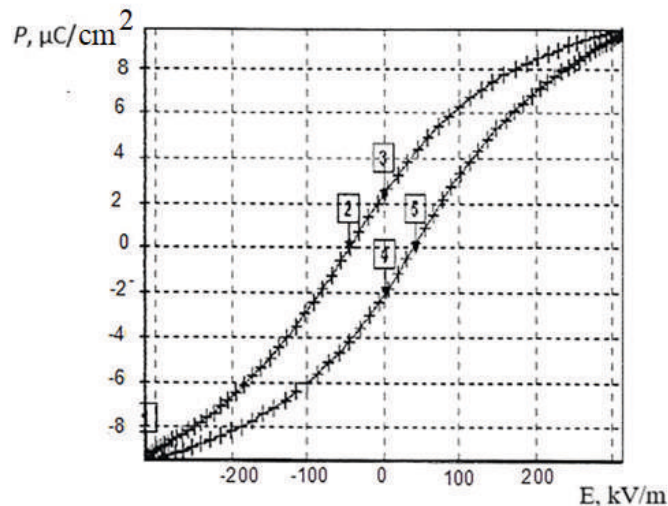


Fig. 3. Experimental dependence of the polarization of a ferroelectric ceramic sample based on barium titanate on the electric field strength at a temperature of  $80^\circ\text{C}$

#### Methods for measuring the tangent of the dielectric loss angle

To measure the dielectric loss tangent, the authors used two modifications of the Sawyer-Tower scheme (Fig. 4, *a*, *b*).

When using the first of the proposed methods, based on the scheme shown in Fig. 4, *a*, an indirect determination of the capacitance  $C_x$  is performed using the following formula:

$$c_x = \frac{U_y C_0}{U}, \quad (1)$$

where  $U_y$  is the voltage across a capacitor of known value, included in the lower arm of the capacitive divider.

Using scheme in Fig. 3, *b*, an indirect determination of  $r_x$  (the resistance) was made using the following formula:

$$r_x = \frac{\tau_1 r_1 - \tau_2 r_2}{\tau_2 - \tau_1}, \quad (2)$$

where  $r_1, r_2$  are the known resistances of the resistors, which are connected in turn in series to the capacitor with the materials under study (Fig. 4, *b*);  $\tau_1, \tau_2$  and  $r_1, r_2$  are connected.

It should be noted that the relative measurement error is the sum of the relative measurement errors of frequency, capacitance and resistance:

$$\delta_1(tg\delta) = \delta f + \delta C_x + \delta r_x. \quad (3)$$

Next, we consider another method for indirectly measuring the dielectric loss tangent, which involves determining the area of the hysteresis loop of the dependence  $U(U_{cx})$ , where  $U = U - U_y = UC_0 / (C_0 + C_x)$  is the voltage across the capacitor with the active dielectric under study. The power  $W_0$  dissipated in the ferroelectric during the period of the sinusoidal signal  $T$  is directly proportional to the area of the hysteresis loop (see Fig. 3),  $W_0 = (1/T) \oint U_{cx} dq$ , and under study  $dq = C_0 dU_y$ . Let us denote the integral in the numerator  $J = \oint U_{cx} dU_y$ , for its calculation it is advisable to use the methods of numerical integration. In this case, there is an error  $\Delta_J$ , due, firstly, to the presence of a truncation error due to the replacement of curvilinear trapezoids by rectilinear ones and, secondly, to an error component caused by errors in measuring the values of the function  $U(U_{cx})$ .

To estimate the standard deviation of the instrumental error of indirect measurement under the normal distribution law, the expression is applicable:

$$\sigma_{tg\delta_2} = \pm \sqrt{\left(\frac{\partial tg\delta}{\partial J} \sigma_J\right)^2 + \left(\frac{\partial tg\delta}{\partial U_x} \sigma_{U_x}\right)^2 + \left(\frac{\partial tg\delta}{\partial U_y} \sigma_{U_y}\right)^2}, \quad (4)$$

where  $J = \oint U_{cx} dU_y$ .

To calculate the ultimate absolute resulting error  $\Delta_2$ , it is necessary to find the sum  $\Delta_2 = \Delta_J + \Delta_{tg\delta_2}$ , where  $\Delta_{tg\delta_2} = 3.09 \sigma_{tg\delta_2}$ . In turn, in relative units, the measurement error of the dielectric loss tangent is determined by the expression:

$$\delta_2 = \frac{\Delta_2}{tg\delta} = \frac{\Delta_2 \pi (U_{C_x})_m (U_y)_m}{\oint U_{C_x} dU_y}. \quad (5)$$

The instrumental implementation of the Sawyer–Tower scheme modifications proposed by the authors makes it possible to measure the dielectric loss tangent with relative errors not exceeding, respectively,  $\delta_1 \leq 0.60\%$ ,  $\delta_2 \leq 0.65\%$ .

### Results and Discussion

As a result of studying the dependences of the electrophysical parameters of BCZT piezoceramics samples on temperature and electric field strength, graphs of the porosity dependence on influencing factors were obtained, which made it possible to study dielectric relaxation as a response of polarization to an external electric field. The relationship between the complex permittivity and temperature indicated a diffuse transformation confirming the relaxor-type behavior.

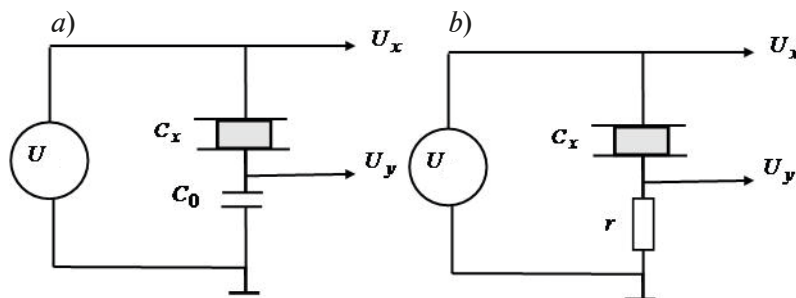


Fig. 4. Modified Sawyer-Tower circuits



Two modifications of the Sawyer–Tower scheme, the use of which is dictated by research goals: the hysteresis loops measurement (the scheme in Fig. 4,*a*) or the study of the repolarization of piezoceramic images, the measurement of the switching current versus time (the scheme in Fig. 4,*b*) are proposed. Both modifications make it possible to indirectly determine the parameters characterizing the dielectric hysteresis. Two methods for measuring the tangent of the dielectric loss angle based on metrological analysis are considered, formulas for estimating the limiting measurement errors, which in relative form do not exceed 0.60% and 0.65%, respectively, are obtained.

It is expedient to use the results presented in the study of ceramic piezos with ferroelectric properties, as well as in the design of functional electronics products based on active dielectrics.

## REFERENCES

1. **Kolthoum I. Othman, Ahmed A. Hassan, Amr. Hashim, A .M . Emam, E. E-Kashif**, Synthesis and characterization of  $\text{Ba}_{0.85}\text{Ca}_{0.15}\text{Zr}_{0.1}\text{Ti}_{0.9}\text{O}_3$  Lead-Free Piezoelectric Ceramic Materials, Technology Reports of Kansai University. 62(11) (2020) 6535–6546.
2. **Vernigora G.D., Lupeiko T.G., Skaliukh A.S., Solovyov A.N.**, About polarization and determination of the porous piezoceramics effective characteristics, Physical and mathematical sciences, Bulletin of the DSTU. 4(55) (2011) 463–469.
3. **Asma Dahri, Yaovi Gagou, Najmeddine Abdelmoula, Hamadi Khemakhem, Mimoun E Marssi**, The structural, dielectric, electrocaloric, and energy storage properties of lead-free  $\text{Ba}_{0.85}\text{Ca}_{0.15}\text{Zr}_{0.1}\text{Ti}_{0.9}\text{O}_3$ , Ceramics International 48 (2022) 3157–3171.
4. **Alexei A. Bokov, Zuo-Guang Ye**, Dielectric relaxation in relaxor ferroelectrics, Journal of Advanced Dielectrics. 2(2) (2012) 24 pages.
5. **Hamad Rahman Jappor, Majeed Ali Habeeb Hamad Rahman Jappor, Majeed Ali Habeeb**, Optical properties of two-dimensional GaS and GaSe monolayers, Physica E: Low-dimensional Systems and Nanostructures. 101 (2018) 251–255.
6. **Belkhadir S., Neqali A., Amjoud M., Mezzane D., Alimoussa A., Choukri E., Gagou Y., Raevski I., El Marssi M., Luk'yanchuk I. A., Rožič B., Kutnjak Z.**, Structural, dielectric and electrocaloric properties of  $(\text{Ba}_{0.85}\text{Ca}_{0.15})(\text{Ti}_{0.9}\text{Zr}_{0.1-x}\text{Sn}_x)\text{O}_3$  ceramics elaborated by sol-gel method, Journal of Materials Science: Materials in Electronics. 30(15) (2019) 14099–14111.
7. **Larionov A.N., Bogdanov D.L., Larionova N.N., Efremov A.I., Toshchenko K.A.**, Dielectric relaxation and viscoelastic properties of nematic liquid crystals, Condensed Media and Interfacial Boundaries. 17(3) (2015) 364–370.
8. **Rybakov D.O. and Belyaev V.V.**, Temperature Dependences of Molecular Coefficients and Activation Energy of Nematic Mixture 2F-3333, Zhid. crist. and their practical use / Liq. Cryst. and their Appl. 18(3) (2018) 94–103.
9. **Gurin S.A., Pecherskaya E.A., Spitsyna K.Y., Fimin A.V., Artamonov D.V., Shepeleva A.E.**, Thin piezoelectric films for micromechanical systems, Moscow Workshop on Electronic and Networking Technologies, MWENT 2020 – Proceedings.
10. **Pecherskaya E.A., Golubkov P.E., Fimin A.V., Zinchenko T.O., Pechersky A.V., Shepeleva J.V.**, Intelligent system for active dielectrics parameters research, Procedia Computer Science 132 (2018) 1163–1170.
11. **Golubkov P.E., Pecherskaya E.A., Golovyashkin A.N., Golovyashkin A.A., Pecherskiy, A.V., Shepeleva, Y.V.**, Analysis of the technological parameters influence on the reproducibility of the active dielectrics properties, International Conference of Young Specialists on Micro/Nanotechnologies and Electron Devices, EDM. (2018) 57–61.
12. **Artamonov, D.V., Baranov, V.A., Pecherskaya, E.A., Pushkareva A.V., Tsy-pin, B.V., Fimin, A.V.**, Application of a Hyper-Complex Impedance Model for Indirect Measurements of Materials Parameters of Functional Electronics, International Conference of Young Specialists on Micro/Nanotechnologies and Electron Devices, EDM. (2019) 760–764.

## THE AUTHORS

**ZHURINA Angelina**

gelya.zhurina@mail.ru

ORCID: 0000-0002-5076-3191

**ZINCHENKO Timur**

scar0243@gmail.com

ORCID: 0000-0002-9342-9345

**PECHERSKAYA Ekaterina**

pea1@list.ru

ORCID: 0000-0001-5657-9128

**KOZLOV Gennady**

politeh@pnzgu.ru

ORCID: 0000-0002-5113-1305

**FIMIN Andrey**

mr.l0tus@mail.ru

ORCID: 0000-0001-6527-9944

*Received 11.07.2022. Approved after reviewing 19.07.2022. Accepted 19.07.2022.*

Conference materials

UDC 539.234

DOI: <https://doi.org/10.18721/JPM.153.249>

## Ferroelectric films for renewable energy

Z. E. Vakulov <sup>1</sup>✉, R. V. Tominov <sup>2</sup>, D. A. Dzyuba <sup>2</sup>,  
I. A. Shihovcov <sup>2</sup>, V. A. Smirnov <sup>2</sup>, O. A. Ageev <sup>2</sup>

<sup>1</sup> Southern Scientific Centre of the Russian Academy of Sciences, Rostov-on-Don, Russia;

<sup>2</sup> Southern Federal University, Rostov-on-Don, Russia

✉ zakhar.vakulov@gmail.com

**Abstract.** This paper shows the results of the development of an energy harvester based on hybrid carbon nanostructures. SiO<sub>2</sub>/TiN/LiNbO<sub>3</sub> and SiO<sub>2</sub>/TiN/BaTiO<sub>3</sub> samples were fabricated by pulsed laser deposition to study the piezoelectric effect. It is shown that the obtained nanocrystalline ferroelectric films exhibit a stable piezoelectric effect, which weakly depends on the nanoscale structure. An energy harvester architecture based on hybrid carbon nanostructures is developed. The use of the developed technology will improve the operational parameters of the converters, as well as replace toxic materials in their composition with lead-free ones, reducing the harmful anthropogenic impact on the nature. The obtained results can be used to create promising lead-free energy harvesters based on ferroelectric films for renewable energy and internet of things devices.

**Keywords:** renewable energy, energy harvesting, ferroelectric films, pulsed laser deposition

**Funding:** The study was supported by the Russian Foundation for Basic Research as part of Projects 19-38-60052 and 19-29-03041 мк, Agreement of Foundation for Assistance to Small Innovative Enterprises in Science and Technology 53ГУРЭС14/72779, Grant of the President of the Russian Federation МК-6252.2021.4 and Agreement of the Government of the Russian Federation 075-15-2022-1123.

**Citation:** Vakulov Z. E., Tominov R. V., Dzyuba D. A., Shihovcov I. A., Smirnov V. A., Ageev O.A., Ferroelectric films for renewable energy, St. Petersburg State Polytechnical University Journal. Physics and Mathematics. 15 (3.2) (2022) 269–273. DOI: <https://doi.org/10.18721/JPM.153.249>

This is an open access article under the CC BY-NC 4.0 license (<https://creativecommons.org/licenses/by-nc/4.0/>)

Материалы конференции

УДК 539.234

DOI: <https://doi.org/10.18721/JPM.153.249>

## Сегнетоэлектрические пленки для возобновляемой энергетики

З. Е. Вакулов <sup>1</sup>✉, Р. В. Томинов <sup>2</sup>, Д. А. Дзюба <sup>2</sup>, И. А.  
Шиховцов <sup>2</sup>, В. А. Смирнов <sup>2</sup>, О. А. Агеев <sup>2</sup>

<sup>1</sup> Южный научный центр Российской академии наук (ЮНЦ РАН), г. Ростов-на-Дону, Россия;

<sup>2</sup> Южный федеральный университет, г. Ростов-на-Дону, Россия

✉ zakhar.vakulov@gmail.com

**Аннотация.** В работе представлены результаты разработки преобразователя энергии на основе гибридных углеродных наноструктур. Для исследования пьезоэлектрических параметров методом импульсного лазерного напыления были изготовлены образцы SiO<sub>2</sub>/TiN/LiNbO<sub>3</sub> и SiO<sub>2</sub>/TiN/BaTiO<sub>3</sub>. Показано, что полученные нанокристаллические сегнетоэлектрические пленки проявляют устойчивый пьезоэлектрический эффект, слабо зависящий от наноразмерной структуры. Разработана архитектура преобразователя энергии на основе гибридных углеродных наноструктур. Полученные результаты могут

быть использованы для создания перспективных бессвинцовых преобразователей энергии на основе сегнетоэлектрических пленок для устройств возобновляемой энергетики и Интернета вещей.

**Ключевые слова:** возобновляемые источники энергии, преобразование энергии, сегнетоэлектрические пленки, импульсное лазерное осаждение

**Финансирование:** Исследование выполнено при финансовой поддержке РФФИ в рамках научных проектов № 19-38-60052 и № 19-29-03041 мк, поддержано Фондом содействия инновациям, Договор № 53ГУРЭС14/72779, Грантом Президента Российской Федерации МК-6252.2021.4 и Правительством РФ, Соглашение № 075-15-2022-1123.

**Ссылка при цитировании:** Вакулов З. Е., Томинов Р. В., Дзюба Д. А., Шиховцов И. А., Смирнов В. А., Агеев О. А. Сегнетоэлектрические пленки для возобновляемой энергетики // Научно-технические ведомости СПбГПУ. Физико-математические науки. Т. 15. № 3.2. С. 269–273. DOI: <https://doi.org/10.18721/JPM.153.249>

Статья открытого доступа, распространяемая по лицензии CC BY-NC 4.0 (<https://creativecommons.org/licenses/by-nc/4.0/>)

## Introduction

Today energy harvesting is considered as one of the alternatives to electrochemical batteries and can be applied as an autonomous power supply for portable IoT devices and wireless sensors [1, 2]. Energy harvesting is prospective to minimize the harmful anthropogenic impact on nature. In [3, 4] has been shown that piezoelectric nanowires, composites, ferroelectric films, and hybrid carbon nanostructures are promising materials for mechanical energy harvesting. The study of the ferroelectric materials synthesis process is urgent since it determines the parameters of fabricated piezoelectric energy harvesters [5, 6]. A large number of piezoelectric materials studies make it possible to design prototypes of energy harvesters, while the manufacture of commercial converters requires a comprehensive solution of a number of technical issues related to the optimization of the fabrication process [7]. Thus, the purpose of the work is to study the synthesis process of ferroelectric films by pulsed laser deposition and develop a mechanical energy harvester based on hybrid carbon nanostructures.

## Materials and Methods

$\text{SiO}_2/\text{TiN}/\text{LiNbO}_3$  and  $\text{SiO}_2/\text{TiN}/\text{BaTiO}_3$  samples were fabricated by pulsed laser deposition to study the piezoelectric effect [8]. The growth of  $\text{LiNbO}_3$  and  $\text{BaTiO}_3$  films was carried out in Pioneer 180 PLD module (Neocera LCC, USA) for 50,000 pulses at a laser pulse repetition rate of 10 Hz and an oxygen pressure of  $1 \times 10^{-2}$  Torr.

The substrate temperature varied from 300 °C to 600 °C. Oxide films were grown using the mask-template to provide electrical contact to TiN layer. Atomic force microscopy (AFM) at the Ntegra probe nanolaboratory (NT-MDT Spectrum Instruments, Russia) in the piezoresponse force microscopy (PFM) mode was used to study piezoelectric parameters of the fabricated samples. The influence of oxide films morphology on the piezoelectric parameters was studied by a two-stage approach. Two regions were scanned on the surface of the oxide films of each sample in the AFM contact mode at constant voltages of opposite polarity. At the first stage, a region of  $7 \times 7 \mu\text{m}^2$  was formed by scanning the surface of the oxide film with the voltage between the probe and the sample of  $-10$  V. At the second stage, an area of  $3 \times 3 \mu\text{m}^2$  inside the region was formed with the voltage between the probe and the sample of  $+10$  V.

The study of the piezoelectric response of the formed regions was carried out in the mode of applying an AC voltage to the probe (the TiN film is grounded) at a frequency of 16 kHz with an amplitude of 1 V. The sample was studied in a capacitor-like structure, (conducting AFM probe and the TiN layer are electrodes). In order to minimize the number of distortions in the measurement process, as well as to correctly compare the piezoelectric parameters of samples from the same experimental series, all measurements were carried out using one AFM probe with the same laser parameters on a microcantilever.



## Results and Discussion

It was established that the PFM signal amplitude in  $7 \times 7 \mu\text{m}^2$  area is less than the amplitude in of  $3 \times 3 \mu\text{m}^2$  the area with the phase ( $\varphi$ ) in  $7 \times 7 \mu\text{m}^2$  area of is equal to  $\varphi = -180^\circ$ , and  $\varphi = 0^\circ$  in of  $3 \times 3 \mu\text{m}^2$  area, respectively (Fig. 1). It can be explained by the fact that a negative voltage applied to the probe leads to an upward electric field, which also orients the polarization vector from the substrate towards the probe, while a positive voltage orients the polarization vector away from the probe towards the substrate. So, one can conclude that the AC voltage signal applied to the probe and the electric field generated in the oxide film are in antiphase in the  $7 \times 7 \mu\text{m}^2$  region. Therefore, the PFM amplitude in the region is less than in  $3 \times 3 \mu\text{m}^2$ .

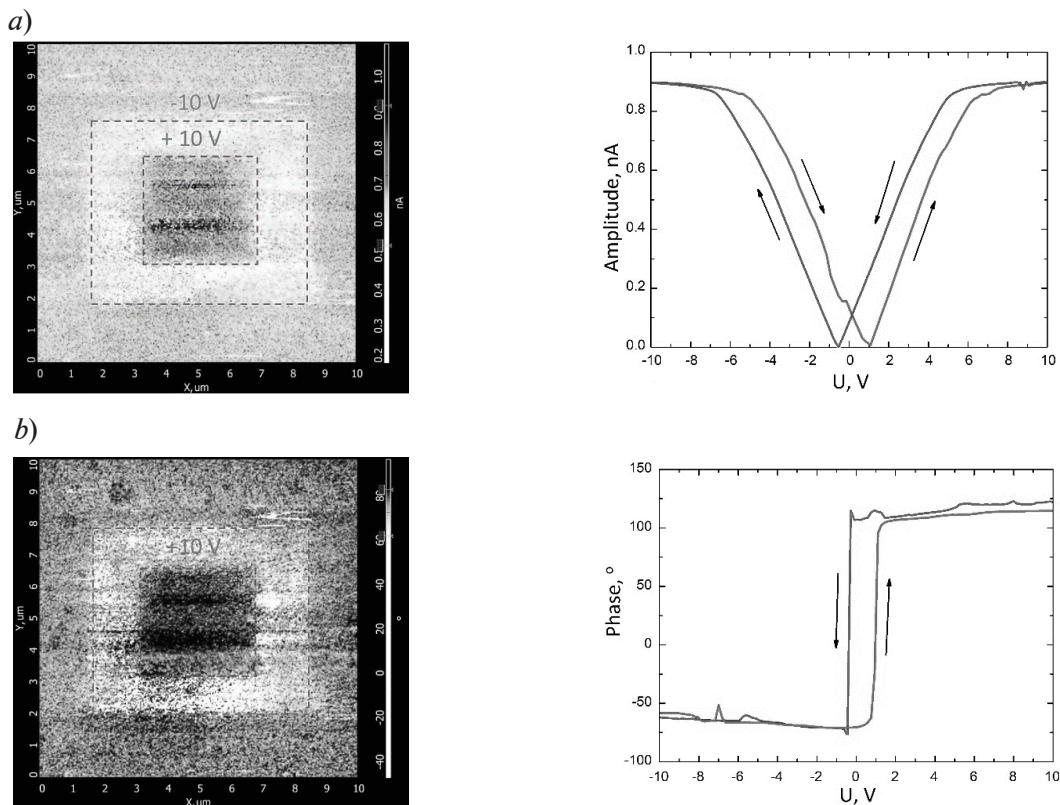


Fig. 1. Results of PFM study: amplitude (a), phase (b)

Obtained nanocrystalline ferroelectric films exhibit a stable piezoelectric effect, which weakly depends on their nanoscale structure (Fig. 1). On the phase curves, one can observe the presence of intrinsic lattice polarization and 180-degree switching, which indicates the existence of domains.

Based on the obtained experimental results, the piezoelectric parameters for  $\text{LiNbO}_3$  and  $\text{BaTiO}_3$  films fabricated under different substrate temperatures were determined (Fig. 2). The piezoelectric coefficient  $d_{33}$  was determined from the slope of the PFM amplitude vs. bias voltage curves measured between the probe and the sample (Fig. 1,a). We used the curve of the approach of the probe to the sample obtained on single-crystal silicon to calculate  $d_{33}$ .

An increase in the substrate temperature under PLD from  $300^\circ\text{C}$  to  $600^\circ\text{C}$  leads to an increase in the piezoelectric coefficient  $d_{33}$  from  $(3.22 \pm 0.41)$  pm/V to  $(6.84 \pm 1.13)$  pm/V for films  $\text{LiNbO}_3$ , and from  $(17.42 \pm 1.32)$  pm/V to  $(32.12 \pm 2.17)$  pm/V for  $\text{BaTiO}_3$  films. The obtained result can be explained by the different growth kinetics of oxide films: the higher mobility of adatoms  $\text{LiNbO}_3$  and  $\text{BaTiO}_3$ , with an increase in the substrate temperature, favors more oriented film growth and the increase in  $d_{33}$ .

Based on the obtained results, the energy harvester was developed (Fig. 3).

The harvester has a carbon nanotube [9] coated with a ferroelectric film ( $\text{LiNbO}_3$  or  $\text{BaTiO}_3$ ) as an active element. A stretched part (positive strain) will create a positive electrical potential, while a compressed part (negative strain) will create a negative electrical potential across the device.

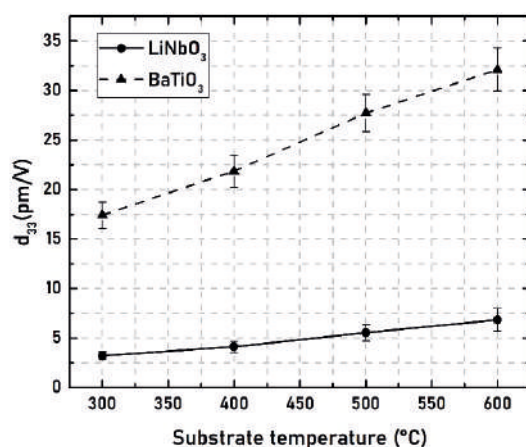


Fig. 2. Dependences of  $d_{33}$  piezoelectric coefficient on the substrate temperature under PLD:  $\text{LiNbO}_3$  and  $\text{BaTiO}_3$

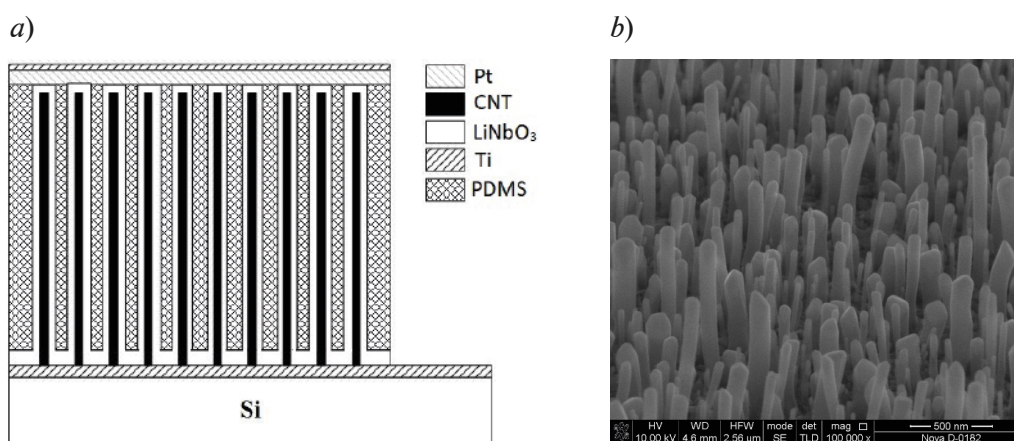


Fig. 3. Piezoelectric energy harvester based on hybrid nanostructures: architecture (a), SEM image of carbon nanotubes coated with  $\text{BaTiO}_3$  (b)

As a result, a potential difference will be created at the top of the nanostructure, distributed over the surface of the structure. The obtained results can be used to create next-generation lead-free energy harvesters based on ferroelectric films for renewable energy and IoT devices.

### Conclusion

Studies of the piezoelectric properties of the obtained nanocrystalline  $\text{LiNbO}_3$  and  $\text{BaTiO}_3$  films have been carried out. The method of atomic force microscopy in the mode of force microscopy of the piezoresponse to study the piezoelectric parameters of the films has been used. It is shown that all the obtained nanocrystalline  $\text{LiNbO}_3$  and  $\text{BaTiO}_3$  films exhibit a stable piezoelectric effect, which is weakly dependent on their nanoscale structure. The phase curves of the obtained films show the presence of intrinsic lattice polarization and  $180^\circ$  switching, which indicates the existence of the domains in the lattice. The obtained experimental results were used to determine the piezoelectric parameters of  $\text{LiNbO}_3$  and  $\text{BaTiO}_3$  films formed at different substrate temperatures. An analysis of the obtained results showed that an increase in the substrate temperature from 300 °C to 600 °C leads to an increase in the piezoelectric coefficient  $d_{33}$  from  $(3.22 \pm 0.41)$  pm/V to  $(6.84 \pm 1.13)$  pm/V for films  $\text{LiNbO}_3$ , and from  $(17.42 \pm 1.32)$  pm/V to  $(32.12 \pm 2.17)$  pm/V for  $\text{BaTiO}_3$  films.



## REFERENCES

1. **Harb A.**, Energy harvesting: State-of-the-art, *Renewable Energy*. 10 (36) (2011) 2641–2654.
2. **Vullers, R. J. M., van Schaijk, R., Doms, I., Van Hoof, C., Mertens, R.**, Micropower energy harvesting, *Solid-State Electronics*. 7 (53) (2009) 684–693.
3. **Wang Z. L., Song J.**, Piezoelectric nanogenerators based on zinc oxide nanowire arrays, *Science*. 5771 (312) (2006) 242–246.
4. **Song J., Zhou J., Wang Z. L.**, Piezoelectric and semiconducting coupled power generating process of a single ZnO belt/wire. A technology for harvesting electricity from the environment, *Nano letters*. 8 (6) (2006) 1656–1662.
5. **Bowen C. R., Kim H. A., Weaver P. M., Dunn S.**, Piezoelectric and ferroelectric materials and structures for energy harvesting applications, *Energy & Environmental Science*. 1 (7) (2014) 25–44.
6. **Topolov V. Y., Isaeva A. N., Bisegna P.**, Squared Figs. of merit and electromechanical coupling factors of a novel lead-free 1–3–0 composite for sensor and energy-harvesting applications, *Sensors and Actuators A: Physical*. (318) (2021) 112473–1–112473–11.
7. **Ryu H., Yoon H. J., Kim S. W.**, Hybrid energy harvesters: toward sustainable energy harvesting, *Advanced Materials*. 34 (31) (2019) 1802898–1–1802898–19.
8. **Vakulov Z., Khakhulin D., Zamburg E., Mikhaylichenko A., Smirnov V. A., Tominov R., Klimin V. S., Ageev O.A.**, Towards scalable large-area pulsed laser deposition, *Materials*. 17 (14) (2021) 4854–1–4854–14.
9. **Il'in O. I., Il'ina M. V., Rudyk N. N., Polyvyanova O. R., Saenko A. V., Fedotov A. A.**, Effect of the sublayer material on geometric dimensions and piezoelectric response of vertically aligned carbon nanotubes, Fullerenes, Nanotubes and Carbon Nanostructures. 30 (1) (2022) 185–190.

## THE AUTHORS

**VAKULOV Zakhar**

zakhar.vakulov@gmail.com

ORCID: 0000-0003-3084-4522

**TOMINOV Roman**

tominov@sfedu.ru

ORCID: 0000-0002-1263-2158

**DZYUBA Dmitry**

dmdzyuba@sfedu.ru

ORCID: 0000-0002-6028-9518

**SHIHOVCOV Ivan**

shihovcov@sfedu.ru

ORCID: 0000-0002-0355-9665

**SMIRNOV Vladimir**

vasmirnov@sfedu.ru

ORCID: 0000-0001-7130-2194

**AGEEV Oleg**

agevoa@gmail.com

ORCID: 0000-0003-1755-5371

*Received 12.07.2022. Approved after reviewing 24.07.2022. Accepted 26.07.2022.*

Conference materials

UDC 538.953

DOI: <https://doi.org/10.18721/JPM.153.250>

## Laser surface treatment of aluminum: correlation between thermal modeling and experimental study

A. A. Mozhayko <sup>1, 2</sup>✉, D. A. Gerashchenkov <sup>2</sup>,

E. Yu. Gerashchenkova <sup>2</sup>, V. V. Davydov <sup>1, 3</sup>

<sup>1</sup> Peter the Great St. Petersburg Polytechnic University, St. Petersburg, Russia;

<sup>2</sup> NRC Kurchatov Institute – CRISM Prometey, St. Petersburg, Russia;

<sup>3</sup> All-Russian Research Institute of Phytopathology, Moscow Region, Russia

✉ [annaanna-1996@mail.com](mailto:annaanna-1996@mail.com)

**Abstract.** In recent years, laser surface treatment was widely used to improve the properties of aluminum coatings. This paper implements a thermal model to simulate the laser treatment effects on a cold-sprayed aluminum coating and St3 substrate. As a result of the work, a model has been developed to evaluate the thermal fields and the melt pool during the laser surface treatment process, and laser treatment modes have been identified, with the help of which a high-alloyed aluminum layer on the surface of steel has been obtained.

**Keywords:** laser surface treatment, aluminum, intermetallides, thermal fields, thermal modeling

**Funding:** This study was funded by RFBR and ROSATOM, grant number 20-21-00024.

**Citation:** Mozhayko A. A., Gerashchenkov D. A., Gerashchenkova E. Yu., Davydov V. V., Laser surface treatment of aluminium: correlation between thermal modeling and experimental study, St. Petersburg State Polytechnical University Journal. Physics and Mathematics. 15 (3.2) (2022) 274–279. DOI: <https://doi.org/10.18721/JPM.153.250>

This is an open access article under the CC BY-NC 4.0 license (<https://creativecommons.org/licenses/by-nc/4.0/>)

Материалы конференции

УДК 538.953

DOI: <https://doi.org/10.18721/JPM.153.250>

## Лазерная обработка поверхности алюминия: тепловое моделирование и экспериментальное исследование

А. А. Можайко <sup>1, 2</sup>✉, Д. А. Геращенко <sup>2</sup>, Е. Ю. Геращенко <sup>2</sup>, В. В. Давыдов <sup>1, 3</sup>

<sup>1</sup> Санкт-Петербургский политехнический университет Петра Великого, Санкт-Петербург, Россия;

<sup>2</sup> НИЦ «Курчатовский институт» – ЦНИИ КМ «Прометей», Санкт-Петербург, Россия;

<sup>3</sup> Всероссийский научно-исследовательский институт фитопатологии, Московская область, Россия

✉ [annaanna-1996@mail.ru](mailto:annaanna-1996@mail.ru)

**Аннотация.** В последние годы для улучшения свойств алюминиевых покрытий широко применяется лазерная обработка поверхности. В данном исследовании разработана тепловая модель для изучения процесса лазерной обработки алюминиевого покрытия, нанесенного методом холодного напыления на подложку из стали Ст3. В результате работы создана модель для оценки тепловых полей и ванны расплава в процессе лазерной обработки поверхности, а также выявлены режимы лазерной обработки, с помощью которых на поверхности стали формируется высоколегированный алюминием слой.

**Ключевые слова:** лазерная обработка поверхности, алюминий, интерметаллиды,



тепловые поля, тепловое моделирование

**Финансирование:** Исследование выполнено при поддержке гранта РФФИ и Росатома № 20-21-00024.

**Ссылка при цитировании:** Можайко А. А., Геращенко Д. А., Геращенко Е. Ю., Давыдов В. В. Лазерная обработка поверхности алюминия: тепловое моделирование и экспериментальное исследование // Научно-технические ведомости СПбГПУ. Физико-математические науки. Т. 15. № 3.2. С. 274–279. DOI: <https://doi.org/10.18721/JPM.153.250>

Статья открытого доступа, распространяемая по лицензии CC BY-NC 4.0 (<https://creativecommons.org/licenses/by-nc/4.0/>)

### Introduction

The laser surface treatment (LST) of metals enables the production of a surface layer with a thickness of under a millimeter to several millimeters and with special functional properties: high hardness and wear resistance, while maintaining the properties of the substrate material [1-4]. This makes it possible to obtain various compounds of materials for scientific research [5–9]. This is confirmed by the study of materials on various devices [10–13].

Currently, LST is widely used to improve the properties of aluminum coatings, since aluminum has a high specific strength, thermal and electrical conductivity, and corrosion resistance [14, 15]. Laser power and speed conditions the structure and properties of the surface layer [16].

An important step in laser surface treatment is the mode selection. The mismatch of the process parameters leads to various adverse outcomes, such as inefficient processing, in which the conditions necessary for the formation of intermetallides are not met, and damage to the processed sample [17]. It is advantageous to select the modes of the laser surface treatment process using computer modeling. With the help of modern numerical simulation packages, it is possible to calculate thermal fields in a sample during surface treatment. This significantly saves time and production resources [18-22].

The aim of the study was to better understand the behavior of aluminum deposited by gas dynamic spraying during laser treatment. At the modeling stage, treatment modes are identified in which the conditions for the formation of intermetallic compounds are fulfilled. For this purpose, a thermal finite element model of laser processing was implemented to evaluate the thermal fields occurring in the deposited coating. Using the selected modes, heat treatment of aluminum deposited by gas-dynamic spraying on a steel substrate is carried out.

### Materials and Methods

Fig. 1 schematically depicts the process of laser surface treatment. When a laser beam interacts with a material, part of the heat is dissipated as a result of convective and radiative heat transfer. The remaining laser energy is absorbed by the material. The main mechanisms of heat transfer during laser treatment are the thermal conductivity of the sample and thermal convection between the material and the environment [18].

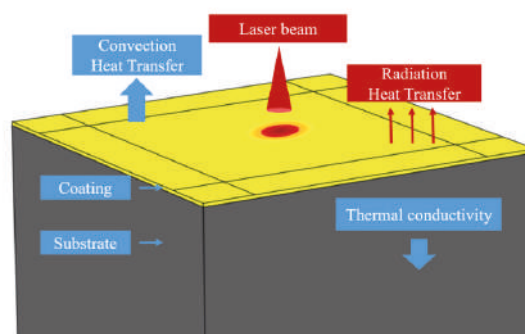


Fig. 1. Schematic illustration of the LST process

In general, heat transfer can be described by the heat conduction equation:

$$\rho C_p \left( \frac{\partial T}{\partial t} + (\vec{u} \cdot \vec{\nabla} T) \right) = \vec{\nabla} \cdot (k \vec{\nabla} T), \quad (1)$$

where  $\rho$  is the material density,  $C_p$  is the heat capacity,  $T$  is the temperature,  $\vec{u}$  is the fluid velocity vector,  $k$  is the thermal conductivity.

The laser source is represented by a heat source with a Gaussian distribution:

$$Q_{in} = \frac{2PA}{\pi r^2} \exp\left(-\frac{2(x-vt)^2 + y^2}{r^2}\right), \quad (2)$$

where  $P$  is the laser power,  $A$  is the laser energy absorption coefficient,  $r$  is the radius of the laser beam, and  $v$  is the laser speed.

When the laser interacts with the material, heat losses due to convection and radiation are taken into account:

$$-k \frac{\partial T}{\partial t} = Q_{in} - \alpha(T_w - T_0) - \sigma \varepsilon (T_w^4 - T_0^4), \quad (3)$$

where  $\alpha$  is the heat transfer coefficient,  $T_w$  is the surface temperature, and  $T_0$  is the ambient temperature,  $\sigma$  is the Stefan-Boltzmann constant, and  $\varepsilon$  is the surface absorption coefficient.

The phase transition of melting and evaporation is considered in the equation of heat capacity [23]:

$$C_p^{eq} = C_p + D_m L_m + D_v L_v, \quad (4)$$

where  $C_p$  is the heat capacity as a temperature dependent function,  $L_m$  is the latent heat of fusion,  $D_m$  and  $D_v$  is the Gaussian function normalized around the melting and evaporation temperature  $T_m$  and  $T_v$ .

In the process of heating and cooling, the thermophysical properties of materials change, since they depend on temperature. The model has the ability to set such properties as thermal conductivity, heat capacity, density, as a function of temperature. Also, before starting the calculation, you can change the values of process parameters, such as power, scanning speed, laser beam diameter, hatch spacing, sample dimensions and coating thickness.

The Comsol Multiphysics package and 3D finite element method are used to model thermal effects. A three-dimensional numerical model was built with dimensions of 2 mm x 2 mm x 4 mm. Aluminum was chosen as the coating material, and St3 steel as the substrate material. Steel St3 was chosen for modeling, since its physical properties are known from open sources, and it is similar to steel 09G2S. The studies were carried out for speeds of 100–800 mm/s and for the thickness of the aluminum coating from 20  $\mu\text{m}$  to 180  $\mu\text{m}$ . The hatch spacing, power and diameter of the laser beam were set constant for all modes and were equal to 75  $\mu\text{m}$ , 180 W and 100  $\mu\text{m}$ , respectively.

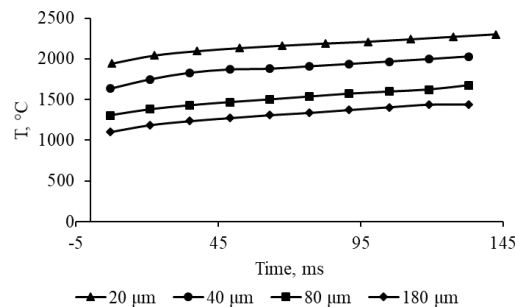


Fig. 2. Dependence of the maximum surface temperature on the scanning time for different coating thicknesses at a laser speed of 100 mm/s

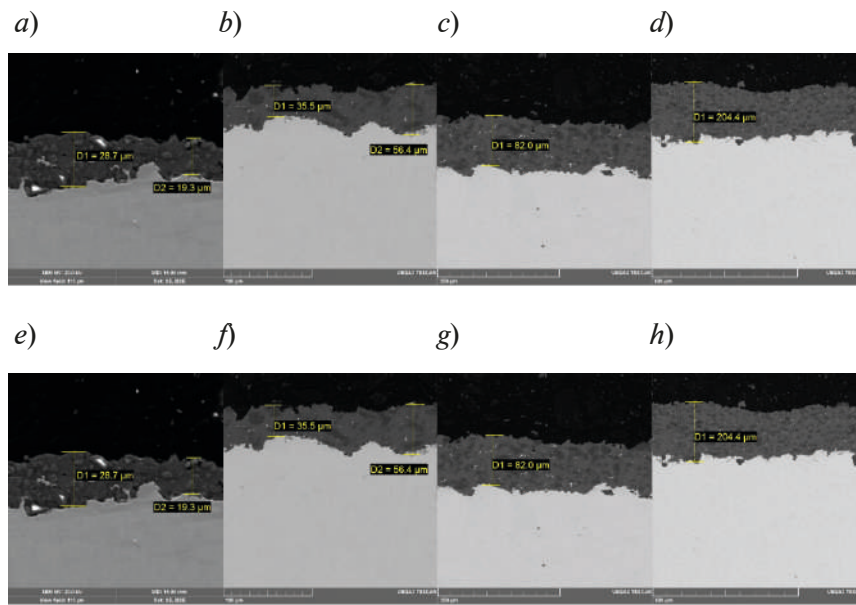


Fig. 3. Cross section of a coating 20 thick (*a, e*); 40 (*b, f*); 80 (*c, g*) and 180  $\mu\text{m}$  (*d, h*) after cold spraying (*a–d*) and after subsequent laser treatment (*e–h*)

The experiment consists of two stages. At the first stage, the cold spraying method [24] forms an aluminum coating with a thickness of 20–180  $\mu\text{m}$ . PA-VCh grade aluminum powder was used as the starting powder material. For applying coatings by cold spraying, a Dimet-403 installation was used. The 09G2S steel substrate was coated with different thicknesses: 20, 40, 80, and 180  $\mu\text{m}$ .

The second stage includes laser surface treatment to form a coating with improved characteristics [25]. Laser surface treatment is performed at the Russian SLM Factory using an ytterbium fiber laser in a protective argon atmosphere.

### Results and Discussion

Ten laser beam passes were simulated for samples made of St3 steel with different thickness of aluminum coating. The maximum temperatures for each pass of the laser beam are found (Fig. 2). It has been found that with increasing coating thickness, the maximum temperature on the surface decreases. This is due to the high thermal conductivity of aluminum.

The melt pool depth was measured for all modes under study. It has been established that at a laser speed of 400 mm/s, 800 mm/s and a power of 180 W, there is no mixing of the components in the laser impact zone, since the energy input is insufficient. For a coating thickness of 20  $\mu\text{m}$  and 40  $\mu\text{m}$ , the components are mixed in a ratio of 2:1 and 1:2, respectively, at a scanning speed of 100 mm/s and a power of 180 W, from which it can be assumed that under these modes, intermetallic compounds are formed in the resulting coating.

As a result of the experiment, samples were made in two stages. At the first stage, an aluminum coating was applied by gas-dynamic spraying, after which the surface was treated with a laser to change the microstructure, reduce the level of porosity, and improve the mechanical properties of the coating (Fig. 3). The cross section of a coating were studied by scanning electron microscopy using the TESCAN Vega 3.

Table 1

**Comparison of the melt pool depth obtained from modeling and experimental study for a scanning speed of 100 mm/s**

	20 $\mu\text{m}$	40 $\mu\text{m}$	80 $\mu\text{m}$	180 $\mu\text{m}$
<i>d</i> , $\mu\text{m}$ (modeling)	70	58	80	180
<i>d</i> , $\mu\text{m}$ (experiment)	63.3	62.9	74.2	230.3

As a result of the study, the dependence of the size of the melt mixing zone on the scanning mode (different scanning speeds and coating depth) was established. Table 1 compares the melt pool depth obtained from the simulation with the mixing zone of the components measured in the experimental samples.

It was found that for a coating thickness of 20  $\mu\text{m}$  and 40  $\mu\text{m}$ , a scanning speed of 100 mm/s, and a power of 180 W, intermetallic compounds are formed in the mixing zone of the components.

The discrepancies with the simulation results when comparing the values in Table 1 are caused by the uneven distribution of the precursor coating over the substrate, as well as the presence of corundum in the coating, which was not taken into account in the simulation.

### Conclusion

As a result of the work, a model was developed for estimating thermal fields in an aluminum coating deposited by gas-dynamic spraying during laser treatment. It was found that for a coating thickness of 20 microns and 40 microns, a scanning speed of 100 mm/s, and a power of 180 W, intermetallic compounds are formed in the mixing zone of the components.

### Acknowledgments

Experimental studies were carried out on the equipment of the Core shared research facilities “Composition, structure and properties of structural and functional materials” of the NRC «Kurchatov Institute» - CRISM “Prometey” with the financial support of the state represented by the Ministry of Education and Science of the Russian Federation under agreement No. 13.CKP.21.0014 (075-11-2021-068). The unique identifier is RF-2296.61321X0014.

### REFERENCES

1. **Fribourg G., Deschamps A., Bréchet Y., Mylonas G., Labeas G., Heckenberger U., Perez M.**, Microstructure modifications induced by a laser surface treatment in an AA7449 aluminium alloy, *Materials Science and Engineering*. 528 (2011) 2736–2747.
2. **Syed B., Maurya P, Lenka S., Padmanabham G., Shariff S. M.**, Analysis of high strength composite structure developed for low-carbon-low-manganese steel sheet by laser surface treatment, *Optics & Laser Technology*. 143 (2021) 107285.
3. **Samant A. N., Du B., Paital S. R., Kumar S., Dahotre N. B.**, Pulsed laser surface treatment of magnesium alloy: Correlation between thermal model and experimental observations, *Journal of Materials Processing Technology*. 209 (2009) 5060–5067.
4. **Chauhan A. S., Jha J. S., Telrandhe S., S. V, Gokhale A. A., Mishr S. K.**, Laser surface treatment of  $\alpha$ - $\beta$  titanium alloy to develop a  $\beta$ -rich phase with very high hardness, *Journal of Materials Processing Technology*. 288 (2021) 116873.
5. **Dyumin V., Smirnov K., Myazin N.**, Charge-coupled Device with Integrated Electron Multiplication for Low Light Level Imaging, *Proceedings of the 2019 IEEE International Conference on Electrical Engineering and Photonics, EExPolytech*. 8906868 (2019) 308–310.
6. **Kruzhhalov S. V., Grebenikova N. M., Smirnov K. J.**, Method for Determining Defects on the Inner Walls of Tubing from the Velocity Distribution of the Flowing Fluid, *Measurement Techniques*. 61(4) (2018) 365–372.
7. **Makeev S. S., Grevtzeva A. S., Glinushkin A. P., Matorin D. N.**, Possibilities of using spectral analysis in method of nuclear magnetic spectroscopy for condensed media investigation, *Journal of Physics: Conference Series*. 1695(1) (2020) 012112.
8. **Davydov V. V.**, Determination of the Composition and Concentrations of the Components of Mixtures of Hydrocarbon Media in the Course of its Express Analysis, *Measurement Techniques*. 62(2) (2020) 1090–1098.
9. **Davydov V. V., Davydova T. I.**, A nondestructive method for express testing of condensed media in ecological monitoring, *Russian Journal of Nondestructive Testing*. 53(7) (2017) 520–529.
10. **Myazin N. S., Dudkin V. I., Grebenikova N. M.**, On the Possibility of Express Recording of Nuclear Magnetic Resonance Spectra of Liquid Media in Weak Fields, *Technical Physics*. 63(12) (2018) 1845–1850.
11. **Kuzmin M. S., Rogov S. A.**, On the use of a multi-raster input of one-dimensional signals in two-dimensional optical correlators, *Computer Optics*. 43(3) (2019) 391–396.



12. **Grebenikova N. M., Smirnov K. J., Rud V. Yu., Artemiev V. V.**, Features of monitoring the state of the liquid medium by refractometer, *Journal of Physics: Conference Series*. 1135(1) (2018) 012055.
13. **Myazin N. S.**, Features of formation of structure of a nuclear magnetic resonance signal in weak magnetic field, *Journal of Physics: Conference Series*. 1135(1) (2018) 012061.
14. **Wu Y., Lin J., Carlson B. E., Lu P., Balogh M. P., Irish N. P., Mei Y.**, Effect of laser ablation surface treatment on performance of adhesive-bonded aluminum alloys, *Surface and Coatings Technology*. 304 (2016) 340–347.
15. **Makarov A. M., Gerashchenkov D. A., Kuznetsov P. A., Ryabov V. V., Vasiliev O. S.**, Investigation of the influence of laser treatment modes on coatings of aluminum, nickel, nickel-titanium systems, *J. Phys. Conf. Ser.* 1758 (2021) 12024.
16. **Dobrzański L. A., Tański T., Dobrzańska-Danikiewicz A. D., Jonda E., Bonek M., Drygala A.**, Structures, properties and development trends of laser-surface-treated hot-work steels, light metal alloys and polycrystalline silicon, *Laser Surface Engineering*. 1 (2015) 3–32.
17. **Rubino F., Astarita A., Carlone P.**, Thermo-Mechanical Finite Element Modeling of the Laser Treatment of Titanium Cold-Sprayed Coatings, *Coatings*. 8(6) (2018) 219.
18. **Dong Z., Liu Y., Wen W., Ge J., Liang J.**, Effect of Hatch Spacing on Melt Pool and As-built Quality During Selective Laser Melting of Stainless Steel: Modeling and Experimental Approaches, *Materials*. 12 (2019) 50.
19. **Mohanty S., Hattel J. H.**, Numerical model based reliability estimation of selective laser melting process // *Phys. Procedia*. 56 (2014) 379–389.
20. **Kuznetsov P., Shakirov I., Mozhayko A., Zhukov A., Bobyr V.**, Comparison of sequential and circular scanning thermal fields and their influence on microstructure of Alnico alloy produced by laser powder bed fusion, *J. Phys.: Conf. Ser.* 1967 (2021) 012064.
21. **Ansari M. J., Nguyen D.-S., Park H. S.**, Investigation of SLM Process in Terms of Temperature Distribution and Melting Pool Size: Modeling and Experimental Approaches, *Materials*. 12 (2019) 1272.
22. **Chaurasia J. K., Jinoop A. N., Paul C. P., Bindra K. S., Bontha S.**, Study of melt pool geometry and solidification microstructure during laser surface melting of Inconel 625 alloy, *Optik*. 246 (2021) 167766.
23. **Bonacina C., Comini G., Fassano A., Primicerio M.**, Numerical solutions of phase change problems, *Int. J. Heat Mass Transfer*. 16 (1973) 1825–1832.
24. **Gerashchenkov D. A., Vasiliev A. F., Farmakovskiy B. V., Mashek A. Ch.**, Study of the flow temperature in the process of cold gas-dynamic spraying of functional coatings, *Materials Science*. 1 (2014) 87–96.
25. **Gerashchenkov D. A., Kuznetsov P. A., Makarov A. M., Krasikov A. V., Markov M. A.**, Investigation of the intermetallic coating of the Ni-Fe system obtained by surface laser treatment on a steel substrate, *J. Phys. Conf. Ser.* 1758 (2021) 12011.

#### THE AUTHORS

**MOZHAYKO Anna**  
Annaanna-1996@mail.ru  
ORCID: 0000-0002-9146-4286

**GERASHCHENKOVA Elena**  
e.burkanova@gmail.com  
ORCID: 0000-0003-1082-2000

**GERASHCHENKOV Dmitry**  
gda.prometey@mail.ru  
ORCID: 0000-0003-0185-8087

**DAVYDOV Vadim**  
davydov.vv@spbstu.ru  
ORCID: 0000-0001-9530-4805

*Received 15.07.2022. Approved after reviewing 21.07.2022. Accepted 16.08.2022.*

Conference materials

UDC 53.097

DOI: <https://doi.org/10.18721/JPM.153.251>

## Ruthenium as an electrode material for the fast electrochemical actuator

P. S. Shlepakov<sup>1, 2✉</sup>, I. V. Uvarov<sup>1, 2</sup>, V. B. Svetovoy<sup>3</sup>

<sup>1</sup> Valiev Institute of Physics and Technology RAS, Yaroslavl Branch, Yaroslavl, Russia;

<sup>2</sup> P.G. Demidov Yaroslavl State University, Yaroslavl, Russia;

<sup>3</sup> A.N. Frumkin Institute of Physical Chemistry and Electrochemistry RAS, Moscow, Russia

✉ p.shlepakov@bk.ru

**Abstract.** Electrolysis of water performed by alternating polarity (AP) voltage pulses increases the operating frequency of the electrochemical actuator by several orders of magnitude due to the fast recombination of the produced gas. The gas is collected in nanobubbles that disappear quickly due to spontaneous combustion of hydrogen and oxygen. However, this type of electrolysis damages the electrodes and the actuator performance deteriorates with time. Platinum electrodes suffer from mechanical action of nanobubbles, while titanium structures are oxidized. A promising material is ruthenium due to its chemical inertness and mechanical strength. In this work, we test Ru, Pt and Ti electrodes in the AP electrolysis. The degree of wear, current flowing through the cell, and threshold voltage are analyzed and compared.

**Keywords:** alternating polarity electrolysis, nanobubbles, electrodes, ruthenium, degradation

**Funding:** The study was supported by RSF, grant 18-79-10038.

**Citation:** Shlepakov P. S., Uvarov I. V., Svetovoy V. B., Ruthenium as an electrode material for the fast electrochemical actuator, St. Petersburg State Polytechnical University Journal. Physics and Mathematics. 15 (3.2) (2022) 280–284. DOI: <https://doi.org/10.18721/JPM.153.251>

This is an open access article under the CC BY-NC 4.0 license (<https://creativecommons.org/licenses/by-nc/4.0/>)

Материалы конференции

УДК 53.097

DOI: <https://doi.org/10.18721/JPM.153.251>

## Рутений как материал электродов быстрого электрохимического актюатора

П.С. Шлепаков<sup>1, 2✉</sup>, И.В. Уваров<sup>1, 2</sup>, В. Б. Световой<sup>3</sup>

<sup>1</sup> Ярославский Филиал Федерального государственного бюджетного учреждения науки Физико-технологического института имени К.А. Валиева Российской академии наук, г. Ярославль, Россия;

<sup>2</sup> Ярославский государственный университет им. П.Г. Демидова, г. Ярославль, Россия;

<sup>3</sup> Институт физической химии и электрохимии им. А. Н. Фрумкина  
Российской академии наук, г. Москва, Россия

✉ p.shlepakov@bk.ru

**Аннотация.** Электролиз воды, выполняемый микросекундными импульсами напряжения переменной полярности, повышает рабочую частоту электрохимического актюатора на несколько порядков вследствие быстрой рекомбинации произведенного газа. Газ производится в виде нанопузырьков, которые быстро растворяются в результате спонтанной реакции горения водорода и кислорода. Однако электроды быстро разрушаются под механическим воздействием нанопузырьков, в то время как титановые электроды окисляются. Перспективным материалом является рутений, обладающий



высокой химической инертностью и твердостью. В данной работе выполнено сравнение рабочих характеристик рутениевых, платиновых и титановых структур в электролизе переменной полярности.

**Ключевые слова:** электролиз биполярными импульсами, нанопузыри, электроды, рутений, деградация

**Финансирование:** Работа выполнена при финансовой поддержке РФФИ, проект № 18-79-10038.

**Ссылка при цитировании:** Шлепаков П. С., Уваров И. В., Световой В. Б. Рутений как материал электродов быстрого электрохимического актюатора // Научно-технические ведомости СПбГПУ. Физико-математические науки. Т. 15. № 3.2. С. 280–284. DOI: <https://doi.org/10.18721/JPM.153.251>

Статья открытого доступа, распространяемая по лицензии CC BY-NC 4.0 (<https://creativecommons.org/licenses/by-nc/4.0/>)

### Introduction

Electrochemical production of gas in a closed chamber provides extra pressure that pushes a flexible membrane up. This phenomenon is used as a working principle for the electrochemical actuators [1], which are good candidates for various microfluidic systems. Conventional actuators based on the DC electrolysis suffer from a long response time due to slow recombination of the produced gas [2]. The use of microsecond AP voltage pulses instead of DC voltage solves the problem. The chamber is filled with nanobubbles (NBs) with a diameter of 100 nm, which disappear in milliseconds due to spontaneous combustion of hydrogen and oxygen. A fast electrochemical actuator was demonstrated, which works several orders of magnitude faster than conventional devices [3]. However, the electrodes of the actuator have a limited lifecycle because of two factors. The first one is a strong mechanical action of NBs on the electrode surface, while the second factor is the oxidation of the electrode material. Platinum electrodes are not oxidized, but are destroyed quickly by the mechanical action of NBs [4] due to a relatively low hardness of Pt (3.5 units on Mohs scale) [5]. Titanium is much harder material (6 units), but it is prone to oxidation that reduces the current flowing through the electrolyte and suppresses the gas production [6]. A promising electrode material is ruthenium. It has high hardness of 6.5 units and a conductive oxide. The resistivity of poor ruthenium is  $7.1 \mu\Omega\cdot\text{cm}$ , while  $\text{RuO}_2$  demonstrates a comparable value of  $35 \mu\Omega\cdot\text{cm}$  [7]. These properties allow one to expect that Ru electrodes withstand the mechanical action of NBs and can be oxidized without significant decrease of the gas production. In this work, we investigate the degradation of Ru electrodes in the AP electrolysis in comparison with Pt and Ti structures.

### Materials and methods

The electrodes of the concentric shape (see Fig. 1,*a*) are fabricated on a silicon wafer with  $0.9 \mu\text{m}$   $\text{SiO}_2$  layer grown by thermal oxidation in wet oxygen. The electrode material is deposited by magnetron sputtering. The sample is placed in a Petri dish filled with the electrolyte, which is a molar solution of  $\text{Na}_2\text{SO}_4$  in distilled water. A layer of SU-8 protects the signal lines from the electrolyte. Square AP voltage pulses are generated by a homemade generator and applied to the working electrode, while the other one is grounded. It was shown that the degradation of the electrodes goes slower at a higher frequency of pulses  $f$  [6]. Here we use  $f = 500 \text{ kHz}$  that is the upper limit of the generator.

The samples are tested in two regimes. In the first one, the pulses with an amplitude of 11 V are applied continuously during 30 min. The voltage is not large enough to produce explosion of a microbubble, so the electrode surface is affected only by NBs. The experiment is performed at 100 nm thick Pt and Ru electrodes, as illustrated in Fig. 1,*b*. The current flowing through the electrochemical cell is recorded every 10 s by an oscilloscope Pico-Scope 5000 and the average absolute value  $I_{av}$  is calculated. SEM investigation of Ru electrodes is performed by SEM Zeiss

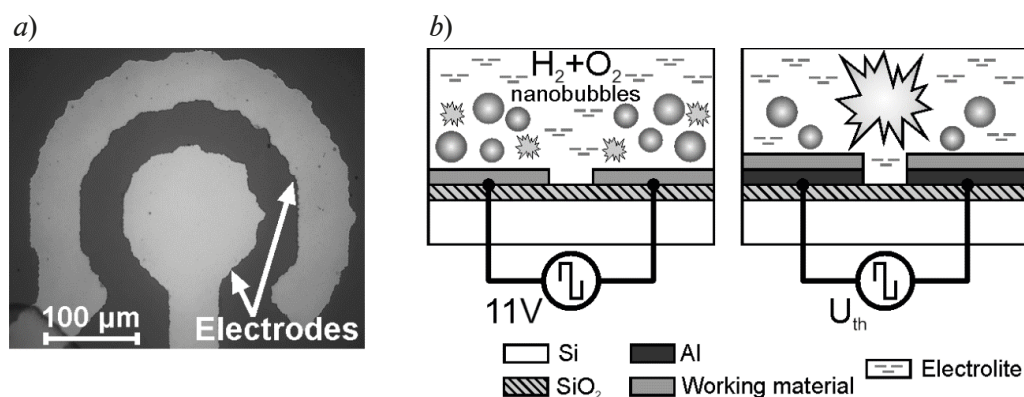


Fig. 1. Photograph of the electrodes, top view (a); schematic illustration of the continuous (left) and explosive (right) testing regimes (b)

Supra 40. Chemical composition is measured by energy dispersive X-ray (EDX) spectrometer Oxford Instruments INCA X-act at the acceleration voltage 6 kV.

In the second regime, the amplitude is adjusted to the threshold level  $U_{th}$ , at which the concentration of NBs in the electrolyte reaches a critical value. The NBs merge into a microbubble, which explodes with the release of a large amount of energy, as shown in Fig. 1, b. AP pulses are applied to the electrodes every 2 s until one explosion happens. The current drop in the cell during the explosion is tracked by our generator and voltage pulses stopped automatically. It sets the same conditions for each sample. The experiment lasts until no explosion happens during the 0.5 s of the AP pulses applying or the  $U_{th}$  reaches 19 V, which is the maximal voltage of the generator. The lifecycle and durability are investigated for Al/Ti and Al/Ru electrodes with a thickness of 500/100 nm. Aluminium layer is included to reduce electrical resistance of the signal lines.

### Results and discussion

The time dependence of the current for Ru and Pt electrodes in the continuous regime is shown in Fig. 2, a. At the beginning of the test, the samples demonstrate similar  $I_{av}$  of 35.0 and 32.5 mA, respectively due to close values of electrical resistivity. Then  $I_{av}$  for Pt decreases as a result of the electrode damage. At the 13th minute the central electrode is almost completely destroyed as shown in Fig. 2, b, which is accompanied by a drop of the current. At the same time, Ru electrodes demonstrate a slight increase in the current throughout the test. The reason for the increase is the heating of the electrolyte and the chip. The damage is not observed, as one can see in Fig. 2, b.

SEM investigation of Ru electrodes revealed nanoparticles appeared on the surface after the electrolysis. Their concentration is higher at the edge of the electrode than at the central part.

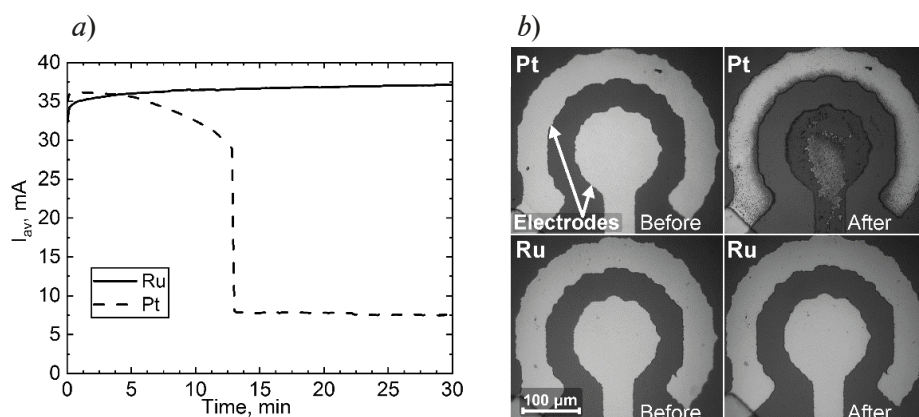


Fig. 2. The results of continuous test: time dependence of the current flowing through the electrodes (a); photographs of the electrodes before and after the test (b)

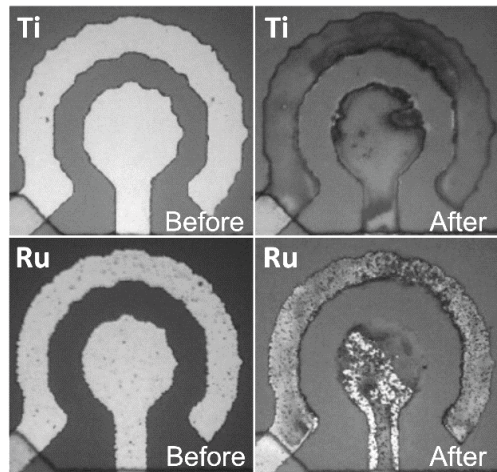


Fig. 3. Ti and Ru electrodes before and after the explosive test

EDX analysis shows the oxidation of the electrodes. The process goes faster at the edge because of higher current density. As was expected, the oxidation of Ru electrodes does not reduce the current due to metallic conductivity of ruthenium oxide.

In the explosive regime, Ti and Ru electrodes have an initial threshold voltage of 12-13 and 10-11 V, respectively. Ti electrodes darken due to oxidation (see Fig. 3), and  $U_{th}$  reaches the limit value of 19 V in 18 min. Ruthenium structures generate explosions during 2 hours. The threshold voltage increases to 12 V because of mechanical damage by explosions, and the test continues until the fatal destruction of the central electrode. Thus, Ru structures exhibit several times longer lifecycle compared to Ti samples. This result makes Ru a preferable material for the fast electrochemical actuator.

### Conclusions

Ruthenium electrodes are tested in the electrochemical process performed by AP voltage pulses with the frequency of 500 kHz. In the continuous regime, Ru and Pt structures are compared. The platinum sample demonstrates high current in the beginning of the test, but  $I_{av}$  falls to the minimal value in 13 min due to mechanical damage by NBs. At the same time, the ruthenium electrodes provide a slightly increasing current due to heating of the electrolyte and do not show signs of wear. Ruthenium layer is oxidized in the electrochemical process, but this effect does not reduce the current due to a high conductivity of the ruthenium oxide. In the explosive mode, Ru and Ti electrodes are compared. Titanium structures start to produce explosions at  $U_{th} = 12$  V. The maximal voltage is reached in 18 min because of oxidation, and the test is stopped. Ruthenium electrodes generate explosions at the pulse amplitude of 10-12 V and operate more than 6 times longer than Ti structures. The limiting factor is the significant damage of the central electrode by explosive microbubbles. Based on the results obtained, Ru is considered a preferable electrode material for the fast electrochemical actuator.

### REFERENCES

1. Villarruel Mendoza L. A., Scilletta N. A., Bellino M. G., Desimone M. F., Catalano P. N., Recent advances in micro-electro-mechanical devices for controlled drug release applications. *Frontiers in Bioengineering and Biotechnology*. (2020) 827.
2. Yi Y., Buttner U., Carreno A. A., Conchouso D., Foulds I. G., A pulsed mode electrolytic drug delivery device. *Journal of Micromechanics and Microengineering*. 25 (10) 2015 105011.
3. Uvarov I. V., Lokhanin M. V., Postnikov A. V., Melenev A. E., Svetovoy V. B., Electrochemical membrane microactuator with a millisecond response time. *Sensors and Actuators B: Chemical*. 260 (2018) 12–20.
4. Uvarov I. V., Shlepakov P. S., Postnikov A. V., Svetovoy V. B., Highly energetic impact of H<sub>2</sub> and O<sub>2</sub> nanobubbles on Pt surface. *Journal of Colloid and Interface Science*. 582, (2021) 167–176.

5. **Szymansky A., Szymansky J.**, Hardness estimation of minerals, rocks and ceramic materials. Amsterdam: Elsevier Science Publishers, 1990.

6. **Shlepakov P. S., Uvarov I. V., Naumov V. V., Mazaletskiy L. A., Svetovoy V. B.**, Degradation of titanium electrodes in the alternating polarity electrolysis. Int. J. Electrochem. Sci, 1 (2019). 5211–5225.

7. **Ryden W. D., Lawson A. W., Sartain C. C.**, Electrical Transport Properties of IrO<sub>2</sub> and RuO<sub>2</sub>. Physical Review B. 1(4) (1970) 1494.

#### THE AUTHORS

**SHLEPAKOV Pavel**

p.shlepakov@bk.ru

ORCID: 0000-0002-1255-791X

**SVETOVOY Vitaliy**

svetovoy@yandex.ru

ORCID: 0000-0002-9649-5663

**UVAROV Ilia**

i.v.uvarov@bk.ru

ORCID: 0000-0002-6882-0625

*Received 14.07.2022. Approved after reviewing 19.07.2022. Accepted 08.09.2022.*

Conference materials

UDC 577.344

DOI: <https://doi.org/10.18721/JPM.153.252>

### Physicochemical analysis of bisretinoid A2E photooxidative destruction products

M. A. Yakovleva <sup>1</sup>, A. A. Vasin <sup>2</sup>✉, A. E. Dontsov <sup>1</sup>, A. A. Gulin <sup>2</sup>, A. V. Aybush <sup>2</sup>,  
T. B. Feldman <sup>1,3</sup>, M.A. Ostrovsky <sup>1,3</sup>

<sup>1</sup> Emanuel Institute of Biochemical Physics, RAS, Moscow, Russia;

<sup>2</sup> N.N. Semenov Federal Research Center for Chemical Physics, RAS, Moscow, Russia;

<sup>3</sup> Lomonosov Moscow State University, Moscow, Russia

✉ [a2vasin@yandex.ru](mailto:a2vasin@yandex.ru)

**Abstract.** Bisretinoid N-retinyl-N-retinylidene ethanolamine (A2E) of the retinal pigment epithelium (RPE) lipofuscin granules is a side product of visual cycle. Its accumulation is associated with degenerative diseases of the retina and retinal pigment epithelium. In this study A2E photooxidation and photodegradation products were studied. Absorption and 2D fluorescence spectra of these substances were detected. Time-of-flight secondary ion mass spectrometry (ToF-SIMS) and Fourier-transform infrared spectroscopy (FTIR) revealed chemical changes during the A2E photooxidation process. Aldehyde accumulation was observed and new structure one of the resulting compounds was proposed.

**Keywords:** Retinal pigment epithelium, bisretinoid A2E, photooxidation, carbonyls

**Funding:** Russian Science Foundation Grant 22-24-00549.

**Citation:** Yakovleva M. A., Vasin A. A., Dontsov A. E., Gulin A. A., Aybush A. V., Feldman T.B., Ostrovsky M.A., Physicochemical analysis of bisretinoid A2E photooxidative destruction products, St. Petersburg State Polytechnical University Journal. Physics and Mathematics. 15 (3.2) (2022) 285–290. DOI: <https://doi.org/10.18721/JPM.153.252>

This is an open access article under the CC BY-NC 4.0 license (<https://creativecommons.org/licenses/by-nc/4.0/>)

Материалы конференции

УДК 577.344

DOI: <https://doi.org/10.18721/JPM.153.252>

### Физико-химический анализ продуктов фотодеструкции бисретиноида А2Е

М. А. Яковлева <sup>1</sup>, А. А. Васин <sup>2</sup>✉, А. Е. Донцов <sup>1</sup>, А. А. Гулин <sup>2</sup>, А. В. Айбуш <sup>2</sup>,  
Т. Б. Фельдман <sup>1,3</sup>, М. А. Островский <sup>1,3</sup>

<sup>1</sup> Институт биохимической физики им. Н.М. Эмануэля РАН, г. Москва, Россия ;

<sup>2</sup> Федеральный исследовательский центр химической физики им. Н.Н. Семёнова РАН, г. Москва, Россия;

<sup>3</sup> Московский государственный университет им. М.В. Ломоносова, г. Москва, Россия

✉ [a2vasin@yandex.ru](mailto:a2vasin@yandex.ru)

**Аннотация.** Бисретиноид А2Е, содержащийся в липофусциновых гранул в клетках ретинального пигментного эпителия глаза является побочным продуктом зрительного цикла. Его накопление связано с дегенеративными заболеваниями сетчатки. В данной работе были изучены продукты фотоокисления и фотодеградаци А2Е, их флуоресцентные свойства, а также химические изменения в процессе фотоокисления. Обнаружено накопление соединений, содержащих альдегидную группу. Предложена новая структура одного из полученных соединений.

**Ключевые слова:** ретиновый пигментный эпителий, бисретиноид А2Е, фотоокисление, карбонилы

**Финансирование:** Российский Научный Фонд № 22-24-00549.

**Ссылка при цитировании:** Яковлева М. А., Васин А. А., Донцов А. Е., Гулин А. А., Айбуш А. В., Фельдман Т. Б., Островский М. А. Физико-химический анализ продуктов фотодеструкции бисретиноида А2Е // Научно-технические ведомости СПбГПУ. Физико-математические науки. Т. 15. № 3.2. С. 285–290. DOI: <https://doi.org/10.18721/JPM.153.252>

Статья открытого доступа, распространяемая по лицензии CC BY-NC 4.0 (<https://creativecommons.org/licenses/by-nc/4.0/>)

### Introduction

*N*-retinyl-*N*-retinylidene ethanolamine (A2E) is the main bisretinoid of the lipofuscin granules (LGs) in the retinal pigment epithelium cells. It is the side product of the visual cycle. A2E biogenesis occurs when two molecules of *all*-trans retinal condense with one molecule of phosphatidylethanolamine in the photoreceptor membrane, followed by uptake into RPE and conversion to stable pyridinium bisretinoid [1]. In the RPE, LGs are formed by incomplete lysosomal degradation of photoreceptor outer segment debris following phagocytosis of shed outer segments by RPE cells. LGs accumulate in the RPE of the human eye during aging, particularly in patients with hereditary diseases [2,3] and progressive age-related macular degeneration (AMD) [4].

A2E and its photooxidation and photodegradation products (A2Eox,deg) are major sources of LG fluorescence. The compounds investigated in LGs include A2E [5], A2Eox,deg [6–7] and a series of *all*-trans retinal conjugates [8]. It is known, that A2E is a photoinducible generator of reactive oxygen species (ROS) [9–10] and able to damage cellular structures *in situ* [11–12].

Earlier we demonstrated [13], the LG photooxidation results in the formation of toxic water-soluble thiobarbituric acid (TBA)-reactive products. However, the nature of these products is not fully understood. There is evidence that the source of TBA-reactive products are the lipid peroxidation end-products, i.e., highly reactive electrophilic aldehydes like malondialdehyde (MDA) and 4-hydroxynonenal (HNE) in LGs, that suggests a connection between its formation and increased oxidative stress [14]. We assume that the source of highly active aldehydes and ketones may be A2Eox,deg in LGs [13].

Thus, the main goal of this work is to characterize the A2Eox,deg using the 2D fluorescence spectroscopy and time-of-flight secondary ion mass spectrometry (ToF-SIMS).

### Materials and Methods

**A2E synthesis and photooxidation.** A2E was synthesized from *all*-trans retinal and ethanolamine in acetic acid and ethanol, as described previously [15]. A2E purity was monitored by high performance liquid chromatography (HPLC) [13]. A2E concentration was determined spectrally using a Shimadzu UV-1700 spectrophotometer (Japan) at a wavelength of 430 nm with  $\epsilon = 3.1 \cdot 10^4 \text{ M}^{-1} \cdot \text{cm}^{-1}$ . For photooxidative destruction, 0.4 ml of A2E in methanol (with concentration of 1.8 mM) was irradiated for 120 min at room temperature under constant stirring using a 150 W incandescent lamp with a heat filter (KGM 24-150, 400–700 nm). The luminous flux density irradiating the sample was  $80 \text{ mWm}^{-2}$  for visible light (400–700 nm), as determined by a photometer (Spectra-Physics 407A, USA).

**Spectroscopy.** Absorption spectra were recorded on a Shimadzu 3600 UV–vis near-infrared spectrophotometer (Japan). Fluorescence data were recorded on a Horiba Fluoromax. 2D analysis was performed with excitation wavelength step 2 nm. IR spectra were taken with a Fourier IR (FTIR) microscope LUMOS II (Bruker) in ATR mode. The samples were applied dropwise to CaF<sub>2</sub> glass and dried in an argon atmosphere before analysis.

**Mass spectrometry.** Time-of-flight secondary ion mass spectrometry (ToF-SIMS) (ION-ToF, Germany) with 30 keV Bi<sub>3</sub><sup>+</sup> primary ions were used to detect A2E photooxidation products. 10 spectra were recorded from different regions for each sample.

## Results and Discussion

A large number of products of A2E photooxidation and photodegradation are formed when A2E is irradiated with visible light. Previously we have shown using HPLC analysis the formation of these products [7, 16]. Fig. 1a demonstrates absorption spectra of synthesized A2E before and after irradiation by visible light. It is clearly seen that during irradiation there is a decrease in absorption in the region of 430 nm, and an increase in the region of 280 nm. These results are in good agreement with the literature data [7, 13, 17].

2D fluorescence map spectra were collected for non-irradiated (Fig 1,b) and irradiated A2E (Fig. 1,c). Three fluorescence sites detected for the non-irradiated A2E: excitation at 263 nm with emission at 580 nm; two excitations at 340 and 440 nm with emission at 610 nm (Fig 1b). These excitation maxima are in good accordance with absorption spectra. However, excitation at 263 nm is not clearly expressed in the absorption spectrum. Interestingly, the UV excitation site has a much larger extinction coefficient and a large Stokes shift. Probably, such shift is present due to the existence of pyridinium in A2E. Pyridinium is known to form a fluorescent complex with charge transfer [18].

Blue shift of fluorescence emission sites were observed for A2E irradiated. Two fluorescence sites of A2E irradiated showed up: excitation at 270 nm with emission at 470 nm, excitation at 370 nm with emission at 460 nm (Fig 1c). The fluorescence profile shows that the emission maxima in the area  $< 500$  nm, which are likely associated with the fluorescence of A2E oxidized products. This is probably due to the destruction of the original A2E conjugated structure and the accumulation of oxidation products with a shorter conjugated structure.

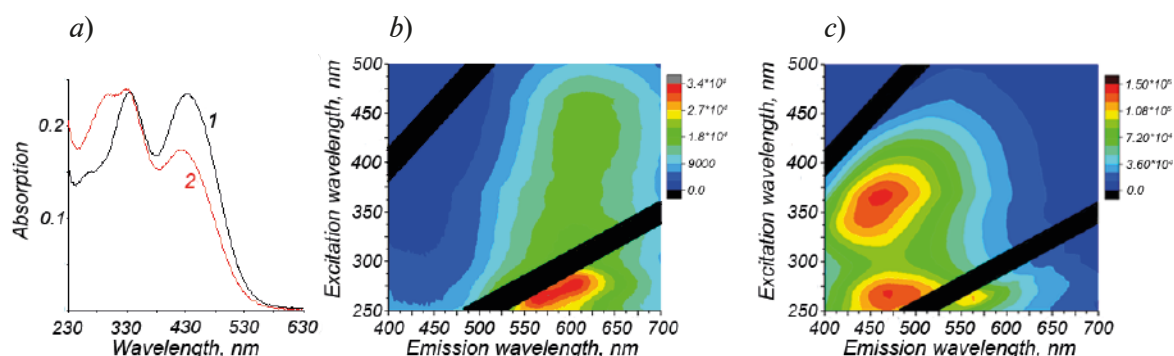


Fig. 1. Absorption spectra before and after irradiation (a); fluorescence profiles of unirradiated A2E (b); fluorescence profiles of A2E irradiated by visible light (c).

The color of the area is responsible for the fluorescence intensity from blue (no fluorescence observed) to red (maximum fluorescence signal)

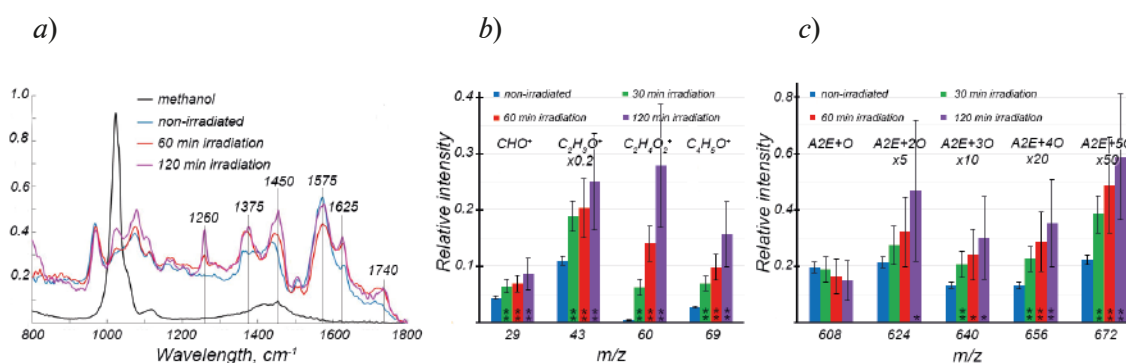


Fig. 2. Chemical changes during oxidation: IR-spectra of unirradiated A2E (blue), A2E after irradiation for 60 min (red) and A2E after irradiation for 120 min (purple) (a), the spectrum of the solvent (methanol) is also shown (black); oxidized A2E formation after light exposure revealed by ToF-SIMS (b), the intensities of all ions were normalized to the ion intensity with  $m/z$  592 (A2E); formation of ions containing carbonyl groups after light exposure revealed by ToF-SIMS (c)

Data are presented as means  $\pm$ SD from 9 independent experiments. \* $p < 0.05$ ; \*\* $p < 0.005$

A2E was irradiated during 30 min, 60 min and 120 min for chemical changes observation. IR spectrum were collected for irradiated and non-irradiated A2E samples (Fig. 2). IR spectra of methanol were received to exclude solvent bands.

The band at  $1740\text{ cm}^{-1}$  could be attributed to the stretching vibrations of the carbonyl group. The bands at  $1375$  and  $1450\text{ cm}^{-1}$  are probably deformational bands of  $\text{CH}_3\text{C(O)-}$  and  $-\text{CH}_2\text{C(O)-}$ , respectively. The band at  $1625\text{ cm}^{-1}$  is probably related to the presence of the pyridine ring. Band  $1260\text{ cm}^{-1}$  is expected epoxy group. Growing bands at  $1740\text{ cm}^{-1}$  identified the aldehyde accumulation. It was also confirmed by the growth of deformation bands at  $1375\text{ cm}^{-1}$  and  $1450\text{ cm}^{-1}$ . Wider band at  $1740\text{ cm}^{-1}$  for the 60 min irradiated sample indicates presence unsaturated conjugate aldehyde in middle of oxidation act. Significant difference was observed for IR band  $1260\text{ cm}^{-1}$ . It could be result in epoxides accumulation during photooxidation process. Thus, formation of both the oxidation products of A2E epoxides and furanoids and the products of their further destruction – aldehydes and ketones were demonstrated.

Using ToF-SIMS relative intensities of A2E oxidized forms were obtained before and after exposure of A2E by light. It can be seen, that during the photooxidation process, the amount of oxidized A2E forms such as A2E+2O, A2E+3O, A2E+4O, A2E+5O A2E increases by about 3 times relative to non-irradiated A2E. These results are the evidence of the accumulation of A2E oxidized forms during irradiation, which contributes to further oxidative degradation. The A2E+O ion intensity ( $m/z$  608) decreases during the oxidation process, because it gradually oxidizes more strongly, turning into compounds with a mass of 624, 656 and 672 (Fig. 2,b). The formation of oxygen-containing products such as epoxides, peroxides, ketones, and aldehydes, was revealed by ToF-SIMS analysis of characteristic fragment ions containing carbonyl groups (Fig. 2,c). There was a significant increase in carbonyl ions after exposure A2E to light as it can be seen in the diagram. For example, the ion with  $m/z = 60$  ( $\text{C}_2\text{H}_4\text{O}_3^+$ ) increase is particularly significant (about 100 times). Based on the data obtained and the A2E structure, an ion with  $m/z = 205.07$  was identified ( $\text{C}_{11}\text{H}_{11}\text{NO}_3^+$ ), assuming it is an aldehyde. The exact mechanism of oxidative degradation of A2E has not yet been described. However, the A2E tail groups show significant similarity to carotenoids. Therefore, the mechanism of ion formation with  $m/z$  205 may be similar to the mechanism of carotenoid oxidation [19]. Fig. 3 represents the proposed scheme of the product with  $m/z = 205.07$  formation.

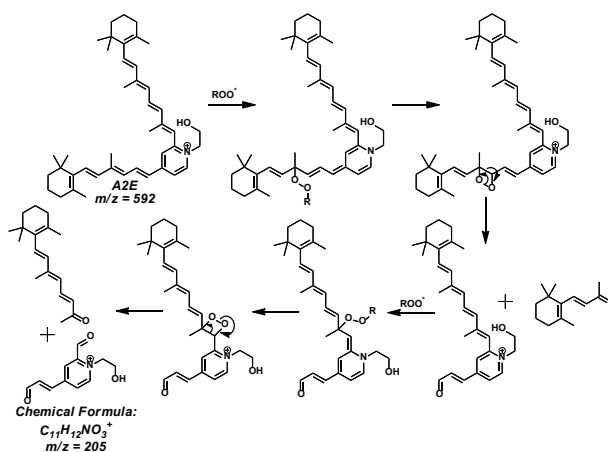


Fig. 3. The proposed scheme of A2E oxidative degradation resulting in formation of aldehyde product with  $m/z = 205.07$

### Conclusion

The photooxidation of A2E leads to generation of highly reactive products containing aldehyde groups. We have previously shown that as a result of visible light exposure of LG aldehydes are accumulated in them in a free state and are able to diffuse from the LG into the cytoplasm of the RPE cell [13, 17]. Obtained results allow us to propose other mechanism of cytotoxic action of LGs. A2E, which is the side product of the visual cycle, can also be a source of such compounds in addition to lipid peroxidation products.



## REFERENCES

1. **Wolf G.**, Lipofuscin and macular degeneration. *Nutrition Reviews*. 61 (2003) 342–346.
2. **Sparrow J.R., Boulton M.E.**, RPE lipofuscin and its role in retinal pathobiology. *Experimental Eye Research*. 80 (2005) 595–606.
3. **Feeney L.**, The phagosomal system of the pigment epithelium: a key to retinal disease, *Investigative Ophthalmology & Visual Science*. 12 (1973) 635–638.
4. **Holz F.G., Pauleikhoff D., Klein R., Bird A.C.**, Pathogenesis of lesions in late age-related macular disease, *American Journal of Ophthalmology*. 137 (2004) 504–510.
5. **Lamb L.E., Simon J.D.**, A2E: a component of ocular lipofuscin, *Photochemistry and Photobiology*. 79 (2004) 127–136.
6. **Ben-Shabat S., Itagaki Y., Jockusch S., Sparrow J.R., Turro N.J., Nakanishi K.**, Formation of a nona-oxirane from A2E, a lipofuscin fluorophore related to macular degeneration, and evidence of singlet oxygen involvement, *Angewandte Chemie International Edition*. 41 (2002) 814–817.
7. **Yakovleva M.A., Sakina N.L., Kononikhin A.S., Feldman T.B., Nikolaev E.N., Dontsov A.E., Ostrovsky M.A.**, Detection and study of the products of photooxidation of N-Retinyldene-N-retinylethanolamine (A2E), the fluorophore of lipofuscin granules from retinal pigment epithelium of human donor eyes, *Doklady Biochemistry and Biophysics*. 409 (2006) 223–225.
8. **Kim S.R., Jang Y.P., Jockusch S., Fishkin N.E., Turro N.J., Sparrow J.R.**, The all-trans-retinal dimer series of lipofuscin pigments in retinal pigment epithelial cells in a recessive Stargardt disease model, *Proceedings of the National Academy of Sciences*. 104 (2007) 19273–19278.
9. **Boulton M., Dontsov A., Jarvis-Evans J., Ostrovsky M., Svistunencko D.**, Lipofuscin is a photoinducible free radical generator, *Journal of Photochemistry and Photobiology B*. 19 (1993) 201–204.
10. **Sparrow J.R., Boulton M.**, RPE lipofuscin and its role in retinal pathobiology, *Experimental Eye Research*. 80 (2005) 595–606.
11. **Dontsov A.E., Sakina N.L., Golubkov A.M., Ostrovsky M.A.**, Light-induced release of A2E photooxidation toxic products from lipofuscin granules of human retinal pigment epithelium, *Doklady Biochemistry and Biophysics*. 425 (2009) 98–101.
12. **Sparrow J.R., Vollmer-Snarr H.R., Zhou J., Jang Y.P., Jockusch S., Itagaki Y., Nakanishi K.**, A2E-epoxides damage DNA in retinal pigment epithelial cells. Vitamin E and other antioxidants inhibit A2E-epoxide formation, *Journal of Biological Chemistry*. 278 (2003) 18207–18213.
13. **Yakovleva M., Dontsov A., Trofimova N., Sakina N., Kononikhin A., Aybush A., Gulin A., Feldman T., Ostrovsky M.**, Lipofuscin granule bisretinoid oxidation in the human retinal pigment epithelium forms cytotoxic carbonyls, *International Journal of Molecular Sciences*. 23 (2022) 222.
14. **Schutt F., Bergmann M., Holz F.G., Kopitz J.**, Proteins modified by malondialdehyde, 4-hydroxynonenal, or advanced glycation end products in lipofuscin of human retinal pigment epithelium. *Investigative Ophthalmology & Visual Science*. 44 (2003) 3663–3668.
15. **Adler L. 4<sup>th</sup>., Boyer N.P., Anderson D.M., Spraggins J.M., Schey K.L., Hanneken A., Ablonczy Z., Crouch R.K., Koutalos Y.**, Determination of N-retinyldene-N-retinylethanolamine (A2E) levels in central and peripheral areas of human retinal pigment epithelium, *Photochemical & Photobiological Sciences*. 14 (11) (2015) 1983–1990.
16. **Feldman T.B., Yakovleva M.A., Arbukhanova P.M., Borzenok S.A., Kononikhin A.S., Popov I.A., Nikolaev E.N., Ostrovsky M.A.**, Changes in spectral properties and composition of lipofuscin fluorophores from human retinal pigment epithelium with age and pathology, *Analytical and Bioanalytical Chemistry*. 407 (2015) 1075–1088.
17. **Dontsov A., Yakovleva M., Trofimova N., Sakina N., Gulin A., Aybush A., Gostev F., Vasin A., Feldman T., Ostrovsky M.**, Water-soluble products of photooxidative destruction of the bisretinoid A2E cause proteins modification in the dark. *International Journal of Molecular Sciences*. 23 (2022) 1534.
18. **Kosower E. M., Skorcz, J. A.**, Pyridinium Complexes. III. Charge-Transfer Bands of Polyalkylpyridinium Iodides, *Journal of the American Chemical Society*. 82 (9) (1960) 2195–2203.
19. **Mordi R. C., Walton J. C.**, Identification of products from canthaxanthin oxidation, *Food Chemistry*. 197 (2016) 836–840.

## THE AUTHORS

**YAKOVLEVA Marina**

lina.invers@gmail.com

ORCID: 0000-0003-4243-2787

**VASIN Alexander**

a2vasin@yandex.ru

ORCID: 0000-0003-0152-3391

**DONTSOV Alexander**

adontsovnick@yahoo.com

ORCID: 0000-0002-8367-5008

**GULIN Alexander**

aleksandr.gulin@phystech.edu

ORCID: 0000-0001-7117-4276

**AYBUSH Arseny**

aiboosh@gmail.com

ORCID: 0000-0002-0496-9105

**FELDMAN Tatiana**

feldmantb@mail.ru

ORCID: 0000-0003-2613-056X

**OSTROVSKY Mikhail**

ostrovsky3535@mail.ru

ORCID: 0000-0003-4350-2812

*Received 15.07.2022. Approved after reviewing 17.07.2022. Accepted 19.07.2022.*

## BIOPHYSICS AND MEDICAL PHYSICS

Conference materials

UDC 539.192

DOI: <https://doi.org/10.18721/JPM.153.253>

### **Peculiarity of electron density calculation during interaction of ultrashort laser pulse with nitrogenous base of DNA molecule adenine**

A. A. Kharlamova <sup>1</sup>✉, D. N. Makarov <sup>1</sup>

<sup>1</sup> Northern (Arctic) Federal University named after M.V. Lomonosov, Arkhangelsk, Russia

✉ [kharlamova.anastasya2015@yandex.ru](mailto:kharlamova.anastasya2015@yandex.ru)

**Abstract.** Today, ultrashort laser pulses are used to study and analyze biomolecules. Their advantages over X-rays lie in the speed of measurement and accuracy, which allows studying the structure of a molecule on a time scale commensurate with the time of various biochemical processes in it. However, the practical possibility of studying chemical and biological processes in facilities using existing and promising X-ray free-electron lasers requires the development of a theory of the interaction of laser pulses with matter. In this article we will consider the interaction of an ultrashort laser pulse (USPs) with the base of the DNA (Deoxyribonucleic acid) molecule - adenine. In more detail we will consider the calculation of the photon birth probability, after the interaction of the pulse with the molecule. We will build a model of the base of the molecule and propose a method for calculating the electron density for the case when the substance has a different elemental composition.

**Keywords:** Deoxyribonucleic acid, ultrashort laser pulse, photon, electron density, elemental composition

**Funding:** The research was supported by State Task of the Russian Federation FSRU-2021-0008.

**Citation:** Kharlamova A. A., Makarov D. N., Peculiarity of electron density calculation during interaction of ultrashort laser pulse with nitrogenous base of DNA molecule adenine, St. Petersburg State Polytechnical University Journal. Physics and Mathematics. 15 (3.2) (2022) 291–295. DOI: <https://doi.org/10.18721/JPM.153.253>

This is an open access article under the CC BY-NC 4.0 license (<https://creativecommons.org/licenses/by-nc/4.0/>)

Материалы конференции

УДК 539.192

DOI: <https://doi.org/10.18721/JPM.153.253>

### **Особенность расчета электронной плотности при взаимодействии ультракороткого лазерного импульса с азотистым основанием молекулы ДНК аденином**

A. A. Харламова <sup>1</sup>✉, Д. Н. Макаров <sup>1</sup>

<sup>1</sup> Северный (Арктический) федеральный университет им. М.В. Ломоносова, г. Архангельск, Россия

✉ [kharlamova.anastasya2015@yandex.ru](mailto:kharlamova.anastasya2015@yandex.ru)

**Аннотация.** Сегодня применяются для изучения и анализа биомолекул ультракороткие лазерные импульсы. Их преимущества по сравнению с рентгеновским излучением заключается в быстроте измерения и точности. Однако, практическая возможность изучения химических и биологических процессов требует разработки теории взаимодействия лазерных импульсов с веществом. В данной статье мы рассмотрим взаимодействие ультракороткого лазерного импульса (УКИ) с основанием молекулы ДНК - аденином. Подробнее рассмотрим расчет вероятности рождения фотона, предложим способ расчета электронной плотности для случая, когда вещество имеет разный элементный состав.

**Ключевые слова:** Дезоксирибонуклеиновая кислота, ультракороткий лазерный импульс, фотон, электронная плотность, элементный состав

**Финансирование:** Исследование выполнено при поддержке государственного задания Российской Федерации № FSRU-2020-0008.

**Ссылка при цитировании:** Харламова А. А., Макаров Д. Н. Особенность расчета электронной плотности при взаимодействии ультракороткого лазерного импульса с азотистым основанием молекулы ДНК аденином // Научно-технические ведомости СПбГПУ. Физико-математические науки. Т. 15. № 3.2. С. 291–295. DOI: <https://doi.org/10.18721/JPM.153.253>

Статья открытого доступа, распространяемая по лицензии CC BY-NC 4.0 (<https://creativecommons.org/licenses/by-nc/4.0/>)

## Introduction

Imaging techniques from diffraction data obtained using ultrashort laser pulses are being actively developed for applications in nanotechnology and structural biology. Methods of X-ray diffraction analysis of matter (XRD) as well as X-ray crystallography (XRC) are well studied and underlie many modern discoveries in physics, chemistry, biology, medicine [1,2]. The structure of a molecule is determined from the time-domain infinite plane wave scattering spectrum [1,2]. But recently scientists have started to apply ultrashort laser pulses for investigation. In this case the scattering spectrum moves into the femto and atto-second time range, which is poorly understood up to now.

The use of (USPs) to analyze the structure of molecules is a very promising area of research. As noted, ultrashort laser pulses (USPs) operate on a small time scale. This is very convenient for the description of organic structures, as such materials can be both stationary and non-stationary. Non-stationary objects, such as DNA, for example, can only be studied using (USPs), because the characteristic time in such systems is smaller or comparable to the femtosecond time scale. The non-stationarity in them may be caused by the formation and rearrangement of chemical bonds, intra-atomic and molecular processes, etc. [3].

Experimental studies of molecules using (USPs) on European X-Ray Free Electron Laser (XFEL) are already in progress [3]. The technique of introducing the molecules into the X-ray beam (e.g. XFEL) is being actively researched and improved. In order to analyse the experimentally obtained data, theoretical descriptions of the interaction processes between (USPs) and biostructures are urgently needed.

So far, a lot of theoretical studies on the specificity of scattered (USPs) on various multi-atomic systems have been carried out. However, despite this fact the theoretical base is still weak and does not take into account all specific features of diffuse (USPs).

In this paper we will consider the DNA molecule as a promising and poorly studied biomolecule at the atomic level. The molecule stores biological information in the form of a genetic code consisting of a sequence of nucleotides. Consequently, a defect on a nucleotide can indicate the presence of a defect in the molecule. In [4] we considered the interaction of an ultrashort laser pulse with a DNA molecule in a simplified form, considering each nucleotide as a separate unit of matter, within the whole molecule. We now focus in detail on a single nucleotide with the nitrogenous base adenine. The difficulty of the new calculation is that now it is necessary to take into account the elemental composition of the molecule. It is possible to take it into account through the electron density of the molecule, which we will consider in this work.

In the following, the atomic system of units will be used, where  $\hbar = 1$ ,  $|e| = 1$ ,  $m_e = 1$ .

## Materials and Methods

A nucleotide is a compound of a phosphate group, a carbohydrate, and a nitrogenous base – adenine. Let us imagine it as an arbitrary polyatomic system, on which the (USPs) falls in the direction  $n_0$ . The duration of such a pulse will be considered much less than the characteristic atomic time  $\tau_a = 1$ , i.e.,  $\tau/\tau_a = 1$ . This will allow us to use the sudden perturbation approximation.



In this approximation, the proper Hamiltonian of the system can be neglected, since the electron in the atom does not have time to evolve under the action of the atom's field due to the too fast interaction of the momentum with the electron in the atom [5]. It should be added that the condition  $\tau/\tau_a = 1$  for using our approximation is not strict. To do this, it is sufficient to assume, as was shown in [5], that,  $\omega_0\tau_a = 1$ , where  $\omega_0$  is the carrier frequency of the incident (USPs). Obviously, the condition  $\omega_0\tau_a = 1$  holds for X-ray frequencies. The intensity of the electromagnetic field of the (USPs)  $\tilde{\mathbf{E}}(\mathbf{r}, t)$  is considered in general terms, i.e., we will consider it to depend on the coordinates and time. We are interested in electromagnetic fields that are not strong enough to account for relativistic effects. As was obtained in [6], taking into account these approximations, the probability of the birth of a photon  $W$  of a given frequency  $\omega$  per unit solid angle  $\Omega$  with the simultaneous transition of the polyatomic system from the ground state to all possible final states (hereinafter, the scattering spectrum of the USPs)

$$\frac{d^2W}{d\omega d\Omega} = \frac{1}{(2\pi)^2} \frac{1}{c^3 \omega} (N_a N_b G(\omega, \mathbf{n}, \mathbf{n}_0) + \delta_N(\mathbf{p})(N_b - 1)F(\omega, \mathbf{n}, \mathbf{n}_0)), \quad (1)$$

where  $N_a$  is the total number of atoms in the system,  $N_b$  is the number of electrons in the atom,  $\mathbf{n}$  is the speed of light,  $G(\omega, \mathbf{n}, \mathbf{n}_0)$  is the direction of escape of the born photon,  $F(\omega, \mathbf{n}, \mathbf{n}_0)$  and the mean values expressed in terms of electron density  $\rho(\mathbf{r})$  as

$$G(\omega, \mathbf{n}, \mathbf{n}_0) = \frac{1}{N_b} \int \rho(\mathbf{r}) |\mathbf{f}(\mathbf{r})|^2 d\mathbf{r}, \quad (2)$$

$$F(\omega, \mathbf{n}, \mathbf{n}_0) = \frac{1}{N_b} \left| \int \rho(\mathbf{r}) \mathbf{f}(\mathbf{r}) e^{-i\mathbf{k}\mathbf{r}} d\mathbf{r} \right|^2, \quad (3)$$

where  $\mathbf{k} = \mathbf{n}\omega/c$ ,  $\mathbf{f}(\mathbf{r}_a) = [\tilde{\mathbf{E}}(\omega) \times \mathbf{n}]$ ,

$$\tilde{\mathbf{E}}(\omega) = \int_{-\infty}^{+\infty} \left( \mathbf{E}(\mathbf{r}_{a,e}, t) - \frac{1}{2} \nabla_a \left( \frac{\mathbf{E}(\mathbf{r}_{a,e}, t)}{c} \right)^2 \right) e^{i\omega t} dt,$$

where  $\nabla_{a,e} = \frac{\partial}{\partial \mathbf{r}_{a,e}}$ .

Furthermore,  $\delta N(\mathbf{p})$  in (2) is a factor which completely determines the geometrical arrangement of the atoms in the target, which is calculated in general form

$$\delta_N(\mathbf{p}) = \sum_{a,b} e^{i\mathbf{p}(\mathbf{R}_a - \mathbf{R}_b)} = \left| \sum_a e^{i\mathbf{p}\mathbf{R}_a} \right|^2. \quad (4)$$

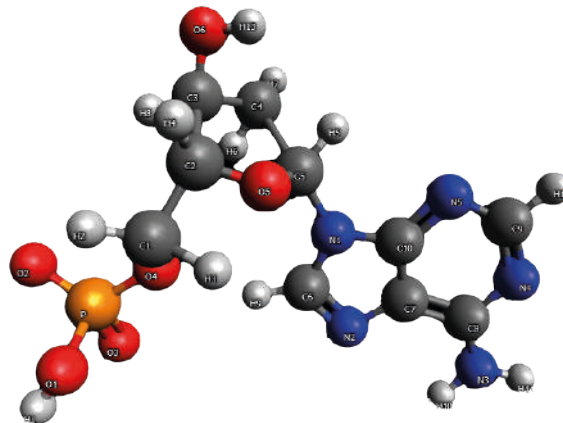


Fig. 1. 3D model of the nucleotide: C corresponds to carbohydrate, N to nitrogen, O to oxygen, P to phosphorus, H to hydrogen  
[source: Avogadro software]

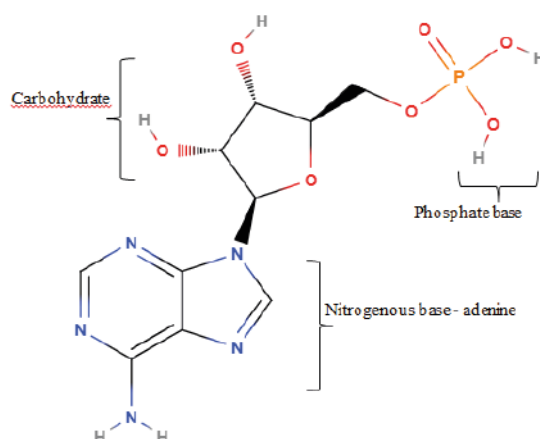


Fig. 2. Arrangement of atoms in a nucleotide: C corresponds to carbohydrate, N to nitrogen, O to oxygen, P to phosphorus, H to hydrogen [source: Avogadro software]

The summation in (3) is carried out for all atoms of the system in question. The electron density can be taken in different models. We will use the Dirac–Hartree–Fock–Slater model from [7]:

$$\rho(r) = \frac{N_e}{4\pi r} \sum_{i=1}^3 A_i \alpha_i^2 e^{-\alpha_i r},$$

where  $A_i$ ,  $\alpha_i$  are the table coefficients giving the electron density in the atom [7]. In our case we cannot use this form of electron density since the base of the molecule consists of different elements. Let us present a 3D model of the nucleotide (Fig. 1.). Using the given distances of 1.372 Å between the elements and their coordinates in space we will find the electron density.

In general, phosphate consists of 5 atoms bonded together by covalent bonds. The covalent radius of oxygen is 73 pm, the radius of the atomic nucleus is 3.27 fm, for phosphorus respectively 106 pm and 3.27 fm. The radius of the atomic nucleus is calculated as  $r = A^{1/3}$ , where A is the number of nucleons. We can assume that the nuclei of atoms are at a distance many times larger than their own radius.

### Results and Discussion

Let us set in Avogadro the coordinates of all elements. Then the electron density of the phosphate group will take the form.

$$\rho(\mathbf{r}_{ph}) = \rho_1(\mathbf{r}_1) + \rho_2(\mathbf{r}_2) + \rho_3(\mathbf{r}_3) + \rho_4(\mathbf{r}_4) + \rho(\mathbf{r}_i), \quad (5)$$

where  $\rho_i$  is the electron of the relevant element

$$\rho_1(\mathbf{r}_1) = \frac{N_e}{4\pi(r)} A_p \alpha_p^2 e^{-\alpha_p r}. \quad (6)$$

We will use the following data for further calculations (Table 1).

Then the expression  $G_i(\omega, \mathbf{n}, \mathbf{n}_0)$  for each atom, taking formula (4) into account, will take the form:

$$G_i(\omega, \mathbf{n}, \mathbf{n}_0) = \frac{1}{N_e} \int \rho_i(\mathbf{r}) |\mathbf{f}(\mathbf{r})|^2 d\mathbf{r}, \quad (7)$$

For the whole phosphate group, let us do the summation:

$$G_{ph}(\omega, \mathbf{n}, \mathbf{n}_0) = \sum_{i=1}^5 G_i(\omega, \mathbf{n}, \mathbf{n}_0), \quad (8)$$

Using this model it is possible to find expressions  $G_i(\omega, \mathbf{n}, \mathbf{n}_0)$  for and go on to further calculate the interaction of USPs with the molecule.



Table 1

**Distribution of atoms at the base  
of adenines by coordinates**

Number	Element	X(A)	Y(A)	Z(A)
Atom 1	H	-1.547	9.377	-1.216
Atom 2	O	-1.44	8.896	-0.401
Atom 3	P	0.038	8.907	0.116
Atom 4	O	0.220	10.175	0.734
Atom 5	O	0.790	8.733	-1.239
...				
Atom 34	H	2.147	0.165	2.718
Atom 35	H	1.815	6.312	5.385

**Conclusion**

The paper considers the probability of photon emission of a given frequency during the interaction of USPs with the nitrogenous base of DNA molecule, adenine. The peculiarities of the calculation of complex molecule with different elemental chemical composition were pointed out. A method of quantitative finding of electron density to refine the probability calculation is proposed.

**Acknowledgments**

The research was supported by the state task of the Russian Federation No. FSRU-2021-0008.

**REFERENCES**

1. **Suryanarayana C., Norton M.**, X-Ray Diffraction: A Practical Approach. Springer Science & Business Media. ISBN 9781489901484.
2. **Poletto F.C.**, Optical Technologies for Extreme-Ultraviolet and Soft X-ray Coherent Sources, Springer-Verlag Berlin Heidelberg, 2015.
3. **Zewail A.**, Voyage through Time: Walks of Life to the Nobel Prize. — World Scientific, 2002.
4. **Makarov D.N., Kharlamova A.A.**, Scattering of ultrashort electromagnetic field pulses by biomolecules, AIP Conference Proceedings 2313, 030070, 2020.
5. **Goshev A.A., Eseev M.K., Makarov D.N.**, Scattering of Attosecond Electromagnetic Field Pulses by Molecular Anions Including the Magnetic Field Component, J. Exp. Theor. Phys. 130 (1), 28–34, 2020.
6. **Eseev M.K., Goshev A.A., Makarov D.N.**, Scattering of Ultrashort X-ray Pulses by Various Nanosystems, Nanomaterials, 10(7), 1355, 2020.
7. **Salvat F., Martinez J. D., Mayol R., Parellada J.**, Analytical Dirac-Hartree-Fock-Slater screening function for atoms ( $Z = 1-92$ ), Phys. Rev. A, 36 (2), 467–474, 1987.

**THE AUTHORS**

**KHARLAMOVA Anastasya**  
Kharlamova.anastasya2015@yandex.ru  
ORCID: 0000-0002-8192-615X

**MAKAROV Dmitry**  
d.makarov@narfu.ru  
ORCID: 0000-0003-1999-1433

*Received 11.07.2022. Approved after reviewing 24.07.2022. Accepted 25.07.2022.*

Conference materials

UDC 53.082

DOI: <https://doi.org/10.18721/JPM.153.254>

## Development of a control algorithm for a fluid flow monitoring system in a microfluidic system

E. D. Serov <sup>1,2✉</sup>, A. I. Kavalier <sup>1,2</sup>, V. A. Kruglov <sup>2</sup>,  
V. S. Reznik <sup>2</sup>, A. S. Saraev <sup>2</sup>, V. V. Davydov <sup>1,3</sup>

<sup>1</sup> Peter the Great St. Petersburg Polytechnic University, St. Petersburg, Russia;

<sup>2</sup> Institute for Analytical Instrumentation of the Russian Academy of Sciences, St. Petersburg, Russia;

<sup>3</sup> All-Russian Research Institute of Phytopathology, Moscow Region, Russia

✉ [egorserov22021998@gmail.com](mailto:egorserov22021998@gmail.com)

**Abstract.** Microfluidic systems are widely used in the preparation and analysis of liquid samples in biology, pharmacology and medicine. Each individual device using microfluidic systems differs in structure from others, and the accuracy of fluid control inside is an important factor. In this paper, we will consider the microfluidic system of a DNA analyzer. An algorithm that reads information from flow sensors in real time and transfers it to microcontroller STM32 has been developed for it. The received information was further processed, and on the basis of the received data, a conclusion was drawn about the correctness of the work performed by the device. The error handler, in case of deviation from the process, made the necessary adjustments by sending an error code to the necessary part of the device.

**Keywords:** Microfluidic system, control algorithm, fluid control, flow sensor, DNA analysis

**Funding:** The work was carried out within the framework of State Task 075-00761-22-00 of the Ministry of Science and Higher Education.

**Citation:** Serov E. D., Kavalier A. I., Kruglov V. A., Reznik V. S., Saraev A. S., Davydov V. V., Development of a control algorithm for a fluid flow monitoring system in a microfluidic system, St. Petersburg State Polytechnical University Journal. Physics and Mathematics. 15 (3.2) (2022) 296–301. DOI: <https://doi.org/10.18721/JPM.153.254>

This is an open access article under the CC BY-NC 4.0 license (<https://creativecommons.org/licenses/by-nc/4.0/>)

Материалы конференции

УДК 53.082

DOI: <https://doi.org/10.18721/JPM.153.254>

## Разработка алгоритма контроля системы мониторинга потока жидкости в микрофлюидной системе

Е. Д. Серов <sup>1,2✉</sup>, А. И. Кавалер <sup>1,2</sup>, В. А. Круглов <sup>2</sup>,  
В. С. Резник <sup>2</sup>, А. С. Сараев <sup>2</sup>, В. В. Давыдов <sup>1,3</sup>

<sup>1</sup> Санкт-Петербургский Политехнический Университет Петра Великого, Санкт-Петербург, Россия;

<sup>2</sup> Институт Аналитического Приборостроения Российской Академии Наук, Санкт-Петербург, Россия;

<sup>3</sup> Всероссийский Научно-Исследовательский Институт Фитопатологии, Московская область, Россия

✉ [egorserov22021998@gmail.com](mailto:egorserov22021998@gmail.com)

**Аннотация.** В данной работе рассматривается микрофлюидная система анализатора ДНК. Для нее был разработан алгоритм, считывающий информацию с датчиков потока в режиме реального времени и передающий ее на микроконтроллер STM32. Полученная информация подвергается дальнейшей обработке и на основании полученных данных делается вывод о правильности работы прибора. Обработчик ошибок при необходимости вносит необходимые коррективы, отправляя код ошибки в нужную часть устройства.



**Ключевые слова:** Микрофлюидная система, алгоритм контроля, контроль потоков, датчик потока, анализ ДНК

**Финансирование:** Работа выполнена в рамках Госзадания 075-00761-22-00 Минобрнауки РФ.

**Ссылка при цитировании:** Серов Е. Д., Кавалер А. И., Круглов В. А., Резник В. С., Сараев А. С., Давыдов В. В. Разработка алгоритма контроля системы мониторинга потока жидкости в микрофлюидной системе // Научно-технические ведомости СПбГПУ. Физико-математические науки. Т. 15. № 3.2. С. 296–301. DOI: <https://doi.org/10.18721/JPM.153.254>

Статья открытого доступа, распространяемая по лицензии CC BY-NC 4.0 (<https://creativecommons.org/licenses/by-nc/4.0/>)

## Introduction

At present, with the development of scientific and technological progress, much attention is paid to various research methods [1–8]. This is especially true in the context of an increase in the influence of various negative factors on biological systems [8–14]. Therefore, for the study of biological systems, as well as condensed media associated with them, a large number of methods have been developed [2–5, 7–9, 15–21]. They have various advantages and disadvantages. This determines their direct application.

The sequencing method of DNA is currently extremely demand for solving of the different tasks in medicine and biology [22–27]. For example, sequencing methods widely used in different medical researchers related with viruses and diseases.

Thus, in sequencing devices, it is necessary to transfer a given volume of liquid at a given speed for the correct analysis.

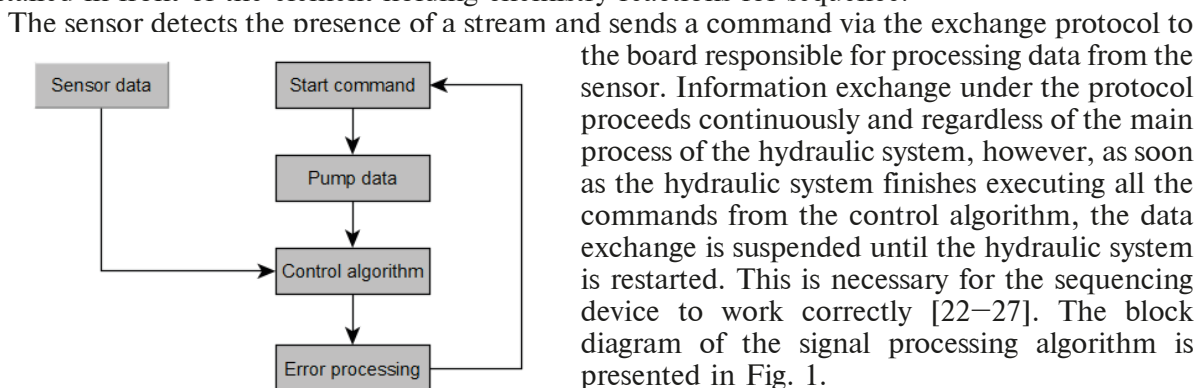
The performance of microfluidic systems depends on monitoring and adjusting the fluid flow in them. The various sensors or flowmeters are performing this task, in particular, a fluid flow sensor [28–31]. Information from the sensor must be read and processed during the entire operation of the hydraulic system.

Therefore, it is important to create an optimal algorithm that is able to carry out the task throughout the entire sequencing process. Also, an important part of this algorithm is the logging of all received data to eliminate and troubleshoot microfluidic systems.

As a consequence of this, the algorithm described above serves not only as a way to control and adjust the hydraulic system, but also to collect data for post-processing of the experiment.

## Structure of the algorithm

The fluid in the microfluidic system of the sequencer moves through thin capillaries using a pump. The pump, having received a command from the control algorithm, adjusts the direction and speed of the fluid supply. To check the correctness of its operation, a liquid flow sensor is installed in front of the element holding chemistry reactions for sequence.



The sensor detects the presence of a stream and sends a command via the exchange protocol to the board responsible for processing data from the sensor. Information exchange under the protocol proceeds continuously and regardless of the main process of the hydraulic system, however, as soon as the hydraulic system finishes executing all the commands from the control algorithm, the data exchange is suspended until the hydraulic system is restarted. This is necessary for the sequencing device to work correctly [22–27]. The block diagram of the signal processing algorithm is presented in Fig. 1.

Fig. 1. Data processing algorithm

The data exchange between the sensor control board and the fluid flow sensor is carried out using the symbols of the binary system, where the unit corresponds to the state of the sensor in which the fluid flow is fixed, and zero corresponds to the state in which the sensor does not observe the flow. Obviously, this information is not enough to control the algorithm, so the data received from the sensor must be compared with what is expected to be seen at the present moment. In other words, starting its work, the pump sends information about how long it is necessary to observe the fluid flow at the sensor installation point. Thus, having received a signal from the pump and the sensor, it is necessary to compare them.

As shown in Fig 1, when a command is received from the program controlling the device, the pump starts its work, while sending the necessary information to the control algorithm. At the same time, the interrogation of the flow sensor begins. In case of discrepancy between the expected and accepted values from the flow sensor, this data goes through the error processing algorithm.

Further, the processor can continue the operation of the device, if the error was not critical, or suspend the experiment by calling the user's dialog box with a choice of further actions.

The entire process of polling the sensor and the operation of the hydraulic system is logged with time stamps. Thus, if necessary, it could be determined the cause of the failure by examining the relevant documentation.

### Realization of algorithm in hydraulic test model

The main aim of developing described algorithm is to use it in sequencing systems. To ensure that described algorithm correctly works the hydraulic system test model was developed. This system is shown in Fig. 2.

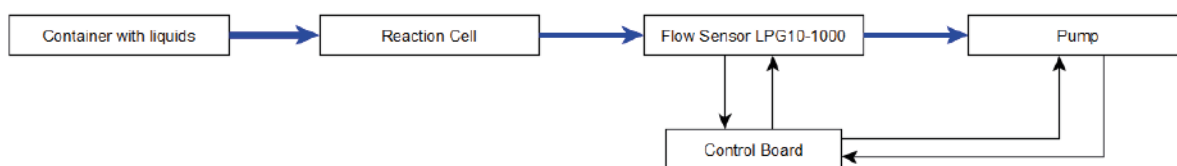


Fig. 2. Block scheme of hydraulic system test model; blue lines correspond to liquid capillaries, black lines to data exchange

One of the parts of the hydraulic system test model is flow sensor LPG10-1000. The parameters of this sensor are presented in Fig. 3. It is necessary to define flow state (logical unit corresponds to fixed fluid flow, logical zero to absence of fluid flow) for algorithm to work correctly. Because of described sensor could perform information about flow rate, it is necessary to determine flow rate threshold value. The threshold value was equalized to 50  $\mu\text{l}/\text{min}$ , due to the LPG10-1000 characteristics. Thus, the flow rate values below the determined threshold are defined as logical zeroes for algorithm.

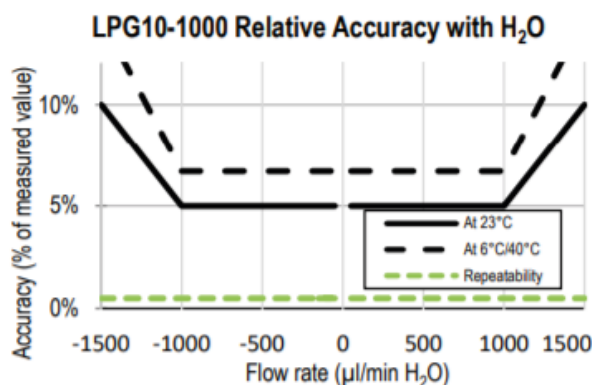


Fig. 3. LPG10-1000 sensor accuracy and repeatability (% of measured value) across the sensor's flow range

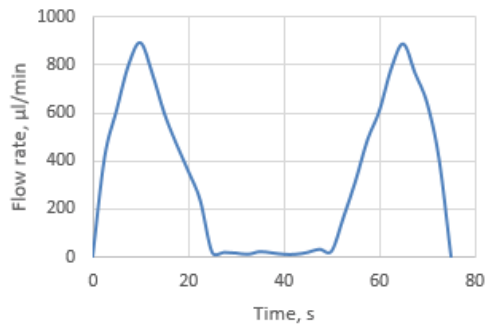


Fig. 4. Visualization of flow rate data from sensor

In developed test model, the control algorithm is performed via control board with microprocessor. The board is connected to pump via UART protocol and to flow sensor via I<sup>2</sup>C protocol. The connection between the board and the pump is necessary to get data from pump (pump status – in work or not).

The control board sends command to pump to start aspirating then control board receives the answer from pump with its status. While pump is aspirating the flow sensor is exchanging its data with control board every 1 second. That provides control of flow status in every iteration. The data from pump and flow sensor is processed on

control board and goes through error processing afterwards. It is necessary to avoid issues such as value below threshold on flow sensor while pump is aspirating.

### Results

As a result, the algorithm was implemented in hydraulic system test model and the acquired information is confirming correctness of described algorithm. This information shows correlations between flow rate from flow sensor, working state of pump and real aspiration process as shown in Fig. 4.

### Conclusions

The developed algorithm allows to control the correct operation of the hydraulic system of the sequencing device. If necessary, the algorithm has the ability to suspend the operation of the entire device, or a specific part thereof, notifying the user at the same time, and will wait for further instructions.

Moreover, developed algorithm can be used not only in sequencing system which described below, but also in another types of hydraulic systems, where is necessary to control the flow rate or flow status.

### Acknowledgment

The work was carried out within the framework of the state task 075-00761-22-00 of the Ministry of Science and Higher Education.

### REFERENCES

1. Grevtseva A. S., Smirnov K. J., Rud V. Yu., Development of methods for results reliability raise during the diagnosis of a person's condition by pulse oximeter, *Journal of Physics: Conference Series*. 1135(1) (2018) 012056.
2. Grevtseva A. S., Smirnov K. J., Greshnevikov K. V., Rud, V. Yu., Glinushkin, A. P., Method of assessment the degree of reliability of the pulse wave image in the rapid diagnosis of the human condition, *Journal of Physics: Conference Series*. 1368(2) (2019) 022072.
3. Marusina M. Y., Karaseva E. A., Automatic segmentation of MRI images in dynamic programming mode Asian Pacific, *Journal of Cancer Prevention*. 19(10) (2018) 2771–2775.
4. Davydov R. V., Rud V. Yu., Yushkova V. Y., On the possibility of analysis using the wavelet transform of the pulse waveform from the bloodstream, *Journal of Physics: Conference Series*. 1695(1) (2020) 012064.
5. Myazin N. S., Yushkova V. V., Rud V. Y., On the possibility of recording absorption spectra in weak magnetic fields by the method of nuclear magnetic resonance, *Journal of Physics: Conference Series*. 1038(1) (2018) 012088.
6. Logunov S. E., Vysoczky M. G., New method of researches of the magnetic fields force lines structure, *Journal of Physics: Conference Series*. 1038(1) (2018) 012093.
7. Kuzmin M. S., Rogov S. A., On the use of a multi-raster input of one-dimensional signals in two-dimensional optical correlators, *Computer Optics*. 43(3) (2019) 391–396.

8. **Makeev S. S., Grevtzeva A. S., Glinushkin A. P., Matorin D. N.**, Possibilities of using spectral analysis in method of nuclear magnetic spectroscopy for condensed media investigation, *Journal of Physics: Conference Series*. 1695(1) (2020) 012112.
9. **Mazing M. S., Zaitceva A. Yu., Kislyakov Yu. Ya., Kondakov N. S., Avdushenko S. A., Davydov V. V.**, Monitoring of Oxygen Supply of Human Tissues Using A Noninvasive Optical System Based on A MultiChannel Integrated Spectrum Analyzer, *International Journal of Pharmaceutical Research*. 12(2) (2020) 1974–1978.
10. **Dyachenko S. V., Vaseshenkova M. A., Martinson K. D., Cherepkova I. A., Zhernovoi A. I.**, Synthesis and properties of magnetic fluids produced on the basis of magnetite particles, *Russian Journal of Applied Chemistry*. 89(5) (2016) 690–696.
11. **Grebenikova N. M., Smirnov K. J., Rud V. Yu., Artemiev V. V.**, Features of monitoring the state of the liquid medium by refractometer, *Journal of Physics: Conference Series*. 1135(1) (2018) 012055.
12. **Nikitina M., Grebenikova N., Dudkin V., Batov Y.**, Methodology for assessing the adverse effects of the use of nuclear energy on agricultural land, *IOP Conference Series: Earth and Environmental Science*. 390(1) (2019) 012024.
13. **Gryznova E., Batov Y., Rud V.**, Methodology for assessing the environmental characteristics of various methods of generating electricity, *E3S Web of Conferences*. 140 (2019) 09001.
14. **Davydov R., Antonov V., Moroz A.**, Parameter Control System for a Nuclear Power Plant Based on Fiber-Optic Sensors and Communication Lines, In: *IEEE International Conference on Electrical Engineering and Photonics (EExPolytech)*, Saint Petersburg, Russia, 13-15 October 2019. Vol. 8906791 (2019) 295–297.
15. **Smirnov K.J., Glagolev S.F., Tushavin G.V.**, High speed near-infrared range sensor based on InP/InGaAs heterostructures, *Journal of Physics: Conference Series*. 1124(2) (2018) 022014.
16. **Dyumin V., Smirnov K., Myazin N.**, Charge-coupled Device with Integrated Electron Multiplication for Low Light Level Imaging, *Proceedings of the 2019 IEEE International Conference on Electrical Engineering and Photonics, EExPolytech*. 8906868 (2019) 308–310.
17. **Myazin N. S., Dudkin V. I., Grebenikova N. M.**, On the Possibility of Express Recording of Nuclear Magnetic Resonance Spectra of Liquid Media in Weak Fields, *Technical Physics*. 63(12) (2018) 1845–1850.
18. **Rakhmatullin I., Efimov S., Tyurin V., Varfolomeev M., Klochkov V.**, Qualitative and quantitative analysis of heavy crude oil samples and their SARA fractions with  $^{13}\text{C}$  nuclear magnetic resonance, *Processes*. 8(8) (2020) 995–1009.
19. **Myazin N. S.**, Features of formation of structure of a nuclear magnetic resonance signal in weak magnetic field, *Journal of Physics: Conference Series*. 1135(1) (2018) 012061.
20. **Davydov R.V., Antonov V.I., Molodtsov D.V.**, Computer implementation of the mathematical model for water flow management by a hydro complex. *Journal of Physics: Conference Series*. 1135(1) (2018) 012088.
21. **Kruzhalov S. V., Grebenikova N. M., Smirnov K. J.**, Method for Determining Defects on the Inner Walls of Tubing from the Velocity Distribution of the Flowing Fluid, *Measurement Techniques*. 61(4) (2018) 365–372.
22. **Reznik V. S., Kruglov V. A.**, Using of «bubble sensors» to control the quality of sequencing by the Illumina / Solexa method, *Journal of Physics: Conference Series*. 2086(1) (2021) 012120.
23. **Kruglov V. A., Reznik V. S., Glinushkin A. P.**, Development of a hydraulic system for bridge amplification, *Journal of Physics: Conference Series*. 1695(1) (2020) 012067.
24. **Reznik V. S., Kruglov V. A., Petrov A. I., Glinuchkin A. P., Rud V. Y.**, Development of a measuring device for the study of thermal processes during the polymerase chain reaction, *Journal of Physics: Conference Series*. 1410(1) (2019) 012078.
25. **Matvienko I. V., Bayramov V. M., Parygina N. A., Kurochkin V. E., Alekseev Y. I.**, Synthesis of Dihydroquinoline-Based Derivatives of Fluorescent Rhodamine Dyes for Nucleic Acid Analysis by a Real-Time Polymerase Chain Reaction, *Russian Journal of Bioorganic Chemistry*. 46(3) (2020) 349–359.
26. **Fedorov A. A., Berdnikov A. S., Kurochkin V. E.**, The polymerase chain reaction model analyzed by the homotopy perturbation method, *Journal of Mathematical Chemistry*. 57(4) (2019) 971–985.
27. **Natyrov A. N., Vlasova N. A., Matvienko I. V., Kurochkin V. E., Alexeev J. I.**, Synthesis of Unsymmetrical Polymethine Cyanine Fluorescent Dyes for Nucleic Acid Analysis by Real-Time PCR, *Russian Journal of Bioorganic Chemistry*. 44(5) (2018) 562–571.



28. **Davydov V.V.**, Nuclear magnetic spectrometer for studying flows of liquid media, *Measurement Techniques*. 59(1) (2017) 1202–1209.
29. **Davydov R., Davydov V., Dudkin V.**, The Nuclear Magnetic Flowmeter for Monitoring the Consumption and Composition of Oil and Its Complex Mixtures in Real-Time, *Energies*. 15(9) (2022) 3259.
30. **Myazin N.S., Dudkin V.I., Davydov R.V.**, Determination of the Longitudinal Relaxation Time of a Flowing Liquid Using a Differential Nuclear Magnetic Spectrometer, *Technical Physics Letters*. 46(11) (2020), 1147–1151
31. **Myazin N.S., Kiryukhin A.V.**, Nuclear-Magnetic Flowmeter-Relaxometers for Monitoring Coolant and Feedwater Flow and Status in Npp, *Atomic Energy*. 127(5) (2020) 274–279.

#### THE AUTHORS

**SEROV EGOR**

egorserov22021998@gmail.com  
ORCID: 0000-0002-2083-4091

**KAVALER Alexey**

RepelLeha@yandex.ru  
ORCID: 0000-0003-2991-9072

**KRUGLOV Vladislav**

vladislav.kruglov98@yandex.ru  
ORCID: 0000-0001-5370-6224

**REZNIK Vladislav**

vlreznik97@gmail.com  
ORCID: 0000-0003-3545-8620

**SARAEV Alexey**

alex.niispb@yandex.ru  
ORCID: 0000-0003-4387-996X

**DAVYDOV Vadim**

davydov\_vadim66@mail.ru  
ORCID: 0000-0001-9530-4805

*Received 09.08.2022. Approved after reviewing 10.08.2022. Accepted 16.09.2022.*

Conference materials

UDC 57.089.3

DOI: <https://doi.org/10.18721/JPM.153.255>

## Femtosecond laser is an effective instrument to remove DNA in pronuclei of mouse zygotes

U. A. Tochilo <sup>1</sup>✉, A. A. Osychenko <sup>1</sup>, A. D. Zalessky <sup>1</sup>,  
D. Yu. Martirosyan <sup>1</sup>, V. A. Nadtochenko <sup>1</sup>

<sup>1</sup>N.N. Semenov Federal Research Center for Chemical Physics Russian Academy of Sciences, Moscow, Russia  
✉ yanulyana@gmail.com

**Abstract.** Applying femtosecond lasers in assisted reproductive technologies is very promising. The removing of a pronucleus (called epronucleation) in three-pronuclear zygotes may help to increase the number of normal diploid embryos. In this work we demonstrated the possibility of epronucleation in mouse zygotes by the femtosecond laser irradiation. We showed that the femtosecond laser could effectively destroy the pronuclei. At the same time, zygotes retained their viability and did not destroy.

**Keywords:** epronucleation, zygote, femtosecond laser, nanosurgery, non-invasive

**Funding:** This work is supported by the Russian Science Foundation under grant 21-75-10155. The work was performed on facilities of ACBS Center of the Collective Equipment (no. 506694, FRCCP RAS) and large-scale research facilities 1440743.

**Citation:** Tochilo U. A., Osychenko A. A., Zalessky A. D., Martirosyan D. Yu., Nadtochenko V. A., Femtosecond laser is an effective instrument to remove DNA in pronuclei of mouse zygotes, St. Petersburg State Polytechnical University Journal. Physics and Mathematics. 15 (3.2) (2022) 302–305. DOI: <https://doi.org/10.18721/JPM.153.255>

This is an open access article under the CC BY-NC 4.0 license (<https://creativecommons.org/licenses/by-nc/4.0/>)

Материалы конференции

УДК 57.089.3

DOI: <https://doi.org/10.18721/JPM.153.255>

## Фемтосекундный лазер – эффективный инструмент энуклеации зигот

У. А. Точило <sup>1</sup>✉, А. А. Осыченко <sup>1</sup>, А. Д. Залесский <sup>1</sup>,  
Д. Ю. Мартиросян <sup>1</sup>, В. А. Надточенко <sup>1</sup>

<sup>1</sup>Федеральный исследовательский центр химической физики им. Н.Н. Семенова  
Российской академии наук (ФИЦ ХФ РАН), г. Москва, Россия  
✉ yanulyana@gmail.com

**Аннотация.** В работе мы показали возможность удаления пронуклеусов в зиготе с помощью фемтосекундного лазерного облучения. Мы полагаем, что этот метод более эффективен и менее инвазивен, чем механическое удаление микроманипулятором. Цитопласты, подготовленные с помощью лазера, более жизнеспособны и пригодны для дальнейших биотехнологических манипуляций.

**Ключевые слова:** энуклеация, зиготы, фемтосекундный лазер, пронуклеусы зигот, микрохирургия, малая инвазивность

**Финансирование:** Работа выполнена при поддержке РФФИ грант No 21-75-10155. Работа выполнена на оборудовании ЦКП ФИЦ ХФ 506694 и УНУ ФИЦ ХФ РАН 1440743.



**Ссылка при цитировании:** Точило У. А., Осыченко А. А., Залесский А. Д., Мартиросян Д. Ю., Надточенко В. А. Фемтосекундный лазер - эффективный инструмент энуклеации зигот // Научно-технические ведомости СПбГПУ. Физико-математические науки. Т. 15. № 3.2. С. 302–305. DOI: <https://doi.org/10.18721/JPM.153.255>

Статья открытого доступа, распространяемая по лицензии CC BY-NC 4.0 (<https://creativecommons.org/licenses/by-nc/4.0/>)

## Introduction

Triploidy is the most common [1] abnormality of the chromosome set. Triploid embryos usually abort the development at early post-implantation stages, which results in miscarriages. In artificial human technologies triploid zygotes can be easily identified by the presence of extra pronucleus (normal diploid zygotes have two pronuclei). These zygotes are always considered as abortive material and does not used for transfer. The removing of extra pronucleus could help to obtain diploid, transferable embryos for couples with exclusively abnormally or few normally fertilized oocytes [2].

Another application of epronucleation is preparation of recipient cytoplasm for mitochondrial replacement therapy (MRT) [3]. MRT is applied to avoid mitochondrial diseases and it realized by two different approaches: spindle transfer and pronuclear transfer. The quality of the recipient cytoplasm may be the key factor of MRT efficiency.

Epronucleation by a microneedle is only existed technique to perform this manipulation. It implies the cell puncturing and using cytoskeleton relaxants. The survival rate after epronucleation by a microneedle is able to reach 100%, but an ability of blastocyst formation is not very high [4]. In this work we suggest a novel approach of epronucleation, which does not require the use of cytoskeleton relaxants and the cell puncturing. We used mouse eggs as a model object and we showed that the destruction of a pronucleus by a near-infrared femtosecond laser does not disturb the whole oocyte and does not accompany with the loss of cytoplasm. Although the pronuclei are clearly visible without any staining, we applied Hoechst 33342 dye to reduce the threshold of DNA breakdown.

## Materials and Methods

**Oocyte collection and staining.** C57Bl/6 female mice aged eight- to ten weeks were mated with males of the same strain. Mice were sacrificed and the oviducts were removed. Fertilized oocytes with two pronuclei were washed and then cultured in KSOM culture medium (MR-101-D, EmbryoMax). The zygotes were stained with 5  $\mu\text{g}/\text{ml}$  Hoechst 33342 dye (B2261, Sigma-Aldrich) for 15 minutes in KSOM medium in the incubator and then washed twice. During the experiment the zygotes were placed onto a cover glass in a 50  $\mu\text{l}$  drop of M2 (M7167, Sigma) medium.

**Laser parameters and enucleation process.** Femtosecond radiation ( $\lambda=790$  nm) was generated by a reformed laser (Chameleon Discovery, Coherent) and coupled to an inverted microscope Olympus IX71. In our experiments we used following parameters for the irradiation of the pronuclei:  $\lambda = 795$  nm,  $\nu = 80$  MHz, pulse energy 0,5 nJ (40 mW power); 100 fs pulse duration, pulse train duration 60 ms. Laser radiation was focused by 60 $\times$  objective lens (NA = 0.7). Pronuclei are easily visualized, we exposed laser on one of them. We repeated the exposure multiple times, until the DNA luminescence had stopped.

**Confocal imaging.** Fluorescence imaging was performed using a laser scanning confocal microscope Zeiss LSM 980 (Carl Zeiss Microscopy, Jena, Germany), 63 $\times$  Plan-Apochromat objective (NA = 1.4, oil immersion). The oocytes were placed in M2 medium drop on a 0.17 mm cover glass (Zeiss). Hoechst 33342 luminescence excitation were performed by 405 nm laser, detection range 410–479 nm.

## Results and Discussion

Femtosecond laser was successfully applied for elimination of one or two pronucleus in the mouse oocytes. At the first moment, two pronuclei were clearly visible (Fig. 1, *a*). After the laser irradiation contour and nucleoli of the pronucleus disappeared (Fig. 1, *b*, *c*). The oocytes retained their viability after the irradiation at least for 24 hours.

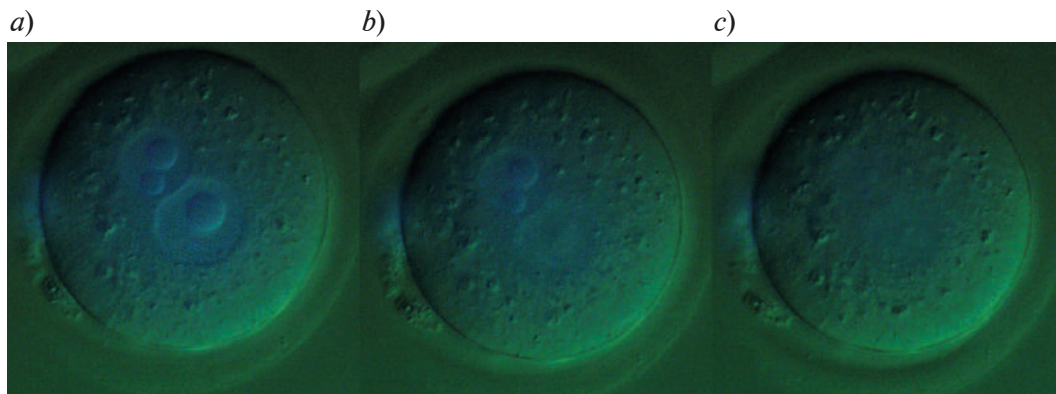


Fig. 1. Femtosecond laser destruction of the pronuclei in the mouse zygote: before the irradiation (*a*); after irradiation of one pronucleus (*b*); after irradiation of two pronuclei (*c*)

To control enucleation, we observed a decrease in the level of DNA luminescence. We measured the initial level of luminescence, then destroyed one of the pronuclei and compared the levels of luminescence after the exposure. Fig. 2 shows the pronuclei, they are in different focal planes. In this experiment, the pronucleus shown in the images on the left (*a*) was irradiated. Fig. 2,*b* shows the second, right pronucleus, without laser irradiation. The average luminescence intensity of the region in which the irradiated pronucleus is located decreased by more than half (73.5 before, 31.6 after). The intensity of the luminescence of the non-irradiated pronucleus practically did not change (27.7 before, 27.6 after).

A decrease in DNA luminescence by two times can be observed for the left protonucleus, and no significant changes for the right one

We examined an ability of epronucleated zygotes to develop in vitro. Oocytes with one irradiated pronucleus completely stopped the development (cleaved 0 of 13) as well as oocytes with two irradiated pronucleus (cleaved 0 of 10), whereas control zygotes successfully formed blastocysts (12 of 13). However, fragmentation or degradation of epronucleated zygotes was not observed at least for 24 hours. We admit that these results are preliminary and require further investigation.

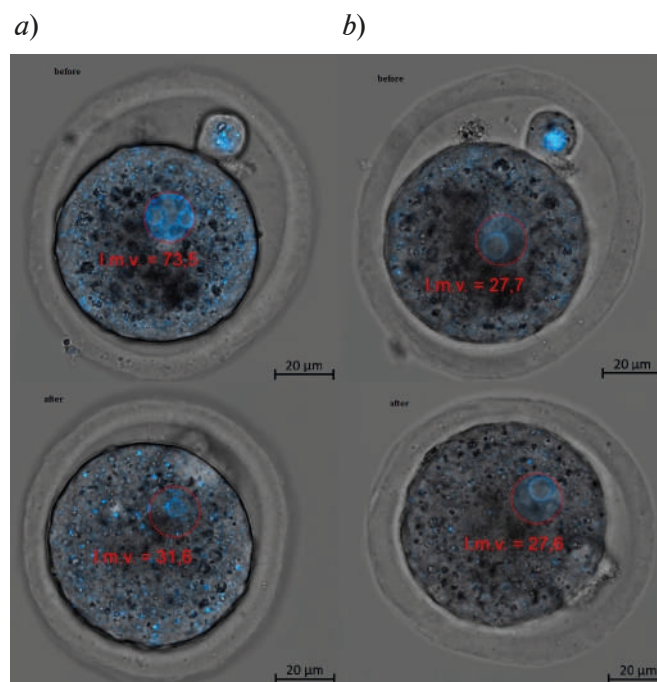


Fig. 2. Pronucleus after irradiation by a femtosecond laser (*a*); non-irradiated protonucleus (*b*)



## Discussion

The use of femtosecond lasers for the oocyte and embryo manipulation can significantly improve some important techniques in artificial human technologies, but it requires considerable effort and fundamental research. We have already studied the range of non-invasive near-infrared laser impact [5] and examined viability of mouse germinal vesicle oocytes [6] and two-cell embryos development [7] after the laser exposure within this range. Moreover, we have successfully performed enucleation of metaphase II oocyte [8] and we demonstrated the efficiency and safety of this method. Thereby we assume that epronucleation within the range of non-invasive diapason could be effective and low-invasive as well. Nonetheless, the proper study of viability after the epronucleation ought to be performed. Another important thing that must be studied is the process of DNA destruction by the femtosecond laser: it is not yet clear, is there any remains of DNA after the exposure.

## REFERENCES

1. **Tarin J. J., Trounson A. O., Sathananthan H.**, Origin and ploidy of multipronuclear zygotes. *Reprod Fertil Dev.* 1999; 11(4-5):273–9.
2. **Czernik M., Anzalone D. A., Palazzese L., Oikawa M., Loi P.**, Somatic cell nuclear transfer: failures, successes and the challenges ahead. *Int J Dev Biol.* 2019; 63(3-4-5):123–130.
3. **Dougherty M. P., Dolitsky S., Chattopadhyay R., Sauer M. V.**, Mitochondrial replacement therapy. *Curr Opin Obstet Gynecol.* 2018 Aug;30(4):217–222.
4. **Escribá M.-J., Martin J., Rubio C., Valbuena D., Remohi J., Pellicer A.**, Heteroparental blastocyst production from microsurgically corrected tripronucleated human embryos IN VITRO FERTILIZATION 2006 86(6) 1601–1607.
5. **Osychenko A. A., Tochilo U. A., Astafiev A. A., Zalessky A. D., Shakhov A. M., Krivokharchenko A. S., Nadtochenko V. A.**, Determining the Range of Noninvasive Near-Infrared Femtosecond Laser Pulses for Mammalian Oocyte Nanosurgery *Sovremennye tehnologii v medicine* 2017; 9(1): 21.
6. **Astafiev A. A., Zalesskiy A. D., Zatssepina O. V. et al.** Impact of tightly focused femtosecond laser pulses on nucleolus-like bodies of mouse GV oocyte and the ability of mouse oocytes to mature. *Dokl. Biochem. Biophys.* 467 (2016) 136–140.
7. **Osychenko A. A., Zalesskii A. D., Kostrov A. N., Ryabova A. V., Krivokharchenko A. S., and Nadtochenko V. A.**, Femtosecond laser surgery of two-cell mouse embryos: Effect on viability, development, and tetraploidization. *Journal of Biomedical Optics.* 22. 1 2017.
8. **Osychenko A. A., Zalessky A. D., Tochilo U. A., Martirosyan D. Yu., Silaeva Y. Yu. and Nadtochenko V. A.**, Femtosecond laser oocyte enucleation as a low-invasive and effective method of recipient cytoplasm preparation, *Biomedical Optics Express* 13(3) (2022) 1447–1456.

## THE AUTHORS

**TOCHILO Uliana**  
yanulyana@gmail.com  
ORCID: 0000-0002-4511-6109

**MARTIROSYAN David**  
petrosyan359@gmail.com  
ORCID: 0000-0002-2952-8867

**OSYCHENKO Alina**  
alina.chemphys@gmail.com  
ORCID: 0000-0002-7519-2479

**NADTOCHENKO Victor**  
nadtochenko@gmail.com  
ORCID: 0000-0002-6645-692X

**ZALESSKY Alexandr**  
aleksandr.zalesskij@phystech.edu  
ORCID: 0000-0002-1992-0574

*Received 29.09.2022. Approved after reviewing 01.10.2022. Accepted 02.10.2022.*

Conference materials

UDC 535-15

DOI: <https://doi.org/10.18721/JPM.153.256>

## Photoluminescent $\alpha\text{-NaYbF}_4\text{:Er}_{0.02}\text{Ce}_{0.02}\text{Zn}_{0.1}$ nanoparticles for bioimaging in visible and infrared ranges

E. M. Trifanova , A. V. Koshelev, K. V. Khaydukov, I. V. Krylov, V. K. Popov

Federal Scientific Research Center "Crystallography and Photonics" RAS, Moscow, Russia

 [katikin@mail.ru](mailto:katikin@mail.ru)

**Abstract.** Nowadays noninvasive optical technologies require multifunctional nanomarkers, that can perform photoluminescence in different ranges of spectrum to provide broad possibilities for bioimaging. Photoluminescent nanoparticles doped with rare earth elements meet these requirements and are very promising for biological tissue visualization.  $\alpha\text{-NaYbF}_4\text{:Er}_{0.02}\text{Ce}_{0.02}\text{Zn}_{0.1}$  nanoparticles were characterized, had narrow and intensive photoluminescent peaks. Experiments were carried out on visualization in the visible and IR ranges of the spectrum. It was shown that a long photoluminescence lifetime made it possible to use the method of time-gated luminescence imaging. Visualization experiments with phantoms of biotissue both 3.5% fat milk and distilled water showed that nanoparticles can be used for multipurpose bioimaging.

**Keywords:** Photoluminescent nanoparticles, bioimaging, biotissue transparency windows, time-gated luminescence imaging

**Funding:** The study was funded by the Ministry of Science and Higher Education of the Russian Federation within the State Assignment FSRC 'Crystallography and Photonics' of RAS and RFBR, Project 20-32-90218.

**Citation:** Trifanova E. M., Koshelev A. V., Krylov I. V., Khaydukov K. V., Popov V. K., Photoluminescent  $\alpha\text{-NaYbF}_4\text{:Er}_{0.02}\text{Ce}_{0.02}\text{Zn}_{0.1}$  nanoparticles for bioimaging in visible and infrared ranges, St. Petersburg State Polytechnical University Journal. Physics and Mathematics. 15 (3.2) (2022) 306–310. DOI: <https://doi.org/10.18721/JPM.153.256>

This is an open access article under the CC BY-NC 4.0 license (<https://creativecommons.org/licenses/by-nc/4.0/>)

Материалы конференции

УДК 535-15

DOI: <https://doi.org/10.18721/JPM.153.256>

## Фотолюминесцентные наночастицы $\alpha\text{-NaYbF}_4\text{:Er}_{0.02}\text{Ce}_{0.02}\text{Zn}_{0.1}$ для биоимиджинга в видимом и инфракрасном диапазонах

Е. М. Трифанова , А. В. Кошелев, К. В. Хайдуков, И. В. Крылов, В. К. Попов

Федеральный научно-исследовательский центр "Кристаллография и фотоника" РАН, г. Москва, Россия

 [katikin@mail.ru](mailto:katikin@mail.ru)

**Аннотация.** В настоящее время для неинвазивных оптических технологий требуются многофункциональные наномаркеры, способные люминесцировать в различных диапазонах спектра, что обеспечивает широкие возможности для биоимиджинга. Фотолюминесцентные наночастицы, легированные ионами редкоземельных элементов, отвечают этим требованиям и весьма перспективны для визуализации биологических тканей. Наночастицы  $\alpha\text{-NaYbF}_4\text{:Er}_{0.02}\text{Ce}_{0.02}\text{Zn}_{0.1}$ , демонстрирующие интенсивную фотолюминесценцию в широком спектральном диапазоне, выбраны в качестве объекта исследования. Эксперименты по визуализации в видимом и ИК-диапазонах спектра сквозь сильно рассеивающую среду (3,5% цельное коровье молоко) и дистиллированную воду показали, что наночастицы  $\alpha\text{-NaYbF}_4\text{:Er}_{0.02}\text{Ce}_{0.02}\text{Zn}_{0.1}$  могут быть использованы для мультифункционального биоимиджинга.

**Ключевые слова:** Фотолюминесцентные наночастицы, биоимиджинг, окна прозрачности биотканей, фотолюминесцентная визуализация с отложенной регистрацией сигнала

**Финансирование:** Работа выполнена при поддержке Министерства науки и высшего образования в рамках выполнения работ по Государственному заданию ФНИЦ «Кристаллография и фотоника» РАН и РФФИ (проект № 20-32-90218\_Аспиранты).

**Ссылка при цитировании:** Трифанова Е. М., Кошелев А. В., Крылов И. В., Хайдуков К. В., Попов В. К. Фотолюминесцентные наночастицы  $\alpha\text{-NaYbF}_4\text{:Er}_{0.02}\text{Ce}_{0.02}\text{Zn}_{0.1}$  для биоимиджинга в видимом и инфракрасном диапазонах // Научно-технические ведомости СПбГПУ. Физико-математические науки. Т. 15. № 3.2. С. 306–310. DOI: <https://doi.org/10.18721/JPM.153.256>

Статья открытого доступа, распространяемая по лицензии CC BY-NC 4.0 (<https://creativecommons.org/licenses/by-nc/4.0/>)

### Introduction

Noninvasive optical technologies including NIR and SWIR regions of spectrum usually use three biotissue transparency windows (BTW): I-BTW (650–950 nm), II-BTW (1000–1350 nm), III-BTW (1500–1870 nm) for bioimaging. Biological tissue has deeper penetration depths according to local minimum of loss coefficient in these wavelength ranges compared with visible range of spectrum [1]. Technologies that use I-BTW and III-BTW attract significant interest due to high signal-to-noise ratio, high spatial and time resolution [2]. Biological tissues have different compositions, but almost all of them consist water [3]. Water has a high absorption coefficient in III-BTW, which can complicate visualization at these wavelengths [4]. Therefore, to implement bioimaging in several BTWs at once, depending on optical properties of a biological object under study, it is important to develop universal multimodal nanomarkers with several photoluminescence peaks in a wide spectral range. Inorganic fluoride nanocrystals, doped with lanthanide ( $\text{Ln}^{3+}$ ) ions, demonstrated the required spectral characteristics [5]. Compared with other luminophores (quantum dots, fluorescent dyes and proteins)  $\text{Ln}^{3+}$  doped fluoride nanoparticles (NPs) have a number of advantages for bioimaging applications [6]. They demonstrate superior chemical and photostability, narrow band and large luminescence shifts relative to excitation light [7]. Depending on the specific application, the luminescence characteristics of fluoride NPs can be varied by changing the nature of the host lattice and doping elements. NPs  $\text{NaYbF}_4$ , co-doped with  $\text{Er}^{3+}$  and  $\text{Ce}^{3+}$  can be used in fast in vivo brain imaging in the IR region above 1500 nm [8]. Temperature dependent NIR emission band pairs in II-BTW and III-BTW can be received by doping  $\text{NaGdF}_4$  NPs with  $\text{Ho}^{3+}/\text{Nd}^{3+}$  or  $\text{Er}^{3+}/\text{Nd}^{3+}$  [9].  $\text{NaYF}_4$  nanocrystals doped with  $\text{Yb}^{3+}$  and  $\text{Tm}^{3+}$  ions have been successfully used for bioimaging of the ovarian cancer cells line at the wavelength of  $\lambda = 800$  nm corresponding to I-BTW [10]. Also, presence of a large number of metastable long-lived excited 4f-states of  $\text{Ln}^{3+}$  ions makes it possible to use such NPs for time-gated luminescence imaging. In the context of non-invasive optical technologies this method allows the laser excitation signal and autoluminescence with a short lifetime to decay before the signal from the NPs with a long lifetime is received [11].

In this work, we demonstrated the possibility of using  $\text{Ln}^{3+}$ -doped  $\alpha\text{-NaYbF}_4$  NPs, which exhibit high intensity up- ( $\sim 650$  nm) and down-conversion ( $\sim 1530$  nm) photoluminescence under  $\lambda = 976$  nm irradiation, as imaging instrument. Two visualization experiments were carried out: imaging through a strongly scattering medium (3.5% fat cow milk) and distilled water aiming to imitate scattering and absorption coefficient of biotissue. Our experiments showed broad perspective in multipurpose visualization with photoluminescent NPs and recommendations on the choice of the detecting range depending on specificity of the application.

### Materials and Methods

Lanthanide doped  $\alpha\text{-NaYbF}_4\text{:Er}_{0.02}\text{Ce}_{0.02}\text{Zn}_{0.1}$  NPs were synthesized by thermolysis method. The phase composition of the obtained nanocrystals was studied using an X-ray powder diffractometer Rigaku Miniflex 600 (radiation  $\text{CuK}\alpha$ ) in the range of angles  $10^\circ \leq 2\theta \leq 120^\circ$  with  $1^\circ$  scan step. The phases were identified using the ICDD PDF-2 (2014). The unit-cell parameters were calculated by the Le Bail full-profile fitting (the Jana2006 software). A semiconductor ATC-laser

with radiation peak at  $\lambda = 976$  nm (Semiconductor Devices, Russia) was used to excite the NPs. The study of photoluminescence spectrum of NPs was carried out on a spectrofluorimeter Fluorolog 3 (HJY, France). The photoluminescence lifetime was measured under excitation of the semiconductor laser in a pulsed mode. The excitation laser beam was divided by splitter  $\sim 20/80\%$ . 20% went on a silicon photodetector APDF and the rest 80% - on photomultiplier (PMT, Hamamatsu, Japan). The PMT signal corresponding to the decay kinetics was recorded on a TDS 6804B high-speed oscilloscope (Tektronix Inc., United States). TEM analysis was performed on a Tecnai Osiris (FEI, Hillsboro, OR, USA) electron microscope operated at 200 kV.

Experimental samples were prepared as follows: two pieces (1x10 mm) of white paper were covered with the NPs. The paper pieces were placed on a quartz cuvette with a 0.7 mm gap between them. 3.5% fat cow milk was chosen as a strongly scattering medium and distilled water was chosen as a medium with high absorption coefficient at  $\lambda = 1530$  nm [4]. Quartz cuvettes with optical paths length of 1–11 mm were used for experiments with distilled water.

For visualization in the visible range, we used a custom-build imaging system with EMCCD camera (Raptor Photonics Incorporated, USA). PC with the software controlled laser galvanometer scanner (Ateco Technocenter, Russia) for precise aiming of the laser beam on the sample. The system of interference filters (Semrock, USA) was used to notch the exciting radiation off. For visualization in the IR range, we performed time-gated luminescence imaging, using InGaAs camera (Hamamatsu, Japan). A chopper wheel was controlled by MC2000B optical light modulator (Thorlabs, USA) and installed between the InGaAs camera and the sample. The laser was in a pulsed mode.

### Results and Discussion

The XRD analysis results of  $\alpha\text{-NaYbF}_4\text{:Er}_{0.02}\text{Ce}_{0.02}\text{Zn}_{0.1}$  NPs are shown in Fig. 1a. The reflections on the X-ray diffraction pattern correspond to the cubic structure of  $\alpha\text{-NaYbF}_4$  (space group  $Fm\bar{3}m$ ,  $a = 5.469(6)$  Å). According to the TEM data, the obtained nanocrystals were monodisperse particles of irregular shape with an average size of 36 nm (Fig. 1b).

The photoluminescent properties of NPs are due to successive absorption of photons by ytterbium ions and further resonant nonradiative energy transfer to erbium ions within the crystalline matrix. The photoluminescence spectrum of NPs is shown in Fig. 2a. The spectrum exhibits luminescence peaks in the visible and IR ranges of the spectrum, which correspond to characteristic electronic transitions in  $\text{Er}^{3+}$  ion.  $\text{Yb}^{3+}$  ions populate the  $^2F_{5/2}$  excited state during absorption of IR radiation at  $\lambda = 976$  nm. Then this ion nonradiatively transfers this energy to closely spaced neighboring  $\text{Er}^{3+}$ . The  $\text{Er}^{3+}$  ions populate the metastable  $^4I_{11/2}$  excited state, where it can participate in synchronous energy exchange with the neighboring excited  $\text{Yb}^{3+}$ , so that  $\text{Er}^{3+}$  populate higher energy levels  $^4F_{7/2}$  and  $^2G_{7/2}$ . From an excited states  $^2H_{9/2}$ ,  $^2H_{11/2}$ / $^4S_{3/2}$ ,  $^4F_{9/2}$  it passes into a state  $^4I_{15/2}$  with the emission of photons with  $\lambda = 407, 525, 540, 652$  nm respectively. When interacting with  $\text{Ce}^{3+}$ , a resonant population of levels of  $\text{Er}^{3+}$  occurs above  $^4I_{13/2}$ . As a result, the NPs have an intense luminescence peak at  $\lambda = 1530$  nm (Fig. 2b). We measured the photoluminescence lifetime. At  $\lambda = 1530$  nm, it is 5.7 ms, which is suitable for time-gated photoluminescence imaging.

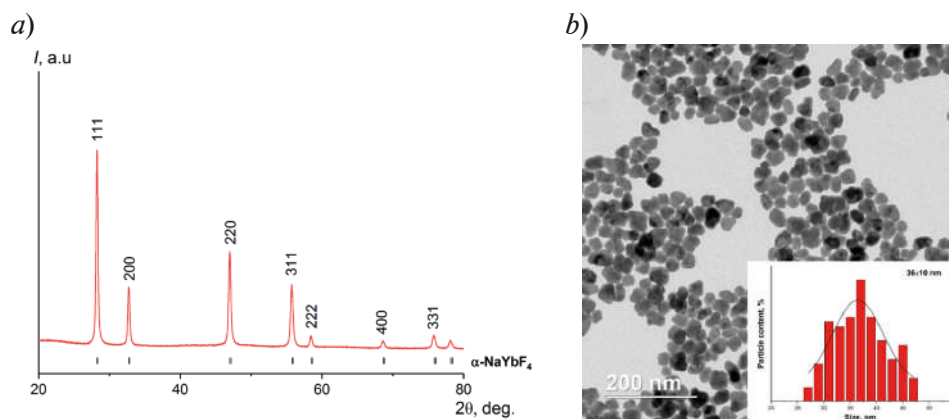


Fig. 1. X-ray diffraction pattern (a), TEM images and histograms of size distribution of  $\alpha\text{-NaYbF}_4\text{:Er}_{0.02}\text{Ce}_{0.02}\text{Zn}_{0.1}$  nanoparticles (b)

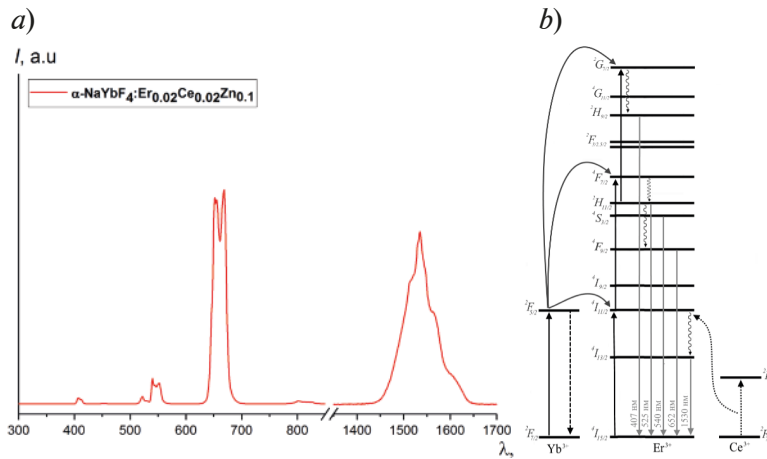


Fig. 2. Photoluminescence spectrum (a) energy level diagram of  $\alpha\text{-NaYbF}_4\text{:Er}_{0.02}\text{Ce}_{0.02}\text{Zn}_{0.1}$  nanoparticles (b)

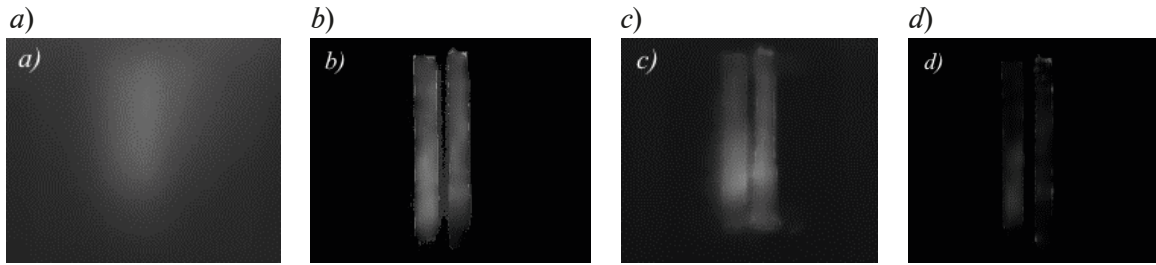


Fig. 3. Images of the samples obtained through a 1 mm layer of 3.5% fat milk in visible (a) and NIR (b) region and through a 4 mm layer of water in visible (c) and NIR (d) region

We obtained images of samples in the visible and IR ranges of the spectrum through 1 mm layer of 3.5% fat cow milk. In the first case gap between the pieces is not observed, it is impossible to separate the image of one paper band from the other (Fig. 3,a). In contrast to the image obtained at  $\lambda = 1530 \text{ nm}$  (Fig. 3,b). The two luminescent bands are clearly visible. This can be explained by the Mie scattering effect – greater the wavelength, less light is scattered [12].

Several experiments were carried out with distilled water. The results are shown in Fig. 3,c and 3,d. The thickness of the water layer was increased from 1 mm to 11 mm. After 4 mm layer of water, the image in the IR range disappears. This is due to the high absorption coefficient of water at  $\lambda = 1530 \text{ nm} \sim 10^3 \text{ cm}^{-1}$ , while at  $\lambda = 652 \text{ nm}$  it is only  $\sim 10^{-2} \text{ cm}^{-1}$  [4]. In the visible range the image is preserved up to a layer 11 mm thick, the gap is clearly visible in all images.

### Conclusion

Various visualization tasks sometimes require individual solutions. Therefore, it is so important to find universal multifunctional nanomarkers performing photoluminescent radiation in different ranges of the spectrum. Clear images of NPs were  $\alpha\text{-NaYbF}_4\text{:Er}_{0.02}\text{Ce}_{0.02}\text{Zn}_{0.1}$  on the surface the paper pieces obtained through media with different optical properties. It was shown that for visualization through a strongly scattering medium, the time-gated photoluminescence imaging in IR region of the spectrum was perfectly suitable due to the long photoluminescence lifetime (more than 5 ms) of the NPs. While the experiment with increasing the thickness of the water layer showed that there was a strong absorption of radiation at  $\lambda = 1530 \text{ nm}$ . Therefore, it is possible to conduct through a medium with a high water content at  $\lambda \leq 700 \text{ nm}$ . The  $\alpha\text{-NaYbF}_4\text{:Er}_{0.02}\text{Ce}_{0.02}\text{Zn}_{0.1}$  NPs can be used as multipurpose photoluminescent nanomarkers both in I-BTW and III-BTW region of the spectrum.

### Acknowledgments

The study was funded by the Ministry of Science and Higher Education within the State assignment FSRC ‘Crystallography and Photonics’ RAS and RFBR according to the project 20-32-90218. The authors are grateful to D.N. Karimov, and E.V. Khaydukov for fruitful discussions.

## REFERENCES

1. Hemmer E., Venkatachalam N., Hyodo H., Hattori A., Ebina Y., Kishimoto H., Soga K., Upconverting and NIR emitting rare earth based nanostructures for NIR-bioimaging, *Nanoscale*. 5 (23) (2013) 11339.
2. Hemmer E., Benayas A., Légaré F., Vetrone F., Exploiting the biological windows: Current perspectives on fluorescent bioprobes emitting above 1000 nm, *Nanoscale Horizons*. 1 (3) Royal Society of Chemistry, (2016) 168–184.
3. Bachmann L., Zezell D.M., Ribeiro A. da C., Gomes L., Ito A.S., Fluorescence Spectroscopy of Biological Tissues—A Review, *Applied Spectroscopy Reviews*. 41 (6) (2006) 575–590.
4. Beć K.B., Huck C.W., Breakthrough Potential in Near-Infrared Spectroscopy: Spectra Simulation. A Review of Recent Developments, *Frontiers in Chemistry*. 7 (FEB) (2019) 1–22.
5. Zhong Y., Dai H., A mini-review on rare-earth down-conversion nanoparticles for NIR-II imaging of biological systems, *Nano Research*. 13 (5) (2020) 1281–1294.
6. Cheng L., Yang K., Zhang S., Shao M., Lee S., Liu Z., Highly-sensitive multiplexed in vivo imaging using pegylated upconversion nanoparticles, *Nano Research*. 3 (10) (2010) 722–732.
7. Zhou J., Liu Z., Li F., Upconversion nanophosphors for small-animal imaging, *Chem. Soc. Rev.* 41 (3) (2012) 1323–1349.
8. Zhong Y., Ma Z., Zhu S., Yue J., Zhang M., Antaris A.L., Yuan J., Cui R., Wan H., Zhou Y., Wang W., Huang N.F., Luo J., Hu Z., Dai H., Boosting the down-shifting luminescence of rare-earth nanocrystals for biological imaging beyond 1500 nm, *Nature Communications*. 8 (1) Springer US, (2017) 737.
9. Skripka A., Benayas A., Marin R., Canton P., Hemmer E., Vetrone F., Double rare-earth nanothermometer in aqueous media: Opening the third optical transparency window to temperature sensing, *Nanoscale*. 9 (9) Royal Society of Chemistry, (2017) 3079–3085.
10. Boyer J.-C., Manseau M.-P., Murray J.I., van Veggel F.C.J.M., Surface Modification of Upconverting NaYF<sub>4</sub> Nanoparticles with PEG–Phosphate Ligands for NIR (800 nm) Biolabeling within the Biological Window, *Langmuir*. 26 (2) (2010) 1157–1164.
11. Khaydukov E. V., Boldyrev K.N., Khaydukov K. V., Krylov I. V., Asharchuk I.M., Savelyev A.G., Rocheva V. V., Karimov D.N., Nechaev A. V., Zvyagin A. V., Deferred Registration of Nanophosphor Photoluminescence As a Platform for Optical Bioimaging, *Optics and Spectroscopy*. 126 (1) (2019) 95–101.
12. Mie G., Sättigungsstrom und Stromkurve einer schlecht leitenden Flüssigkeit, *Annalen der Physik*. 331 (8) (1908) 597–614.

## THE AUTHORS

**TRIFANOVA Ekaterina**  
katikin@mail.ru  
ORCID: 0000-0003-4320-6917

**KHAYDUKOV Kirill**  
haidukov\_11@mail.ru  
ORCID: 0000-0001-5898-2404

**KOSHELEV Alexander**  
avkoshelev03@gmail.com  
ORCID: 0000-0002-2119-6992

**POPOV Vladimir**  
popov@laser.ru  
ORCID: 0000-0002-9305-6964

**KRYLOV Ivan V.**  
ivan\_krylov@bk.ru

*Received 15.07.2022. Approved after reviewing 18.07.2022. Accepted 19.07.2022.*

Conference materials

UDC 617.7

DOI: <https://doi.org/10.18721/JPM.153.257>

### **Oxidative destruction of human RPE melanosomes induced by superoxide radicals leads to the formation of reactive aldehydes and ketones**

A. A. Gulin <sup>1</sup>✉, A. E. Dontsov <sup>2,3</sup>, M. A. Yakovleva <sup>2,3</sup>, N. N. Trofimova <sup>2</sup>,  
A. V. Aybush <sup>1</sup>, A. A. Vasin <sup>1</sup>, M. A. Ostrovsky <sup>2,3</sup>

<sup>1</sup>N.N. Semenov Federal Research Center for Chemical Physics RAS, Moscow, Russia;

<sup>2</sup>Emanuel Institute of Biochemical Physics RAS, Moscow, Russia;

<sup>3</sup>Koltzov Institute of Developmental Biology RAS, Moscow, Russia

✉ [aleksandr.gulin@phystech.edu](mailto:aleksandr.gulin@phystech.edu)

**Abstract:** Oxidative destruction of the natural pigment melanin leads to a decrease in its concentration in the cell, a decrease of antioxidant properties and the accumulation of products that exhibit prooxidant activity. This work shows for the first time that oxidative destruction of melanosomes from human retinal pigment epithelium (RPE) cells induced by superoxide radicals results in the formation of toxic carbonyl compounds, namely aldehydes and ketones. Analysis of the products of oxidative degradation of melanosomes was performed by absorption and fluorescence spectroscopy and time-of-flight secondary ion mass spectrometry (ToF-SIMS). It has been shown the water-soluble products of oxidative destruction of RPE melanosomes induce proteins modification with the formation of fluorescent Schiff bases. It is assumed that carbonyl products of oxidative destruction of melanosomes can have a toxic effect on RPE cells, which is important for understanding the mechanisms of development of retina senile degenerative diseases.

**Keywords:** Retinal pigment epithelium, melanosomes, superoxide, carbonyl stress

**Funding:** Grant of the Ministry of Science and Higher Education of the Russian Federation 075-15-2020-773.

**Citation:** Gulin A. A., Dontsov A. E., Yakovleva M. A., Trofimova N. N., Aybush A. V., Vasin A. A., Ostrovsky M. A., Oxidative destruction of human RPE melanosomes induced by superoxide radicals leads to the formation of reactive aldehydes and ketones, St. Petersburg State Polytechnical University Journal. Physics and Mathematics. 15 (3.2) (2022) 311–316. DOI: <https://doi.org/10.18721/JPM.153.257>

This is an open access article under the CC BY-NC 4.0 license (<https://creativecommons.org/licenses/by-nc/4.0/>)

Материалы конференции

УДК 617.7

DOI: <https://doi.org/10.18721/JPM.153.257>

### **Окислительная деструкция меланосом из клеток рпэ человека, индуцированная супероксидными радикалами, приводит к образованию реакционноспособных альдегидов и кетонов**

А. А. Гулин <sup>1</sup>✉, А. Е. Донцов <sup>2,3</sup>, М. А. Яковлева <sup>2,3</sup>, Н. Н. Трофимова <sup>2</sup>,  
А. В. Айбуш <sup>1</sup>, А. А. Васин <sup>1</sup>, М. А. Островский <sup>2,3</sup>

<sup>1</sup>Федеральный исследовательский центр химической физики им. Н.Н. Семёнова РАН, г. Москва, Россия;

<sup>2</sup>Институт биохимической физики им. Н.М. Эмануэля РАН, г. Москва, Россия;

<sup>3</sup>Институт биологии развития им. Н.К. Кольцова РАН, г. Москва, Россия

✉ [aleksandr.gulin@phystech.edu](mailto:aleksandr.gulin@phystech.edu)

**Аннотация.** В работе впервые показано, что в результате окислительной деструкции меланосом из клеток ретиального пигментного эпителия (РПЭ) глаза человека, вызванной супероксидными радикалами, образуются токсичные карбонильные соединения, в частности альдегиды и кетоны. Показано, что водорастворимые продукты окислительной деструкции РПЭ меланосом индуцируют модификацию белков с образованием флуоресцентных оснований Шиффа.

**Ключевые слова:** ретиальный пигментный эпителий, меланосомы, супероксид, карбонильный стресс

**Финансирование:** Грант Министерства науки и высшего образования Российской Федерации № 075-15-2020-773.

**Ссылка при цитировании:** Гулин А. А., Донцов А. Е., Яковлева М. А., Трофимова Н. Н., Айбуш А. В., Васин А. А., Островский М. А. Окислительная деструкция меланосом из клеток РПЭ человека, индуцированная супероксидными радикалами, приводит к образованию реакционноспособных альдегидов и кетонов // Научно-технические ведомости СПбГПУ. Физико-математические науки. Т. 3.2 № .15. С. 311–316. DOI: <https://doi.org/10.18721/JPM.153.257>

Статья открытого доступа, распространяемая по лицензии CC BY-NC 4.0 (<https://creativecommons.org/licenses/by-nc/4.0/>)

### Introduction

Melanosomes contained in RPE cells of the eye perform the function of screening photoreceptor cells from excessive illumination and the function of antioxidant protection of the cell from free radical oxidation caused by irradiation and reactive oxygen species [1–4]. Aging leads to a significant decrease in the number of melanosomes in RPE cells. While in the age group below 20 years melanosomes occupy up to 8% of the RPE cell volume, in the age group 40–90 years this volume gradually decreases to 3.5% [5]. At the same time the total concentration of melanin in the RPE cell decreases by 2.5 times [6]. It is assumed the content of melanin decreases due to its photooxidative and/or oxidative destruction [6, 7]. Oxidative destruction of RPE melanosomes leads on the one hand to a decrease in their antioxidant activity and on the other hand, to the appearance of prooxidant properties and an increase in photoreactivity [8–11]. In other words the oxidative destruction of melanin in RPE melanosomes causes the degradation of native organelles, significant decrease of their antioxidant activity and the resulting destruction products can exhibit prooxidant activity. All this leads to a decrease in the antioxidant status of RPE cells. It is known that oxidative destruction of melanin can be caused by hydrogen peroxide and UV irradiation [12, 13], as well as by the action of superoxide radicals [7]. In this case a mixture of water-soluble fluorescent products is formed. The aim of this work was to study the nature and physicochemical properties of water-soluble products formed during the oxidative degradation of RPE melanosomes induced by potassium superoxide. The results obtained indicate that during the oxidative destruction of melanosomes toxic carbonyls are formed that can damage cell structures in the dark.

### Materials and methods

**Obtaining water-soluble degradation products of melanosomes.** Melanosomes were isolated from RPE cells of human donor eyes obtained from the eye tissue bank of the S.N. Fedorov NMRC “MNTK Eye Microsurgery”, according to the standard method [7, 14]. Oxidative degradation of melanosomes was carried out by incubating a suspension of melanosomes in 0.1 M K-phosphate buffer, pH 7.4, ( $1.0 \times 10^8 - 5.0 \times 10^8$  granules/mL) with dry potassium superoxide (3–8 mg) at room temperature for 1–2 hours. At the end of the reaction, the water-soluble degradation products of melanosomes were separated by centrifugation in a Beckman Allegra 64R centrifuge at 10,000xg for 20 min.

**Measurement of melanosome degradation products.** RPE melanosome degradation products obtained in the reaction with superoxide radicals were registered by the accumulation of low molecular weight fluorescent compounds, which were measured at an exciting light wavelength of 450–470 nm [7]. The emission intensity was measured on a Shimadzu RF5301PC Spectro fluorophotometer (Japan). Water-soluble degradation products had an emission maximum in the



region of 520–525 nm. Melanosome samples not treated with potassium superoxide were used as controls. A calibration dependence curve of the emission intensity at 520–525 nm on the concentration of synthetic DOPA-melanin completely oxidized by  $\text{KO}_2$  was used to estimate the concentration of melanosome destruction products.

**Determination of the concentration of products that react with thiobarbituric acid (TBA-reactive products).** Water-soluble degradation products of RPE melanosomes were evaluated for the content of reactive carbonyls reacting with thiobarbituric acid [15]. The concentration of TBA-reactive products was determined spectrophotometrically at a wavelength of 532 nm [16] on a Shimadzu UV-1700 spectrophotometer (Japan). The initial samples of melanosomes not oxidized with superoxide served as the control.

**Analysis of melanosome degradation products by time-of-flight secondary ion mass spectrometry.** Mass spectrometry experiments were performed on the TOF.SIMS.5 instrument (ION-TOF, Germany) equipped with 30 keV  $\text{Bi}_3^+$  cluster beam. At least 10 measurements for each sample were recorded in both positive and negative ion modes. An electron flood gun was activated to avoid charging effect during analysis. Due to high energy of bismuth projectiles organic species are regularly fragmented and therefore presented on mass spectrum as a set of characteristic ions.

**Measurement of protein modification by water-soluble degradation products of RPE melanosomes.** The process of protein modification was assessed by the formation of fluorescent Schiff bases in the reaction between free amino groups of proteins and aldehydes. Modification of proteins (bovine serum albumin BSA or hemoglobin from human erythrocytes) with water-soluble products of melanosomes oxidative degradation was carried out by incubation at 37°C for 24–48 hours, followed by dialysis to remove low molecular weight unreacted substances. The incubation medium contained: 0.1 M sterile potassium phosphate buffer, pH 7.4; 2–4 mg/ml BSA (or 2–3 mg/ml hemoglobin), 3–4 mM sodium azide and 0.4–0.7 ml supernatants of oxidized and non-oxidized (control) RPE melanosomes. Samples containing only proteins without supernatants and supernatants without added proteins were used as additional control samples. The content of modified proteins was estimated by fluorescence spectrum at the emission maximum at 440–455 nm (an excitation wavelength of 365 nm) after dialysis.

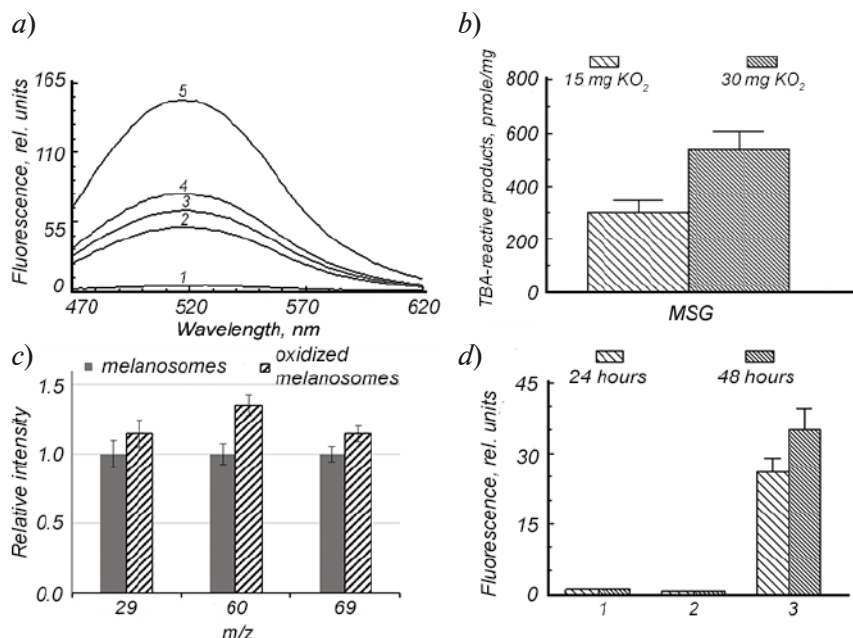


Fig. 1. Melanin suspension fluorescence spectra at different incubation times with  $\text{KO}_2$  (curves 1–5 correspond incubation during 0 min, 30 min, 60 min, 90 min and 180 min, respectively) (a); excitation wavelength was 450 nm; content of TBA-reactive products in melanin for different amounts of added  $\text{KO}_2$  (b); carbonyl ion signals in melanin samples under the destructive effect of  $\text{KO}_2$  (c); the corresponding chemical formulas are given in the text; integrated fluorescence signal from albumin and modified albumin (d)

## Results and discussion

Fig. 1,*a* shows that, under normal physiological conditions, potassium superoxide causes the destruction of melanin with the formation of fluorescent degradation products with an emission maximum at 520–525 nm. Time-of-flight mass spectrometry was performed to determine the presence of aldehydes in water-soluble fractions of melanosomes in human eye RPE cells. As can be seen from the diagram (Fig. 1,*c*), there is a significant increase in carbonyl ions ( $m/z = 29 - \text{CHO}^+$ ,  $m/z = 60 - \text{C}_2\text{H}_4\text{O}_2^+$ ,  $m/z = 69 - \text{C}_4\text{H}_7\text{O}^+$ ) after exposure to superoxide. The ion with  $m/z = 60$  shows the largest increase (about 1.5 times). This indicates the presence of aldehydes in the water-soluble degradation products formed during the oxidation of melanosomes by superoxide radicals. These results are confirmed by experiments on the content of carbonyl compounds that react with thiobarbituric acid (TBA-reactive products) (Fig. 1,*b*). One can see that the supernatants of oxidized samples contain significantly more TBA-reactive products than the supernatants of control samples and higher dose of added  $\text{KO}_2$  formed more TBA-reactive products.

Obtained results indicate that the oxidation of melanosomes with potassium superoxide leads to the formation of carbonyl products that are readily soluble in the aqueous phase. The degree of melanin destruction depends on the melanin/superoxide ratio. Increased superoxide concentration results in increased accumulation of TBA-reactive products (Fig. 1,*b*). Calculations show that one RPE cell with a volume of  $2 \times 10^{-9}$  ml contains about 10–20 picograms of melanin and with its complete destruction up to 0.3 nmol of TBA-reactive products can be accumulated. This amount is quite a lot for the manifestation of the toxic effect of carbonyls. It was also found that the aldehydes and ketones contained in the water-soluble fraction obtained as a result of the oxidative degradation of melanosomes are quite stable, since the content of TBA-reactive products in them practically did not change. The appearance of such long-lived and active chemicals during oxidative destruction of RPE melanosomes may contribute to the development of various eye pathologies.

To the best of our knowledge, it was shown for the first time that water-soluble products of oxidative degradation of RPE melanosomes showed the ability to modify proteins. Thus, incubation of BSA at 37 °C for 24 and 48 h in the presence of water-soluble melanosome degradation products leads to a significant increase in the intensity of albumin fluorescence (Fig. 1*d*, bars 3). On the contrary, only a slight increase in the fluorescence intensity is observed in the control samples (Fig. 1,*d*, bars 1 and 2). This indicates the formation of Schiff bases during the reaction between the amino groups of albumin and aldehydes contained in water-soluble fractions of oxidized melanosomes. The process of BSA modification depended on the incubation time and was absent in the case of BSA incubation with water-soluble products of unoxidized melanin.

Obtained results indicate the toxicity of the products of oxidative degradation of RPE melanosomes. The accumulation of carbonyl products in the cell can lead to an increase in carbonyl stress, the development of inflammatory processes and be of great importance in the pathogenesis of senile eye pathologies. Previously we have shown that during the oxidative destruction of RPE human melanosomes the polymer structure of melanin is destroyed, which is accompanied by a decrease in the concentration of paramagnetic centers and the accumulation of water-soluble fluorescent products of melanin oxidation [7]. This work presented a detailed study of the melanin oxidative destruction induced by the action of superoxide radicals. The oxidative destruction of melanosomes leads to the formation of TBA-reactive products containing highly active carbonyl compounds. Water-soluble products formed during the oxidation of melanosomes cause the modification of bovine serum albumin with the formation of fluorescent Schiff bases.

## Conclusion

It is assumed that one of the main mechanisms of age-related melanin concentration decrease in human RPE cells is its destruction in melanolipofuscin granules. Melanin in the melanolipofuscin granule is in close contact with lipofuscin and lipofuscin fluorophores are capable of forming reactive oxygen species, superoxide radicals, under the action of light [17]. Hence, the age-related decrease of melanosomes amount [5] and melanin concentration [6] in the RPE cell and the formation of reactive aldehydes and ketones, that are toxic to the cell, can be explained by the action of reactive oxygen species formed during photoinduced oxygen reduction by lipofuscin fluorophores [7].



The accumulation of carbonyl products in the cell as a result of the melanin oxidative breakdown can lead to the development of carbonyl stress, inflammatory processes and therefore this process is of great importance for understanding the pathogenesis of senile eye pathologies. In addition, our results suggest that under oxygen stress caused by various reasons and accompanied by the generation of superoxide radicals one of the mechanisms of the toxic effect on RPE cells may be connected with accumulation of highly reactive aldehydes and ketones formed during the destruction of melanosomes by superoxide radicals.

### Acknowledgments

The work was supported by the Ministry of Science and Higher Education of the Russian Federation (No. 075-15-2020-773).

### REFERENCES

1. **Ostrovsky M.A., Sakina N.L., Dontsov A.E.**, Antioxidative role of eye screening pigments, *Vision Research*. 27 (1987) 893–899.
2. **Dontsov A.E., Ostrovsky M.A.**, The antioxidant role of screening eye pigments – melanins and ommochromes, and physicochemical mechanism of their action. In: Varfolomeev SD, Burlakova EB, editors. *Chemical and Biological Kinetics*. New Horizons. Danvers; MA 0193, USA; 2005. 2: 133–150.
3. **Ostrovsky M.A., Zak P.P., Dontsov A.E.**, Vertebrate eye melanosomes and invertebrate eye ommochromes as screening cell organelles, *Biology Bulletin*. 45 (2018) 570–579.
4. **Ostrovsky M.A., Dontsov A.E.**, Vertebrate Eye Melanosomes and Invertebrate Eye Ommochromes as Antioxidant Cell Organelles: Part 2, *Biology Bulletin*. 46 (2019) 105–116.
5. **Feeney-Burns L., Hilderbrand E.S., Eldridge S.**, Aging human RPE: morphometric analysis of macular, equatorial, and peripheral cells. *Investigative Ophthalmology & Visual Science*. 25 (1984) 195–200.
6. **Sarna T., Burke J.M., Korytowski W., Ryzanowska M., Skumatz C.M.B., Zareba A., Zareba M.**, Loss of melanin from human RPE with aging: possible role of melanin photooxidation, *Experimental Eye Research*. 76 (2003) 89–98.
7. **Dontsov A.E., Sakina N.L., Ostrovsky M.A.**, Loss of melanin by eye retinal pigment epithelium cells is associated with its oxidative destruction in melanolipofuscin granules, *Biochemistry (Moscow)*. 82 (2017) 916–924.
8. **Zadlo A., Rozanowska M.B., Burke J.M., Sarna T.J.**, Photobleaching of retinal pigment epithelium melanosomes reduces their ability to inhibit iron induced peroxidation of lipids, *Pigment Cell Research*. 20 (2007) 52–60.
9. **Rozanowski B., Burke J.M., Boulton M.E., Sarna T., Ryzanowska M.**, Human RPE melanosomes protect from photosensitized and iron-mediated oxidation but become pro-oxidant in the presence of iron upon photodegradation, *Investigative Ophthalmology & Visual Science*. 49 (2008) 2838–2847.
10. **Zadlo A., Burke J.M., Sarna T.**, Effect of untreated and photobleached bovine RPE melanosomes on the photoinduced peroxidation of lipids, *Photochemical & Photobiological Sciences*. 8 (2009) 830–837.
11. **Olchawa M.M., Szewczyk G.M., Zadlo A.C., Krzysztynska-Kuleta O.I., Sarna T.J.**, The effect of aging and antioxidants on photoreactivity and phototoxicity of human melanosomes: in vitro study, *Pigment Cell & Melanoma Research*. 34 (2020) 670–682.
12. **Ito S., Nakanishi Y., Valenzuela R.K., Brilliant M.H., Kolbe L., Wakamatsu K.**, Usefulness of Alkaline Hydrogen Peroxide Oxidation to Analyze Eumelanine and Pheomelanine in Various Tissue Samples: Application to Chemical Analysis of Human Hair Melanins, *Pigment Cell Melanoma Research* 24 (2011) 605–613.
13. **Wakamatsu K., Nakanishi Y., Miyazaki N., Kolbe L., Ito S.**, UVA-induced oxidative degradation of melanins: Fission of indole moiety in eumelanin and conversion to benzothiazole moiety in pheomelanin, *Pigment Cell Melanoma Research*. 25 (2012) 434–445.
14. **Feldman T.B., Yakovleva M.A., Arbukhanova P.M., Borzenok S.A., Kononikhin A.S., Popov I.A., Nikolaev E.N., Ostrovsky M.A.**, Changes in spectral properties and composition of lipofuscin fluorophores from human retinal pigment epithelium with age and pathology, *Analytical and Bioanalytical Chemistry*. 407 (2015) 1075–1088.

15. **Esterbauer H., Cheeseman K.H.**, Determination of aldehydic lipid peroxidation products: Malonaldehyde and 4-hydroxynonenal, *Methods in Enzymology*. 186 (1990) 407–421.
16. **Buege J.A., Aust S.D.**, Microsomal lipid peroxidation, *Methods in Enzymology*. 52 (1978) 302–310.
17. **Boulton M., Dontsov A., Jarvis-Evans J., Ostrovsky M., Svistunenko D.**, Lipofuscin is a photoinducible free radical generator, *Journal of Photochemistry and Photobiology B: Biology*. 19 (1993) 201–204.

#### THE AUTHORS

**GULIN Alexander**

aleksandr.gulin@phystech.edu  
ORCID: 0000-0001-7117-4276

**DONTSOV Alexander**

adontsovnick@yahoo.com  
ORCID: 0000-0002-8367-5008

**YAKOVLEVA Marina**

lina.invers@gmail.com  
ORCID: 0000-0003-4243-2787

**TROFIMOVA Natalia**

ntrofimova@mail.ru  
ORCID: 0000-0001-8951-7134

**AYBUSH Arseny**

aiboosh@gmail.com  
ORCID: 0000-0002-0496-9105

**VASIN Alexander**

a2vasin@yandex.ru  
ORCID: 0000-0003-0152-3391

**OSTROVSKY Mikhail**

ostrovsky3535@mail.ru  
ORCID: 0000-0003-4350-2812

*Received 15.07.2022. Approved after reviewing 24.07.2022. Accepted 25.07.2022.*

Conference materials

UDC 57.089.38

DOI: <https://doi.org/10.18721/JPM.153.258>

## **Oocyte enucleation by 795 nm femtosecond laser is a precise and effective method of recipient cytoplasm preparation**

A. A. Osychenko <sup>✉</sup>, A. D. Zalessky, U. A. Tochilo, D. Yu. Martirosyan

N.N. Semenov Federal Research Center of Chemical Physics, Russian Academy of Sciences, Moscow, Russia

<sup>✉</sup> [alina.chemphys@gmail.com](mailto:alina.chemphys@gmail.com)

**Abstract.** Oocyte enucleation by femtosecond (fs) laser radiation is low-invasive and effective method of recipient cytoplasm preparation. We have already demonstrated an ability to completely eliminate the metaphase plate by the fs laser without significant oocyte morphology and viability impairment. Considering further development of femtosecond laser oocyte enucleation for artificial reproductive technologies in humans and for the somatic cell nuclear transfer in mammals, the persistence of any DNA fragments after the fs laser enucleation must be studied thoroughly. In this work we revealed the remains of the metaphase plate by super resolution confocal microscopy after the laser enucleation of mouse oocytes at metaphase II stage. The laser was set up on 795 nm in 80 MHz mode with 0,5 nJ pulse energy. By the super resolution microscopy (Airyscan 2) we have detected minor fragments of the metaphase plate in the laser-exposed oocytes. However, the careful laser treatment is able to provide the recipient cytoplasm without any detectable DNA fragments.

**Keywords:** recipient cytoplasm, femtosecond laser, super resolution microscopy

**Funding:** This work is supported by the Russian Science Foundation under grant № 21-75-10155. The work was performed on facilities of ACBS Center of the Collective Equipment (no. 506694, FRCCP RAS) and large-scale research facilities № 1440743.

**Citation:** Osychenko A. A., Zalessky A. D., Tochilo U. A., Martirosyan D. Yu., Oocyte enucleation by 795 nm femtosecond laser is a precise and effective method of recipient cytoplasm preparation, St. Petersburg State Polytechnical University Journal. Physics and Mathematics. 15 (3.2) (2022) 317–320. DOI: <https://doi.org/10.18721/JPM.153.258>

This is an open access article under the CC BY-NC 4.0 license (<https://creativecommons.org/licenses/by-nc/4.0/>)

Материалы конференции

УДК 57.089.38

DOI: <https://doi.org/10.18721/JPM.153.258>

## **Энуклеация ооцитов с помощью фемтосекундного лазера с длиной волны 795 нм – точный и эффективный метод подготовки реципиентного цитопласта**

А. А. Осыченко <sup>✉</sup>, А. Д. Залесский, У. А. Точило, Д. Ю. Мартиросян

Федеральный исследовательский центр химической физики  
им. Н.Н. Семенова Российской академии наук, г. Москва, Россия

<sup>✉</sup> [alina.chemphys@gmail.com](mailto:alina.chemphys@gmail.com)

**Аннотация.** Энуклеация ооцитов фемтосекундным (фс) лазерным излучением является малоинвазивным и эффективным методом подготовки реципиентного цитопласта. Мы уже продемонстрировали возможность полного удаления метафазной пластинки с помощью фс лазера без значительного ухудшения морфологии и жизнеспособности ооцитов. Учитывая дальнейшее развитие фемтосекундной лазерной энуклеации

ооцитов для искусственных репродуктивных технологий у человека и переноса ядер соматических клеток у млекопитающих, необходимо тщательно изучить присутствие любых фрагментов ДНК после фс лазерной энуклеации. В данной работе мы выявляли остатки метафазной пластинки с помощью конфокальной микроскопии сверхвысокого разрешения после лазерной энуклеации ооцитов мыши на стадии метафазы II. Лазер был настроен на 795 нм в режиме 80 МГц с энергией в импульсе 0,5 нДж. С помощью микроскопии сверхвысокого разрешения (Airyscan 2) мы обнаружили незначительные фрагменты метафазной пластинки в ооцитах, подвергшихся воздействию лазера. Однако тщательная лазерная обработка способна обеспечить реципиентный цитопласт без каких-либо обнаруживаемых фрагментов ДНК.

**Ключевые слова:** реципиентный цитопласт, фемтосекундный лазер, микроскопия сверхвысокого разрешения

**Финансирование:** Работа выполнена при поддержке гранта РФФИ № 21-75-10155. Работа выполнена на ЦКП № 506694 ФИЦ ХФ РАН и УНУ № 1440743.

**Ссылка при цитировании:** Осыченко А. А., Залесский А. Д., Точило У. А., Мартиросян Д. Ю. Энуклеация ооцитов с помощью фемтосекундного лазера с длиной волны 795 нм – точный и эффективный метод подготовки реципиентного цитопласта // Научно-технические ведомости СПбГПУ. Физико-математические науки. Т. 15. № 3.2. С. 317–320. DOI: <https://doi.org/10.18721/JPM.153.258>

Статья открытого доступа, распространяемая по лицензии CC BY-NC 4.0 (<https://creativecommons.org/licenses/by-nc/4.0/>)

### Introduction

Removing the DNA from the living cell is of relevance for medical and biomedical applications, including somatic cell nuclear transfer (SCNT) in animals and mitochondrial replacement therapy (MRT) in humans. In particular, DNA removal is commonly performed for these purposes, by nucleus or metaphase plate aspiration with a needle, which can be resulted in the loss of reprogramming factors [1]. More, aspiration by a needle implies the cell puncturing, and requires applying cytoskeleton poisons, e.g., cytochalasin B [2]. As an alternative for aspiration, near-infrared femtosecond lasers are able to perform intracellular incisions with the submicron resolution, acting locally in the focal volume of the laser beam [3, 4]. In our recent research we have shown that near-infrared femtosecond laser effectively destroys the metaphase plate but does not affect oocyte viability and development by itself. Double fluorescent staining as well as the disability to develop parthenogenetically after the laser exposure confirm the lack of DNA in enucleated oocytes [5]. However, the question of the persistence of any DNA fragments after the fs laser enucleation must be studied thoroughly. In this work we have studied the remains of the metaphase plate by super resolution confocal microscopy. We have detected minor fragments of the metaphase plate in the laser-exposed oocytes. However, the careful laser treatment is able to provide the recipient cytoplasm without any detectable DNA fragments.

### Materials and Methods

**Oocyte collection.** To obtain oocytes at metaphase II stage, C57Bl/6 female mice were induced to superovulate by the standard scheme [5]. Mice were sacrificed and the oviducts were removed. Cumulus-oocyte complexes were purified from cumulus by 0.1% hyaluronidase (H4272, Sigma-Aldrich) in M2 culture medium (M7167, Sigma-Aldrich). For the metaphase plate visualization, the oocytes were stained with 5 µg/ml Hoechst 33342 dye (B2261, Sigma-Aldrich) for 15 minutes in M2 medium and then washed twice. During the experiment the oocytes were cultured in M2 medium.

**Laser parameters and enucleation process.** The detailed scheme of the oocyte enucleation is described here [5]. Briefly, in these experiments we used following parameters for the irradiation of the metaphase plate:  $\lambda = 795$  nm,  $\nu = 80$  MHz, pulse energy 0.5 nJ (40 mW power); 100 fs pulse duration, pulse train duration 60 ms. Laser radiation was focused by 60× objective lens ( $NA = 0.7$ ). Before the enucleation we performed the metaphase plate visualization by UV illumination. Then the metaphase plate was exposed to laser. The exposure was repeated multiple times until the DNA luminescence stopped.

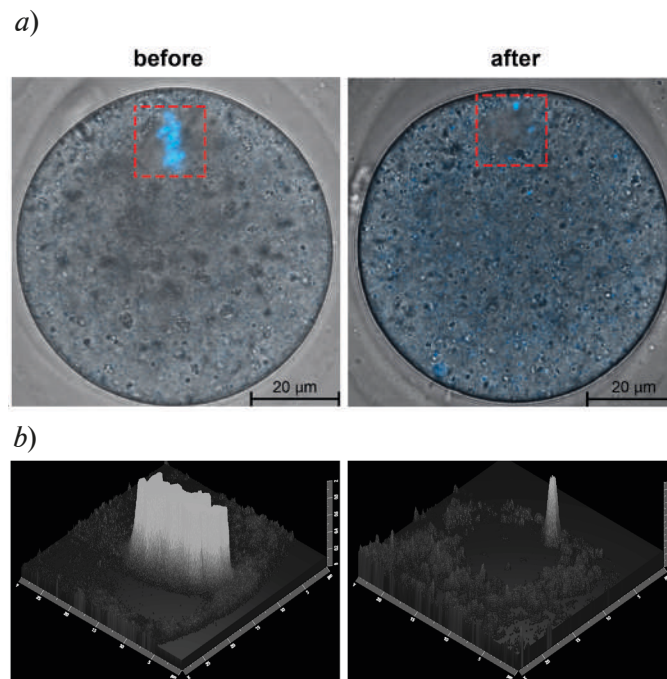


Fig. 1. Confocal images of the oocytes before and after the laser enucleation: brightfield + luminescence images (*a*). The red square shows an area containing the metaphase plate. These areas were further investigated by Airyscan 2. Super resolution image, presented in 2.5 D mode (*b*). *X* and *Y* axes show the distance (5  $\mu\text{m}$  scale), *Z* axis shows the intensity.

**Confocal imaging.** Fluorescence imaging was performed using a laser scanning confocal microscope Zeiss LSM 980 (Carl Zeiss Microscopy, Jena, Germany), 63x Plan-Apochromat objective (NA = 1.4; oil immersion). The oocytes were placed in M2 medium drop on a 0.17 mm cover glass (Zeiss). Hoechst 33342 luminescence excitation were performed by 405 nm laser, detection range 410-479 nm. Super resolution was obtained by Airyscan 2 with 5 AU pinhole (251  $\mu\text{m}$ ).

### Results and Discussion

The oocytes were exposed to the laser radiation as described [5]. In short, the femtosecond laser pulses were applied in the area of the metaphase plate, and fluorescence was observed in the focal spot with each pulse simultaneously. Laser exposure on the metaphase plate was repeated multiple times until the DNA luminescence stopped. Fig. 1 represents the oocytes before and after the femtosecond enucleation. Clearly visible at the left image (Fig. 1,*a*), DNA luminescence is almost undetectable at the right image, obtained after the laser exposure. The remains of the metaphase plate are slightly visible in super resolution mode (Fig. 1,*b*). A single peak of the luminescence, shown at right B image, could be easily eliminated by more careful laser exposure and control. The rest of the laser-exposed area has practically zero luminescence signal. Note that the oocytes retain their morphology and viability after the laser exposure.

### Conclusion

We have detected minor fragments of the metaphase plate in the oocytes, enucleated by 795 nm femtosecond laser. However, the careful laser treatment is able to provide the recipient cytoplasm without any detectable DNA fragments.

### Acknowledgments

This work is supported by the Russian Science Foundation under grant 21-75-10155. The work was performed on facilities of ACBS Center of the Collective Equipment (no. 506694, FRCCP RAS) and large-scale research facilities 1440743.

## REFERENCES

1. **Ogura A., Inoue K., Wakayama T.**, Recent advancements in cloning by somatic cell nuclear transfer, *Phil Trans R Soc B* 368 (2012) 20110329.
2. **Ogura A.**, **Cloning Mice**, *Cold Spring Harb Protoc.* 8 (2017) pdb.prot094425.
3. **Shakhbazyan A.K., Sviridova-Chailakhyan T.A., Karmenyan A.K., Krivokharchenko A.S., Chiou A., Chailakhyan L.M.**, The Use of Laser for Obtaining Recipient Cytoplasts for Mammalian Nuclear Transfer, *Doklady Biological Sciences* 428 (2009) 1–4.
4. **Kuetemeyer K., Lucas-Hahn A., Petersen B., Lemme E., Hassel P., Niemann H., Heisterkamp A.**, Combined multiphoton imaging and automated functional enucleation of porcine oocytes using femtosecond laser pulses, *Journal of Biomedical Optics* 15 (4) (2010) 046006.
5. **Osychenko A.A., Zalessky A.D., Tochilo U.A., Martirosyan D.Yu., Silaeva Y.Yu., Nadtochenko V.A.**, Femtosecond laser oocyte enucleation as a low-invasive and effective method of recipient cytoplast preparation, *Biomed. Opt. Express* 13 (3) (2022) 1447–1456.

## THE AUTHORS

**OSYCHENKO Alina**  
alina.chemphys@gmail.com  
ORCID: 0000-0002-7519-2479

**TOCHILO Uliana**  
yanulyana@gmail.com  
ORCID: 0000-0002-4511-6109

**ZALESSKY Alexandr**  
aleksandr.zalesskij@phystech.edu  
ORCID: 0000-0002-1992-0574

**MARTIROSYAN David**  
petrosyan359@gmail.com  
ORCID: 0000-0002-2952-8867

*Received 16.07.2022. Approved after reviewing 19.07.2022. Accepted 20.07.2022.*

## PHYSICS OF MOLECULES

Conference materials

UDC 535-47

DOI: <https://doi.org/10.18721/JPM.153.259>

### Nonlinear circular dichroism in dielectric nanoparticle dimers and trimers

A. D. Nikitina <sup>1</sup>✉, A. A. Nikolaeva <sup>1</sup>, M. I. Petrov <sup>1</sup>, K. S. Frizyuk <sup>1</sup>

<sup>1</sup> ITMO University, St. Petersburg, Russia

✉ [anastasia.nikitina@metalab.ifmo.ru](mailto:anastasia.nikitina@metalab.ifmo.ru)

**Abstract.** We performed the theoretical study of circular dichroism (CD) in the second harmonic (SH) signal generated in nanostructures of different symmetries. In particular, we explored nonlinear response of dielectric AlGaAs nanoparticles and showed that even in the case of symmetric achiral shape circular dichroism is possible only for some specific shapes and crystalline lattice orientations. Using the apparatus of group theory, we compared dimer and C<sub>3v</sub> symmetric trimer structures, and explained the appearance of SH-CD in dimer, as well as the absence of dichroism in AlGaAs trimers. In summary, we proved, that knowing the general symmetry of the nanostructure with crystalline lattice is not enough, and detailed analysis of the eigenmodes and nonlinear polarization symmetry is required.

**Keywords:** second harmonic generation, nonlinear circular dichroism, AlGaAs, dielectric nanoparticle, Mie resonance

**Funding:** This work was supported by the Russian Science Foundation Project 22-12-00204. K.F. acknowledges support from the Foundation for the Advancement of Theoretical Physics and Mathematics "BASIS" (Russia).

**Citation:** Nikitina A. D., Nikolaeva A. A., Petrov M. I., Frizyuk K. S., Nonlinear circular dichroism in dielectric nanoparticle dimers and trimers, St. Petersburg State Polytechnical University Journal. Physics and Mathematics. 15 (3.2) (2022) 321–325. DOI: <https://doi.org/10.18721/JPM.153.259>

This is an open access article under the CC BY-NC 4.0 license (<https://creativecommons.org/licenses/by-nc/4.0/>)

Материалы конференции

УДК 535-47

DOI: <https://doi.org/10.18721/JPM.153.259>

### Нелинейный циркулярный дихроизм в димерах и тримерах диэлектрических наночастиц

А. Д. Никитина <sup>1</sup>✉, А. А. Николаева <sup>1</sup>, М. И. Петров <sup>1</sup>, К. С. Фризык <sup>1</sup>

<sup>1</sup> Университет ИТМО, Санкт-Петербург, Россия

✉ [anastasia.nikitina@metalab.ifmo.ru](mailto:anastasia.nikitina@metalab.ifmo.ru)

**Аннотация.** В работе проведено теоретическое исследование кругового дихроизма (КД) в сигнале второй гармоники (ВГ), генерируемом в наноструктурах различной симметрии. В частности, был изучен нелинейный отклик диэлектрических наночастиц AlGaAs симметричной ахиральной формы и показано, что даже в этом случае нелинейный круговой дихроизм возможен только для некоторых определенных форм и ориентаций кристаллической решетки. С использованием аппарата теории групп были проанализированы димерные и тримерные структуры и объяснено появление ВГ-КД в димерных структурах, а также отсутствие дихроизма в тримерах AlGaAs. Как итог, было

продемонстрировано, что знания общей симметрии наноструктуры с кристаллической решеткой недостаточно, требуется проводить детальный анализ собственных мод и симметрии нелинейной поляризации.

**Ключевые слова:** генерация второй гармоники, нелинейный круговой дихроизм, AlGaAs, диэлектрическая наночастица, резонанс Ми

**Финансирование:** Работа выполнена при поддержке РФФ (проект 22-12-00204). К.Ф. выражает благодарность за поддержку Фонду развития теоретической физики и математики «БАЗИС».

**Ссылка при цитировании:** Никитина А. Д., Николаева А. А., Петров М. И., Фризюк К. С. Нелинейный циркулярный дихроизм в димерах и тримерах диэлектрических наночастиц // Научно-технические ведомости СПбГПУ. Физико-математические науки. Т. 15. № 3.2. С. 321–325. DOI: <https://doi.org/10.18721/JPM.153.259>

Статья открытого доступа, распространяемая по лицензии CC BY-NC 4.0 (<https://creativecommons.org/licenses/by-nc/4.0/>)

### Introduction

Circular dichroism is a relevant phenomenon in nanophotonic for exploring the properties of media and molecules. Meanwhile, the nonlinear circular dichroism such as dichroism of the second harmonic (SH-CD) opens new prospective for various application of nonlinear photonics [1–5].

One of the recent works on CD in the SH signal considered a structure that consists of two identical AlGaAs cylinders irradiated by circularly polarized light [5]. The crystalline lattice has a specific orientation  $[100] \parallel x$ ,  $[001] \parallel z$ , and the structure can be rotated around the  $z$ -axis. The study revealed that CD exists only if the dimer's axis is rotated with the respect to the  $[100]$  crystalline axis. An erroneous conclusion can be drawn, that this is due to the low total symmetry of the structure with lattice.

In this work, we demonstrated that the existence of CD in the SHG signal depends on the symmetry in a tricky way, and one should always consider the symmetry of the induced nonlinear polarization and the nanostructure's eigenmodes. To show that the total symmetry does not play a major role, we compared the nonlinear response of dimers and  $C_{3v}$  symmetric trimers and obtained and explained via the group theory the total absence of CD in the trimer. All our results were also verified using numerical modeling in COMSOL Multiphysics™.

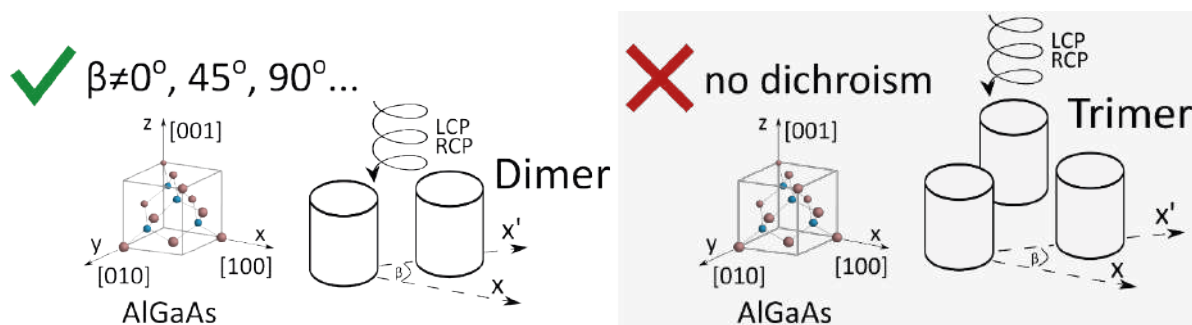


Fig. 1. Illustration of main result of the study of CD in SH signal in AlGaAs nanoparticles.

On the left side of the figure, a dimer structure shows a nonvanishing nonlinear CD. It exists only if  $\beta \neq Z\pi/4$ , where  $\beta$  is the angle between the crystalline  $x$ -axis and the sample's  $x'$ -axis and  $Z$  is an integer number. On the right side of the figure, a trimer structure is shown. SH-CD never appears here for any lattice orientation.



## Materials and Methods

We study dielectric AlGaAs nanostructures with particular symmetry. One can achieve an efficient second-harmonic generation signal because of the lack of inversion symmetry of the crystalline lattice. In this case, nonlinear circular dichroism can appear. The size of the nanostructure is about 1  $\mu\text{m}$ , and the incident wavelength is in the infrared range, while the SH wavelength is in visible range. The size of the AlGaAs nanostructure should be large enough to allow obtaining hexadecapole ( $n = 4$ ) Mie resonances, as it allows us to observe a significant nonlinear circular dichroism in the vicinity of these resonances, which will be explained later. The particular shape of the nanostructure does not play a significant role, only the symmetry group is important. Thus, our considerations are the same for a dimer and rectangular prism, or for a trimer and triangular prism, or any other shapes with these symmetries. For both dimer and trimer structures, we consider the same AlGaAs lattice orientation,  $[001] \parallel z$ ,  $[100] \parallel x$ . The structures are irradiated by normally incident circularly polarized plane wave and can be rotated around the  $z$ -axis by arbitrary angle  $\beta$  as it is shown in Fig. 1.

## Results and Discussion

Nonlinear circular dichroism manifests itself in the different nonlinear responses of structure for left and right polarization (LCP and RCP). It is described by the formula

$$\text{SH-CD} = 2 \frac{(I_{\text{RCP}}^{2\omega} - I_{\text{LCP}}^{2\omega})}{(I_{\text{RCP}}^{2\omega} + I_{\text{LCP}}^{2\omega})}.$$

Considering the dimer, i.e., two identical AlGaAs cylinders, we obtain the nonvanishing nonlinear CD for majority of angles. To provide the theory of the appearance of the nonlinear CD, we should analyse SH polarization  $\mathbf{P}^{2\omega}(\mathbf{r})$ , defined by the formula

$$\mathbf{P}^{2\omega}(\mathbf{r}) = \varepsilon_0 \hat{\chi}^{(2)} \mathbf{E}^{\text{inc}}(\mathbf{r}) \mathbf{E}^{\text{inc}}(\mathbf{r}),$$

where  $\hat{\chi}^{(2)}$  is the nonlinear second-order susceptibility of the crystalline lattice, and  $\mathbf{E}^{\text{inc}}(\mathbf{r})$  is the fundamental field inside the nanoparticle. We use the dyadic Green's function formalism to describe the second harmonic field [6, 7]

$$\begin{aligned} \mathbf{E}^{2\omega}(\mathbf{r}) &= (2\omega)^2 \mu \int_V dV' \hat{\mathbf{G}}(\mathbf{r}, \mathbf{r}', k) \mathbf{P}^{2\omega}(\mathbf{r}') = \\ &= (2\omega)^2 \mu \int_V dV' \sum_n \frac{\mathbf{E}_n(\mathbf{r}) \otimes \mathbf{E}_n(\mathbf{r}')}{2k(k - k_n)} \mathbf{P}^{2\omega}(\mathbf{r}'), \end{aligned}$$

where the contribution of each eigenmode  $\mathbf{E}_n(\mathbf{r})$  to the SH is described by an overlap integral:

$$D_n = \int_V dV \mathbf{E}_n(\mathbf{r}') \mathbf{P}^{2\omega}(\mathbf{r}').$$

We use the approximation for the field on the fundamental frequency inside the nanostructure, assuming that it is the same as in cylindrically symmetric nanoparticle. This approximation is valid, while it is possible to show that taking the exact form of this field does not change the considerations. Thus, field inside the nanoparticle in cylindrical coordinate system is written as follows

$$\mathbf{E}^{\text{inc}} = (E_r(r, z) \mathbf{e}_r + E_z(r, z) \mathbf{e}_z \pm i E_\phi(r, z) \mathbf{e}_\phi) e^{\pm i\varphi},$$

where  $\varphi$  is an angle in cylindrical coordinates, and  $\pm$  sign stands for two different circular polarizations. Rewriting the susceptibility tensor in cylindrical coordinates, we obtain that the SH polarization for AlGaAs contains two terms:

$$\mathbf{P}^{2\omega}(r, z, \varphi) \propto \mathbf{P}_0^{2\omega}(r, z) + \mathbf{P}_4^{2\omega}(r, z) e^{\pm 4i(\varphi - \beta)},$$

where  $\beta$  is the angle between the crystalline  $x$ -axis and sample's  $x'$ -axis. The particular form of SH polarization does not matter, we should know only how it depends on  $\varphi$  and  $\beta$ . Let us note that the first term does not transform under rotations around the  $z$ -axis, while the second is proportional to exponential term and transforms as the functions with  $m = \pm 4$ .

Then we should find out which modes are excited in second harmonic, which is defined by the overlap integral. If the integral with a mode is non-zero, it will be excited. The mode content for dimer and trimer is shown in Fig. 2.  $\mathbf{W}_{\pm 1 m l}$  denote vector spherical harmonics in the far-field of the mode with angular momentum  $l$  and projection  $m$ . Index  $\pm 1$  refers to the parity under reflection in  $y = 0$  plane [8]. The symmetry group of the dimer is  $C_{2v}$  [8]. It has four irreducible representations; hence, it has four types of modes. However, considering the selection rules [7] and overlap integral, we obtain, that only two of them are excited in second harmonic, A1 and A2. We will only consider A1 mode, while for the A2 mode all considerations are the same. According to the group theory, multipoles with indexes  $m = 0$  and  $m = 4$  both correspond to the A1 irrep (see the multipolar content in Fig. 2). In this case both terms of nonlinear polarization  $\mathbf{P}^{2\omega}(\mathbf{r})$  give nonzero overlap integral  $D_n$  with the eigenmode A1. Comparing accurately the complex overlap integral for RCP and LCP polarizations [5] and different  $\beta$ , one can obtain that nonlinear circular dichroism appears for proper orientation between the lattice and pattern axis. In contrast, symmetry group of the trimer is  $C_{3v}$ . Its eigenmodes with  $m = 0$  and  $m = 4$  belong to different irreps, A1 and E (see Fig. 2). So, the first term of nonlinear polarization will excite the A1 mode, and the second term the E mode. These two modes are excited independently, and due to this fact, the coefficients of their excitation are equal for both polarizations. As a result, in trimers, nonlinear CD cannot be observed, despite the low symmetry of a timer.

Mode $C_{2v}$	Far-field multipoles $x, y, z$	Dimer	Mode $C_{3v}$	Far-field multipoles $x, y, z$	Trimer
A1		$\mathbf{W}_{1(2k)}$ ✓	A1		$\mathbf{W}_{1(3k)}$ ✓
A2		$\mathbf{W}_{-1(2k)}$ ✓	A2		$\mathbf{W}_{-1(3k)}$ ✓
B1		$\mathbf{W}_{1(2k-1)}$	E		$\mathbf{W}_{\pm 1(3k-2)}$ $\mathbf{W}_{\pm 1(3k-1)}$ ✓
B2		$\mathbf{W}_{-1(2k-1)}$			

Fig. 2. Comparison of multipolar content of the modes of a dimer and a trimer.  $\mathbf{W}_{\pm 1 m l}$  denote vector spherical harmonics in the far-field of the mode with angular momentum  $l$  and projection  $m$ . Index  $\pm 1$  refers to the parity under reflection in  $y = 0$  plane. The modes excited in SH are marked by a tick. In case if A1 mode is excited in dimer by both terms of the polarization, in trimer A1 mode is excited by the first term, and E by the second. This leads to independent contribution of these two modes in the intensity.

### Conclusion

In summary, we provide the theoretical description of SH-CD. We describe, how the symmetry of the crystalline lattice and the structure together affect nonlinear response. We show that the symmetry behaviour of nonlinear polarization, as well as the mode content in the SH plays a crucial role. For considered case, the nonlinear polarization contains two terms with a different symmetry behaviour, each of them excites modes of the same symmetry in dimer case, and of different symmetries in case of a trimer. This leads to the presence of circular dichroism in case of a dimer structure and the absence in case of a trimer.

**REFERENCES**

1. Berova N., Nakanishi, K., Woody R. W., Circular Dichroism: Principles and Applications, 2nd ed.; Wiley-VCH: Hoboken, NJ, 2000.
2. Wang Z., Cheng F., Winsor T., Liu Y., (2016). Optical chiral metamaterials: a review of the fundamentals, fabrication methods and applications. *Nanotechnology*, 27(41), 412001.
3. Slocik J. M., Govorov A. O., Naik R. R., (2011). Plasmonic Circular Dichroism of Peptide-Functionalized Gold Nanoparticles. *Nano Lett.*, 11(2), 701–705.
4. Belardini A., Larciprete M. C., Centini M., Fazio E., Sibilica C., Chiappe D., Buatier de Mongeot F., (2011). Circular Dichroism in the Optical Second-Harmonic Emission of Curved Gold Metal Nanowires. *Phys. Rev. Lett.*, 107(25), 257401.
5. Frizyuk K., Melik-Gaykazyan E., Choi J.-H., Petrov M. I., Park H.-G., Kivshar, Y., (2021). Nonlinear Circular Dichroism in Mie-Resonant Nanoparticle Dimers. *Nano Lett.*, 21(10), 4381–4387.
6. Doost M. B., Langbein W., Muljarov E. A., (2014). Resonant-state expansion applied to three-dimensional open optical systems. *Phys. Rev. A*, 90(1), 013834.
7. Frizyuk K., Volkovskaya I., Smirnova D., Poddubny A., Petrov M., (2019). Second-harmonic generation in Mie-resonant dielectric nanoparticles made of noncentrosymmetric materials. *Phys. Rev. B*, 99(7), 075425.
8. Gladyshev S., Frizyuk K., & Bogdanov A., (2020). Symmetry analysis and multipole classification of eigenmodes in electromagnetic resonators for engineering their optical properties. *Phys. Rev. B*, 102(7), 075103.

**THE AUTHORS**

**NIKITINA Anastasia**  
anastasia.nikitina@metalab.ifmo.ru  
ORCID: 0000-0002-0396-2761

**PETROV Mihail**  
m.petrov@metalab.ifmo.ru  
ORCID: 0000-0001-8155-9778

**NIKOLAEVA Anna**  
anna.nikolaeva@metalab.ifmo.ru  
ORCID: 0000-0003-1692-9298

**FRIZYUK Kristina**  
k.frizyuk@metalab.ifmo.ru  
ORCID: 0000-0002-0506-464X

*Received 13.07.2022. Approved after reviewing 14.07.2022. Accepted 15.07.2022.*

Conference materials

UDC 621.382

DOI: <https://doi.org/10.18721/JPM.153.260>

### **Optimization of heterostructure transistor parameters for the monolithic integrated circuits of the amplifying path of a medical radiothermograph**

V. G. Tikhomirov <sup>1</sup>, S. V. Chizhikov <sup>2✉</sup>, A. G. Gudkov <sup>2</sup>, A. V. Nikolaenkov <sup>1</sup>, G. A. Gudkov <sup>3</sup>

<sup>1</sup> Saint Petersburg State Electrotechnical University "LETI", St. Petersburg, Russia;

<sup>2</sup> Bauman Moscow State Technical University, Moscow, Russia;

<sup>3</sup> Hyperion Ltd., Moscow, Russia

✉ [chigikov95@mail.ru](mailto:chigikov95@mail.ru)

**Abstract.** The amplifying path of a modern miniature medical radiothermograph should provide a gain of about 80 dB with minimal intrinsic noise levels. The construction of such a path, even on the most modern element base, requires the use of several microcircuits with a significant resulting current consumption. The existing problem can be solved by creating new active elements of specialized monolithic microcircuits - low-noise transistors, for which the requirements of high energy efficiency will be taken into account when designing heterostructures. The paper presents the results of optimizing the design of a heterostructure low-noise transistor for use in microcircuits of the amplifying path of a miniature medical radiothermograph.

**Keywords:** medical radiothermography, heterostructure transistor, optimization, amplifying path

**Funding:** The research was carried out with the financial support of the Russian Science Foundation as part of the scientific project 19-19-00349-П dated 19.05.2022.

**Citation:** Tikhomirov V. G., Chizhikov S. V., Gudkov A. G., Nikolaenkov A. V., Gudkov G. A., Optimization of heterostructure transistor parameters for the monolithic integrated circuits of the amplifying path of a medical radiothermograph, St. Petersburg State Polytechnical University Journal. Physics and Mathematics. 15 (3.2) (2022) 326–330. DOI: <https://doi.org/10.18721/JPM.153.260>

This is an open access article under the CC BY-NC 4.0 license (<https://creativecommons.org/licenses/by-nc/4.0/>)

Материалы конференции

УДК 621.382

DOI: <https://doi.org/10.18721/JPM.153.260>

### **Оптимизация параметров гетероструктурного транзистора для монолитных интегральных схем усилительного тракта медицинского радиотермографа**

В. Г. Тихомиров <sup>1</sup>, С. В. Чижиков <sup>2✉</sup>, А. Г. Гудков <sup>2</sup>, А. В. Николаенков <sup>1</sup>, Г. А. Гудков <sup>3</sup>

<sup>1</sup> Санкт-Петербургский государственный электротехнический университет «ЛЭТИ» им. В.И. Ульянова (Ленина), Санкт-Петербург, Россия;

<sup>2</sup> МГТУ им. Н.Э. Баумана, г. Москва, Россия;

<sup>3</sup> ООО «НПИ ФИРМА «ГИПЕРИОН», г. Москва, Россия

✉ [chigikov95@mail.ru](mailto:chigikov95@mail.ru)

**Аннотация.** В работе представлены результаты оптимизации конструкции гетероструктурного маломощного транзистора для применения в микросхемах усилительного тракта миниатюрного медицинского многоканального многочастотного радиотермографа. Достигнуто значительное повышение крутизны передаточной характеристики предложенной конструкции маломощного транзистора.



**Ключевые слова:** медицинская радиотермография, гетероструктурный транзистор, оптимизация, усилительный тракт

**Финансирование:** Работа выполнена при поддержке РНФ в рамках научного проекта № 19-19-00349-П от 19.05.2022.

**Ссылка при цитировании:** Тихомиров В. Г., Чижиков С. В., Гудков А. Г., Николаенков А. В., Гудков Г. А. Оптимизация параметров гетероструктурного транзистора для монолитных интегральных схем усилительного тракта медицинского радиотермографа // Научно-технические ведомости СПбГПУ. Физико-математические науки. Т. 15. № 3.2. С.–. DOI: <https://doi.org/10.18721/JPM.153.260>

Статья открытого доступа, распространяемая по лицензии CC BY-NC 4.0 (<https://creativecommons.org/licenses/by-nc/4.0/>)

### Introduction

Very high requirements are traditionally placed on the amplifying path of a radiothermograph. In addition, radiothermographs for medical use have a number of other features (for example, the requirements for a very small error in determining body temperature, not exceeding tenths of a kelvin, a record low level of intrinsic noise in the microwave range, etc.), which further tightens the characteristics of the amplifying path. Moreover, there are additional limitations when designing a miniature medical radiothermograph. Indeed, to provide a gain of about 80 dB with minimal levels of intrinsic noise, designing of such a path even on the most modern Monolithic Integrated Circuit (MIC) Low Noise Amplifier (LNA) requires several chips with a total current consumption in the operating mode of the order of hundreds of milliamps. Such current consumption of amplifying stages in a miniature case of a radiothermograph leads to a significant increase in temperature inside the case with the reference noise source located there. This is a significant problem for designers of modern miniature medical radiothermographs. The existing problem can be solved by creating new active elements of specialized monolithic microwave microcircuits - low-noise transistors, for which the requirements of high energy efficiency, primarily low current consumption, low heat release into the surrounding space, low noise level and sufficient gain factor will be taken into account when designing heterostructures [1–2].

### Results and Discussion

A promising system of materials for solving the above problem can reasonably be considered heterostructures of semiconductors of the A3-B5 group. The experience accumulated by the author of successful mathematical modeling and practical implementation of heterostructural microwave transistors with high electron mobility allows to speak about the reasonable probability of successfully solving the above problem of creating a special low-noise microwave transistor with reduced current consumption [3].

Analysis of the possibility of reducing the energy consumption of the amplifying tract of a miniature medical radiothermograph suggested that one of the most significant resources for reducing the energy consumption of the amplifying tract is a change in the design of the active elements of monolithic integrated circuits of low-noise amplifiers. Indeed, almost all modern monolithic integrated circuits of low-noise microwave amplifiers are based on heterostructural pseudomorphic transistors with high electron mobility based on gallium arsenide with an indium channel [4]. The basic structure of the transistor (Fig. 1) is formed on a semi-insulating GaAs substrate, on which a buffer layer is created in the form of an AlAs/GaAs superlattice, an InGaAs channel layer and an AlGaAs n-type barrier layer. Above and below the channel layer adjoins the so-called spacer, a thin layer of unalloyed AlGaAs. The concentration of conduction electrons in the channel reaches  $1.0 \times 10^{12} \text{ cm}^{-2}$ , and their mobility is  $6500 \text{ cm}^2/\text{V}\cdot\text{s}$ . As a result, the maximum current of the transistor channel can be 600 mA/mm (at a channel voltage of 1.5 V), the breakdown voltage is 13 V, the boundary frequency  $f_i$  is 60 Hz, the maximum power amplification frequency  $f_{max}$  is 150 Hz. The optimal operating voltage of the transistor is 6 V.

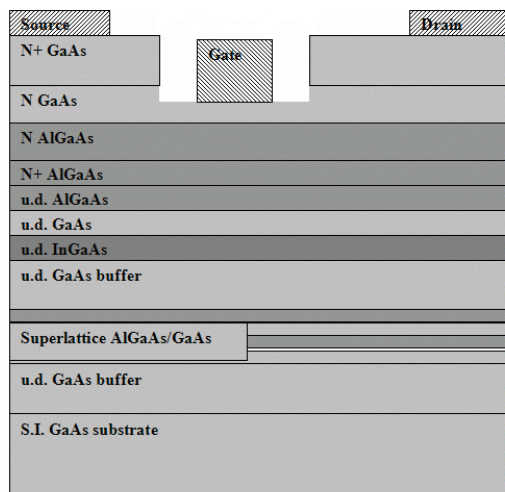


Fig. 1. Schematic cross section of a base transistor with high electron mobility based on gallium arsenide with an indium channel

In order to reduce the current consumption of the active element of such MIC, while maintaining a high gain, which means a high transconductance of the transfer characteristics along the gate, attention should be paid to an effect that is almost imperceptible in other conditions, seriously hindering the reduction of current consumption in such devices. Indeed, as the estimates of the behavior of charge carriers in the transistor channel show, with an increase in the locking potential at the gate, the shape of the quantum well is distorted and some of the electrons can move away from the gate and react less to the controlling effects of its electric field.

This leads to the fact that in the area of low currents, the transconductance of the transfer characteristic becomes insufficient to maintain a high gain of the base active element of the MIC LNA.

In modern devices, in order to reduce the effect of this effect, it is necessary to increase the quiescent current of the operating mode of a low-noise transistor, which leads to an increase in the total current consumption of the MIC, which is usually tolerated against the background of significantly higher current consumption by other elements of the path, for example, the MIC of a power amplifier [5].

However, in our case, it is here that the main reserve for improving the efficiency of a low-noise transistor, as a basic element of a microcircuit, as part of a microwave MIC, can be concentrated, without changing its schematic diagram and manufacturing technology.

By analyzing the effect of changes in the thickness of various layers on the transfer characteristics of the device, we were able to determine the topological parameter that most effectively affects the transfer characteristic of the transistor. This parameter turned out to be the depth of etching of the gate groove. Fig. 2 shows the main results of the analysis.

Analyzing the results shown in Fig. 2, it can be clearly seen that in order to achieve the same transconductance, a new version of the transistor design requires about half the value of the quiescent current. So, for a transistor with a gate width of 100 microns, to reach the transconductance of the characteristic in the region of 400 mSm/mm, it was required to have a quiescent current of about 20 mA. In our proposed version of a transistor with increased energy efficiency, to achieve the same transconductance (static gain), it is sufficient to provide a quiescent current in the region of 10–15 mA. As a result, we can expect a significant reduction in the current consumption of the entire chip, which also depends on typical circuit solutions. Among the disadvantages of the proposed solution, it can be noted that the upgraded transistor design will require increasing the accuracy of the etching processes of the barrier layer.

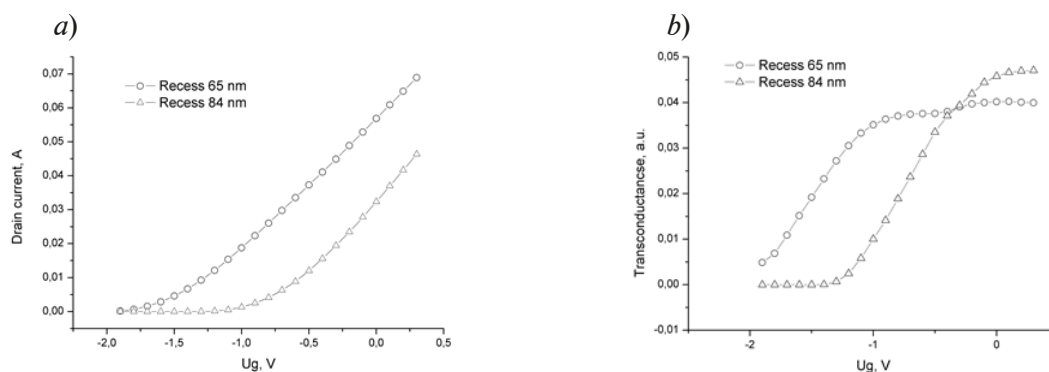


Fig. 2. Effect of the depth of the gate electrode on the transfer characteristic (a) and static transconductance (b)



As a result of optimizing the transistor design based on these requirements, a calculated slope characteristic was obtained, clearly showing the good amplifying capabilities of the proposed transistor in the low current region, which directly leads to the possibility of a significant reduction in the current consumption of the entire microcircuit. The results of calculated characteristics are shown in Fig. 3.

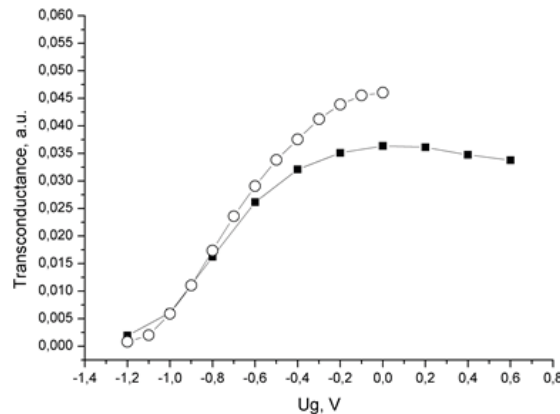


Fig. 3. Calculated characteristic of the slope of the transistor transfer characteristic (squares correspond to conventional design; circles to topology-optimized design)

### Conclusion

Thus, the paper presents the results of optimization by numerical simulation of a low-noise p-HEMT transistor based on a domestic heterostructure. A significant increase in the transconductance of the transfer characteristic of the proposed transistor design indicates the possibility of using this promising element base as part of microwave radiometers, which will allow combining the principles of multichannel, multifrequency and miniaturization in one radiometric complex and will lead to the expansion of its functionality and a significant reduction in size.

### Acknowledgments

The research was carried out with the financial support of the Russian Science Foundation as part of the scientific project 19-19-00349- $\Pi$  dated 19.05.2022.

### REFERENCES

1. Vesnin S., Sedankin M., Leushin V., Skuratov V., Nelin I., Konovalova A., Research of a microwave radiometer for monitoring of internal temperature of biological tissues, *Eastern-European Journal of Enterprise Technologies*. 4 (5) (2019) 6–15.
2. Gudkov A.G., Leushin V.Y., Vesnin S.G. et al., Studies of a Microwave Radiometer Based on Integrated Circuits, *Biomedical Engineering*. 53 (2020) 413–416.
3. Tikhomirov V, Zemlyakov V, Volkov V. et al., Optimization of the parameters of HEMT GaN/AlN/AlGaIn heterostructures for microwave transistors using numerical simulation, *Semiconductors*. 50 (2) (2016) 244–248.
4. Tikhomirov V.G., Gudkov A.G., Agasieva S.V., Dynaiev D. D., Popov M.K., Chizhikov S.V., Increasing efficiency of GaN HEMT transistors in equipment for radiometry using numerical simulation, *Journal of Physics Conference Series*. 2019. 1410:012191
5. Duffy S.J. et al., Strain-reduction induced rise in channel temperature at ohmic contacts of GaN HEMTs, *IEEE Access*. 6 (2018) 42721–42728.

## THE AUTHORS

**TIHKOMIROV Vladimir**  
vv11111@yandex.ru

**NIKOLAENKOV Alexander**  
vv11111@yandex.ru

**CHIZHIKOV Sergey**  
chigikov95@mail.ru  
ORCID: 0000-0001-7272-2916

**GUDKOV Grigoriy**  
ooo.giperion@gmail.com

**GUDKOV Alexander**  
profgudkov@gmail.com

*Received 05.08.2022. Approved after reviewing 08.08.2022. Accepted 16.08.2022.*

Conference materials  
UDC 543.9, 546.06, 57.083.3  
DOI: <https://doi.org/10.18721/JPM.153.261>

## Study of quantum dots conjugation with antibodies to be used in a lateral flow immunochromatographic assay

E. A. Sidorov , V. V. Kriger, P. D. Nasirov,  
S. A. Novikova, E. D. Gribova, P. P. Gladyshev

Dubna State University, Dubna, Russia  
 siea.18@uni-dubna.ru

**Abstract.** Lateral-flow immunochromatographic assays (LFIA) is one of the most common low-cost, simple-to-use and rapid methods for point-of-care determining various types of bacterial, viral and autoimmune diseases. The selectivity and sensitivity of the analysis is determined by the complementarity interactions of protein molecules and attaching an analytical label to the protein. Recently, quantum dots (QDs) have been considered the most promising protein labels. In this study, oriented conjugation of QDs with antibodies (Abs) to glycoprotein B (gB) of the Aujeszky's disease was conducted by the carbodiimide-succinimide method. There has been proposed a polymer coating of QDs suitable for site-specific conjugation based on the vinylpyrrolidone-maleic anhydride-ethylene glycol dimethacrylate (VP-MAN-EGDMA) copolymer. Using a portable fluorescent reader the minimum detection limits of the considered immunochromatographic test-systems with QDs as Abs labels were determined.

**Keywords:** bioconjugation, immunochromatographic assay, quantum dots, antibodies

**Funding:** This study was carried out with the financial support of The Foundation for Assistance to Small Innovative Enterprises in Science and Technology (17262ГУ/2022).

**Citation:** Sidorov E. A., Kriger V. V., Nasirov P. D., Novikova S. A., Gribova E. D., Gladyshev P. P., Study of quantum dots conjugation with antibodies to be used in a lateral flow immunochromatographic assay, St. Petersburg State Polytechnical University Journal. Physics and Mathematics. 15 (3.2) (2022) 331–335. DOI: <https://doi.org/10.18721/JPM.153.261>

This is an open access article under the CC BY-NC 4.0 license (<https://creativecommons.org/licenses/by-nc/4.0/>)

Материалы конференции  
УДК 543.9, 546.06, 57.083.3  
DOI: <https://doi.org/10.18721/JPM.153.261>

## Исследование процесса конъюгации антител с квантовыми точками для создания иммунохроматографических тест-систем на их основе

Е. А. Сидоров , В. В. Кригер, П. Д. Насиров,  
С. А. Новикова, Е. Д. Грибова, П. П. Гладышев

Государственный университет «Дубна», г. Дубна, Россия  
 siea.18@uni-dubna.ru

**Аннотация.** Иммунохроматографический анализ (ИХА) является одним из наиболее распространенных экспресс-методов для определения различных видов бактериальных, вирусных и аутоиммунных заболеваний. Селективность анализа определяется комплементарностью взаимодействий белковых молекул, а чувствительность анализа достигается присоединением аналитической метки к белку. В последнее время к наиболее перспективным меткам белков относятся квантовые точки (КТ). В данной работе была проведена ориентированная конъюгация КТ с антителами (АТ) к гликопротеину В (gB) вируса болезни Ауески карбодиимид-сукцинимидным методом. Предложено подходящее для ориентированной конъюгации полимерное покрытие КТ на основе сополимера

винилпирролидон – малеиновый ангидрид – этиленгликольдиметакрилат (ВП-МАН-ЭГДМА). С помощью портативного флуоресцентного ридера были определены минимальные пределы обнаружения рассматриваемых иммунохроматографических тест-систем с КТ в качестве меток АТ.

**Ключевые слова:** биоконъюгация, иммунохроматографический анализ, квантовые точки, антитела

**Финансирование:** Работа выполнена при финансовой поддержке Фонда содействия развитию малых форм предприятий в сфере науки и техники по договору 17262ГУ/2022 от 05.04.2022.

**Ссылка при цитировании:** Сидоров Е. А., Кригер В. В., Насиров П. Д., Новикова С. А., Грибова Е. Д., Гладышев П. П., Исследование процесса конъюгации антител с квантовыми точками для создания иммунохроматографических тест-систем на их основе // Научно-технические ведомости СПбГПУ. Физико-математические науки. Т. 15. № 3.2. С. 331–335. DOI: <https://doi.org/10.18721/JPM.153.261>

Статья открытого доступа, распространяемая по лицензии CC BY-NC 4.0 (<https://creativecommons.org/licenses/by-nc/4.0/>)

### Introduction

LFIA is an immunochemical method for the qualitative and quantitative identification of viral diseases. The widespread use of LFIA is due to the fact that this method is express (analysis time is 10–30 minutes), reproducible, requires the use of a minimum number of instruments and devices, and is suitable for point-of-care screening of infectious diseases. Currently, one of the most promising fields is the use of colloidal QDs as analytical labels for protein molecules. QDs have a number of unique properties, including a narrow symmetrical fluorescence peak, high fluorescence brightness, a wide excitation band, and high photostability. Due to these properties, it is possible to reduce detection limits and increase the sensitivity of test systems. The surface of the label and protein, as well as the method of conjugation are important parameters affecting the result of conjugation of protein molecules.

To ensure the spatial accessibility of antigen-binding fragments, it is preferable that Fab regions of Ab do not participate in the conjugation process. Some of the protocols used for the functionalization of nanoparticles (NPs) are based on the attachment of Abs to the surface in a random orientation, which leads to a partial loss of sensitivity and increase detection limits of test-systems [1]. Thus, the development of strategies of site-specific conjugation is a key challenge to overcome the reduction of randomly immobilized Abs.

Two-stage approaches to oriented conjugation which consists in a combination of electrostatic adsorption and covalent bonding are promising. Since electrostatic adsorption is a multipoint interaction, the orientation of Abs will depend on the number of positively or negatively charged regions on the surface of the protein molecule. A region with a higher density of charged residues will have a higher adsorption rate and, as a result, Abs will be attached to QDs predominantly through it, providing the optimal orientation on the surface.

### Materials and Methods

CdSe/CdS/CdS/ZnS QDs, coated with vinylpyrrolidone-maleic anhydride-ethylene glycol dimethacrylate copolymer (VP-MAN-EGDMA), monoclonal Abs ADV 34/2 gB of the Aujeszky's disease (Institute of Cell Biophysics of the Russian Academy of Sciences, Pushchino, Russia), phosphate-buffered saline (PBS) tablets (for biological research, Sigma Aldrich), 2-(N-morpholino)ethanesulfonic acid (MES) monohydrate ( $\geq 99.0\%$ , Sigma-Aldrich), N-Hydroxysuccinimide (NHS,  $\geq 97\%$ , Sigma-Aldrich), Dimethyl sulfoxide (CH<sub>3</sub>)<sub>2</sub>SO (99.7%, SigmaAldrich), N-(3-Dimethylaminopropyl)-N'-ethylcarbodiimide hydrochloride (EDC,  $\geq 98\%$ , Sigma Aldrich), tris(hydroxymethyl)aminomethane (HOCH<sub>2</sub>)<sub>3</sub>CNH<sub>2</sub> ( $\geq 99.9\%$ , Trizma base, Sigma-Aldrich), bovine serum albumin (Sigma-Aldrich), Superose 6 Prep Grade (Sigma-Aldrich), anti-mouse monoclonal antibodies (Institute of Cell Biophysics of the Russian Academy of Sciences, Pushchino, Russia), deionized water.



Microcentrifuge Eppendorf 5425, magnetic stirrer IKA C-MAG HS 7, analytical balance CAUX-120 (weighing limit 120 g), polyethersulfone (PES) syringe filters with 0.22  $\mu\text{m}$  pores, Amicon ultra-0.5 mL centrifugal filters (Merck, standard deviation - 0.1 mg), spectrophotometer UNICO-2100/2800 (wavelength range: 190–1100 nm), spectrofluorimeter FluoroLog 3 model FL3–21, Zetasizer Nano S Size Analyzer (Malvern Panalytical).

### Conjugation of QDs with Abs

The conjugation of QDs with Abs is conducted in a 0.01 M PBS solution with pH = 7.4 with a molar ratio of QDs:Abs 1:10. To activate carboxyl groups on the surface of QDs, a 0.1 M EDC solution (at a molar ratio of QDs:EDC 1:2000) and a 0.1 M solution of NHS (at a molar ratio of QDs:NHS 1:1000) are added to the QDs and left under constant stirring for 30 minutes. After activation of carboxyl groups, the calculated amount of Abs is added to the reaction mixture and left for 1.5 hours in the dark with constant stirring. After completion of the conjugation process, the free NHS-ester groups are blocked with a blocker solution in an amount of 1/10 of the total volume of the conjugate for 30 minutes. The resulting conjugates are purified from free components using gel-filtration chromatography.

### Oriented conjugation of QDs with Abs

The conjugation of QDs with Abs is conducted in a 10 mM MES solution with pH = 5 with a molar ratio of QDs:Abs 1:10. To activate carboxyl groups on the surface of QDs, a 0.1 M EDC solution (at a molar ratio of QDs:EDC 1:2000) and a 0.1 M solution of NHS (at a molar ratio of QDs:NHS 1:1000) is added to the QDs and leave under constant stirring for 30 minutes. Abs are incubated in 10 mM MES pH = 5 with constant stirring for 30 minutes at room temperature. After activation of the carboxyl groups, the QDs are purified from excess activating agents by ultrafiltration. Then, the calculate amount of purified Abs is adding to the reaction mixture and leave for 1.5 hours in the dark with constant stirring. After completion of the conjugation process, a blocker solution is added to the reaction mixture in an amount of 1/10 of the total volume of the conjugate and leave for 30 minutes with constant stirring. The resulting conjugates are transferred into a 0.01 M PBS solution, then purified from the components of the reaction mixture using gel-filtration chromatography.

### Results and Discussion

To use QDs as analytical labels in LFIA, it is necessary to conjugate them with analyte-specific protein molecules. Immobilization of Abs by antigen-binding fragments on the QDs surface leads to a decrease in sensitivity and an increase in the detection limits of immunochromatographic test-systems. Currently, have been developed various approaches for the site-specific conjugation of NPs with biomolecules. They include the selective interaction of a crystallizing antibody fragment with proteins A, G, and A/G [2, 3], binding through sulfhydryl groups formed during the reduction of antibodies [4], aldehyde groups [5], and histidine labels [6] located in the constant region of Abs.

The binding of Abs to the A/G protein does not require chemical modification of Abs, but it is due to physical adsorption, which leads to low stability of the NP-Abs complex. This approach is also costly. The other methods described above are labor intensive as they require the chemical modification of the Abs for the conjugation.

The most promising are site-specific covalent binding approaches that do not require chemical modification of Abs. These methods include the two-stage immobilization of biomolecules through electrostatic interactions and the subsequent formation of a covalent bond [7, 8].

In this study, oriented conjugation of CdTe/CdSe/CdS/ZnS-VP-MAN-EGDMA QDs with Abs to gB of the Aujeszky's disease was conducted by using the carbodiimide-succinimide method.

The absorption and luminescence spectra of CdTe/CdSe/CdS/ZnS-VP-MAN-EGDMA QDs and their conjugates with antibodies to gB of the Aujeszky's disease shows in Fig. 1. The peak in the absorption spectrum of QDs and conjugates in the region of 470 nm match to the formation energy of an electron-hole pair (exciton). After immobilization of Abs on the QD surface, the intensity of the exciton peak decreases, which indicates the formation of conjugates. The maximum luminescence intensity is at a wavelength of 680 nm. Abs immobilized on the QD surface screen the secondary radiation, which leads to a decrease in the luminescence intensity. After performing oriented

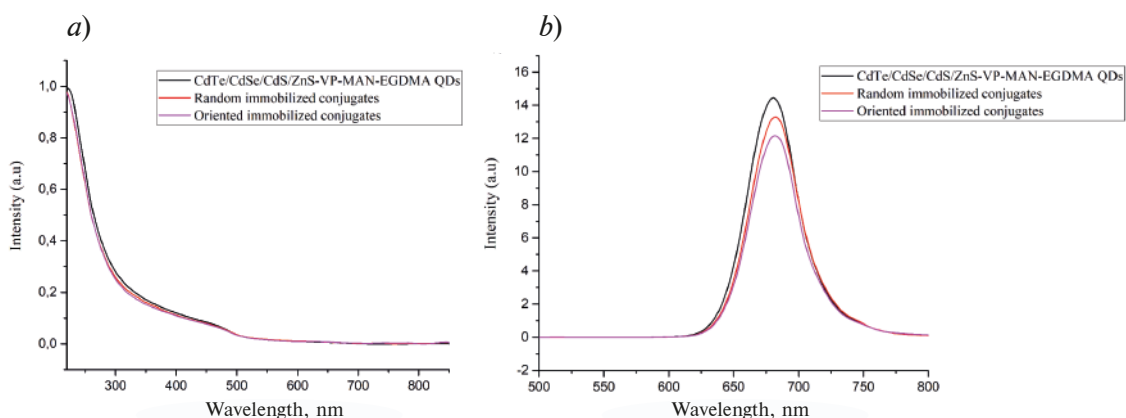


Fig. 1. Absorption (a) and luminescence (b) spectra of QDs and their conjugates

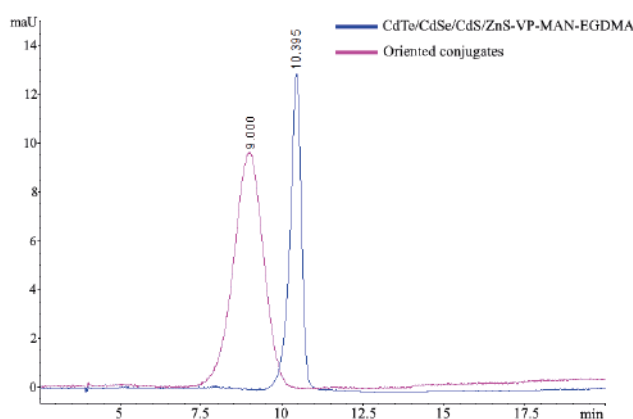


Fig. 2. Overlay of electropherograms of QDs and their conjugates. Analysis conditions: detection wavelength 220 nm, voltage +30 kV, supporting electrolyte 2 mM PBS pH = 7

conjugation based on fast electrostatic interactions, Abs are immobilized in a flat orientation, which leads to a larger area of QD coverage, and hence a larger reduction in quantum yield. However, with this conjugation approach, the number of antigen-binding fragments available for binding increases, which leads to a decrease in the detection limits of immunochromatographic test systems.

After conjugation of Abs with QDs, the resulting conjugates are purified from unbound components by gel chromatography. The purity of conjugates was determined by capillary zone electrophoresis. Electropherograms of CdTe/CdSe/CdS/ZnS-VP-MAN-EGDMA QDs and their conjugates are shown in Fig. 2.

The migration time of QDs is 10.4 minutes, and that of their conjugates is 9 minutes, which evidence an increase in the hydrodynamic size and surface charge of QDs after conjugation due to the immobilization of protein molecules. The electrophoretic zone is evidence for the homogeneity and purity of the conjugates.

Dynamic light scattering (DLS) was used to determine the sizes of QDs and their conjugates. The QDs size was 67.8 nm, random immobilized, oriented immobilized conjugates 71 nm and 70.6 nm, respectively.

The orientation of immobilized protein molecules can be estimated by the minimum detection limit of test-systems created on their basis. Conjugates with optimal orientation are capable of interacting with a large number of antigens, which leads to an increase in the number of QD-Ab-antigen complexes in the test zone of the test-strip. It is possible to quantify antigens in the analyzed sample using a fluorescent reader. When studying the intensity of the analytical fluorescence signal on the test zone of the test strip, it was found that the minimum limit of antigen detection in the sample was 0.8  $\mu\text{g/ml}$ .



### Conclusion

There were study the optical properties of QDs of composition CdTe/CdSe/CdS/ZnS-VP-MAN-EGDMA and their conjugates with Abs to gB of the of the Aujeszky's disease. As a result of site-specific conjugation of protein molecules, the fluorescence intensity of the conjugate decreases compared to QDs, however, the spatial availability of sites for antigen binding leads to a decrease in the detection limits of immunochromatographic test systems.

### Acknowledgments

This study was carried out with the financial support of The Foundation for Assistance to Small Innovative Enterprises in Science and Technology (17262FY/2022).

### REFERENCES

1. Xu Y., Ma B., Chen E., Yu X., Ye Z., Sun C., Zhang M., Dual fluorescent immunochromatographic assay for simultaneous quantitative detection of citrinin and zearalenone in corn samples, Food Chemistry. 336 (2021) 127713.
2. K. Luo, J. Ryu, I.H. Seol, K.B. Jeong, S.M. You, Y.R. Kim., Paper-Based radial chromatographic immunoassay for the detection of pathogenic bacteria in milk, ACS applied materials & interfaces. 11 (50) (2019) 46472–46478.
3. Liao B. Y., Chang C. J., Wang C. F., Lu C. H., Chen J. K., Controlled antibody orientation on Fe<sub>3</sub>O<sub>4</sub> nanoparticles and CdTe quantum dots enhanced sensitivity of a sandwich-structured electrogenerated chemiluminescence immunosensor for the determination of human serum albumin, Sensors and Actuators B: Chemical. 336 (2021) 129710.
4. Robotham A. C., Kelly J. F., Detection and quantification of free sulfhydryls in monoclonal antibodies using maleimide labeling and mass spectrometry, MAbs. – Taylor & Francis. 11 (4) (2019) 757–766.
5. Hu J., Zhou S., Zeng L., Chen Q., Duan H., Chen X., Xiong Y., Hydrazide mediated oriented coupling of antibodies on quantum dot beads for enhancing detection performance of immunochromatographic assay, Talanta. 223 (2021) 121723.
6. Hwang D., Tsuji K., Park H., Burke Jr T. R., Rader, C., Site-Specific Lysine Arylation as an Alternative Bioconjugation Strategy for Chemically Programmed Antibodies and Antibody–Drug Conjugates, Bioconjugate chemistry. 30 (11) (2019) 2889–2896.
7. Gao S., Rojas-Vega F., Rocha-Martin J., Guisán, J. M., Oriented immobilization of antibodies through different surface regions containing amino groups: Selective immobilization through the bottom of the Fc region, International Journal of Biological Macromolecules. 177 (2021) 19–28.
8. Gao S., Guisán J. M., Rocha-Martin J., Oriented immobilization of antibodies onto sensing platforms-A critical review, Analytica chimica acta. 1189 (2022) 338907.

### THE AUTHORS

**SIDOROV Evgeniy**  
siea.18@uni-dubna.ru  
ORCID: 0000-0003-0326-3554

**NOVIKOVA Sagila**  
ibragimova21@yandex.ru

**KRIGER Vladlena**  
vladlena.k576@mail.ru

**GRIBOVA Elena**  
elena\_g67@mail.ru

**NASIROV Pavel**  
CHemBioslne@gmail.com

**GLADYSHEV Pavel**  
pglad@yandex.ru

*Received 28.07.2022. Approved after reviewing 11.08.2022. Accepted 05.09.2022.*

Conference materials

UDC 621.359.3

DOI: <https://doi.org/10.18721/JPM.153.262>

### Features of the formation super C45-RuO<sub>2</sub>-based planar supercapacitor structures

Yu. I. Kakovkina<sup>1</sup>, Sh. Sh. Isokjanov<sup>1✉</sup>, R. M. Ryazanov<sup>2</sup>, E. A. Lebedev<sup>1,2</sup>, E. Kitsyuk<sup>2</sup>

<sup>1</sup> National Research University of Electronic Technology, Moscow, Russia;

<sup>2</sup> Scientific-Manufacturing Complex "Technological Centre", Moscow, Russia

✉ [isakjanov2997@gmail.com](mailto:isakjanov2997@gmail.com)

**Abstract.** A method for forming electrodes of a planar supercapacitor based on Super C45 and RuO<sub>2</sub> by electrophoretic deposition is considered. The possibility of controlling the sediment composition by changing the composition of the initial suspension is shown. The suspension was subjected to dispersion, after which electrophoresis was performed in an electrophoretic cell consisting of two electrodes and a power source. The features of electrophoretic deposition and the influence of the main technological regimes on the morphology and composition of the formed layers of electrode materials are considered. A technological route was developed for manufacturing prototypes of planar supercapacitors using laser engraving to apply a topological pattern. The dependence of the specific capacitance on the electric field strength during electrophoretic deposition has been studied. Thus, it became possible to create designs of planar supercapacitors for a wide range of applications in microelectronics.

**Keywords:** planar supercapacitor, laser engraving, electrophoretic deposition, suspension, electrode material

**Funding:** The work is partially supported by the Ministry of Science and Higher Education of the Russian Federation (project FNRМ-2021-0002) and by the Russian Federation President's grant (МК-1823.2021.4).

**Citation:** Kakovkina Yu. I., Isokjanov Sh. Sh., Ryazanov R. M., Lebedev E. A., Kitsyuk E. P., Features of the formation super C45-RuO<sub>2</sub> based planar supercapacitor structures, St. Petersburg State Polytechnical University Journal. Physics and Mathematics. 15 (3.2) (2022) 336–339. DOI: <https://doi.org/10.18721/JPM.153.262>

This is an open access article under the CC BY-NC 4.0 license (<https://creativecommons.org/licenses/by-nc/4.0/>)

Материалы конференции

УДК 621.359.3

DOI: <https://doi.org/10.18721/JPM.153.262>

### Особенности формирования структур планарного суперконденсатора на основе super C45-RuO<sub>2</sub>

Ю. И. Каковкина<sup>1</sup>, Ш. Ш. Исокжанов<sup>1✉</sup>, Р. М. Рязанов<sup>2</sup>, Е. А. Лебедев<sup>1,2</sup>, Е. П. Кицюк<sup>2</sup>

<sup>1</sup> Национальный исследовательский университет «Московский институт электронной техники», г. Москва, Россия;

<sup>2</sup> НПК «Технологический центр», г. Москва, Россия

✉ [isakjanov2997@gmail.com](mailto:isakjanov2997@gmail.com)

**Аннотация.** Рассмотрен способ формирования электродов планарного суперконденсатора на основе Super C45 и RuO<sub>2</sub> методом электрофоретического осаждения. Изучены особенности электрофоретического осаждения и влияние основных технологических режимов на морфологию и состав формируемых слоев электродных материалов. Был разработан технологический маршрут изготовления прототипов планарных суперконденсаторов с применением лазерной гравировки для нанесения топологического рисунка. Таким образом, стало возможным создание конструкций планарных суперконденсаторов для широкого спектра применений в микроэлектронике.

**Ключевые слова:** планарный суперконденсатор, лазерная гравировка, электрофоретическое осаждение, суспензия, электродный материал

**Финансирование:** Работа выполнена при частичной поддержке Минобрнауки РФ (проект FNRМ-2021-0002) и гранта Президента РФ (МК-1823.2021.4).

**Ссылка при цитировании:** Каковкина Ю. И., Исокжанов Ш. Ш., Лебедев Е. А., Рязанов Р. М., Кищук Е. П. Особенности формирования структур планарного суперконденсатора на основе super C45-RuO<sub>2</sub> // Научно-технические ведомости СПбГПУ. Физико-математические науки. Т. 15. № 3.2. С. 336–339. DOI: <https://doi.org/10.18721/JPM.153.262>

Статья открытого доступа, распространяемая по лицензии CC BY-NC 4.0 (<https://creativecommons.org/licenses/by-nc/4.0/>)

## Introduction

Composite materials based on various modifications of carbon with a large surface area and transition metal compounds have become quite promising due to their unique properties: high specific capacity and power due to fast redox reactions [1–2]. This increases the demand for various power sources, including supercapacitors. The main efforts of researchers were aimed at maximizing their productivity, increasing their specific capacity and energy density. In this work, we study the manufacturing technology of planar supercapacitor structures by laser engraving. As the electrode layer, we used a composite based on Super C45 and RuO<sub>2</sub>, formed by electrophoretic deposition (EPD), which makes it possible to form multicomponent materials and create nanostructured coatings of a given composition at room temperature [3–5].

## Materials and Methods

Sital plates were used as substrates, on which a nickel layer 300 nm thick was deposited by means of magnetron sputtering. For the manufacture of electrodes, as the main material, we used Super C45 and RuO<sub>2</sub>. All components (Super C45, RuO<sub>2</sub>·xH<sub>2</sub>O, cellulose and iodine) were mixed in a test tube with a mixture of acetone and isopropyl alcohol (Table 1).

Dispersion of the resulting solution was carried out by submersible ultrasonic disperser. The electrode material was deposited in an electrophoretic cell consisting of two electrodes: a cathode (sital with nickel coating) and an anode (gold electrode). Electrophoretic deposition of composite materials was carried out in a potentiostatic mode at an electric field strength of 50 and 100 V/cm. The duration of the process was 60 seconds. To determine the mass of the deposit, the substrate was weighed before and after the deposit. After electrophoretic precipitation using laser engraving on a CNC machine, a layer of the structure of a planar supercapacitor was formed, which is an interdigital comb, nested on top of each other. With the help of laser engraving, not only the electrode composite material was locally removed, but also the nickel layer, which ultimately made it possible to electrically isolate the electrodes from each other (Fig. 1).

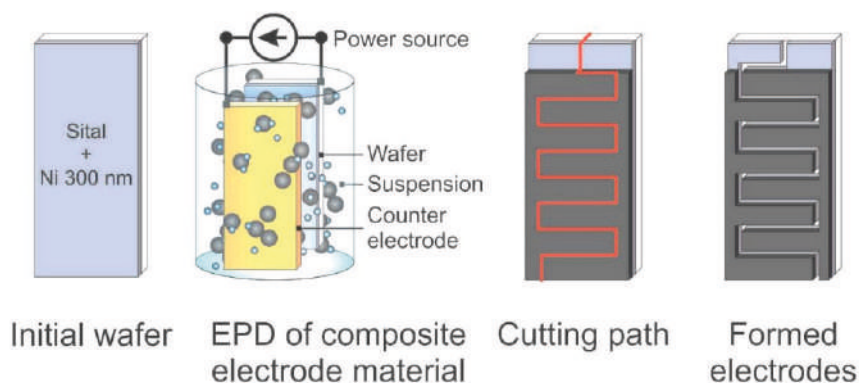


Fig. 1. Schematic representation of the route for creating a planar supercapacitor with composite electrodes based on Super C45-RuO<sub>2</sub>

Table 1

Suspension composition

Super C45, (g)	RuO <sub>2</sub> *xH <sub>2</sub> O, (g)	Cellulose, (g)	Iodine, (g)	Acetone, (l)	Isopropyl alcohol, (l)
0.01	0.01	0.01	0.02	0.025	0.025

The morphology and composition of the surface of the resulting coatings were studied by scanning electron microscopy. To study the electrophysical characteristics, supercapacitors were placed in a beaker with a 1 M KOH solution, and their capacitance characteristics were measured using an Elins-45X potentiostat with the supplied ES8 software for PC.

Results and Discussion

Electrophoretic deposition is a technique that can not only deposit multi-component materials and locally deposit on a conductive pattern, but also control the composition, thickness, and porosity of the layer. Samples after composite deposition by this method were examined using a scanning electron microscope (SEM).

SEM images of samples based on Super C45 and RuO<sub>2</sub> at 50 V/cm and 100 V/cm deposition show differences in the morphology of the composite layers (Fig. 2). The sample deposited at 100 V/cm has a more distinct uniform, porous and rough structure compared to the sample deposited at 50 V/cm. This feature can make a positive impact on the capacitive characteristics of a supercapacitor, since the effective electrode-electrolyte contact area will be larger, and, hence, the contribution to the total capacity of the electric double layer.

For two samples formed at field strengths of 50 and 100 V/cm, cyclic sweeps were taken at different scanning rates from 10 to 500 mV/s. Based on the data obtained, the values of the specific capacity of the samples were calculated, after which the dependences of the capacity on the scanning speed for both samples were plotted, which are shown in Fig. 3.

There is a tendency for capacitance to decrease as sweep speed increases. It can be seen from the dependence graphs that the specific capacitance of the sample deposited at 50 V/cm is almost 2,5 times less than that of the sample deposited at 100 V/cm. At an electric field strength of

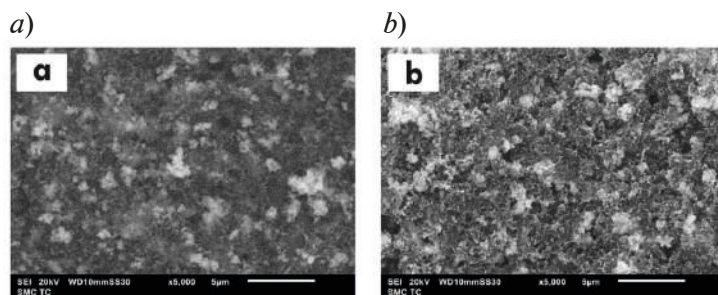


Fig. 2. SEM images of samples based on Super C45-RuO<sub>2</sub> at 50V (a) and 100V (b)

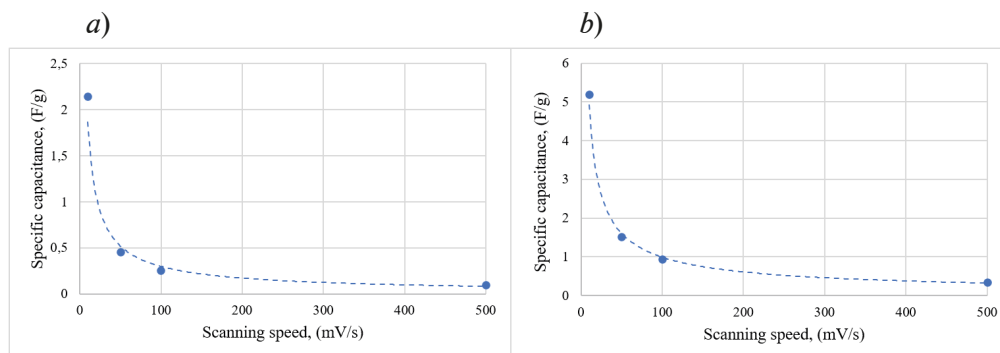


Fig. 3. Dependence of the scanning speed on the specific capacitance of the samples upon deposition of 50 V/cm (a) and 100 V/cm (b), respectively



100 V/cm, compared to 50 V/cm, the composite clings better and is more uniformly distributed on the substrate surface, which has a good effect on the contribution of redox reactions.

With an increase in the sweep rate on both samples, one can see a decrease in the capacitive characteristics of the planar supercapacitor. This may be due to the low rate of redox reactions compared to the rate of potential change in the cell. The higher it is, the smaller the contribution of Faraday processes and the greater the contribution due to the formation of a double electric layer. As the sweep rate increases, the resistance to internal diffusion of the active material may increase.

### Conclusion

In this work, we studied planar supercapacitors with composite electrodes based on Super C45 and ruthenium oxide. The electrode materials were formed using electrophoretic deposition, and the planar power supply structure was formed using laser engraving. The technology for manufacturing structures of planar supercapacitors was worked out, and the modes of laser engraving were optimized. The dependence of the capacitive characteristics of planar supercapacitors on the measurement modes is also studied. A maximum capacitance of 5.2 F/g was found with a minimum sweep rate of 10 mV/s at 100 V/cm deposition and 2.15 F/g at 50 V/cm deposition.

Super C45 and RuO<sub>2</sub> are materials whose measured parameters have good prospects, and the proposed planar supercapacitor assembly option can allow it to be widely used on various electronic devices, and EPD will bring the deposition process to a new level of application when creating functional layers with various required characteristics.

### REFERENCES

1. Liu Y., Zeng Z., Wei J., Frontiers in nano-architected carbon-metal oxide electrodes for supercapacitance energy storage: a review, *Frontiers in Nanoscience and Nanotechnology*, 2(2) (2016) 78–85.
2. Brisse A. L., Stevens P., Toussaint G., et al., Ni(OH)<sub>2</sub> and NiO Based Composites: Battery Type Electrode Materials for Hybrid Supercapacitor Devices, *Materials*, 11(7) (2018) 1178–1193.
3. Kaewpijit P., Qin J., Pattanauwat P., Preparation of MXene/N, S doped graphene electrode for supercapacitor application, *Chemical Engineering Journal*, 317 (2019) 1026–1036.
4. Argüello J. A., Rojo J. M., Moreno R., One-pot synthesis of manganese oxide/graphene composites via plasma-enhanced electrochemical exfoliation process for supercapacitors, *Electrochimica Acta*, 294 (2019) 102–109.
5. Kakovkina Yu. I., Lebedev E. A., Kitsyuk E. P., Kuzmin D. A., Alekseyev A. V., Shaman Yu. P., Electrophoretic deposition and capacitive characteristics of composite electrode materials based on CNTs and ruthenium oxide for planar supercapacitors, *Journal of Physics: Conference Series – IOP Publishing*, 2086 (2021) 1 012183.

### THE AUTHORS

**KAKOVKINA Yuliya**  
kakovkinaj@mail.ru  
ORCID: 0000-0003-1255-3043

**LEBEDEV Egor**  
dr.beefheart@gmail.com  
ORCID: 0000-0002-5085-5408

**ISOKJANOV Shakhboz**  
Isakjanov2997@gmail.com  
ORCID: 0000-0001-6009-9039

**KITSYUK Evgeny**  
Kitsyuk.e@gmail.com  
ORCID: 0000-0002-4166-8408

**RYAZANOV Roman**  
r.m.ryazanov@gmail.com  
ORCID: 0000-0002-2464-8712

*Received 15.07.2022. Approved after reviewing 24.07.2022. Accepted 16.08.2022.*

## RADIOPHYSICS

Conference materials

UDC 623.6

DOI: <https://doi.org/10.18721/JPM.153.263>

### Monitoring of radioactive contamination in the atmosphere using radar systems

D. A. Ryzhova <sup>1</sup>✉, V. V. Davydov <sup>1, 2, 3</sup>

<sup>1</sup> Peter the Great St. Petersburg Polytechnic University, St. Petersburg, Russia;

<sup>2</sup> Bonch-Bruевич Saint Petersburg State University of Telecommunications, St. Petersburg, Russia;

<sup>3</sup> All-Russian Research Institute of Phytopathology, Moscow Region, Russia

✉ [qwdarya1234@gmail.com](mailto:qwdarya1234@gmail.com)

**Abstract.** The necessity of monitoring the state of the environment is justified. Various methods of environmental monitoring were analyzed. The radar method for monitoring radioactive contamination in the atmosphere was considered in detail. The monitoring data using radar stations were processed and analyzed. The efficiency of this method was estimated. Recommendations were proposed to expand the monitoring capabilities using radars to assess the environmental situation.

**Keywords:** radar systems, radar station, radioactive contamination, environmental monitoring, plasmoid, atmosphere, microwave radiation

**Citation:** Ryzhova D. A., Davydov V. V., Monitoring of radioactive contamination in the atmosphere using radar systems, St. Petersburg State Polytechnical University Journal. Physics and Mathematics. 15 (3.2) (2022) 340–345. DOI: <https://doi.org/10.18721/JPM.153.263>

This is an open access article under the CC BY-NC 4.0 license (<https://creativecommons.org/licenses/by-nc/4.0/>)

Материалы конференции

УДК 623.6

DOI: <https://doi.org/10.18721/JPM.153.263>

### Мониторинг радиоактивных загрязнений в атмосфере с использованием радиолокационных систем

Д. А. Рыжова <sup>1</sup>✉, В. В. Давыдов <sup>1, 2, 3</sup>

<sup>1</sup> Санкт-Петербургский политехнический университет Петра Великого, Санкт-Петербург, Россия;

<sup>2</sup> Санкт-Петербургский государственный университет связи им. проф.  
М.А. Бонч-Бруевича, Санкт-Петербург, Россия;

<sup>3</sup> Всероссийский научно-исследовательский институт фитопатологии, Московская область, Россия

✉ [qwdarya1234@gmail.com](mailto:qwdarya1234@gmail.com)

**Аннотация.** Обоснована необходимость контроля за состоянием окружающей среды. Проанализированы различные методы экологического мониторинга. Подробно рассмотрен радиолокационный метод для мониторинга радиоактивных загрязнений в атмосфере. Обработаны и проанализированы данные мониторинга с использованием радиолокационных станций. Оценена эффективность данного метода. Предложены рекомендации для расширения возможностей мониторинга с использованием радиолокационных станций для оценки экологической ситуации.

**Ключевые слова:** радиолокационные системы, радиолокационная станция, радиоактивное загрязнение, мониторинг окружающей среды, плазмод, атмосфера, СВЧ излучение

**Ссылка при цитировании:** Рыжова Д. А., Давыдов В. В. Мониторинг радиоактивных загрязнений в атмосфере с использованием радиолокационных систем // Научно-технические ведомости СПбГПУ. Физико-математические науки. Т. 15. № 3.2. С. 340–345. DOI: <https://doi.org/10.18721/JPM.153.263>

Статья открытого доступа, распространяемая по лицензии CC BY-NC 4.0 (<https://creativecommons.org/licenses/by-nc/4.0/>)

## Introduction

The deterioration of ecology and emergence of different negative factors for various reasons led to a decrease in the quality of the air environment [1–4], that affects the person health [5–8]. For various reasons, pollution is formed in the air environment, which must be determined by various methods [9–16]. Due to the constant increase in the number of industrial enterprises, the study of radiation formations in the air is extremely important for humans, especially in high-risk areas, such as places located in close proximity to radiation-hazardous objects. The amount of radioactive substances released into the atmosphere is also increasing every year [17–23]. These dangerous substances get into the air masses and can be transported over vast distances, and thus get to the ground and to water bodies in the form of precipitation. This is confirmed by various studies [18–27].

Many methods have been developed to control the radiation situation and respond to emergencies in a timely manner [2, 5, 7, 9, 11–14, 21, 23, 24, 26, 28]. Over time, most of them have become obsolete, and the remaining ones have a number of disadvantages [17–20, 28–31]. Among the various methods, the radar method is the most optimal, since it is remote, which is important when working with radioactive particles. It should be noted that the radar method of studying the state of the environment is a direct measurement of the degree of ionization of air masses containing radioactive elements (pollution level). This is extremely important, especially when taking measurements in difficult conditions.

## Materials and Methods

The principle of the radar method of finding radioactive particles consists of several points. First, radioactive substances are released into the atmosphere. Next, a plasmoid is formed in the atmosphere, which can change locations with the help of air masses. This plasmoid can be detected using a radar station that is located at a fairly safe distance from the object under study. Radiation directed at the plasmoid is reflected from it and then enters the receiving path of the radar station. Due to the fact that the reflected signal has a small power, the signal is amplified in the receiving path and transmitted to the control panel using fiber-optic communication lines. Fig. 1 presents a block diagram of the operation of the radar station.

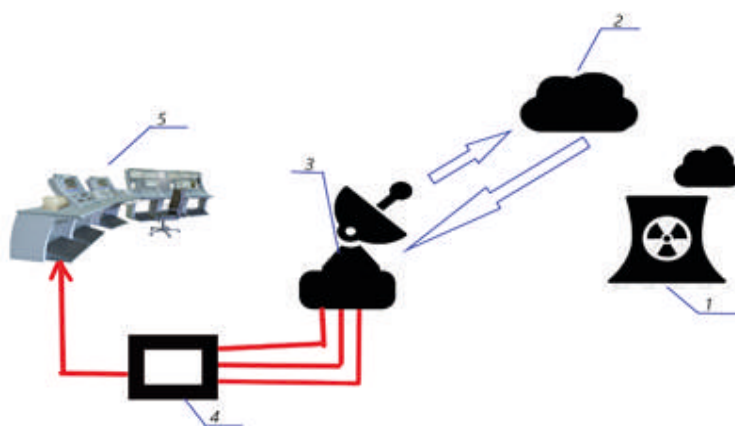


Fig. 1. Structural diagram of the radar operation: radiation-hazardous object 1, plasmoid 2, radar antenna complex 3, radar receiving path 4, remote control 5

An important feature of the plasmoid is that the refractive index of ionization formations and the density are quite different from the parameters of air formations in the atmosphere. This fact indicates the ability of the plasmoid to reflect the microwave radiation that hits it from the radar station. The reflection coefficient  $R$  depends on the degree of ionization of the plasmoid. Taking into account the fact that the distribution of charges in the ionization formation is random, it is possible to represent the reflection coefficient  $R$  from the plasmoid in the form of formula (1):

$$R \approx \frac{0.2V\Delta\varepsilon^2}{\sqrt[3]{L_0^2\lambda}}, \quad (1)$$

where  $V$  is the plasmoid volume,  $\Delta\varepsilon^2$  is the average square of the dielectric constant of the ionization formation,  $L_0$  is the reduced plasmoid length,  $\lambda$  is the wavelength of microwave radiation.

The layered structure of the ionization formation can be described by changing the value of the permittivity of the atmosphere in the plasmoid, which was formed as a result of the release of radioactive elements. In this case, the permittivity of the medium  $\varepsilon$  can be estimated using the formula (2):

$$\varepsilon = 1 - \frac{4\pi N_e e^2}{m_e(\omega^2 + \nu^2)} - \frac{4\pi N_+ e^2}{M_+(\omega^2 + \nu^2)} - \frac{4\pi N_- e^2}{M_-(\omega^2 + \nu^2)}, \quad (2)$$

where  $N_e$  is the electron concentration,  $N_+$  is the concentration of positive ions,  $N_-$  is the concentration of negative ions,  $\nu$  is the frequency of collisions,  $\omega$  is the radiation frequency,  $M_+ = M_-$  is the mass of ions,  $m_e$  is the electron mass.

A layer-by-layer change in the permittivity value of the atmosphere leads to a corresponding change in the electric field strength and conductivity in comparison with the airspace, which does not contain contamination by radioactive particles.

In order to determine the parameters of the plasmoid, it is necessary to describe its shape. Thus, a mathematical model is compiled. Often radioactive contamination enters the atmosphere with the help of pipes that have the shape of a cylinder. Therefore, the volume of the plasmoid is found using the formula (3) of the volume of the cylinder.

$$V = \pi r^2 L, \quad (3)$$

where  $r$  is cylinder radius;  $L$  is the height of the cylinder.

The radar method provides advantages in the ability to detect ionization formations in almost any weather conditions. The detection distance is quite large. In comparison with other methods for detecting radioactive substances in the atmosphere, the radar method has proven itself as a method with only one significant drawback. In the presence of a strong wind, it is difficult to detect and study the plasmoid, since the plasmoid is prone to rapid dispersion. It breaks down into smaller particles that are difficult to detect.

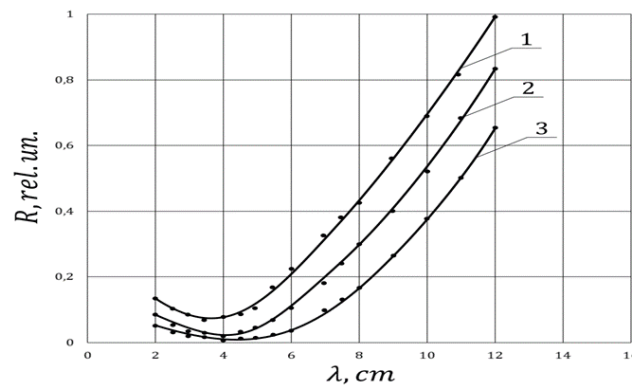


Fig. 2. Dependence of the reflection coefficient  $R$  on the wavelength of radiation  $\lambda$  at different levels of concentration of ions of the isotope  $^{16}\text{N}$  in the atmosphere

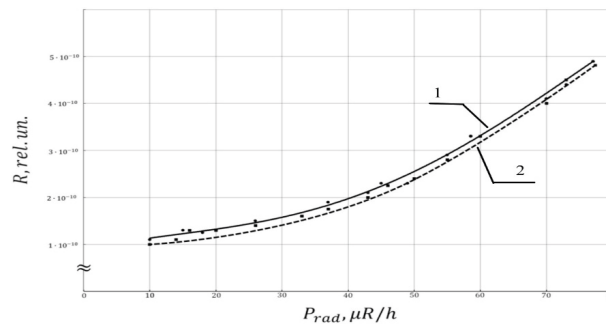


Fig. 3. Dependence of the reflection coefficient  $R$  on the power of the exposure dose of radiation for different wavelengths  $\lambda$  of microwave radiation  
Graphs 1 and 2 correspond to the values of 8 cm and 5 cm of the radiation wavelength  $\lambda$

### Results and Discussion

The main objective of the study of a cloud of radioactive particles is to estimate the dependence of the reflection coefficient  $R$  of the electromagnetic wave on ionization formations on the wavelength of radiation  $\lambda$ . During the study of ionization formations formed from ions of the nitrogen isotope  $^{16}\text{N}$ , the following dependences  $R(\lambda)$ , shown in Fig. 2, were obtained at different concentration levels.

The analysis of the dependencies shows that different levels of nitrogen ion concentration in the plasmoid correspond to their own schedule. The higher the concentration of ions, the higher the reflectivity of the ionization formation, with increasing concentration, the dependence  $R(\lambda)$  is located higher. In addition, it can be noted that all dependencies have a characteristic shape, an important feature is the presence of a minimum reflection coefficient at a certain value of  $\lambda$ . Starting from this value, there is a continuous increase in the reflection coefficient with an increase in the wavelength of the microwave radiation  $\lambda$ .

Moreover, it can be established that the minimum reflection coefficient  $R$  is achieved at different  $\lambda$  for each type of isotope ions of radioactive elements. Thus, after conducting an additional study of various plasmoids formed as a result of the release of pollutants in the presence of radioactive particles, it will be possible to determine which isotope ion formed the plasmoid and what its concentration is.

Another dependence was also revealed, which was obtained experimentally – this is the dependence of the reflection coefficient  $R$  from the plasmoid on the irradiation power of the  $P_{\text{rad}}$ , which is shown in Fig. 3.

A change in the value of the wavelength  $\lambda$  makes it possible to estimate the exposure dose in various areas of the plasmoid with an error of about 10%.

### Conclusion

The use of the proposed methodology during environmental monitoring makes it possible to more effectively detect ionization formations resulting from the release of radioactive elements into the atmosphere. This is especially true on mobile objects, where the radar complex, in addition to monitoring the state of the atmosphere, will monitor the air situation. In the future, it is possible to develop a complex that will not only detect ionization formations, but also determine their composition.

### REFERENCES

1. Gryaznova E. M., Rud V. Y., On the possibility of using the optical method for express quality control of fruits, *Journal of Physics: Conference Series*. Vol. 2086(1) (2021) 012143.
2. Davydov V. V., Determination of the Composition and Concentrations of the Components of Mixtures of Hydrocarbon Media in the Course of its Express Analysis, *Measurement Techniques*. 62(2) (2020) 1090–1098.
3. Nikitina M., Grebenikova N., Dudkin V., Batov Y., Methodology for assessing the adverse effects of the use of nuclear energy on agricultural land, *IOP Conference Series: Earth and Environmental Science*. 390(1) (2019) 012024.

4. **Gryznova E., Batov Y., Rud V.**, Methodology for assessing the environmental characteristics of various methods of generating electricity, *E3S Web of Conferences*. 140 (2019) 09001.
5. **Mazing M. S., Zaitceva A. Yu., Kislyakov Yu. Ya., Kondakov N. S., Avdushenko S. A., Davydov V. V.**, Monitoring of Oxygen Supply of Human Tissues Using A Noninvasive Optical System Based on A MultiChannel Integrated Spectrum Analyzer, *International Journal of Pharmaceutical Research*. 12(2) (2020) 1974–1978.
6. **Kislyakov Yu. Ya., Avdyushenko S. A., Kislyakova I. P., Zaitceva A. Yu.**, Analytical multisensory trainable system for diagnosing vocational aptitude of military medical specialists by ion content in the expired breath condensate, *Journal of Computational and Theoretical Nanoscience*. 16(11) (2019) 4502–4507.
7. **Davydov R. V., Yushkova V. V., Stirmanov A. V., Rud V. Yu.**, A new method for monitoring the health condition based on nondestructive signals of laser radiation absorption and scattering, *Journal of Physics: Conference Series*. 1410(1) (2019) 012067.
8. **Grebenikova N. M., Smirnov K. J., Rud V. Yu., Artemiev V. V.**, Features of monitoring the state of the liquid medium by refractometer, *Journal of Physics: Conference Series*. 1135(1) (2018) 012055.
9. **Antonov V.I., Davydov R.V., Maslikov V.I., Molodtsov D.V., Badenko V.L.**, Simulation of water flow management by the flood control facilities in the adjacent river basins, *Journal of Physics: Conference Series*. 1400(7) (2019) 077049.
10. **Davydov V. V., Davydova T. I.**, A nondestructive method for express testing of condensed media in ecological monitoring, *Russian Journal of Nondestructive Testing*. 53(7) (2017) 520–529.
11. **Smirnov K.J., Glagolev S.F., Tushavin G.V.**, High speed near-infrared range sensor based on InP/InGaAs heterostructures, *Journal of Physics: Conference Series*. 1124(2) (2018) 022014.
12. **Dyumin V., Smirnov K., Myazin N.**, Charge-coupled Device with Integrated Electron Multiplication for Low Light Level Imaging, *Proceedings of the 2019 IEEE International Conference on Electrical Engineering and Photonics, EExPolytech*. 8906868 (2019) 308–310.
13. **Kuzmin M. S., Rogov S. A.**, On the use of a multi-raster input of one-dimensional signals in two-dimensional optical correlators, *Computer Optics*. 43(3) (2019) 391–396.
14. **Myazin N. S., Dudkin V. I., Grebenikova N. M.**, On the Possibility of Express Recording of Nuclear Magnetic Resonance Spectra of Liquid Media in Weak Fields, *Technical Physics*. 63(12) (2018) 1845–1850.
15. **Marusina M. Ya., Karaseva E. A.**, Application of fractal analysis for estimation of structural changes of tissues on MRI images *Russian Electronic Journal of Radiology*. 8(3) (2018) 107–112.
16. **Gizatullin B., Gafurov M., Murzakhanov F., Mattea C., Stapf S.**, Molecular Dynamics and Proton Hyperpolarization via Synthetic and Crude Oil Porphyrin Complexes in Solid and Solution States, *Langmuir*. 37(22) (2021) 6783–6791.
17. **Davydov R., Davydov V., Myazin N., Dudkin V.**, The Multifunctional Nuclear Magnetic Flowmeter for Control to the Consumption and Condition of Coolant in Nuclear Reactors, *Energies*. 15(5) (2022) 1748.
18. **Davydov V.V., Kiryukhin A.V.**, Nuclear-Magnetic Flowmeter-Relaxometers for Monitoring Coolant and Feedwater Flow and Status in Npp Atomic, *Energy*. 127(5) (2020) 274–279.
19. **Fadeenko V., Fadeenko I., Popovskiy N., Rud V.**, Multifunctional method for remote monitoring of the environment in the area of nuclear facilities, *E3S Web of Conferences*. 140 (2019) 07006.
20. **Davydov R., Antonov V., Moroz A.**, Parameter Control System for a Nuclear Power Plant Based on Fiber-Optic Sensors and Communication Lines, In: *IEEE International Conference on Electrical Engineering and Photonics (EExPolytech)*, Saint Petersburg, Russia, 13-15 October 2019 8906791 (2019) 295–297.
21. **Elokhin A.P.**, On the longitudinal stability of technogenic ionized formations, *Technical Physics*. 46(8) (2001) 1026–1036.
22. **Davydov R.V., Antonov V.I., Molodtsov D.V.**, Computer implementation of the mathematical model for water flow management by a hydro complex. *Journal of Physics: Conference Series*. 1135(1) (2018) 012088.
23. **Elokhin A.P., Zhilina M.V.**, Determination of gas-aerosol radioactive impurity characteristics from arms  $\gamma$ -ray detector indications, *Atomic Energy*. 112(4) (2012) 269–280.
24. **Elokhin A.P., Zhilina M.V., Parkhoma P.A.**, Particulars of scanning an underlying surface using a pilotless dosimetric complex, *Atomic Energy*. 107(2) (2009) 130–143.



25. **Grevtseva A. S., Smirnov K. J., Rud V. Yu.**, Development of methods for results reliability raise during the diagnosis of a person's condition by pulse oximeter, *Journal of Physics: Conference Series*. 1135(1) (2018) 012056.
26. **Marusina M. Y., Karaseva E. A.**, Automatic segmentation of MRI images in dynamic programming mode Asian Pacific, *Journal of Cancer Prevention*. 19(10) (2018) 2771–2775.
27. **Myazin N. S.**, Features of formation of structure of a nuclear magnetic resonance signal in weak magnetic field, *Journal of Physics: Conference Series*. 1135(1) (2018) 012061.
28. **Elokhin A.P., Ulin S.E., Vasilenko A.A.**, Method for Determining and Transmitting Data on Radioactive Contamination of the Sea-Bottom in Deep-Water Areas, *Atomic Energy*. 130(6) (2021) 360–366.
29. **Fadeenko V.B., Fadeenko I.V., Vasiliev D.A., Rud V.Yu.**, Investigation of radiation formation (plasmoid) in the air environment by radar method, *Journal of Physics: Conference Series*. 1697(1) (2020) 012057.
30. **Fadeenko V.B., Pchelkin G.A., Rud V.Yu.**, Features of the transmission of microwave signals in the range of 8-12 GHz in the maritime radar station over fiber-optic communication line, *Journal of Physics: Conference Series*. 1400(4) (2019) 044010.
31. **Davydov V.V., Myazin N.S., Logunov S.E.**, A Contactless Method for Testing Inner Walls of Pipelines Russian, *Journal of Nondestructive Testing*. 54(3) (2018) 213–221.

#### THE AUTHORS

**RYZHOVA Daria**

qwdarya1234@gmail.com

ORCID: 0000-0002-7155-1892

**DAVYDOV Vadim**

davydov\_vadim66@mail.ru

ORCID: 0000-0001-9530-4805

*Received 15.07.2022. Approved after reviewing 21.07.2022. Accepted 13.09.2022.*

Conference materials

UDC 543.4

DOI: <https://doi.org/10.18721/JPM.153.264>

## Method for constructing NMR signal spectra using the discrete Fourier transform

S. S. Makeev <sup>1</sup>✉

<sup>1</sup> Peter the Great St. Petersburg Polytechnic University, St. Petersburg, Russia

✉ [st\\_makeev@mail.ru](mailto:st_makeev@mail.ru)

**Abstract.** The article deals with studies of the structure of the nuclear magnetic resonance signal, which is recorded using the modulation technique. The influence of the properties of the medium on the possibility of registering an NMR signal in a weak magnetic field using a modulation technique for measuring is established. A new method for describing the registered NMR signal using the modulation technique is proposed, taking into account the contributions of absorption and dispersion signals. The features of the use of spectral analysis in the study of the NMR signal from liquid media are determined. The results of theoretical calculation and experimental studies are compared.

**Keywords:** condensed medium, nuclear magnetic resonance, amplitude spectrum, phase spectrum, absorption signal, dispersion signal

**Citation:** Makeev S. S., Method for constructing NMR signal spectra using the discrete Fourier transform, St. Petersburg State Polytechnical University Journal. Physics and Mathematics. 15 (3.2) (2022) 346–351. DOI: <https://doi.org/10.18721/JPM.153.264>

This is an open access article under the CC BY-NC 4.0 license (<https://creativecommons.org/licenses/by-nc/4.0/>)

Материалы конференции

УДК 543.4

DOI: <https://doi.org/10.18721/JPM.153.264>

## Методика построения спектров сигнала ЯМР с использованием дискретного преобразования Фурье

С. С. Макеев <sup>1</sup>✉

<sup>1</sup> Санкт-Петербургский политехнический университет Петра Великого, Санкт-Петербург, Россия

✉ [st\\_makeev@mail.ru](mailto:st_makeev@mail.ru)

**Аннотация.** В статье рассмотрены исследования структуры сигнала ядерного магнитного резонанса, который регистрируется с помощью модуляционной методики. Установлено влияние свойств среды на возможности регистрации сигнала ЯМР в слабом магнитном поле с использованием модуляционной методики для проведения измерения. Предложена новая методика описания регистрируемого сигнала ЯМР с использованием модуляционной методики с учетом вкладов сигналов поглощения и дисперсии. Определены особенности использования спектрального анализа при исследовании сигнала ЯМР от жидких сред. Проведено сравнение результатов теоретического расчета и экспериментальных исследований.

**Ключевые слова:** конденсированная среда, ядерный магнитный резонанс, амплитудный спектр, фазовый спектр, сигнал поглощения, сигнал дисперсии

**Ссылка при цитировании:** Макеев С. С. Методика построения спектров сигнала ЯМР с использованием дискретного преобразования Фурье // Научно-технические ведомости СПбГПУ. Физико-математические науки. Т. 15. № 3.2. С. 346–351. DOI: <https://doi.org/10.18721/JPM.153.264>

Статья открытого доступа, распространяемая по лицензии CC BY-NC 4.0 (<https://creativecommons.org/licenses/by-nc/4.0/>)



## Introduction

The deterioration of the environment and the emergence of various negative factors for various reasons led to a decrease in the quality of liquid media [1–8]. Therefore, when conducting various experiments, manufacturing products, environmental control of hard-to-reach reservoirs and water protection zones, means of express control become extremely in demand [8–14]. In recent years, the division of this control into two parts which are control tools that conduct research in express mode (located in small stationary and mobile laboratories, require electrical power from the network) [15–18]. Measuring instruments that can be moved around the territory are battery-operated and allow obtaining information about the state of the environment at the sampling site [8, 19–21]. In these cases, new tasks arise that are associated with obtaining new information about the state of the environment from the data obtained during express control. One of these problems is considered in our work.

### Method of nuclear magnetic resonance for express control and formation of the spectrum of NMR signals

The main condition for a qualitative study of liquid media is the preservation of their physical structure and chemical composition of the medium under study [21–24]. The fulfillment of this condition in the express control of any liquid can be achieved only with the help of devices whose operation is based on the phenomenon of nuclear magnetic resonance (NMR) [21–26]. Other types of devices for express control of the state of a liquid, such as optical, ultrasonic and X-ray devices, can fulfill this condition only when they work with a certain class of media [27–29].

The modulation technique is used to register the NMR signal in weak magnetic fields. The registered NMR signal in this case is obtained in the form of damped oscillations [8, 19, 26, 30, 31]. Using the shape of this signal, one can measure the relaxation constants  $T_1$  and  $T_2$  and determine the state of the medium [8, 19, 26, 30, 31]. When solving a number of problems, more information is required. To obtain it, we propose methods for processing NMR signals using spectral analysis.

One of the features of the application of spectral analysis is that the registered NMR signal is a non-periodic oscillation in the form of damped peaks. Therefore, it is advisable to use the discrete Fourier transform to describe the signal  $G(t)$ , as well as the calculated absorption and dispersion signals:

$$y_k = \sum_{n=0}^{N-1} x_n e^{-j2\pi kn/N}, \quad (1)$$

where  $n = 0, 1, 2, \dots, N-1$ ;  $x_n$  is the input data sequence;  $N$  is the number of elements of the input data sequence  $x_n$ .

The harmonics of the spectrum are located on the frequency axis with a discreteness  $\Delta f = f_s/N$ , where  $f_s$  is the sampling frequency of the initial sequence  $x$ . The sampling rate is determined as follows. Let  $\tau$  be the duration of the NMR signal. Then  $f_s$  can be calculated using the following relation:

$$f_s = N/\tau, \quad (2)$$

In addition, when  $N$  is a power of two, the DFT is calculated by the FFT (Fast Fourier Transform) algorithm. It requires less computing resources and is much faster than the discrete Fourier transform. The DFT is symmetrical about the Nyquist frequency, which is equal to  $f_s/2$ , so harmonics with numbers  $(N/2-k)$  and  $(N/2+k)$  can be combined. The result is a one-sided complex spectrum with frequencies from 0 to  $f_s/2$ , which corresponds to indices  $k = 0 \dots (N/2-1)$ .

The scaled one-sided complex spectrum of the discrete input sequence  $x_n$  is given by:

$$y_k = \begin{cases} y_0 & k = 0 \\ \sqrt{2} \frac{y_k}{N} & k = 1, 2, \dots, \left[ \frac{N}{2} - 1 \right] \end{cases}. \quad (3)$$

In relation (3), the operation in brackets  $[N/2-1]$  represents rounding to the nearest whole number. In this case, the amplitude spectrum  $S$  is equal to the modulus of the one-sided complex spectrum and the phase spectrum  $P(f) = \arg y_k$  is its argument, where  $f = k\Delta f$ .

### Comparison of the technique for forming the spectrum of NMR signals with the results of the experiment

To obtain information about the contribution of absorption and dispersion signals to the registered NMR signals, it is necessary to calculate the values of  $v(t)$  and  $u(t)$ . Fig. 1 shows the calculated dependences  $v(t)$ ,  $u(t)$  and  $G(t)$  for oil.

An analysis of the received signals shows the absence of a period at the location of the decaying peaks, which makes it possible to use the DFT to calculate the spectra. For absorption and dispersion signals, the amplitude and phase spectra are calculated (Figs. 2 and 3).

$T_2^* = 144$  ms is calculated and NMR signal spectra for oil are plotted using (1)–(3). Fig. 4 shows the amplitude and phase spectra of the NMR signal for oil.

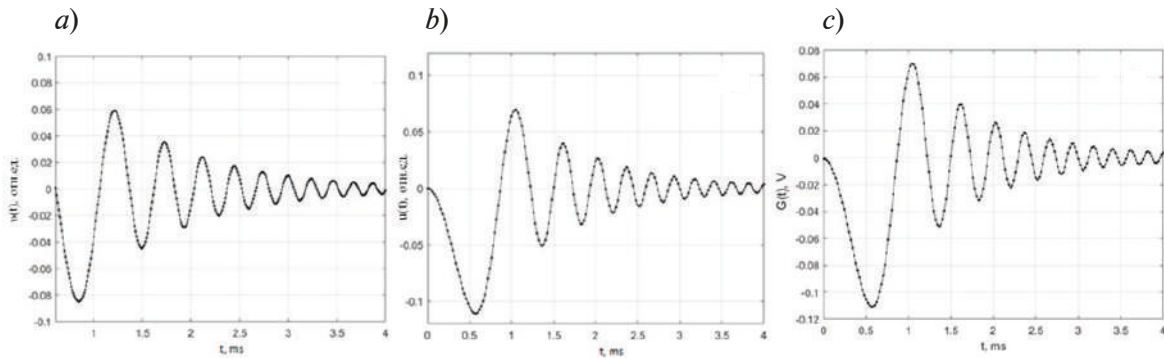


Fig. 1. Calculation forms of NMR signals from oil: absorption (a); dispersion (b); sum signal  $G(t)$  (c)

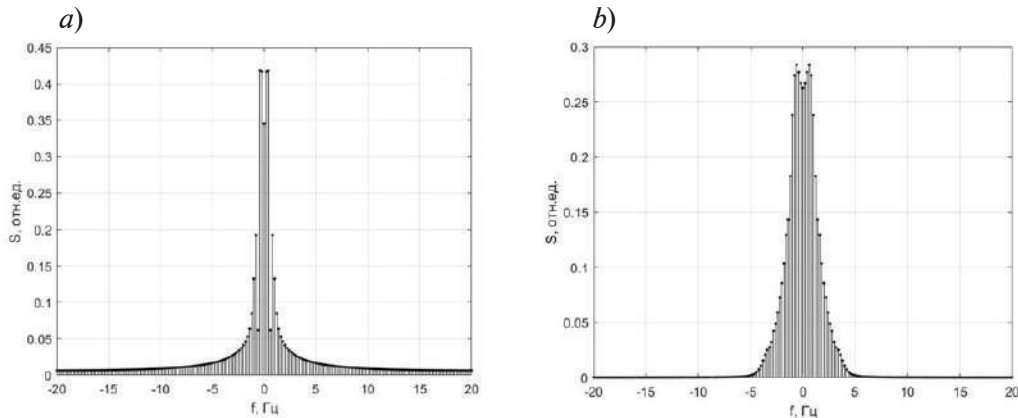


Fig. 2. Amplitude spectra from the calculated NMR signal for oil: absorption (a); dispersion (b)

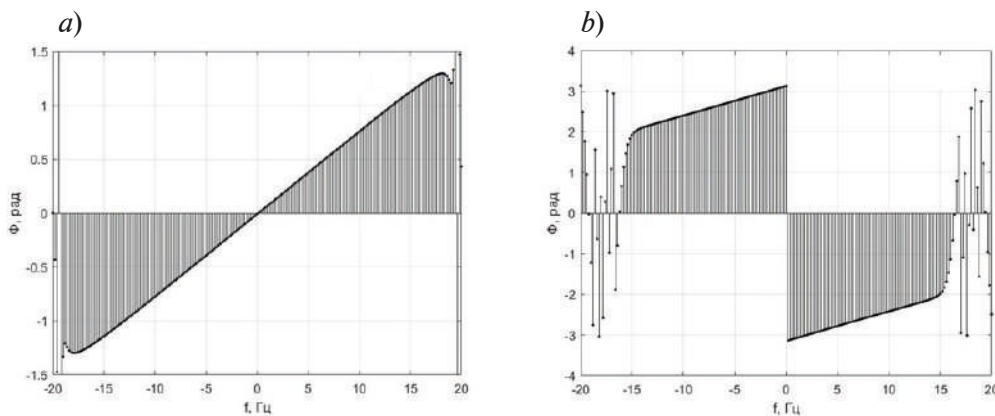


Fig. 3. Phase spectra from the calculated NMR signal for oil: absorption (a); dispersion (b)

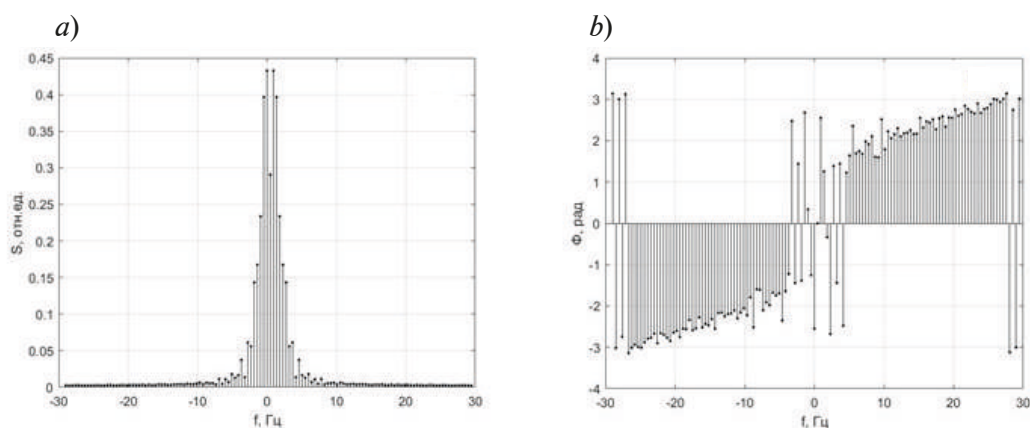


Fig. 4. Spectra from calculated NMR signal for oil: amplitude (a); phase (b)

The obtained results show that the spectral components of the amplitude and phase spectrum can be expressed in terms of the spectral components of the amplitude and phase spectra of the signals  $v(t)$  and  $u(t)$ . The coefficients that determine this relationship will be the contribution of these signals to the recorded NMR signal.

To test our proposed method, experimental studies of liquid media were carried out. With the help of the Matlab package, the amplitude and phase spectra of the NMR signals recorded from the oil sample were constructed, obtained using relations (1)–(3). Fig. 5 shows the spectra of the experimental NMR signal for oil.

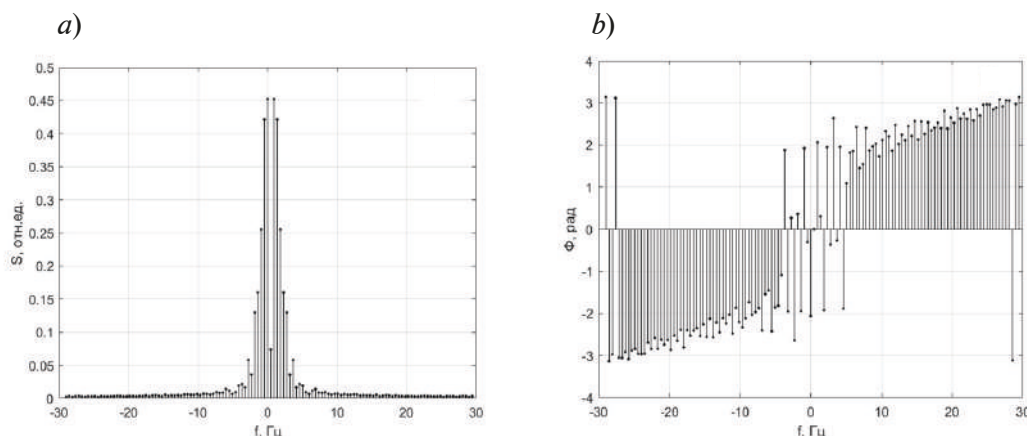


Fig. 5. Spectra from experimental NMR signal for oil: amplitude (a); phase (b)

Analysis of the presented spectra in Fig. 5 shows that the method proposed by us for modeling the spectra of NMR signals makes it possible to obtain good agreement between the theoretical and experimental data. This allows it to be used for effective express control of condensed media.

Having made similar calculations,  $T_2^* = 360$  ms for kerosene and  $T_2^* = 440$  ms for gasoline were obtained and the amplitude and phase spectra were plotted from the calculated NMR signals for kerosene and gasoline.

Further, using the Matlab package, the amplitude and phase spectra of NMR signals for kerosene and gasoline were constructed, obtained using relations (1)–(3). Figs. 6 and 7 show the spectra of the experimental NMR signal for kerosene and gasoline.

It should be noted that the registration of the NMR signal in a weak field is carried out at the maximum signal-to-noise ratio of the signal. In this case, the absorption signal is always greater than the signal dispersion, the coefficients are uniquely determined. In the study of such mixtures, the number of coefficients increases, and coefficients appear corresponding to the concentrations of media in the mixture. Their determination makes it possible to determine the composition and concentration of the components in the mixture.

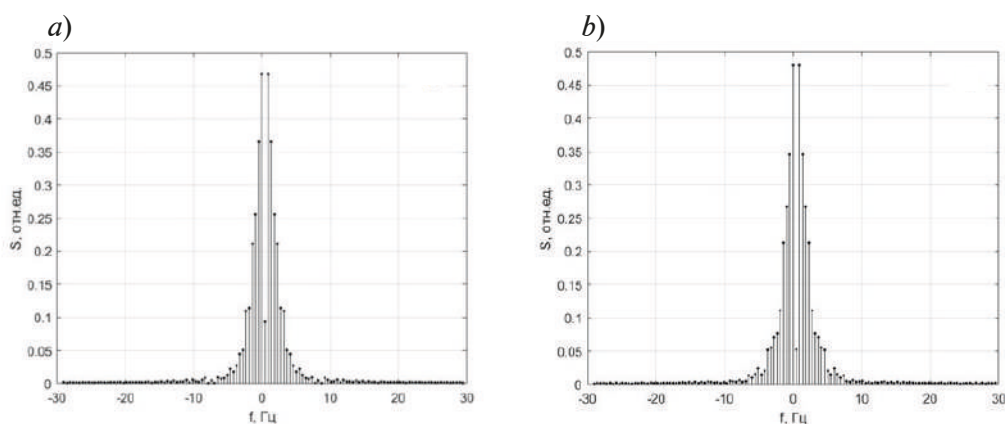


Fig. 6. Amplitude spectra from the experimental NMR signal: kerosene (a); gasoline (b)

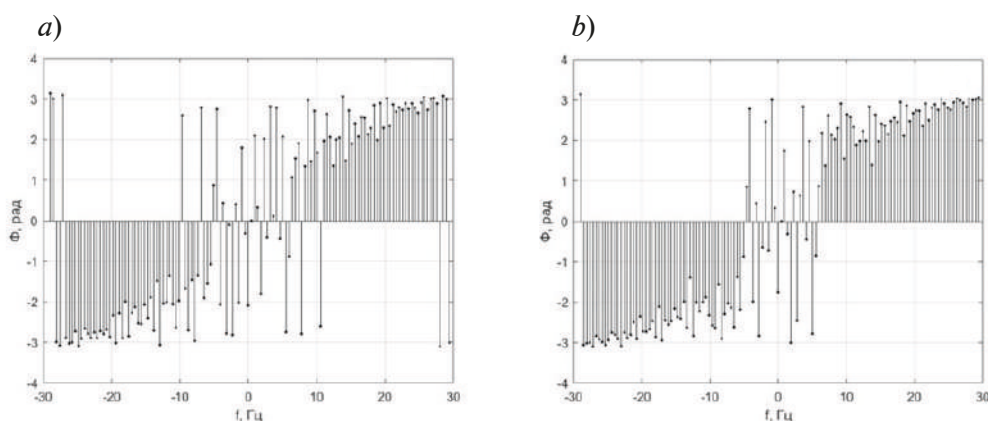


Fig. 7. Phase spectra from the experimental NMR signal: kerosene (a); gasoline (b)

### Conclusion

As a result, it was found that the proposed spectral research method has no restrictions on its use. To use it, it is necessary to register the NMR signal from a medium containing nuclei with magnetic moments, for example, at the resonant frequency of protons (more than 99% of liquid media contain protons) and measure the relaxation constants  $T_1$  and  $T_2$  to calculate absorption and dispersion signals.

### REFERENCES

1. Mazing M. S., Zaitceva A. Yu., Kislyakov Yu. Ya., Kondakov N. S., Avdushenko S. A., Davydov V. V., Monitoring of Oxygen Supply of Human Tissues Using A Noninvasive Optical System Based on A MultiChannel Integrated Spectrum Analyzer, International Journal of Pharmaceutical Research. 12(2) (2020) 1974–1978.
2. Kislyakov Yu. Ya., Avdyushenko S. A., Kislyakova I. P., Zaitceva A. Yu., Analytical multisensory trainable system for diagnosing vocational aptitude of military medical specialists by ion content in the expired breath condensate, Journal of Computational and Theoretical Nanoscience. 16(11) (2019) 4502–4507.
3. Gryaznova E. M., Rud V. Y., On the possibility of using the optical method for express quality control of fruits, Journal of Physics: Conference Series 2086(1) (2021) 012143.
4. Davydov R. V., Yushkova V. V., Stirmanov A. V., Rud V. Yu., A new method for monitoring the health condition based on nondestructive signals of laser radiation absorption and scattering, Journal of Physics: Conference Series. 1410(1) (2019) 012067.
5. Davydov, V. V., Myazin, N. S., Grebenikova, N. M., & Dudkin, V. I., Determination of the Composition and Concentrations of the Components of Mixtures of Hydrocarbon Media in the Course of its Express Analysis. Measurement Techniques, 62(12), 1090–1098.



6. Grebenikova N. M., Smirnov K. J., Rud V. Yu., Artemiev V. V., Features of monitoring the state of the liquid medium by refractometer, *Journal of Physics: Conference Series*. 1135(1) (2018) 012055.
7. Grebenikova N. M., Smirnov K. J., Features of optical signals processing for monitoring the state of the flowing liquid medium with a refractometer, *Journal of Physics: Conference Series*. 1368(2) (2019) 022057.
8. Davydov V. V., Davydova T. I., A nondestructive method for express testing of condensed media in ecological monitoring, *Russian Journal of Nondestructive Testing*. 53(7) (2017) 520–529.
9. Nikitina M., Grebenikova N., Dudkin V., Batov Y., Methodology for assessing the adverse effects of the use of nuclear energy on agricultural land, *IOP Conference Series: Earth and Environmental Science*. 390(1) (2019) 012024.
10. Gryznova E., Batov Y., Rud V., Methodology for assessing the environmental characteristics of various methods of generating electricity, *E3S Web of Conferences*. 140.
11. Davydov R.V., Antonov V.I., Yushkova V.V., Smirnov K.J., A new method of processing a pulse wave in rapid diagnosis of the human health, *Journal of Physics: Conference Series*. 1400(6) (2019) 066037.
12. Antonov V.I., Badenko V.L., Davydov R.V., Maslikov V.I., Molodtsov D.V., Modeling parameters of the flood control facilities adapted to climate change, *Journal of Physics: Conference Series*. 1236(1) (2019) 012049.
13. Davydov R.V., Antonov V.I., Molodtsov D.V., Computer implementation of the mathematical model for water flow management by a hydro complex. *Journal of Physics: Conference Series*. 1135(1) (2018) 012088.
14. Kuzmin M. S., Rogov S. A., On the use of a multi-raster input of one-dimensional signals in two-dimensional optical correlators, *Computer Optics*. 43(3) (2019) 391–396.
15. Davydov R., Antonov V., Moroz A., Parameter Control System for a Nuclear Power Plant Based on Fiber-Optic Sensors and Communication Lines, In: *IEEE International Conference on Electrical Engineering and Photonics (EExPolytech)*, Saint Petersburg, Russia.
16. Davydov V. V., Kruzhalov S. V., Grebenikova N. M., Smirnov K. J., Method for Determining Defects on the Inner Walls of Tubing from the Velocity Distribution of the Flowing Fluid, *Measurement Techniques*. 61(4) (2018) 365–372.
17. Dyumin V., Smirnov K., Myazin N., Charge-coupled Device with Integrated Electron Multiplication for Low Light Level Imaging, *Proceedings of the 2019 IEEE International Conference on Electrical Engineering and Photonics, EExPolytech*. 8906868 (2019) 308–310.
18. Myazin N. S., Dudkin V. I., Grebenikova N. M., On the Possibility of Express Recording of Nuclear Magnetic Resonance Spectra of Liquid Media in Weak Fields, *Technical Physics*. 63(12) (2018) 1845–1850.
19. Grevtseva A. S., Smirnov K. J., Rud V. Yu., Development of methods for results reliability raise during the diagnosis of a person's condition by pulse oximeter, *Journal of Physics: Conference Series*. 1135(1) (2018) 012056.

#### THE AUTHOR

**MAKEEV Sergey**

st\_makeev@mail.ru

ORCID: 0000-0003-1669-0539

*Received 23.07.2022. Approved after reviewing 07.09.2022. Accepted 14.09.2022.*

Conference materials

UDC 53.084.6

DOI: <https://doi.org/10.18721/JPM.153.265>

## Application of a broadband Josephson parametric amplifier

A. E. Dorogov <sup>1, 3, ✉</sup>, G. P. Fedorov <sup>1, 2, 3</sup>, D. A. Kalacheva <sup>1, 2, 4</sup>,  
A. Yu. Dmitriev <sup>1</sup>, A. N. Bolgar <sup>1, 4</sup>, N. N. Abramov <sup>2</sup>, O. V. Astafiev <sup>1, 4</sup>

<sup>1</sup> Moscow Institute of Physics and Technology, Moscow, Russia;

<sup>2</sup> National University of Science and Technology MISIS, Moscow, Russia;

<sup>3</sup> Russian Quantum Center, Moscow, Russia;

<sup>4</sup> Skolkovo Institute of Science and Technology, Moscow, Russia

✉ Dorogov.AE@phystech.edu

**Abstract.** We examine the performance of a Josephson Parametric Amplifier (JPA) which uses an array of SNAILs (Superconducting Nonlinear Asymmetric Inductive eLements) as the source of nonlinearity and leverages the technique of impedance engineering (introducing a positive linear slope in the imaginary part of the input impedance seen by the SNAILs) to overcome a traditional gain-bandwidth product and increase the 1-dB compression point. We experimentally demonstrate an 18 dB gain over a 586 MHz band, along with a 1-dB compression point -101.9 dBm. All these characteristics are of great importance for the quantum devices measurements and in particular for the single-shot readout of a multi-qubit system. The signal-to-noise ratio after the application of the JPA was increased by 3 times. That led to the improvement of separation fidelity of single-shot dispersive measurements of a transmon qubit from 30.6% to 97.2%.

**Keywords:** parametric amplifier, Josephson junction, gain-bandwidth product, 1-dB compression point, single-shot readout

**Funding:** Russian Science Foundation Grant No. 21-72-30026.

**Citation:** Dorogov A. E., Fedorov G. P., Kalacheva D. A., Dmitriev A. Yu., Bolgar A. N., Abramov N. N., Astafiev O. V., Application of a broadband Josephson parametric amplifier, St. Petersburg State Polytechnical University Journal. Physics and Mathematics. 15 (3.2) (2022) 352–357. DOI: <https://doi.org/10.18721/JPM.153.265>

This is an open access article under the CC BY-NC 4.0 license (<https://creativecommons.org/licenses/by-nc/4.0/>)

Материалы конференции

УДК 53.084.6

DOI: <https://doi.org/10.18721/JPM.153.265>

## Применение широкополосного джозефсоновского параметрического усилителя

А. Е. Дорогов <sup>1, 3, ✉</sup>, Г. П. Федоров <sup>1, 2, 3</sup>, Д. А. Калачева <sup>1, 2, 4</sup>,  
А. Ю. Дмитриев <sup>1</sup>, А. Н. Болгар <sup>1, 4</sup>, Н. Н. Абрамов <sup>3</sup>, О. В. Астафьев <sup>1, 4</sup>

<sup>1</sup> Московский физико-технический институт, г. Москва, Россия;

<sup>2</sup> Национальный исследовательский технологический университет «МИСиС», г. Москва, Россия;

<sup>3</sup> Российский квантовый центр, г. Москва, Россия;

<sup>4</sup> Сколковский институт науки и технологий, г. Москва, Россия

✉ Dorogov.AE@phystech.edu

**Аннотация.** В данной работе исследуется применение широкополосного джозефсоновского параметрического усилителя на основе сверхпроводящих нелинейных асимметричных индуктивных элементов SNAIL в качестве источника нелинейности и с использованием

техники трансформации импеданса (введение частотной зависимости мнимой части входного импеданса) для увеличения gain-bandwidth product и мощности насыщения. Были экспериментально продемонстрированы коэффициент усиления 18 дБ в полосе 586 МГц и мощность насыщения -101.9 дБм. Эти характеристики очень важны для измерений квантовых устройств, и в частности для проективного считывания многокубитной системы. Благодаря использованию усилителя отношение сигнал-шум измерительной цепи было увеличено в три раза. Это привело к улучшению точности погрешности разделения состояний проективного дисперсионного считывания кубита-трансмона с 30.6% до 97.2%.

**Ключевые слова:** параметрический усилитель, джозефсоновский переход, мощность насыщения, дисперсионное считывание

**Финансирование:** Грант РНФ 21-72-30026.

**Ссылка при цитировании:** Дорогов А. Е., Федоров Г. П., Калачева Д. А., Дмитриев А. Ю., Болгар А. Н., Абрамов Н. Н., Астафьев О. В. Применение широкополосного джозефсоновского параметрического усилителя // Научно-технические ведомости СПбГПУ. Физико-математические науки. Т. 15. № 3.2. С. 352–357. DOI: <https://doi.org/10.18721/JPM.153.265>

Статья открытого доступа, распространяемая по лицензии CC BY-NC 4.0 (<https://creativecommons.org/licenses/by-nc/4.0/>)

### Introduction

As the field of quantum computing is rapidly evolving, quantum devices incorporate more and more qubits, inevitably forming a demand for broadband parametric amplifiers which can be used for multiplexed qubit readout. Commercially available HEMT amplifiers are not sufficient because of high added noise,  $T_{\text{HEMT}} = 3\text{--}5$  K. Josephson Parametric Amplifiers (JPAs) are capable of reaching the minimum added noise imposed by quantum mechanics,  $T_q \sim 0.3$  K, and consequently can increase the signal-to-noise ratio (SNR) several-fold. Enhancement of SNR is a vital task for qubit measurements because it allows to speed up readout and improve the fidelity.

Moreover, JPAs have to provide a decent gain  $G_{\text{JPA}}$  to overcome the noise from the subsequent HEMT amplifiers, as follows from the expression for the chain noise:

$$T_{\text{chain}} = T_{\text{JPA}} + \frac{T_{\text{HEMT}}}{G_{\text{JPA}}}. \quad (1)$$

Thus, the crucial requirements which define the performance of the JPA are low added noise, high gain (15–20 dB), large bandwidth and dynamic range, as well as ease of operation.

Generally, a parametric amplifier is just a nonlinear oscillator, where the nonlinearity provides the power transfer from the strong pump to the weak quantum signal. JPAs employ the Josephson junctions (JJs) to introduce the required nonlinearity: their inductance depends on the phase drop  $\varphi$  across the JJ as

$$L_J = \frac{\Phi_0 / I_0}{\cos(\varphi)},$$

where  $\Phi_0$  is a magnetic flux quantum and  $I_0$  is the junction's critical current.

The performance of JPAs is fundamentally confined by several factors. First of all, there is a trade-off between the power gain and the bandwidth of amplification, namely the 'gain-bandwidth product' [1]:

$$G = 1 + \frac{G_{\text{max}} - 1}{1 + (\omega / \Gamma)^2}, \quad \Gamma \propto \frac{1}{\sqrt{G_{\text{max}} - 1}}. \quad (2)$$

Thus, there is no sense to strive to reach the gain more than 15–20 dB because that is enough to overcome the noise from HEMT amplifiers and further increase in gain will just lead to the decrease in bandwidth.

Next, the amplification decreases at high signal powers as it is provided by plentiful though still depletable photons from the pump. To quantify this effect, the so-called 1-dB compression point is introduced as the signal power at which the gain drops by 1 dB.

Seeking the way to sidestep negative influence of the aforementioned factors, we study a JPA which uses an array of  $M = 23$  SNAILs (Superconducting Nonlinear Asymmetric elements) as a nonlinear element [2]. This architecture offers great flexibility while designing the device. A single SNAIL consists of 3 large Josephson junctions (inductance  $L_j$ ) in a loop with one smaller junction (inductance  $L_j/\alpha$ ) (Fig. 1).

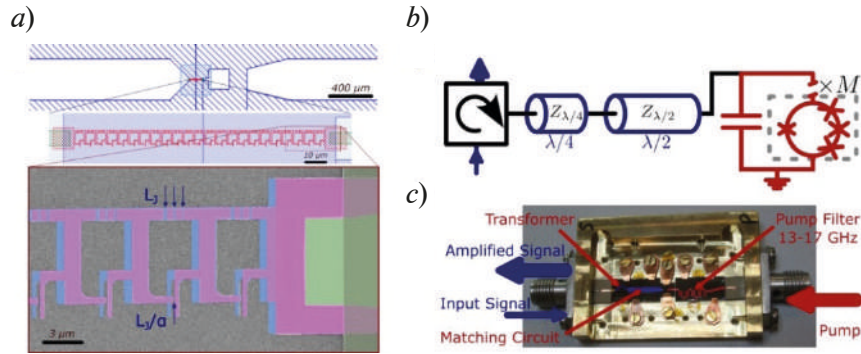


Fig. 1. Design (top) and false color scanning electron micrograph (bottom) of the structure (a); the Al-based tunnel junctions are shaded in pink and blue for two different evaporation angles, respectively. Nonlinear resonator composed of a capacitively shunted SNAIL array (red) coupled to the source impedance via two transmission line segments (blue) introducing a positive linear slope in the imaginary part of the input impedance  $Z_{in}[\omega]$  (b). Implementation of the circuit in (b) using microstrip geometry (c); the transformer and the pump filter are fabricated on separate chips

The Hamiltonian of such amplifier can be approximated as [2]:

$$\frac{H_{JPA}}{\hbar} = \omega_a \hat{a}^\dagger \hat{a} + g_3 (\hat{a} + \hat{a}^\dagger)^3 + g_4 (\hat{a} + \hat{a}^\dagger)^4. \quad (3)$$

Then the power gain for a signal at frequency  $\omega_s$  and the pump at  $\omega_p$  is

$$G[\omega] = 1 + \frac{4\kappa^2 |g|^2}{(\Delta_p^2 - \omega^2 + \frac{\kappa^2}{4} - 4|g|^2)^2 + (\kappa\omega)^2}, \quad (4)$$

where  $\omega = \omega_s - \frac{\omega_p}{2}$ ,  $g = 2g_3\alpha_p$ ,  $\Delta_p = \omega_a - \frac{\omega_p}{2} + \frac{32}{3}g_4|\alpha_p|^2$ ;

$\alpha_p$  is the mean intracavity amplitude and  $\kappa$  is the dissipation rate defined by coupling to the transmission line. The performance of an amplifier depends only on  $\omega_a$ ,  $g_3$ ,  $g_4$  and  $\kappa$ , which can be tuned via engineering  $L_j$ ,  $M$ ,  $\alpha$ ,  $\omega_0$ .

The expression for  $G[\omega]$  (4) may lead to a confusion that the gain-bandwidth product can be set arbitrarily large by applying a stronger pump. However, that is not so. Higher-order terms will appear in Hamiltonian (3) with the extreme increase in pump power making the further analysis invalid. Moreover, as regards experimental setup, huge pump may cause the increase in the cryostat base temperature and interfere with the experimental process.

The device under study leverages another technique to go beyond the gain-bandwidth product, impedance engineering [1]. The design uses a combination of a  $\lambda/4$  and a  $\lambda/2$  impedance transformers to introduce the frequency dependence of the environmental impedance:

$$Z_{in}[\omega] = R + i\xi\omega. \quad (5)$$

It turns out that by tuning  $\xi$  it is possible to eliminate the leading-order quadratic dependence of  $G[\omega]$ .

Thereby the modified gain-bandwidth product can be rewritten as:

$$\tilde{G}[\omega] = 1 + \frac{G_{max} - 1}{1 + (\omega/\tilde{\Gamma})^4}, \quad \tilde{\Gamma} \propto \frac{1}{\sqrt[4]{G_{max} - 1}}. \quad (6)$$

As one can see, application of impedance engineering makes the trade-off between gain and bandwidth less severe.

SNR measurement can be used to estimate the JPA's added noise. When the pump is off JPA provides no amplification so the only active amplifiers in the chain are HEMTs:

$$SNR_{HEMT} = \frac{A}{T_{HEMT}}. \quad (7)$$

After turning the pump on, the signal  $A$  is amplified in JPA as well:

$$SNR_{JPA} = \frac{G_{HEMT} G_{JPA} A}{G_{HEMT} G_{JPA} T_{JPA} + G_{HEMT} T_{HEMT}} = \frac{A}{T_{JPA} + \frac{T_{HEMT}}{G_{JPA}}} \equiv \frac{A}{T_{chain}}. \quad (8)$$

Combining (7) and (8),

$$T_{JPA} = T_{HEMT} \frac{SNR_{HEMT}}{SNR_{JPA}} - \frac{T_{HEMT}}{G_{JPA}}. \quad (9)$$

Eq. (9) provides an easy way to learn  $T_{JPA}$  in situ.

### Materials and Methods

The fabrication of the device starts with the aluminum evaporation on a silicon substrate followed by etching of a patterned optical resist mask in  $Cl_2$  plasma. To minimize the amount of native oxide on silicon substrate, piranha solution and buffered HF treatment were implemented [3]. The Josephson junctions for the device were fabricated using electron lithography and the aluminum was evaporated using Dolan bridge technique [4].

### Results and Discussion

The characterization is done by monitoring the transmission through the amplifier while sweeping the signal frequency and the pump power. The results are shown in Fig. 2, *a*. The flattest gain profile is shown in Fig. 2, *b*. The saturation power measurement is shown in Fig. 2, *c*, demonstrating the high 1-dB compression point  $-101.9$  dBm which is on par with the best reported amplifiers [2], [1].

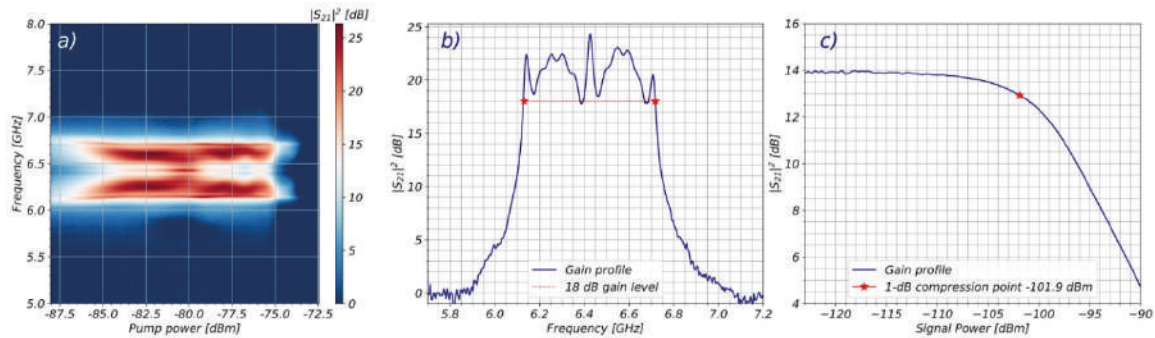


Fig. 2. Characterization of amplifier: amplification (color) versus signal frequency and pump power (*a*), the huge bandwidth is detected in a wide range on the pump power scale; slice of the dependence in (*a*) at the pump power  $-80$  dBm (*b*), 18 dB gain is reached in a bandwidth of 586 MHz; 1-dB compression point measurement (*c*) (signal frequency 7.34 GHz)

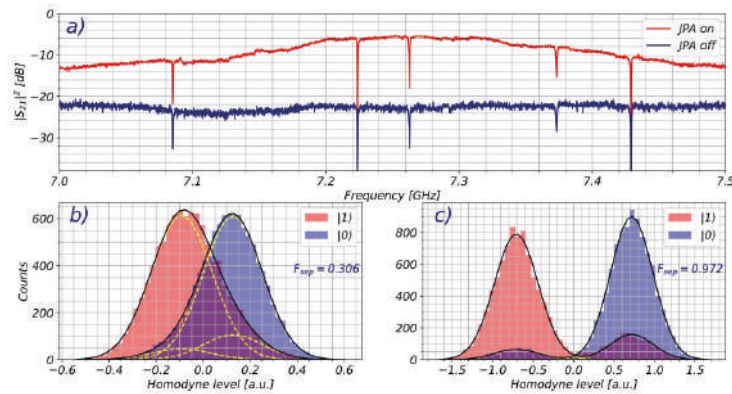


Fig. 3. Application of the amplifier. Comparison between the transmission profiles through the readout line of the 5-qubit sample with active JPA (red, pump signal on) and inactive (blue, pump signal off) (a): in ‘off’-state, the JPA has almost no effect on transmission. The SNR at resonator frequencies (sharp dips in transmission) in ‘on’-state is increased by approximately 3 times (see Table 1). Applying the device for single-shot qubit measurements (resonator II at 7.232 GHz) (b): the  $|0\rangle$  and  $|1\rangle$  states are nearly indistinguishable after I-pulse (blue) and  $\pi$ -pulse (red) without JPA (b) providing poor separation fidelity of 30.6%. After turning on the JPA, the state histograms become well-separated with decent fidelity of 97.2% (c)

For the ease of application of the amplifier for any quantum device the optimization algorithm was developed. It takes as input the needed gain and bandwidth and seeks for the parameters (bias magnetic flux, pump frequency and power) which provide the best performance. Using it, a suitable working regime for a 5-qubit device was found. The improvement of the SNR is shown in Fig. 3,a. Due to improved SNR, the fidelity of single-shot IQ-clouds measurement [5] was also enhanced (Fig. 3 b, c).

The SNR was measured for the resonant frequencies of the resonators for dispersive readout. Results are shown in Table 1. It can be seen that a three-fold increase in SNR was achieved in the entire band. According to Eq. (9), one can estimate the additional noise of JPA knowing the  $T_{\text{HEMT}} \approx 5 \text{ K} : T_{\text{JPA}} \approx 0.4 \text{ K}$  which is comparable to the quantum noise.

Table 1

**Improvement of SNR for resonant frequencies**

Frequency (GHz)	$\text{SNR}_{\text{JPA off}}$	$\text{SNR}_{\text{JPA on}}$	$\text{SNR}_{\text{JPA off}}/\text{SNR}_{\text{JPA on}}$
7.086	16.6	47.2	2.8
7.232	19.0	61.9	3.3
7.262	16.4	48.4	2.9
7.374	17.9	54.1	3.0
7.429	7.3	20.4	2.8

### Conclusion

The performance of the Josephson Parametric Amplifier was examined. The design leveraging the techniques of SNAILS and Impedance Engineering allows for high 1-dB compression point -101.9 dBm and power gain 18 dB in a bandwidth 586 MHz. The amplifier was used for the measurement of a 5-qubit processor. It tripled the signal-to-noise ratio and increased the separation fidelity of single-shot measurements from 30.6% to 97.2%.

### Acknowledgements

A.E.D. acknowledges fruitful discussions with Alexei Tolstobrov and Oleg Li. The JPA was fabricated at the cleanroom facility of MIPT. This research is supported by Russian Science Foundation under Grant 21-72-30026.

**REFERENCES**

1. **Roy T., Kundu S., Chand M., et al.**, Broadband parametric amplification with impedance engineering: Beyond the gain-bandwidth product. *Applied Physics Letters* 107 (26) (2015): 262601.
2. **Frattini N.E., Sivak V.V., Lingenfelter A., et al.**, Optimizing the nonlinearity and dissipation of a snail parametric amplifier for dynamic range. *Physical Review Applied* 10 (5) (2018): 054020.
3. **Kalacheva D., Fedorov G., Kulakova A., et al.**, Improving the quality factor of superconducting resonators by post-process surface treatment. *AIP Conference Proceedings* 2241 (1). AIP Publishing LLC, 2020.
4. **Dolan G. J.**, Offset masks for lift-off photoprocessing. *Applied Physics Letters* 31 (5) (1977): 337–339.
5. **Walter T., Kurpiers P., Gasparinetti S., et al.**, Rapid high-fidelity single-shot dispersive readout of superconducting qubits. *Physical Review Applied* 7 (5) (2017): 054020.

**THE AUTHORS****DOROGOV Aleksandr**

Dorogov.AE@phystech.edu

ORCID: 0000-0003-2708-6409

**FEDOROV Gleb**

gleb.fedorov@phystech.edu

ORCID: 0000-0001-9144-6179

**KALACHEVA Daria**

d.kalacheva@gmail.com

ORCID: 0000-0002-6931-0686

**DMITRIEV Aleksei**

dmitrmipt@gmail.com

ORCID: 0000-0001-9493-6739

**BOLGAR Aleksey**

alexgood@list.ru

ORCID: 0000-0001-7559-2336

**ABRAMOV Nikolay**

abramov.nn@misis.ru

ORCID: 0000-0003-0461-642X

**ASTAFIEV Oleg**

O.Astafiev@skoltech.ru

ORCID: 0000-0001-5763-589X

*Received 29.07.2022. Approved after reviewing 08.08.2022. Accepted 11.08.2022.*

Conference materials

UDC 612.166

DOI: <https://doi.org/10.18721/JPM.153.266>

## New technique for researching the absorption signal fronts of laser radiation on blood vessels

I. M. Gureeva <sup>1</sup>✉, V. V. Davydov <sup>1, 2, 3</sup>

<sup>1</sup> Peter the Great St. Petersburg Polytechnic University, St. Petersburg, Russia;

<sup>2</sup> Bonch-Bruевич Saint Petersburg State University of Telecommunications, St. Petersburg, Russia;

<sup>3</sup> All-Russian Research Institute of Phytopathology, Moscow Region, Russia

✉ irena-gureeva@mail.ru

**Abstract.** The analysis of pulse oximetry as a method of rapid diagnosis of the state of the body in real time was performed. Data are presented that the high rate of pulse wave propagation through the arteries in patients with COVID-19 may indicate a high risk of death. It is noted that modern device designs and pulse wave signal processing methods have a number of disadvantages. This leads to an unreliable interpretation of the data. Using a charge-coupled device increases the accuracy of measuring the position of maxima and minima on the time scale. This makes it possible to determine the moment of closure of the aortic valves of the left ventricle more accurately. The registered pulse waves of various people are presented, as well as the results of the study of the time intervals of the rising and falling fronts.

**Keywords:** blood flow, pulse wave, laser radiation, absorption signal, oxygen, time, rise and fall front, measurement error

**Citation:** Gureeva I. M., Davydov V. V., A new technique for researching the absorption signal fronts of laser radiation on blood vessels, St. Petersburg State Polytechnical University Journal. Physics and Mathematics. 15 (3.2) (2022) 358–363. DOI: <https://doi.org/10.18721/JPM.153.266>

This is an open access article under the CC BY-NC 4.0 license (<https://creativecommons.org/licenses/by-nc/4.0/>)

Материалы конференции

УДК 612.166

DOI: <https://doi.org/10.18721/JPM.153.266>

## Новая методика исследования фронтов пульсовой волны, регистрируемой на кровеносных сосудах

И. М. Гуреева <sup>1</sup>✉, В. В. Давыдов <sup>1, 2, 3</sup>

<sup>1</sup> Санкт-Петербургский политехнический университет Петра Великого, Санкт-Петербург, Россия;

<sup>2</sup> Санкт-Петербургский государственный университет телекоммуникаций им. проф. М.А. Бонч-Бруевича, Санкт-Петербург, Россия;

<sup>3</sup> Всероссийский научно-исследовательский институт фитопатологии, Московская область, Россия

✉ irena-gureeva@mail.ru

**Аннотация.** Выполнен анализ пульсоксиметрии как метода экспресс-диагностики состояния организма в режиме реального времени. Представлены данные о том, что высокая скорость распространения по артериям пульсовой волны у пациентов с COVID-19 может свидетельствовать о высоком риске летального исхода. Отмечено, что современные конструкции приборов и методы обработки сигнала пульсовой волны обладают рядом недостатков. Это приводит к недостоверной интерпретации данных. Использование прибора с зарядовой связью увеличивает точность измерений положения максимумов и минимумов на временной шкале. Это позволяет более точно определить момент закрытия аортальных клапанов левого желудочка. Представлены зарегистрированные пульсовые волны различных людей, а также результаты исследования временных интервалов фронтов нарастания и спада.

**Ключевые слова:** кровоток, пульсовая волна, лазерное излучение, сигнал поглощения,

© Gureeva I. M., Davydov V. V., 2022. Published by Peter the Great St. Petersburg Polytechnic University.



кислород, время, фронт нарастания и спада, погрешность измерения

**Ссылка при цитировании:** Гуреева И. М., Давыдов В. В. Новая методика исследования фронтов пульсовой волны регистрируемой на кровеносных сосудах // Научно-технические ведомости СПбГПУ. Физико-математические науки. Т. 15. № 3.2. С. 358–363. DOI: <https://doi.org/10.18721/JPM.153.266>

Статья открытого доступа, распространяемая по лицензии CC BY-NC 4.0 (<https://creativecommons.org/licenses/by-nc/4.0/>)

## Introduction

In conditions of environmental degradation, acceleration of the rhythm of life and the level of stress load, people began to regularly monitor their health [1–6]. Express diagnostic methods in the modern world are very often used to solve various problems [6–9]. It is very important for a person to be able to perform this diagnosis independently. Therefore, pulse oximetry has become widespread among express diagnostics, in addition to measuring temperature and pressure [3, 4, 9–11]. Its advantages include noninvasiveness of measurements when obtaining pulse data and percentage of oxygen saturation of the blood.

In addition, studies by various scientists have shown that a number of patients with COVID-19 have a higher rate of pulse wave propagation through the arteries. Considering this factor, sources of laser radiation at various wavelengths for pulse oximeters are being developed for its registration [12, 13]. According to British and Italian researchers, the probability of death in COVID-19 can be considered increased if the pulse wave velocity does not exceed 13 meters per second. It should be noted that for most people of different ages (the norm in terms of velocity) is 5.5–8 meters per second [14, 15].

It should be noted that modern pulse oximeter designs and pulse wave signal processing methods have a number of disadvantages [16–21]. This leads to errors in measuring the pulse and the percentage of oxygen saturation of the blood (up to 50%), as well as distortion of the pulse wave shape. Therefore, the purpose of our work is to study the pulse wave fronts to obtain additional information about the state of human health. This is extremely relevant recently, especially in the context of a pandemic.

## Features of pulse wave fronts formation and methods of their investigation

Numerous studies have shown that transmission pulse oximetry using a laser radiation absorption signal has the greatest advantages for personal use at various times (for example, with deterioration of health, heavy loads, etc.) [16–18]. The classical form of the laser radiation absorption signal (pulse wave) recorded using a photodetector is shown in Fig. 1.

The presented signal has two peaks (maxima) and three minima. The pulse value per minute is determined by the distance between the main maxima (corresponding to time  $t_2$ ) in the pulse wave and their number. By registering two absorption signals of laser radiation with different wavelengths  $\lambda_1 = 662$  nm and  $\lambda_2 = 907$  nm, the percentage saturation of blood hemoglobin with oxygen is determined.

To obtain additional information about the state of human health, the values of the time intervals  $\Delta t_1 = t_2 - t_1$ ,  $\Delta t_2 = t_3 - t_2$ ,  $\Delta t_3 = t_4 - t_3$  and  $\Delta t_4 = t_5 - t_4$  are important. As well as the nature of the change in the fronts of the rise and fall of the pulse wave. These data may make it possible in the future to noninvasively determine the compliance of the cardiovascular system, as well as to evaluate (determine the order of magnitude) the value of the

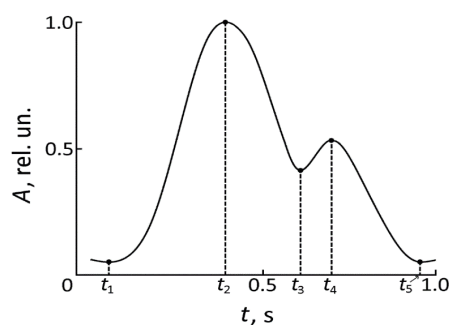


Fig. 1. Pulse wave shape detected by the photodetector from the laser radiation absorption signal

blood velocity in the veins and arteries. Data on the intervals  $\Delta t_1$ ,  $\Delta t_2$ ,  $\Delta t_3$  and  $\Delta t_4$  were used by a number of authors to construct mathematical models of rising and falling fronts [16, 18, 20–23].

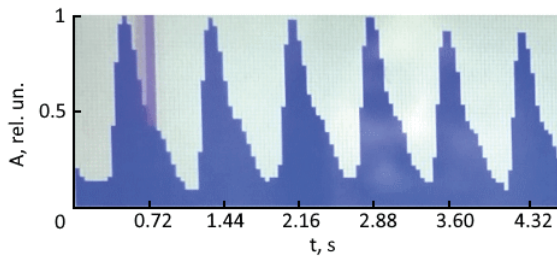


Fig. 2. Shape of the absorption signal of the recorded signal in transmission pulse oximetry Data for female patient showing symptoms of COVID-19 for less than 2 weeks (age 22)

In a number of papers, the authors tried to obtain additional information about the state of human health using envelopes [21–26], for the mathematical description of which an exponential function of the form  $\exp(-Kt)$  was used. This method turned out to be ineffective. Therefore, the most appropriate decision in this situation was to register the absorption signal of laser radiation using a CCD array. In this case, the pulse wave signal is recorded in the form of steps that correspond to the levels of cell filling with charge (quantization of the shape of the pulse wave fronts). Fig. 2 shows the recorded signal of laser radiation absorption using a CCD.

Our research has shown that for different people, the parameters of the steps (amplitude and their duration), as well as their number in the pulse wave, differ from each other. These differences are related to the pulsation of the walls of the blood vessel during the passage of blood flow during contraction of the heart muscle, the elasticity of blood vessels and veins, and may also be the composition of blood. The technique of recording absorption signals using CCD does not significantly affect the change in the parameters of the steps. Other factors influence, for example, when changing the position of a person’s placement, the recorded pulse wave signal changed (the number and parameters of the steps changed).

When using the parameters of the steps to measure the characteristics of the pulse wave (time intervals  $\Delta t$ ), the signal-to-noise ratio of the recorded absorption signal will be of great importance. As a result of various studies [18, 21, 22, 24, 25] of measuring the amplitude of the recorded laser radiation from the angle of incidence of the laser beam on the surface of the finger, the following was established. The value of the signal-to-noise ratio in the recorded absorption signal will be maximum if the direction of the angle of incidence of the laser radiation on the surface of the finger is perpendicular to the blood flow in the vessel. Therefore, choosing the appropriate sensor configuration, which is installed on the finger, allows you to get an increase in the signal-to-noise ratio by 5-10%, which in some cases can affect the accuracy of diagnostics with a weak absorption signal (very thin blood vessels). It should be noted that the wavelength  $\lambda$  has the greatest influence on the signal-to-noise ratio of the recorded absorption signal. In modern industrial devices, two laser radiation sources with  $\lambda_1 = 662 \pm 2$  nm and  $\lambda_2 = 940 \pm 2$  nm are used to register a pulse wave based on measurements of the amplitudes of the absorption signal. These wavelengths have been calculated for a long time for typical human data from the twentieth century.

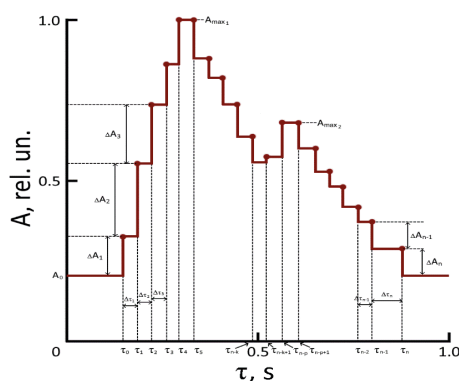


Fig. 3. Shape of the absorption signal recorded in transmission pulse oximetry

The results obtained showed that in most people, the maximum amplitude of the pulse wave is shifted to the region of smaller wavelengths of the red laser radiation range. Therefore, in order to increase the signal/noise of the recorded signal of absorption of reduced hemoglobin in these cases, it is necessary to use laser radiation with  $\lambda_1$  less than 650 nm. Similar studies have been done to change  $\lambda_2$ . It was found that to increase the signal/noise of the detected absorption signal of

In case of using a CCD, will reduce the resolution of the device in the formation of steps in the pulse wave signal, part of the steps with a small amplitude will either not be formed or them combination with the neighboring one will occur, which will lead to measurement errors of the values of  $\Delta t_T$ . To increase the accuracy of measuring the time intervals of the pulse

wave fronts  $\Delta t_1, \Delta t_2, \Delta t_3$  and  $\Delta t_4$ , it is proposed to use the following technique. Fig. 4 shows the pulse wave signal formed in the form of steps. The timeline scale is defined as follows. The counter counts  $N_m$  correspond to the number of peaks per minute (amplitude maxima). Maxima ( $A_{max_2}$ ) corresponding to the dirotic rise (Fig. 3) are not considered.



Next, a time ruler is built with a scale of  $60/N_m$  in seconds. The grid labels correspond to the maxima of the signal peaks. There is already an error in this approach, since the integer number of peaks does not fit into 60 s. Therefore, we propose to introduce a correction factor  $\Delta T = 30/(N_m)^2$ . In this case, the following formula should be used to determine the distance between the peaks of  $T$ :

$$T = \frac{60}{N_m} + \frac{30}{(N_m)^2}. \tag{1}$$

In the case of small values (less than 70 beats per minute), it is proposed to introduce additional coefficients in (1):

$$T = 60 \left( \frac{1}{N_m} + \frac{2}{(N_m)^2} + \dots + \frac{n}{(N_m)^n} \right), \tag{2}$$

where  $n$  can vary from 3 to 10 or more.

With an increase in  $n$ , the accuracy of determining  $T$  increases. The conducted studies have shown that the use of formula (2) reduces the error of determining the scale several times. This makes it possible to determine the values of  $t_n$  at least twice as accurately as in the methods previously used in pulse oximetry. Considering the peculiarities of recording the absorption signal using CCD, we propose to determine the position of points  $t_1, t_2, t_3, t_4, t_5$  on the time scale by separating the processes of formation and decay of pulse wave fronts. The position on the timeline of points with  $t_2$  and  $t_4$  will be determined as follows. Consider the definition of time  $t_2$  according to the waveform in Fig. 3. The moment of the end of the step formation (register charge) is determined – this is the time  $t_5$ . At time  $t_6$ , the formation of a step ends, which corresponds to the front of the pulse wave decline. In this case, the time value  $t_2$  is located between  $\tau_5$  and  $\tau_6$ .

Since the formation did not begin with the increase of another step, but there was a decrease in amplitude  $\Delta A_5$  (Fig. 3), which is smaller in amplitude  $\Delta A_4$ , it can be argued that  $t_2$  is located in the interval between  $t_5$  and  $t_6 - (t_6 - t_4)/2$ . In this case, the value  $t_2 = \tau_5 + (\tau_6 - \tau_4)/4$  is selected. The error in determining  $t_2$  in this case is at least two times less than when using photodiodes to register the absorption signal. Similarly, using a comparison of the amplitudes of the  $\Delta A_n$  steps, the value of  $t_4$  is determined.

The position of points  $t_3$  and  $t_5$  will be determined as follows. Let us take this as an example of determining the value of  $t_3$ . The moment of the end of the step formation (register charge) is also determined: this is the time  $t_{n-k}$ . At the moment of time  $t_{n-k+1}$ , the formation of a step ends, which corresponds to the front of the pulse wave rise. In this case, the time value  $t_3$  is located between  $t_{n-k}$  and  $t_{n-k+1}$ .

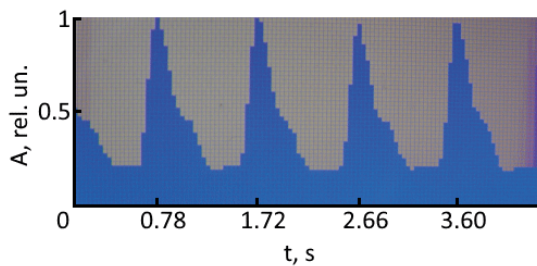


Fig. 3. Shape of the absorption signal recorded by the CCD matrix in transmission pulse oximetry  
Data given for male patient (age 50)

Since the formation of another step did not begin with a decrease in amplitude, but there was an increase in the amplitude of  $\Delta A_{n-k+1}$  (Fig. 3), which is smaller in amplitude of  $\Delta A_{n-k}$ , it can be argued that  $t_3$  is located in the interval between  $t_{n-k+1}$  and  $\tau_{n-k+1} + (\tau_{n-k+1} - \tau_{n-k})/2$ . In this case, the value  $t_3 = \tau_{n-k} + (\tau_{n-k+1} - \tau_{n-k})/4$  is selected. The error in determining  $t_3$  in this case is at least two times less than when using photodiodes to register the absorption signal. Similarly, using a comparison of the amplitudes of the  $\Delta A_n$  steps, the value of  $t_5$  and  $t_1$  is determined.

### Results of human health studies and their discussion

Figs. 3 and 4, for example, show registered pulse wave signals from people with various health conditions.

Visual analysis of the pulse waves presented in Fig. 3 and 4 makes it possible to notice minor deviations in their wave forms, which are quite difficult to associate with diseases. Therefore, we performed using the developed methods and ratios (1) and (2) measurements of the times  $t_1, t_2, t_3, t_4, t_5$  by the values of which the time intervals  $\Delta t_1, \Delta t_2, \Delta t_3$  and  $\Delta t_4$  were determined.

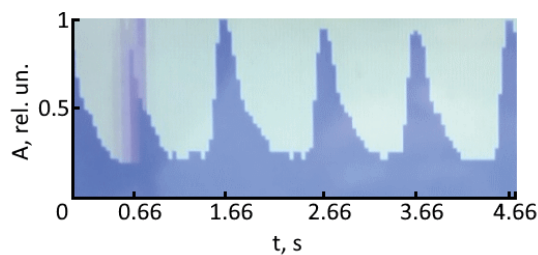


Fig. 4. Shape of the absorption signal recorded by the CCD matrix in transmission pulse oximetry  
Data given for male patient (age 55)

Analysis of the data obtained shows that at higher values of the human pulse, the rate of formation of the pulse wave front is higher (the value of  $\Delta t_1$  decreases) than at a low pulse. An increase in the percentage of hemoglobin oxygen saturation in the blood during the examination of 20 people showed an increase in the value of  $\Delta t_3$ . At the same time, in almost all of these people, the value of  $\Delta t_2$  differs slightly from the values of  $\Delta t_1$  and  $\Delta t_4$ . With a decrease in the percentage of oxygen in the blood, this difference increases. Comparisons of information about the health status of people whose pulse waves were measured

and  $\Delta t$  determined show the possibilities of obtaining additional information for express diagnostics.

Prerequisites for further studies using the developed techniques will be an array of data from various patients for statistical processing [18–25]. In most cases, information about the disease of the cardiovascular system in these patients has been established using other methods used in clinical medicine. This will allow a more correct comparison of research results and establish new relationships between the parameters of the pulse wave to identify a number of changes in the state of the body at an early stage.

### Conclusion

The obtained research results show the expediency of using the techniques developed by us for processing pulse wave fronts to obtain additional information about the work of the human cardiovascular system.

The use of the proposed methodology allows us to reduce the error by at least two times compared to previously performed measurements in determining the time intervals of  $\Delta t$ , which allows them to be used to determine the compliance of the arterial system.

### REFERENCES

1. Guedes A. F., Carvalho F. A., Moreira C., Nogueira J. B., Santos N. C., Essential arterial hypertension patients present higher cell adhesion forces, contributing to fibrinogen-dependent cardiovascular risk, *Nanoscale*. 9(39) (2017) 14897.
2. Leitão C., Ribau V., Afreixo V., Clinical evaluation of an optical fiber-based probe for the assessment of central arterial pulse waves, *Hypertension Research*. 41(11) (2018) 904.
3. Gommer E. D., Shijaku E., Mess W. H., Reulen J. H., Dynamic cerebral autoregulation: different signal processing methods without influence on results and reproducibility, *Medical and Biological Engineering and Computing*. 48 (12) (2010) 1243.
4. Luo J. W., Guo S. W., Cao S. S., The Construction of Unsmooth Pulse Images in Traditional Chinese Medicine Based on Wave Intensity Technology, *Evidence-based Complementary and Alternative Medicine*. 2468254 (2016).
5. Guo R., Wang Y., Yan H., Analysis and Recognition of Traditional Chinese Medicine Pulse Based on the Hilbert-Huang Transform and Random Forest in Patients with Coronary Heart Disease, *Evidence-based Complementary and Alternative Medicine*. 895749 (2015).
6. Frolov M., Chistiakova O., Adaptive Algorithm Based on Functional-Type A Posteriori Error Estimate for Reissner-Mindlin Plates, *Lecture Notes in Computational Science and Engineering*. 128 (2019) 131.
7. Davydov R. V., Dudkin V. I., Nikolaev D. I., Makeev S. S., Moroz A. V., Structure of a Nuclear Magnetic Resonance Signal in a Small Relaxometer, *Journal of Communications Technology and Electronics*. 66(5) (2021) 632.
8. Davydov V. V., Dudkin V. I., Nikolaev D. I., Moroz A. V., Features of Studying Liquid Media by the Method of Nuclear Magnetic Resonance in a Weak Magnetic Field, *Journal of Communications Technology and Electronics*. 66(10) (2021) 1189.
9. Davydov V. V., Myazin N. S., Makeev S. S., Dudkin V. I., Method for Monitoring the Longitudinal Relaxation Time of Flowing Liquids Over the Entire Range of Flow Rate Measurements, *Measurement Techniques*. 63(5) (2020) 368.



10. **Davydov V. V., Dudkin V. I., Vysoczky M. G., Myazin N. S.**, Small-size NMR Spectrometer for Express Control of Liquid Media State, *Applied Magnetic Resonance*. 51(7) (2020) 653.
11. **Myazin N. S., Yushkova V. V., Rud' V. Yu.**, A new method of determining the state of water and agricultural areas in real time, *Environmental, Research, Engineering and Management*. 75(2) (2019) 28.
12. **Antonov V., Efremov P.**, Malformations as a violation of the fractal structure of the circulatory system of an organism, *Technical Physics*. 65(9) (2020) 1446.
13. **Baskurt O. K., Meiselman H. J.**, Blood Rheology and Hemodynamics, *Semin Thromb Hemost*. 29(5) (2003) 435.
14. **Gataulin Y. A., Yukhnev A. D., Zaitsev D. K., Smirnov E. M., Kulikov V. P., Kirsanov V. A.**, Structure of the secondary flow in the bifurcation of a blood vessel: patient-specific modeling and clinical Doppler measurements, *Journal of Physics: Conference Series*. 1135 (1) (2018) 012089.
15. **Zhang Y., Wang R., Zhou Y., Han W., Liu J.**, Diode-pumped Dy<sup>3+</sup>, Tb<sup>3+</sup>:LuLiF<sub>4</sub> continuous-wave and passively Q-switched yellow lasers, *Optics Communications*. 510(2) (2022) 127917.
16. **Miller P., Wang J.**, Effect of pulse duration and confinement on laser-induced stress waves for high strain-rate material testing, *Optics and Lasers in Engineering*. 151(3) (2022) 106919.
17. **He X.-W., Park J., Huang W.-S., Zhu G., Wu S.**, Usefulness of estimated pulse wave velocity for identifying prevalent coronary heart disease: findings from a general Chinese population, *BMC Cardiovascular Disorders*. 22(4) (2022) 9.
18. **Zaunseder S., Vehkaoja A., Fleischhauer V., Hoog C. Antink**, Signal-to-noise ratio is more important than sampling rate in beat-to-beat interval estimation from optical sensors, *Biomedical Signal Processing and Control*. 74(3) (2022) 103538.
19. **Mazing M. S., Zaitceva A. Y., Kislyakov Y. Y., Avdyushenko S. A.**, Monitoring of oxygen supply of human tissues using a noninvasive optical system based on a multi-channel integrated spectrum analyzer, *International Journal of Pharmaceutical Research*. 12 (2020) 1974.
20. **Gataulin Y. A., Zaitsev D. K., Smirnov E. M., Yukhnev A. D.**, Structure of unsteady flow in the spatially curved model of the common carotid artery with stenosis: a numerical study, *Russian Journal of Biomechanics*. 23 (1) (2019) 58.
21. **Davydov R. V., Yushkova V. V., Glinushkin A. P., Stirmanov A. V., Rud V. Yu.**, A new method for monitoring the health condition based on nondestructive signals of laser radiation absorption and scattering, *Journal of Physics: Conference Series*. 1410(1) (2019) 012067.
22. **Zaitseva A. Y., Kislyakova L. P., Kislyakov Y. Y., Avduchenko S. A.**, Development of a multi-sensor analytical trainable system for non-invasive evaluation of adaptedness status of hazardous occupation specialists, *Journal of Physics: Conference Series*. 1400(3) (2019) 033022.
23. **Davydov R. V., Antonov V. I., Yushkova V. V., Grebenikova N. M., Dudkin V. I.**, A new algorithm for processing the absorption and scattering signals of laser radiation on a blood vessel and human tissues, *Journal of Physics: Conference Series*. 1236(1) (2019) 012079.
24. **Grevtseva A. S., Smirnov K. J., Greshnevikov K. V., Rud V. Yu., Glinushkin A. P.**, Method of assessment the degree of reliability of the pulse wave image in the rapid diagnosis of the human condition, *Journal of Physics: Conference Series*. 1368(2) (2019) 022072.
25. **Grevtseva A. S., Smirnov K. J., Rud V. Yu.**, Development of methods for results reliability raise during the diagnosis of a person's condition by pulse oximeter, *Journal of Physics: Conference Series*. 1135(1) (2018) 012056.
26. **Zhernovoi A. I., Komlev A. A., D'yachenko S. V.**, Magnetic characteristics of MgFe<sub>2</sub>O<sub>4</sub> nanoparticles obtained by glycine–nitrate synthesis, *Technical Physics*. 61(2) (2016) 302.

#### THE AUTHORS

**GUREEVA Irena M.**  
irena-gureeva@mail.ru  
ORCID: 0000-0001-8353-6553

**DAVYDOV Vadim V.**  
davydov\_vadim66@mail.ru  
ORCID: 0000-0001-9530-4805

*Received 03.08.2022. Approved after reviewing 15.08.2022. Accepted 18.08.2022.*

Conference materials

UDC 53.06

DOI: <https://doi.org/10.18721/JPM.153.267>

## Development of automatic gain control for atomic frequency standard on rubidium-87 atoms

A. V. Shavshin <sup>1</sup>✉, V. V. Davydov <sup>1, 2, 3</sup>

<sup>1</sup> Peter the Great St. Petersburg Polytechnic University, St. Petersburg, Russia;

<sup>2</sup> Bonch-Bruевич Saint Petersburg State University of Telecommunications, St. Petersburg, Russia;

<sup>3</sup> All-Russian Research Institute of Phytopathology, Moscow Region, Russia

✉ [shavshin2107@gmail.com](mailto:shavshin2107@gmail.com)

**Abstract.** The necessity of upgrading the optical path of the atomic frequency standard based on rubidium-87 atoms is substantiated. A new scheme for automatic gain control in the optical path of an atomic frequency standard based on rubidium-87 atoms is presented. The amplifier of the error signal formed on the photodetector for controlling the microwave signal is considered in detail. Experimental studies of the metrological characteristics of an atomic frequency standard based on rubidium-87 atoms with automatic gain control are presented. The validity of the developed automatic amplification scheme for the new frequency standard based on rubidium-87 atoms is confirmed.

**Keywords:** time scale, stabilization, automatic frequency control, rubidium frequency standard, gain control, operational amplifier, Allan dispersion

**Citation:** Shavshin A. V., Davydov V. V., Development of automatic gain control for a atomic frequency standard on rubidium-87 atoms, St. Petersburg State Polytechnical University Journal. Physics and Mathematics. 15 (3.2) (2022) 364–369. DOI: <https://doi.org/10.18721/JPM.153.267>

This is an open access article under the CC BY-NC 4.0 license (<https://creativecommons.org/licenses/by-nc/4.0/>)

Материалы конференции

УДК 53.06

DOI: <https://doi.org/10.18721/JPM.153.267>

## Разработка автоматической регулировки усиления для квантового стандарта частоты на атомах рубидия-87

А. В. Шавшин <sup>1</sup>✉, В. В. Давыдов <sup>1, 2, 3</sup>

<sup>1</sup> Санкт-Петербургский политехнический университет Петра Великого, Санкт-Петербург, Россия;

<sup>2</sup> Санкт-Петербургский государственный университет телекоммуникаций им. проф. М. А. Бонч-Бруевича, Санкт-Петербург, Россия;

<sup>3</sup> Всероссийский научно-исследовательский институт фитопатологии, Московская область, Россия

✉ [shavshin2107@gmail.com](mailto:shavshin2107@gmail.com)

**Аннотация.** Обоснована необходимость модернизации оптического тракта квантового стандарта частоты на атомах рубидия-87. Представлена новая схема автоматической регулировки усиления в оптическом тракте квантового стандарта частоты на атомах рубидия-87. Подробно рассмотрен усилитель сигнала ошибки, формируемого на фотоприемнике для управления СВЧ-сигналом. Представлены экспериментальные исследования метрологических характеристик квантового стандарта частоты на атомах рубидия-87 с автоматической регулировкой усиления. Подтверждена правомерность разработанной схемы автоматического усиления для нового стандарта частоты на атомах рубидия-87.

**Ключевые слова:** шкала времени, стабилизация, автоматическая подстройка частоты, рубидиевый стандарт частоты, регулировка усиления, операционный усилитель, дисперсия Аллана



**Ссылка при цитировании:** Шавшин А. В., Давыдов В. В. Разработка автоматической регулировки усиления для квантового стандарта частоты на атомах рубидия-87 // Научно-технические ведомости СПбГПУ. Физико-математические науки. Т. 15. № 3.2. С. 364–369. DOI: <https://doi.org/10.18721/JPM.153.267>

Статья открытого доступа, распространяемая по лицензии CC BY-NC 4.0 (<https://creativecommons.org/licenses/by-nc/4.0/>)

## Introduction

At present, with the advent of new technologies, the need for accurate measurement of frequency and time is the most relevant topic in various areas of life [1–8]. In this case, it is necessary to divide the requirements for ensuring the accuracy of determining time and frequency into several areas [8–12]. The maximum accuracy of determining the frequency and time is extremely important when conducting scientific experiments and in spacecraft used in satellite navigation [13–20]. Atomic frequency standards are one of the main instruments that can provide the greatest accuracy in determining time and frequency [2, 3, 6, 11, 14–18, 20–25]. When used in navigation, they provide synchronization of satellites with each other or synchronization of a satellite with base stations on Earth [20–29]. At present, a large number of AFS models for space applications have been developed [20–35]. One of them is the atomic frequency standard on rubidium atoms-87 [21, 23, 24, 29, 31, 35, 36].

Similar frequency standards are used in GLONASS and GPS systems as synchronizing generators, as well as on moving objects in the earth's atmosphere. Performing accurate synchronization in satellite systems has a number of difficulties associated with both the features of the operating environment and the autonomy of the object itself. One of the main factors affecting the accuracy is the system errors introduced by the equipment of the space complex. This leads to errors in the formation of a signal from a highly sensitive photodetector after registration of optical radiation. These errors need to be compensated.

One of the elements of their elimination is automatic gain control (AGC) for the rubidium frequency standard. When the ambient temperature or other external influence changes, the output characteristic of the frequency standard without the AGC system changes. This change must be compensated to ensure stable operation of spacecraft systems. The paper considers the development of a new AGC system, which is necessary to modernize the design of AFS based on rubidium-87 atoms under the conditions of changing its operation in a spacecraft and new tasks when conducting sounding of the Earth's surface.

### Atomic frequency standard based on rubidium-87 atoms and an automatic gain control system

The principle of operation of rubidium frequency standards lies in the resonant absorption of microwave electromagnetic waves in the beam of a rubidium atom; therefore, it is called a passive atomic standard [21, 31, 35]. A passive atomic frequency standard is a standard in which the

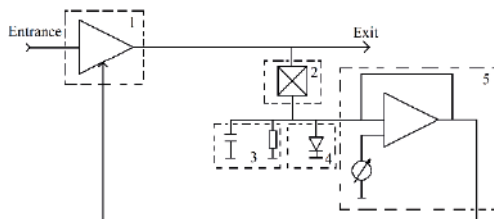


Fig. 1. Scheme of automatic gain control: voltage amplifier 1 of the microwave signal on a field-effect transistor; directional coupler 2; low-pass filter 3; detector diode 4; 'error' signal amplifier 5 to control the power supply of the field effect transistor, the first amplifier

frequency of absorption of electromagnetic waves of one of the energy transitions of atoms is used as a reference. The passive standard uses an atomic discriminator as a stabilizer. Atomic generators as part of frequency standards produce signals with a low output power, so they are first amplified using a microwave receiver. And only then stabilize the frequency of the quartz oscillator. Fig. 1 shows the automatic gain control circuit we developed to solve this problem.

A voltage-attenuated signal is supplied to the input of the circuit, which must be amplified so that the total signal power at the system output is 20  $\mu$ W. The signal is preliminarily amplified in 1 in a FET circuit. Further, to generate an 'error'

signal, part of the signal passes through a directional coupler 2 to the power control circuit of the field-effect transistor of the first amplifier, and part of the signal goes to the system output. Then it is necessary to detect the future ‘error’ signal in order to obtain the DC component of the signal. For these purposes, a detector microwave diode 4 will be used. After detection, the signal will have a different amplitude in different cases, so it is necessary to be able to adjust its amplitude to the level we need. To do this, use the ‘error’ signal amplifier on the operational amplifier 5.

### Calculation of the elements of the automatic gain control system

In the simplest case, a directional coupler on coupled microstrip lines is an eight-terminal network consisting of two parallel microstrip lines, the electrical length of which is equal to a quarter of the excitation wavelength Fig. 2.

Such a coupler has two planes of symmetry, so the calculation of the bridge elements and the scattering matrix takes the following form:

$$\begin{aligned} 1/Z_{A2}^2 - 1/Z_{A1}^2 &= 1, \quad s_{ii} = 0, \quad s_{14} = s_{32} = 0, \\ s_{21} &= -jZ_{B2}, \quad s_{31} = -Z_{B2}/Z_{B1}, \\ |s_{21}| &= |s_{31}| \Rightarrow Z_{B2} = \frac{Z_{B2}}{Z_{B1}} \Rightarrow Z_{B1} = 1 = Z_0 = 1 \text{ Ohm}, \\ Z_{Bi} &= \frac{Z_{Bi}}{Z_0}; \quad 1/Z_{B2}^2 - 1/Z_{B1}^2 = 1 \Rightarrow 1/Z_{B2}^2 = 2 \Rightarrow \\ &\Rightarrow Z_{B2} = \frac{1}{\sqrt{2}} = \frac{Z_0}{\sqrt{2}} = 0.707 \text{ Ohm}. \end{aligned}$$

Let us compose the scattering matrix for the directional coupler

$$S = \frac{1}{\sqrt{2}} * \begin{pmatrix} 0 & 1 & -j & 0 \\ 1 & 0 & 0 & -j \\ -j & 0 & 0 & 1 \\ 0 & -j & 1 & 0 \end{pmatrix}.$$

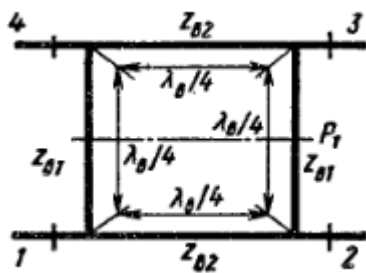


Fig. 2. Microstrip directional coupler

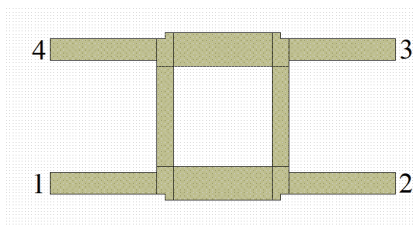


Fig. 3. Microstrip directional coupler topology

To synthesize the required directional coupler, you need to calculate its dimensions for a signal of a specific frequency. In our case, the directional coupler will be synthesized for a frequency of 6.834 GHz. Fig. 3 shows the topology of a microstrip directional coupler. To create a bridge, the following elements were used: MLIN to simulate microstrip lines, MTEE to implement separation into two channels.

Further, we obtain the final parameters of the microstrip directional coupler (Fig. 4).

As can be seen from the graphs, the directional coupler was successfully synthesized at -3 dB at 6.834 GHz. Fig. 5 shows a graph of the phase-frequency response of a directional coupler.

The obtained results of tuning the directional coupler and its phase-frequency characteristic completely satisfy the set requirements. On the phase-frequency characteristic graph, we can observe that the phase between outputs 3 and 2 differs by 90° (taking into account the allowable error), which indicates the correct setting of the directional coupler.

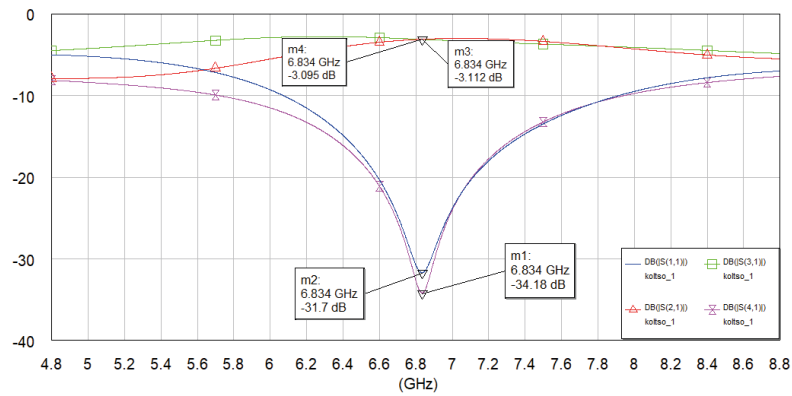


Fig. 4. Final parameters of the microstrip directional coupler

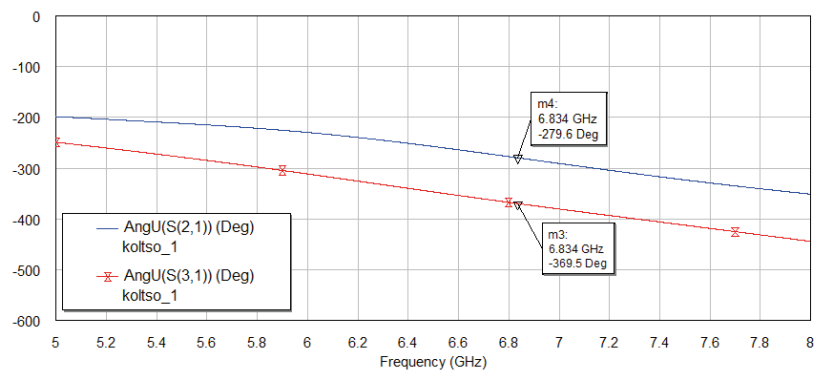


Fig. 5. Phase-frequency response of a directional coupler

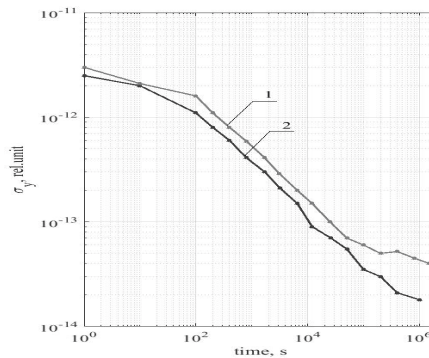


Fig. 6. Dependence of the change on the Allan variance  
Graphs 1 and 2 correspond to QSC using the old system and the new AGC system

### Results of experimental studies of the characteristics of the quantum frequency standard

As an example, the paper presents the results of a study of the characteristics of AFS in the temperature range from 253 to 308 K in accordance with the possible technical conditions for the operation of the device. The AGC prototype was included in the composition of the AFS, the output characteristics of which were measured. After processing the obtained data, plots of the dependence of the values of the Allan variance  $\sigma(\tau)$  on time  $\tau$  were plotted for the modernized and previous AFS designs (Fig. 6).

The results obtained show an improvement in the Allan variance  $\sigma(\tau)$  by 12%. Studies of the work of AGC were carried out for 12 days in a heat chamber.

### Conclusion

The results of the analysis of the operation of the prototype AFS with the new AGC system showed that there was no malfunction due to a low signal level at the input of the frequency converter. This confirms the adequacy of the AGC design scheme proposed by us.

In addition, it was found that the introduction of an automatic gain control system improves the output characteristics of the frequency converter, which affects both the Allan dispersion value and the long-term frequency value (LFC).

### REFERENCES

1. **Semenov V. V., Nikiforov N. F., Ermak S. V.**, Calculation of stationary magnetic resonance signal in optically oriented atoms induced by a sequence of radio pulses, *Soviet journal of Communications Technology and Electronics*. 36(4) (1991) 59–63.
2. **Lukashev N. A., Davydov R. V., Glinushkin A.P., Rud' V.Y.**, Improving characteristics of microwave frequency standard on Hg-199 ions for telecommunication systems, *Journal of Physics: Conference Series*. 1326(1) (2019) 012046.
3. **Petrov A. A.**, Improvement frequency stability of caesium atomic clock for satellite communication system, *Lecture Notes in Computer Science*. 9247 (2015) 739–744.
4. **Myazin N. S., Dudkin V. I., Grebenikova N. M., Davydov R. V., Podstrigaev A. S.**, Fiber - optical system for governance and control of work for nuclear power stations of low power, *Lecture Notes in Computer Science*. 11660 (2019) 744–756.
5. **Kuzmin M. S., and Rogov S. A.**, On the use of a multi-raster input of one-dimensional signals in two-dimensional optical correlators, *Computer Optics*. 43(3) (2019) 391–396.
6. **Petrov A. A., Zaletov D. V., Shapovalov D. V.**, Peculiarities of Constructing a Scheme for Formation of a Microwave Excitation Signal in a Cesium Atomic Clock, *Journal of Communications Technology and Electronics*. 66(3) (2021) 295–299.
7. **Davydov V. V., Davydova T. I.**, A nondestructive method for express testing of condensed media in ecological monitoring, *Russian Journal of Nondestructive Testing*. 53(7) (2017) 520–529.
8. **Dudkin V.I., Myazin N.S., Davydov R.V.**, On the Possibility of Studying Ferrofluids by a Nuclear Magnetic Magnetometer with a Flowing Sample, *Journal of Communications Technology and Electronics*. 65 (5) (2020) 558–564.
9. **Mihov E.D., Nepomnyashchiy O.V.**, Selecting informative variables in the identification problem *Journal of Siberian Federal University - Mathematics and Physics*. 9(4) (2016) 473–480.
10. **Ryzenko I.N., Lutsenko A.E., Varygin O.G., Nepomnyashchiy O.V.**, Carrier compensation mode implementation in satellite communication channels. In: *Proceedings of 2019 International Siberian Conference on Control and Communications, SIBCON 2019*, vol. 8729665 (2019) 23–29.
11. **Petrov A. A., Grebenikova N. M.**, Some Directions of Quantum Frequency Standard Modernization for Telecommunication Systems, *Lecture Notes in Computer Science (including subseries Lecture Notes in Artificial Intelligence and Lecture Notes in Bioinformatics)*. 11118 LNCS (2018) 641–648.
12. **Davydov V.V., Kiryukhin A.V.**, Nuclear-Magnetic Flowmeter-Relaxometers for Monitoring Coolant and Feedwater Flow and Status in Npp Atomic Energy. 127 (5) (2020) 274–279.
13. **Davydov R., Antonov V., Moroz A.**, Parameter Control System for a Nuclear Power Plant Based on Fiber-Optic Sensors and Communication Lines, In: *IEEE International Conference on Electrical Engineering and Photonics (EExPolytech)*, Saint Petersburg, Russia, 13–15 October 2019 8906791 (2019) 295–297.
14. **Petrov A. A., Shabanov V. E., Zalyotov D. V., Bulyanitsa A. L., Shapovalov D. V.**, Modernization of the frequency synthesizer of cesium atomic clock, *IEEE International Conference on Electrical Engineering and Photonics, EExPolytech 2018*, Saint Petersburg, October 2018 8564389 (2018) 52–55.
15. **Lukashev N.A., Moroz A.V.**, Compact microwave frequency standard on Hg-199 ions for navigation systems, *Journal of Physics: Conference Series*. 1236(1) (2019) 012068.
16. **Tarasov A. D., and Milder O. B.**, Gradation traectories as an analog of gradation curves in the metric cie lab space discrete approche, *Computer Optics*. 43(1) (2018) 104–110.
17. **Lukashev N. A., Petrov A.A., Grebenikova N.M.**, Improving performance of quantum frequency standard with laser pumping, *Proceedings of 18th International conference of Laser Optics ICLO-2018 Saint Petersburg, 2018*, vol. 8435889, (2018) 271.
18. **Petrov A. A.**, Digital Frequency Synthesizer for <sup>133</sup>Cs-Vapor Atomic Clock, *Journal of Communications Technology and Electronics*. 62(3) (2017) 289–293.



19. **Davydov V. V., Kruzhalov S. V., Vologdin V. A.**, Concerning some features of studying the flow of liquid media by a Doppler method: *Journal of Optical Technology (A Translation of Opticheskiy Zhurnal)*. 84 (8) (2017) 568–573.
20. **Mazing M.S., Zaitceva A. Yu., Kislyakov Yu. Ya., Kondakov N. S., Avdushenko S. A.**, Monitoring of Oxygen Supply of Human Tissues Using A Noninvasive Optical System Based on A MultiChannel Integrated Spectrum Analyzer, *International Journal of Pharmaceutical Research*. 12 (2) (2020) 1974–1978.
21. **Riehle F.**, Frequency standard. Basic and applications, WILEY-VCH Verlag GmbH & Co. KGaA: New York, 2008.
22. **Almat N., Pellaton M., Moreno W.**, et al., Rb vapor-cell clock demonstration with a frequency-doubled telecom laser, *Appl. Opt.* 57 (2008) 4707.
23. **Valov, A.P., Arinushkina, K.G.**, The use of digital data processing to improve the metrological characteristics of the rubidium frequency standard, *Journal of Physics: Conference Series*. 2086(1) (2021) 012070.
24. **Arinushkina K. G., Valov A. P.**, Digital processing of optical signals in the frequency standard based in rubidium atoms - 87, In: *Proceedings of ITNT 2021 - 7th IEEE International Conference on Information Technology and Nanotechnology, 2021 Samara, Russia, 20–24 September 2021* 44026298 (2021) 44–49.
25. **Lukashev N. A., Glinushkin A. P., Rud V. Yu., Lukyantsev V. S.**, Microwave low mass-dimensional frequency standard on Hg-199 ions, *Journal of Physics: Conference Series*. 1410(1) (2019) 012211.
26. **Bandi T., Affolderbach C., Calosso C.E.**, et al., High-performance laser-pumped rubidium frequency standard for satellite navigation, *Electron. Lett.* 47(2001) 698–699.
27. **Petrov A. A., Vologdin V. A., Zalyotov D. V.**, Dependence of microwave – excitation signal parameters on frequency stability caesium atomic clock, *Journal of Physics: Conference Series*. 643(1) (2015) 012087.
28. **Petrov A. A., Zalyotov D. V., Shabanov V. E., Shapovalov D. V.**, Features of direct digital synthesis applications for microwave excitation signal formation in quantum frequency standard on the atoms of cesium, *Journal Physics: Conference Series*. 1124(1) (2018) 041004.
29. **Grevtseva A. S., Dmitriev R. A.**, Features of the formation of the frequency of the microwave excitation signal in the quantum frequency standard on rubidium atoms–87, *Journal of Physics: Conference Series*. 2086(1) (2021) 012055.
30. **Grevtseva A., Rud V.**, Method of processing velocity increase of measuring results of quantum frequency standard parameters for information transfer velocity increase in satellite communication systems, *CEUR Workshop Proceedings*. 2667 (2020) 15–18.
31. **Pashev G. P.**, Optimal algorithm for synchronizing the quantum clock timeline, *Measurement Techniques*. 59(6) (2016) 1005–1012.
32. **Lukashev N. A., Rud V. Yu.**, Microwave frequency standard on Hg-199 ions for space stations and vehicles *Journal of Physics: Conference Series*. 1400(2) (2019) 022050.
33. **Petrov A. A., Zaletov D. V., Shapovalov D. V.**, Peculiarities of Constructing a Scheme for Formation of a Microwave Excitation Signal in a Cesium Atomic Clock, *Journal of Communications Technology and Electronics*. 66(3) (2021) 295–299.
34. **Petrov A. A.**, New scheme of the microwave signal formation for quantum frequency standard on the atoms of caesium-133 *Journal of Physics: Conference Series*. 769(1) (2016) 012065.
35. **Wang, D., Rud, V.Y.** Prospective directions for the development of microwave frequency standards for satellite navigation systems *Journal of Physics: Conference Series*. 2086(1) (2021) 012073.
36. **Petrov A.A., Myazin N.S., Kaganovskiy V.E.**, Rubidium atomic clock with improved metrological characteristics for satellite communication system, *Lecture Notes in Computer Science*. 10531 LNCS (2017) 561–568.

#### THE AUTHORS

**SHAVSHIN Artyom**  
shavshin2107@gmail.com  
ORCID: 0000-0002-3597-8901

**DAVYDOV Vadim V.**  
davydov\_vadim66@mail.ru  
ORCID: 0000-0001-9530-4805

*Received 04.08.2022. Approved after reviewing 08.08.2022. Accepted 13.08.2022.*

Conference materials

UDC 537.876

DOI: <https://doi.org/10.18721/JPM.153.268>

## Simulation of terahertz photonic integrated antenna

S. V. Seliverstov <sup>1</sup>✉, S. S. Svyatodukh <sup>1,2</sup>, A. I. Prokhodtsov <sup>1</sup>, G. N. Goltsman <sup>1,2</sup>

<sup>1</sup>Moscow State Pedagogical University, Moscow, Russian Federation;

<sup>2</sup>HSE Moscow Institute of Electronics and Mathematics, Moscow, Russian Federation

✉ seliverstovsv@mail.ru

**Abstract.** The rapid development of wireless devices, that take place over the last decade, is associated with an increase in the need to achieve a higher data transfer rate. To achieve this goal, it is necessary to use the terahertz (THz) range. The vast majority of THz devices (no matter bulk or integrated) require fast, non-mechanical beam shape control, which is generally defined as the ability to manipulate the shape of the radiation pattern in the desired way. But it is hard to implement without the use of photonic integrated phased array antennas. In this paper, the possibility of the creation of photonic integrated antenna which is a basic element of such a system is investigated and confirmed. The antenna is based on a platform of metamaterial silicon with perforations, the dimensions of which are in the deep subwavelength region, which makes it possible to provide a wide bandwidth with low dispersion.

**Keywords:** Phased array antennas, THz range, photonic integrated circuits, coupling devices, metamaterials

**Funding:** Russian Science Foundation Grant 21-72-10119.

**Citation:** Seliverstov S. V., Svyatodukh S. S., Prokhodtsov A. I., Goltsman G. N., Simulation of terahertz photonic integrated antenna, St. Petersburg State Polytechnical University Journal. Physics and Mathematics. 15 (3.2) (2022) 370–374. DOI: <https://doi.org/10.18721/JPM.153.268>

This is an open access article under the CC BY-NC 4.0 license (<https://creativecommons.org/licenses/by-nc/4.0/>)

Материалы конференции

УДК 537.876

DOI: <https://doi.org/10.18721/JPM.153.268>

## Моделирование терагерцовой фотонной интегральной антенны

С. В. Селиверстов <sup>1</sup>✉, С. С. Святодух <sup>1,2</sup>, А. И. Проходцов <sup>1</sup>, Г. Н. Гольцман <sup>1,2</sup>

<sup>1</sup>Московский педагогический государственный университет, г. Москва, Россия;

<sup>2</sup>Московский институт электроники и математики НИУ ВШЭ, г. Москва, Россия

✉ seliverstovsv@mail.ru

**Аннотация.** Бурное развитие беспроводных устройств, наблюдающееся в последнее десятилетие, связано с увеличением потребности в достижении более высокой скорости передачи данных. Для достижения этой цели необходимо использовать терагерцовый (ТГц) диапазон. Подавляющее большинство ТГц-устройств (независимо от того, объемные они или интегрированные) требуют быстрого немеханического управления диаграммой направленности выходного излучения. Эту задачу трудно реализовать без использования фотонных интегрированных фазированных антенных решеток. В данной работе исследуется и подтверждается возможность создания фотонной интегральной антенны, которая является базовым элементом такой системы. В основе антенны лежит платформа из метаматериального кремния с перфорациями, размеры которых находятся в глубоко субволновой области, что позволяет обеспечить широкую полосу пропускания при малой дисперсии.

**Ключевые слова:** фазированная антенная решетка, ТГц-диапазон, фотонные интегральные схемы, устройства связи, метаматериалы



**Финансирование:** Грант РФФ № 21-72-10119.

**Ссылка при цитировании:** Селиверстов С. В., Святодух С. С., Проходцов А. И., Гольцман Г. Н. Моделирование терагерцовой фотонной интегральной антенны // Научно-технические ведомости СПбГПУ. Физико-математические науки. Т. 15. № 3.2. С. 370–374. DOI: <https://doi.org/10.18721/JPM.153.268>

Статья открытого доступа, распространяемая по лицензии CC BY-NC 4.0 (<https://creativecommons.org/licenses/by-nc/4.0/>)

## Introduction

In recent years, there has been a significant increase in the need to achieve higher wireless data transfer rates. This is due to progress in such fields as big data processing [1] and applications related to augmented reality [2]. This can be achieved by using higher signal frequencies. The most promising is the terahertz (THz) range. It has already been demonstrated that the data transfer rate can be increased to 1 Tb per second and higher due to the transition to the THz frequency region [3]. At the same time, the transition to THz radiation is associated with a number of difficulties. First of all, this is a high absorption of THz radiation in the atmosphere, which limits the use of such systems over long distances. Because of this, in particular, the most powerful telescopes in the THz range are placed in the stratosphere [4] or in space [5]. There are some transparency windows in the THz range, but they still do not allow signals to be transmitted over long distances [6]. In practice, this means that such THz data transfer systems can be used inside buildings, like Wi-Fi, but with orders of magnitude higher data transfer rate. Another problem is the large signal loss during radiation propagation in metal waveguides (on the order of several dB per cm [7]). The solution to this problem can be the use of dielectric waveguides, which are characterized by much lower values of absorption of THz radiation [8].

A large number of leading scientific teams around the world are working on their development, and to date, some success has been achieved. In particular, paper [9] demonstrates a silicon strip waveguide optimized for two frequency ranges: 90–140 GHz and 140–220 GHz. In this work, authors achieved low losses in the waveguide and small values of dispersion, but at the same time, this type of waveguides is poorly integrated with other components on the same chip due to its design features. These limitations can be avoided by using waveguides formed in a single dielectric photonic crystal, made on a silicon substrate platform. For example, in [10], a photonic crystal waveguide with an isosceles triangular lattice based on a silicon slab at a frequency of 0.3 THz was demonstrated. Unfortunately, this type of waveguide is characterized by a relatively low bandwidth and high dispersion. These problems greatly complicate the use of such waveguide technologies in real practical applications. In addition, the development of THz communication systems is associated with the need for a rapid (non-mechanical) change of the radiation pattern of THz emitters. But it's hard to implement without using of phased antenna arrays [11], in which this change is carried out due to phase adjustment.

Phased array antennas in the THz range have been actively investigated in the last few years and some promising results have already been achieved. In particular, a phased array antenna based on the platform of optical photonic integrated circuits matched with femtosecond laser was demonstrated. Laser radiation undergoes a phase change like in conventional optical phased antenna arrays. The conversion of the laser infrared radiation into THz is carried out by mixing it with the tunable laser radiation using a photodiode [12]. It should be noted that the use of femtosecond laser greatly increases the cost and complexity of this system, which makes it impossible for widespread use. Another approach is based on employing of an array of millimeter-wave sources with their subsequent synchronization [13, 14]. However, synchronization of a large number of sources is an extremely difficult task both in implementation and in compact integration, and also has a rather high cost. This greatly complicates its practical application.

To solve this problem, it is necessary to develop a simple and effective technology for creating THz phased array antennas. In this article the possibility of creation of the photonic integrated horn based on a platform of metamaterial silicon with perforations is studied. It will be the key component for the future THz phased array antennas available for widespread use. The

dimensions of the perforations are in the deep subwavelength region which makes it possible to provide a wide bandwidth with low dispersion.

### Materials and Methods

The structures of the waveguides and the integrated horn were specified by a lattice of periodic through holes in a high-resistance silicon substrate. A square lattice of holes was chosen (see Fig. 1). The permittivity of the obtained effective medium for TE ( $\epsilon_{TE}$ ) and TM ( $\epsilon_{TM}$ ) polarizations was calculated by the following formulas [15]:

$$\epsilon_{TE} = \epsilon_{Si} \frac{1+k+\epsilon_{Si}(1-k)}{1-k+\epsilon_{Si}(1+k)}, \quad (1)$$

$$\epsilon_{TM} = k + \epsilon_{Si}(1-k), \quad (2)$$

$$k = \frac{\pi d^2}{4a^2}. \quad (3)$$

where  $\epsilon_{Si}$  is the relative permittivity of silicon,  $k$  is the filling factor. Note that the above formulas are valid for the case of filling the space inside the holes with air with a permittivity equal to 1.

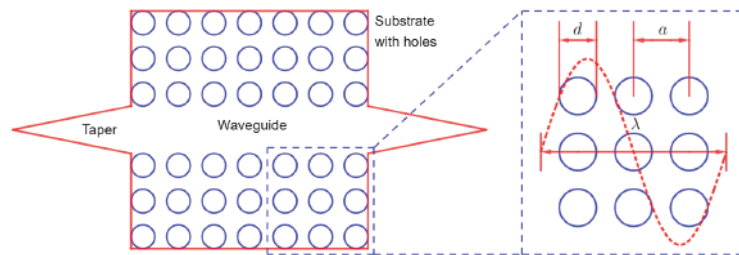


Fig. 1. Topology of the waveguide given by a square lattice of cylindrical perforations (through holes) in a high-resistance silicon substrate  
A taper can be used as a coupling element

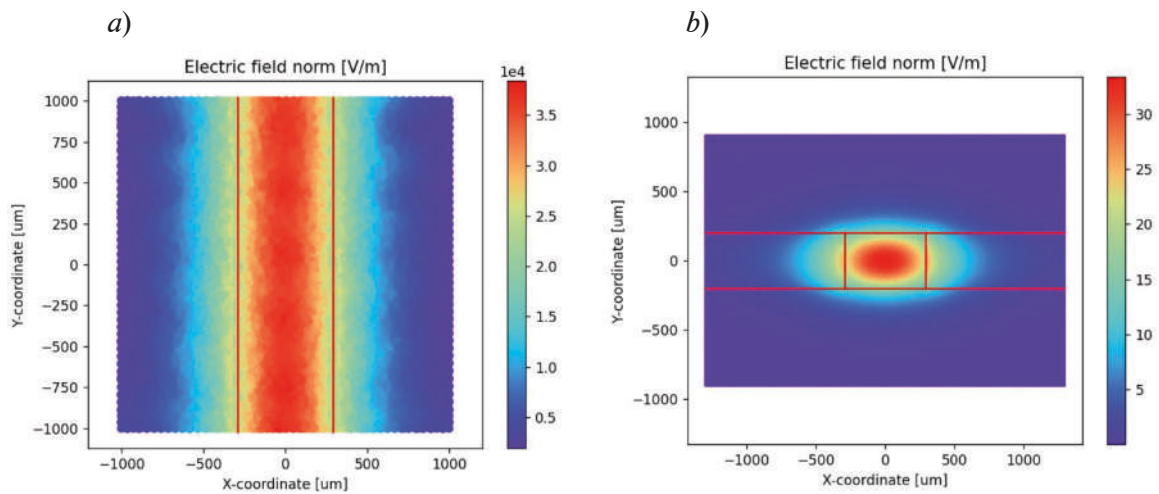


Fig. 2. Electric field distribution in the waveguide structure: top view (a); end view (b)

The following parameters were set in the simulation. The substrate thickness was 400  $\mu\text{m}$ . The radius of the air sphere around the substrate was 3500  $\mu\text{m}$ . The frequency was 150 GHz. The permittivity of silicon was 11.7. The diameter of holes was 73  $\mu\text{m}$ . The distance between centers of perforations was 165  $\mu\text{m}$ . The waveguide effective width was 585  $\mu\text{m}$ . The last value equals to the wavelength of the radiation in silicon. The permittivities of the obtained effective medium for TE and TM polarizations calculated by formulas (1) and (2) were equal to 9 and 10 respectively.

A single  $\text{TE}_1$  mode was implemented for the given configuration of the antenna with this set of parameters (see Fig. 2).

The power of radiation supplied to the incoming ports was equal to 1 W in 3D models. The boundary conditions were defined at the edge of the substrate where the input ports were located and specified on the sphere bounding the model in such a way that it completely scattered the radiation incident on it. The given model was discretized into finite elements (tetrahedra). After that, the following equation was numerically solved for the obtained mesh of elements to find the space distribution of the electric field vector:

$$\nabla \times \frac{1}{\mu} (\nabla \times \vec{E}) + k_0^2 \left( \frac{i\sigma}{\omega \epsilon_0} - \epsilon \right) \vec{E} = 0, \quad (4)$$

where  $\mu$  is the relative permeability,  $\epsilon$  is the relative permittivity,  $\sigma$  is the specific conductivity,  $\epsilon_0$  is the dielectric constant,  $k_0$  is the vacuum wave number,  $\omega$  is the angular frequency of radiation,  $i$  is the imaginary unit. Iterations of discretization into a smaller elements and recalculations were carried out until the required accuracy was achieved.

### Results and Discussion

During the simulation of the integrated horn radiation pattern, the length of the input waveguide was fixed at 1000  $\mu\text{m}$  and the flare angle of the horn was varied. One can see from the Fig. 3, *b* that the flare angle of about 10 degrees turned out to be optimal for providing the required shape of the radiation pattern and a sufficient area of overlap by the radiation beams from different elements of the proposed phased array antenna. The field distribution in the structure at the given angle is shown in Fig. 3, *a*.

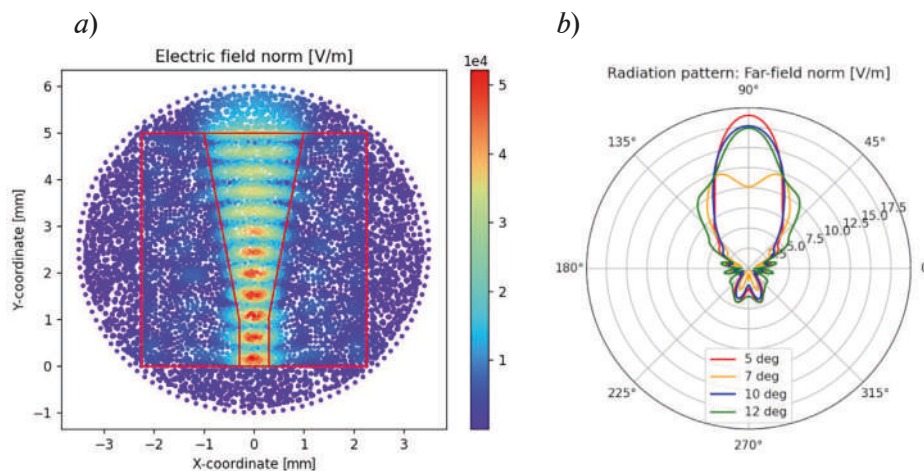


Fig. 3. Simulation results of the integral horn: distribution of the electric field in the central plane of the structure (*a*); radiation pattern of the integral horn at different values of its flare angle (*b*)

### Conclusion

The presented results of simulation confirm the possibility of practical implementation of the proposed concept of integrated horn antennas on a perforated high-resistance silicon substrate platform. These antennas will be used to create devices for controlling the parameters of the output THz radiation beam, which will be the main components for next-generation data transfer systems. It should be noted that the fabrication of the simulated structures will be implemented using standard CMOS technologies, which will allow their mass production.

## REFERENCES

1. Zhang C., Ota K., Jia J., Dong M. (2018). Breaking the blockage for big data transmission: Gigabit road communication in autonomous vehicles. *IEEE Communications Magazine*, 56(6), 152–157.
2. Chaccour C., Saad W. (2020, December). On the ruin of age of information in augmented reality over wireless terahertz (THz) networks. In *GLOBECOM 2020-2020 IEEE Global Communications Conference* (pp. 1-6). IEEE.
3. Corre Y., Gougeon G., Doré J. B., Bicans S., Miscopein B., Faussurier E., Saad M., Bader F. (2019, March). Sub-THz spectrum as enabler for 6G wireless communications up to 1 Tbit/s. In *6G Wireless Summit*.
4. Krabbe A. (2000, June). SOFIA telescope. In *Airborne Telescope Systems* (Vol. 4014 276-281). International Society for Optics and Photonics.
5. Pilbratt G. L., Riedinger J. R., Passvogel T., Crone G., Doyle D., Gageur U., Heras A. M., Jewell C., Metcalfe L., Ott S. Schmidt M., (2010). Herschel Space Observatory-An ESA facility for far-infrared and submillimetre astronomy. *Astronomy & Astrophysics*, 518, L1.
6. Boronin P., Petrov V., Moltchanov D., Koucheryavy Y., Jornet J. M., (2014). Capacity and throughput analysis of nanoscale machine communication through transparency windows in the terahertz band. *Nano Communication Networks*, 5(3), 72–82.
7. Frankel M. Y., Gupta S., Valdmanis J. A., Mourou G. A. (1991). Terahertz attenuation and dispersion characteristics of coplanar transmission lines. *IEEE Transactions on microwave theory and techniques*, 39(6), 910–916.
8. Gao W., Yu X., Fujita M., Nagatsuma T., Fumeaux C., Withayachumnankul W., (2019). Effective-medium-cladded dielectric waveguides for terahertz waves. *Optics Express*, 27(26), 38721–38734.
9. Malekabadi A., Charlebois S. A., Deslandes D., Boone F. (2014). High-resistivity silicon dielectric ribbon waveguide for single-mode low-loss propagation at F/G-bands. *IEEE Transactions on Terahertz Science and Technology*, 4(4), 447–453.
10. Yu X., Sugeta M., Yamagami Y., Fujita M., Nagatsuma T., (2019). Simultaneous low-loss and low-dispersion in a photonic-crystal waveguide for terahertz communications. *Applied Physics Express*, 12(1), 012005.
11. Fu X., Yang F., Liu C., Wu X., Cui T. J., (2020). Terahertz Beam Steering Technologies: From Phased Arrays to Field-Programmable Metasurfaces. *Advanced optical materials*, 8(3), 1900628.
12. Lu P., Steeg M., Kolpatzeck K., Dülme S., Khani B., Czulwik A., Stöhr A., (2018, September). Photonic assisted beam steering for millimeter-wave and THz antennas. In *2018 IEEE Conference on Antenna Measurements & Applications (CAMA)* (pp. 1-4). IEEE.
13. Tousei Y., Afshari E. (2014). A high-power and scalable 2-D phased array for terahertz CMOS integrated systems. *IEEE Journal of Solid-State Circuits*, 50(2), 597–609.
14. Sengupta K., Hajimiri A., (2015). Mutual synchronization for power generation and beam-steering in CMOS with on-chip sense antennas near 200 GHz. *IEEE Transactions on Microwave Theory and Techniques*, 63(9), 2867-2876.
15. Subashiev A. V., Luryi S., (2006). Modal control in semiconductor optical waveguides with uniaxially patterned layers. *Journal of lightwave technology*, 24(3), 1513.

## THE AUTHORS

**SELIVERSTOV Sergey**  
sv.seliverstov@mpgu.su  
ORCID: 0000-0001-9624-5325

**PROKHODTSOV Aleksey**  
alexabrest@yandex.ru  
ORCID: 0000-0001-5159-3043

**SVYATODUKH Sergey**  
sergey.svetodux@gmail.com  
ORCID: 0000-0001-9436-6641

**GOLTSMAN Gregory**  
goltsman10@mail.ru  
ORCID: 0000-0002-1960-9161

*Received 08.08.2022. Approved after reviewing 11.08.2022. Accepted 12.08.2022.*

Conference materials

UDC 57.087.1

DOI: <https://doi.org/10.18721/JPM.153.269>

## Processing of qPCR signals obtained on microfluidic chips in the measurement sequence disorder event

D. Yu. Klimenko <sup>1</sup>, N. A. Esikova <sup>2</sup>, A. L. Bulyanitsa <sup>2</sup>, R. V. Davydov <sup>1,3</sup>, D. A. Belov <sup>2</sup>✉

<sup>1</sup> Peter the Great St. Petersburg Polytechnic University, St. Petersburg, Russia;

<sup>2</sup> Institute of Analytical Instrumentation of the Russian Academy of Sciences, St. Petersburg, Russia;

<sup>3</sup> All-Russian Research Institute of Phytopathology, Moscow Region, Russia

✉ [dasha.klimenko.01@inbox.ru](mailto:dasha.klimenko.01@inbox.ru)

**Abstract.** The formation and movement of gas bubbles in microfluidic chips leads to the measurement sequence disorder in the form of a signal distortion. Two new methods for automatic processing of distorted qPCR signals were developed and implemented. Methods are based on the qPCR signals approximation by a sigmoid function and make it possible to successfully perform a microfluidic chips qPCR analysis in the event of bubbles, which is demonstrated on experimental and simulation curves.

**Keywords:** microfluidics, microfluidic chip, qPCR, bubbles, approximation

**Funding:** The work was carried out within the framework of the state task of the Ministry of Science and Higher Education of the Russian Federation 075-00761-22-00.

**Citation:** Klimenko D. Yu., Esikova N. A., Bulyanitsa A. L., Davydov R. V., Belov D. A., Processing of qPCR signals obtained on microfluidic chips in the measurement sequence disorder event, St. Petersburg State Polytechnical University Journal. Physics and Mathematics. 15 (3.2) (2022) 375–380. DOI: <https://doi.org/10.18721/JPM.153.269>

This is an open access article under the CC BY-NC 4.0 license (<https://creativecommons.org/licenses/by-nc/4.0/>)

Материалы конференции

УДК 57.087.1

DOI: <https://doi.org/10.18721/JPM.153.269>

## Обработка полученных на микрофлюидных чипах сигналов ПЦР-РВ при разладке последовательности измерений

Д. Ю. Клименко <sup>1</sup>✉, Н. А. Есикова <sup>2</sup>, А. Л. Буляница <sup>2</sup>, Р. В. Давыдов <sup>1,3</sup>, Д. А. Белов <sup>2</sup>

<sup>1</sup> Санкт-Петербургский политехнический университет Петра Великого, Санкт-Петербург, Россия;

<sup>2</sup> Институт аналитического приборостроения Российской академии наук, Санкт-Петербург, Россия;

<sup>3</sup> Всероссийский научно-исследовательский институт фитопатологии, Московская область, Россия

✉ [dasha.klimenko.01@inbox.ru](mailto:dasha.klimenko.01@inbox.ru)

**Аннотация.** Одним из основных недостатков микрофлюидных чипов является образование пузырей, приводящее к возникновению разладки в последовательности измерений в форме искажения сигналов ПЦР-РВ. Разработаны и реализованы две новые методики автоматической обработки искаженных сигналов, основанные на аппроксимации сигмоидальной функцией. Выполнена апробация методов на экспериментальных и имитационных сигналах. Данные методики позволяют получать удовлетворяющие значения погрешностей при определении порогового цикла и успешно выполнять количественный анализ ПЦР-РВ в микрофлюидных чипах при возникновении пузырей.

**Ключевые слова:** микрофлюидика, микрофлюидный чип, ПЦР-РВ, пузыри, аппроксимация

**Финансирование:** Работа выполнена в рамках Госзадания Минобрнауки РФ 075-00761-22-00.

**Ссылка при цитировании:** Клименко Д. Ю., Есикова Н. А., Буляница А. Л., Давыдов Р. В., Белов Д. А. Обработка полученных на микрофлюидных чипах сигналов ПЦР-РВ при разладке последовательности измерений // Научно-технические ведомости СПбГПУ. Физико-математические науки. Т. 15. № 3.2. С. 375–380. DOI: <https://doi.org/10.18721/JPM.153.269>

Статья открытого доступа, распространяемая по лицензии CC BY-NC 4.0 (<https://creativecommons.org/licenses/by-nc/4.0/>)

## Introduction

Recently, a large number of methods [1–4] and instruments [5–7] for diagnosing condensed matter have been developed in the world. The main disadvantages of such instruments are their large size, high consumption of reagents and samples, etc. [8, 9]. The use of microfluidic chips for the study of liquids and solutions in microsystems allows solving many of these problems. These chips provide reproducible control of the laminar flows of nano- and picoliter volumes of liquid in microsized channels, high sensitivity and low power, reagents and samples consumption [10–12]. So they are widely used in chemical engineering, pharmaceuticals, biotechnology, and medicine [13].

Quantitative polymerase chain reaction (qPCR) is a popular method of genetic analysis, which makes it possible to quantify the content of the target nucleotide sequence in a sample by determining quantification cycle values  $C_q$  [14]. Microfluidic qPCR chips are being actively developed and improved in the world [15–20]. A significant disadvantage of performing PCR in a chip chamber compared to test tubes is the formation of gas bubbles during thermal cycling. It has no noticeable effect on the reaction result, but prevents correct optical detection. Several methods have been used to inhibit the bubble generation: (i) the design of PCR chamber, (ii) the surface treatment, (iii) the sealing pressurization of the PCR chamber (iv) degasification of the PCR sample and (v) the addition of high boiling-point biocompatible reagents to the PCR sample [13]. Mathematical processing of qPCR signals makes it possible to evaluate the analysis result, despite the gas bubbles formation influence on signal. The PCR efficiency evaluation depending on the materials and design of the chips, the reagents used, and the reaction conditions is complex due to the occurrence of discord in the measurement sequence due to the formation and movement of bubbles. This results in a fluorescence intensity decrease over several cycles. Therefore, the development of methods for processing of qPCR signals distorted due to the formation of bubbles is an extremely urgent task.

## Materials and Methods

Microchips for qPCR analysis were made of polycarbonate Novattro (SafPlast, Russia) and polypropylene PP 4445S (PJSC Nizhnekamskneftekhim, Russia) by thermal pressing in a MM-100 hydraulic press (MTDI, Korea) on a stainless steel master mold made by laser micro-processing. Microchip topology represents 3 chambers with supply channels [21]. Polymer film P-500 (LLC PKF Modern technologies, Russia) was used for sealing microchips.

The obtained microchips were used for qPCR of soybean DNA isolated manually using a set of M-sorb-OOM (LLC Sintol, Russia). The experiments were carried out for the initial concentration of isolated nucleic acids, for dilutions of 1, 2 and 3 orders, and for a positive control in three repeats for each variant. R6G and Cy5 dyes were used to detect soybean DNA samples and confirm a positive control respectively.

The measurements were carried out on a specially designed model that provides a thermal cycling mode for qPCR, dyes excitation at wavelengths of 530, 570 and 685 nm and signal registration at 580, 630 and 660 nm. The microchip chambers were filled with a reaction mixture with the addition of nucleic acids; the inputs/outputs were sealed with PCR film. The microchip was placed on the heating element with the film facing down. Overall, 114 experimental qPCR plots were obtained, about 70 % had distortion caused by bubbles.



Two signal processing methods, based on the qPCR plots approximation by a known sigmoid function [22] (formula 1) were developed and implemented in the MATLAB software to identify the correct  $C_q$  values:

$$F_c = \frac{F_m}{1 + e^{-k(C - C_q)}} + f_0, \quad (1)$$

where  $F_c$  is the fluorescence signal at cycle  $C$ , RFU;  $F_m$  is the maximal reaction fluorescence, RFU;  $C_q$  is the fractional cycle at which reaction fluorescence reaches half of  $F_m$ ;  $k$  is related to the slope of the curve,  $f_0$  is the fluorescence background, RFU.

Each cycle of the program, when implementing the developed methods, the graph is approximated. In method No. 1, the signal value with the largest absolute deviation from the approximating function (1)  $\Delta F$  is assigned the value corresponding to the approximating dependence point. In method No. 2, the value corresponding to the deviation  $\Delta F$  is excluded from the experimental set. The program end is determined automatically.

The use of the program on experimental data does not allow estimating the errors in determining the threshold cycle values since there is no a priori information about the true  $C_q$  values. The experimental curves errors study was carried out, which revealed the following:

- the mathematical expectation of errors close to zero;
- the distribution of errors is more consistent with the normal law: information discrepancy of the Kullback–Leibler histogram of the real distribution of interference over 6 intervals with a uniform law of 0.0710 nits, with a normal one – 0.0422 nits, a coefficient of kurtosis – 3.07;
- the error is close to multiplicative, its standard deviation is possibly proportional to the value of the average signal.

Based on the results of the error study, Set A was created from 10000 simulation curves (Fig. 1, *a*) with parameters  $F_m = 1000$ ;  $C_q = 30$ ;  $k = 1$ ,  $f_0 = 600$ , the dependence law of errors normally distributed standard deviations (RMS) on the signal value  $\sigma = 0.0024F_c + 1.1368$ , uniform distributions of the duration of signal distortion from 3 to 7 cycles, and the intensity of the signal drop when a bubble occurs  $(0.22–0.24) \cdot F_c$ . The beginning of the bubble is also random, its distribution is even.

We separately created five sets of 10000 curves: with signal distortion caused by bubbles that occur in the ranges: Set B from 1 to 24 cycles, Set C from 25 to 35 cycle and Set D from 36 to 50 cycle; as well as with signal distortions of duration: Set E 3 cycles and Set F 7 cycles.

### Results and Discussion

As a result of applying the method No. 1 (Fig. 1, *b*) on Set A errors 76.41 % of values  $C_q$  lie in the range  $\pm 0.15$  cycle from the true value, as a result of applying method No. 2, 77.39 %. The mean  $C_q$  scores for the methods were  $30.36 \pm 0.84$  and  $30.52 \pm 1.30$ , respectively. The estimate bias is caused by large positive errors, the proportion of which is about 20 %. The acceptable value of 0.15 cycles corresponds to a quantification error of less than 10 % and was chosen as the deviation in the determination of  $C_q$ , which is acceptable for most tasks of qPCR analysis. According to this criterion, method No. 2 has advantages.

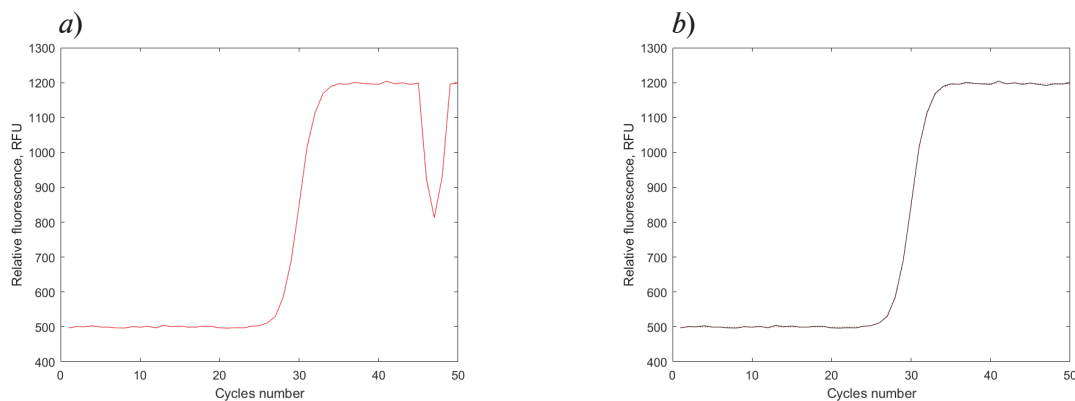


Fig. 1. Graphs for qPCR: model graph (*a*); model graph with eliminated distortion according to Method No. 1 (*b*)

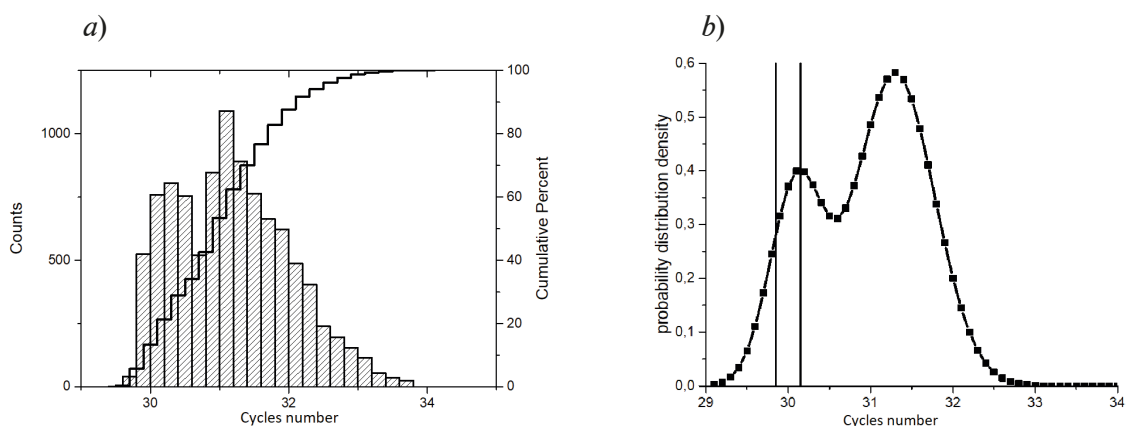


Fig. 2. Results of Method No. 1 application in Set C: threshold cycle position estimates histogram (a); possible probabilistic model for the distribution of scores (b), which is the sum of two Gaussian distributions

In case of distortion in the initial (Set B) or final (Set D) section of the kinetic curve, the average errors in estimating the position of the inflection point are at an acceptable level: 0.013 for the initial section and 0.022 for the final section when choosing any of the two methods. Permissible error in determining  $C_q$  obtained in 100 % of cases.

The main errors occur when the signal is distorted in the central section of the qPCR graph. 11% of the curves fall within the allowable range of  $\pm 0.15$  cycles (Fig. 2).

The mathematical expectation ( $M$ ) of the threshold cycle position in method No. 1 was 31.18 cycles. As follows from the histogram, the distribution is close to bell-shaped. According to the Novickij-Zograf rule, at least 90 % of the sample must fall within the interval  $M \pm m \cdot \sigma$  standard deviation at  $m = (1.65 \pm 0.05)$  [23], in our case in the interval  $\{29.81; 32.55\}$  with  $m = 1.65$ .

Set analysis shows that 9329 out of 10000 results fell into this interval (i.e., 93.3 %), which correlates well with the Novickij-Zograf rule. Depending on the method for constructing an approximating dependence and estimating the inflection point of the kinetic curve in the presence of bubbles in the section 25–35 cycles, the estimation error are given in Table 1. The average error according to method No. 1 is 1.18 cycles, according to method No. 2 0.99 cycles.

With method No. 2, the proportion of small (up to 0.3 cycles) errors is much larger (29.5 versus 18.5 %). However, the proportion of super-large estimation errors is almost the same: 20 % of the largest errors with method No. 1 - 1.89 cycles or more, with method No. 2 - 1.80 cycles or more. Approximately every 10th quantitative qPCR analysis, when distortion is on the central part, we will mistakenly exclude a reasonable and correct result.

Another stage of the simulation involved introducing a discord corresponding to a 3 or 7 distortion duration (Sets E and F).

Table 1

Comparison of the errors distribution in determining  $C_q$  by two methods when processing the Set C

Method No. 1		Method No. 2	
Level, cycle	Probability, %	Level, cycle	Probability, %
0.30	18.5	0.30	29.5
0.50	25.2	0.50	38.0
1.00	42.6	0.85	50.0
1.12	50.0	1.00	56.8
1.89	80.0	1.80	80.0



According to method No. 1 with the replacement of values with a distortion duration of 3 cycles, the average error in threshold cycle determining was 0.135; with an alternative method of exclusion, it was 0.065 cycles. That is, for a “small” bubble, it is more reasonable to exclude the corresponding 3 measurements from the signal.

When simulating a bubble with distortion duration of 7 cycles, the average errors in estimating the position of the threshold cycle are practically the same with an accuracy of several thousandths and are approximately equal to 0.254 cycles.

### Conclusion

Two automated methods have been developed that allow to obtain a satisfying RMS value when determining the threshold cycle and successfully perform a quantitative analysis of qPCR in microfluidic chips when bubbles occur. Approbation on a set of 10000 created simulation curves showed that the acceptable error in determining  $C_q$  values, method No. 1 provides in 76.41 % of cases, method No. 2 - in 77.39 %. The main errors occur when the distortion is in the central section of the curve, which is characterized by the most intense fluorescence intensity change. When using the developed methods, 11 % of the processed curves fall within the allowable range of  $C_q$  value errors. Methods allow identifying such cases and recommending the operator to discard the values as false.

As a result, developed methods approbation on sets of simulation curves with different signal distortion lengths revealed that for short distortion durations, it is more reasonable to exclude the corresponding measurements from the signal, for large ones, the choice of the method is not fundamental.

### REFERENCES

1. **Zheng Q., Chu W., Zhao C., Zhang L., Guo H., Wang Y., Jiang X., Zhao J.**, Ab initio nonadiabatic molecular dynamics investigations on the excited carriers in condensed matter systems. *Wiley Interdisciplinary Reviews: Computational Molecular Science*. 9(8) (2019) e1411.
2. **Makeev S. S., Grevtzeva A. S., Glinushkin A. P., Matorin D. N.**, Possibilities of using spectral analysis in method of nuclear magnetic spectroscopy for condensed media investigation, *Journal of Physics: Conference Series*. 1695(1) (2020) 012112.
3. **Kuzmin M. S., Rogov S. A.**, On the use of a multi-raster input of one-dimensional signals in two-dimensional optical correlators, *Computer Optics*. 43(3) (2019) 391–396.
4. **Mazing M. S., Zaitceva A. Yu., Kislyakov Yu. Ya., Kondakov N. S., Avdushenko S. A., Davydov V. V.**, Monitoring of Oxygen Supply of Human Tissues Using A Noninvasive Optical System Based on A MultiChannel Integrated Spectrum Analyzer, *International Journal of Pharmaceutical Research*. 12(2) (2020) 1974–1978.
5. **Grebenikova N. M., Smirnov K. J., Rud V. Yu., Artemiev V. V.**, Features of monitoring the state of the liquid medium by refractometer, *Journal of Physics: Conference Series*. 1135(1) (2018) 012055.
6. **Myazin N. S., Yushkova V. V., Rud V. Y.**, On the possibility of recording absorption spectra in weak magnetic fields by the method of nuclear magnetic resonance, *Journal of Physics: Conference Series*. 1038(1) (2018) 012088.
7. **Grebenikova N. M., Smirnov K. J.**, Features of optical signals processing for monitoring the state of the flowing liquid medium with a refractometer, *Journal of Physics: Conference Series*. 1368(2) (2019) 022057.
8. **Davydov V.V., Dudkin V.I., Karseev A.Y.**, A Compact Nuclear Magnetic Relaxometer for the Express Monitoring of the State of Liquid and Viscous Media, *Measurement Techniques*. 57(8) (2014) 912–918.
9. **Karseev A., Vologdin V., Davydov V.**, Features of nuclear magnetic resonance signals registration in weak magnetic fields for express - Control of biological solutions and liquid medium by nuclear magnetic spectroscopy method, *Journal of Physics: Conference Series*. 643(1) (2015) 012108.
10. **Evstrapov A.A.**, Microfluidic chips for biological research and research, *Russian Chemical Journal*. 55 (2) (2011) 99–110.
11. **Bruus H.**, Theoretical microfluidics. Lecture notes third edition. MIC Department of Micro and Nanotechnology Technical University of Denmark, 2006.
12. **Fiorini G. S., Chiu D. T.**, Disposable microfluidic devices: fabrication, function and application, *BioTechniques*. 38(3) (2005) 429–446.

13. **Zhang C., Xing D.**, Miniaturized PCR chips for nucleic acid amplification and analysis: latest advances and future trends, *Nucleic Acids Research*. 35(13) (2007) 4223–4237.
14. **Nakayama T., Kurosawa Y., Furui S., Kerman K., Kobayashi M., Rao S. R., Tamiya E.**, Circumventing air bubbles in microfluidic systems and quantitative continuous-flow PCR applications. *Analytical and Bioanalytical Chemistry*, 386(5) (2006) 1327–1333.
15. **Fedorov A. A., Berdnikov A. S., Kurochkin V. E.**, The polymerase chain reaction model analyzed by the homotopy perturbation method, *Journal of Mathematical Chemistry*. 57(4) (2019) 971–985.
16. **Natyrov A. N., Vlasova N. A., Matvienko I. V., Kurochkin V. E., Alexeev J. I.**, Synthesis of Unsymmetrical Polymethine Cyanine Fluorescent Dyes for Nucleic Acid Analysis by Real-Time PCR, *Russian Journal of Bioorganic Chemistry*. 44(5) (2018) 562–571.
17. **Reznik V. S., Kruglov V. A., Petrov A. I., Glinuchkin A. P., Rud V. Y.**, Development of a measuring device for the study of thermal processes during the polymerase chain reaction, *Journal of Physics: Conference Series*. 1410(1) (2019) 012078.
18. **Kiselev I. G., Belov D. A.**, Physical processes simulation in a precision device for liquid samples thermal cycling, *Journal of Physics: Conference Series*. 2131(2) (2021) 022061.
19. **Matvienko I. V., Bayramov V. M., Parygina N. A., Kurochkin V. E., Alekseev Y. I.**, Synthesis of Dihydroquinoline-Based Derivatives of Fluorescent Rhodamine Dyes for Nucleic Acid Analysis by a Real-Time Polymerase Chain Reaction, *Russian Journal of Bioorganic Chemistry*. 46(3) (2020) 349–359.
20. **Zubik A. N., Rudnitskaya G. E., Bulyanitsa A. L., Lukashenko T. A., Evstrapov A.A.**, Microfluidic chips for real-time PCR, *Journal of Physics: Conference Series*. 2086 (2021) 012124.
21. **Yesikova N.A., Germash N.N., Evstrapov A.A.**, Operational production of microchips for PCR analysis from polymer materials in laboratory conditions, *Scientific instrumentation*. 30 (4) (2020) 21–6.
22. **Novickij P.V., Zograf I.A.**, Ocenka pogreshnostej rezul'tatov izmerenij [Assessment of errors of observed data], Nauka, Leningrad, 1991.
23. **Rutledge R.G., Stewart D. A.**, Kinetic-based sigmoidal model for the polymerase chain reaction and its application to high-capacity absolute quantitative real-time PCR. *BMC Biotechnol.* (2008) 8:47.

#### THE AUTHORS

**KLIMENKO Daria**

dasha.klimenko.01@inbox.ru  
ORCID: 0000-0002-1216-2192

**DAVYDOV Roman**

davydovroman@outlook.com  
ORCID: 0000-0003-1958-4221

**ESIKOVA Nadezhda**

elpis-san@yandex.ru  
ORCID: 0000-0002-0145-6451

**BELOV Dmitrii**

belov.da@list.ru  
ORCID: 0000-0003-3219-0446

**BULYANITSA Anton**

antbulyan@yandex.ru  
ORCID: 0000-0002-9235-8549

*Received 14.08.2022. Approved after reviewing 16.08.2022. Accepted 16.08.2022.*

Conference materials

UDC 681.7

DOI: <https://doi.org/10.18721/JPM.153.270>

## Application of a fiber-optic communication line for transmitting RF-signal in system for measuring parameters of active phased antenna arrays

E. M. Gryaznova <sup>1</sup>✉, V. V. Davydov <sup>1, 2, 3</sup>, K. Yu. Malanin <sup>4</sup>

<sup>1</sup> Peter the Great St. Petersburg Polytechnic University, St. Petersburg, Russia;

<sup>2</sup> All-Russian Research Institute of Phytopathology, Moscow Region, Russia;

<sup>3</sup> Bonch-Bruевич Saint Petersburg State University of Telecommunications, St. Petersburg, Russia;

<sup>4</sup> JSC Zaslou, St. Petersburg, Russia

✉ [katya.gryaznova@mail.ru](mailto:katya.gryaznova@mail.ru)

**Abstract.** The necessity of using fiber-optic communication lines (FOCL) for transmitting microwave signals in radar complexes is substantiated. The advantages of the use of FOCL when working with microwave signals and testing various antennas are noted. A system with a fiber optic system has been developed to measure the parameters of an active phased array antenna (APAA) in the far zone. The choice of the components of the system is justified and their characteristics are measured. The results of research on the operation of the developed system are presented.

**Keywords:** fiber-optic communication line, active phased array antenna, radiophotonics, frequency range, microwave signal, far zone

**Citation:** Gryaznova E. M., Davydov V. V., Malanin K. Yu., Application of a fiber-optic communication line for transmitting RF-signal in system for measuring parameters of active phased antenna arrays, St. Petersburg State Polytechnical University Journal. Physics and Mathematics. 15 (3.2) (2022) 381–387. DOI: <https://doi.org/10.18721/JPM.153.270>

This is an open access article under the CC BY-NC 4.0 license (<https://creativecommons.org/licenses/by-nc/4.0/>)

Материалы конференции

УДК 681.7

DOI: <https://doi.org/10.18721/JPM.153.270>

## Использование волоконно-оптической линии связи для передачи РЧ-сигнала в системе измерения параметров активных фазированных антенных решеток

Е. М. Грязнова <sup>1</sup>✉, В. В. Давыдов <sup>1, 2, 3</sup>, К. Ю. Маланин <sup>4</sup>

<sup>1</sup> Санкт-Петербургский политехнический университет Петра Великого, Санкт-Петербург, Россия;

<sup>2</sup> Санкт-Петербургский государственный университет связи  
им. проф. М.А. Бонч-Бруевича, Санкт-Петербург, Россия;

<sup>3</sup> Всероссийский научно-исследовательский институт фитопатологии, Московская область, Россия;

<sup>4</sup> ЗАО «Заслон», Санкт-Петербург, Россия

✉ [katya.gryaznova@mail.ru](mailto:katya.gryaznova@mail.ru)

**Аннотация.** Обоснована необходимость использования волоконно-оптических линий связи (ВОЛС) для передачи сигналов СВЧ в радиолокационных комплексах. Отмечены преимущества использования ВОЛС при работе с СВЧ-сигналами и тестировании различных антенн. Разработан комплекс с волоконно-оптической системой для измерения параметров активной фазированной антенной решетки (АФАР) в дальней зоне. Обоснован выбор компонентов системы и измерены их характеристики. Представлены результаты исследования работы разработанной системы.

**Ключевые слова:** волоконно-оптическая линия связи, активная антенная фазированная решетка, радиофотоника, диапазон частот, СВЧ сигнал, дальняя зона

**Ссылка при цитировании:** Грязнова Е. М., Давыдов В. В., Маланин К. Ю. Использование волоконно-оптической линии связи для передачи РЧ-сигнала в системе измерения параметров активных фазированных антенных решеток // Научно-технические ведомости СПбГПУ. Физико-математические науки. Т. 15. № 3.2. С. 381–387. DOI: <https://doi.org/10.18721/JPM.153.270>

Статья открытого доступа, распространяемая по лицензии CC BY-NC 4.0 (<https://creativecommons.org/licenses/by-nc/4.0/>)

### Introduction

The development of efficient high-speed optoelectronic devices has aroused great interest in the use of optoelectronic and optical technologies in microwave technology [1–9]. Various developments of laser systems also contributed to the emergence of radiophotonics [10–14], which allows to create devices and systems of the microwave range with parameters unattainable by traditional electronic means. The main advantages of radiophotonics devices and systems are related to the properties of optical fiber: ultra-low losses during transmission of a microwave signal, a wide frequency band, immunity to electromagnetic interference, complete galvanic isolation, mechanical flexibility, low weight and dimensions [13, 15–20]. A during are solving various tasks in radar, the use of FOCL allows obtaining the necessary results [15–25]. It should be noted that the transmission of microwave signals is carried out mainly at distances less than 1000 m. In this case, different types of dispersion do not have time to form in the fiber and affect the transmitted signal [22–27]. This greatly simplifies the design of the FOCL [20–30].

One of the most difficult tasks is to set up various radar antenna systems in an enterprise environment. The greatest difficulties arise when setting up an air-based radar with APAA operating in review mode. In this mode precise measurements of radiation diagram are very important, in the far zone especially [21, 28, 30]. The far zone of the radar is determined by the following ratio:

$$R_0 \gg 2L^2 / \lambda, \quad (1)$$

where  $R_0$  is the distance between antennas,  $L$  is the distance between the marginal transmitting elements of the antenna array,  $\lambda$  is the wavelength of the radiation.

The angular distribution of the field in the far zone does not significantly depend on the change in the distance to the antenna. In most APAAs in operation, the far zone corresponds to a distance of about several hundreds meters. This creates big problems when setting up and testing the radars in an anechoic chamber (AEC). Therefore, field tests are necessary. In the conditions of the polygon, the amount of interference of various kinds can be very large, which will lead to signal distortion and errors in the antenna setup. The use of fiber-optic communication lines can help solve this problem.

### Fiber optical communication system

In analog fiber-optic information transmission systems, modulation methods are used, characterized by a continuous change in one of the parameters of the signal carrier (optical radiation power during intensity modulation, the position of the optical pulse during positional pulse modulation or its duration during pulse width modulation, etc.).

One of the ways to transmit a microwave signal to a FOCL is direct modulation. The principle of direct modulation is as follows: the input of a laser diode with direct modulation receives a microwave signal that modulates the output optical signal of the laser diode. The modulated optical signal is transmitted with the help of a fiber-optic line to an optoelectronic receiving module, in which it is converted into a microwave signal. The developed direct-modulated FOCL can be used to transmit an analog signal over long distances (more than 500 m) in the frequency band from 0.1 to 12 GHz (currently unknown direct-modulated FOCL in the diapason from 0 to 40 GHz).

Similar FOCL have two main disadvantages: limited bandwidth and significant nonlinear distortions caused by the direct arrival of the microwave signal to the laser. In order to avoid these disadvantages, it is recommended to use a FOCL with external modulation. The principle of external modulation is as follows: the electro-optical modulator receives an optical signal from a semiconductor laser module, which is modulated by an input microwave signal. The modulated optical signal is transmitted via a fiber-optic line to an optoelectronic receiving module, in which it is converted into a microwave signal.

The peculiarity of analog transmission in comparison with digital is the need to ensure a large signal-to-noise ratio at the output of the optical receiver and high linearity along the entire path, since otherwise mutual interference from various frequency components of the transmitted analog signal is possible.

Fig. 1 shows a block diagram of a system in transmitting mode for measuring APAA parameters in the far zone.

The system includes two antenna posts:

- antenna post 1 (AP I) includes the studied APAA, optoelectronic converters (receivers) and spectrum analyzers.
- antenna post 2 (AP II) includes receiving antennas - horns 1 and 2, low-noise amplifiers, transmitters, as well as a power source.

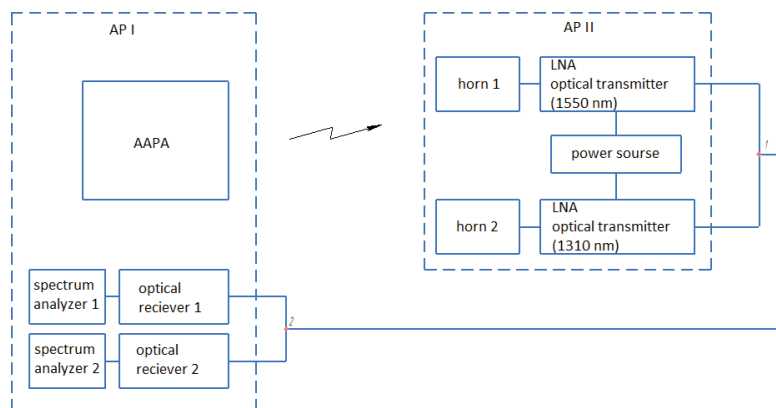


Fig. 1. Block diagram of the developed system

Two different devices were selected as transmitters - transmitter with direct modulation in the 1310 nm window and with external modulation for the 1550 nm wavelength. Direct modulation is a cheap solution used for 1310 nm window. Because 1310 nm wave is not subject to amplification by EDFA (Erbium Doped Fiber Amplifiers) amplifiers at longer lengths, there are problems with optical noise and, in particular, with signal attenuation. It has one big drawback: the presence of a chirp effect, which occurs only in lasers with direct modulation. That is why the length of the emitted lightwave is volatile and depends on the current of light source. The corruption created by this is very high in the 1550 nm window. Therefore, external modulation is usually used for transmission on the 1550 nm and direct modulation is used for 1310 nm, so the signal covering distances are increased up to 20 km. External modulation is much complex modulation type that provides attenuation of the optical signal of a laser in accordance with the RF input signal, but through the use of amplifiers, it allows covering distances up to 120 km.

Devices paired with transmitters were selected as receivers. In optical networks they must have a large dynamic range, good linearity, high sensitivity, even sensitivity in its spectral waveband. The photodetector must be fully compatible with the transmitting device, in terms of spectral sensitivity, transmission wavelengths and temporal modulation characteristics. High resistance to errors occurring in the signal when passing through the medium and other optical components is also important.

A single-mode fiber was chosen to transmit the analog microwave signal. Multi-year fiber has much more loss and multi-year dispersion is present, and the most important disadvantage is the small broadband coefficient.

For the developed FOCL, the main factors are high reverse losses and the strength of the connector. The best reverse losses of connectors with APC polishing, one of the most reliable and convenient are FC connectors. Therefore, FC-APC connectors were used in the FOCL. Also, an optical insulator was used to reduce the possible reflection of the signal along the entire length of the line.

The concept of the microwave path operation of the VOLS is as follows: the microwave signal received by the horn goes to a broadband low-noise amplifier, then the amplified microwave signal goes to an optical modulator and modulates the light beam coming from the laser module. From the modulator, the modulated optical signal is transmitted across a fiber-optic line to the optoelectronic receiving module, in which the light signal is converted back into a microwave signal with minimal distortion. Then the converted microwave signal is sent to the measuring receiver for further processing, after which it is sent to the spectroanalyzer.

The principle of operation of the microwave path of the FOCL is as follows: the microwave signal received by the horn goes to a broadband low-noise amplifier, then the amplified microwave signal goes to an optical modulator and modulates the light beam coming from the laser module. From the modulator, the modulated optical signal is transmitted through a fiber-optic line to the optoelectronic receiving module, in which the light signal is converted back into a microwave signal with minimal distortion. Then the converted microwave signal is sent to the measuring receiver for further processing, after which it is sent to the spectroanalyzer.

### Results and Discussion

Fig. 2 shows, as an example, the radar radiation diagrams in a rectangular coordinate system, measured using an electrical cable and designed FOCL in landfill conditions.

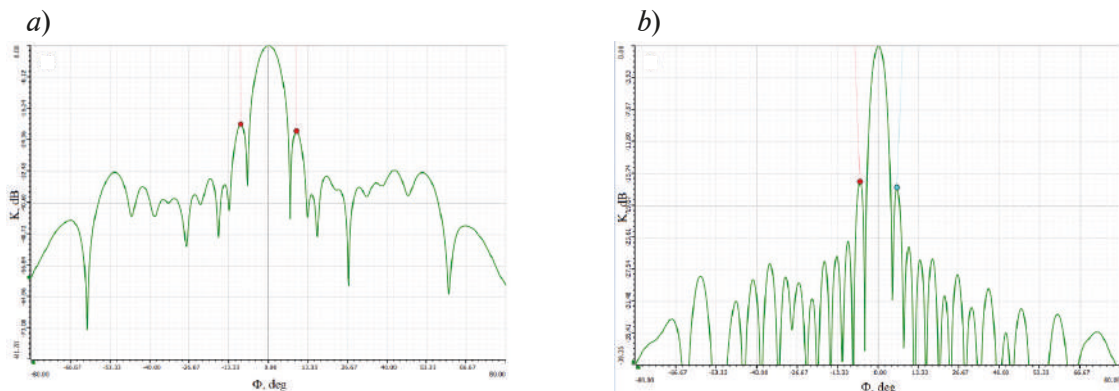


Fig. 2. AFAR directional diagram: electrical cable is used to transmit signal (a), FOCL is used to transmit the signal (b)

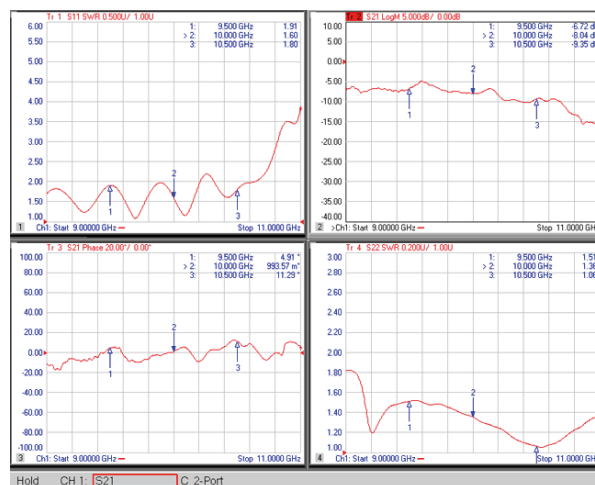


Fig. 3. Frequency characteristics of the experimental stand

Results show that the radiation pattern measured with FOCL allows an approximation to be performed to assess the stable APAA radar survey zone. Allows you to adjust the APAA to the maximum suppression of the side lobes for reducing the impact on the determination accuracy for the coordinates of moving objects, repeatedly reflected electrical signals.

Fig. 3 shows the frequency characteristics of the stand measured by the analyzer.

The usage of designed FOCL made it possible, as experiments have shown, to study, in addition to the radiation spectrum of the entire APAA in various operating modes, as well as the radiation spectra of its single active elements. These studies were previously not possible because of the presence of interference and noise in the transmission path.

As an example, in Fig. 4 shows the emission spectra of a single active element (rod) of the APAA transmitted to the control sector from the microwave signal recording device via a coaxial cable and the perceived.

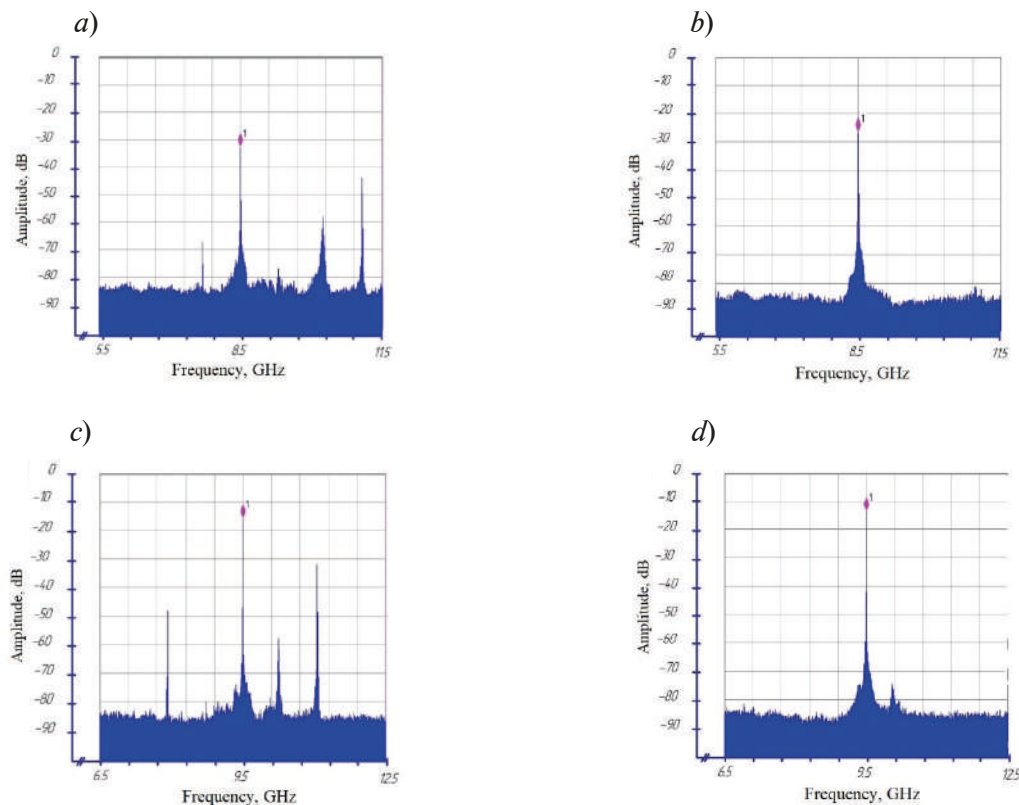


Fig.4. Radiation spectra transmitted via coaxial cable (*a, c*) and optical fiber (*b, d*)

The obtained graphs show that the measured spectra of the transceiver modules transmitted via a coaxial cable contain parasitic components in the spectrum, whereas the spectra obtained by the fiber optic have no interference. This fact indicates the expediency of using FOCL for APAA testing.

### Conclusion

The results obtained demonstrate that our designed FOCL makes it possible to make insignificant the effect of distortion when transmitting a microwave signal over the territory of the landfill over long distances to the equipment for subsequent processing. It also allows to identify different mistakes in the radar elements that cannot be established when using electrical cable.

## REFERENCES

1. **Davydov R., Antonov V., Moroz A.**, Parameter Control System for a Nuclear Power Plant Based on Fiber-Optic Sensors and Communication Lines, In: IEEE International Conference on Electrical Engineering and Photonics (EExPolytech), Saint Petersburg, Russia, 13-15 October 2019. Vol. 8906791 (2019) 295–297.
2. **Dyumin V., Smirnov K., Myazin N.**, Charge-coupled Device with Integrated Electron Multiplication for Low Light Level Imaging, Proceedings of the 2019 IEEE International Conference on Electrical Engineering and Photonics, EExPolytech. Vol. 8906868 (2019) 308–310.
3. **Grebenikova N. M., Davydov R. V., Rud V. Yu.**, Features of the signal registration and processing in the study of liquid flow medium by the refraction method, Journal of Physics: Conference Series. 1326(1) (2019) 012012.
4. **Grebenikova N. M., Smirnov K. J., Rud V. Yu., Artemiev V. V.**, Features of monitoring the state of the liquid medium by refractometer, Journal of Physics: Conference Series. 1135(1) (2018) 012055.
5. **Skidanov R.V., Blank V.A., Morozov A.A.**, Study of an imaging spectrometer based on a diffraction lens, Computer Optics. 39(3) (2015) 384–392.
6. **Kuzmin M. S., Rogov S. A.**, On the use of a multi-raster input of one-dimensional signals in two-dimensional optical correlators, Computer Optics. 43(3) (2019) 391–396.
7. **Myazin N.S., Smirnov K.J., Logunov S.E.**, Spectral characteristics of InP photocathode with a surface grid electrode, Journal of Physics: Conference Series. 929(1) (2017) 012080.
8. **Nalimov A.G., Kozlova E.S.**, Inversion of the longitudinal component of spin angular momentum in the focus of a left-handed circularly polarized beam, Computer Optics. 44(5) (2020) 699–706.
9. **Kozlova E.S., Kotlyar V.V.**, Refined dispersion model for quartz glass, Computer Optics. 38(1) (2014) 132–138.
10. **Stafeev S.S., Kozlova E.S., Nalimov A.G.**, Focusing a second-order cylindrical vector beam with a gradient index mikaelian lens, Computer Optics. 44(1) (2020) 29–33.
11. **Davydov V. V., Kruzhalov S. V., Grebenikova N. M., Smirnov K. J.**, Method for Determining Defects on the Inner Walls of Tubing from the Velocity Distribution of the Flowing Fluid, Measurement Techniques. 61(4) (2018) 365–372.
12. **Davydov V. V.**, Determination of the Composition and Concentrations of the Components of Mixtures of Hydrocarbon Media in the Course of its Express Analysis, Measurement Techniques. 62(2) (2020) 1090–1098.
13. **Dmitrieva D.S., Pilipova V.M., Rud V.Y.**, Fiber-optical communication line with a system for compensation of radiation-induced losses during the transmission of information. Lecture Notes in Computer Science (including subseries Lecture Notes in Artificial Intelligence and Lecture Notes in Bioinformatics). 12526 LNCS (2020) 348–356.
14. **Fadeenko V.B., Kuts V.A., Vasiliev V.D.**, New design of fiber-optic communication line for the transmission of microwave signals in the X-band, Journal of Physics: Conference Series. 1135(1) (2018) 012053.
15. **Petrov A. A.**, Digital Frequency Synthesizer for  $^{133}\text{Cs}$ -Vapor Atomic Clock, Journal of Communications Technology and Electronics. 62(3) (2017) 289–293.
16. **Davydov V.V.**, Some specific features of the NMR study of fluid flows, Optics and Spectroscopy (English translation of Optika i Spektroskopiya). 121(1) (2016) 18–24.
17. **Pchelkin G.A.**, Features of the transmission of microwave signals at offshore facilities, Journal of Physics: Conference Series. 1368(2) (2019) 022045.
18. **Fadeenko V.B., Pchelkin G.A., Rud V.Yu.**, Features of the transmission of microwave signals in the range of 8-12 GHz in the maritime radar station over fiber-optic communication line, Journal of Physics: Conference Series. 1400(4) (2019) 044010.
19. **Lenets V.A., Tarasenko M.Yu., Rodygina N.S., Moroz A.V.**, New method for testing of antenna phased array in X frequency range, Journal of Physics: Conference Series. 1038(1) (2018) 012037.
20. **Davydov V., Fadeenko V., Fadeenko I., Popovskiy N., Rud V.**, Multifunctional method for remote monitoring of the environment in the area of nuclear facilities, E3S Web of Conferences. 140 (2019) 07006.
21. **Moroz A.V., Malanin K.Y., Krasnov A.A.**, Development of a Compensation System Based on Horn Antennas for an Active Phased Antenna Array, Proceedings of the 2019 Antennas Design and Measurement International Conference, ADMInC 2019, vol. 8969090 (2019) 114–116.



22. **Moroz A.V.**, Features of transmission bearing and heterodyne receivers for signals in fiber-optic communication line in active phased array antenna, *Journal of Physics: Conference Series*. 1410(1) (2019) 012212.
23. **Filatov D.L., Galichina A.A., Vysoczky M.G., Rud V.Y.**, Features of transmission at analog intermediate frequency signals on fiber - Optical communication lines in radar station, *Journal of Physics: Conference Series*. 917(8) (2017) 082005.
24. **Petrov A. A., Grebenikova N.M.**, On the Potential Application of Direct Digital Synthesis in the Development of Frequency Synthesizers for Quantum Frequency Standards, *Journal of Communications Technology and Electronics*. 63(11) (2018) 1281–1285.
25. **Fadeenko V.B., Pchelkin G.A., Beloshapkina O.O., Rud V.Yu.**, Features of construction of the scheme of fiber-optic communication system for transmission of analog signals in the frequency range from 0.135 to 40 GHz, *Journal of Physics: Conference Series*. 1410(1) (2019) 012238.
26. **Moroz A. V., Davydov R. V.**, A New Scheme for Transmitting Heterodyne Signals Based on a Fiber-Optical Transmission System for Receiving Antenna Devices of Radar Stations and Communication Systems, *Lecture Notes in Computer Science (including subseries Lecture Notes in Artificial Intelligence and Lecture Notes in Bioinformatics)*. 11660 (2019) 710–718.
27. **Fadeenko V.B., Vasiliev D.A.**, Multifunctional radar system for remote control of environment and the Earth's surface, *Journal of Physics: Conference Series*. 1745(1) (2021) 012023.
28. **Moroz A.V.**, Fiber-optical system for transmitting heterodyne signals in active phased antenna arrays of radar stations, *Journal of Physics: Conference Series*. 1368(2) (2019) 022024, December 2019.
29. **Petrov A. A., Shabanov V. E., Zalyotov D. V., Bulyanitsa A. L., Shapovalov D. V.**, Modernization of the frequency synthesizer of cesium atomic clock, *IEEE International Conference on Electrical Engineering and Photonics, EExPolytech 2018, Saint Petersburg, October 2018*. vol. 8564389 (2018) 52–55.
30. **Moroz A.V., Krasnov K.Yu.**, Features of the construction of the noise compensation circuit of a small-sized active phased antenna array, *Journal of Physics: Conference Series*. 1400(4) (2019) 044009.

#### THE AUTHORS

**GRYAZNOVA Ekaterina**  
katya.gryaznova@mail.ru  
ORCID: 0000-0001-6761-251X

**MALANIN Kirill**  
kymalanin@gmail.com  
ORCID: 0000-0001-7511-0819

**DAVYDOV Vadim**  
davydov\_vadim66@mail.ru  
ORCID: 0000-0001-9530-4805

*Received 15.08.2022. Approved after reviewing 17.08.2022. Accepted 07.09.2022.*

Conference materials

UDC 537.86

DOI: <https://doi.org/10.18721/JPM.153.271>

## Additive manufacturing of an antenna array

V. D. Burtsev <sup>1</sup>✉, K. A. Rogozhkin <sup>1</sup>, T. S. Vosheva <sup>1</sup>,  
A. A. Khudykin <sup>1</sup>, D. S. Filonov <sup>1</sup>

<sup>1</sup> Moscow Institute of Physics and Technology, Moscow, Russia

✉ [burtsev.vd@phystech.edu](mailto:burtsev.vd@phystech.edu)

**Abstract.** Antenna arrays are essential elements in modern wireless communication technologies. Capabilities to perform real-time beamforming with millisecond-scale latencies enable supporting frontier 5G communication protocols. Being based on standard lithography methods, printed board antenna arrays are two-dimensional by design. However, exploration of the third dimension allows for obtaining new capabilities, including wide-angle scanning, broadband impedance matching, higher directivity, and several others. Here we demonstrate an additively manufactured volumetric antenna array, where each individual element is 3D-printed and subsequently metalized with the aid of electrochemical deposition. Additive manufacturing is foreseen to provide capabilities of a complete production cycle, including electronics and peripheries, being fabricated within the same machine. Here, the full potential of volumetric antenna arrays will be revealed.

**Keywords:** additive manufacturing, antennae, 3D print, radio frequency, telecommunications, electrostatics, antenna arrays

**Funding:** The study was supported by the Federal Academic Leadership Program Priority-2030.

**Citation:** Burtsev V. D., Rogozhkin K. A., Vosheva T. S., Khudykin A. A., Filonov D. S., Additive manufacturing of an antenna array, St. Petersburg State Polytechnical University Journal. Physics and Mathematics. 15 (3.2) (2022) 388–392. DOI: <https://doi.org/10.18721/JPM.153.271>

This is an open access article under the CC BY-NC 4.0 license (<https://creativecommons.org/licenses/by-nc/4.0/>)

Материалы конференции

УДК 537.86

DOI: <https://doi.org/10.18721/JPM.153.271>

## Аддитивное изготовление антенной решетки

В. Д. Бурцев <sup>1</sup>✉, К. А. Рогожкин <sup>1</sup>, Т. С. Вошева <sup>1</sup>,  
А. А. Худыкин <sup>1</sup>, Д. С. Филонов <sup>1</sup>

<sup>1</sup> Московский физико-технический институт, Москва, Россия

✉ [burtsev.vd@phystech.edu](mailto:burtsev.vd@phystech.edu)

**Аннотация.** Антенные решетки на печатных платах, основанные на стандартных методах литографии, по своей конструкции являются двумерными. Однако открытие третьего измерения позволяет получить новые возможности, включая широкоугольное сканирование, широкополосное согласование импеданса, более высокую направленность и ряд других. Здесь мы демонстрируем аддитивно изготовленную объемную антенную решетку, каждый отдельный элемент которой напечатан на 3D-принтере и впоследствии металлизирован с помощью электрохимического осаждения.

**Ключевые слова:** аддитивные технологии, антенны, 3D печать, радиотехнологии, системы связи, электродинамика, антенные решетки

**Финансирование:** Это исследование поддержано федеральной академической передовой программой «Приоритет 2030».



**Ссылка при цитировании:** Бурцев В. Д., Рогожкин К. А., Вошева Т. С., Худыкин А. А., Филонов Д. С. Аддитивное изготовление антенной решетки // Научно-технические ведомости СПбГПУ. Физико-математические науки. Т. 15. № 3.2. С. 388–392. DOI: <https://doi.org/10.18721/JPM.153.271>

Статья открытого доступа, распространяемая по лицензии CC BY-NC 4.0 (<https://creativecommons.org/licenses/by-nc/4.0/>)

## Introduction

The development of various additive technologies has been gaining momentum recently [1]. Additive manufacturing technology is a mixture of several traditional manufacturing methods for layer-by-layer manufacturing of the final product. Additive technologies serve science in various industries, ranging from ordinary applications (surface anodizing, decorative metallization with a thin shiny metal layer of plastic coatings) and to space applications. A bright example of an additive technology is three-dimensional metal printing, when a powerful laser, sintering metal dust, forms the frame of the test sample [2, 3]. Also, there already exists a set of developments in the field of printing with conductive ink for the manufacture of electrical circuits for the needs of electronics [4]. The range of applications of additive manufacturing methods is quite large. Their scope of applicability extends in the field of radio engineering and data transmission. There are a number of works devoted to obtaining electrodynamic structures using laser sintering [5, 6], drawing with conductive ink [7–9], polymer deposition [10], and others [11–13]. Some researchers use electrically conductive plastic to make antenna frames, which are subsequently metallized in a galvanic bath [14, 15]. The antennas obtained by this method practically do not differ from all-metal analogues and are well predicted using numerical modeling [16].

However, in advanced works, mainly one-sided metallization of the skeleton is considered, implying that the plastic sublayer is covered with metal only on one side, while the other boundaries are opened. This entails locking up the energy of the electromagnetic field in the dielectric. In order to estimate the effective electrical length of such an antenna, it is necessary to know the exact value of the dielectric constant of the plastic. There are several basic methods for measuring this value, for example, the NRW method [17], slot-line based methods [18] or various measurement methods using microstrip lines [19–22]. These methods suit well for planar structures or structures of simple shapes. For 3D objects of complex shape, their impedance is difficult to calculate. To overcome this limitation, in this work we are targeting at the frequency of 2.0 GHz, since above 5 GHz plastic begins to have a strong negative effect on the emitter performance [23], while below it does not have such an impact.

In this paper, we are going to highlight the possibility of assembling antenna arrays based on additively manufactured antennas.

## Methods

We use 3D printing on a BCN3D SigmaX device with PLA-plastic filling. After that, the surface of the skeleton is covered with a thin layer of electrically conductive varnish, which allows subsequent metal deposition onto its surface. After the coverage process the whole structure is believed to be an antenna array which should not significantly differ from the one that could be obtained from pure metal.

To test the proposed method of 3D printing and electroplating, it was decided to use a model of an antenna array consisting of four three-dimensional antennas (2x2) located in the corners of a square with a side of 120 mm. The design of each standalone antenna was taken from a work on 3D evolved antennas prototyping [24].

Fig. 1,*a* shows the general geometry of the printed circuit board (PCB) layout for this antenna, where all the dimensions are given in millimeters. The thickness of the metallization is about 0.1 mm. The thickness of substrate is 1.5 mm. The reverse side of the PCB is the full metal ground. Fig. 1,*b* shows the general 3D view of the constructed antenna array.

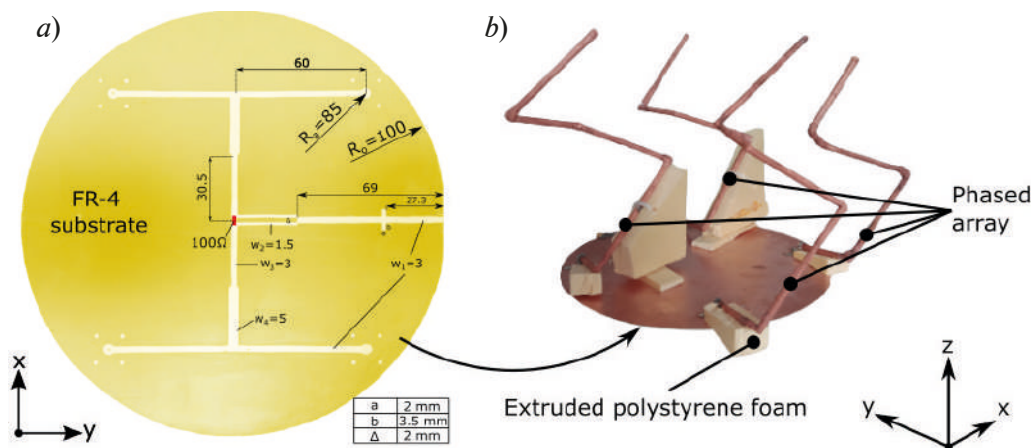


Fig. 1. Geometry properties of the antenna array: design of power supply wiring on the PCB with FR-4 substrate (a), photo of the general view of the antenna array (b)

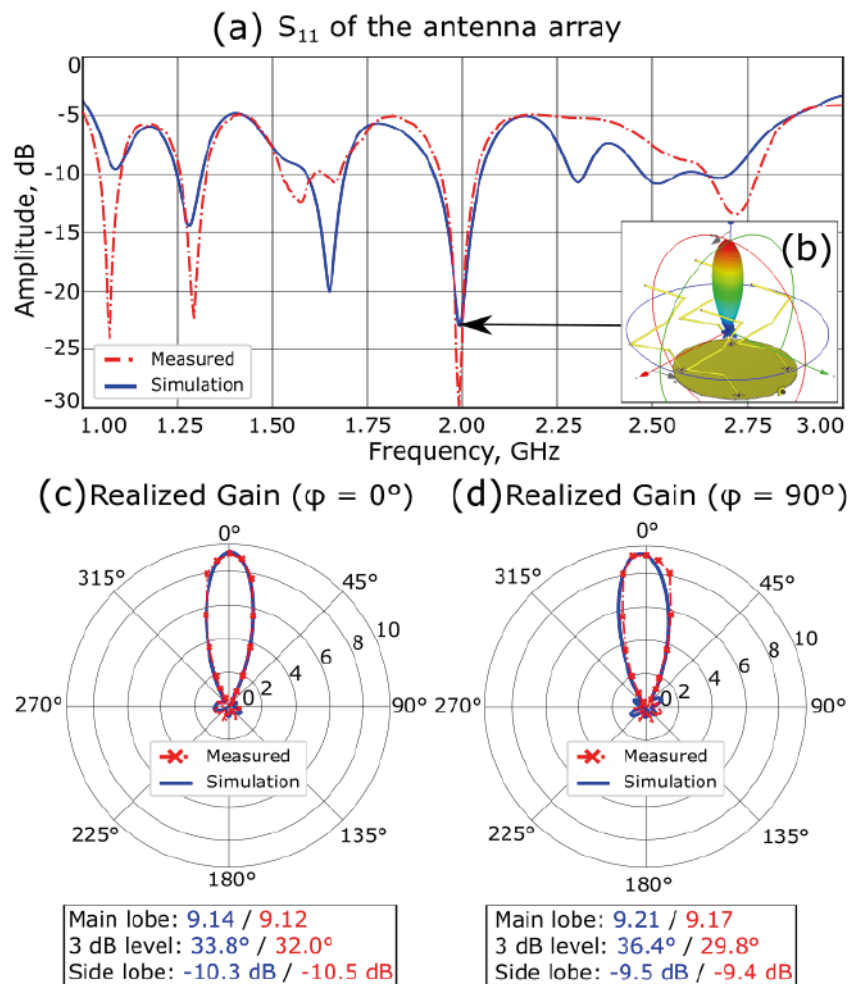


Fig. 2. Radiation properties of the antenna array: experimental (red dot-dashed line) and numerical simulation (blue line) data representation in comparison of reflection coefficient of the antenna array (a), radiation pattern at 2.0 GHz in numeric simulation (b), comparison of the realized gain patterns in orthogonal cuts  $\varphi = 0^\circ$  and  $\varphi = 90^\circ$  for experimental setup (red dot-dashed line with X marks) and computational results (blue line) (c) and (d)



The antenna array was prototyped in the CST Studio Suite software package. It was assumed that an antenna array with an aperture of 200 mm, consisting of 4 monopole antennas, should create a highly directional beam with a relatively high realized gain. Numerical modeling of the antenna was carried out by two different methods. The first of them is a simulation in the Time Domain Solver based on the finite integration method, when a solver in a wide frequency band calculates the development of an electromagnetic field propagating from the energy supply port of the system, launching a pulse. This method made it possible to obtain all the electrodynamic characteristics of the antenna in a wide frequency band. The second, clarifying method was modeling in the frequency domain, when Maxwell's equations are solved in the frequency domain, determining which part of the signal exists at the calculation frequency. This method made it possible to specify the exact frequencies of dips on the reflection coefficient graph (Fig. 2, *a*).

After the numerical simulation, to verify its results, the experimental study has been performed. The antenna measurements were carried out using the vector network analyzer Keysight P9374A, the signals from which were fed to the inputs of the measured antenna array and the measuring logoperiodic antenna with known efficiency. The reflection coefficient of the measuring antenna over the entire measured frequency range is below -12 dB, which allows us to assert the effectiveness of signal transmission at these frequencies. The distance between the antennas satisfied the far-field criterion, and was also much larger than the characteristic size of the antenna array. The angular dependences of the realized gain (Fig. 2, *c*, *d*), blue) are based on the matrix of the S-parameters of the antenna and represent  $S_{21}$ -parameter taken at the same frequency using a rotary device and VNA. Fig. 2, *a* demonstrates the similarity between reflection coefficient from the simulation and from the real experiment. Numerical have shown that at 2 GHz, the antenna array has radiation pattern of single beam (inset in *b*). The discrepancies in this plot are explained by incomplete impedance matching of PCB structure and 3D emitters and irregularities in FR-4 substrate. Fig. 2 (*c* and *d*) shows a complete comparison of the emitted beam for a numerical experiment and for a real antenna array manufactured using additive technologies. It is noticeable that the results shown by the metallized antenna array agree well with the prediction of the computational algorithm. The gain is slightly lower due to additional losses in the dielectric, as well as power cables. The angle at the level of -3 dB from the main lobe remains, and the level of the side lobes remains approximately the same, which suggests that the signal will not have noticeable distortions when transmitting it using this antenna array.

### Conclusion

In this paper, a 2x2 antenna array with three-dimensional emitters was described, manufactured using additive 3D printing technologies and selective metallization in a galvanic solution. Numerical simulation predicted results of the antenna array performance, and the results obtained in a real experiment coincide with the data of the computational algorithm with high accuracy. Thus, 3D antenna arrays can be used for receiving and transmitting information.

### Acknowledgments

The research was supported by of the Federal Academic ILeadership Program Priority 2030.

### REFERENCES

1. Dilberoglu U. M., Gharehpapagh B., Yaman U., Dolen M., The Role of Additive Manufacturing in the Era of Industry 4.0, *Procedia Manuf.* 11 (2017) 545–554.
2. Kruth J. P., Leu M. C., Nakagawa T., Progress in Additive Manufacturing and Rapid Prototyping, *CIRP Ann.* 47(2) (1998) 525–540.
3. Roy N. K., Behera D., Dibua O. G., Foong C. S., Cullinan M. A., A novel microscale selective laser sintering ( $\mu$ -SLS) process for the fabrication of microelectronic parts, *Microsystems Nanoeng.* 5(1) (2019) 1–14.
4. Pandey R., et al., Highly Conductive Copper Film on Inkjet-Printed Porous Silver Seed for Flexible Electronics, *J. Electrochem. Soc.* 165(5) (2018) D236.
5. Ferrando-Rocher M., Herranz-Herruzo J. I., Valero-Nogueira A., Bernardo-Clemente B., Selective Laser Sintering Manufacturing as a Low Cost Alternative for Flat-Panel Antennas in Millimeter-Wave Bands, *IEEE Access.* 9 (2021) 45721–45729.
6. Sigmarsson H., Kinzel E., Chappell W., Xu X., Selective laser sintering of patch antennas on FR4, *IEEE Antennas Propag. Soc. AP-S Int. Symp.* 1 (2005) A 280–283.

7. **Kazani I., et al.**, Performance study of screen-printed textile antennas after repeated washing, *Autex Res. J.* 14(2) (2014) 47–54.
8. **Merilampi S. L., Bjorninen T., Vuorimaki A., Ukkonen L., Ruuskanen P., Sydanheimo L.**, The effect of conductive ink layer thickness on the functioning of printed UHF RFID antennas, *Proc. IEEE*. 98(9) (2010) 1610–1619.
9. **Kim D., Moon J.**, Highly conductive ink jet printed films of nanosilver particles for printable electronics, *Electrochem. Solid-State Lett.* 8(11) (2005) J30.
10. **Olejník R., Goňa S., Slobodian P., Matyáš J., Moučka R., Daňová R.**, Polyurethane-Carbon Nanotubes Composite Dual Band Antenna for Wearable Applications, *Polym.* 12(11) (2020) 2759.
11. **Maurya D., et al.**, 3D printed graphene-based self-powered strain sensors for smart tires in autonomous vehicles, *Nat. Commun.* 11(1) (2020) 1–10.
12. **Ferrando-Rocher M., Herranz J. I., Valero-Nogueira A., Bernardo B.**, Performance Assessment of Gap Waveguide Array Antennas: CNC Milling vs. 3D Printing, *IEEE Antennas Wirel. Propag. Lett.* 1225(c) (2018) 1–1.
13. **Liang M., Wu J., Yu X.**, 3D printing technology for RF and THz antennas, *IEEE*, (2) (2016) 536–537.
14. **Kyovtorov V., Georgiev I., Margenov S., Stoychev D., Oliveri F., Tarchi D.**, New antenna design approach – 3D polymer printing and metallization. experimental test at 14–18 GHz, *AEU - Int. J. Electron. Commun.* 73 (2017) 119–128.
15. **Thévenard J., Lo Hine Tong D., Louzir A., Nicolas C., Person C., Coupez J. P.**, 3D multi-sector vivaldi antennas based on metallized plastic technology, *IEEE Antennas Propag. Soc. AP-S Int. Symp.* (2007) 5849–5852.
16. **Filonov D., Kolen S., Shmidt A., Shacham-Diamand Y., Boag A., Ginzburg P.**, Volumetric 3D-Printed Antennas, Manufactured via Selective Polymer Metallization, *Phys. status solidi – Rapid Res. Lett.* 13(6) (2019).
17. **Nicolson A. M., Ross G. F.**, Measurement of the Intrinsic Properties Of Materials by Time-Domain Techniques, *IEEE Trans. Instrum. Meas.* 19(4) (1970) 377–382.
18. **Janaswamy R., Schaubert D. H.**, Characteristic Impedance of a Wide Slotline on Low-Permittivity Substrates, *IEEE Trans. Microw. Theory Tech.* 34(8) (1986) 900–902.
19. **Ramzan R., Siddiqui O. F., Arshad M. W., Ramahi O. M.**, A Complex Permittivity Extraction Method Based on Anomalous Dispersion, *IEEE Trans. Microw. Theory Tech.* 64(11) (2016) 3787–3796.
20. **Lu X., et al.**, A ceramic-based microwave sensor for both permittivity and permeability characterization of materials, *J. Phys. D. Appl. Phys.* 53(34) (2020) 345103.
21. **Siddiqui O., Ramzan R., Amin M., Ramahi O. M.**, A Non-Invasive Phase Sensor for Permittivity and Moisture Estimation Based on Anomalous Dispersion, *Sci. Rep.* 6(1) (2016) 1–9.
22. **Burtsev V., Vosheva T., Filonov D.**, Extracting Dielectric Permittivity with a Cross-Like Stripline, *J. Phys. Conf. Ser.* 2015(1) (2021) 012026.
23. **Burtsev V. D., Vosheva T. S., Khudykin A. A., Ginzburg P., Filonov D. S.**, Simple low-cost 3D metal printing via plastic skeleton burning, *Sci. Rep.* 12(1) (2022) 7963.
24. **Santarelli S., et al.**, Military antenna design using simple and competent genetic algorithms, *Math. Comput. Model.* 43(9–10) (2006) 990–1022.

## THE AUTHORS

**BURTSEV Vladimir**  
 burtsev.vd@phystech.edu  
 ORCID: 0000-0002-7988-5213

**KHUDYKIN Anton**  
 khudykin.aa@mipt.ru  
 ORCID: 0000-0001-7992-7981

**ROGOZHKIN Kirill**  
 rogozhkinkirill@gmail.com

**FILONOV Dmitry**  
 filonov.ds@mipt.ru  
 ORCID: 0000-0002-5394-8677

**VOSHEVA Tatyana**  
 Vosheva.ts@mipt.ru  
 ORCID: 0000-0002-5786-4972

*Received 30.08.2022. Approved after reviewing 09.09.2022. Accepted 09.09.2022.*

© Peter the Great St. Petersburg Polytechnic University, 2022

Conference materials

UDC 537.86

DOI: <https://doi.org/10.18721/JPM.153.272>

### RFID-based sensor for insect detection

N. O. Bulatov <sup>1</sup>✉, T. S. Vosheva <sup>1</sup>, A. A. Khudykin <sup>2</sup>, D. S. Filonov <sup>1</sup>

<sup>1</sup> Moscow Institute of Physics and Technology, Moscow, Russia

✉ [separatast@gmail.com](mailto:separatast@gmail.com)

**Abstract.** Real-time monitoring of insects is an important objective across many life-science disciplines. Here we demonstrate the first of its kind disposable wireless detector, capable of monitoring insect activity. Our solution is based on an indirect indicator, based on sugar consumption by insects. We develop a caramel-based antenna device, linked with an RFID chip. Apart from its nutrition value, caramel is a dielectric material, affecting electromagnetic interactions between waves and matter. Being consumed by insects, changes the electromagnetic properties of the antenna, deactivating the tag. The failure in the readout suggests an active presence of insects in the surrounding. Adding control bits, weather sustainability, and other functions, required for a reliable outdoor operation, will be reported in the future.

**Keywords:** RFID, insect detection, microwave sensor, agricultural monitoring

**Funding:** The study was supported by the federal academic leadership program Priority-2030.

**Citation:** Bulatov N. O., Vosheva T. S., Khudykin A. A., Filonov D. S., RFID-based sensor for insect detection, St. Petersburg State Polytechnical University Journal. Physics and Mathematics. 15 (3.2) (2022) 393–398. DOI: <https://doi.org/10.18721/JPM.153.272>

This is an open access article under the CC BY-NC 4.0 license (<https://creativecommons.org/licenses/by-nc/4.0/>)

Материалы конференции

УДК 537.86

DOI: <https://doi.org/10.18721/JPM.153.272>

### RFID сенсор для детектирования насекомых

Н. О. Булатов <sup>1</sup>✉, Т. С. Вошева <sup>1</sup>, А. А. Худыкин <sup>1</sup>, Д. С. Филонов <sup>1</sup>

<sup>1</sup> Московский физико-технический институт, г. Долгопрудный, Россия

✉ [separatast@gmail.com](mailto:separatast@gmail.com)

**Аннотация.** Мониторинг насекомых в режиме реального времени является важной задачей во аспектах естественных наук. В данной работе мы демонстрируем первый в своем роде беспроводной сенсор-расходник, способный отслеживать активность насекомых. Наше решение основано на наблюдениях о потреблении насекомыми частиц сахара, в результате чего разрабатывается антенное устройство на карамельной основе, связанное с RFID-чипом. Помимо своей питательной ценности, карамель является диэлектрическим материалом, влияющим на взаимодействие между электромагнитными волнами и веществом. Поедание карамели насекомыми изменяет геометрию метки и, как следствие, электромагнитные свойства антенны, деактивируя метку. Особенности в показаниях детектора говорят о наличии насекомых в окружающей среде. Также о добавлении управляющих элементов, об устойчивости к погодным условиям и других функциях, необходимых для надежной работы на открытом воздухе, будет сообщено в будущем.

**Ключевые слова:** RFID, детектор насекомых, СВЧ сенсор, мониторинг в сельском хозяйстве

**Финансирование:** Работа выполнена в рамках федеральной академической передовой программы «Приоритет 2030».

**Ссылка при цитировании:** Булатов Н. О., Вошева Т. С., Худыкин А. А., Филонов Д. С. RFID сенсор для детектирования насекомых // Научно-технические ведомости СПбГПУ. Физико-математические науки. Т. 15. № 3.2. С. 393–398. DOI: <https://doi.org/10.18721/JPM.153.272>

Статья открытого доступа, распространяемая по лицензии CC BY-NC 4.0 (<https://creativecommons.org/licenses/by-nc/4.0/>)

### Introduction

Real-time monitoring of the distribution, migration, and population of insects provides valuable information in ecology, agriculture, and other life science disciplines. Quite a few methods of detection and monitoring have been developed. These include components, driven by optical, acoustic, acousto-optic, chemical, radiofrequency-based, and other elements [1–6]. The vast majority of the devices are based on active sensing schemes and therefore require power sources. The main fundamental challenge, faced by radiofrequency approaches, is the small size of insects relative to operational wavelengths. For example, the average size of ants is 3.5–5.5 mm, which makes them weakly interact with electromagnetic waves owing to characteristic size mismatch and relatively low average refractive index. A probable solution to this problem is shifting operation frequencies towards the sub-terahertz region. However, the penalty of this approach is high atmospheric decay, making the wireless detection extremely short-range and not practical. Camera-based monitoring is an appealing solution but comes with a penalty if an elevated cost.

Here we propose a sensor, based on mature RFID technology. Capable to accommodate multiple information bits with a capability of a mid-range interrogation (typically, several meters for passive schemes), RFID tags were used to monitor migrations of bees and bumblebees [7, 8]. However, only a limited number of species were labeled to make statistical estimates of the population behavior. Furthermore, this approach is inapplicable to most species, which cannot be RFID-labeled owing to their small size, appearance, and other possible constraints. Pests monitoring is also not possible owing to their rather unexpected appearance.

Our proposed solution is based on an indirect indicator, based on sugar consumption by insects. We develop a caramel-based antenna device, linked with an RFID chip. Apart from its nutrition value, caramel is a dielectric material, affecting electromagnetic interactions between waves and matter. It is well-known that placing a dielectric in the vicinity of an RFID tag can change its resonant frequency, antenna gain, efficiency, and other electromagnetic parameters [9, 10]. Here we use this concept and functionalize a tag with a biodegradable dielectric. Being consumed by insects, changes the electromagnetic properties of the antenna, deactivating the tag. The failure in the read-out suggests an active presence of insect in the surrounding. Adding control bits, weather sustainability, and other functions, required for a reliable outdoor operation, will be reported in the future.

### Geometry and design

The basic structure of the proposed RFID sensor is PCB meander whose configuration and parameters is shown in Fig. 1 and summarized in Table 1. The proposed design is printed on 1 mm FR-4 substrate with 36  $\mu\text{m}$  copper metal layer. Chosen geometry of tag reduced overall size (40 x 40  $\text{mm}^2$ ) related to UHF RFID wavelength (370–330 mm) and increase thickness homogeneity of caramel layer during manual crafting. Other geometric characteristics is shown in Table 1. Lumped port with 20 ohm impedance replaces IC chip. Dielectric properties of caramel are  $\epsilon = 3$  (without dispersion) and  $\text{tg}\delta = 0$  (in the model loss in caramel is neglected). Numerical simulation of sensor shows its high sensitivity to caramel layer thickness as a resonant structure.

Table 1

Dimensions of RFID tag

$L_1$	$L_2$	$w_1$	$w_2$
36.5	32.5	3.4	1.4

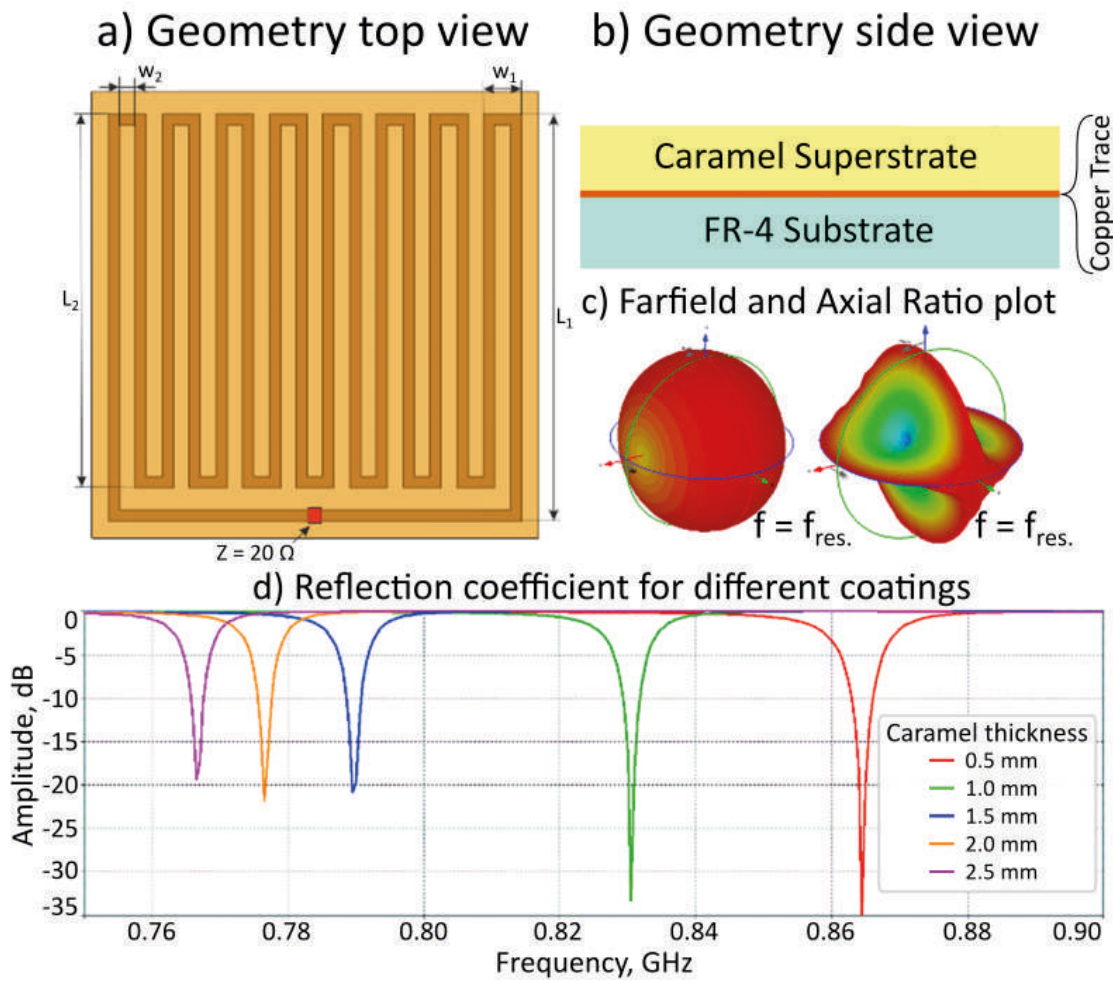


Fig. 1. Proposed design of sensor with tag geometry of tag in top view (a) and side view (b) Properties of model sensor: far-field and axial ratio 3D plots on resonant frequency of tag (c), influence of caramel layer thickness on tag resonance position (d)

### Results and Discussion

Measurements of the passive RFID tag were based on the near-field response. For this purpose, a special magnetic probe, sensitive to electro-dynamics structures, was numerically simulated (Fig. 2) and fabricated (Fig. 3,a). Its own first eigenmode is much higher in frequency (Fig. 4, orange circle) than the expected resonance of the tag, thus there was no coupling between them. The distance between the sensor and the magnetic probe is 2 mm.

The probe diameter is 40 mm, feeder length 110 mm and gap size 4.5 mm. Special labels were applied on its top (Fig. 3,b) to simplify the placement of the tag (Fig. 3,c).

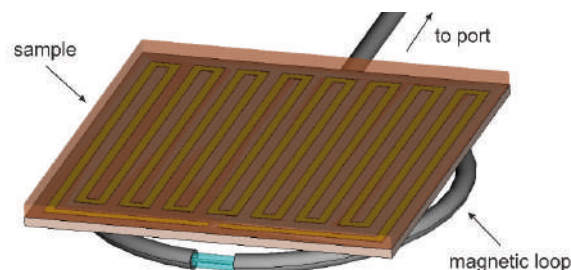


Fig. 2. Sensor model taking into account the influence of the magnetic loop

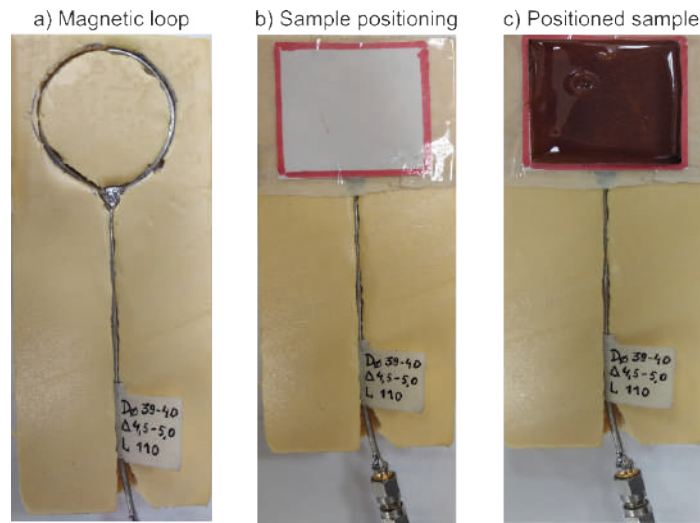


Fig. 3. Measurement setup: standalone probe on a stand (a), probe with a sample positioning mark (b) and probe with a positioned sample (c)

General setup Near-field probe measurements

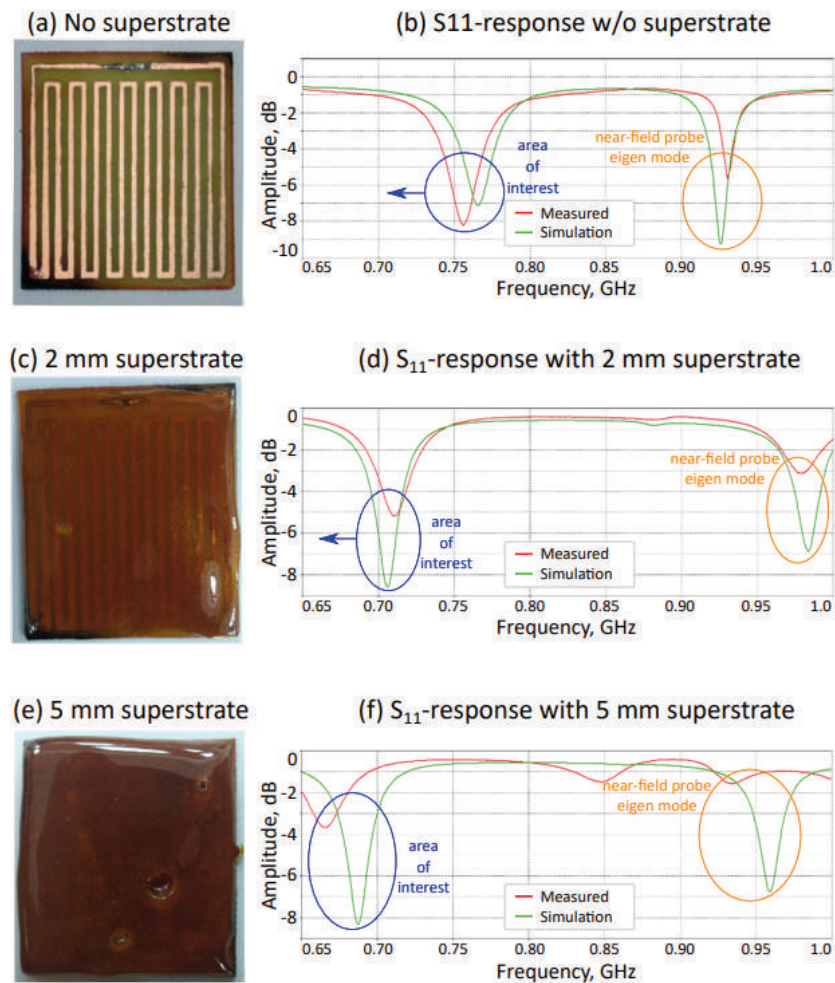


Fig. 4. Manufactured RFID tags without caramel superstrate (a), with 2 mm (c) and 5 mm of caramel thickness (e) and their  $S$  parameters (b, d and f, respectively)



Three samples were analyzed numerically, manufactured and then measured (near-field measurements of  $S_{11}$  parameters via magnetic loop). The first of them does not have caramel layer, the second is covered with only 2 mm thickness superstrate and the third one has 5 mm thickness overlayer. Fig. 4, *b, d, f* illustrates the positioning dynamics of the RFID tag resonance (blue circle) depending on the changing thickness of the caramel coating. It is noticeable that, according to the expectations and to the numerical experiment (Fig. 4, *b, d, f*), green curve), the greater the superstrate thickness, the lower the resonance frequency, while the eigen frequency of the probe still lies much higher and does not affect the structure.

The results show general convergence between the numerical simulation data and experimental data. While the convergence remains high at small coating thickness (Fig. 4 (d)), for large thickness (Fig. 4, *f*), the uniformity of the layer starts to play a leading role, which can cause additional discrepancy.

At the same time, it is important to note that in this frequency range, a caramel covered tag can not have a second resonance, as long as it retains the original geometry of the metal. Therefore, when describing the interaction of insects with the tag, even allowing for an uneven coating it with caramel at an arbitrary moment in time, it is possible to describe the superstrate using an effective dielectric permittivity index. Thus, keeping the fact that the RFID reader's channel bandwidth is quite narrow (about 20 MHz), it can be concluded that the label maintains the ability to enter or exit this range when the coating thickness changes. At the same time, due to the continuity and unambiguity of the impact of insects on the caramel, such an event as described will occur only once and will immediately activate the detector.

In continuation of this study it is required to measure dielectric characteristics of caramel and obtain precise convergence of model and experiments. The current task is to make additional samples and increase the homogeneity of caramel thickness.

### Conclusion

The relationship with caramel covering layer thickness and resonant frequency of structure was shown. In addition, the possibility of using caramel covering RFID tag for insect detection was demonstrated.

### Acknowledgments

The research was supported by of the federal academic leadership program Priority 2030.

### REFERENCES

1. **Lu J., et al.**, Monitoring of Flying Insects using a Dual-Wavelength CW Lidar System, 2019 Asia Communications and Photonics Conference (ACP), 2019 1–3.
2. **Izumi K., Ishibashi S., Tsujimura T.**, Exploring of gas source location using behavioral model of insects, 2017 56th Annual Conference of the Society of Instrument and Control Engineers of Japan, SICE 2017, vol. 2017–November 180–181, Nov. 2017, doi: 10.23919/SICE.2017.8105747.
3. **Pan W., Kong X., Xu J., Pan W.**, Measurement and analysis system of vibration for the detection of insect acoustic signals, 2016 Asia-Pacific International Symposium on Electromagnetic Compatibility, APEMC 2016 1090–1092, Jul. 2016, doi: 10.1109/APEMC.2016.7522953.
4. **Wu H. Y., et al.**, A Bio-Inspired Motion Detection Circuit Model for the Computation of Optical Flow: The Spatial-Temporal Filtering Reichardt Model, 2021 IEEE 3rd International Conference on Artificial Intelligence Circuits and Systems, AICAS 2021, Jun. 2021, doi: 10.1109/AICAS51828.2021.9458450.
5. **Makuhin A. A., Vybornov N. A., Likhter A. M.**, Selective sources' using of the electromagnetic radiation in the optical range detection and collecting systems of Colorado Beetle, Conference Proceedings - 2014 International Conference on Actual Problems of Electron Devices Engineering, APEDE 2014, vol. 2 300–307, Nov. 2014, doi: 10.1109/APEDE.2014.6958266.
6. **Tahir N., Brooker G.**, The investigation of millimetre wave optical harmonic transponders and radar for monitoring small insects, WiSNet 2013 - Proceedings: 2013 IEEE Topical Conference on Wireless Sensors and Sensor Networks - 2013 IEEE Radio and Wireless Week, RWW 2013 22–24, 2013, doi: 10.1109/WISNET.2013.6488621.
7. **P. de Souza et al.**, Low-Cost Electronic Tagging System for Bee Monitoring, Sensors 2018, Vol. 18, Page 2124, vol. 18, no. 7, p. 2124, Jul. 2018, doi: 10.3390/S18072124.

8. **Barlow S. E., O'Neill M. A., Pavlik B. M.**, A prototype RFID tag for detecting bumblebee visitations within fragmented landscapes, *Journal of Biological Engineering*, vol. 13, no. 1, Feb. 2019, doi: 10.1186/S13036-019-0143-X.

9. **Yunos M. F. A. M., et al.**, RF Remote Blood Glucose Sensor and a Microfluidic Vascular Phantom for Sensor Validation, *Biosensors 2021*, Vol. 11, Page 494, vol. 11, no. 12, p. 494, Dec. 2021, doi: 10.3390/BIOS11120494.

10. **Gao M., Qiang T., Ma Y., Liang J., Jiang Y.**, RFID-Based Microwave Biosensor for Non-Contact Detection of Glucose Solution, *Biosensors*.

#### THE AUTHORS

**BULATOV Nikita**

separatast@gmail.com

ORCID: 0000-0003-1145-3075

**KHUDYKIN Anton**

khudykin.aa@mipt.ru

ORCID: 0000-0001-7992-7981

**VOSHEVA Tatyana**

vosheva.ts@mipt.ru

ORCID: 0000-0002-5786-4972

**FILONOV Dmitriy**

dimfilonov@gmail.com

ORCID: 0000-0002-5394-8677

*Received 30.08.2022. Approved after reviewing 09.09.2022. Accepted 09.09.2022.*

Conference materials

UDC 53.089

DOI: <https://doi.org/10.18721/JPM.153.273>

## Design improvements of nuclear magnetic resonance magnetometer to study magnetic mid-fields variations

N. S. Myazin <sup>1</sup>✉, V. V. Davydov <sup>1, 2, 3</sup>

<sup>1</sup> Peter the Great St. Petersburg Polytechnic University, St. Petersburg, Russia;

<sup>2</sup> Bonch-Bruевич Saint Petersburg State University of Telecommunications, St. Petersburg, Russia;

<sup>3</sup> All-Russian Research Institute of Phytopathology, Moscow Region, Russia

✉ [myazin.n@list.ru](mailto:myazin.n@list.ru)

**Abstract.** The necessity to develop a magnetometer for variations research in the mid-fields magnetic strength with a relative error of  $10^{-6}$  is justified. A modernization design of magnetometer to nuclear magnetic resonance with using to maser with flowing liquid is presented. The block diagram of nuclear magnetic resonance magnetometer is given. The core principle of its working is described. The results of experimental investigations of various variations to magnetic fields are presented. Further directions of modernization of the design of the magnetometer are determined.

**Keywords:** nuclear magnetic resonance, magnetic field, magnetometer, magnetic field variations, maser

**Funding:** The study was funded by RFBR as part of research project 2032-90012.

**Citation:** Myazin N. S., Davydov V. V., Design improvements of nuclear magnetic resonance magnetometer to study magnetic mid-fields variations, St. Petersburg State Polytechnical University Journal. Physics and Mathematics. 15 (3.2) (2022) 399–405. DOI: <https://doi.org/10.18721/JPM.153.273>

This is an open access article under the CC BY-NC 4.0 license (<https://creativecommons.org/licenses/by-nc/4.0/>)

Материалы конференции

УДК 53.089

DOI: <https://doi.org/10.18721/JPM.153.273>

## Модернизация конструкции магнетометра на ядерном магнитном резонансе для исследования вариаций средних магнитных полей

Н. С. Мязин <sup>1</sup>✉, В. В. Давыдов <sup>1, 2, 3</sup>

<sup>1</sup> Санкт-Петербургский политехнический университет Петра Великого, Санкт-Петербург, Россия;

<sup>2</sup> Санкт-Петербургский государственный университет телекоммуникаций им. проф. М. А. Бонч-Бруевича, Санкт-Петербург, Россия;

<sup>3</sup> Всероссийский научно-исследовательский институт фитопатологии, Московская область, Россия

✉ [myazin.n@list.ru](mailto:myazin.n@list.ru)

**Аннотация.** Обоснована необходимость разработки магнитометра для исследования вариаций средней напряженности магнитного поля с относительной погрешностью  $10^{-6}$ . Представлена конструкция модернизации магнитометра до ядерного магнитного резонанса с использованием мазера с проточной жидкостью. Приведена блок-схема магнитометра ядерного магнитного резонанса. Подробно представлен принцип его работы. Представлены результаты экспериментальных исследований различных вариаций магнитных полей. Определены дальнейшие направления модернизации конструкции магнитометра.

**Ключевые слова:** ядерный магнитный резонанс, магнитометр, магнитное поле, вариации магнитного поля, мазер

**Финансирование:** Исследование выполнено при финансовой поддержке РФФИ в рамках научного проекта № 2032-90012.

**Ссылка при цитировании:** Мязин Н. С., Давыдов В. В. Модернизация конструкции магнетометра на ядерном магнитном резонансе для исследования вариаций средних магнитных полей // Научно-технические ведомости СПбГПУ. Физико-математические науки. Т. 15. № 3.2. С. 399–405. DOI: <https://doi.org/10.18721/JPM.153.273>

Статья открытого доступа, распространяемая по лицензии CC BY-NC 4.0 (<https://creativecommons.org/licenses/by-nc/4.0/>)

### Introduction

The development of technological progress and scientific investigations has led to an increase in the number of negative factors affecting various processes. [1–9]. A wide variety of negative factors led to the development of various instruments for measuring different kinds of physical parameters [10–19]. One of these parameters is the magnetic field [20–25], the amplitude and variation of which contains a lot of useful information [22–30]. That’s why recently more and more areas of science and technologies have started demanding a lot of data on the magnetic field properties and characteristics [26–32]. Usually, it means that magnetic fields parameters must be measured and controlled with high accuracy. Such kind of problems can be successfully solved with modern devices like quantum magnetometers (which are based on nuclear magnetic resonance (NMR)). They are one of most precise devices for measuring magnetic fields variations. [17, 18, 21, 30–33]. It should be noted that there are several designs to such nuclear-magnetic magnetometers. The very popular ones include devices based on a nuclear resonance filter [31]. In this device is realized to the frequency of the passive NMR line and the spin generator of phase or frequency self-tuning of the external generator frequency [32]. However, they do have disadvantages. For example, the first one has quite narrow NMR line, thus imposes grand demands for the tracking system. Because of it, several measurement problems occur. For example, temperature variations can cause noticeable significant dynamic errors. There are solutions to this issue, but they significantly complicate the overall device design.

Because of the reasons mentioned above, most of the industrial models of the quantum NMR magnetometers usually have upper limit around 100  $\mu\text{T}$ . There are custom versions of these devices with upper limit of measurement before value of 0.0002 T, but they specifically designed to solve a small set of tasks. Overall, the values of the magnetic field were discussed above belong to so called low magnetic fields. However, the invention of generations of devices like particle accelerators, tokamaks, tracking devices for underwater objects requires new generations of magnetometers that will be able to measure the parameters of magnetic field in the diapason from 0.0002 to 0.2 mT with a relative error of measurement no more than 0.000001.

Nowadays, strength of the magnetic in in so called mid-fields ( $0.0002 \text{ T} < B < 1.0 \text{ T}$ ) is measured using the Hall effect magnetometers. However, even one of the best devices in this area (magnetic induction meter DX-180) has a relative error of measurement is the value of 0.000050.0005 in the measurement range from 0.01 mT to 300 mT with a resolution of 10100 nT. Therefore, it is extremely relevant to develop a new magnetometer design that will allow making measurements with a relative error no more than 0.000001.

### Experiment and theory

Results of the analysis of current scientific state have shown that there is in fact only one manuscript that has been presented in the open sources and covers this topic [34]. This paper considers a scheme for self-tuning to the receiving circuit NMR resonant frequency of a maser with a flowing medium. Unfortunately, the data presented in [35] do not provide all required details, which prevents from full understanding of the device features. Also, it was found to be quite hard to reproduce the device design which is crucial to make required modifications to perform measuring of variations in mid-field magnetic strength in a wide range. This is vital for solving special tasks. Therefore, this article provides a detailed description of magnetometers components, as well as its structural diagram. The magnetometer is based on a maser with a flowing medium. In addition, the maser implements automatic tuning to the frequency of the NMR signal from the center of the generation zone.

Fig. 1 shows the structure scheme of the magnetometer developed by us. In time a development of NMR magnetometer we used the data about the Benoit maser [35]. A mixture of alcohol and filtered tap water is used as a liquid.

Centrifugal pump 1 allows to vary consumption  $q$  from 0 to 0.020 l/s. The polarized vessel 3 is placed in magnet 2 (polarizer). Its magnet has an induction  $B_p = 1250$  mT. The mixture magnetizes of magnet 2. Inverse population of the flowing liquid molecules is created by inverse coil 4 and radiofrequency generator 5. Not that inversion coil 4 is located in the magnet 3 stray field. Protons with the inverted (negative) magnetization are passed to the sensor 7 (for measuring magnetic field), which is located in electromagnet 6 that has an induction  $B_E$  (can take magnitude from 0 to 230 mT). The presented magnetometer uses 26 sensors. This allows us to measure the variations of magnetic field in the diapason from 0.2 to 200 mT.

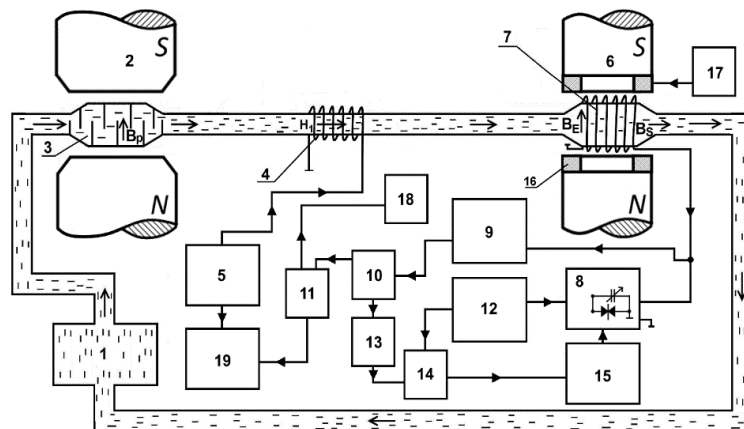


Fig. 1. Block diagram of a nuclear magnetic magnetometer: centrifugal pump 1, polarizer magnet 2, polarizer vessel 3, pulse coil of water proton magnetization inversion 4, radiofrequency generator 5, electromagnet 6, measuring sensor 7, receiving circuit 8, regenerator 9, resonance amplifier 10, registration device 11, low-frequency generator 12, low-frequency amplifier 13, synchronous detector 14, control circuit 15, excitation coils 16, pulse radiofrequency generator 17, oscilloscope 18 and frequency meter 19

Let us describe in detail how the magnetometer works with one of the sensors that allows measurements of field variations in the diapason  $60 \pm 13$  mT. Measuring sensor 7 is a coil of 40 turns of copper wire with a winding length of 3 mm and a winding duty cycle  $\eta = 0.2$ . The receiving circuit intrinsic quality factor at frequency  $f_{\text{nmr}} = 2500$  kHz of nuclear magnetic resonance has a value of more than 30. This circuit includes the coil of the measuring sensor 7 and is connected to the regenerator 9 input. In the developed by us of magnetometer design, it was decided to adjust level of positive feedback in the receiving circuit  $Q_c$  in order to compensate for the losses during the signal registration of nuclear magnetic resonance. To measure magnetic field variations in other sources, for example,  $43 \pm 14$  mT, it is necessary to use another sensor 7.

This allowed to set  $Q_c$  set higher than the threshold quality factor of self-excitation that is equal to  $Q_c^{\text{th}} = 350$ . The generation EMF is created by magnetic moments of protons that are passed into the receiving circuit and then is amplified by resonance amplifier 10 with amplification bandwidth of 0.17 MHz and then is registered in the registration scheme 11. The frequency and the overall shape of the NMR signal is being monitored using an oscilloscope and a frequency meter that are connected to the registration scheme 11. It should be noted that by changing the capacitance of the receiving system it is possible to reconfig. the maser generation zone. This is possible because it includes two oppositely connected variable capacitors (so called varicaps) that are connected to the audio generator 12 which provides an auxiliary voltage with a frequency of 10 to 20 Hz. The provided voltage basically modulates the circuit resonance frequency, which in turn modulates the voltage amplitude of the maser generation. Then, the low-frequency amplifier 13 detects the value of the modulated signal which comes from the resonant amplifier 10. Then the signal is passed to the synchronous detector 14. Note that this detector also has an input that

receives the voltage, which is the reference, created by the generator 12. If there is a detuning between the maser generation frequency and the resonant frequency of the receiving circuit, then at the output of the synchronous detector 13 a control voltage appears. This voltage is of interest because its sign and amplitude are proportional to the detuning. That's why it is fed to the control scheme 15 which was developed and assembled using integrated operational amplifiers. Finally, this signal is passed to varicaps that allows to control the receiving circuit resonant frequency thus adjusting it to the resonant line center.

The transverse relaxation time  $T_2$  can be evaluated in two ways:

- by exciting the spin system with a  $\pi/2$  pulse and measuring the free induction signal decay time;
- by modulating the magnetic field while disconnecting generator 5 from nutation coils 4 and switching the regenerator to self-excitation mode, and measuring the NMR signal decay time.

Having the relaxation time value determined, variations of the magnetic field strength can be evaluated as follows:

$$\Delta\omega_{\max} = \frac{1}{\left(T_2 \sqrt{\frac{Q_c}{Q_0} - 1}\right)}, \quad (1)$$

where  $Q_c$  is the receiving circuit quality factor and  $Q_0$  is the threshold quality factor at zero detuning.

The measurement error of the magnetic field in the developed magnetometer is determined as follows. Measurements of the induction  $B_0$  are carried out at the resonant frequency of protons (frequency measurements).

$$\gamma B_0 = \omega_0. \quad (2)$$

The frequency value  $\omega_0$  is determined using a modern frequency comparator (for example, on a gas rubidium cell or a cesium atomic beam tube) with an accuracy of  $10^{-9}$ . The gyromagnetic ratio  $\gamma$  for protons is determined with an accuracy of  $10^{-7}$ . According to the rules of indirect measurements, the  $B_0$  measurement error will be no worse than  $10^{-6}$ . The signal-to-noise ratio during measurements should be greater than 3.5 for direct measurements or greater than 1.5 for accumulation measurements. In the developed magnetometer, the signal-to-noise ratio is greater than 5. If necessary, it can be increased at least 2–3 times by increasing the induction  $B_p$  of the polarizer magnet. The higher the magnetization of the flowing liquid, the higher the signal-to-noise ratio of the registered NMR signal.

To obtain a higher accuracy for all NMR magnetometers operating at the resonant frequency of protons, it is necessary to determine the value of  $\gamma$  with an error of  $10^{-8}$  or less.

### Experimental results and discussion

An example of the NMR signal registered with using the modulation of the magnetic field  $B_E = 59.52$  mT is shown in Fig. 2. The envelope decay of the signal peaks is used to determine the transverse relaxation effective time  $T_2^*$  of the media (in this case, it is a flowing liquid). Specifically,  $T_2^*$  is measuring by the decrease in NMR signal amplitude in range from  $U_{\max}$  to  $U_t = U_{\max}/10$ .

Knowing the effective relaxation time, it is possible to determine the relaxation time  $T_2$  as follows:

$$\frac{1}{T_2^*} = \frac{1}{T_2} + \frac{\gamma^* \Delta H}{\pi}, \quad (3)$$

where  $\Delta H$  is the magnetic field uniformity in the in the place of the sensor 7.

The magnetic field uniformity is roughly equal to  $10^{-4}$  cm<sup>-1</sup> in the magnetometer design considered in this paper.

The magnetization  $M_0$  of a liquid entering the sensor 7 is one of the important characteristics for performing measurements. That is because the amplitude of the recorded NMR signal is proportional to the value of magnetization  $M_0$ . Therefore, the higher the  $M_0$  value, the higher the measurement accuracy of the magnetic field variation. Thus, it is feasible to conduct research on the correlation between flow rate  $q$  and the NMR signal amplitude  $U$  using the considered sensor 7. Results of this research are shown in Fig. 3.

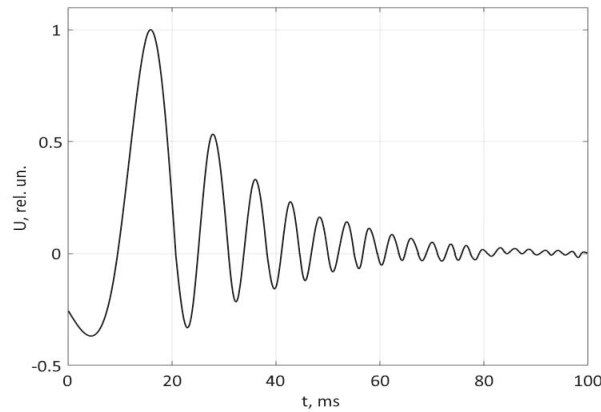


Fig. 2. Registered NMR signal from a mixture of alcohol with filtered tap water at  $T = 295.3$  K

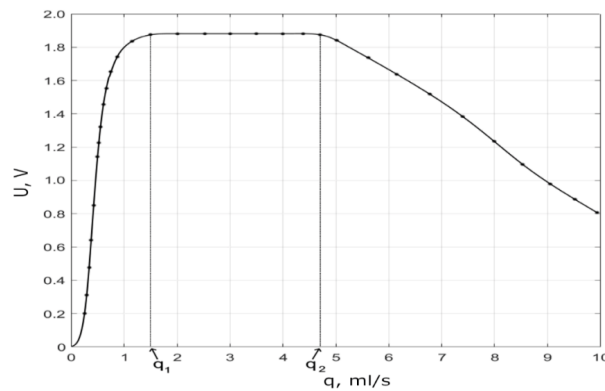


Fig. 3. Dependence of the NMR signal amplitude  $U$  on the flow rate  $q$  of a mixture of alcohol with a filtered tap water at  $T = 295.3$  K

According to the results of the research, there is a fairly wide range of a flow rate  $q$  in which the signal-to-noise (SNR) ratio is high enough (i.e., more than 20). Specifically, this range is from  $q_1 = 0.02 \pm 1.59$  ml/s to  $q_2 = 0.05 \pm 4.74$  ml/s. If the device operates in this range, significant changes in the flow rate (up to 10 %) will not affect the measurement error if the overall flowrate is close to the middle of the range.

Using the obtained data, the transverse relaxation time  $T_2$  was determined in two described above ways for fluid flow  $q = 0.02 \pm 2.99$  ml/s. The result of the free induction decay method is  $T_2 = 0.18 \pm 23.21$  ms. The result of the free magnetic field modulation is  $T_2 = 0.23 \pm 23.04$  ms. It should be noted that in order to estimate a measurement error using standard methods, in both cases measurements were repeated 10 times with subsequent data averaging.

Also, to additionally validate the obtained data, characteristics of the same solution at the temperature  $T = 294.9$  K were measured on a stationary NMR relaxometer Minispec mq 20M (made by BRUKER company). The measured value was  $T_2 = 0.065 \pm 23.198$  ms. Thus, it can be concluded that all obtained transverse relaxation time values coincided within the measurement error.

### Conclusion

The results of research have showed that the self-generating NMR magnetometer considered in this paper allows measuring variations of the magnetic field in the diapason of 0.2 to 200 mT. This becomes possible because magnetometer uses automatic tuning to center of the generation zone for the proton resonance frequency. What's more important, in both dynamic and static modes the relative measurement error doesn't exceed  $10^{-6}$  at input signal variations with frequency  $f_v \leq 0.25$  Hz and amplitude up to from  $5 \cdot 10^{-10}$  to  $2 \cdot 10^{-10}$  T, depending on the measuring range.

## REFERENCES

1. **Nikitina M., Grebenikova N., Dudkin V., Batov Y.**, Methodology for assessing the adverse effects of the use of nuclear energy on agricultural land, IOP Conference Series: Earth and Environmental Science. 390(1) (2019) 012024.
2. **Davydov R., Antonov V., Moroz A.**, Parameter Control System for a Nuclear Power Plant Based on Fiber-Optic Sensors and Communication Lines, In: IEEE International Conference on Electrical Engineering and Photonics (EExPolytech), Saint Petersburg, Russia, 13-15 October 2019. Vol. 8906791 (2019) 295–297.
3. **Kuzmin M. S., Rogov S. A.**, On the use of a multi-raster input of one-dimensional signals in two-dimensional optical correlators, Computer Optics. 43(3) (2019) 391–396.
4. **Gryznova E., Batov Y., Rud V.**, Methodology for assessing the environmental characteristics of various methods of generating electricity, E3S Web of Conferences. 140 (2019) 09001.
5. **Grebenikova N. M., Smirnov K. J., Rud V. Yu., Artemiev V. V.**, Features of monitoring the state of the liquid medium by refractometer, Journal of Physics: Conference Series. 1135(1) (2018) 012055.
6. **Davydov V. V.**, Determination of the Composition and Concentrations of the Components of Mixtures of Hydrocarbon Media in the Course of its Express Analysis, Measurement Techniques. 62(2) (2020) 1090–1098.
7. **Davydov R. V., Yushkova V. V., Stirmanov A. V., Rud V. Yu.**, A new method for monitoring the health condition based on nondestructive signals of laser radiation absorption and scattering, Journal of Physics: Conference Series. 1410(1) (2019) 012067.
8. **Mazing M. S., Zaitceva A. Yu., Kislyakov Yu. Ya., Kondakov N. S., Avdushenko S. A.**, Monitoring of Oxygen Supply of Human Tissues Using A Noninvasive Optical System Based on A MultiChannel Integrated Spectrum Analyzer, International Journal of Pharmaceutical Research. 12(2) (2020) 1974–1978.
9. **Davydov V. V., Davydova T. I.**, A nondestructive method for express testing of condensed media in ecological monitoring, Russian Journal of Nondestructive Testing. 53(7) (2017) 520–529.
10. **Grebenikova N. M., Smirnov K. J.**, Features of optical signals processing for monitoring the state of the flowing liquid medium with a refractometer, Journal of Physics: Conference Series. 1368(2) (2019) 022057.
11. **Antonov V.I., Davydov R.V., Maslikov V.I., Molodtsov D.V., Badenko V.L.**, Simulation of water flow management by the flood control facilities in the adjacent river basins, Journal of Physics: Conference Series. 1400(7) (2019) 077049.
12. **Davydov V. V., Kruzhalov S. V., Grebenikova N. M., Smirnov K. J.**, Method for Determining Defects on the Inner Walls of Tubing from the Velocity Distribution of the Flowing Fluid, Measurement Techniques. 61(4) (2018) 365–372.
13. **Dyumin V., Smirnov K.**, Charge-coupled Device with Integrated Electron Multiplication for Low Light Level Imaging, Proceedings of the 2019 IEEE International Conference on Electrical Engineering and Photonics, EExPolytech. 8906868 (2019) 308–310.
14. **Grevtseva A. S., Smirnov K. J., Rud V. Yu.**, Development of methods for results reliability raise during the diagnosis of a person's condition by pulse oximeter, Journal of Physics: Conference Series. 1135(1) (2018) 012056.
15. **Marusina M. Y., Karaseva E. A.**, Automatic segmentation of MRI images in dynamic programming mode Asian Pacific, Journal of Cancer Prevention. 19(10) (2018) 2771–2775.
16. **Marusina M. Ya., Karaseva E. A.**, Application of fractal analysis for estimation of structural changes of tissues on MRI images Russian Electronic Journal of Radiology. 8(3) (2018) 107–112.
17. **Gizatullin B., Gafurov M., Murzakhanov F., Mattea C., Stapf S.**, Molecular Dynamics and Proton Hyperpolarization via Synthetic and Crude Oil Porphyrin Complexes in Solid and Solution States, Langmuir. 37(22) (2021) 6783–6791.
18. **Rakhmatullin I., Efimov S., Tyurin V., Varfolomeev M., Klochkov V.**, Qualitative and quantitative analysis of heavy crude oil samples and their SARA fractions with <sup>13</sup>C nuclear magnetic resonance, Processes. 8(8) (2020) 995–1009.
19. **Shurtakova D.V., Yavkin B.V., Mamin G.V., Gafurov M.R., Komlev V.S.**, X-ray diffraction and multifrequency epr study of radiation-induced room temperature stable radicals in octacalcium phosphate, Radiation Research. 195(2) (2021) 200–210.



20. Sapunov V. A., Rasson J., Sergeev A. V., Rubinstein B. Y., Sapunov A. V., Application of overhauser DNP and K optics INTERMAGNET quantum magnetometers to fundamental physics and cosmology, *Magnetic Resonance in Solids*. 18(2) (2016) 16210.
21. Sapunov V.A., Denisov A.Y., Saveliev D.V., Sergeev A.V., Shirokov A.N., New vector/scalar overhauser DNP magnetometers POS-4 for magnetic observatories and directional oil drilling support, *Magnetic Resonance in Solids*. 18(2) (2016) 16209.
22. Kashaev R.S., Suntsov I.A., Tung C.V., Usachev A.E., Kozelkov O.V., Apparatus for Rapid Measurement of Oil Density and Molecular Mass Using Proton Magnetic Resonance, *Journal of Applied Spectroscopy*. 86(2) (2019) 289–293.
23. Davydov R.V., Dudkin V.I., Nikolaev D.I., Makeev S.S., Moroz A.V., Structure of a Nuclear Magnetic Resonance Signal in a Small Relaxometer, *Journal of Communications Technology and Electronics*. 66(5) (2021) 632–636.
24. Ryzhenko I.N., Lutsenko A.E., Varygin O.G., Nepomnyashchiy O.V., Carrier compensation mode implementation in satellite communication channels. In: *Proceedings of 2019 International Siberian Conference on Control and Communications, SIBCON 2019*, vol. 8729665 (2019) 23–29.
25. Petrov A. A., Zaletov D. V., Shapovalov D. V., Peculiarities of Constructing a Scheme for Formation of a Microwave Excitation Signal in a Cesium Atomic Clock, *Journal of Communications Technology and Electronics*. 66(3) (2021) 295–299.
26. Davydov V.V., Dudkin V.I., Karseev A.Y., A two-channel nutation nuclear-magnetic magnetometer for remote control of the magnetic-field induction, *Instruments and Experimental Techniques*. 58(6) (2015) 787–793.
27. D'yachenko S.V., Zhernovoi A.I., The Langevin formula for describing the magnetization curve of a magnetic liquid, *Technical Physics*. 61(12) (2016) 1835–1837.
28. Zhernovoi A.I., Komlev A.A., D'yachenko S.V., Magnetic characteristics of  $\text{MgFe}_2\text{O}_4$  nanoparticles obtained by glycine–nitrate synthesis, *Technical Physics*. 305–302 (2016) (2)61.
29. Davydov V.V., Velichko E.N., Dudkin V.I., Karseev A.Y., A Nutation Nuclear-Magnetic Teslameter for Measuring Weak Magnetic Fields, *Measurement Techniques*. 57(6) (2014) 684–689.
30. Marusina M.Y., Fedorov A.V., Prokhorovich V.E., Tkacheva N.V., Mayorov A.L., Development of Acoustic Methods of Control of the Stress-Strain State of Threaded Connections, *Measurement Techniques*. 61(3) (2018) 297–302.
31. Ledbetter M., Pustelny S, Budker D., Blanchard J.W., Pines A., Liquid-state nuclear spin comagnetometers, *Physical Review Letters*. 108(24) (2012) 243001.
32. Xu S., Crawford C., Rochester S., Budker D., Pines A., Submillimeter-resolution magnetic resonance imaging at the Earth's magnetic field with an atomic magnetometer, *Physical Review A - Atomic, Molecular, and Optical Physics*. 78(1) (2008) 013404.
33. Sheinker A., Frumkis L., Ginzburg B., et. al. Magnetic Anomaly Detection Using a Three-Axis Magnetometer, *IEEE Transactions on Magnetics*. 45(1) (2009) 160–167.
34. Romer G., Self-generating magnetometer, *Archive Science*. 14 (1961) 273–286.
35. Benoit H., Friver P., Guibe L., Maser with resonant line auto-tuning, *Compt. Rend.*, vol. 246 (1958) 3608–3614.

#### THE AUTHORS

**MYAZIN Nikita**  
myazin.n@list.ru  
ORCID: 0000-0002-9423-9068

**DAVYDOV Vadim**  
davydov\_vadim66@mail.ru  
ORCID: 0000-0001-9530-4805

*Received 07.09.2022. Approved after reviewing 15.09.2022. Accepted 15.09.2022.*

Conference materials

UDC 6

DOI: <https://doi.org/10.18721/JPM.153.274>

## Possibility of using atomic clocks on mercury-199 ions in satellite navigation systems

Wang Ding <sup>1</sup>✉, V. V. Davydov <sup>1, 2, 3</sup>

<sup>1</sup>Peter the Great St. Petersburg Polytechnic University, St. Petersburg, Russia;

<sup>2</sup>Bonch-Bruевич Saint Petersburg State University of Telecommunications, St. Petersburg, Russia;

<sup>3</sup>All-Russian Research Institute of Phytopathology, Moscow Region, Russia

✉ [jssdwang06@mail.ru](mailto:jssdwang06@mail.ru)

**Abstract.** The necessity of developing atomic clocks with high long-term stability for space exploration and improving the operation of satellite systems is substantiated. The photon detection system for the design of atomic clocks on mercury-199 ions for space applications is developed. A comparison is made of various data on the Allan deviation for various models of atomic clocks based on mercury-199 ions. For comparison, we used the results obtained by us and other scientists. The directions for further research are determined.

**Keywords:** satellite navigation system, atomic clock, atomic clock on mercury-199 ions, Paul ion trap, Allan deviation

**Citation:** Wang D., Davydov V.V., Possibility of using atomic clocks on mercury-199 ions in satellite navigation systems, St. Petersburg State Polytechnical University Journal. Physics and Mathematics. 15 (3.2) (2022) 406–411. DOI: <https://doi.org/10.18721/JPM.153.274>

This is an open access article under the CC BY-NC 4.0 license (<https://creativecommons.org/licenses/by-nc/4.0/>)

Материалы конференции

УДК 6

DOI: <https://doi.org/10.18721/JPM.153.274>

## Возможность использования атомных часов на ионах ртути-199 в спутниковых навигационных системах

Ван Дин <sup>1</sup>✉, В. В. Давыдов <sup>1, 2, 3</sup>

<sup>1</sup>Санкт-Петербургский политехнический университет Петра Великого, Санкт-Петербург, Россия;

<sup>2</sup>Санкт-Петербургский государственный университет телекоммуникаций им. проф. М.А. Бонч-Бруевича, Санкт-Петербург, Россия;

<sup>3</sup>Всероссийский научно-исследовательский институт фитопатологии, Московская область, Россия

✉ [jssdwang06@mail.ru](mailto:jssdwang06@mail.ru)

**Аннотация.** Обоснована необходимость разработки атомных часов с высокой долговременной стабильностью для исследования космического пространства и улучшения работы спутниковых систем. Разработана система регистрации фотонов для конструкции атомных часов на ионах ртути-199 для космического применения. Проведено сравнение различных данных по девиации Аллана для различных моделей атомных часов на ионах ртути-199. Для сравнения использовались результаты, полученные нами и другими учеными. Определены направления для дальнейших исследований.

**Ключевые слова:** спутниковая навигационная система, атомные часы, атомные часы на ионах ртути-199, ионная ловушка Паули, девиация Аллана



**Ссылка при цитировании:** Ван Д., Давыдов В. В. Возможность использования атомных часов на ионах ртути-199 в спутниковых навигационных системах // Научно-технические ведомости СПбГПУ. Физико-математические науки. Т. 15. № 3.2. С. 406–411. DOI: <https://doi.org/10.18721/JPM.153.274>

Статья открытого доступа, распространяемая по лицензии CC BY-NC 4.0 (<https://creativecommons.org/licenses/by-nc/4.0/>)

## Introduction

Modern society in the age of advanced technologies cannot function without the exact time [1–7]. Especially in such areas as information transmission and navigation [1, 3, 8–12]. Atomic clocks or quantum frequency standards as high-precision devices provide a time reference for solving problems of information transfer and determination of object coordinates at any time [10–14]. The accuracy of positioning and synchronization of satellite navigation and positioning in outer space depends on the reliable operation of atomic clocks [15–20]. According to the positioning principle of navigation systems, and small deviation in time can lead to huge deviations, for example, if the time shift is 1  $\mu$ s, the positioning accuracy will be shifted by 300 m, so to reduce the positioning deviation caused by time shift, increased requirements are imposed on the accuracy of atomic clocks [15–23].

At present, there are three types of modern space atomic clocks that are relatively well developed and widely used in global navigation satellite systems: cesium atomic clocks, rubidium atomic clocks, and passive hydrogen masers, these atomic clocks use the spectral lines of transitions of hyperfine energy levels of the ground states of atomic systems, to distinguish appropriate excitation signals and receive error signals, and then adjust the output frequency of the crystal oscillator to output a stable and accurate time-frequency signal [20–26]. There are problems when using these standards. In cesium atomic clocks the frequency instability is mainly influenced by the second-order Doppler effect and magnetic field, in rubidium atomic clocks it is mainly influenced by external environments such as optical shifts and buffer gases, and passive hydrogen masers it is mainly influenced by collisions with the vessel walls [16–29]. Therefore, it is necessary to adjust the frequency standards during the communication session with the Earth. With the development of satellite navigation system technology and deep space exploration technology, the characteristics of these space satellite atomic clocks no longer meet the requirements, and atomic clocks with better characteristics are needed as time standards, we have noticed that atomic clocks on mercury-199 ions can be the best solution.

Atomic clocks on mercury-199 ions are microwave atomic clocks, which entered the space after cesium atomic clocks, rubidium atomic clocks, and passive hydrogen masers, compared to them this new generation of atomic clocks uses the Paul ion trap to trap mercury ions, this device effectively reduces the collisions of ions with the wall and reduces interference from the external environment, eliminates the second-order Doppler effect [30–33]. The main problem in the development of atomic clocks on mercury-199 ions is associated with reducing the size and weight of the Paul ion trap, as well as reducing power consumption while maintaining the metrological characteristics that have been obtained for atomic clocks on mercury-199 ions ground application.

## Principles of trapped mercury-199 ions to provide the necessary precision performance

The working principles of capturing mercury ions using the Paul ion traps have been described in detail in several papers [13–15, 19, 30–33]. Mercury-199 ions captured by the Paul ion trap interact with a wavelength  $\lambda = 194$  nm (this can be provided by a laser, but the simplest option is to use a lamp with mercury-202 ions) and a microwave field, whose frequency is formed by the transition with a frequency equal to  $c/\lambda$ . When the frequencies match exactly, the maximum fluorescence signal is formed, which is registered by the photodetector. If the frequencies do not match, an error signal is generated and the frequency of the crystal oscillator is adjusted to the transition frequency. In this case, an important element is the photo counter. We proposed a new design for the photo counter (the block diagram is shown in Fig. 1).

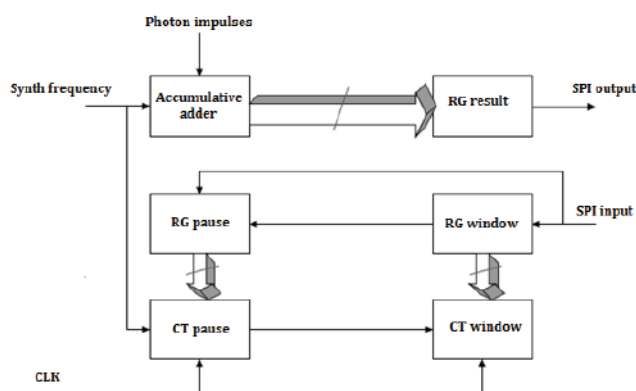


Fig. 1. Block diagram of the photon counting functional block

The input to the counter has three components: the modulation frequency, the signal of the clock frequency and the input data received from the microcontroller, which were sent to the input of counter, which generated a signal with variable counting and pause windows, and the counting of photon pulses at the corresponding time interval.

The sign of the pulse count is positive or negative due to the difference in the half-period of the signal of the frequency synthesizer signal, where the photons were recorded. The count result of the counter characterizes the frequency detuning of the crystal oscillator, on which basis the microcontroller forms a control voltage to change the output frequency of the crystal oscillator.

It is used to count photons by transferring signal parameters through the serial peripheral interface SPI. The data transfer standard of this interface allows the microcontroller and the peripheral to work in full duplex mode (receiving and transmitting information), where the data transfer is performed bit by bit.

On the one hand, using this design allowed to improve the signal-to-noise ratio, which depends on the number of photons and determines the accuracy of frequency tuning. On the other hand, it allowed reducing the weight and size of the frequency standard design.

### Frequency stability analysis of quantum frequency standards

The following experimental setup (Fig. 2) was assembled for experimental studies of the output characteristics of the quantum frequency standard on cesium-133 and rubidium-87 atoms and the laboratory model of the standard on mercury-199 ions.

The signals from the reference and studied quantum frequency standards are fed to the VCH-308A comparator (Fig. 2). In the comparator, the phase-time method is implemented. Information about the signals is converted into time intervals, which are measured using a digital time interval meter. Then the signal is transmitted to a personal computer, where the information is archived and processed.

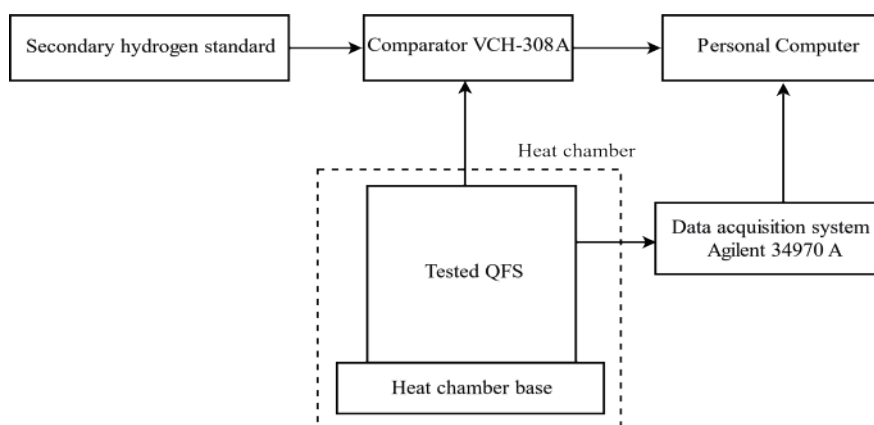


Fig. 2. Block diagram of the installation for the study of metrological characteristics

The measured parameters were controlled and monitored through a control circuit using the Agilent 34970A data acquisition system. The data acquisition system is connected to the same computer as the comparator. Every 100 seconds the frequency of the studied standards was measured. The obtained frequency values were recorded in the computer memory and then used to calculate the parameters that make it possible to estimate the frequency instability.

The Allan variance was chosen as a parameter to estimate the frequency instability and was calculated by using the following equation:

$$\sigma_y^2 = \frac{\sum_{i=1}^n \sigma_{0i}^2}{2(n-1)}, \quad (1)$$

where  $\sigma_{0i} = \frac{f_{i+1} - f_i}{f}$  is the relative  $i$ th variation of the measured value of the frequency measure,

$n$  is the number of variations.

After processing the obtained data, graphs of the dependence of the values of the Allan deviation on time were plotted (Fig. 3). For comparison, Fig. 3 shows the results of the Allan deviation for other types of atomic clocks, which are placed on satellites. These data are obtained by other scientists.

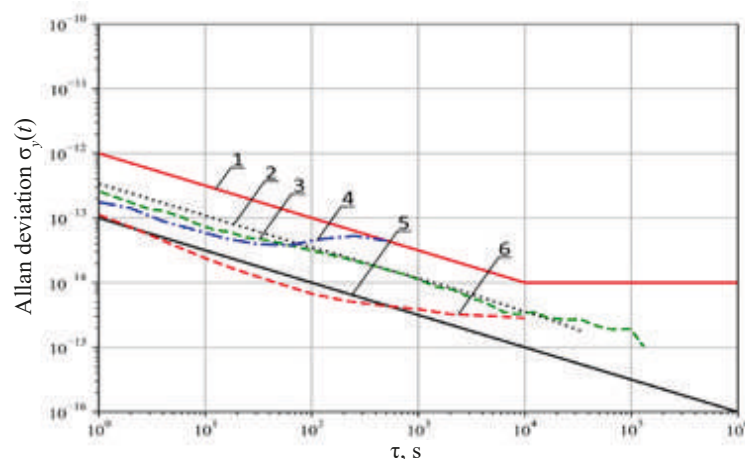


Fig. 3. Allan deviation of different current space atomic clocks and station communication on Earth. Curves 1, 2, 3, 4, 5, and 6 correspond to the following atomic clock: Cs-133; Rb-87;  $^{199}\text{Hg}$  ion – experimental layout; Leonardo RAFS – Galileo; PHM – ship communication station; PHM – communication station on Earth

Analysis of the Allan deviation data for various model atomic clocks shows that the atomic clocks on mercury-199 ions have better characteristics than others in some cases.

### Conclusion

The obtained results showed that the atomic clocks on mercury-199 ions, compared with other types of atomic clocks, have higher stability of the output characteristics. This allows their use in spacecraft during flights to other planets, as well as in situations where the space orbit is already overloaded by other satellites.

The main problem of atomic clocks on mercury-199 ions is related to keeping the necessary number of charged ions in a fixed zone while reducing the size of the trap is now being addressed by groups of other scientists, to expand the possibilities for their use in various space systems.

## REFERENCES

1. **Myazin N. S., Dudkin V. I., Grebenikova N. M., Davydov R. V., Podstrigaev A. S.**, Fiber - optical system for governance and control of work for nuclear power stations of low power, *Lecture Notes in Computer Science*. 11660 (2019) 744–756.
2. **Semenov V. V., Nikiforov N. F., Ermak S. V.**, Calculation of stationary magnetic resonance signal in optically oriented atoms induced by a sequence of radio pulses, *Soviet journal of Communications Technology and Electronics*. 36(4) (1991) 59–63.
3. **Davydov R., Antonov V., and Moroz A.**, Parameter Control System for a Nuclear Power Plant Based on Fiber-Optic Sensors and Communication Lines, In: *IEEE International Conference on Electrical Engineering and Photonics (EExPolytech)*, Saint Petersburg, Russia, 13-15 October 2019. Vol. 8906791 (2019) 295–297.
4. **Makeev S. S., Grevtzeva A. S., Glinushkin A. P., Matorin D. N.**, Possibilities of using spectral analysis in method of nuclear magnetic spectroscopy for condensed media investigation, *Journal of Physics: Conference Series*. 1695(1) (2020) 012112.
5. **Davydov V. V., Kruzhalov S. V., Grebenikova N. M., Smirnov K. J.**, Method for Determining Defects on the Inner Walls of Tubing from the Velocity Distribution of the Flowing Fluid, *Measurement Techniques*. 61(4) (2018) 365–372.
6. **Lukashev N.A., Davydov R.V., Glinushkin A.P., Rud' V.Y.**, Improving characteristics of microwave frequency standard on Hg-199 ions for telecommunication systems *Journal of Physics: Conference Series*. 1326(1) (2019) 012046.
7. **Kuzmin M. S., Rogov S. A.**, On the use of a multi-raster input of one-dimensional signals in two-dimensional optical correlators, *Computer Optics*. 43(3) (2019) 391–396.
8. **Fadeenko V.B., Pchelkin G.A., Rud V.Yu.** Features of the transmission of microwave signals in the range of 8-12 GHz in the maritime radar station over fiber-optic communication line, *Journal of Physics: Conference Series*. 1400(4) (2019) 044010.
9. **Wang D., Davydov V.V., Rud V.Y.**, Prospective directions for the development of microwave frequency standards for satellite navigation systems, *Journal of Physics: Conference Series*. 2086(1) (2021) 012073.
10. **Mihov E.D., Nepomnyashchiy, O.V.**, Selecting informative variables in the identification problem, *Journal of Siberian Federal University: Mathematics and Physics*. 9(4) (2016) 473–480.
11. **Ryzenko I.N., Lutsenko A.E., Varygin O.G., Nepomnyashchiy O.V.**, Carrier compensation mode implementation in satellite communication channels 2019 International Siberian Conference on Control and Communications, *SIBCON 2019 – Proceedings*. 8729665 (2019).
12. **Petrov A. A., Grebenikova N. M.**, Some Directions of Quantum Frequency Standard Modernization for Telecommunication Systems, *Lecture Notes in Computer Science (including subseries Lecture Notes in Artificial Intelligence and Lecture Notes in Bioinformatics)*. 11118 LNCS (2018) 641–648.
13. **Burt E.A., Prestage J.D., Tjoelker R.L., Enzer D.G., Kuang D., Murphy D.W., Robison D.E., Seubert J.M., Wang R.T., Ely T.A.**, Demonstration of a trapped-ion atomic clock in space, *Nature*. 595 (7865) (2021) 43–47.
14. **Batori E., Almat N., Affolderbach C., Mileti G.**, GNSS-grade space atomic frequency standards: Current status and ongoing developments, *Advances in Space Research*. 68 (12) (2021) 4723–4733.
15. **Lukashev N. A., Petrov A.A., Grebenikova N.M.**, Improving performance of quantum frequency standard with laser pumping, *Proceedings of 18th International conference of Laser Optics ICLO-2018 Saint Petersburg, 2018, vol. 8435889*, (2018) 271.
16. **Valov, A.P., Arinushkina, K.G.**, The use of digital data processing to improve the metrological characteristics of the rubidium frequency standard, *Journal of Physics: Conference Series*. 2086(1) (2021) 012070.
17. **Arinushkina K. G., Valov A. P.**, Digital processing of optical signals in the frequency standard based in rubidium atoms - 87, In: *Proceedings of ITNT 2021 - 7th IEEE International Conference on Information Technology and Nanotechnology, 2021 Samara, Russia, 20-24 September 2021. vol. 44026298* (2021) 44–49.
18. **Petrov A. A.**, Improvement frequency stability of caesium atomic clock for satellite communication system, *Lecture Notes in Computer Science (including subseries Lecture Notes in Artificial Intelligence and Lecture Notes in Bioinformatics)*. 9247 (2015) 739–744.
19. **Lukashev N. A., Glinushkin A. P., Rud V. Yu., Lukyantsev V. S.**, Microwave low mass-dimensional frequency standard on Hg- 199 ions, *Journal of Physics: Conference Series*. 1410(1) (2019) 012211.



20. **Jaduszliwer B., Camparo J.**, Past, present and future of atomic clocks for GNSS, GPS Solutions. 25 (1) (2021) 27.
21. **Grevtseva A., Rud V.**, Method of processing velocity increase of measuring results of quantum frequency standard parameters for information transfer velocity increase in satellite communication systems, CEUR Workshop Proceedings. 2667 (2020) 15–18.
22. **Pashev G. P.**, Optimal algorithm for synchronizing the quantum clock timeline, Measurement Techniques. 59(6) (2016) 1005-1012.
23. **Petrov A. A., Vologdin V. A., Zalyotov D. V.**, Dependence of microwave – excitation signal parameters on frequency stability caesium atomic clock, Journal of Physics: Conference Series. 643(1) (2015) 012087.
24. **Petrov A.A., Shabanov V.E., Zalyotov D.V., Bulyanitsa A.L., Shapovalov D.V.**, Modernization of the frequency synthesizer of cesium atomic clock, Proceedings of the 2018 IEEE International Conference on Electrical Engineering and Photonics, EExPolytech - 2018), Saint Petersburg, Vol. 8564389. (2018). 56–61.
25. **Grevtseva A. S., Dmitriev R. A.**, Features of the formation of the frequency of the microwave excitation signal in the quantum frequency standard on rubidium atoms – 87, Journal of Physics: Conference Series. 2086(1) (2021) 012055.
26. **Petrov A. A., Zalyotov D. V., Shabanov V. E., Shapovalov D. V.**, Features of direct digital synthesis applications for microwave excitation signal formation in quantum frequency standard on the atoms of cesium, Journal Physics: Conference Series. 1124(1) (2018) 041004.
27. **Petrov A. A.**, Digital Frequency Synthesizer for <sup>133</sup>Cs-Vapor Atomic Clock, Journal of Communications Technology and Electronics. 62(3) (2017) 289–293.
28. **Petrov A. A., Zalyotov D. V., Shapovalov D. V.**, Peculiarities of Constructing a Scheme for Formation of a Microwave Excitation Signal in a Cesium Atomic Clock, Journal of Communications Technology and Electronics. 66(3) (2021) 295–299.
29. **Petrov A. A.**, New scheme of the microwave signal formation for quantum frequency standard on the atoms of caesium-133 Journal of Physics: Conference Series. 769(1) (2016) 012065.
30. **Hoang T.M., Chung S.K., Le T., Prestage J.D., Yi L., Tjoelker R.L., Yu N., Park S., Park S.-J., Eden J.G., Holland C.**, Demonstration of a Mercury Trapped Ion Clock Prototype, 2021 Joint Conference of the European Frequency and Time Forum and IEEE International Frequency Control Symposium, EFTF/IFCS 2021 - Proceedings (2021).
31. **Hoang T.M., Chung S.K., Le T., Prestage J.D., Yi L., Tjoelker R.I., Yu N.**, Performance of Micro Mercury Trapped Ion Clock, IFCS/EFTF 2019 - Joint Conference of the IEEE International Frequency Control Symposium and European Frequency and Time Forum, Proceedings, (2019) 8856065.
32. **Liu H., Yang Y., He Y., Li H., Yang Z., Chen Y., She L., Li J.**, Progress on linear ion trap mercury-ion frequency standard, Lecture Notes in Electrical Engineering, 245 LNEE, (2013) 335–340.
33. **Lukashev N. A., Rud V. Yu.**, Microwave frequency standard on Hg-199 ions for space stations and vehicles Journal of Physics: Conference Series. 1400(2) (2019) 022050.

#### THE AUTHORS

**WANG Ding**

jssdwang06@mail.ru

ORCID: 0000-0002-3698-6700

**DAVYDOV Vadim**

davydov\_vadim66@mail.ru

ORCID: 0000-0001-9530-4805

*Received 13.07.2022. Approved after reviewing 21.07.2022. Accepted 07.09.2022.*

Conference materials

UDC 53.043

DOI: <https://doi.org/10.18721/JPM.153.275>

## Improvement of the characteristics of the frequency synthesizer in the quantum frequency standard on caesium-133 atoms

E. V. Isupova <sup>1</sup>✉, A. S. Budnikov <sup>1</sup>, S. Y. Shvetsov <sup>2</sup>, V. V. Davydov <sup>1, 3, 4</sup>

<sup>1</sup> Peter the Great St. Petersburg Polytechnic University, St. Petersburg, Russia;

<sup>2</sup> Russian Institute of Radionavigation and Time, St. Petersburg, Russia;

<sup>3</sup> Bonch-Bruевич Saint Petersburg State University of Telecommunications, St. Petersburg, Russia;

<sup>4</sup> All-Russian Research Institute of Phytopathology, Moscow Region, Russia

✉ [isupova.e24@mail.ru](mailto:isupova.e24@mail.ru)

**Abstract.** A new circuit of a frequency synthesizer is presented, which is an important functional node in the quantum frequency standard on cesium atoms. The advantages and disadvantages of the new signal synthesis method are considered in detail. By increasing the bit depth of the accumulating adder, it was possible to reduce the step of tuning the output frequency by several orders of magnitude. This method meets all the requirements for the parameters of frequency synthesizers.

**Keywords:** quantum frequency standard, frequency synthesizer, direct digital synthesis, accumulating adder, frequency tuning, cesium atomic clocks

**Citation:** Isupova E. V., Budnikov A. S., Shvetsov S. Y., Davydov V. V., Improvement of the characteristics of the frequency synthesizer in the quantum frequency standard on caesium-133 atoms, St. Petersburg State Polytechnical University Journal. Physics and Mathematics. 15 (3.2) (2022) 412–418. DOI: <https://doi.org/10.18721/JPM.153.275>

This is an open access article under the CC BY-NC 4.0 license (<https://creativecommons.org/licenses/by-nc/4.0/>)

Материалы конференции

УДК 53.043

DOI: <https://doi.org/10.18721/JPM.153.275>

## Улучшение метрологических характеристик синтезатора частоты для квантового стандарта частоты на атомах цезия-133

Е. В. Исупова <sup>1</sup>✉, А. С. Будников <sup>1</sup>, С. Ю. Швецов <sup>2</sup>, В. В. Давыдов <sup>1, 3, 4</sup>

<sup>1</sup> Санкт-Петербургский Политехнический университет Петра Великого  
Санкт-Петербург, Россия;

<sup>2</sup> Российский институт навигации и времени, Санкт-Петербург, Россия;

<sup>3</sup> Санкт-Петербургский государственный университет телекоммуникаций  
им. проф. М.А. Бонч-Бруевича, Санкт-Петербург, Россия;

<sup>4</sup> Всероссийский научно-исследовательский институт фитопатологии, Московская область, Россия

✉ [isupova.e24@mail.ru](mailto:isupova.e24@mail.ru)

**Аннотация.** Представлена новая схема синтезатора частот, который является важным функциональным узлом в квантовом стандарте частоты на атомах цезия. Подробно рассмотрены достоинства и недостатки нового метода синтеза сигнала. С помощью увеличения разрядности накапливающего сумматора удалось добиться уменьшения шага перестройки выходной частоты на несколько порядков. Сделан вывод о том, что данный метод удовлетворяет всем требованиям, предъявляемым к параметрам синтезаторов частоты.

**Ключевые слова:** квантовый стандарт частоты, синтезатор частоты, прямой цифровой синтез, накапливающий сумматор, перестройка частоты, цезиевые атомные часы

**Ссылка при цитировании:** Исупова Е. В., Будников А. С., Швецов С. Ю., Давыдов В. В. Улучшение метрологических характеристик синтезатора частоты для квантового стандарта частоты на атомах цезия-133 // Научно-технические ведомости СПбГПУ. Физико-математические науки. Т. 15. № 3.2. С. 412–418. DOI: <https://doi.org/10.18721/JPM.153.275>

Статья открытого доступа, распространяемая по лицензии CC BY-NC 4.0 (<https://creativecommons.org/licenses/by-nc/4.0/>)

## Introduction

The frequency can be determined with the greatest precision among all physical quantities [1–8]. The development of frequency measurement methods has increased the accuracy of measuring quantities that can be determined through it [1, 3, 4, 7–14]. The international system of units, using physical laws and fundamental constants, defines other units of measure in terms of seconds. Frequency standards are often used as reference standards [1, 3, 4, 15–22]. The frequency standard is a source of electromagnetic pulses that generates the desired frequency signal with a given accuracy and provides the consumer with frequency references from a wide range. The 1 second time standard is defined in world science as the time interval during which 9,192,631,770 periods of electromagnetic radiation occur during the transition between two hyperfine levels of the fundamental state of the  $^{133}\text{Cs}$  atom. That is why the  $^{133}\text{Cs}$  frequency standard was used as the primary reference on the basis of which the international time scale is based [1, 15, 22–26].

The first frequency standard for  $^{133}\text{Cs}$  was developed in the mid-20th century. It is this standard which, unlike others, has a precise unit of time and a uniform time scale. Since then, the quantum frequency standard on cesium atoms has been modified due to the development of electronics, materials, and more. The diagram of quantum frequency standard on  $^{133}\text{Cs}$  is given in Fig. 1.

Quantum frequency standards are divided into two types. Active quantum standards emit

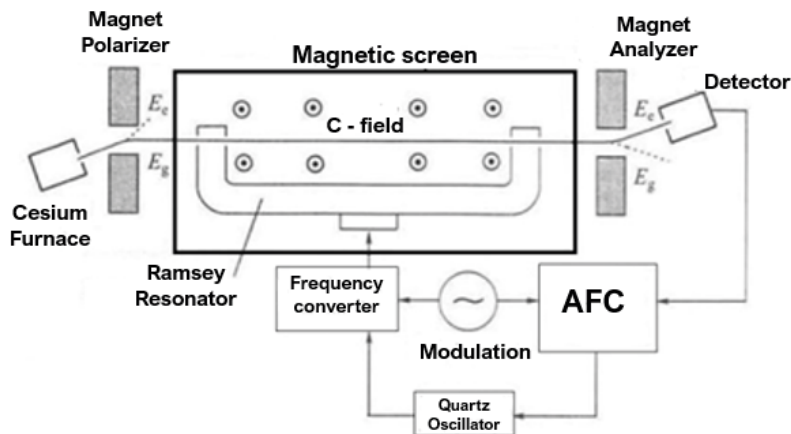


Fig. 1. Diagram of cesium atomic clock

electromagnetic waves, the frequency of which is determined by the spectral line of matter. Such devices are also called quantum generators. In passive quantum standards, the measured oscillation frequency of the external generator is compared to the spectral line frequency. Cesium atomic clocks are passive quantum frequency standards.

One of the important functional nodes of the quantum frequency standard is the frequency synthesizer [26–33]. The synthesizer is a source of stable fluctuations in devices that require tuning to different frequencies in a wide range and high stability of the selected frequency. It should be noted that the accuracy of the output signal generated by the synthesizer affects the

accuracy of the transition resonance frequency and other characteristics of the quantum standard output signal. Therefore, in the context of increasing requirements to the frequency standard, this issue requires increased attention. One of the solutions is presented in our work.

### Materials and Methods

The most common methods to date are the following methods of frequency synthesis:

**Direct analog synthesis.** This method is called so because it does not have a stage of error correction. Because of this, the accuracy of synthesizer output signal synthesis depends on the quality of input clock. Several support generators are used to quickly change the frequency of the device. The need to synthesize a signal from a wide range of frequencies forces designers to use a large number of support generators. Direct synthesis devices are cumbersome and expensive.

**Indirect synthesis.** This method is based on phase automatic frequency adjustment. The output frequency is formed by an additional generator, which is covered by a loop of phase automatic frequency adjustment. The presence of a phase detector in the synthesizer design causes phase noises. In order to reduce the frequency rearrangement step, it is necessary to work at a low frequency of comparison, which forces to reduce the frequency of the loop filter cutting. It also negatively affects the phase noise of the device. The design of such a frequency synthesizer does not allow for a high rate of frequency adjustment.

**Direct digital synthesis.** This is a relatively new method of frequency synthesis, which appeared in the early 1970s. All described synthesis methods have been available to developers for quite a long time, but only recently has the method of direct digital synthesis been given close attention. This method is special because the generated signal is synthesized with the inherent precision of digital systems.

**Hybrid synthesis.** A synthesis method in which a combination of several previously described methods takes place.

The new design of the digital frequency synthesizer uses the above method of direct digital synthesis. This is due to some advantages compared to other frequency synthesis methods. Digital systems synthesize a signal with precise specified characteristics. The parameters of the output signal, such as frequency, amplitude and phase, are precisely known and continuously controlled by the system. High frequency and phase resolution, fast switching to another frequency and high rate of adjustment in the absence of emissions or other distortions that may occur due to timing, a wide range of generated frequencies are also advantages of this method.

The synthesizer circuit based on this method includes only one unstable element, the digital-analog converter. This instability is common to all analog circuits.

Modern synthesizers use an updated version of direct digital synthesis. For this reason, the ROM address counter has been replaced by an accumulating adder. The accumulating adder is a case, at each stroke of which the device reboots. Also, for each stroke of the device, there is a summation of the value obtained earlier, and the constant - summing with accumulation. The resulting synthesizer diagram is shown in Fig. 2.

The value contained within the register is constantly increasing over time, the value of the

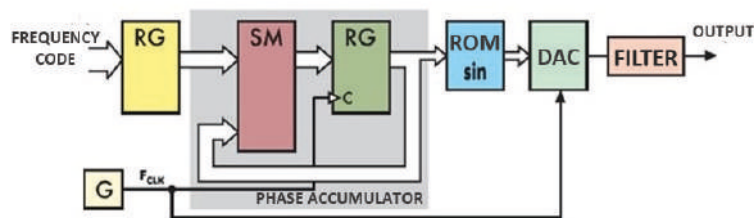


Fig. 2. Digital synthesizer circuit

additive depends on the constant term. At the output of the accumulating adder a code is obtained, which corresponds to the phase of the signal at the current time. The addressable, which is used in the operation of the device, corresponds to the growth of the signal phase in one cycle of operation. The amount of frequency of the synthesized signal is directly proportional to the rate of change of the phase of the signal in time. Thus, the phase increase value corresponds

to the binary frequency code at the register output.

So the accumulating adder, also called the phase battery, synthesizes a sequence of binary codes from the linearly changing phase of the signal. The phase battery overflow frequency corresponds to the output signal frequency. The output frequency is determined by the formula:

$$F_{out} = \frac{M \cdot F_{clk}}{2^N},$$

where  $F_{out}$  is the output frequency,  $F_{clk}$  is the clock speed,  $M$  is the binary frequency code,  $N$  is the discharge of the accumulating adder.

The frequency represented as a binary code determines the speed at which the signal phase will change. The increasing phase is converted into output signal values, from which the DAC generates a signal of sinusoidal form, consisting of 'steps'. The lower frequency filter smooths the 'steps', and thus the sinusoidal output signal is formed (Fig. 3).

The signal at the output of the device is created from separate counts. Not always in the sine

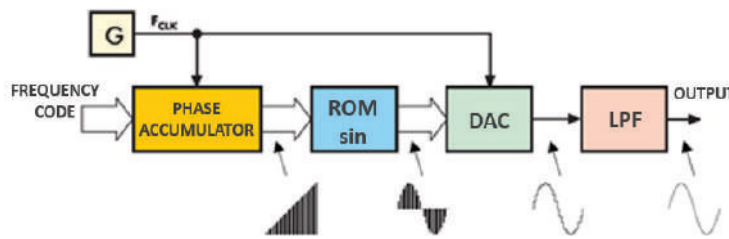


Fig. 3. Principle of the synthesizer

period is placed an integer number of counts. More often than not, the periods are different, differing from previous and subsequent periods. In some cases, it is possible that the location of the readings may be repeated with a certain period, but this period of repetition is very different throughout the signal. This period is determined by a number of factors, such as frequency code, adder discharge and phase code bit. Thus, a sinusoidal signal can be formed from a sequence of readings.

Despite the fact that noise is reduced when the frequency is divided, the main cause of the phase noise in the scheme is the presence of a source of clock signal. In theory, the phase noise of the clock signal is greater than that of the output signal. In fact, noise reduction is limited to the noise threshold of the circuits used, and the phase output reduction is limited to the amount of clock noise. Residual phase noise is the amount of noise below which the output noise cannot be lowered.

### Results and Discussion

In the course of the study, modeling was carried out in a specialized development tool Quartus II, which is focused on the work with FPGA firm Altera. A program code was written to implement direct digital frequency synthesis in VHDL. The data was loaded from the microcontroller using the peripheral interface SPI (Serial Peripheral Interface). Fig. 4 presents the results of modeling.

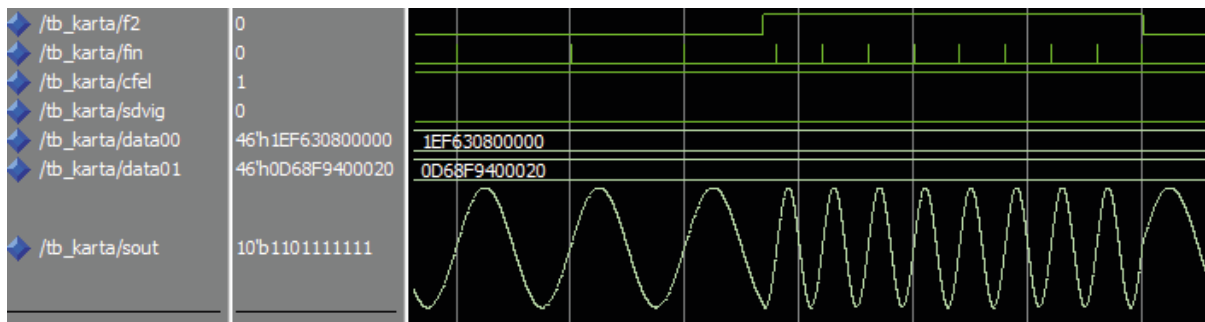


Fig. 4. Simulation result

An earlier version of the synthesizer used a 32-bit phase battery. Increasing the number of discharges of the device to 40 allowed to lower the value of the step of frequency adjustment. The scheme created when operating at 15 MHz has an output frequency change step:

$$\Delta F_{out} = \frac{F_{clk}}{2^N} = \frac{15 \cdot 10^6}{2^{40}} = 1.36 \cdot 10^{-5} \text{ Hz.}$$

When operating at 25 MHz, the rearrangement step will be:

$$\Delta F_{out} = \frac{F_{clk}}{2^N} = \frac{25 \cdot 10^6}{2^{40}} = 2.27 \cdot 10^{-5} \text{ Hz,}$$

where  $\Delta F_{out}$  is the step of restructuring the output frequency,  $F_{clk}$  is the clock speed,  $N$  is the discharge of the accumulating adder.

The resulting value of the synthesizer  $\Delta F_{out}$  frequency restructuring step is an order of magnitude lower than the value  $\Delta F_{out}$  used in previous frequency synthesizer designs.

### Conclusion

The results obtained by tuning the frequency of the synthesizer output signal made it possible to improve several times the accuracy of the formation of the frequency of the microwave excitation signal corresponding to the resonant transition in the atomic structure.

The parameters of the developed frequency synthesizer based on the DDS method (direct digital synthesis) meet most of the new technical requirements for signals in the quantum frequency standard. In addition, most of the parameters of the developed frequency synthesizer are controlled by the program.

The newly developed design of the frequency synthesizer has reduced energy requirements, which is essential for subsequent use.

This frequency synthesizer design can be successfully used in other types of quantum frequency standards (e.g., rubidium-87 atoms, etc.).

### REFERENCES

1. **Riehle F.**, Frequency standard. Basic and applications, WILEY-VCH Verlag GmbH Co. KGaA: New-York, 2008.
2. **Wang D., Rud V.Y.**, Prospective directions for the development of microwave frequency standards for satellite navigation systems, Journal of Physics: Conference Series. 2086(1) (2021) 012073.
3. **Mihov E.D., Nepomnyashchiy, O.V.**, Selecting informative variables in the identification problem, Journal of Siberian Federal University: Mathematics and Physics. 9(4) (2016) 473–480.
4. **Ryzenko I.N., Lutsenko A.E., Varygin O.G., Nepomnyashchiy O.V.**, Carrier compensation mode implementation in satellite communication channels 2019 International Siberian Conference on Control and Communications, SIBCON 2019 – Proceedings. 8729665 (2019).
5. **Almat N., Pellaton M., Moreno W.**, Rb vapor-cell clock demonstration with a frequency-doubled telecom laser, Appl. Opt. 57 (2008) 4707.
6. **Bandi T., Affolderbach C., Calosso C.E.**, High-performance laser-pumped rubidium frequency standard for satellite navigation, Electron. Lett. 47 (2001) 698–699.
7. **Myazin N. S., Dudkin V. I., Grebenikova N. M., Davydov R. V., Podstrigaev A. S.**, Fiber - optical system for governance and control of work for nuclear power stations of low power, Lecture Notes in Computer Science. 11660 (2019) 744–756.
8. **Semenov V. V., Nikiforov N. F., Ermak S. V.**, Calculation of stationary magnetic resonance signal in optically oriented atoms induced by a sequence of radio pulses, Soviet journal of Communications Technology and Electronics. 36(4) (1991) 59–63.
9. **Davydov R., Antonov V., and Moroz A.**, Parameter Control System for a Nuclear Power Plant Based on Fiber-Optic Sensors and Communication Lines, In: IEEE International Conference on Electrical Engineering and Photonics (EExPolytech), Saint Petersburg, Russia, 13-15 October 2019. Vol. 8906791 (2019) 295–297.



10. **Makeev S. S., Grevtzeva A. S., Glinushkin A. P., Matorin D. N.**, Possibilities of using spectral analysis in method of nuclear magnetic spectroscopy for condensed media investigation, *Journal of Physics: Conference Series*. 1695(1) (2020) 012112.
11. **Davydov V. V., Kruzhalov S. V., Grebenikova N. M., Smirnov K. J.**, Method for Determining Defects on the Inner Walls of Tubing from the Velocity Distribution of the Flowing Fluid, *Measurement Techniques*. 61(4) (2018) 365–372.
12. **Davydov V. V.**, Determination of the Composition and Concentrations of the Components of Mixtures of Hydrocarbon Media in the Course of its Express Analysis, *Measurement Techniques*. 62(2) (2020) 1090–1098.
13. **Myazin N.S., Dudkin V.I., Grebenikova N.M.**, On the Possibility of Express Recording of Nuclear Magnetic Resonance Spectra of Liquid Media in Weak Fields, *Technical Physics*. 63(12) (2018) 1845–1850.
14. **Kuzmin M. S., Rogov S. A.**, On the use of a multi-raster input of one-dimensional signals in two-dimensional optical correlators, *Computer Optics*. 43(3) (2019) 391–396.
15. **Petrov A. A., Shabanov V. E., Zalyotov D. V., Bulyanitsa A. L., Shapovalov D. V.**, Modernization of the frequency synthesizer of cesium atomic clock, *IEEE International Conference on Electrical Engineering and Photonics, EExPolytech, Saint Petersburg*. 8564389 (2018) 52–55.
16. **Lukashev N.A., Davydov R.V., Glinushkin A.P., Rud' V.Y.**, Improving characteristics of microwave frequency standard on Hg-199 ions for telecommunication systems *Journal of Physics: Conference Series*. 1326(1) (2019) 012046.
17. **Valov, A.P., Arinushkina, K.G., Davydov, V.V.**, The use of digital data processing to improve the metrological characteristics of the rubidium frequency standard *Journal of Physics: Conference Series*. 2086(1) (2021) 012070.
18. **Lukashev N.A., Moroz A.V.**, Compact microwave frequency standard on Hg-199 ions for navigation systems, *Journal of Physics: Conference Series*. 1236(1) (2019) 012068.
19. **Tarasov A. D., Milder O. B.**, Gradation trajectories as an analog of gradation curves in the metric lab space discrete approach, *Computer Optics*. 43(1) (2018) 104–110.
20. **Lukashev N. A., Petrov A.A., Grebenikova N.M.**, Improving performance of quantum frequency standard with laser pumping, *Proceedings of 18th International conference of Laser Optics ICLO-2018, Saint Petersburg*. 8435889 (2018) 271.
21. **Arinushkina K. G., Valov A. P., Davydov V. V.**, Digital processing of optical signals in the frequency standard based in rubidium atoms - 87, In: *Proceedings of ITNT 2021 - 7th IEEE International Conference on Information Technology and Nanotechnology, 2021 Samara, Russia, 20-24 September 2021*. Vol. 44026298 (2021) 44–49.
22. **Petrov A. A.**, Improvement frequency stability of caesium atomic clock for satellite communication system, *Lecture Notes in Computer Science (including subseries Lecture Notes in Artificial Intelligence and Lecture Notes in Bioinformatics)*. 9247 (2015) 739–744.
23. **Grevtseva A., Rud V.**, Method of processing velocity increase of measuring results of quantum frequency standard parameters for information transfer velocity increase in satellite communication systems *CEUR Workshop Proceedings*. 2667 (2020) 15–18.
24. **Petrov A. A., Vologdin V. A., Zalyotov D. V.**, Dependence of microwave – excitation signal parameters on frequency stability caesium atomic clock, *Journal of Physics: Conference Series*. 643(1) (2015) 012087.
25. **Pashev G. P.**, Optimal algorithm for synchronizing the quantum clock timeline, *Measurement Techniques*. 59(6) (2016) 1005–1012.
26. **Petrov A. A., Zalyotov D. V., Shabanov V. E., Shapovalov D. V.**, Features of direct digital synthesis applications for microwave excitation signal formation in quantum frequency standard on the atoms of cesium, *Journal Physics: Conference Series*. 1124(1) (2018) 041004.
27. **Lukashev N. A., Glinushkin A. P., Rud V. Yu., Lukyantsev V. S.**, Microwave low mass-dimensional frequency standard on Hg-199 ions, *Journal of Physics: Conference Series*. 1410(1) (2019) 012211.
28. **Petrov A. A., Grebenikova N. M.**, Some Directions of Quantum Frequency Standard Modernization for Telecommunication Systems, *Lecture Notes in Computer Science (including subseries Lecture Notes in Artificial Intelligence and Lecture Notes in Bioinformatics)*. 11118 LNCS (2018) 641–648.
29. **Grevtseva A. S., Dmitriev R. A.**, Features of the formation of the frequency of the microwave excitation signal in the quantum frequency standard on rubidium atoms – 87, *Journal of Physics: Conference Series*. 2086(1) (2021) 012055.

30. **Petrov A. A.**, Digital Frequency Synthesizer for  $^{133}\text{Cs}$ -Vapor Atomic Clock, *Journal of Communications Technology and Electronics*. 62(3) (2017) 289–293.

31. **Lukashev N. A., Rud V. Yu.**, Microwave frequency standard on Hg-199 ions for space stations and vehicles, *Journal of Physics: Conference Series*. 1400(2) (2019) 022050.

32. **Petrov A. A., Zaletov D. V., Shapovalov D. V.**, Peculiarities of Constructing a Scheme for Formation of a Microwave Excitation Signal in a Cesium Atomic Clock, *Journal of Communications Technology and Electronics*. 66(3) (2021) 295–299.

33. **Petrov A. A.**, New scheme of the microwave signal formation for quantum frequency standard on the atoms of caesium-133, *Journal of Physics: Conference Series*. 769(1) (2016) 012065.

#### THE AUTHORS

**ISUPOVA Ekaterina**

isupova.e24@mail.ru

ORCID: 0000-0002-0963-5497

**SHVETSOV Sergey**

shvetsov0000@gmail.com

ORCID: 0000-0001-6849-1481

**BUDNIKOV Andrey**

budnikov.as@edu.spbstu.ru

ORCID: 0000-0002-4096-4598

**DAVYDOV Vadim**

davydov\_vadim66@mail.ru

ORCID: 0000-0001-9530-4805

*Received 29.07.2022. Approved after reviewing 01.08.2022. Accepted 17.08.2022.*

Journal

**ST. PETERSBURG STATE POLYTECHNICAL UNIVERSITY  
JOURNAL: PHYSICS AND MATHEMATICS**

**Vol. 15, No. 3.2, 2022**

Founder and publisher: Peter the Great St. Petersburg Polytechnic University

The journal is registered with the Federal Service for Supervision of Communications,  
Information Technology and Mass Media (Roskomnadzor).  
Certificate ПИИ ФС77-51457 issued 19.10.2012.

Editorial Office

Dr. Prof. *V.K. Ivanov*, Editor-in-Chief  
Dr. Prof. *A.E. Fotiadi*, Deputy Editor-in-Chief  
Dr. Prof. *V.V. Dubov*  
Dr. Prof. *P.A. Karaseov*  
Dr. Assoc. Prof. *V.M. Kapralova*  
*A.S. Kolgatina*, translator  
*N.A. Bushmanova*, editorial manager

*All papers presented are final author versions  
Peer review is under responsibility of the Organizing Committee*

Phone 8 (812) 294-22-85

Website <https://physmath.spbstu.ru/>

E-mail: [physics@spbstu.ru](mailto:physics@spbstu.ru)

Typesetting by *N.A. Bushmanova, A.S. Kolgatina*

---

Published 30.10.2022. Format 60x84/8. Digital print.

Printer's sheets

Print circulation 1000. Order ID .

---